EMBRITTLEMENT MECHANISMS OF

NICKEL-BASE ALLOYS IN WATER

by

IL SOON HWANG

B.S., Seoul National University, Seoul, Korea
(1975)

M.S., Korea Advanced Institute of Science, Seoul, Korea
(1977)

Submitted to the Department of Nuclear Engineering
in Partial Fulfillment of
the Requirements of the Degree of
Doctor of Philosophy in Nuclear Engineering

at the

Massachusetts Institute of Technology

May 1987

Signature of Author _____
Department of Nuclear Engineering
May 15, 1987

Certified by _____
R. B. Ballinger
Associate Professor of Nuclear engineering
Thesis Advisor

_____
R. M. Latanision
Professor of Materials Science and Engineering
Thesis Reader

Accepted by _____
A. F. Henry
Chairman, Departmental Committee

EMBRITTLEMENT MECHANISMS OF

NICKEL-BASE ALLOYS IN WATER

by

IL SOON HWANG

Submitted to the Department of Nuclear Engineering
on May 15, 1987 in partial fulfillment of the
requirements for the Degree of Doctor of Philosophy in
Nuclear Engineering

ABSTRACT

Premature intergranular cracking of nickel-base alloys in Light Water Reactor (LWR) environments has resulted in significant economic impact and safety concern for operating nuclear power plants. A detailed understanding of the embrittlement mechanisms is key to accurate remedial actions and successful alloy development. For alloys 600, X-750 and 718, the fundamental embrittlement mechanisms were determined from the results of grain boundary characterization, galvanic corrosion studies, straining electrode tensile and fatigue tests as well as slow strain rate tests.

Carbon-solution annealing of alloys 600 and X-750 produces extensive intergranular carbides with little intragranular carbides in coarsened grains. Annealing at lower temperatures show opposite microstructure. Intergranular $\gamma'(Ni_3Al)$ and Laves phase (Fe_2Ti) evolve by aging of alloy X-750 at 885 C and by low temperature annealing of alloy 718, respectively. Phosphorus degregation to alloy 600 grain boundaries follows a McLean-type equilibrium relation with a free energy of 58 ± 2 kJ/mole. In alloy X-750, phosphorus segregation below 885 C is much lower than equilibrium level. In both alloys negative correlations are observed between phosphorus and boron levels suggesting a site competition behavior.

Anodic current density of intergranular γ' in galvanic couple with surrounding matrix has an initial value of 0.5 mA/cm^2 and shows $1/\sqrt{t}$ passivation kinetics at 93 C. By cathodic charging at this current density in 0.05M sodium sulphate solution, precracked fatigue specimens in two-step aged X-750 condition exhibit accelerated intergranular crack growth whereas both anodic charging and free corrosion state as well as air environment show a slow crack growth. Discontinuous crack growth and increased crack tip plastic zone support dislocation-assisted hydrogen transport. Galvanically induced hydrogen embrittlement mechanism is proposed as responsible for the accelerated cracking at 93 C. Hydrogen generation reaction is suggested to control crack growth rate.

In high temperature water, localized galvanic corrosion is shown to be significant based on measured corrosion potentials of chromium-depleted

chemistries and γ'. Two distinct embrittlement patterns are observed in slow strain rate test results with various conditions of three alloys in high temperature water with 0.18 MPa hydrogen overpressure. Alloy 600 specimens containing little intergranular carbides exhibit multiple crack initiation after 350 hours with a growth rate of $1x10^{-7}$ mm/sec at a strain rate of $2x10^{-7}$ sec^{-1} and 342±2 C while two-step aged X-750 initiated isolated cracks after only 44 hours with a growth rate of $7x10^{-6}$ mm/sec at a strain rate of $5x10^{-7}$ sec. and 350 C. High temperature annealed and aged X-750 and all conditions of alloy 718 are not embrittled. Analysis of the results and comparison with data in literatures led to a conclusion that both hydrogen embrittlement and film rupture mechanisms are viable at high temperature. With active grain boundary chemistries such as γ', hydrogen embrittlement is suggested to dominate due to localized hydrogen discharge in the acidified crack tip. Slow strain rates allow time for diffusion while minimizing the strain-assisted recombination of hydrogen. Effect of recombination poison is hence significant. With passive grain boundary chemistries such as unsensitized grain boundaries, hydrogen discharge is unlikely due to neutral pH in crack tip and hence film rupture mechnism is expected to dominate. More protective and thinner film structures can maintain sharp crack tip and support preferential intergranular ruptures. Results with materials containing extensive intergranular carbides support a postulation of crack tip blunting and stress relief by carbide-assisted dislocation injection at grain boundaries.

By integrating the mechanistic understandings general principles are suggested for alloy developments. These state 1) active intermetallic precipitates be avoided at grain boundaries, 2) phosphorus segregation be reduced if hydrogen embrittlement persists, 3) extensive intergranular carbide precipitation be developed, and 4) film passivity and structure be optimized.

Thesis Supervisor: Dr. Ronald G. Ballinger
Title: Associate Professor of Nuclear Engineering and Materials Science and Engineering

ACKNOWLEDGEMENTS

This work has been generously funded by the Electric Power Research Institute, Palo Alto, California. In addition their guidance through project managers, Drs. McIlree and Nelson,is deeply appreciated.

My thesis advisor, professor Ballinger, contributed enormously to this thesis from initial program formulation to final conclusions. I express my deep gratitute to him for continual stimulation and close supervision.

I would like to appreciate professors Latanision, Pelloux and Meyer. Professor Latanision was there to guide me whenever I was lost. Professor Pelloux constantly encouraged me to overcome frustrating obstacles throughout this thesis work. Professor Meyer introduced me to this exciting field when I just arrived here. I also have benefited from occasional discussion with honourable professor Uhlig.

This multidisciplinary task was made posiible by friendly cooperation of M.I.T. staffs. Advice and assistance by members of H.H. Uhilg Corrosion Laboratory, Fatigue Research Laboratory, Surface Analytical Laboratory, Electronmicroscopy Laboratory, and Nuclear Reactor Laboratory were instrumental. Skillful word processings by Don Keller, Matthew Friedman and Mrs. Siu are greatly acknowledged.

During experimental works nothing is more demanding than a nice fiend. I was fortunate to have wonderful men in the laboratory. It is a pleasure to remember John Prybylowski, Keizo Hosoya, Glenn Romanoski, Joe Goss, Jerry Martin, Marti Morra, Jun Feng, and more friends. I also would like to appreciate Korean friends in this department for their frequent help and encouragement.

I express my deep gratitute to my family members whose encouragement and partial financial support were essential to my study at M.I.T.. Finally, I dedicate this thesis with love to my wife, Hae-young. She stayed awake as many nights as I did to draw graphs and edit texts. Without her understanding and assistance, completion of this thesis were impossible.

TABLE OF CONTENTS

LIST OF FIGURES

LIST OF TABLES

Chapter 1

INTRODUCTION

1.1 IMPORTANCE OF MECHANISTIC KNOWLEDGE

Nickel-base alloys have been extensively used in light water reactor (LWR) environments due to their good resistance to general corrosion and mechanical strength. The nickel-base alloys used most extensively for LWR applications are alloy 600, alloy X-750 and alloy 718. Their typical compositions and mechanical properties are summarized in Table 1.1.

Alloy 600 is a solid solution strengthened material of which tensile properties are is determined by carbon content and grain size. Compared with austenitic stainless steels, alloy 600 has superior SCC resistance in hot chloride emvironments [1], a higher yield strength and somewhat higher thermal conductivity. Hence, alloy 600 has been historically used for various pressure boundary components such as steam generator tubings in pressurized water reactor (PWR) power plants and nozzle safe-ends in boiling water reactor (BWR) pressure vessels. Despite its superior performance in chloride environments, these components have suffered from various modes of corrosion related failures in the water environment including intergranular attack (IGA) and intergranular stress corrosion cracking (IGSCC).

Alloys X-750 and 718 are high strength alloys which are hardened by intermetallic precipitates such as $Ni_3Al(\gamma')$ and $Ni_3Nb(\gamma'')$, respectively. Depending on heat treatment, these alloys can be produced with a wide range of mechanical properties. As they were originally developed for aircraft turbine applications, thermomechanical processes were optimized for creep-rupture resistance at elevated temperature in gas turbine environments. These alloys were later specified, as shown

Table 1.1

Typical Compositions and Mechanical Properties of Alloys 600, X-750 and 718 for LWR Applications (wt %)

Element	Alloy 600	Alloy X-750	Alloy 718
Ni	75	73	53
Cr	15	15	19
Fe	8	7	18
Ti	-	2.5	0.9
Al	-	0.7	0.5
Nb+Ta	-	1.0	5.1
Mo	-	-	3.0
C	<0.05	0.04	0.04
Mechanical Properties			
0.2% Y.S(MPa)	400	800 - 2000	1400 - 2000
U.T.S.(MPa)	700	1200 - 2000	1400 - 2000
Elongation(%)	30 - 50	1 - 25	16 - 18

in Table 1.2, for high strength fasteners for LWR internals such as bolts, springs, beams and pins. A significant number of failures have been identified as corrosion-related embrittlement which can be attributed to unfavorable microstructures in the water environment.

Corrosion-related failures and subsequent forced outages have had a growing impact on plant availability [2, 3] and often develops serious safety concerns. Primary side stress corrosion crack of alloy 600 steam generator tubing, in one case, caused three forced shutdowns of a plant during the first operation year. Cracking in the primary pressure boundaries such as safe-ends and steam generator tubing may result in safety-related problems. Economic impact of failures of high strength fasteners has been mimimized by effective inspections and replacements during scheduled outages.

An analysis of failure experences and remedial actions taken which are presented in the next section, shows that a number of different degradation phenomena have been involved in the nickel-base alloy/water system. There have been cases of both correct and incorrect remedies. The difference can be traced to one key factor; sound fundamental knowledge of the embrittlement mechanism. This mechanistic knowledge is also essential to various important engineering judgements such as life prediction and failure analysis.

The goal of this thesis is the identification of embrittlement mechanisms in nickel-base alloys in water environments. Microstructural, electrochemical and fracture mechanical experiments were performed on alloys 600, X-750 and 718 in their representative conditions of thermomechanical processes. The results are integrated in a mechanistic framework. As practical applications of the mechanistic knowledge, a principle for metallugical optimization is to be presented.

1.2 FAILURE EXPERIENCE WITH NICKEL-BASE ALLOYS IN LIGHT WATER REACTORS

Alloy 600 - Steam Generator Tubing

Table 1.2

Typical Heat Treatments used for Precipitation-hardened Alloys X-750 and 718

Alloy X-750

A - Hot-Finished(HF) + 885C x 24hr/Air-Cooled (AC) + 704C x 20hr/AC

B - HF + 982C x 1hr/AC + 732C x 8hr/Furnace-Cooled(FC) to 620C x 8hr/AC

C - Cold-Rolled(CR) + Annealed + 704C x 20hr/AC

D - Annealed(≃1065C) + 15-20% Cold Work (CW) + 732 x 16hr/AC (AMS 5698)

E - Annealed(≃1065C) + 30-65%CW + 650C x 4hr/AC (AMS 5699)

F - HF + 1150C x 2hr/AC + 843C x 24hr/AC + 704C x 20hr/AC

Alloy 718

G - HF + 1065C x 1hr/AC + 760C x 10hr/FC to 650C x 20hr/AC

H - CR + Annealed + 718C x 8hr/FC to 620C x 18hr total/AC

I - Annealed + 15-30%CW + 718C x 8hr/FC to 620C x 18hr total/AC

Several forms of degradation have been observed in alloy 600 steam generator tubing. Recently, Green [4] and Green and Paine [5] summarized the steam generator problems by type of failure which included: 1) tube wastage, 2) denting, 3) stress corrosion cracking (SCC), 4) intergranular attack (IGA) and 5) mechanical damage. Out of 65 units with more than five years of operation as of 1985 only one unit was reported to have been without problems. The extent and multiplicity of failure types are indicative of inadequate effort in design and perfomance verification early in the nuclear age when emphasis was on economic considerations in order to compete with conventional energy sources. Existing small heat exhangers were scaled up without laboratory evaluations on the effects of increase temperature, heat flux and steam flow. Secondary system water chemistry standards and operating practices were adopted from low pressure fossile plant experiences [5]. It appears that chloride induced transgranular stress corrosion cracking (TGSCC) was the greatest concern for seawater plants. For this reason sodium phosphate chemistry was employed in the first system. Due to uncontrolled sodium-to-phosphate ratio the formation of free caustic resulted in a significant number of SCC events initiated on the secondary side. The sodium-to-phosphate ratio was thus controlled to 2.0 and caustic SCC was appreciably reduced. However coodinated phosphate chemistry increased general corrosion rate to cause slow consumption or wastage of steam generator tubing. The phenomenon was apparently attributed to sodium phosphate precipitation. To correct this problem the secondary water chemistry was replaced with the current all-volatile-treatment (AVT).

Since 1974 when AVT chemistry was adopted denting at support plates and tube sheets became the most often cited steam generator problem. The phenomenon is characterized by gradual collapse of tubing by compressive radial force due to accelerated buildup of magnetite in the crevices between alloy 600 tubing and carbon steel support plates. Localized chloride concentration at those poorly-circulated regions were found to be upto 60,000 times that of bulk water [5] which is responsible for accelerated corrosion of carbon steel [6].

Another problem which has been observed since AVT chemistry was adopted is the intergranular cracking from the secondary side which has been attributed to IGA and SCC. IGA is characterized by its lack of stress dependence and widely distributed attack morphology while SCC results in a localized penetration as illustrated by a failure example in Figure 1.1. These phenomena are observed primarily at tube sheet crevices where a number of different chemicals are concentrated by the repeated wetting and boiling process. These chemicals are: 1) hydroxides, 2) the reaction products of sulphate and hydrazine, 3) decomposed ion exchanger resins, 4) neutral salt solution and 5) alkaline carbonates [5]. Extensive laboratory tests suggest that concentrated alkaline environment is the most likely single cause for both types of the secondary side intergranular cracking. Remedial actions are therefore aimed at minimizing the occurrence of such high pH crevices. Although problems associated with AVT chemistry has been gradually alleviated as the result of relevant remedial actions, total plugging rate is higher than that with the phosphate chemistry with appropriate slidge control. This has leds some utilities to the conclusion that phosphate chemisry should be revisited. Some units are now operated in the combined AVT/phosphate chemistry for optimal control of tube wastages and chloride related SCC [7].

While the remedies for the secondary side problems have resulted in a decreasing importance, in recent years, primary side SCC becomes the most significant failure phenomenon in steam generator. Unlike other corrosion-related problems, primary side SCC initiates from well-circulated smooth surfaces in the uncontaminated primary water of both LWR's and heavy water reactors(HWR) [7]. The affected locations such as roll transitions on hot leg side, denting areas and minimum radius (row 1) U-bend apex are characterized by the presence of tensile stress due to either residual stress or active load. No SCC has been observed on the cold leg side. This indicates an importance of temperature in the failure process. Extensive research efforts around the world have shown that tubing manufacturing process plays a vital role in determining susceptibility. The undesirable manufacturing process, designed to produce minimal sensitization (chromium depletion

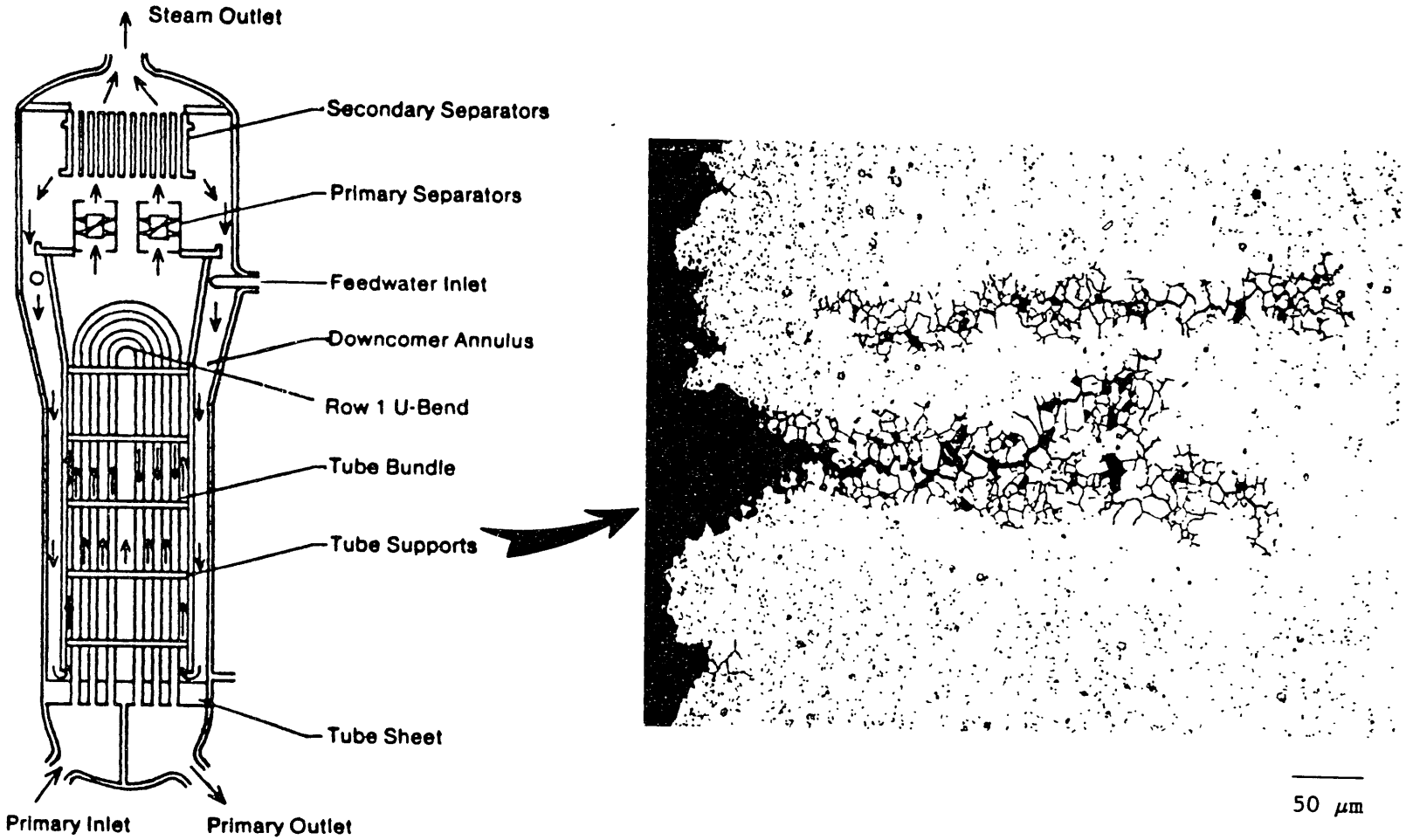

Figure 1.1 Schematic of a Steam Generator Design and Typical Intergranular Stress Corrosion Cracking of Alloy 600 Steam Generator Tubing (cracks initiated from the secondary side).

at grain boundaries), was established about a decade ago when significant IGSCC were observed in sensitized alloy 600 tubing due to faulted acidic environments. In fact some plants with sensitized conditions showed surprisingly good performances in normal water chemistry [3]. Remedial actions for primary side SCC have included lowering tensile stresses, temperature and optimizing the microstructure. The first two approaches are favored as short-term actions on existing steam generators although a number of undesirable effects may limit their usefulness [8]. For new and replacement steam generators metallurgical improvement appears to be the most promising solution as supported by the strong dependence of susceptibility on the tubing manufacturing process.

Mechanical damages to steam generators such as fretting, high-frequency fatigue and water hammering are also significant problems. But these structural design-related problems are beyond the scope of discussion in this thesis.

Alloy 600 - Nozzle Safe-ends

Alloy 600 is used for a transition region to facilitate welding of stainless steel piping to carbon-steel BWR vessel nozzle. Intergranular crackings have been observed within creviced areas in the oxygen-abundant BWR water chemistry. The result of failure analysis [9] indicates that sensitization of the heat affected zone combined with high residual stress are responsible for the IGSCC in the creviced environment. Remedial actions include the use of higher chromium alloys and desensitization as well as stress relief treatments [10].

Alloys X-750 and 718 Fasteners

The concern with the failure of alloy X-750 has developed in recent years. The earliest reported failure occured in the guide-tube support pins of the Mihama Unit 3 in 1978 [11]. A design schematic and an example of such a failure at the built-up end of spring leaves are shown in Figure 1.2. Since then, failures of fasteners made of alloys X-750

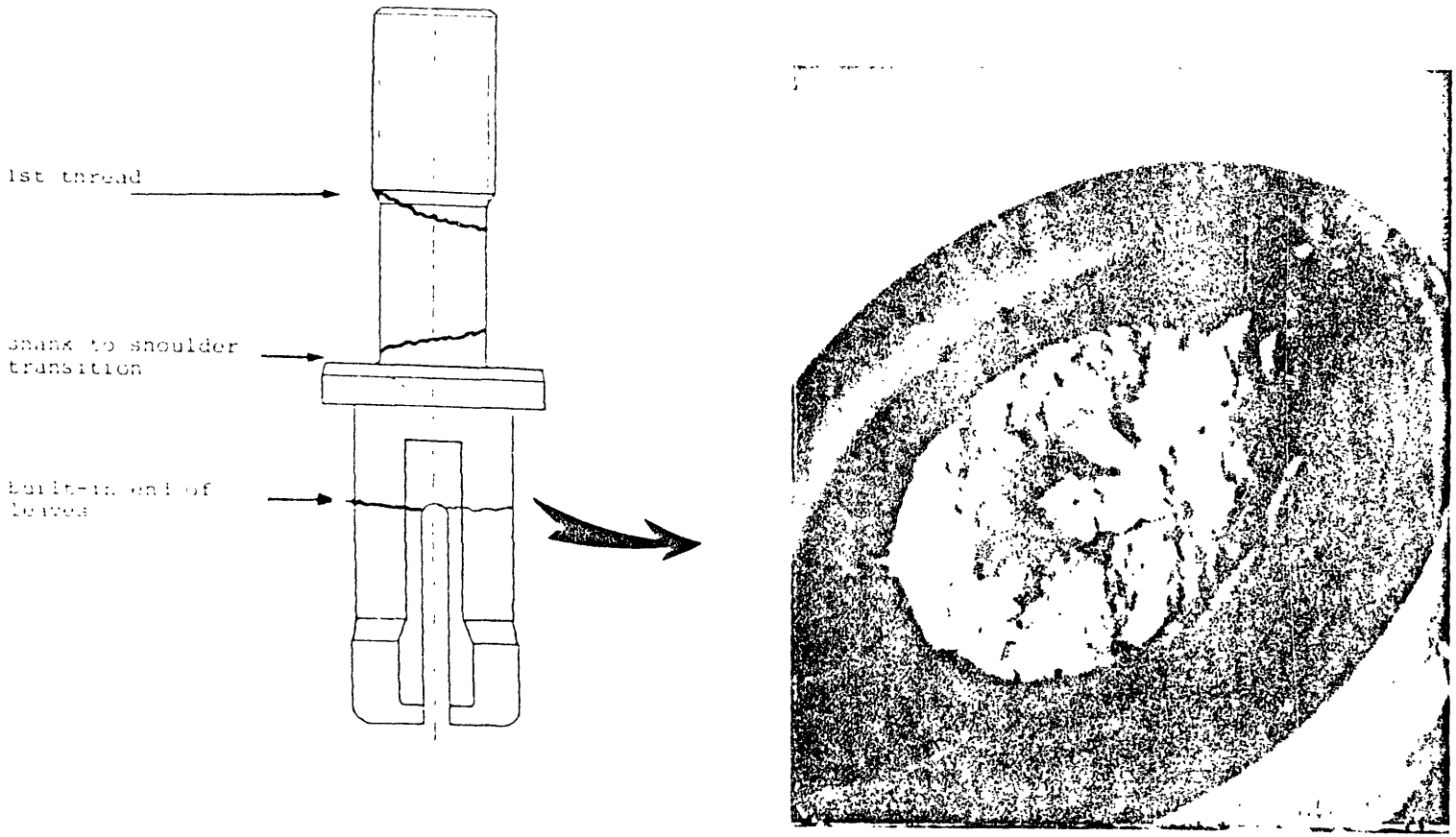

Figure 1.2 Design Schematic and Failure Example of PWR Guide-tube Support Pin (Curtesy: G.O. Hayner, Babcock and Wilcox Co.).

and 718 have become a common problem in all major LWR designs [11-15]. Most significantly affected component designs include the pin, springs, bolts and beams. A typical failure of fuel assembly holddown spring is shown in Figure 1.3.

Due to a wide variation in thermomechanical processes and structural design characteristics, the failure mechanism for these high strength materials is not simple. McIlree [16] and Hayner et al.[14] reviewed field failures of high strength alloys in LWR service. Most of the failure surfaces are characterized by intergranular cracking. The failure data by Hayner et al.[14] are summarized as a function of heat treatment, in Table 1.3. Several important characteristics can be observed from the data. Most of the heat treatments for the alloys using aircraft material specifications (AMS) have resulted in failures when service load was close to the yield strength of the condition. Although comparison between heat treatments is difficult due to the strong dependence on the stress level, no failure has been reported with two particular conditions, heat treatment C and as hot worked conditions. This highligts the sensitivity of suseptibility to microstructure. In addition there is a significant difference in the failure rate between PWR and BWR environments. A more detailed comparison is necessary to see if the trend is systematic.

Currently suggested remedial actions may be divided into three categories; reduction in stress level, microstructural improvements, and replacement with better alloys. The stress level of threaded fasteners can often be reduced by using either reinforcements or a more accurate preload control [17, 18]. It appears unlikely that stress reduction alone can solve the environmental problem. Futhermore some important design features make these options difficult to employ. The last two approaches are generally believed to be more effective considering the sensitivity failure rate on material conditions. These approaches require a detailed understanding of microstructural factors in the embrittlement process.

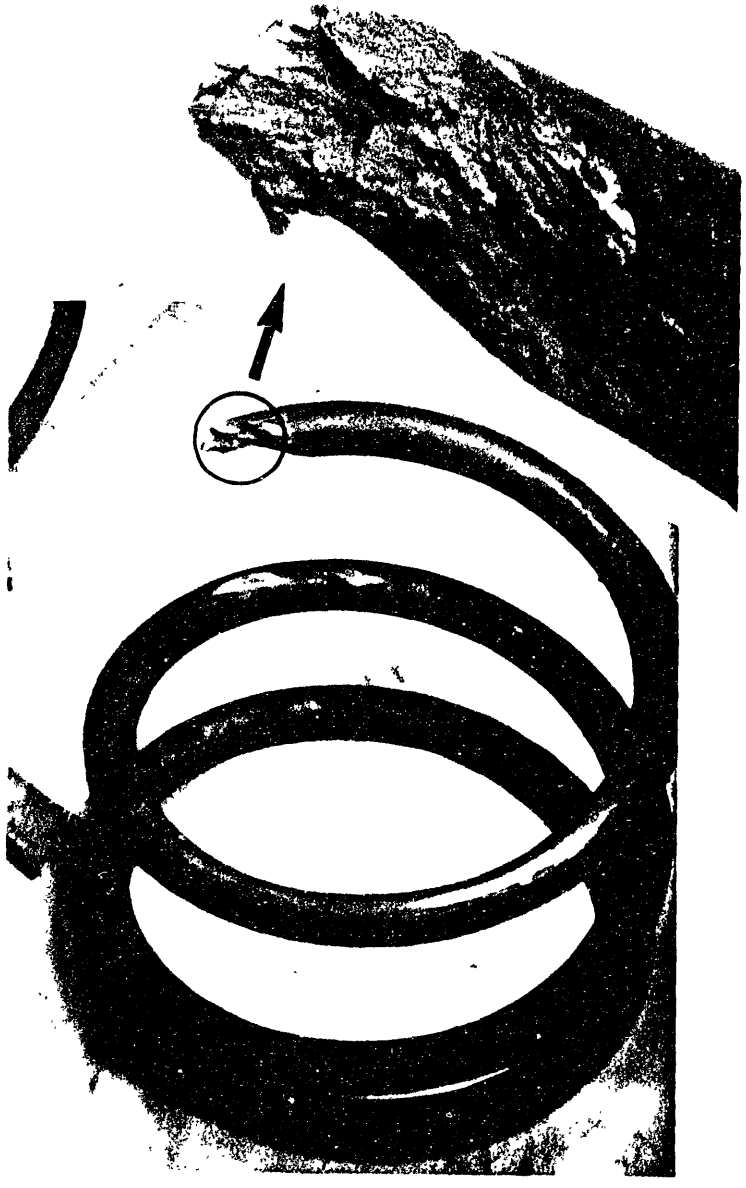

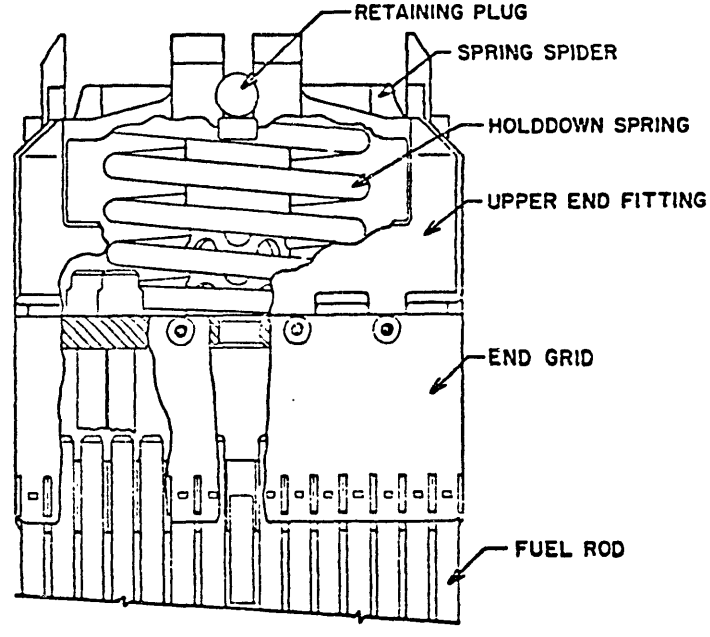

Figure 1.3 Failure Example of PWR Fuel Assembly Holddown Spring (Curtesy: G.O. Hayner, Babcock and Wilcox Co.).

Table 1.3

Failures of Alloys X-750 and 718 in LWR
as a Function of Heat Treatment

Heat Treat*	Component	Total# used	Total# Failed	Failure Mode	Est. Stress	Reactor**
X-750						
A;	Beam	unknown	3	IGSCC	620MPa	B
B;	Bolt	unknown	up to 10%	IGSCC	>700MPa	P
	Bolt	unknown	0	-	$0.7\sigma_Y$	P
	Spring	unknown	0	-	low	P
C;	Bolt	unknown	0	-	unknown	P
D;	Spring	3500	34	Fatigue	430MPa	P
	Spring	unknown	0	-	unknown	B
	Spring	unknown	0	-	low	P
	Plunger	2000	0	-	14MPa	P
E;	Spring	>10,000	few	unknown	unknown	P
	Spring	1000	0	-	300MPa	P
F:	Pin	≈10,000	unknown	IGSCC	high	P
AR***	Spring	unknown	0	-	unknown	P
718						
G;	O-ring	unknown	0	-	unknown	P
H;	Spring	150	2	unknown	450MPa	P
	Grid	300,000	0	-	340MPa	P
I;	Spring	unknown	0	-	med-high	P
	Spring	unknown	12%	Fatigue	unknown	P

Note: * See Table 1.2 for the heat treat code.

** Reactor Type: B = BWR, P = PWR

*** As Hot Worked.

Chapter 2

LITERATURE REVIEW

Evironmentally assisted cracking of nickel-base alloys has received an extensive amount of research effort due to their broad applications ranging from high purity water to deep sour gas. It would require a major effort if one desired to make a complete coverage of the vast amount of literature. For this reason, no such exhaustive review is yet avaiable in open literature.

The scope of the review in this thesis is also limited, primarily to three alloys including 600, X-750 and 718. These alloys have been applied in a wide variation of microstructures tailored to specific requirements for mechanical properties. It is necessary to summarize the relationship between processes and resultant microstructures so that a complicated microstructural dependence of the susceptibility can be discussed. The main discussion is divided into three parts: 1) the role of microstructure; 2) environmental variable effects; and 3) mechanical factors. These are generally accepted as three major parameters. Finally, a mechanistic summary is presented based on generally accepted understanding. This summary would reveal the areas which need further clarification.

2.1 ROLE OF MICROSTRUCTURE

2.1.1 Process-Microstructure Relationship

Typical thermomechanical processes of the three nickel-base alloys can be characterized by the cold or hot work steps followed by annealing treatments. The precipitation hardened alloys X-750 and 718 are further aged for various strengths. The final aging is usually done near 700 C for about 20 hours. The grain size is determined by the competition between recrystallization and grain coarsening phenomena during the

final anneal stage. The grain size varies between 10 μm and 100 μm for typical anneal temperatures between 930 C and 1100 C [21].

Carbides

The carbon solubility in nickel-base alloys is very low and follows an Arrhenius equation type temperature dependence [19,20]. A significant fraction of carbon in the solution is precipitated in the form of carbides during either a slow cooling or subsequent aging stages. X-ray analysis of extracted phases in alloy 600 indicates that most of the carbides are of the Cr_7C_3, $Cr_{23}C_6$, and Ti(C, N) type. Cr_7C_3 is predominant in mill-annealed heats [21,22] while a significant amount of $Cr_{23}C_6$ is formed after subsequent aging at a temperature near 700 C [22]. The latter step is often described as a thermal treatment (TT). In alloy X-750, $Cr_{23}C_6$ is the predominant carbide [23-25]. The difference in the carbide type between mill-annealed alloy 600 and aged alloy X-750 can be understood by the fact that the formation of $Cr_{23}C_6$ requires at least half an hour of aging at 700 C while the mill anneal process with a typical cooling rate of about 130 C/min [21] does not allow adequate time-at-temperature. In alloy 718, only a small amount of carbides are observed in the form of $Cr_{23}C_6$ and Ti(C,N) [26]. This is due to the high carbon solubility in high iron alloys. Ti(C,N) is usually formed in the early step of the process. Due to its high melting temperature, it is not dissolved by any later solution anneal process.

The distribution of chromium carbides in alloy 600 is controlled by the heatup and cooldown rate during the final anneal as well as the annealing temperature. Intragranular carbides are formed during the heatup step preferentially along prior cold worked grain boundaries [27]. Intergranular carbides are formed during the cooldown step or the TT process. Therefore, the intragranular carbide is dominant by mill annealing at a temperature below a solvus for a carbon content while the intergranular carbide is dominant after mill annealing above the solvus.

These two processes are desigated as a low temperature mill anneal(LTMA) and a high temperature mill anneal(HTMA), respectively. Ti(C,N) is usually formed at a higher temperature range and remains unchanged by the thermomechanical processes [15].
Morphology of intergranular carbides has been studied in detail[23-25]. $Cr_{23}C_6$ has a fcc structure with a lattice parameter of 10.36 ^{o}A which is almost exactly three times that of the matrix [23]. Carbide growth at grain boundaries maintains the alignment with every third atom of the lattice. Since there is neither a one-to-one atomic correspondence at the carbide/matrix interface nor strain associated with the alignment, classical form of coherency is not possible. Yonezawa [25] classified the carbide morphologies into two types; one growing in one direction and the other having a mixture of carbides with bidirectional growth morphology. Hosoi et al. [28] found that typical globular shape of carbides changes into a cellular and a finely scattered shapes after 20% and 60% cold work before aging of X-750, respectively.

Chromium Depletion

Precipitation of intergranular carbides results in at least temporary chromium depletion adjacent to the grain boundaries. The kinetics of carbide precipitation determines the rate of initial depletion process while the slower chromium diffusion controls its replenishment with further aging. Therefore, the minimum chromium level at grain boundaries is a complex function of the prior carbon inventory and the temperature history during the final anneal and subsequent aging treatments.

The low temperature mill annealed (LTMA) alloy 600 usually show little chromium depletion after the final anneal and do not respond to the thermal treatment (TT) due to low carbon in solution [27]. In the high temperature mill annealed (HTMA) alloy 600 and the solution annealed and aged X-750, the chromium concentration can be reduced down to 12 weight percent [23].

Airey [29] studied the sensitization kinetics of mill annealed alloy 600. Huey tests showed that the aging at 700 C for 1 hour gives rise to the maximum sensitization which agrees well with subsequent work by Kowaka et al. [30]. Thermal treatment (TT) at 700 C for 15 hours results in a substantial replenishment of chromium in the HTMA condition of alloy 600. Pement [31] and Domian et al. [32] examined microstructures of alloy 600 after 16,000 hours at 332 C and after 14,000 hours at 343 C to find no discernible changes by the exposure. For alloy X-750, aging at 704 C for 20 hours after solution anneal shows a significant chromium depletion [23] indicating that much longer aging may be necessary for the same degree of replenishment. In alloy 718, there is no chromium depletion at grain boundaries where only a marginal quantity of carbides are observed in the form of (Ti, Nb)C [24].

γ' and η Phases

Alloy X-750 has typical heat treatment schedules consisting of hot work, anneal and aging, as shown in Table 1.2. In aged condition of X-750 γ' precipitate, $Ni_3(Al,Ti)$, is the primary hardening phase which comprises up to 15% by volume [23]. Since its solvs is about 980 C [15], only a minimal quantity of γ' is observed in hot finished and annealed conditions. Aging at 885 C, designated as equalizing treatment, results in 0.2 μm size cuboidal coarse γ' precipitation occurring both in matrix and at grain boundaries. This treatment also results in the precipitation of needle-shaped intragranular η phase(Ni_3Ti) [28]. Regions near grain boundaries and η phase are denuded of the coarse γ' precipitates.

Typical aging treatments at 704 C produce fine γ' which are uniformly distributed throughout the matrix including the coarse γ'-denuded zones from prior heat treatment. Due to a small difference in lattice parameter between the γ' and matrix a coherency strain develops [23].

γ'' and Laves Phases

Heat treatment schedules of alloy 718 is similar with those of alloy X-750, as shown in Table 1.2. In alloy 718 γ'' $Ni_3(Cb,Nb)$ are precipitated in Widmann-Staten structure by a typical aging process involving 8 hours at 718 C followed by a furnace cool to 621 C with total aging time of 18 hours which corresponds to Aircraft Materials Specification 5596, as described in Table 1.2. In low temperature annealed conditions, Laves and delta phases are produced at grain boundaries. The Laves phase has a complex chemistry but may be represented by Fe_2Ti [26]. The delta phase(Ni_3Nb) is found in a much smaller amount. When directly aged from a hot finished condition, the precipitation of Laves phase is significantly reduced.

Segregated Elements

Trace elments such as P, B, S and Si are known to segregate to grain boundaries in nickel-base alloys. In mill annealed alloy 600, the phosphorus segregation is too small to be detected by the Auger Electron Spectroscopy [32-34]. Airey [29], Guttmann et al. [32] and Briant et al. [33] found a significant phosphorus segregation in alloy 600 after aging near 700 C. Their independent kinetic studies agree with each other, showing that equlibrium phosphorus segregation is reached within 16 to 24 hours at 700 C. Was and Martin [35] used a laboratory material similar with alloy 600 but with a higher bulk concentration of phosphorus. They showed that the phosphorus segregation follows a McLean-type equilibrium model, i.e.,an Arrhenius-type temperature dependence, and is unaffected by the precipitation of chromium carbides.

Grove and Petzold [36] observed that phosphorus segregation occurs to a greater extent in the equalized and aged condition in alloy X-750. The low temperature annealed and aged condition showed slightly lower segregation but higher than the high temperature annealed and aged condition. Miglin and Domain [24] also studied the segregation in X-750 and 718 for various heat treatment conditions. Although phosphorus, boron and sulphur were detected, their variation due to surface contamination prohibited identification of any dependence on heat

treatments. Ljungberg [37] attempted a segregation study on X-750 by using analytical transmission electron microscopy to find that the method is not suitable for the application. Phosphorus is observed to be narrowly populated near grain boundaries with a depth between 5°A and 25°A [36,38].

No sulphur or silicon segregation has been observed in nickel-base alloys although sulphur segregates in pure nickel. This has been attributed to the strong scavenging effect of alloying elements such as Mg, Al and Cr [32].

2.1.2 Microstructural Dependences of Embrittlement in Deaerated Water

Carbon Content

The possibility of intergranular stress corrosion cracking (IGSCC) in alloy 600 in deaerated high-purity high-temperature water was first detected by Coriou and coworkers [39] as early as 1959. A more detailed investigation by the same group [40] showed a systematic microstructural dependence of the susceptibility in deareated water at 350 C. All the low carbon heats were found more susceptible than the solution annealed and quenched high carbon heats while sensitized high carbon heats showed no cracking. The carbon effect was later reproduced by Domian et al. [41]. U-bend tests near 360 C showed no systematic difference in initiation time in mill annealed material for a carbon range between 0.01% and 0.05% by weight [42,43]. Bulischek and van Rooyen [42] showed that activation energy for initiation increases with carbon content in the temperature range between 325 C and 365 C. These results suggest higher susceptibilty of high carbon heats at much higher temperature. However, accelerated tests in 400 C steam with 76 kPa hydrogen overpresssure showed no such effect [44]. It appears that the carbon content alone does correlate with the susceptibility. Instead specific microstructural characterisitics should be related although the carbon content affects the microstructure to some extent.

Yonezawa et al. [45] found that low carbon X-750 is more susceptible

than the standard X-750 composition. Hence, they sggested a carbon of at least 0.02% forr an improved alloy.

Grain Size and Carbide Morphology

A good correlation exists between susceptibility to embrittlement and microstructural characteristics such as grain size and carbide distribution. The highest susceptibility is found with fine grained heats with a preponderence of intragranular carbides which characterizes the LTMA heats [43,44]. The larger grained heats without intragranular carbides but with intergranular carbides shows much lower susceptibility although these are not completely immune to the IGSCC.

The lower susceptibility of the TT conditions and sensitized conditions of alloy 600 indicates that continuous and semi-continuous morphology of intergranular carbides are beneficial [46]. Alloy X-750 shows high susceptibility at two distinct temperature ranges; near 100 C and above 300 C. The microstructural dependence of the susceptibility appears identical at both temperatures [23,24,36,48].

The smaller grained microstructures showed higher susceptibility in the rising load tests of alloy X-750 [36,48], the stress corrosion tests of alloy 600 and X-750 [23,24,49] and the corrosion fatigue tests of alloy X-750 [23]. In a bi-modal microstructure consisting of both fine grained region and coarse grained region which occurs in the low temperature annealed and aged condition, high susceptibility occurred in the small grained regions [50].

Smaller grained conditions are not susceptible unless they received the final aging treatment which results in the distribution of fine γ' and the increased yield strength [15,28]. Continuous and semi-continuous intergranular carbides ($Cr_{23}C_6$) are found to lower the susceptibility of X-750 [11,24,25,28,48]. Yonezawa [25] and Hosoi [28] suggested that the carbides should be of the globular or finely scattered morphology to achieve the beneficial effect. Moderate degree of sensitization

associated with the carbide precipitation appears not to support the susceptibility.

Intergranular MC carbides are considered as detrimental [48]. The large MC carbides are only by solution anneal at very high temperature [51]. This may correlate with the lower susceptibility of heats with the higher solution anneal temperature [11,51,52]. However, the high temperature solution anneal also affects grain size and intergranular $Cr_{23}C_6$ morphology. No detailed study of carbide precipitation in alloy 718 has been repoted, probably due to minimal carbide precipitation inthis material.

On the effect of intergranular carbide, several early researchers believed that grain boundaries are strengthened by dislocation pinning effect. Recent studies by Airey [46] and Bruemmer et al. [53] revealed that the carbides are in fact dislocation sources. The easy injection of slip steps into the matrix is considered to be an effective mechanism for crack tip blunting [53]. This finding with alloy 600 is likely to be true with alloy X-750 as well. Raymond [54] found the intergranular carbides are dislocation concentrators which result in mechanical rupture along grain boundaries. This is consistent with fractographic observation on the tensile specimens containing intergranular carbides [23]. Seemingly intergranular fracture surfaces contained extensive amount of microvoids conceivably originated from the carbides.

<u>γ' and η Phases</u>

Susceptible microstructures in alloy X-750 are characterized by a coarse intergranular γ' combined with adjacent γ' denuded zone. The coarse γ' structure reduces the tendency for planar slip compared with fne γ' which are easily cut by dislocations [55,56].

Recently, Hosoya et al. [57] found that γ' is electrochemically active with a maximum dissolution rate near 100 C. They also showed that the galvanic coupling bewteen γ' and the surrounding matrix can set up an

active galvanic cell which can support intergranular embrittlement processes. A more detailed electrochemical discussion is left for the next section. Hosoi et al. [28] tested the equalized but unaged condition of alloy X-750 which contains an extensive amount of η phase. No increase in susceptibility was observed indicating that η phase does not support embrittlement.

γ'', δ and Laves Phase

Compared with alloy X-750, few literature citations are available for microstructural dependence in alloy 718. The low temperature annealed and aged condition showed high susceptibility in high temperature water [24,49,58]. This condition is still slightly better than the equalized and aged X-750. When the annealing temperature is slightly increased, susceptibility is decreased [24] while Wilson [49] observed no such improvement.

Prybylowski [26] suggested that Laves phase precipitation during the low temperature anneal is responsible for susceptibility. The direct aged condition, which contains a reduced amount of Laves phase, showed lower susceptibility. Tsubota et al. [58] shortened the aging time to 6 hours and observed a significantly improved performance. This suggests that precipitation of δ or γ' phase during the prolonged conventional aging contributes to the embrittlement process.

Segregation of Trace Elements

Thermally treated or sensitized alloy 600 which contains increased amount of segregated posphorus at grain boundaries showed lower susceptibility in the deaerated high purity water. Since segregation occurs simultaneously with beneficial carbide percipitation, it is difficult to isolate its effect. The segregation effect, if any, seems to be much smaller than the carbide effect. However, further studies are required clarify this effect.

For alloy X-750, Grove and Petzold [36] observed a good correlation

between susceptibility and intergranular phosphorus while Miglin et al.[24] and Yonezawa et al. [25] found no such correlation. Miglin et al. [24] attributed the results to surface contamination. It is not clear yet whether the variation between different laboratories is a real one or associated with experimental technique.

Floreen and Nelson [55] found that a small Zr addition is beneficial. They explained its effect by suggesting that Zr improves γ' stabilization near grain boundaries and possible have scavenging effect against the segregation. No experimental evidence yet exists to verify the latter explanation. Recent results show, however, no effect of Zr on the performance in high temperature water [24].

Cold Work

Cold work increases susceptibility in mill annealed alloy 600 in high purity water [42,43,59]. Airey [43] found that susceptibility increases with cold work up to 35% above which its effect appears to saturate. In constant load tests Bandy and van Rooyen [60] observed thate susceptibility increased with a small (5%) amount of cold work but decreased with further (20%) cold work. Hence, effects of large cold work are yet to be clarified.

The effect of cold work may be related to the development of complex residual stress state. Specimen designs involving such complex residual or applied stress such as the reverse U-bend and cold-pressed hump tensile specimens show much higher susceptibility [59,61]. Slow strain rate tests with uniaxial tensile specimens at 1×10^{-7} sec^{-1} showed the same crack growth rate as the reverse U-bend tests at 365 C [62]. Slow strain rate tests with cold-pressed hump specimen showed much higher crack growth rate than the reverse U-bend tests at the same temperature [59]. Bandy and van Rooyen [60] suggested that small amounts of cold work may increase dislocation density and creep rate and will thus increase the susceptibility to SCC while larger amount of cold work may limit dislocation motions and hence transient creep rate.

For alloy X-750, Hosoi et al. [28] and Tsubota [58] observed a consistent effect of cold work before final aging step. Susceptibility of high temperature annealed and aged conditions increases with cold work up to 30 % while further cold work up to 45% reduced susceptibility. Hosoi et al. [28] correlated the effect of cold work with the carbide morphology. As the amount of cold work increases, the intergranular carbides morphology is changed from a globular to a cellular and finally to a fine scattered shape. The latter morphology is attributed to observed low susceptibility. Tsubota et al. [58] found that there is no effect of cold work on the susceptibility of alloy 718.

2.1.3 Electrochemical Influence of Microstructural Characteristics

Microstructural Galvanic Couples

Due to complex microstructrues of nickel-base alloys, it is necessary to examine the possibility of localized galvanic cell between various phases. Electrochemical studies on sensitized chemistries and γ' chemistries in alloys 600 and X-750 were recetnly reported by Hosoya et al. [57], as shown in Figures 2.1 and 2.2. Figure 2.1 shows that the peak anodic current density increases with decreasing chromium concentration. For realistic chromium concentrations for nickel-base alloys, the current density is small and fairly independent of temperature. In contrast, the peak anodic current density of γ' chemistries is significantly higher and a strong function of temperature, as shown in Figure 2.2. The temperature dependence of current density of Ni_3Al correlates well with that of crack growth rate of the equalized and aged condition containing coarse intergranular γ'. They also applied the mixed potential theory to predict a galvanic current density of 7×10^{-5} mA/cm^2 which agrees well with the experimentally observed value.

Although their analysis was based on the most active chemistry of γ' (Ni_3Al), microchemical analysis of extracted γ' from X-750 shows that the intergranular γ' composition is close to Ni_3 (Ti = 0.1, Al = 0.15)

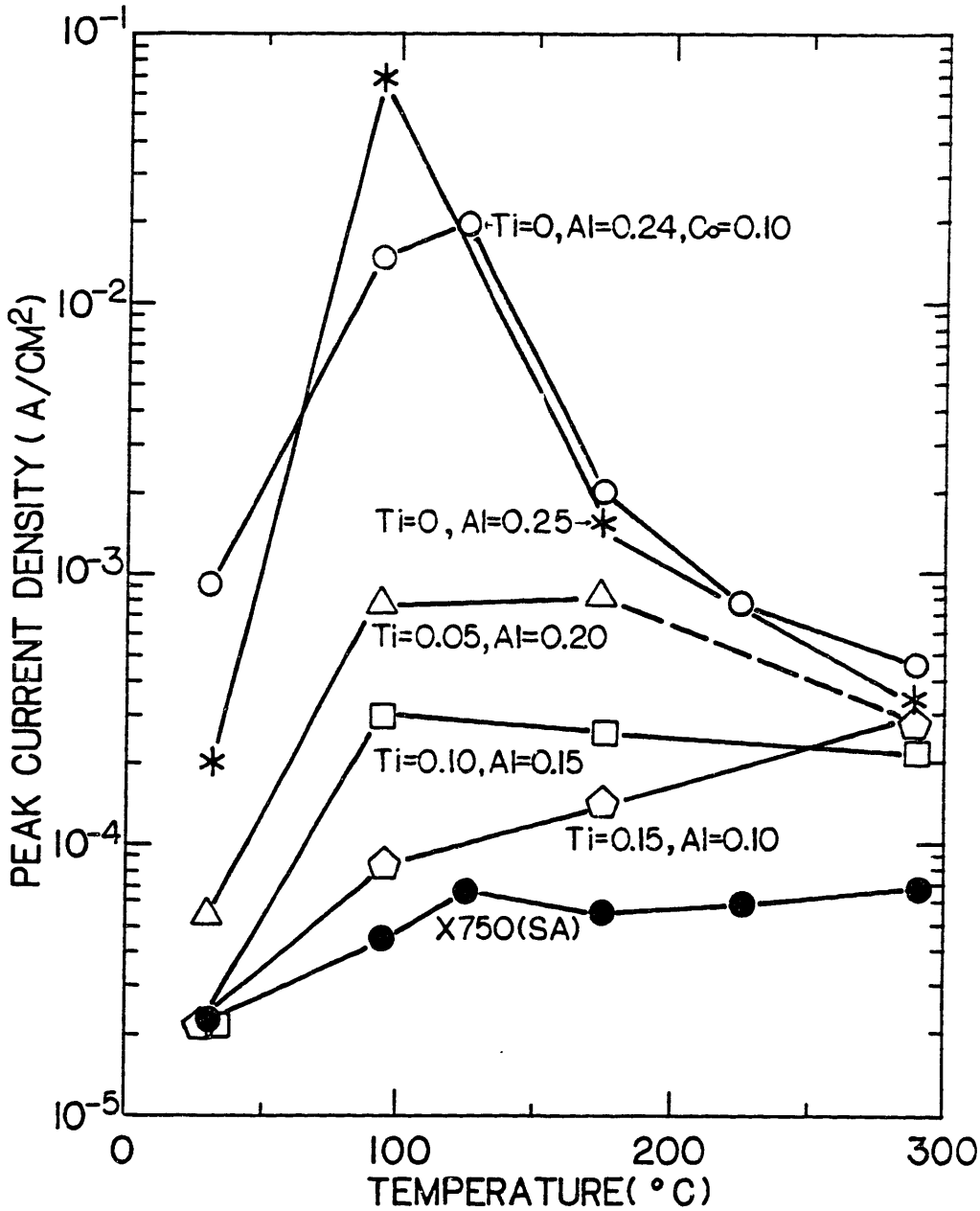

Figure 2.1 Peak Anodic Current Densities of various γ' Chemistries determined by Potentiodynamic Polarization as a Function of Temperature in 0.05M Na_2SO_4(pH 3) Solution [57].

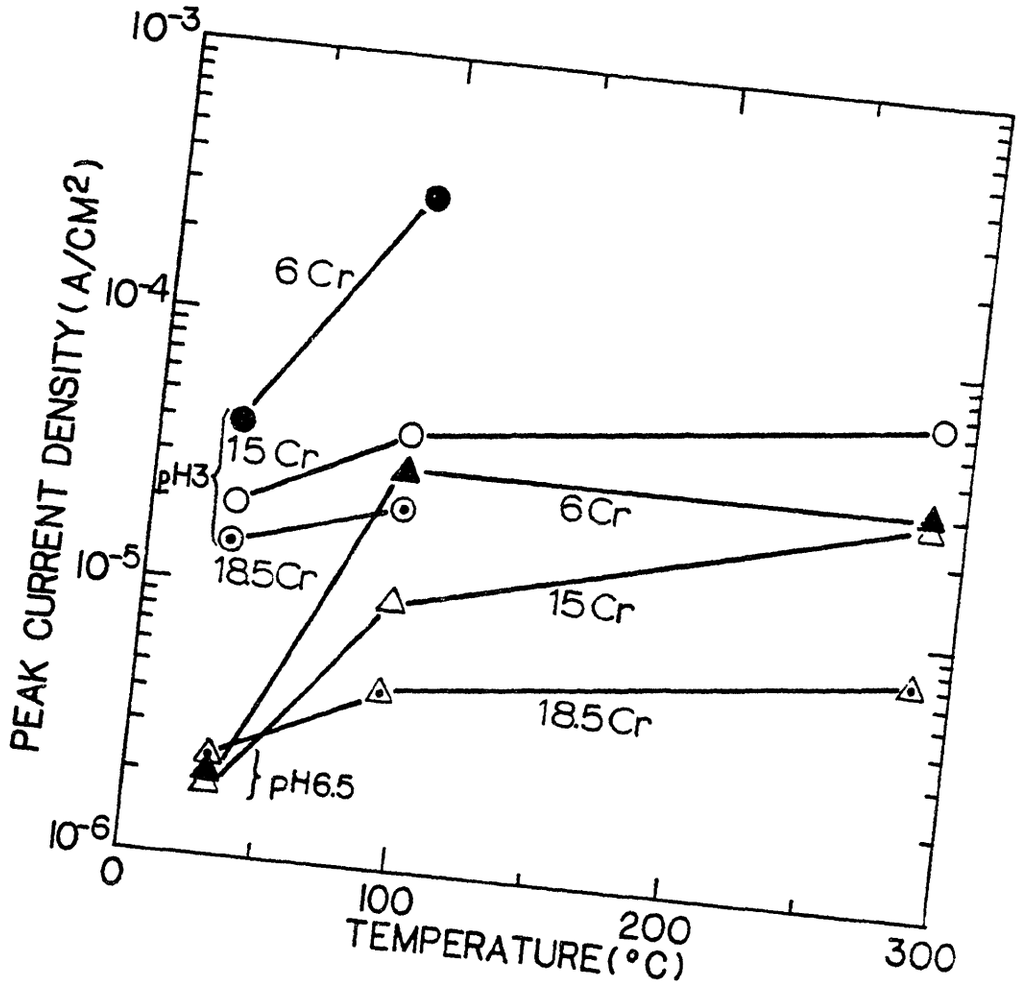

Figure 2.2 Peak Anodic Current Density of Chromium-depleted Chemistries determined by Potentiodynamic Polarization as a Function of Temperature in 0.05M Na_2SO_4 (pH 3) Solution [57].

[23]. The latter composition apparently does not show the high current density and exhibits a passivity at low temperature, according to Figure 2.1. A detailed electrochemical study is desirable to more fully understand galvanic effects with the latter composition.

The galvanic effect between the sensitized chemistry and surrounding carbides or matrix has not been studied due to lack of data on carbides. The polarization experiment in 3.6 N H_2SO_4 with 0.1 N NH_4SCN [63] shows that the peak current density of $M_{23}C_6$ is about two orders of magnitude lower than type 316 stainless steel matrix and the corrosion potential is more noble by 120 mV. Therefore, the development of a galvanic cell is also possible in this case. It should be noted that the magnitude of resultant current density depends not only on the potential difference but also on the hydrogen exchange current density of $M_{23}C_6$ which has not been reported.

Cihal et al. [64] obtained the anodic polarization curves for TiC and NbC in 14.4 N H_2SO_4 at 70 C. Despite an identical corrosion potential, the anodic peak current density of TiC was found to be significantly higher than that of NbC. The electrochemistries of other important phases such as γ'', Laves and δ phases are not found in the literature. However, it is likely that their electrochemical behavior is also different from that of the surrounding matrix.

Effects of Phosphorus Segregation

It is generally agreed that phosphorus acts as a recombination posion for hydrogen recombination reaction. Hence, phosphorus segregation is believed to cause more effective atomic hydrogen accumulation at intergranular regions [65,66,73]. Segregation of sulphur has been shown to promote deuterium segregation in nickel [67,84]. If phosphorus has a similar effect, the hydrogen accumulation can be significant at grain boundaries. However, no data exists to support this contention. The presence of phosphorus also increases peak anodic current density in HCl

[68]. A depassivation effect of phosphorus has recently been confirmed by Jones et al. [69] and Briant et al. [33]. The former also showed that phosphorus has a stronger depassivation effect than sulphur due to self-dissolution characteristics. Hence, phosphorus segregation appears to support both anodic and cathodic mechanisms of embrittlement.

Film Characteristics

Airey [46] analyzed the thickness, composition and structures of the oxide film on alloy 600 which had been exposed to high purity water at 360 C with and without 0.14 MPa of hydrogen overpressure. The hydrogen overpressure increases susceptibility to IGSCC. The oxide formed without hydrogen overpressure was much thicker and rich in NiO while the oxide formed with hydrogen overpressure was rich in elemental nickel as well as NiO. This is consistent with the expected decrease in the corrosion potential with hydrogen. The dominance of NiO in film on alloy 600 exposed to high purity water at 365 C has also been observed by Bandy and van Rooyen [62] who showed, based on thermodynamic data, that the potential of NiO is close to the hydrogen reversible potential at one atmosphere hydrogen overpressure. These observations may be used to explain the results of bi-metal couple tests of alloy 600 in pure water at 350 C by Coriou's group [40]. Coupling with gold would bring alloy 600 to the hydrogen reversible potential which is much higher than the NiO regimeand and then resulted in no embrittlement. Coupling with a mild steel might have lowered the potential down to the NiO regime and produced the susceptible film structure.

Pathania and Cleland [70] showed that the oxide film on thermally treated alloy 800 was substantially thicker than the mill annealed condition after an exposure to a caustic solution at 300 C. Although there are large differences in both material and environmental conditions, the correlation between the thinner film and the higher susceptibility to IGSCC deserves further attentions. It is not understood why that apparently inverse relationship holds.

Airey [46] also found that chromium concentration in film was lower with

the hydrogen overpressure indicating selective dissolution. The Pourbaix diagram on Cr-H_2O system [71] shows that the stable regime of Cr_2O_3 gradually decreases with increasing temperature while NiO regime slightly expands between 100 C and 300 C, as shown in Figures 2.3 and 2.4.

2.2 ENVIRONMENTAL VARIABLES

2.2.1 Localized Environment

It has been demonstrated by a number of investigators that the chemistry in a crack or occluded region can be very different from the bulk [72-77]. The primary side of ally 600 steam generator tubings usually do not have such an occuluded region. However after crack initiate, the environmental condition may be significantly altered. High strength fasteners usually are used in designs where crevices are present along with high stresses.

Major environmental variables to characterize localized environment are oxygen concentration, pH and impurity concentrations. It is generally accepted that the dissolution of material at crack tip or inner crevice region results in oxygen depletion. Gabetta and Rizzi [72] observed that potential of crack tip environment decreases as the crack opens. The active crack tip would consume the oxygen more than the pumping effect can compensate which results in oxygen depletion in the environment. Turnbull [73] analyzed the fatigue crack tip chemistry, taking into account both diffusion and convection effects. The oxygen concentration at crack tip can be about three orders of magnitude lower than bulk. The minimum concentration decreases with decreasing fatigue loading frequency and increasing the ratio of minimum load to maximum load (R-ratio).

The pH in localized environments behaves as a function of the electrochemical reactions. With small bore alloy 600 tubings, Taylor [74] measured a pH of about three in 0.1 M Na_2SO_4 and a pH of about 9 in

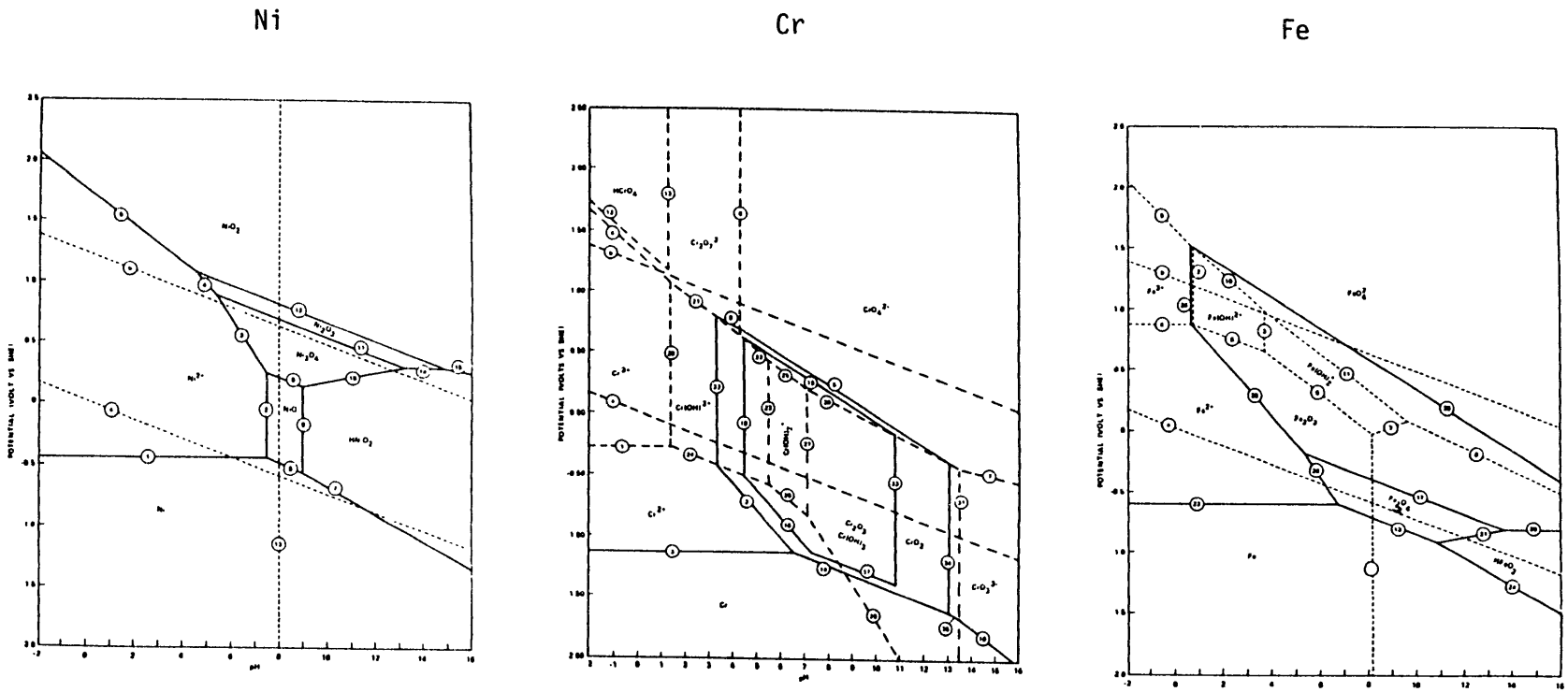

Figure 2.3 Pourbaix Diagrams of Nickel, Chromiium and Iron in Water at 100 C [71].

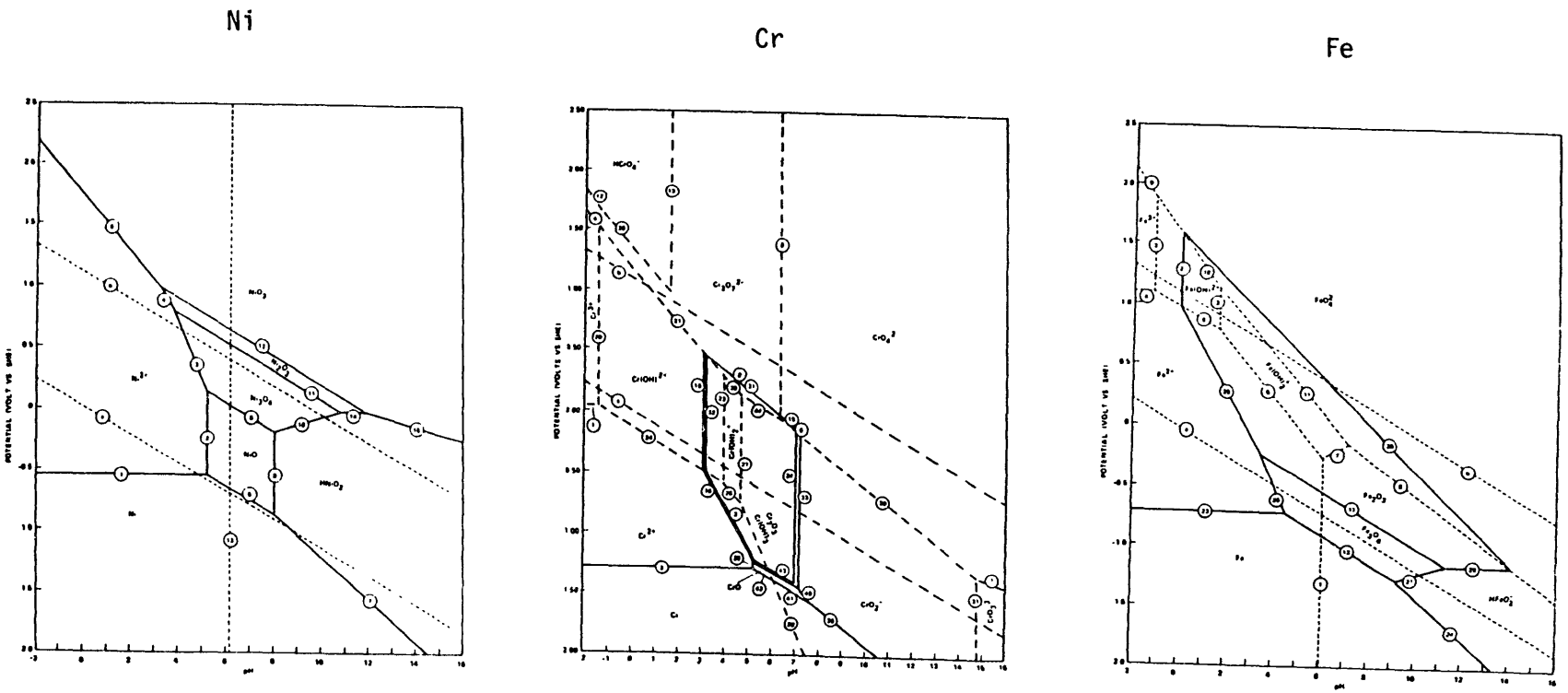

Figure 2.4 Pourbaix Diagrams of Nickel, Chromiium and Iron in Water at 300 C [71].

deareated water at 288 C. In chloride containing electrolyte, the alloy 600 crevice was quickly acidified during the first day and gradually neutralized to a slightly basic pH at 288 C [75]. The attainment of neutrality was attributed to likely consumption of H^+ due to recombination reactions. The same environment, however, acidified the crevice of type 304L stainless steel wthout subsequent neutralization [76]. Therefore the pH appears to be determined by the competition between localized dissolution reaction and the recombination of H^+. An acidic environment is expected for an active crack tip while a slightly basic environment is expected for a passive crack tip. Assuming continuous dissolution without recombination loss, Shuck and Swedlow [77] found that the crack tip pH is lowered to about three for the bulk pH between 3 and 7. Further decrease in the bulk pH results in proportional decrease in crack tip pH.

When an external potential is applied to a material, its crack tip potential is often questioned. In a highly conductive solution (0.5 M NaCl), the potential loss across the crack tip is found to be negligible. If solution conductivity is low, as in case of high purity water, it is likely that crack tip potential is determined by localozed electrochemical reaction regardless of external potential. In a solution with intermediate conductivity external polarization in one direction may induce a shift in crack tip potential in the other direction.

2.2.2 Water Chemistry Effects

A number of test results on nickel-base alloys were obtained from other than the deaerated high purity water. Variation in water chemistries include pH, oxygen content and hydrogen overpressure. These results were also valuable for development of mechanistic understanding of embrittlement in pure water since it has been shown that crack tip or crevices can be significantly different from the bulk.

Solution pH

At low tempeature, nickel-base alloys are susceptible to intergranular embrittlement when a sensitized microstructure is exposed in acidic environments [79]. A sensitized microstructure has also been shown to be susceptible to IGSCC in acidic high temperature water in slow strain rate tests [80]. Lower pH results in a higher susceptibility at a strain rate of 6.7×10^{-7} sec^{-1}. At this strain rate and an oxygen concentration of 8 ppm a maximum susceptibility occurs at 288 C. At the other extreme, highly concentrated caustic environments produces similar IGSCC of alloy 600. Since the latter environment produces a mixture of IGSCC and IGA in mill annealed alloy 600 which is is similar to that observed on the secondary side of operating steam generators, caustic was suggested to be a more appropriate environment [81]. Theus [82] observed that susceptibility in a caustic environment showed the same microstructural dependence as the case of high purity water while an exactly opposite dependence was found in acidic environment. A similar observation was made by corrosion fatigue tests in caustic solution [83]. In spite of this, Taylor [74,75] argued that the crevice pH can not be so high.

Most of caustic SCC studies use highly concentrated solutions. A review by Serra [84] showed that testings in the active-passive transition potential regime produced IGSCC while cathodic potentials produced only transgranular SCC. Bandy et al. [85] later showed a more systematic relation between the two variables, as shown in Figure 2.5. The results indicate that the mechanism of IGSCC in caustic environments is consistent with a film rupture mechanism. If the same microstructural dependences of susceptibility in both caustic and high purity water are truly due to an identical mechanism, the primary side SCC may also be explained by the film rupture mechanism for alloy 600. For alloys X-750 and 718, such a detailed environmental study has not been discussed in the literature.

Oxygen and Hydrogen Effects

Matsushima and Shimiza [80] showed that solution annealed alloy 600 is susceptible in high oxygen water. On the other hand, Airey [43] found

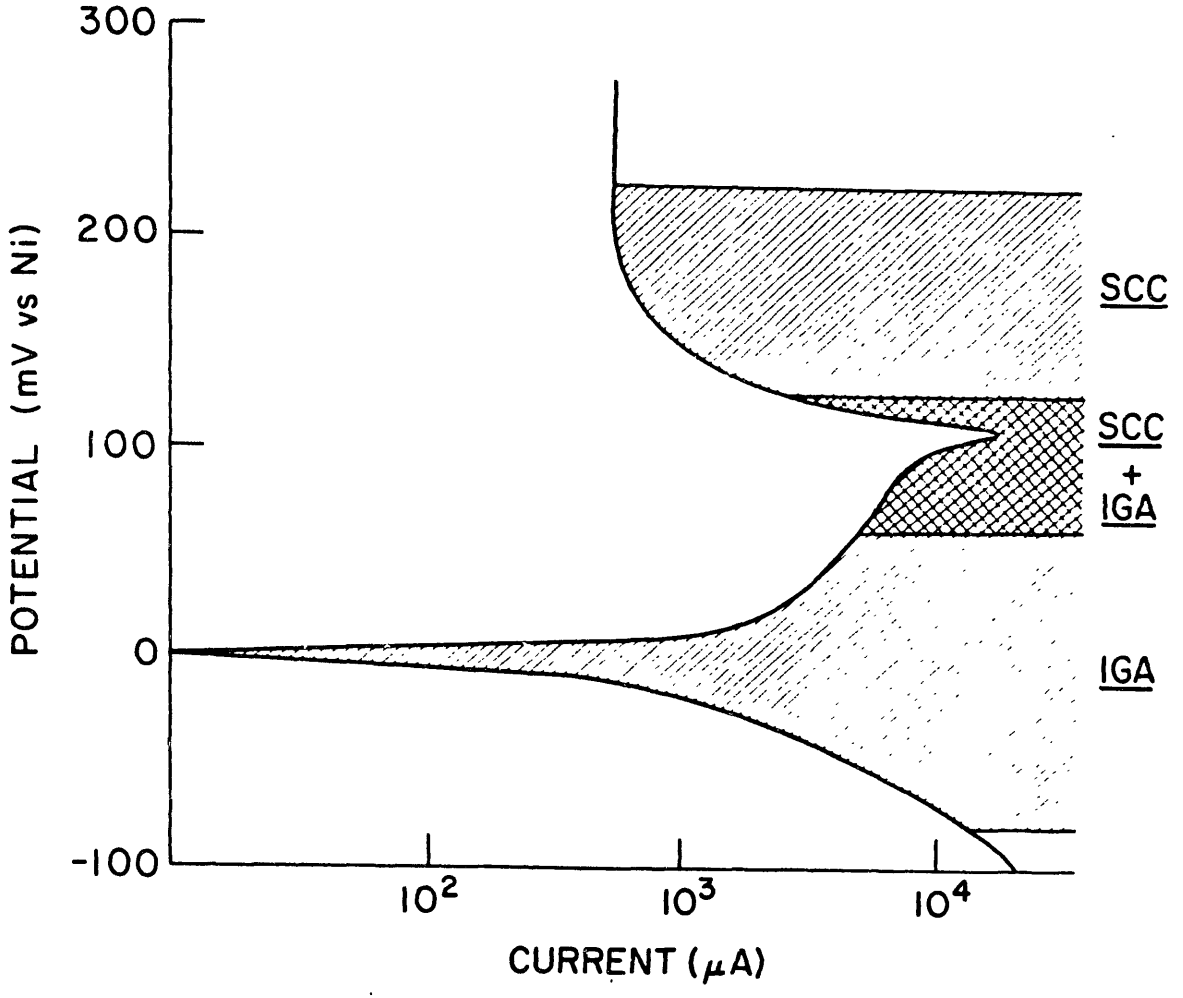

Figure 2.5 Observed Potential Range for Intergranular Stress Corrosion Cracking of Alloy 600 in a High Temperature Caustic Environment [46].

that the hydrogen overpressure of 0.14 MPa can increase susceptibility by several times. The susceptibility of alloy 600 appears to decrease in the sequence of 1) deaerated high purity water with hydrogen; 2) primary water chemistry with hydrogen and finally, 3) pure water. The effect of hydrogen overpressure was mentioned briefly in the previous section in terms of film composition and structure. However, detailed evidences is not available.

Alloy X-750 shows no difference in susceptibility regardless of oxygen content. For the effect of hydrogen overpressure, there are no published results yet. However, it is conceivable that the environmental effect is also valid for the age-hardenable alloys X-750 and 718.

2.2.3 Behaviors of Nickel-base Alloys in Hydrogen Environment

Gaseous Hydrogen Environment

The use of a gaseous environment usually provides true effects of internal hydrogens. Based on tensile tests after gaseous charging, Eastman et al. [86] showed that hydrogen softened the already strengthened nickel-carbon alloy while it strengthened pure nickel. Thompson [87] showed that the ductility of alloys 600 and 625 are lowered by internal hydrogens. Based on ductility measurements based on dimple sizes, a smaller ductility loss with alloy 600 was explained by the higher stacking fault energy (SFE) related to lower chromium content. Igarashi et al. [88] attributed susceptibility of γ' and γ'' hardened nickel-base alloys in a sour gas environment to coplanar dislocation structures. The more massive dislocations in alloy 718 was correlated with lower susceptibility. For thoria dispersed nickels, Thompson and Wilcox [89] suggested that ThO_2 is beneficial due to hydrogen trapping effects. It should be noted that the tendency toward planar dislocation decreases with increasing particle size which in turn would reduce the trapping effect. Therefore, the two observations apparently contradict with each other.

The temperature dependence of embrittlement in gaseous hydrogen environment has been determined for alloy 718 [90]. The susceptibility is highest at 50 C and gradually decreases with temperature change to both directions. It is interesting to note that the temperature dependence of alloy X-750 crack growth rate in water agrees qualitatively with the above data. However, the temperature range of embrittlement in water is more well-defined [23].

Cathodic Charging Environment

The cathodic charging provides an easy and convenient way to introduce hydrogen at high fugacity. Most cathodic charging studies usually involve a high cathodic current density, up to 10 mA/cm^2, using an acidic electrolyte with a hydrogen recombination posion [23,26,91-94]. Hinotani et al. [95] found that f.c.c. nickel hydride can form in an Ni-Cr-Fe alloy during the cathodic charging at 10 mA/cm^2. Hydrides were shown to decompose in air which resulted in surface cracks preferentially along grain boundaries. This was argued to be the results of fast diffusion along grain boundaries. They also showed that the increasing nickel content makes hydride formation easier. There is consistency on the surface crack description between Hinotani et al. [95] and Kekkonen et al. [93] who used 50 mA/cm^2 for unstressed X-750 specimens.

This finding has significances for the mechanistic studies. Hydride formation as not usually taken into account in a number of cathodic charging experiments since it was shown to form only at very high hydrogen fugacity [96] or at very high current density [97]. In aqueous environments, the high fugacity can be easily achieved as predicted by using the Nernst equation [98]. However, an accurate conversion between the fugacity and the overpotential is difficult due to the lack of reliable data. It seems a reasonable first order approximation that 20 kbar of gaseous hydrogen [97] is equivalent to 10 mA/cm^2 of cathodic current density.

Although no data is available, Birnbaum indicated that the presence of stress can further reduce the hydride formation current density. Hence it is necessary to clarify whether or not hydride formation is possible in real service environments. Direct observation would be difficult if hydride decays immediately upon unloading. An indirect method may be the measurement of a realistic galvanic current density. If the galvanic current density compares well with 10 mA/cm^2 the hydride may be suggested to be responsible for the real failure process. Hosoya et al [57] showed the current density can be about 7×10^{-5} A/cm^2. Since the overall reaction rate was limited by small cathodic area it is likely that the true crack tip value can be much higher.

Most results of hydrogen embrittlement studies with cathodic charging at high current densities may be thus understood in term of hydride effects. Like Hinotani et al. [95], Price and Morris [92] also observed that the hydrogen embrittlement increased with higher nickel content in an alloy. They also showed that the rank of susceptibility was preserved in mercury embrittlement test results. Lee [94] found that the embrittlement increased with decreasing strain rate during a straining electrode test with cathodic charging.

One may question if there would be a significant transition in embrittlement near the critical current density for hydride formation. Jones et al. [98] used a wide range of cathodic charging current density for their straining electrode tests on nickel-base alloys. Between 10^{-5} A/cm^2, the embrittlement was increased continuously without any precipitous transition although the fracture mode changed from microvoid coalescence to mixed mode cleavage and finally to intergranular failure. Continuous changes in both ductility and fracture mode may be interpreted as evidence of a continuous transition. There may be mechanical competition between the grain boundary strength and the matrix strength which results in an overlap of two failure modes for an intermediate condition. A continuous transition in fracture mode was also observed by Price and Morris [92].

Although alloy 600 specimens were not significantly embrittled even at

20 mA/cm^3 charging [92], Was and Ballinger [99] used a much smaller overvoltage on the single-edge-notch corrosion fatigue specimen and obtained a significant fraction of intergranular failure. Moshier [100] and Prybylowski [26] attempted cathodic charging in high purity water for corrosion fatigue test specimens of alloys 600 and X-750, respectively. No charging effect was observed on the crack growth rate. Elliot [23] and Prybylowski [26] showed that the microstructural dependences of susceptibility of X-750 conditions in the high purity water is reproduced by the straining electrode tests with cathodic charging at about 10 mA/cm^2.

The effect of nickel content which was observed in the slow strain rate tests is consistent with observations in water [24,47,70]. As the nickel content decreases below 50%, the transgranular SCC become dominant in the chloride environment. As the nickel content increases above 50%, the intergranular cracking increases with nickel content.

2.3 MECHANICAL FACTORS

2.3.1. Crack Tip Strain Rate

The environment assisted embrittlement of the nickel-base alloys show a strong dependence on strain rates. Since there are a number of different testing methods which result in different strain rate, it is difficult to compare one result with another. Ford et al. [101] made the first attempt to interrelate the crack tip strain rate between different testing configurations used in environmental cracking studies. Their results are summarized as follows:

Constant load

$$\dot{\epsilon}_{ct} = 9 \times 10^{-14} K^4 \text{ sec}^{-1} \qquad (2\text{-}1)$$

where $\dot{\epsilon}_{ct}$ is the crack tip strain rate in sec^{-1} and K is the stress intensity factor in MPa$\sqrt{m}$.

Constant Strain Rate

$$\dot{\epsilon}_{ct} = (5 \text{ to } 10)\ \dot{\epsilon} \qquad (2\text{-}2)$$

where $\dot{\epsilon}$ is applied unform strain rate in sec^{-1}.

Cyclic Loading

$$\dot{\epsilon} = (10 \text{ to } 100) \left[\frac{da}{dt}\right]_o \qquad (2.3)$$

where $\left[\frac{da}{dt}\right]_o$ is the crack growth rate in cm/sec in an inert envrionment.

It is expected that the above correlations involve significant amounts of error unless the empirical coefficients are adjusted for a particular material condition. Nevertheless, they provide the only way to compare the results from different tests.

Low Temperature Water

In the low temperature water, alloy X-750 exhibits accelerated crack growth during cyclic loading [23] as well as monotonous loading [48]. Crack growth rate during the cyclic loading shows a maximum at a frequency of about 1 Hz. At a frequency of about 0.3 Hz the crack growth rate drops precipituously accompanied by a fracture mode transition from intergranular to transgranular [26]. For a ΔK at 25 $MPa\sqrt{m}$, the crack growth rate increases with R-ratio. The crack tip strain rate calculated for 1 Hz and 0.1 Hz from Equations (2-2) and (2-3) correspond to about 5×10^{-4} sec^{-1} and 5×10^{-5} sec^{-1}, respectively. These values appear to underestimate the strain rate at crack tip free surface which undergoes a complete slip and reversal ($\epsilon \simeq 1$) during each cycle. Considering that the crack tip strain rate has a steep gradient within a plastic zone, the average value to describe overall plasticity at the crack tip would be much smaller. Hence, these values are tentatively taken for comparisons.

The rising load test is a three point bending test with a constant crosshead speed. Although the geometry is complicated the crack tip strain rate can be estimated by using Eq. (2-3). In air, a complete failure occurs in about 25 minutes [48] which translates into $\left(\frac{da}{dt}\right)_o$ of about 3×10^{-4} cm/sec. The resultant crack tip strain rate is expected to be about 10^{-2} sec^{-1}.

The WOL SCC test [23] at 93 C for the same susceptible X-750 showed almost no crack growth. The crack tip strain rate is calculated using Eq. (2-1). At a stress intensity factor of 40 $MPa\sqrt{m}$, the strain rate is about 2×10^{-7} sec^{-1}. These approximate comparisons indicate that high strain rates are required for low temperature embrittlement.

High Temperature Water

The alloy 600 shows an increasing susceptibility with decreasing strain rate [60]. There is a minimum strain rate to produce the IGSCC which increases with increasing temperature.

For alloy X-750, Miglin et al. [24] observed no embrittlement during a slow strain rate test at 2×10^{-5} sec^{-1} in 288 C water. No significant embrittlement was found at 7×10^{-7} sec^{-1} at the same temperature [102]. At 363 C, a strain rate of 2×10^{-7} results in a crack growth rate of 2×10^{-7} mm/sec while WOL SCC tests [102] at 40 $MPa\sqrt{m}$ shows about 5×10^{-7} mm/sec. The agreement is thus excellent. Tests at high strain rates usually by fatigue loading, have not revealed embrittlement at high temperature up 288 C [23].

2.3.2 Effect of Complex Stress State

There is a consistent trend that a more complex stress state accelerates embrittlement. The reverse U-bend is a more severe test than the C-ring [61]. A cold-pressed hump tensile specimen is more prone to cracking than the standard specimens during slow strain rate tests of alloy 600

[59]. However, there has been no systematic research results applicable to mechanistic understanding.

The mechanical environment in real service involves a complex stress state. The roll transition and U-bend of PWR steam generators and springs, bolts and pins are subjected to a combination of tensile and torsional stress. Hence, further research to address the effect appears to be necessary.

2.4 MECHANISTIC VIEWS

The fundamental mechanisms of environment assisted cracking, in general, include stress corrosion cracking (SCC) and hydrogen embrittlement (HE) mechanisms. The phenomenological similarity and difference between the two fundamental mechanisms has been reviewed in detail by Latanision et al. [104]. For nickel-base alloys a more specific review was made by Prybylowski and Ballinger [105] who suggested the importance of the HE in water environments. Similarly, embrittlement mechanisms are divided into the SCC and the HE in this review. The SCC mechanisms are, in turn, categorized as: 1) active path corrosion mechanism (APCM); 2) film rupture mechanism (FRM) and 3) surface related mechanism (SM). Hydrogen adsorption is however included as a hydrogen embrittlement mechanism (HEM). This review is further focussed to necessary conditions for any of these mechanisms to operate in nickel-base alloys of interest.

2.4.1 Stress Corrosion Cracking Mechanisms

Active Path Corrosion mechanism (APCM)

This mechanism attributes the embrittlement to a continuous dissolution of localized regions. The role of stress is to accelerate the dissolution rate. The SCC of alloy 600 in acidic water containing sulphur ion may be best described by this mechanism. It is observed that the susceptibility increases with the sulphur concentration, oxygen level and the degree of sensitization [79]. There is poor passivity

when the chromium level decreases below 12% which allows for the possibility of the APCM. The role of sulphur and oxygen may be explained in the context of ACPM by the results of Marcus et al. [106,107]. They performed anodic polarization and surface analysis on a nickel-iron alloy. The sulphur was preferentially adsorbed on the surface while the base metal was depassivated in the oxydizing condition. Therefore, the APCM is believed to describe the IGSCC and IGA of a sensitized nickel-base alloy in sulphur containing and oxydizing environments.

The APCM is unlikely to operate in typical microstructures of nickel-base alloys in high purity water due to the observed integrity of passive films. Nevertheless, its operability will be examined later based on the experimental results of this work.

Film Rupture Mechanism (FRM)

The film rupture mechanism describes the crack progression as a repeated rupturing of passive film by the deformation of substrate metal and subsequent repassivation. A sharp crack tip geometry required for growth is believed to be maintained when there is a suitable balance between the corrosion/passivation rate and crack tip strain rate [108]. This mechanism implies that the susceptibility of crack growth rate would be a function of both anodic potential and the strain rate. If one of two variables (for example, the potential determined by the environment) is fixed, the maximum susceptible condition would be found for an intermediate value of the other variable (the strain rate).

Bandy et al. [62,85] suggested the FRM as the possible mechanism for the caustic stress corrosion cracking of alloy 600. The crack growth rate showed a maximum in the active-passive transition potential [109] as shown in Figures 2.5. At these potentials, the grain boundaries of alloy 600 are grooved after a 10 day exposure without stress which indicates a less protective film structure at the grain boundaries. It was discussed earlier that the caustic environment can develop in occuluded regions. An anodic overpotential may develop in the secondary

side of steam generator or in the BWR environment due to the presence of oxygen [110]. These environments can support the FRM in alloy 600.

The intergranular cracking of alloy 600 in the primary water and in the high purity water is also believed to be related with the FRM [68,85,111]. Bandy and van Rooyen [85] pointed out the similarity between the caustic SCC and the primary water SCC as to the microstructural dependence and the active-passive transition behavior. Garud and McIlree [111] showed by comparing the activation energies that the mechanism is different from that controlled by hydrogen diffusion process. They also emphasized the importance of strain rate in the mechanism. Due to difficulties in mechnistic studies associated with the low conductivity of water, high temperature and crack detection, supporting evidences for the FRM mechanism are not sufficient.

Surface Mechanism (SM)

This mechanism, originally proposed by Petch [112], was first applied by Uhlig [113] to explain the specificity of environment-material combination for embrittlement. Crack initiation as well as propagation are assumed to be caused by the decreased surface energy due to adsorption of specific deleterious species which include Cl^-, F^-, SO_4^{--}, NO_3^- and several liquid metals. Hence, the surface active species should be available at the crack tip for the mechanism to operate. If anionic species are, as usual, involved Uhlig suggested that cathodic polarization would retard the embrittlement.

Uhlig also pointed out the role of stress in the context of SM. Fresh surfaces injected by the strain are suggested to promote the adsorption of those species. The stress-sorption mechanism can cause a brittle fracture with little amount of global deformation. In the high purity water, the surface active species may include oxygen, metal hydroxide as well as water molecule. The relevance of the stress-sorption or SM will be examined later in Chapter 7.

2.4.2 Hydrogen Embrittlement Mechanism (HEM)

The HEM is a complex and multiple parameter phenomenon. There are vast amounts of literature regarding the detailed microprocesses of this phenomenon. The present review on HEM is focussed specifically on nickel-base alloys and water environment systems. The microprocesses are discussed in four steps: 1) hydrogen generation in water; 2) hydrogen adsorption; 3) hydrogen transport and 4) fracture.

Hydrogen Generation in Water

Hosoya et al. [57] showed the possibility of microstructural galvanic coupling between electrochemically different phases near grain boundaries. The cathodic reaction is expected to occur in a close proximity of the grain boundaries due to low electrical conductivity of the pure water [114]. The overall reaction rate is governed by the slower step between the anodic and cathodic reactions which is yet undetermined for the nickel-base alloys.

Wei et al. [115] described the microprocess of hydrogen generation from water vapor as the result of reaction with active cementite (Fe_3C) on the prior astenite boundaries in 4340 steel. Chemisorption of water vapor is found to occur very rapidly and subsequent metal/water reaction was identified as the rate controlling step with an activation energy of 8.5 ± 3.3 kcal/mole. This activation energy agrees well with that of the crack growth rate. This also supports their belief that the hydrogen generation rate is governed by the anodic process. The temperature dependence of metal/water reaction holds through 180 C but the crack growth rate data in water environment is published for a temperature only up to 80 C [116].

Based on the study of delayed failures in 18% Ni maraging steel, Asayama [117] suggested that Ni_3Ti precipitates would react with water vapor to produce hydrogens. All of these investigators agree that certain active phases are responsible for hydrogen generation in water.

Hydrogen Adsorption/Desorption

The adsorption/desorption behaviors of hydrogen was recently studied by employing an atomistic approach [118]. However, most of these works are concerned with the gaseous hydrogen environment where dissociation of molecular hydrogen is an important part of adsorption process. Although the adsorption phenomenon is different from that in water, it may be assumed that the desorption phenomenon is very similar.

The adsorption of hydrogen occurs as the result of a charge transfer reaction. For pure nickel in an acidic environment, the adsorption reaction is faster than desorption [119]. Pasco and Ficalora [120] showed that the desorption of hydrogen is accelerated by plastic strains. The creation of catalytic sites by dislocations and surface diffusion to the sites are suggested as the rate controlling step. This explanation is reasonable since the desorption reaction is kinetically dependent on the crystallographic direction of surfaces [121] and dislocations can generate favorable surfaces. Based on surface diffusion analysis, Pasco and Ficalora [120] showed that the crack growth rate in 18% Ni maraging steel is controlled by the desorption kinetics at the upper limit of temperature.

In a passivating system, these cathodic processes may be impeded by the oxide film [122]. Since the anodic reaction is also reduced due to the film it is difficult to determine the rate controlling process. The electrochemical studies to show the individual passivation kinetics are desirable to identify the more likely situation.

Hydrogen Transport

The diffusion coefficient of hydrogen in nickel-base alloys is extremely small. There is direct evidence that hydrogens are transported by mobile dislocations at a speed much faster than the diffusion speed in a type 304L stainless steel [123]. Numerous indirect evidences and supporting theoretical evaluations has been summarized by Hirth and

Johnson [124]. In nickel, the drag velocity of dislocation core atmosphere can be as high as 1 m/sec at room temperature. A large supersaturation is found to be possible due to slow hydrogen leakage by diffusion. Traps for hydrogen are expected to achieve local equilibrium very rapidly. Hence, the trapping of hydrogen is determined by the strain and not by the strain rate.

As the hydrogen is transported by the dislocations, Eastman et al. [86] showed that extrinsic barriers to mobile dislocations can be lowered and the plasticity is increased. Since the alloys 600, X-750 and 718 contain both solute and precipitates as the extrinsic barriers, the increased plasticity may conversely support the hydrogen transport mechanism.

At 350 C, the diffusion coefficient of hydrogen in nickel-base alloys is about 3×10^{-6} cm^2/sec which is still about two orders of magnitude lower than that in iron at room temperature. This suggests that the supersaturation can be somewhat higher than that expected in the iron base alloys at room temperature.

Fracture

Birnbaum summarized the fracture mode of nickel in hydrogen environments [125]. Intergranular fracture was identified as the dominant mode whether or not the nickel hydride is formed. When the hydride is not formed but significant supersaturation can be achieved the decohesion or internal pressure theory can account for any significant ductility loss provided that the fracture surfaces contain microvoids.

Hydride formation was believed to be possible in the presence of local stress concentration [125]. As discussed earlier, Hinotani et al. [95] demonstrated that th γ hyride forms at a cathodic charging current density of 10 mA/cm^2. The γ hydride has a lattice parameter about 4% larger than matrix. Hence, stress induced hydride formation can not be ruled out at low temperature [126]. At high temperature, the hydride formation is less likely due to increased solubility of hydrogen in

the matrix and less allowable supersaturation.

Chapter 3

RESEARCH OBJECTIVES AND PROGRAM

3.1 RESEARCH OBJECTIVES AND SCOPE

The goal of this thesis is the identification of the embrittlement mechanism in three nickel-base alloys; alloy 600, alloy X-750 and alloy 718, in nuclear reactor water environments. The effect of irradiation on embrittlement is not included. High purity water is used as the base-line environment to which variations in oxygen content, electric conductivity as well as pH are made for mechanistic studies.

The literature review in the previous chapter showed that the environment assisted cracking of nickel-base alloys exhibits a specificity with respect to microstructure and environment. For a high purity water environment, a corollary may be stated that there is a microstructural specificity associated with a particular mechanism. The relation between microstructural or process variables and embrittlement susceptibility is to be established. For this goal microstructural characteristics are examined as to: 1) process-microstructure relationships, and 2) microstructure-susceptibility relationships. Mechanistic understanding and the microstructural relationship can be used to develop predictive models and to develope principles for alloy development.

Both crack initiation from smooth surface and growth from existing cracks are studied. Due to the relatively slow kinetics of crack initiation and growth, it was advantageous to use accelerated testing methods. An accelerated testing method was developed that made use of the combined application of slow strain rate and higher temperature. To determine crack initiation time and growth rate without interruption of high temperature slow strain rate tests, a sensitive crack detection technique was also developed using the skin effect of the high frequency

alternating current (AC).

3.2 EXPERIMENTAL PROGRAM

The relationship between process and microstructure was characterized for five heats of alloy 600 tubing, three heats of alloy X-750 and one heat of alloy 718. Grain boundary chemistries and precipitate morpholoy were charaterized by using optical metallography, scanning electron microscopy, transmission electron microscopy, scanning transmission electron microscopy and Auger electron spectroscopy as well as boiling nitric acid (Huey) tests. The data and understanding of the relationship between embrittlement susceptibility and process variables were also used to identify similarity and difference among alloy as to the microstructural role.

Electrochemical studys included anodic and cathodic polarization, galvanic corrosion, the straining electrode experiments as well as high temperature potential measurements. For reasons of time, most of experiments were limited to low temperature environments. Local galvanic corrosion behavior was studied by using specially melted materials designed to have simulated grain boundary chemical compositions. This task was designed to quantify realistic galvanic current densities at grain boundaries taking into account effects of surface area ratio between cathode and anode, and the effect of plastic deformation. A critical experiment was performed to clarify which process, anodic or cathodic, has the faster kinetics and is responsible for the observed low temperature embrittlement. The experiment consisted of straining electrode tensile tests and straining electrode fatigue tests under both anodic and cathodic potentials and currents, the magnitude of which was determined by the galvanic corrosion study.

The mechanical behavior of the material was determined by conventional tensile testing in the laboratory air. Effects of microstructure were determined over the temperature range between 25 C and 360 C and a strain rate range between $2x10^{-4}$ sec^{-1} and $2x10^{-5}sec.^{-1}$. The results of this task were used as the reference properties to compare with slow

strain rate test results in the water environment.

Finally, the kinetics of intergranular crack initiation and growth are determined by using the corrosion fatigue tests and the slow strain rate tests in high purity water. Corrosion fatigue tests were performed for two-step aged X-750 at temperature below 60 C. A simplified apparatus was used to allow direct visual observation of crack tip behavior. For three heats of alloy 600 and one heat from each of alloys X-750 and 718, a few conditions were selected for slow strain rate tests with a temperature range between 93 C and 350 C and a strain rate range between $1x10^{-4}$ $sec.^{-1}$ and $2x10^{-7}$ $sec.^{-1}$. Fractographic analysis was made to determine detailed surface structure in relation to microstructural characteristics and surface film compositions by using optical, scanning electron and Auger electron microscopes.

3.3 MECHANISTIC ANALYSIS PROGRAM

The results of the experimental program were integrated to identify the embrittlement mechanism of nickel-base alloys in water. Incorporating available data in the literature, detailed microprocesses of the embrittlement mechanism was analyzed in order to determine the rate controlling step. Both qualitative and quantitative kinetic models are to be developed to describe microstructural, environmental and mecahnical influence on crack initiation and growth behavior. Finally, a set of general principles is formulated for use in microstructural optimization of nickel-base alloys.

Chapter 4

TEST SYSTEM DEVELOPMENT

4.1 DEVELOPMENT OF THE SLOW STRAIN RATE TEST SYSTEM

It is known that conventional testing methods for stress corrosion cracking such as constant load or constant displacement techniques often require significant lengths of time and expense, especially for tests conducted at service temperatures. Although the test results can be used directly for design, information on mechanistic processes are often not effectively obtained. For these reasons a well characterized, accelerated test method needs to be developed.

Among several techniques for the acceleration of stress corrosion cracking, only two are considered to be appropriate in terms of maintaining true microprocesses of both initiation and propagation. These are: (1) an application of a slow strain rate [111] and, (2) an elevated temperature test [44]. It was the author's belief that a system incorporating the synergistic effects of these two factors would be capable of both an acceleration in test time and at the same time allow for comparison of the SCC susceptibility of various materials as well as allowing a mechanistic understanding of the phenomena. Therefore, one of the major goals of this project was to develop a slow strain rate test (SSRT) system which was capable of testing at temperatures up to 350 C with high sensitivity to detection of crack initiation. This development work was a significant portion of this project.

The developed SSRT system was combined with an AC potential drop (ACPD) system for crack detection. The system allows testings at a minimum strain rate of $1x10^{-7}sec^{-1}$ in various water chemistries at 350 C and pressures up to 18.3 MPa. The system consists of seven subsystems, as follows:

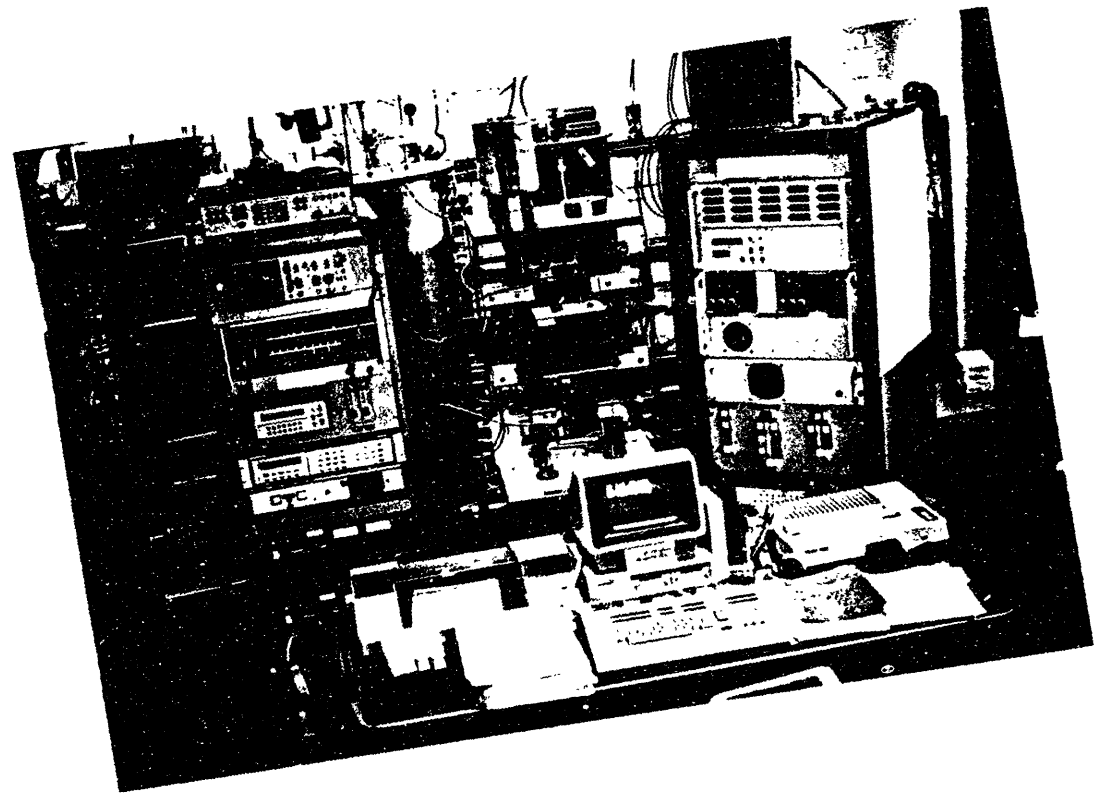

Figure 4.1 Overall View of the Slow Strain Rate Test System (left side ACPD system, central autoclave system, right side test control panel and back side water system).

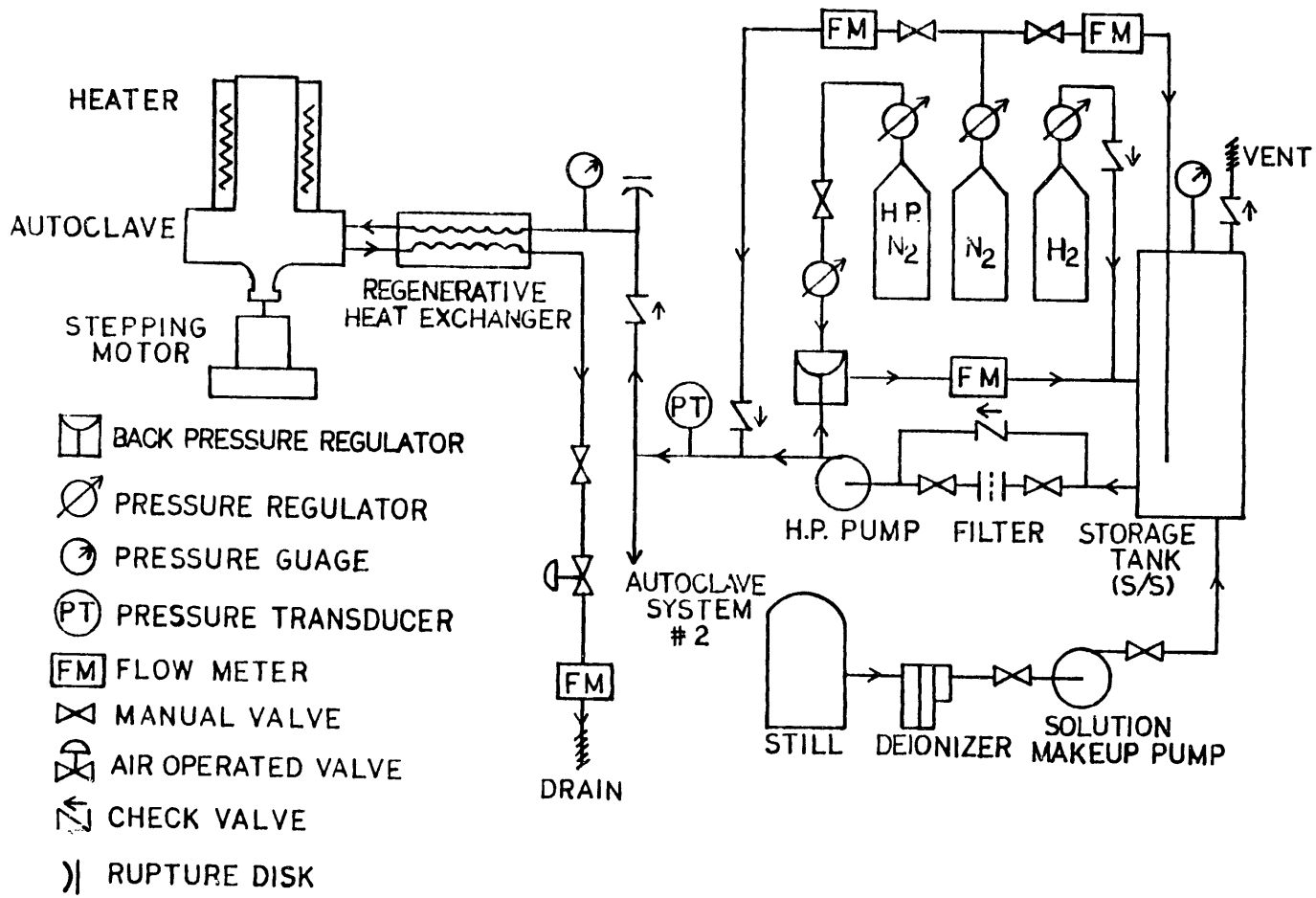

Figure 4.2 Schematic Diagram of the SSRT System Water Flow.

1) Water treatment system
2) High pressure pumping system
3) High pressure autoclave system
4) Tensile test system
5) Data acquisition and control system
6) Safety system
7) AC potential drop system

The design description of the SSRT system is presented in this section. The ACPD system also required major development work. Hence, a detailed characterization of the ACPD system is dealt with separately in the next section. An overall view of the test system is shown in Figure 4.1. A simplified diagram of the system is shown in Figure 4.2.

Water Treatment System

Distilled water is deionized and transferred to a stainless steel storage tank. The oxygen concentration in water is adjusted to the desired value by bubbling gases with controlled composition and/or the use of a pressurized cover gas. To simulate PWR primary chemistry, the storage tank was pressurized by a hydrogen cover gas at 0.177 MPa. The water chemistry, including oxygen concentration, pH and conductivity are frequently monitored.

High Pressure Pumping System

The high pressure pumping system takes water from the storage tank. A Pulsafeeder Co. Model 680-S-E diaphragm metering pump maintains system pressure in combination with a back pressure regulator, of up to 20.7 MPa. The back pressure regulator acted both as system pressure regulator and pulsation damper.

High Pressure Autoclave System

The autoclave system consists of two one-liter type 316 stainless steel autoclaves and associated internal load reaction structures. The design of the autoclave system was patterned after a high temperature corrosion

fatigue test system developed by Ballinger [127]. The inverted autoclave system design keeps the head cool enough to allow the use of teflon sealants for all penetrations through the head.

The autoclave head was designed with a neck extended from the bottom so that the seal around a pull rod could be effectively cooled by the surrounding air. In addition to the central bore for the pull rod, six penetrations were made in accordance with the Section 5 of the ASME Boiler and Pressure Vessel Code [128] for various fluid and instrumentation connections.

Temperature control was achieved using an external heating mantle in combination with a suitable controller. System flow was regulated using a throttle valve on the autoclave exit after a regenerative heat exchanger. Flow rate was measured using a flowmeter installed down stream from the throttle valve.

Tensile Test System

The tensile test system consists of a stepping motor with a gear box, a micro-step control unit, a load frame, a load train reaction cage and a stress/strain measurement device. A Korros-Data Corp. stepping motor and control unit allowed for a minimum displacement rate of 1.5×10^{-8} cm/sec. Linearity and smoothness in the displacement was experimentally confirmed by using a capacitance gage with an accuracy of one part in 10^6. The Korros-Data Corp. load frame was equipped with two identical test units. Each head was supported by two support columns each with a capacity of 30 kN. The load train reactor case consisted of a load reaction cage, specimen grips, pull rods, and a load cell. The load reaction cage consisted of three columns and a top plate for load transmittal. Two types of grip designs were used; one for a pin-loaded plate specimens and the another for threaded button head specimens All grips were fabricated from type 17-4 PH stainless steel. Specimens were electrically insulated from the grips by using ceramic washers which were precisely machined of high density aluminum oxide. Specimen grips were connected to an external load cell using a 1.6cm diameter pull rod.

For this design, the load exerted on the specimen due to hydrostatic pressure on the pull rod contributed to the overall load.

The pull rod surface was polished to minimize the friction load. The measured load due to friction at atmospheric pressure was only about 200 Newton. The contribution due to friction was expected to be higher at temperature and pressure. An accurate estimation of the friction force was important for accuracy in the measured stress. Two types of seals of different composition were used: (1) a glass fiber reinforced teflon (Fluorocarbon model RP208-6), and (2) an ultrahigh molecular weight polyethlene (Fluorocarbon model RP208-8). The first type of seal was used for all tests with alloy 600 specimens. The seal was found to slowly decompose during long tests at high pressure. To correct this problem, two seals were arranged in series with a 3mm separation using a Rulon insert. The arrangement resulted in an increase in friction by a significant amount probably due to compressive load exerted by the upper seal on the lower seal.

The effect of friction during high temperature tests was evaluated, and the results adjusted, by company stress strain behavior of specimens tested in air, but at the same temperature as that for the autoclave tests. The measured flow stress during the autoclave tests was always higher than its non-autoclave counterpart. It was assumed that the elevation in apparent flow stress was due to pull-rod friction. Significant elevation of flow stress was observed only for the double seal arrangement. Strain rate effects on the flow stress were not observed. The estimated friction forces for the alloy 600 tests are plotted as a function of pressure in Figure 4.3. The data shows significant scatter. Deviation from the least squeare fitted line is about 300 Newton at a pressure of 18 MPa. This variation is believed to be read due to unpredictable conditions of the double seal arrangement. The error due to the correction is thus estimated from the test-to-test variation in the measured yield strength of a given condition of alloy 600. Data analysis on the statistically significant number of specimens made in section 6 results in an estimated accuracy better than 20 MPa in the ultimate tensile strength. This represents only 3% of the relative

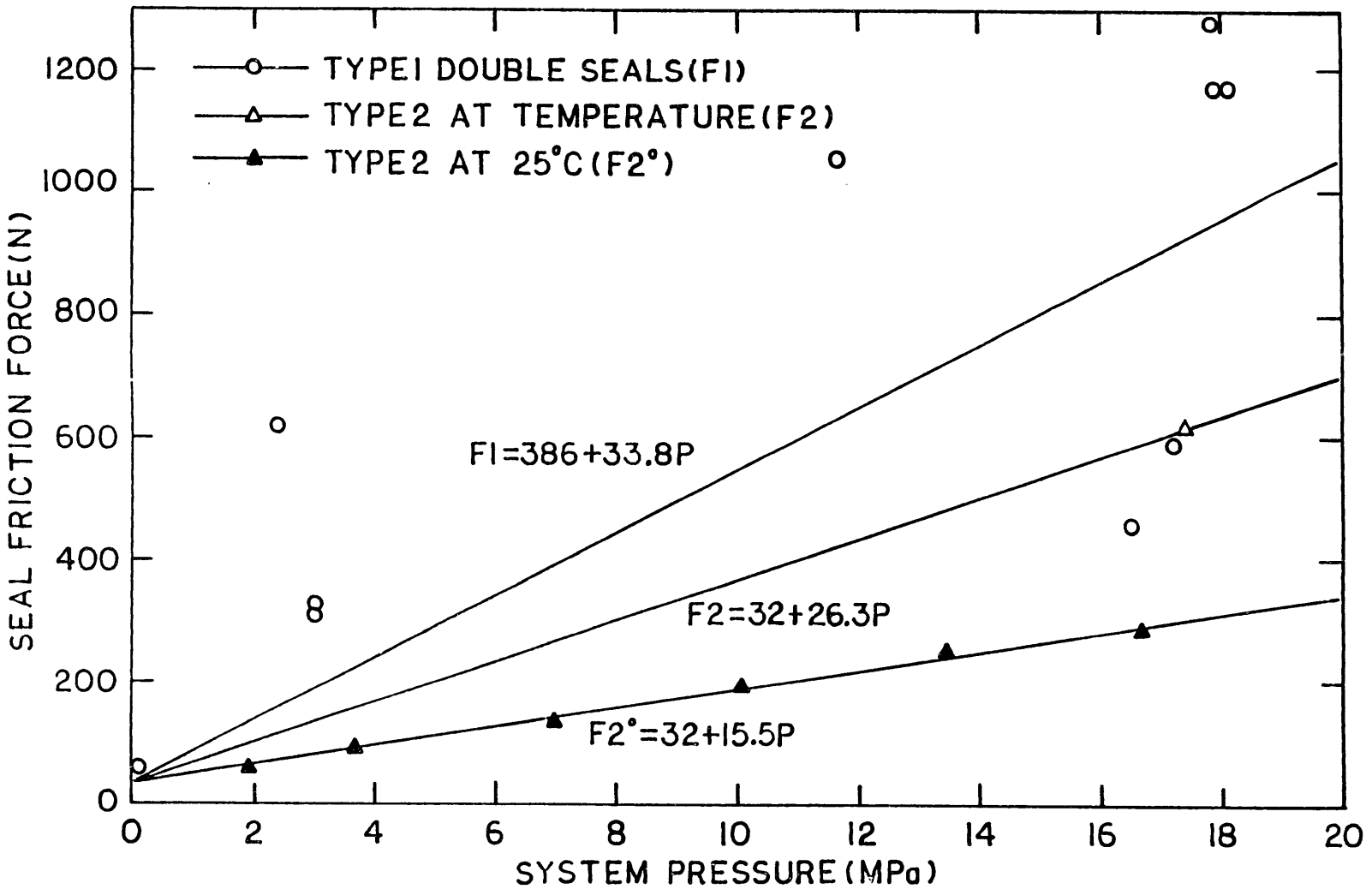

Figure 4.3 Estimated Seal Forces as a Function of the System Pressure for the SSRT of Alloy 600 (F1) and Alloys X-750 and 718 (F2) in comparison with the Measured Friction at 25 C.

error.

The friction forces involved in tests on alloys X-750 and 718 were expected to be much smaller than that for alloy 600 tests since the one seal arrangement was used. The notched specimen design used for these alloys did not show any well-defined yield strength during the SSRT as well as tensile tests. Only two specimen were tested without the notch which allowed the friction estimation. The results are compared with that of alloy 600 tests, in Figure 4.3. A linear interpolation was made to determine correction factors for a specific pressure. Due to the small amount of data, the linearity is, however, questionable. For this reason, the seal friction force was directly measured at room temperture as a function of pressure. Linearity was found to be very good, as shown in Figure 4.3. The values are, however, about two times lower than those linearly interpolated values. This is attributed to the temperature effect which is absent in the measured data at room temperature. Therefore, the interpolated values were assumed to be correct. The standard deviation from the room temperature was applied as the error of this correction. This is equivalent to an error of about 1 MPa or 0.1% on the corrected ultimate tensile strength. The error in the measured strength poses no considerable limitation of data analysis.

Another source of error in the measured strength include the calibration errors of the load cell and the pressure transducer. The load cell was found to be stable within 0.5% over a three month period after calibration which is done against an Material Testing Systems (MTS) load cell with 0.25% accuracy. The pressure calibration error is conservatively estimated to be about 1.0% or 0.2 MPa. Consequentional error is bounded within 0.02% on the measured strength. Therefore, all the combined error in the load measuring system is found to be within 4% for the alloy 600 case and 1% for the allosy X-750 and 718.

Due to the complicated design of the load train, it was difficult to estimate the strain in the specimen simply by the crosshead displacement. Therefore, the deformation of specimen gage length was directly measured by using two linear-variable-differential-transformers

(LVDTs). As shown schematically in Figure 4.4, two knife-edges were attached to the specimen with an accurately known spacing. Magnetic cores were connected to the knife-edges by using tubing of 0.32cm diameter and a solid rod of 0.16cm diameter. The core assembly was contained in a type 316 stainless steel sleeve which acted as the pressure boundary. Then the coils of LVDT were located externally on the tubing with about 3cm spacing between ends. It was necessary to use different exitation frequencies for each LVDT to eliminate interference. Frequencies of 2.5 kHz and 10 kHz were used. The knife-edges were made of a high density zirconium oxide and spring-loaded to stay on the specimen during deformation.

Data Acquistion and Control System

Since the slow strian rate test requires a considerable amount of time, it was necessary to fully automate the data acquistion and control of the test. The data acquisiton and control system consisted of a set of digital and analog electronic devices with a high reliability, as listed in Table 4.1.

Communication between digital devices were made through a General Purpose Interface Bus (IEEE-488). All analog signals except AC potential drop signal were multiplexed and connected to the 16-bit digital multimeter. Thermocouple outputs were multiplexed by an isothermal scanner and compensated with an electronic cold junction. The AC potential drop signal was digitized by a 12-bit A/D converter in the lock-in amplifier.

A computer program was written in BASIC to handle two different modes of test control; a constant load, and a constant extension rate. Each mode was divided into three stages of operation: (1) heatup, (2) test, and (3) cooldown stage controlled by a combination of manual crosshead speed switches and a remote switching of input signals to the stepping motor translator. A constant heatup rate could be maintained during the heatup stage by use of a computer interfaced relay in the heater control circuit. A test was judged to be completed by a sudden drop in load

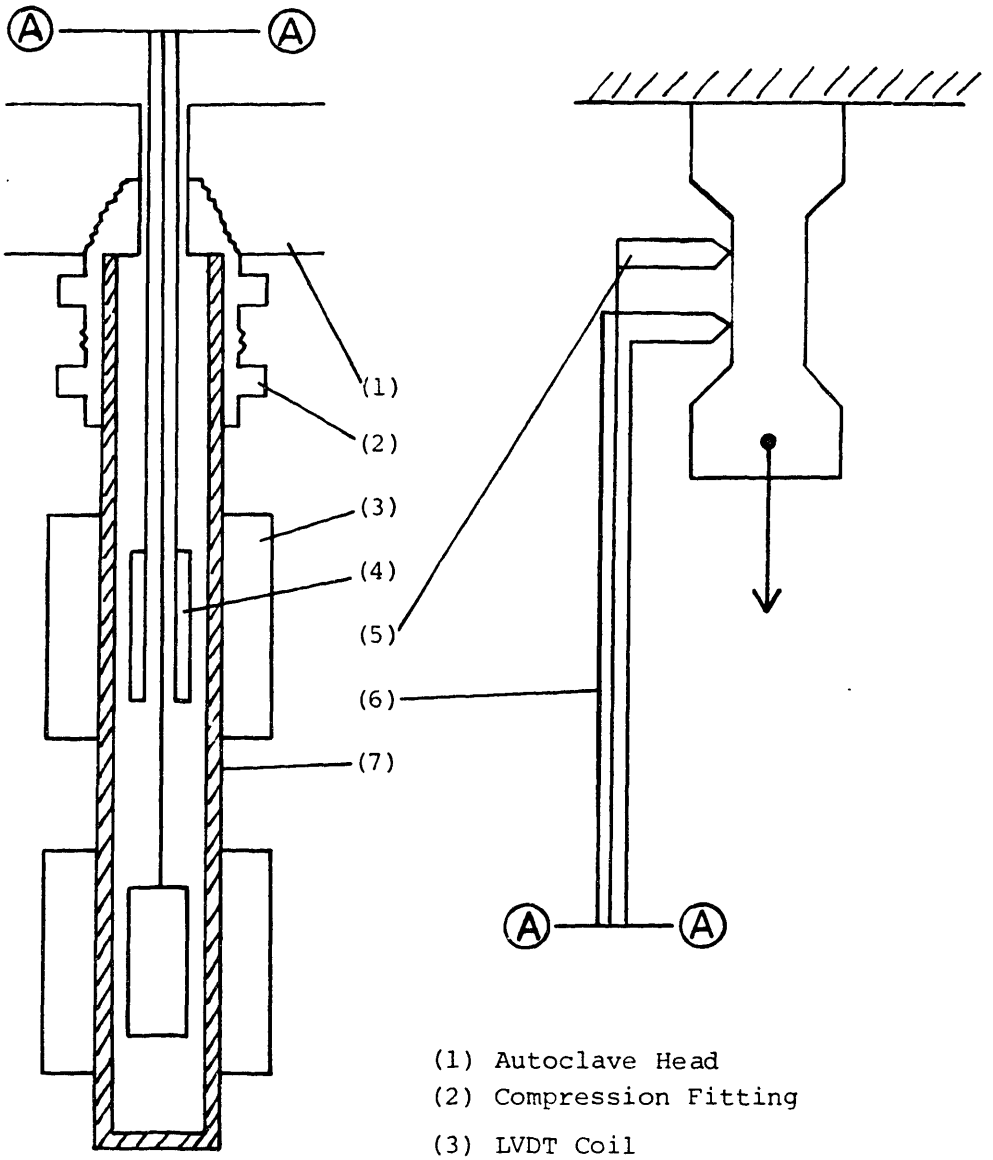

(1) Autoclave Head
(2) Compression Fitting
(3) LVDT Coil
(4) LVDT Core
(5) ZrO_2 Knife Edge
(6) S.S. 316 Connection Rods
(7) Pressure Boundary

Figure 4.4 Schematic of External LVDT Construction for Strain Measurements Using Internal Cores and Knife Edges.

Table 4.1

Computers of the Data Acquisition and Control System

Function	Model
Computer	HP9816
Digital Multimeter	HP3478A
Isothermal Scanner	HP3495A
Switch /Controller	HP3488A
Lock-in Amplifier	PAR5301
Function Generater	HP3325A
Disk Driver	HP9122
AC Current Driver	Perry Amp 465-35
AC Pre-amplifier	Perry Amp 675D
Indicating Switch Board	Home-built
LVDT Signal Conditioner	Schaevitz ATA 101
Load Cell Signal Conditioner	Korros-Data

after which an automatic transition was made to the cooldown stage. Overall flow of the computer program is shown in Figure 4.5.

Safety System

The safety system is designed to protect operating personnel and equipment from the potential consequence of excessive pressure, temperature, and loss of electric power. Each protection scheme contained a redundancy by a serial arrangement of the computer controlled relays and a set of local limit switches. The fail-safe concept was a basic principle in a logic circuit design as shown in Figure 4.6. The design basis for the safety system design is summarized in Table 4.2.

In case of a loss of electric power a solenoid valve is de-energized to open the air supply to air operated isolation valves. The system is then isolated. This is intended to protect sophisticated electronic devices from high temperature water and steam released due to loss of cooling in the regenerative heat exchangers. The electric power system is designed to remain shut off until a loss of power interlock is manually reset.

An overpressure condition is considered to be the most dangerous situation due to the possibility of a mechanical failure. Four independent provisions were made to reduce its probability. A Helicoid model indicating pressure switch was installed on the inlet side of the high pressure line at a close proximity to the autoclave. The overpressure setpoint was set at 0.69 MPa above the normal pressure. A stainless steel rupture disk with a burst pressure of 19.3 MPa was installed to allow a pressure relief through a separate drain system. In addition, the signal from the pressure transducer was monitored by the computer at every 15 seconds. The computer controlled relays was programed to shut off the high pressure pump and energized alarms when an overpressure condition was detected. Lastly, a relief valve built-in to the high pressure pump was set at 20 MPa in order to maintain the charging pressure within the system design limit

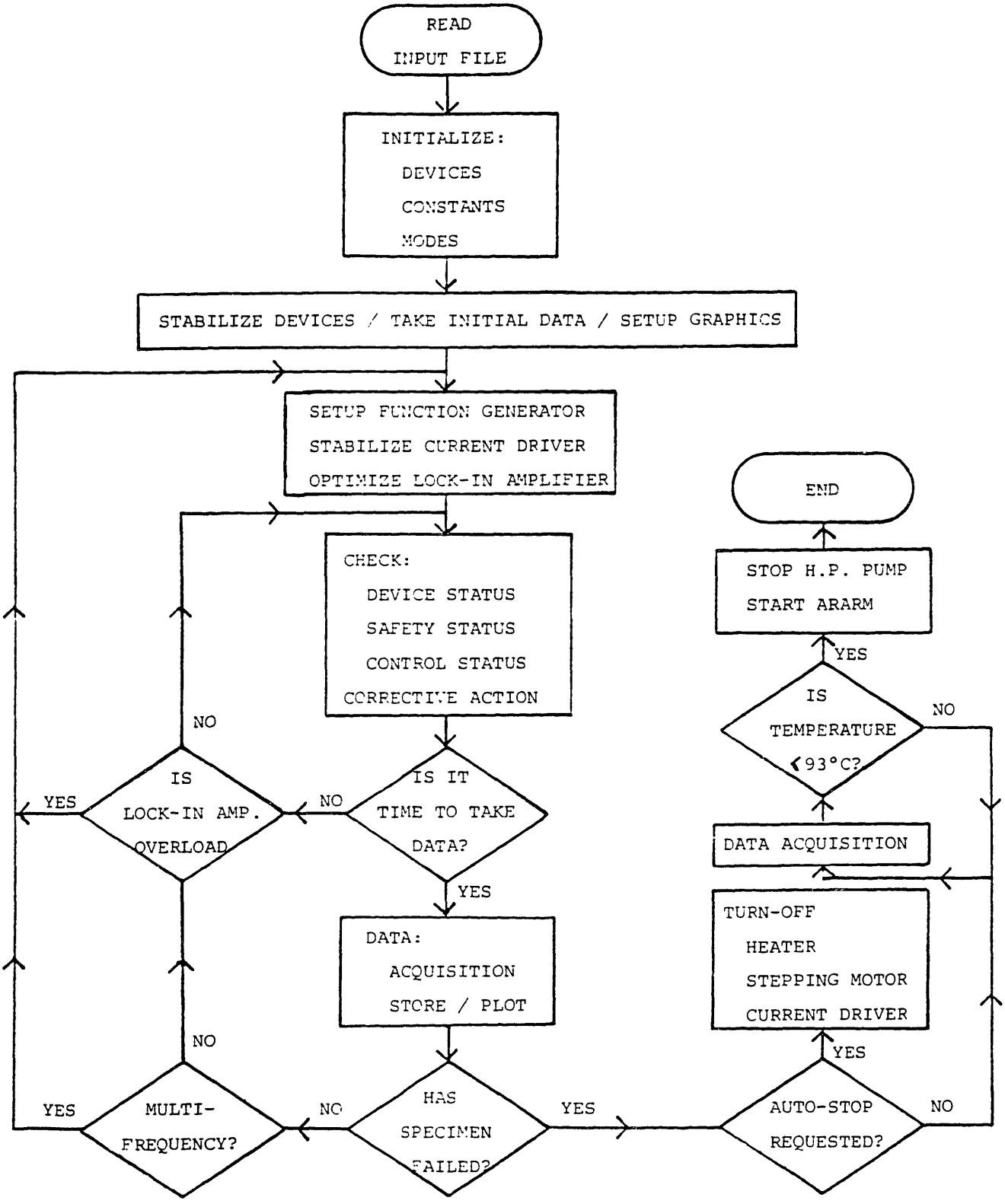

Figure 4.5 Logic Flow Diagram for the SSRT System Software.

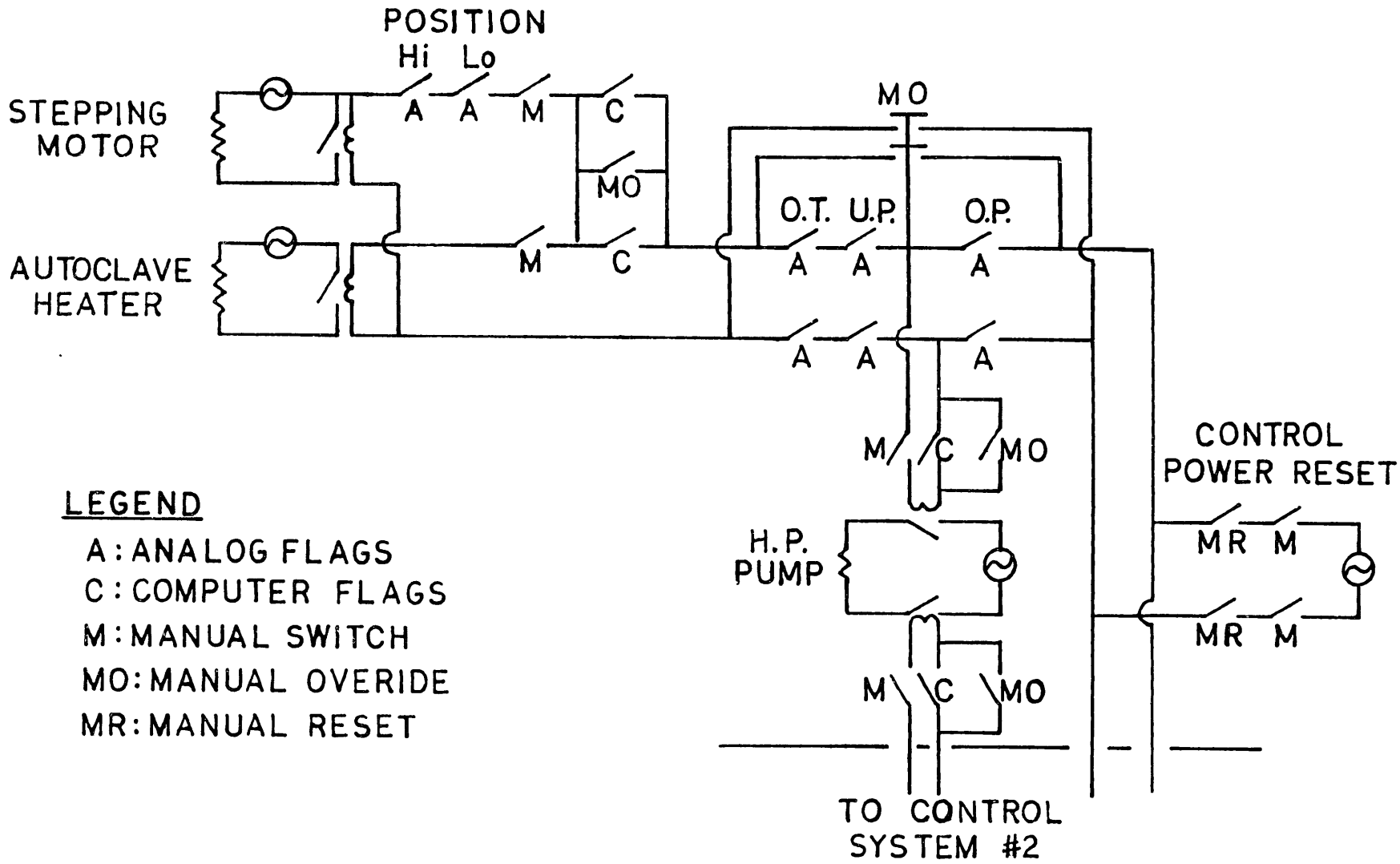

Figure 4.6 Relay Logic Circuit of the Safety and Control Panel of the SSRT System

Table 4.2

Logic Chart for the Safety System of the SSRT System

Event	Heater		Stepping Motor		H.P. Pump	System Isolation	
	Auto-clave1	Auto-clave2	Auto-clave1	Auto-clave2		Auto-clave1	Auto-clave2
Autoclave #1							
Underpressure	OFF	OFF	OFF	OFF	ON	ON	ON
Overpressure	OFF	OFF	OFF	OFF	PFF	OFF	OFF
Overtemperature	OFF	ON	OFF	ON	ON	OFF	OFF
Autoclave #2							
Underpressure	OFF	OFF	OFF	OFF	ON	ON	ON
Overpressure	OFF	OFF	OFF	OFF	OFF	OFF	OFF
Overtemperature	ON	OFF	ON	OFF	ON	OFF	OFF
Loss of Power	OFF	OFF	OFF	OFF	OFF	ON	ON

An underpressure conditon may develop as a result of either leakage through the high pressure boundary or a failure of the high pressure pump. This condition is detected by the pressure indicating switch and the pressure transducer signal which was frequently monitored by the computer. In case of underpressure the heater is turned off and an alarm is energized while the high presure pump is kept operating.

An overtemperature condition may develop due to a malfunction of the heater control unit. This condition is detected either by the high temperature detector or by an independent thermocouple output which is monitored by the computer every 15 seconds. An undertemperature condition is also checked by the computer. The heater is turned off on detection of the overtemperature condition whereas only an alarm is set off during an undertemperature condition. Values of important safety-related parameters are summarized in Table 4.3.

4.2 DEVELOPMENT OF AC POTENTIAL DROP SYSTEM

Potential Drop Techniques

Potential drop techniques are in common use for the detection of crack length in metallic systems. The most common technique makes use of DC potential drop. In this technique DC current is passed through a specimen and the potential drop between probes on either side of a crack is measured. For many systems, the DC technique is adequate. However, DC potential drop techniques have several disadvantages which make it unsuitable for use in many situations including the detection of small cracks. DC techniques, due to the relatively high conductivity of metals, often require large currents to achieve measurable potential drops. Since, in the case of DC, the current distribution in a specimen is uniform, the potential drop between two points will be proportional to the distance between these points and the conductor cross sectional area. The increase in potential drop due to crack initiation is thus due primarily to reduction specimen in cross sectional area and an increase in distance between probes.

Table 4.3

Characteristics of the SSRT System

Parameter	Value
Materials of Construction	Stainless Steel Type 316, 304 and 17-4PH
Operating Pressure	18.3MPa, nominal
Overpressure	Operating Pressure + 0.69MPa
Underpressure	Operating Pressure - 0.69MPa
Rupture Disk Break	19.3MPa
H.P. Pump Relief	20.3MPa
Autoclave System Hydrostatic Test	19.1MPa
H.P. Pumping System Hydrostatic Test	20.7MPa
Operating Temperature	350C, nominal
Saturation Pressure	16.5MPa, nominal
Overtemperature	Operating Temperature + 10C
Undertemperature	Operating Temperature - 10C
Autoclave System Flow	0.2 liter/hr
H.P. Pump Capacity	1.15 liter/hr
Storage Tank Capacity	200 liter
Load Frame Capacity	30kN
Min. Crosshead Speed	1.5×10^{-8} cm/sec
Max. Crosshead Speed	3.0×10^{-4} cm/sec
A.C. Potential Drop System Frequency	0-230 kHz
Current at 200 kHz	1.4A r.m.s.

With DC techniques, to achieve a resolution of 50μm in crack length with common specimen geometries, the variation in specimen current must be less than $\pm$0.01%. This degree of stability is easy to achieve for small currents. However, for a steel with a resistance of a few micro-ohms, the current requirements are on the order of 30-50A. Stability of $\pm$0.01% for this case is more difficult. In addition, for maximum sensitivity, it is important that probes be located as close to the crack faces as possible. This presents problems if the crack initiation site or sites are accurately not known.

A potential concern with the use of electric current in the crack detection system is its possible effect on corrosion behavior at crack tips. Crack closure due to the buildup of conductive oxides or deformation may lead to a situation where stray current can polarize the crack tip environment. Although no quantitative evaluation for the effect is possible, it was believed to be important to minimize this effect. Electrochemical studies on a free surfaces have shown that the effect of stray current on corrosion decreases with increasing frequency [129]; above 10 kHz, the effect is negligible. Hence this provides an important incentive to use an alternating current potential drop (ACPD) technique for crack detection as was the case in this study.

In the past, thermoelectric signals from the thermocouple junction between the probe and speciment have been a limitation with the DC technique. This problem can be solved by employing compensation techniques. On the other hand special compensation is not required in the ACPD technique since only a narrow band of desired frequency can be easily filtered for a signal. In a space-efficient test system such as this SSRT, smaller number of probe wires is beneficial. On the positive side, it should be noted that DC techniques require much lower installation cost and less technical expertise for operation.

AC Potential Drop

The major difficulty, involved in the studies on the initiation of short

cracks is one of limited sensitivity. AC potential techniques have the potential for higher sensitivity, for a given current, that DC techniques. The source of this increased sensitivity is illustrated in Figure 4.7 and as follows. For a round bar geometry, as illustrated in Figure 4.7 the current distribution can be represented by the following relationship.

$$I(r) = \frac{C}{r} \exp\left[- \frac{R - r}{\delta} \right] \qquad (4\text{-}1)$$

where r is the radial position, measured from the center; C is a constant, R is the specimen outer radius, and δ represents the so called "skin depth" and is defined by the relationship

$$\delta = \frac{1}{\pi f \sigma \mu} \qquad (4\text{-}2)$$

where,

f = current frequency (Hz)
σ = material electrical conductivity (Ωm^{-1})
μ = magnetic permeability (H/m)

Inspection of Eq. (4-1) shows that, as the skin depth decreases, the current distribution skews to the outer radius of the conductor. The major variables affecting δ are frequency, electrical conductivity, and magnetic permeability. Table 4.4 shows values for σ and μ for selected materials. As the skin depth decreases and the current distribution shifts to the surface of the specimen, the potential drop for a given probe spacing increases for a given total current. This phenomenon allows for increased sensitivity to the presence of surface defects, such as small cracks. For a material such as carbon steel, an appreciable effect is observed even at low frequencies. For austenitic materials such as stainless steels and nickel base alloys, one must go to higher frequencies to take advantage of the skin effect. Operation at high frequencies (>50 kHz) has, in the past, been difficult, due to

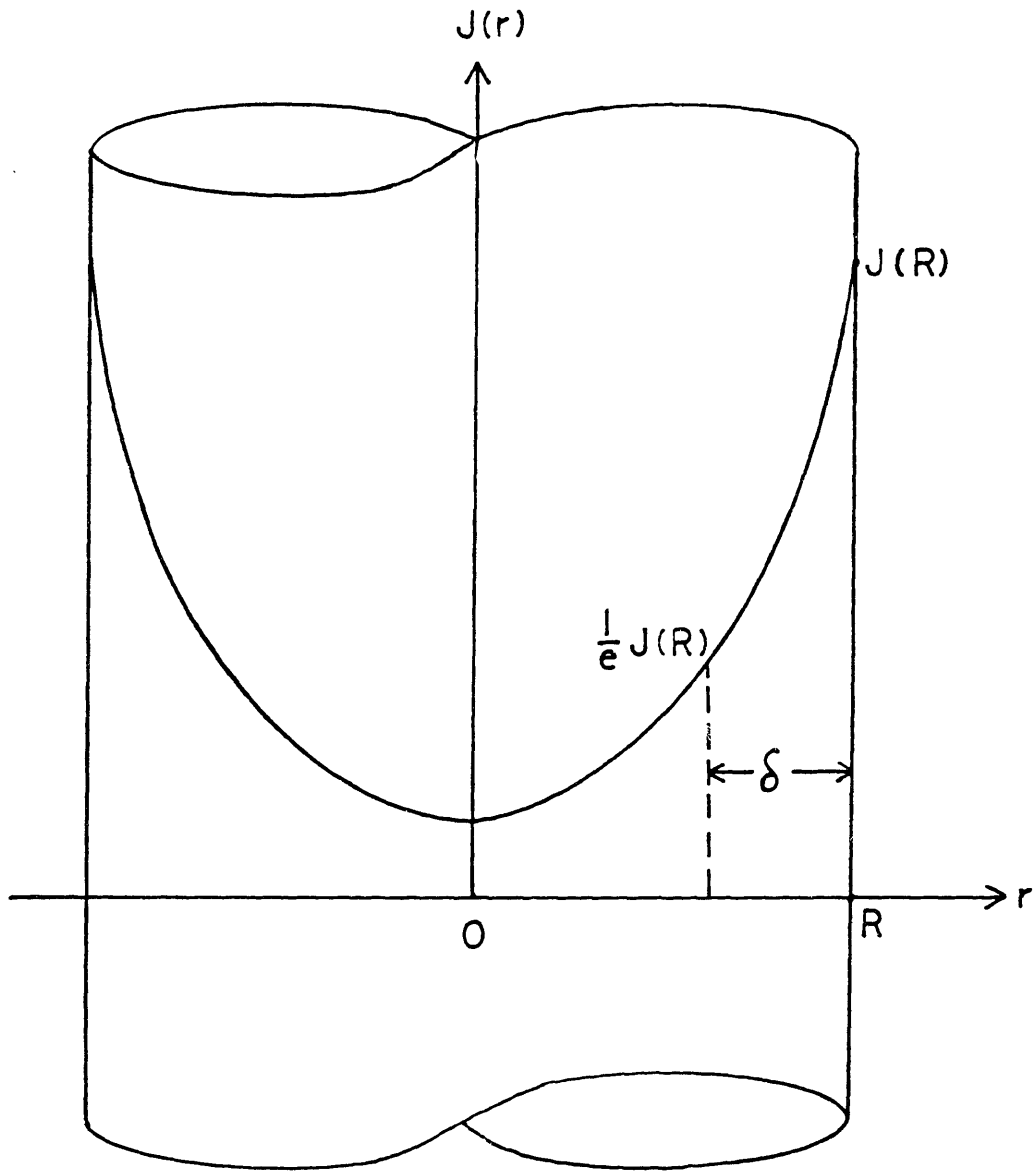

Figure 4.7 Definition of Variables Used in the Skin-effect Analysis of a Round Bar Geometry.

noise problems associated with interference. Recent advances in electroncis have resulted in the development of highly stable, high resolution lock-in amplifiers capable of AC voltage measurements in the nanovolt range. These developments of narrow band filtering techniques have greatly reduced the noise problem. In addition, the cost of these devices, while initially quite expensive to pose a disadvantage with respect to DC methods, becomes a less significant problem. The addition of microprocessor control and multifrequency capability has also expanded the capability of these instruments. Improvements in instrumentation allow operation at higher frequencies than previously used. This is significant since incresaed frequency is the only alternative for increasing senstivity in non-magnetic materials such as stainless steels and nickel base alloys as evidenced by the Eq. (4-2) and illustrated in Table 4.4.

Multifrequency ACPD System Development

An ACPD system was developed by the author as a part of this thesis. A sensitivity of about 50μm in the crack depth has been achieved to date. There is plenty of room for further increase in the sensitivity so that the initiation as well as propagation of short cracks <50μm can be monitored. Figure 4-8 shows a schematic of the system.

The major components of the system include: (1) a high stability AC current driver, (2) a high sensitivity microprocessor controlled lock-in amplifier, (3) associated microprocessor, printer, and data storage, and (4) a high frequency function generator. The potential drop system was incorporated with the slow strain rate testing system to form an integrated system for the studies of environment assisted cracking. The ACPD system was, therefore, also adapted for use at high temperatures and pressures typical of LWR systems. Probes and current lead wires were made of the same material as specimens in order to eliminate thermocouple effects and galvanic corrosion.

The developed system has several advantages over existing ACPD systems. A major advantage is its multifrequency capability. With this

Table 4.4

Physical Constants for Selected Material

Material	$\sigma(\Omega m)^{-1} x10^{-6}$	$\mu(H/m) x10^{-6}$
Ti	1.12	1.25
Zr	2.2	-0.45
In-600	0.97	0.4
In-X-750	0.80	0.4
Stainless Steel	1.4	0.4
Copper	50	0.4
Aluminum	25	0.4
Steel (0.7% C)	5	80

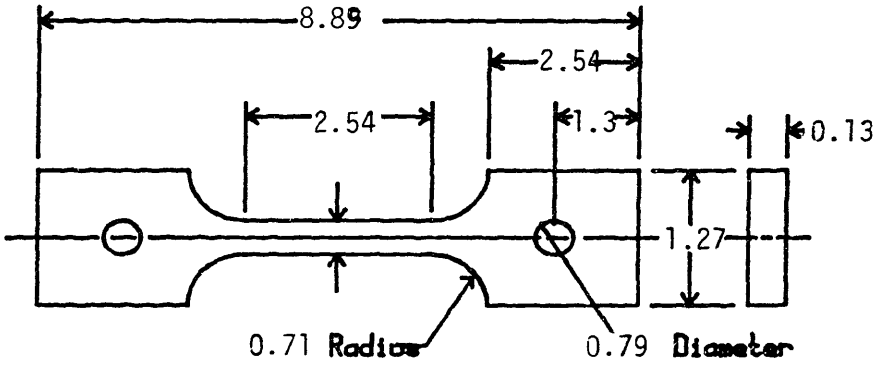

Figure 4.8 Geometry of the Alloy 600 SAS Specimen used in the ACPD Sensitivity Study.

capability it was possible to adjust skin depth during a test and thus, maintain sensitivity as microcracks initiate and grow. High frequency capability allows its use with nickel base and stainless steel alloys. The present system has a maximum operating frequency of 230kHz with corresponding skin depth of about 0.2μm for alloy 600 and x-750. Current staability is 0.5% over a 24 hour period which results in an output stability of 0.1% at 200 kHz. The resultant sensitivity is such that the probes may be placed 1 cm apart and still detect crack initiation at 100μm depth. The frequency used in this system was much higher than any other ACPD system described in the open literature. Further increase in the frequency has been unfavorable for several reasons. Primarily, no lock-in amplifier with multifrequency capability is commercially available for use at the higher frequencies. A single frequency lock-in amplifier is available for use up to 50 MHz. However, due to a lack of optimization and automation features, its application is limited. Noise and signal interference is also expected to be a serious problem at higher frequencies. Coherent noise due to induced currents increases with frequency due to ground loop current induced in probe wires.

Theoretical Analysis on Potential Drop and Current Distribution

It can be shown that a conducting medium passing an AC current, I(t), can be represented by

$$I(t) = I_o \, e^{j\omega t} \tag{4-3}$$

and has an electric field equation as follows;

$$\nabla^2 E(\vec{r}) + k^2 E(\vec{r}) = 0 \tag{4-4}$$

where,

$k^2 = -j\omega\sigma\mu = j^{3/2} \omega\sigma\mu$

E = electric field at position $\vec{r}$ with time dependence $e^{j\omega t}$ omitted.

The solution for the electric field, $E(\vec{r})$ supplies us with valuable pieces of information. One is that the internal current density distribution determined by Ohm's law:

$$J(\vec{r}) = \frac{1}{\sigma} E(\vec{r}) \tag{4-5}$$

shows a dependence of skin depth on physical parameters. This information is essential to optimizing experimental conditions. In addition the theoretical potential drop,

$$\Delta U = \int E(\vec{r}) \cdot dl \tag{4-6}$$

is obtained with explicit parameteric dependence. This expression is a guide to design a good probe system, to explore calibration techniques and to analyze data. Two specimen geometries are considered here, a rectangular bar and a round bar which represent the majority of tensile-testing-specimen designs. In the rectangular bar with 2A by 2B cross section. The solution to Eq. (4-4) requires boundary conditions which are too complicated. Hence the simpler result for the round bar geometry is used as a first approximation.

$$E(x) = \sum_{n=o}^{\infty} C_n \cos kx_y \tag{4-7}$$

where the coefficient C_n is the proportionality constants and k is the eigen value.

The current density and potential drop are determined as follows,

$$J(x) = \sigma \sum_{n=o}^{\infty} C_n \cos kx \tag{4-8}$$

$$\Delta U(x=A) = \sigma L \sum_{n=o}^{\infty} C_n \cos k A \qquad (4\text{-}9)$$

where L is the axial spacing between probes.

In a round bar specimen of radius R, it can be shown that a general expression of the field is,

$$E(r) = \frac{I_o \sigma \kappa}{2\pi R} \frac{J_o(kr)}{J_1(kR)} \qquad (4\text{-}10)$$

where J_o and J_1 are the zeroth and the first order Bessel function of the first kind, respectively. There are computational reasons that suggest that a series solution is preferred to Eq. (4-10). Solutions of this type are,

$$J(r) = \frac{I_o}{\pi R^2} \frac{\sum_{s=o}^{\infty} \frac{J^s}{(s!)^2} (\frac{\omega \sigma \mu}{4} r^2)^s}{\sum_{s=o}^{\infty} \frac{j^s}{s!(sH)!} (\frac{\omega \sigma \mu}{4} R^2)^s} \qquad (4\text{-}11)$$

$$\Delta U(R) = \frac{I_o L}{\pi R^2} \frac{\sum_{s=o}^{\infty} \frac{j^s}{(s!)^2} (\frac{\omega \sigma \mu}{4} R^2)^s}{\sum_{s=o}^{\infty} \frac{j^s}{s!(sH)!} (\frac{\omega \sigma \mu}{4} R^2)^s} \qquad (4\text{-}12)$$

Where J(r) is distrubution of current density as described in Figure 4.7, abd $\Delta U(R)$ is the ACPD between probe spacing L, as described in Figure 4.9. The Eq. (4-6) and (4-8) are general expressions covering from DC current to high their skin case as long as frequency is below

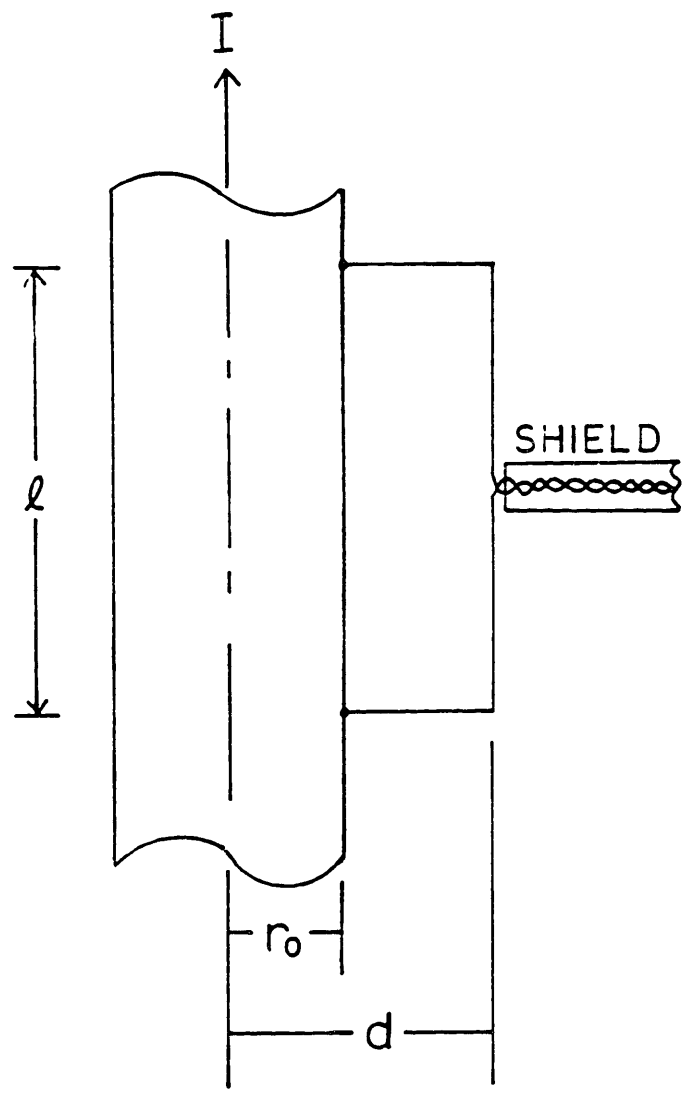

Figure 4.9 Definition of Variables Used in the Analysis of the Parasitic ACPD Due to Induced Current.

optical the region.

Effects of Elastic and Plastic Strains

The strains during slow strain rate testing result in an increase in potential drop due to an increase in the probe spacing and by reducing the cross section. A theoretical expression can be developed for the strain effect using the results of the previous section. Although the elastic strain is small, it is treated separately from plastic strain.

In a rectangular bar, dimensional changes can be expressed as follows,

$$L = L_o \exp(\epsilon_e + \epsilon_p)$$

$$A = A_o \exp(-\nu\epsilon_e - \epsilon_p/2) \qquad (4\text{-}13)$$

$$B = B_o \exp(-\nu\epsilon_e - \epsilon_p/2)$$

where L_o, A_o, B_o = original dimensions

ν = Poisson's ratio

ϵ_e = true elastic strain

ϵ_p = true plastic strain

Similiarly, a round bar specimen has expressions,

$$L = L_o \exp(\epsilon_e + \epsilon_p)$$

$$R = R_o \exp(-\nu\epsilon_e - \epsilon_p/2) \qquad (4\text{-}14)$$

where R_o is original radius.

The expression of dimensional changes can be inserted into Eq. (4-6) and (4-8) to determine the potential drop increase. Due to the complexity

of the resulting expression, a numerical evaluation is feasible only with a computer. In what follows detailed results are presented in conjunction with a sensitivity study. An approximation is, however, valuable for the thin skin case, as given by Verpoest et al.[130],

$$|\Delta U| = \frac{I_o}{2} \cdot \frac{L}{R} \quad \frac{\mu f}{\pi \sigma} \tag{4-15}$$

It is meaningful to examine the strain effect with the thin skin case. For a given frequency and current, it can be easily shown that,

$$\log_{10} \left| \frac{\Delta U}{\Delta U_o} \right| = 0.434(1 + \nu)\ \epsilon_e + 0.651\ \epsilon_p \tag{4-16}$$

For large plastic strain, it is expected that the potential drop plotted on a semi log scale, after normalization to initial value, will be a linear function of strain with a slope of 0.651, for the thin skin case. The numerical computation results to show the strain effect have also been performed for a wide range of skin depths.

Multiple Crack Initiation

Although only one or a few cracks initiate in the earliest stage of fracture, the number of density cracks, at a given time is likely to be high in most cases of environment assisted crackeing. This may be particularly true in application of the ACPD system where the probe spacing is much larger than a grain size and the average spacing between initiating cracks is likely to be as short as the grain size.

A statistical analysis of multiple crack initiation [3] shows that the density-depth profile is bell-shaped over a wide range of average crack depths. If such a characteristic profile can be obtained, the potential drop may be calculated by using the theoretical expressions Eq. (4-6) and (4-8). However, there are several reasons to prefer a simplified handling of multiple crack initiation. The agreement between theoretical results and measurements is not quantitative but only

illustrates to the functional dependence. A simpler expression between the measured potential drop and crack depth may suffice for the purpose of identifying the functional dependence. The second reason derives from the observed density-depth profile of initiating cracks in alloy 600 in both sodium tetrathionate solution and high purity high temperature water. Evidences were obtained that the density-depth profile is not widely distributed so that it can be approximated by average values of crack depth and the number density. These two parameters will be shown to allow useful parametrizations of associated variables without losing their physical significances, as described below.

The practical situation may be characterized by the multiple initiation of cracks with an average depth which is only a fraction of the skin depth. The potential drop may be approximated by the partial loss of current conduction area due to cracking. First of all the average current density in the cracking area is defined as follows:

$$\bar{J}(\bar{a}) = \left[\begin{array}{l} \int_{R_o - \bar{a}}^{R_o} J(r)\, 2\pi r dr \;/\; \int_{R_o - \bar{a}}^{R_o} 2\pi r dr \\ \int_{A_o - \bar{a}}^{A_o} J(x) dx \;/\; \int_{A_o - \bar{a}}^{A_o} dx \end{array} \right. \qquad (4\text{-}17)$$

where $\bar{a}$ is the average crack depth and $\bar{J}(\bar{a})$ is corresponding normalized current density. The cracking area may be characterized as a porous medium passing the average current density determined by the Eq.(4-17). The porosity of the area can be related linearly with the crack number density. Thus the potential drop in the prescence of the multiple crack initiation is expressed as follows:

$$\left[\frac{\Delta \cup (\bar{a})}{\Delta \cup (a=0)} \right]_{\epsilon} = C_1 \cdot \bar{J}(\bar{a}) \cdot n + 1 \qquad (4\text{-}18)$$

where C is a proportionality constant and n is the number of crackes

intersecting a straight line of 1 μm length in the current path direction. The values of average current density are determined numerically using the derived equation. The results are given as a function of the average crack depth in Table 4.5.

For a given test material and environment, it is assumed that the calibration constant can be found with a constan n. Therefore the crack depth can be predicted using the measured potential drop and the data in Table 4.5. Eqations (4-16) and (4-18) are combined to give a final expression including both the effects of deformation and cracking, as follows:

$$\log_{10}\left[\frac{\Delta \cup (\epsilon, \bar{a})}{\Delta \cup (\epsilon=0,\ a=0)}\right] = \log_{10}\left[\frac{\Delta \cup (\bar{\epsilon},\bar{a})}{\Delta \cup_o}\right]$$
$$= (C_2 + C_3)\ \log_{10}\left[\ C_1 n \cdot \bar{J}\ (\bar{a}) + 1\ \right] \qquad (4\text{-}19)$$

where constant C_1, C_2 and C_3 are to be experimentally determined for the specific specimen design and test environment.

System Verification

Due to complicated the electronic systems used for signal detection, it is necessary to make sure that the output behaves in accordance with the theoretical expectations. An alloy 600 specimen shown in Figure 4.8 was used for system verification. Input current lead wires were spot welded at both ends of the specimen. The probes made of 380μm diameter-alloy 600 wires were spot welded at the locations where two LVDT knife-edges were attached so that the probe spacing was kept accurately at 1cm for all the calibration tests.

Due to the wide probe spacing and high frequency used, there was a concern with parasitic signal due to induced current in the probe wire. Charlesworth et al. [132] derived an expression for this as follows,

Table 4.5

Normalized Surface Current Density
as a Function of Frequency and Average Depth of Multiple Cracks
as Predicted by Eq. (4-12).

Crack Depth (μm)	105 kHz	200 kHz	20 MHz
0	1.133	1.402	17.64
5	1.138	1.406	17.68
10	1.142	1.410	17.72
15	1.147	1.414	17.76
20	1.151	1.418	17.80
25	1.156	1.422	17.84
30	1.161	1.426	17.88
35	1.165	1.430	17.92
40	1.170	1.434	17.96
45	1.175	1.439	18.00
50	1.180	1.443	18.05
60	1.189	1.451	18.13
70	1.199	1.460	18.22
80	1.209	1.469	18.32
90	1.220	1.478	18.41
100	1.230	1.487	18.51
125	1.257	1.511	18.78
150	1.285	1.536	19.06
175	1.315	1.561	19.36
200	1.345	1.589	19.70
250	1.411	1.647	20.45
300	1.484	1.711	21.33

$$|U_p| = \frac{I_o M_o L f}{2} \ln \frac{d}{r} \qquad (4\text{-}20)$$

where $|U_p|$ is the parasitic potential drop, and d is height of the probes as shown in Figure 4.9. This expression was derived for a round bar specimen, but the parametric dependence is equally valid for a rectangular bar. The parasitic signal of Eq. (4-20) depends linearly on frequency whereas, at most a square-root dependence is typical for the true signal. The frequency dependence of the signal in the present system was measured and is shown in Figure 4.10. At low frequencies, the current density was uniform due to high skin depth and almost no dependence on frequency was observed. As the frequency increases above 50kHz, the skin effect began to show. The slope became constant at 0.5 as the frequency increased further from 100kHz up to 250kHz which agrees well with the theoretical true signal behavior. The noise was also directly measured by using a separate probe loop. The amplitude of coherent noise was found to be about 4% of the true signal. Therefore, the effect of induced parasitic signals was believed to be small enough in the system.

Sensitivity Measurement

The smallest crack size detectable with the ACPD system was determined by using crack acceleration in an aggressive environment. An alloy 600 steam generator tube was sensitized to facilitate easy cracking in the environment. Sensitization process consisted of an 8 minutes of solution anneal at 1100°C and an aging at 700°C for 8 hours followed by a water quench. Average grain size of the material was measured to be 75μm. The senstized tubing was cut into tensile testing specimens by electro-discharge machining so that original curvature was retained in the test section. The surface of test section was mechanically polished with a grit 600 SiC papers and finished with 1μm alumin powder. A constant load test and slow strain rate tests were performed in a solution of sodim tetrathionate which was applied to one side of the

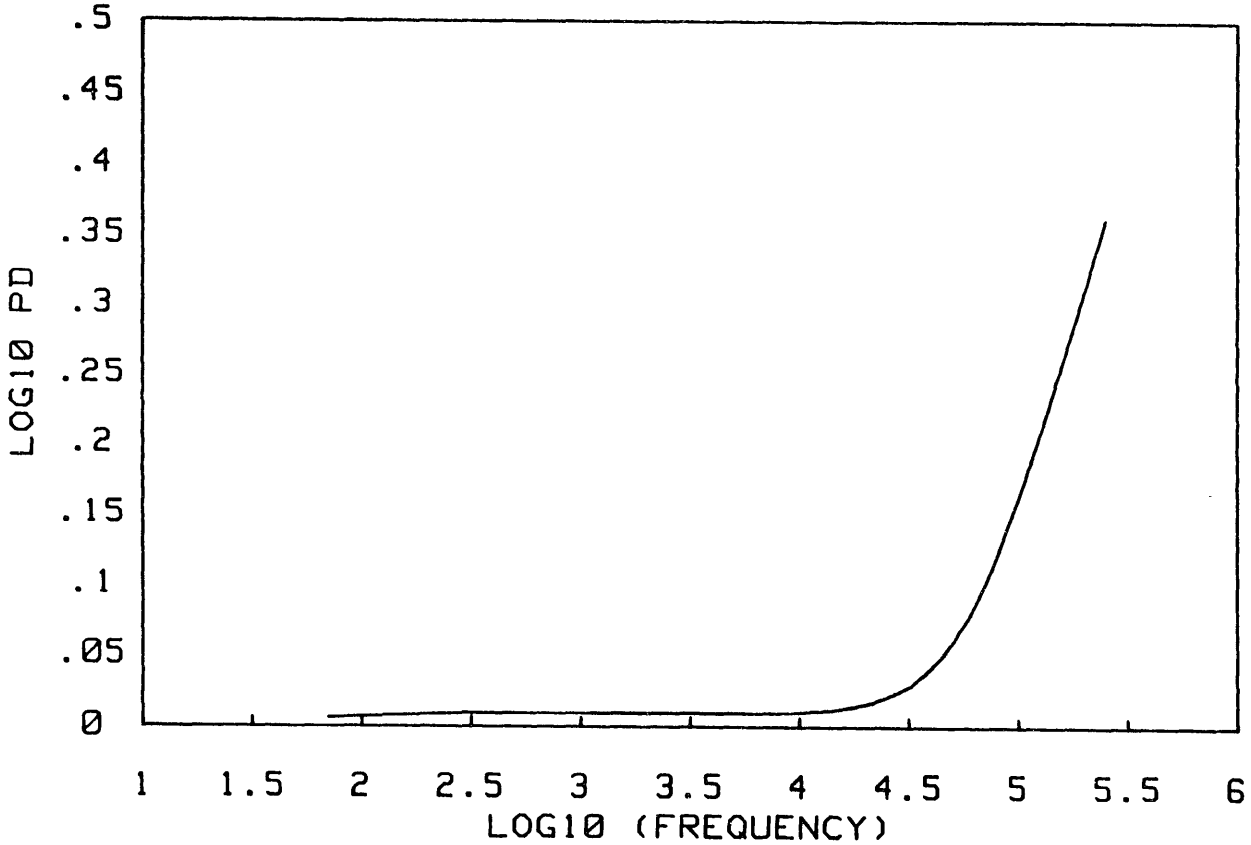

Figure 4.10 Measured ACPD as a Function of Frequency.

specimen gage length using a soaked wick [133].

Figures 4.11 through 4.14 show results of calibration tests to date, using 1.4A at 200kHz. All cracking was initiated in sodium tetrathionate at room temperature. During a constant load test, the ACPD signal begins to deviate from a steady state level as cracks initiate as shown in Figure 4.11. The test is stopped intentionally when the signal was increased by more than two times the previous fluctuation level. Optical micrographs for the cross section and side wall of the specimen are shown in Figure 4.12. The average crack depth is determined as about 50 um which corresponds to the sensitivity of the ACPD system in the constant load test mode with a probe spacing of 1cm. Figure 4.13 shows the results of two tests; one in air, the other with sodium tetrathionate solution with a 1 cm gage length. The slopes of the potential drop vs. strain plots were clearly different from the beginning of the tests. Using a least square fit the strain at which the slope increased above the reference air test case was determined to be about 3.5%. Another test was made in the identical test configuration upto the 3.5% strain so that the crack structue could be obtained. Figure 4.14 shows optical micrographs for the cross section and side wall of the latter specimen after 3.5% plastic strain. The average crack depth was 50μm which agrees well with the case of constant load. The average surface length of the cracks were measured to be about 150 um. The sensitivity of 50 um is considered to be much better than any other techniques applicable to an autoclave environment.

A tentative correlation for the sensitivity may be obtained from the above measurement. Theoretically, the crack is assumed to be detected at a 95% confidence if the ACPD with cracks is increased beyond the reference ACPD at the same plastic strain by more than two times the overall standard error. The overall standard error, s, is defined as a root-mean-square average of two primary errors including the standard error of least square fitting as a funciton of strain and that of electronic stability of the ACPD over a period of test. The standard error of fitting is typically 0.2% on the relative error scale. Electronic stability is measured to be better than 0.1% over a 24 hour

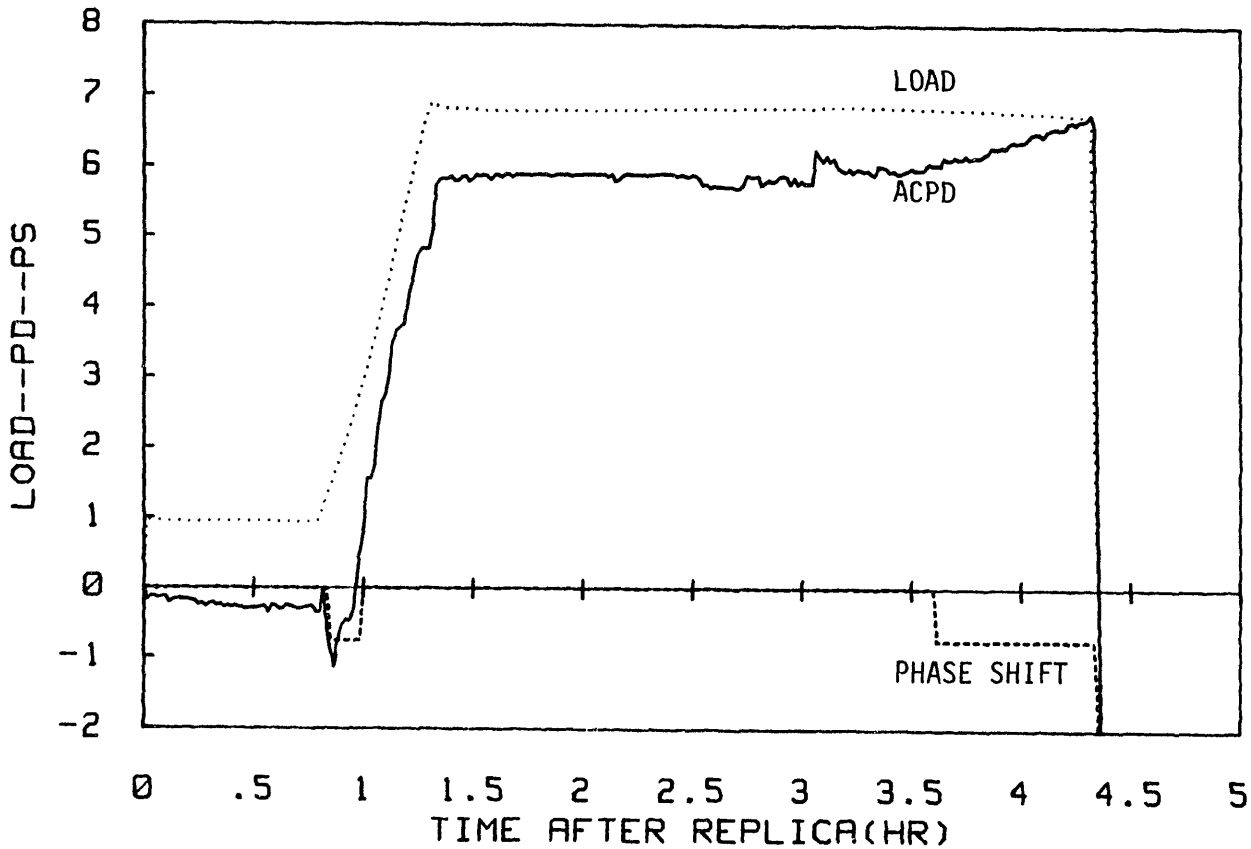

Figure 4.11 Effect of the Multiple Crack Initiation in a Sodium Tetrathionate Solution on the ACPD During a Constant Load Test on the SAS Condition of NX2650.

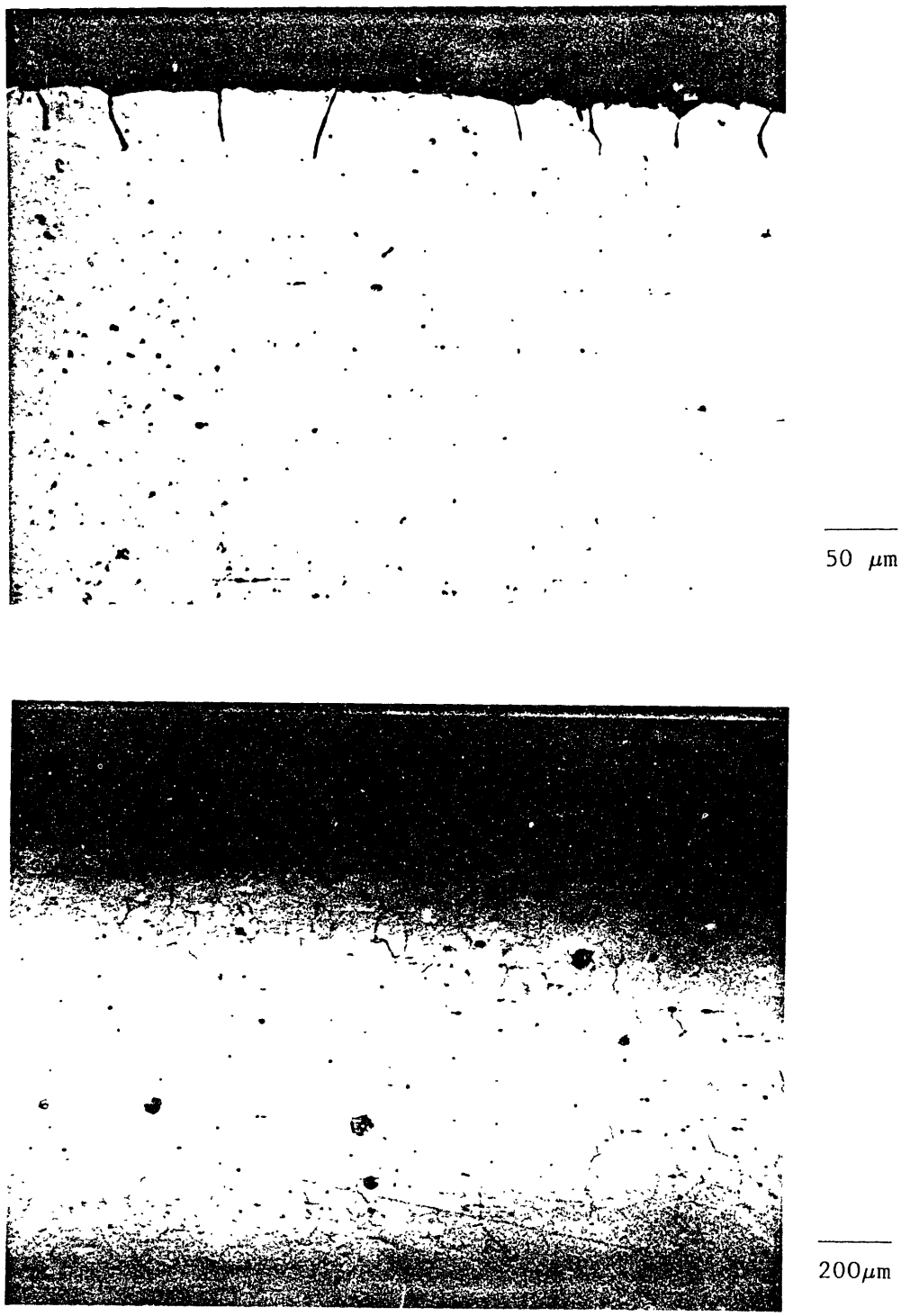

Figure 4.12 Cross Sectional and Surface View of Multiple Cracks initiated during a Constant Load Test on the SAS Condition of NX2650 in a Sodium Tetrathionate Solution

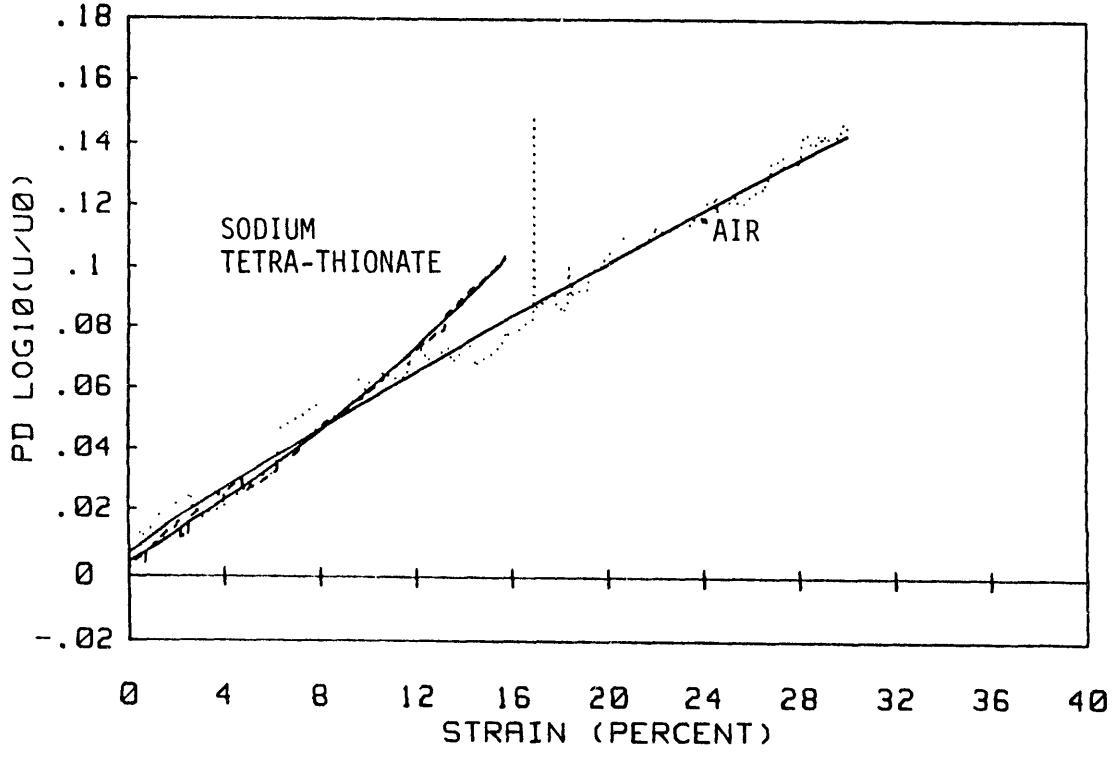

Figure 4.13 Effect of the Multiple Crack Initiation during the SSRT in a Sodium Tetrathionate Solution on the ACPD in Comparison with the Reference ACPD during Tensile Deformation in Air.

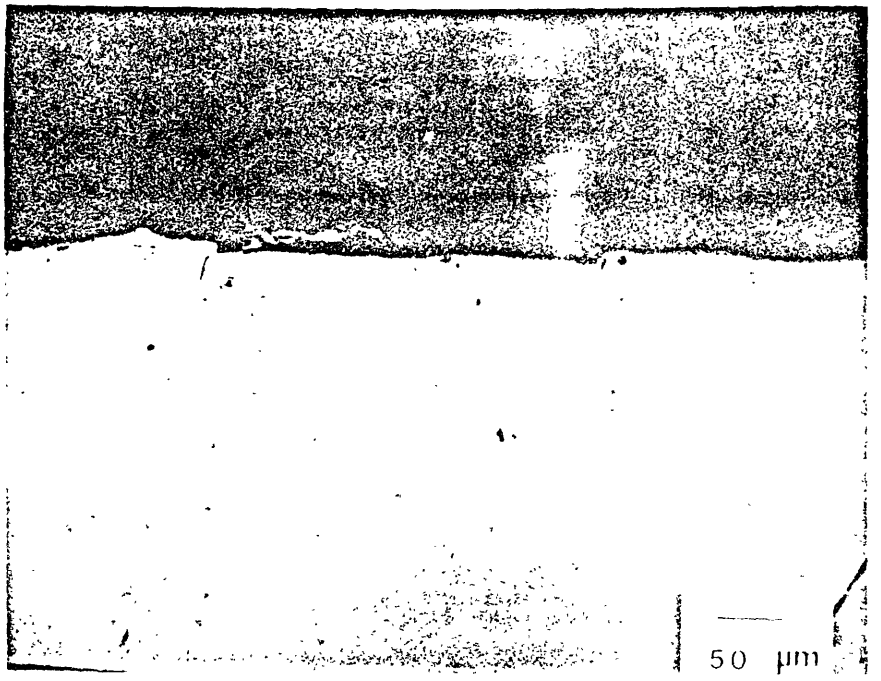

Figure 4.14 Cross Sectional and Surface View of Multiple Cracks initiated during a SSRT on the SAS Condition of NX?650 up to 3.5% Plastic Strain in a Sodium Tetrathionate Solution.

period.

Although tests at low strain rates may take a month, the stability over a five-day period is of practical interest since the ACPD are compared with the previous five-day trend as well as the reference data. Hence the standard error due to electronic instability is estimated to be about 0.5%. The overall standard error is then about 0.54%. The ACPD requirement for crack detection can be translated as follows:

$$\log_{10} \left[C_1 n \cdot \bar{J}(\bar{a}) + 1 \right] \geq 2S \qquad (4\text{-}21)$$

where S is the overall standard error determined to be 0.0054 and n is the number of cracks per 1μm of axial distance. Based on the data from the sensitivity study and values of $\bar{J}(\bar{a})$ in Table 4.5, the constant C_1 is determined to be 2×10^{-4} cm. A number of SSRT results with alloy 600 in the high purity water indicate that the crack number density is close to the calibration test case during the initiation stage. For other cases where crack density is expected to be lower, it is desirable to increase the frequency or reduce the probe spacing to maintain the required sensitivity.

Current system with multifrequency capabilty is described in Figure 4.15. It is possible to employ multifrequency technique up to 210 kHz.

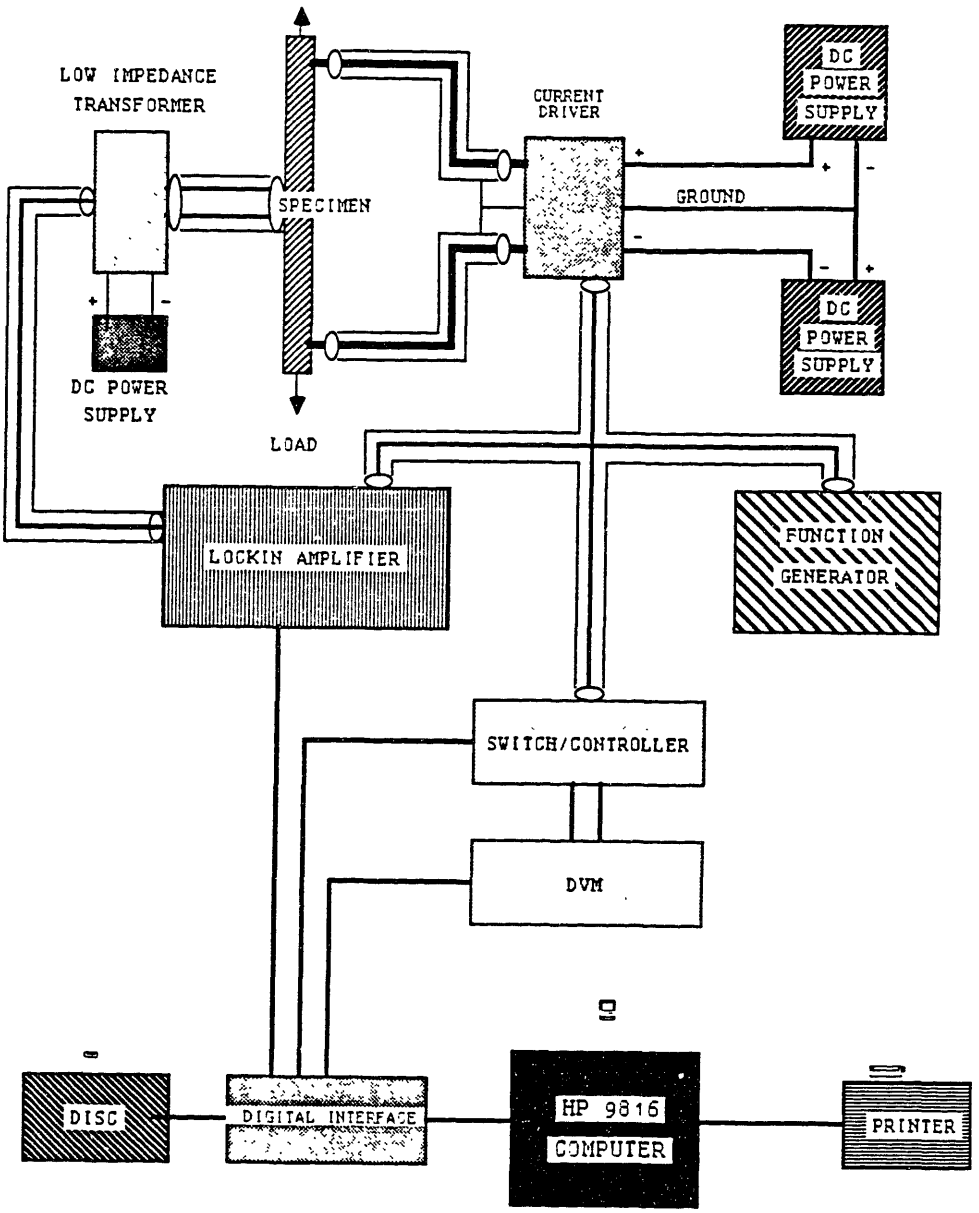

Figure 4.15 Schematic of Developed ACPD Crack Detection System.

Chapter 5

EXPERIMENTAL PROCEDURES

5.1 MATERIAL DESCRIPTION

Alloy 600

A total of five heats of alloy 600 tubing were used in various parts of the experiments. Their compositions represent typical ranges used in commercial steam generator tubing. Their chemistries are summarized in Table 5.1. The individual tubing fabrication schedules, illustrated schematically in Figure 5.1, were designed to simulate or duplicate typical vendor commercial tubing fabrication schedules. In addition, fabrication schedules were designed to encompase current as well as past fabrication practice. Basic fabrication steps included cold drawing and annealing starting from tube reduced extrusions. All anneals were performed using a conveyor furnace in a hydrogen atmosphere.

The first two heats in Table 5.1, NX1638, NX2650 were processed to 2.2 cm diameter using furnace temperatures of 1066 C for intermediate anneals and a 1024 C for final anneal. The carbon content of these two heats represent a lower and an upper bound for commercially produced alloy 600 tubings.

Heats 96834, 763675 and NX3857 were specially produced as a part of EPRI programs using two annealing temperatures of metals; 1024 C and 927 C. For these batches, designated as high temperature mill annealed, HTMA, and low temperature mill annealed, LTMA, the same intermediate and final annealing temperatures were used. In addition, for heat 96834, two final tubing diameters were fabricated for each batch (HTMA and LTMA), 1.905 cm and 2.22 cm. Optical metallographic characterization for the EPRI Specially Processed heats of alloy 600 was preformed by Takemoto and reported elsewhere [21]. Detailed characterization of grain

Table 5.1

Chemical Composition of Alloy 600 Tubing

Supplier	Westinghouse	Westinghouse	Babcock/Wilcox	Sandvik	Huntington Alloys
Heat # Wt.%	NX1638	NX2650	96834	763675	NX3857
Ni	74.68	74.83	74.93	72.49	74.29
Cr	14.95	15.06	15.86	17.02	14.41
Fe	9.60	9.27	8.08	8.77	9.40
Ti	0.22	0.22	---	---	---
Al	0.22	0.24	---	---	---
Co	0.05	0.05	0.021	0.033	0.074
Mn	0.21	0.30	0.26	0.71	0.39
Si	0.22	0.21	0.31	0.39	0.17
Cu	0.33	0.29	0.01	0.01	0.40
C	0.014	0.038	0.039	0.018	0.025
P	0.006	0.008	---	---	---
S	0.003	0.001	0.001	0.004	0.003

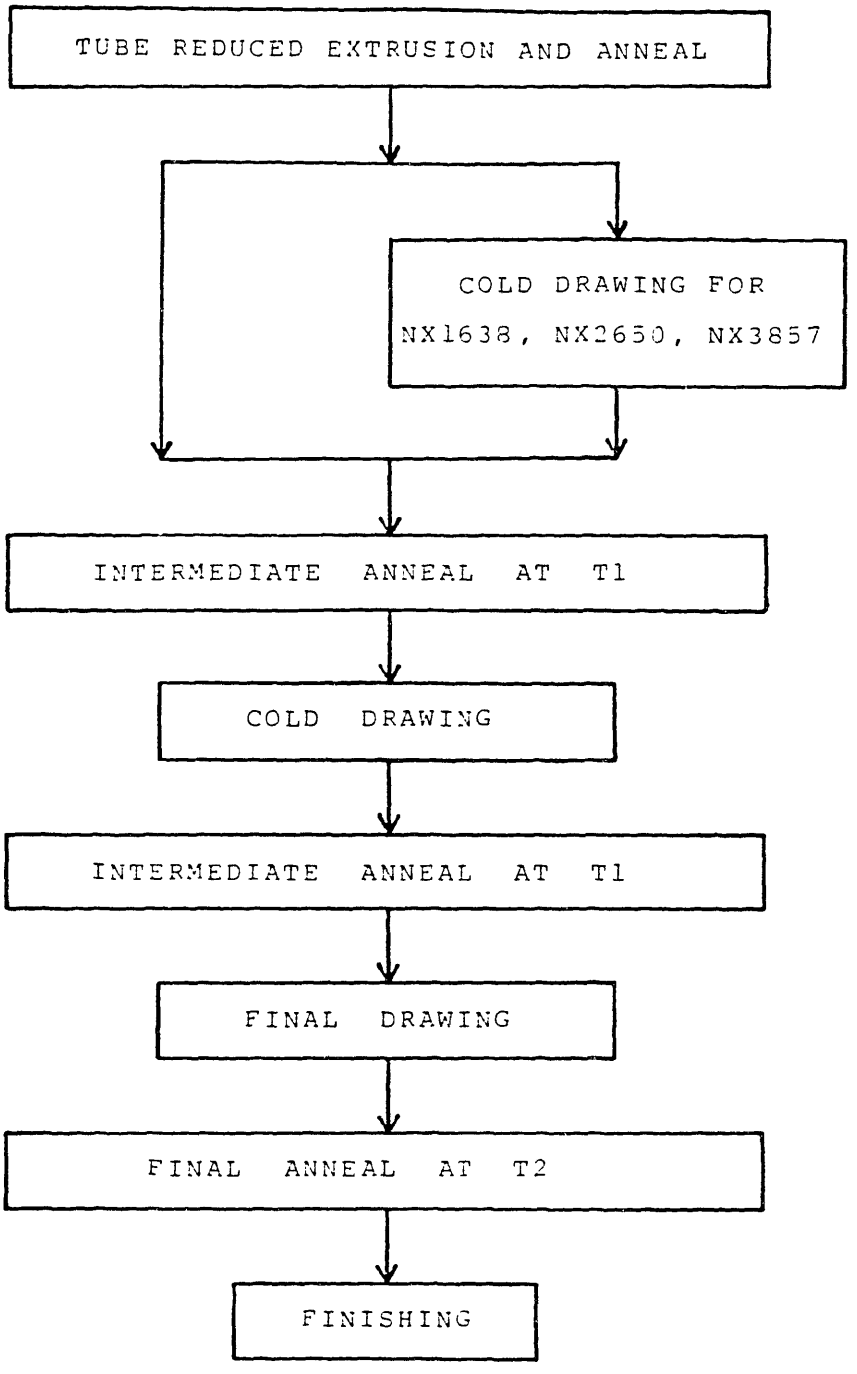

Figure 5.1 Thermomechanical Processes of Alloy 600 Mill Annealed Tubing.

boundary chemistry is made here by using STEM and AES.

Heat NX1638 and NX2650 are classified as HTMA since the furnace temperature was 1024 C during the final anneal. However, the metal temperature during anneal is lower than furnace temperature approximately by 75 to 100 C. Therefore it should be noted that these two heat had metal temperatures close to the case of LTMA of EPRI Specially Processed materials for which metal temperatures were used to control the process. Nevertheless they were designated as HTMA heats.

Alloy X-750

The chemical composition of five heats of alloy X-750, used in this study, are shown Table 5.2. The first heat, No. 96457E6, was acquired as 10 cm by 10 cm by length electroslag remelted (ESR) forging stock. The billet was then hot rolled to 1.3 cm thick, 15 cm wide plates. Initial break down of the billet was performed at 1121 C to a thickness of 7.6 cm. Subsequent passes were taken at 0.6 cm per pass with a reheat at 5 cm when stock temperature had decreased to 954 C. The billet temperature had decreased to 954 C at a thickness of 5 cm and a reheat was necessary. The second heat of X-750 was used only for the corrosion fatigue test where 3.18 mm thick plate was required to fit existing test fixtures. The 3.18 mm thick hot rolled plate was obtained from D. Duquette at the Renssaeler Polytechnic Institute. Its detailed process data was not available. Zirconium modified remelt heats contain two different Zr levels but with the same concentration of other elements. These and heat 90330 were used only for grain boundary segregation analysis.

Heat treatments used in the program are shown in Table 5.3. Three of them, AH, HTH, and HOA were selected for more detailed studies including slow strain rate tests. The remaining heat treatments were used only for microstructural studies. The AH and BH treatments have been used for LWR components. These components have experienced failure by intergranular cracking. Due to a high susceptibility to intergranular cracking, the AH condition has been studied in detail by others

Table 5.2

Chemical Composition of Alloys X-750 and 718 (wt. %)

Element	X-750 96457E6	X-750 Remelt	X-750 90330	X-750 PLATE	718
Ni	70.6	72.56	72.13	71.39	50.3
C	15.0	14.86	15.2	15.54	19.4
Fe	6.78	7.88	8.3	7.53	19.6
Ti	3.94	2.47	2.5	2.34	0.95
Al	1.23	0.57	0.8	0.67	0.43
Nb	1.36	0.90	0.8	0.89	5.2
Co	0.077	0.09	--	0.343	0.26
Mn	0.15	0.22	0.12	0.213	0.16
Si	0.09	0.16	0.11	0.13	0.21
Cu	0.10	0.01	<0.05	--	0.05
C	0.058	0.045	0.036	0.035	0.054
Zr	0.048	0.048(low Zr) 0.086(high Zr)	--	--	--
P	0.048	0.014	0.003	--	0.01
B	0.004	0.0019	--	--	0.005
Ta	0.004	--	--	0.037	0.11
S	<0.002	0.002	0.002	0.003	0.001
Mo	--	0.07	--	--	3.0

Table 5.3

Designation and Heat Treatment Schedules of
Alloy X-750 Conditions Studied.

Condition	Heat Treatment	Description
AR	As Hot Worked	Hot Rolled at 1121 C
EAH	AR + 24 Hr @ 885 C/AC*	Equalized
AH	EAH + 20 Hr @ 704 C/AC	Equalized and Aged
EHTH	AR + 1 Hr @ 1093 C/AC	High Temperature Annealed
HTH	EHTH + 20 Hr @ 704 C/AC	High Temperature Annealed and Aged
HOA	EHTH + 100 Hr @ 760 C/AC	High Temperature Annealed and Overaged
EBH	AR + 1 Hr @ 982 C/AC	Low Temperature Annealed
BH	EBH + 20 Hr @ 704 C/AC	Low Temperature Annealed and Aged
AHTH	EHTH + 24 Hr @ 885 C/AC + 24 Hr @ 704 C/AC	High Temperature Annealed Equalized and Aged

[23, 24]. The HTH condition is currently used as an improvement over AH. HOA conditions are being considered for future generations as an optimized condition.Three intermediate conditions EAH, EBH, and EHTH were used to determine the evolution of grain boundary chemistry and morphology during the heat treatment processes. The sequence and interrelationship of each condition is shown in Figure 5.2.

The chemical composition of Alloy 718 used in the study is shown in Table 5.2. The alloy 718 was obtained in the form of hot-rolled bar with a diameter of 8.25 cm. The as hot rolled materal exhibited grain boundary microstructures essentially free of precipitates due to its processing above the solvus for grain boundary phases such as Laves and delta [25]. Two heat treatments were used for the alloy 718 as follows:

1) CHT (Conventionally Heat Treated - 980 C x 1 hr/Air + 720 C x 8 hr/Furnace Cool + 620 C/Total 18 hours Aging Time):
This heat treatment is typical of alloy 718 used for high temperature service and in existing LWR components. The condition results in a fine grained microstructure with extensive grain boundary precipitates.

2) DA (Direct Aged - 720 C x 8 hr/Furnace Cool + 620 C/Total 18 hours Aging Time):
This condition was suggested by Prybylowski [26] to reduce grain boundary precipitates without grain coarsening.

Materials for Electrochemical Characterization

Electrochemical stueies of intergranular regions in nickel-base alloys were studied by using specially melted materials designed to represent grain boundary chemistries including chromium depleted regions. Intermetallic precipitates chemistries were studied as well as those representing the matrix. Chemical compositions of the materials are summarized in Table 5.4.

Two alloys, #5051 and #5052, represent the chemistry of grain boundary regions with significant chromium depletion from a normal bulk level of 15%. Such a chromium level would be obtained as a result of chromium

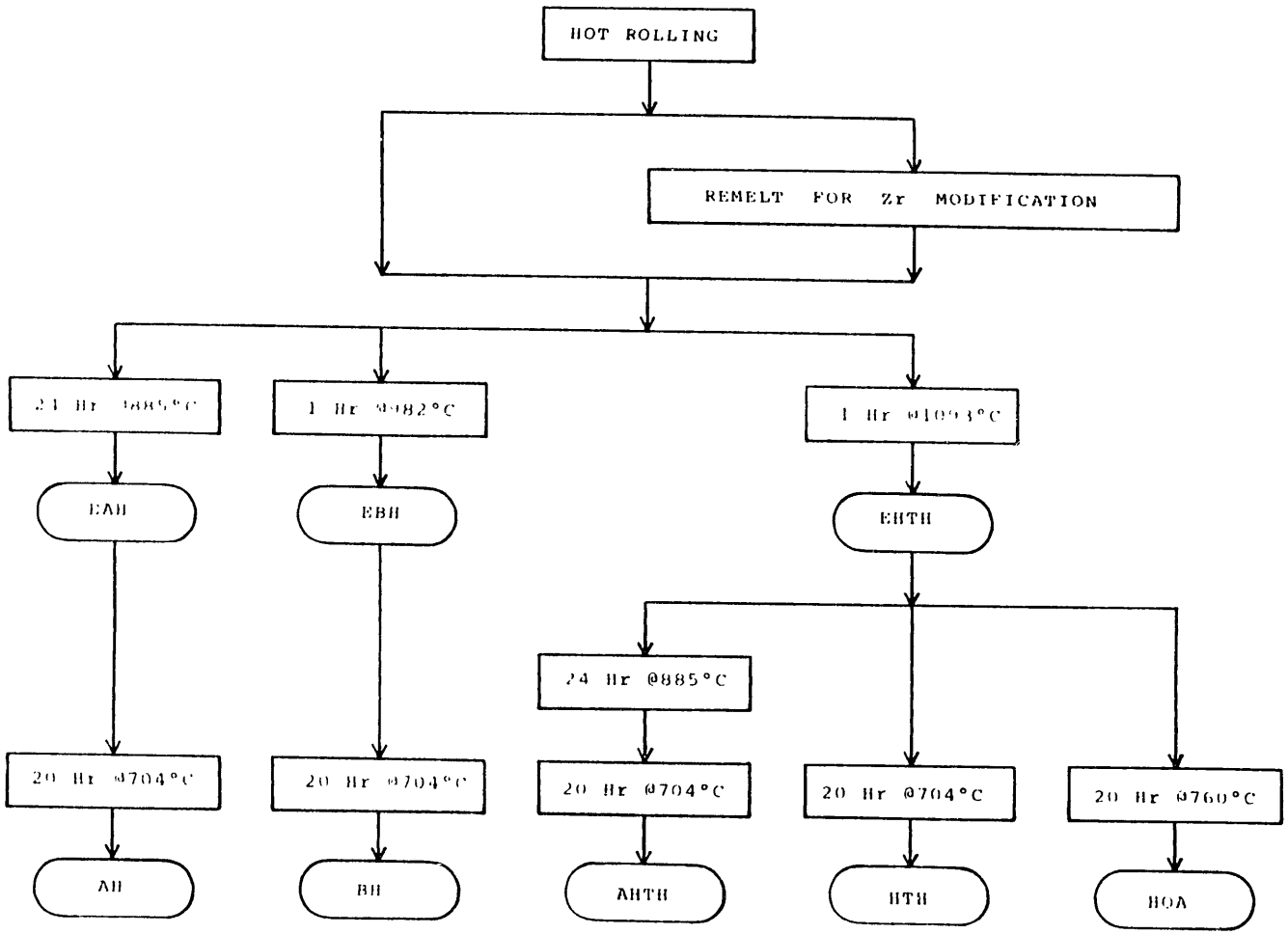

Figure 5.2 Thermomechanical Processes of Alloy X-750.

Table 5.4

Chemical Compositions of Materials for Electrochemical Characterization

Designation Wt.%	#5051	#5052	#5056	Ni_3Al(Co)	Ni_3Al(Ti=0)
Ni	82.05	79.01	73.88	75.3	86.4
Cr	6.3	9.4	15.3	0.01	---
Fe	10.0	10.0	7.1	0.48	---
Ti	1.5	1.5	2.3	---	---
Al	0.04	0.03	0.42	12.6	13.4
Nb	0.01	0.01	0.9	---	---
Co	---	---	---	11.30	---
Mn	0.02	0.02	0.02	<0.005	---
Si	0.03	0.03	0.03	0.03	---
Cu	---	---	---	---	---
C	0.018	0.012	0.012	0.17	---
Zr	---	---	---	---	---
P	0.005	0.005	0.011	<0.005	---
B	---	---	---	0.05	0.2
Ta	---	---	---	---	---
S	0.005	0.011	0.008	0.007	---
Mo	0.02	0.03	0.02	0.02	---

carbide precipitation in either alloy 600 or alloy X-750. In these heats the nickel content was increased to compensate for the lowered chromium. Solution annealed X-750 chemistry was represented by alloy #5056. These materials were provided by S. Floreen at the Knolls Atomic Power Laboratory.

The gamma prime chemistries were selected based on detailed electrochemical studies performed by Hosoya et al. [57]. These results indicated that Ni_3Al without Ti exhibits purely active anodic polarization behavior while Ni_3Al with 15 at.% Ti, which is similar in composition to that of intergranular gamma prime [23], exhibits active/passive transition in 0.05M sodium sulpfate (pH-3) solution. This chemistry is believed to approximate the crack tip environment. A small amount of boron was included to improve ductility. Gamma prime materials were obtained from K. M. Chang at the General Electric Corporate Research and Development Laboraory.

5.2 MICROSTRUCTURAL CHARACTERIZATION

Optical Metallography.

Specimens for optical metallography were prepared by standard methods. Specimens were polished mechanically using SiC papers through 600 grit. Final polishing was done using alumina powders with sizes 10 μm, 0.3 μm, and 0.05μm in sequence. The specimens were then ultrasonically cleaned in distilled water and methanol.

For alloy 600 tubing, longitudinal sections were observed following a standard two-step etch procedure [134]. Specimens are etched using an 8:1 solution of orthophosphoric acid and water at a closed circuit voltage of 3 volts for a time between 15 and 30 seconds. The surface is then ultrasonically cleaned in ethanol and dried. A microhardness indentation is then placed at a location in the field of typical microstructure. Photomicrographs are made at 500 magnification making sure that the microhardness indentation is visible. A second polish of

surface was done by repeating the mechanical steps from 1.0μm to 0.05μm alumina powders. Caution is taken to remove all of the residual etched material from the porthophosphoric acid, but not the microhardness indentation. The specimen is then etched in a solution of 5% nitric acid and 95% methanol at 3 volts for a maximum of 20 seconds. The final photograph was made at the same location as the orthophosphoric etch by matching the indentation marks. This etch procedure allows for a determination of the character of the grain boundaries.

The two-step etch was also used for some alloy X-750 conditions where identification of carbide morphology was important. This procedure, however, often produced insufficient grain boundary definition. Kallings reagent (5g $CuCl_2$, 100ml hydrochloric acid, 100ml ethanol) was successfully used to obtain general microstructural characterization of all X-750 conditions.For alloy 718, specimens were electrolytically etched in a solution of 10% hydrochloric acid and methanol at 10 volts for five seconds [26]. A magnification of 500 was used as a reference for all cases. For grain size determination, a magnification of 200 was used and the linear intercept method was employed according to ASTM Specification E112.

TEM and STEM.

For thin foil preparation, material was cut into a cylinder of a 3mm diameter by electro-discharge machining. The cylinder was then sliced into about 0.5mm thick disks. For alloy 600 tubing specimens, disks were cut directly from the tube wall. Only one specimen was thus made from each cylinder. Disks were thinned further by mechanical grinding with 600 grit SiC paper. Care was made to grind only one particular side when specimens were to be obtained from certain locations in thickness direction of alloy 600 tubing. The final step consists of electrolytic jet-polish in a solution of 50ml butylcellosolve (2-butoxy-ethanol, 60ml perchloric acid, 70ml distilled water, and 350ml of methanol). Mixing of the solution and jet polishing was done at a bath temperature of about -40 C. A condition of 35V and 40 to 60 mA was

typical for all three nickel base alloys in this work. For TEM, a JOEL model JEM-200CX with an LAB6 filament was used at 200 kV. Secondary phases were identified by dark field techniques based on selected area diffraction patterns.

For microchemistry analysis, a Vacuum Generators model HB-5 STEM system was used with an EDAX energy dispersive x-ray spectometer. Spatial resolution for analysis is about 20°A. Therefore, a compositional variation was quantified at a spacing as small as 50°A along a line crossing representative grain boundary. The spacing was, however, relaxed to 200°A or 500°A where compositional gradients are not high.

Data conversion from the spectral x-ray intensities to chemical composition were were done using the Cliff-Lorimer ratio approach [135] as follows:

$$\frac{C_{Ai}}{C_{Bj}} = K_{Aj} \frac{I_{Ai}}{I_{Bj}} \qquad \text{and,} \quad \sum_{i=1}^{n} C_i = 1 \tag{5-1}$$

where I_{Ai} and I_{Bj} are the integrated peak intensities for species Ai and Bj having concentrations of C_{Aj} and C_{Bj}, respectively. The proportionality factor values were obtained from the work of Wood et al. [136]. A portion of K-factors used in this work are listed in Table 5.5.

The standard deviations in chemical compositions were estimated by the square root of the integrated x-ray counts based on the Poisson distribution. Adequate countings were made to keep the standard deviation below 5% relative. Goldstein's thin film criterion [137] was assumed to be met so that absorbed x-rays are limited to less than 10% of the produced x-rays, as follows:

$$(X_i - X_j) * \rho * t/2 \quad < 0.1 \tag{5-2}$$

Table 5.5

$K_{Ai\ Fe}$ Factors for K-lines by Wood et al. [136]

ELEMENT	Ki Fe
Fe	1.00
Ni	1.07
Cr	0.90
Al	0.86
Ti	0.86
Nb	2.14

where

X_i = $(\mu/\rho)_i$ cosec α

$(\mu/\rho)_i$ = mass absorption coefficient for element i

ρ = specimen density

α = detector take-off angle

t = foil thickness

A maximum allowable foil thickness was set for titanium which emits the lowest x-rays and the most absorbed to be 4900^{0}A while the measured thickness [26] of X-750 foils prepared by the same procedure ranges between 380^{0}A and 600^{0}A. Therefore, the errors associated with absorption effects are negligible.

Auger Electron Microscopy.

Due to possible segregation of trace elements to grain boundaries, surface analysis was done on in-situ fracture speciemns. The specimen preparation and analysis procedure are described in this section.

For alloy 600, small tensile fracture specimens were directly cut from the stock tubings by electro-discharge machining (EDM). The axis of specimens are longitudinal direction and the reduced section covers entire thicknesses of the as received tubings. Therefore, the specimen thickness was about 1.35mm with small variations depending on the tubing thickness.

In the case of alloy X-750, small sized blocks, 28mm x 11mm and 3mm thick were taken from the as received plate by using a watercooled diamond wheel saw. Each block was heat treated in an electrical furnace to the specified conditions. Small tensile fracture specimens were made with a thickness, t, of 3mm, as shown in Figure 5.3.

The specimens were spot welded with Inconel 600 wires at the end of longer grip sections. After ultrasonic cleaning in acetone, all of the surface areas to be submerged except the reduced section were coated

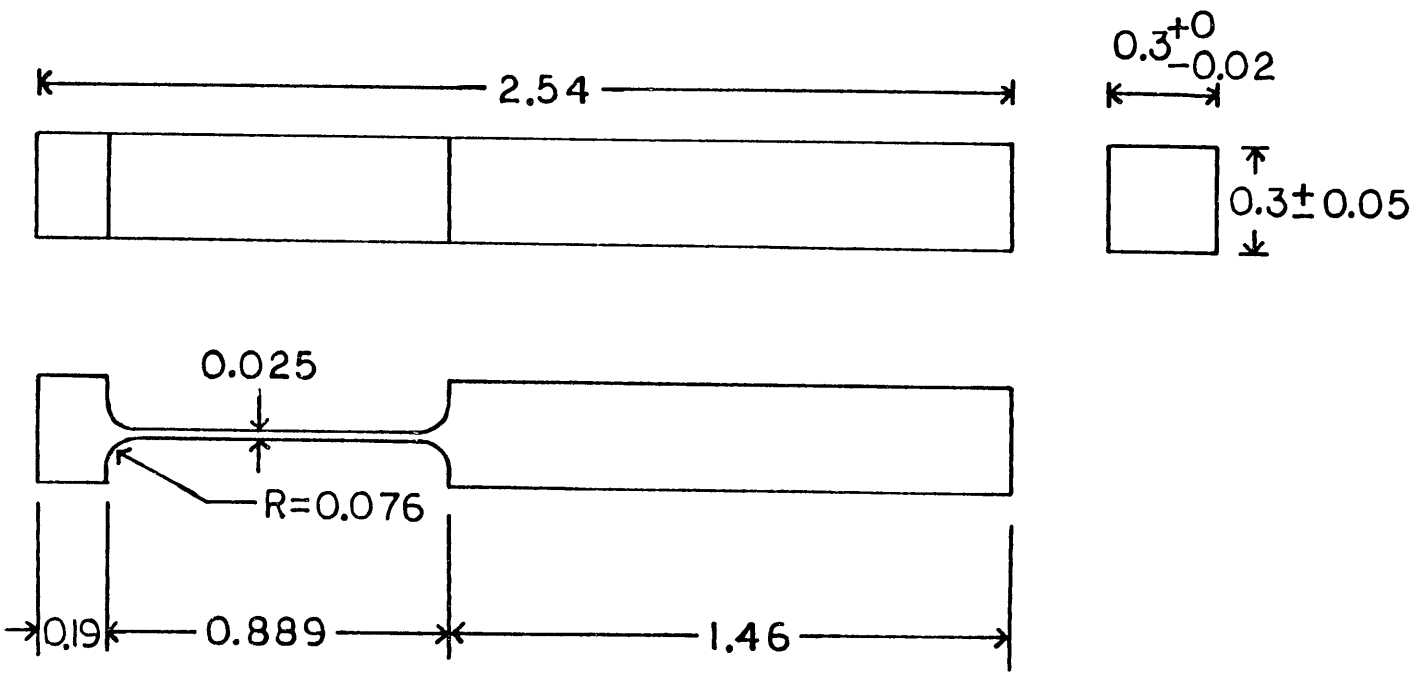

Figure 5.3 Miniature Tensile Fracture Specimen Design for the Auger Electron Spectroscopy.

with stop-off lacquer and dried for a day. Three to four specimens were tied by twisting Inconel lead wires and connected to a negative pole of DC power supply. A platinum plate spot welded with platinum wire was used as an anode. The charging solution was 1 liter of 1 N sulphuric acid with 3ppm of arsenic trioxide as a poison to the hydrogen recombination reaction. The solution was kept stirred slowly inside a hood.

The time of charging for sufficient intergranular fracture was a function of the material condition, charging current density, and temperature. In the case of alloy X-750, about 10 days were required at room temperature with 8 mA/cm^2, whereas only 3 days were required at 60°C with 20 mA/cm^2. It took about twice longer time for the alloy 600 specimens to obtain adequate intergranular fracture surfaces. During the prolonged charging, the solution was replaced after every seven days in order to compensate for arsenic depletion due to arsenic hydride evaporation [138].

Charged specimens were cleaned ultrasonically using the following sequence;

1) acetone to remove the stop-off lacquer
2) a 5% diluted solutionof Contrad 70
3) deionized water
4) air dry.

In most cases, less than five hours were spent from the end of charging to fracture in the Auger system chamber. In a few cases, specimens were kept in liquid nitrogen dewar for storage overnight. A physical electronics model PHI 590 scanning Auger electron microscope (SAM) was used. A vacuum better than $5x10^{-9}$ torr was reached in a few hours and specimens were pulled to fracture by using a slow extension rate in-situ fracture stage [139]. Except for about one third of the total specimens examined in the beginning part of this work, a vacuum better than $2.5x10^{-9}$ torr was reached before the fracture. Under the latter condition, the surface contamination with carbon was tolerable during the first two hours.

A beam energy of 5 kV was used with incident beam current between 90nA and 110nA. The corresponding beam size is about 1μm which is small enough compared with the smallest grain size of 10μm under study. There are two modes of Auger analysis called "survey" and "multiplex". The former represents a continuous detection of Auger electron over a complete energy range to cover all of the element. therefore, a thorough spectrum is obtained by this mode, although the resolution is not better than several percent in atomic concentration. The multiplex mode on the other hand, is designed to focus on a number of particular elements by tuning narrow energy bands of each element involved. It can give a better resolution. Therefore, the multiplex mode was used primarily while a brief survey analysis was supplemented in most cases.

With the help of computerized data analysis, atomic concentration ratios among the involved elements are determined in the multiplex mode. The formula for the concentration analysis is as follows;

$$(\text{\% Atomic concentration of x}) = \frac{\dfrac{I_x}{S_x \quad T_x \quad N_x}}{\displaystyle\sum_{i=1}^{n} \frac{I^2}{S_i \quad T_i \quad N_i}} \times 100, \qquad (5\text{-}3)$$

where:

n = Number of elements under analysis

I = Peak to peak amplitude of the differentiated Auger electron detection amplitude level

S = Sensitivity factor

T = Data acquisition time per sweep

$\bar{N}$ = Number of sweeps

Values of the charateristic parameters used in the above equation are summarized in Table 5.6.

The background noise was found to be a significant problem for the data

Table 5.6

Characteristic Parameters of Auger
Analysis for Nickel-base Alloys

Element	Auger Energy eV	Sensitivity* Factor	Typical Analysis Time, Sec**	Detectability Limit Calculated	Measure***
Ni	840	0.26	2	0.3	---
Cr	489	0.31	2	0.24	---
Fe	598	0.22	2	0.33	---
Ti	385	0.43	5	0.12	---
C	272	0.14	5	0.36	---
P	120	0.45	8	0.06	0.6
B	179	0.11	8	0.3	1.0
S	152	0.75	13	0.04	0.2
Zr	1840	0.21	13	0.14	6.7

NOTE: * Values at 5 keV of incident beam energy
** Equals to time per sweep multiplied by the number of sweep. The time per sweep is fixed at 0.1 second for all measurements.
*** Average measured concentration with S/N = 3

analysis. The peak-to-peak amplitude of the signal may be that of noise when its true concentration is well below certain detectability limit. Therefore, it is important to distinguish true signal from the noise for a trace elements. Since the true signal has a sinusoidal wave from within a given spectral energy band, the noise can be identified by an abrupt deviation from the cuve of differentiated Auger electron signal.

The signal-to-noise ratio (S/N) can be defined as the ratio of the peak-to-peak amplitude of the curve to that of the greatest abrupt change A signal-to-noise ratio of 3 is generally a borderline below which the signal is considered to be meaningless noise. The detectability limit formula has been developed by Clough [140] to provide an approximation as follows:

$$\begin{pmatrix}\text{Detectability limit in \%} \\ \text{Atomic Concentration of x)}\end{pmatrix} = \frac{(S/N)}{S_x \quad H_x} \qquad (5\text{-}4)$$

where

SN = signal-to-noise ratio

S_x = sensitivity factor

H_x = a semi-empirical factor as functionof analysis time and beam current

The detectability limits for the elements of interest calculated by using a signal-to-noise ratio of 3, as listed in Taole 5.6. These numbers are, however, found to be too much optimistic when compared with practically detectable levels at the same signal-to-noise ratio as discussed in the next chapter.

Although both multiplex and survey modes were used quantitative information such as concentration and S/N ratio could be obtained only from themultiplex mode. The trace elements including P, B, S, and Zr do not develop detectable peak on the survey spectra. Total 86 spots were analyzed including 59 spots from 18 commercial material specimens and 27 spots from 9 Zr-modified material specimens.

In order to analyze the data, each surface must be identified as to whether or not it is a true grain boundary. The scanning electron capability, built-in to the Auger System, does not have a resoltuion which is good enough to make such identification of surfaces possible. Attempts to locate the same analysis spot under high resolution SEM were not successful due to difficulties arising from changed view angles, except for large grain specimens. The SEM micropraphs on a typical area are taken to represent the analysis spots. It was speculated, however, that those spots with high signal-to-noise ratio for phosphorous or boron were true grain boundaries since the bulk concentration of the segregants are well below the detectability limits. The remaining spots may be either true grain boundaries with little segregants or transgranular surfaces. If these were transgranular surfaces, their grain boundaries are implied to contain little embrittling segregants such as phosphorus and sulphur. Therefore, it is assumed that significant segregations of phosphorus or sulphur take place at grain boundaries if signal-to-noise ratio is equal to or greater than three. Representative AES spectrum with the signal-to-noise ratio of 2,3,4 and 5, respectively, are shown in Figure 5.4.

The atomic concentration of segregants is calculated as follows: First, the ratio of trace elements to nickel concentration is determined from computer generated raw data. The ratio is multiplied with bulk concentration of nickel which is determined from data in Table 5.2. Although nickel concentration is believed to vary from grain to matrix, the error introduced by the variation would not be significant compared with other errors of this study. Was et al. [35] suggested a better normalization by using the sum of Ni, Cr, and Fe which is more invariable than Ni concentrations alone. In the early part of this work, Cr and Fe were not included in the multiplex, which made use of the latter method impossible. The variation of Ni concentration was estimated by comparing the two procedures. It was found that relative error between the two was within 10%.

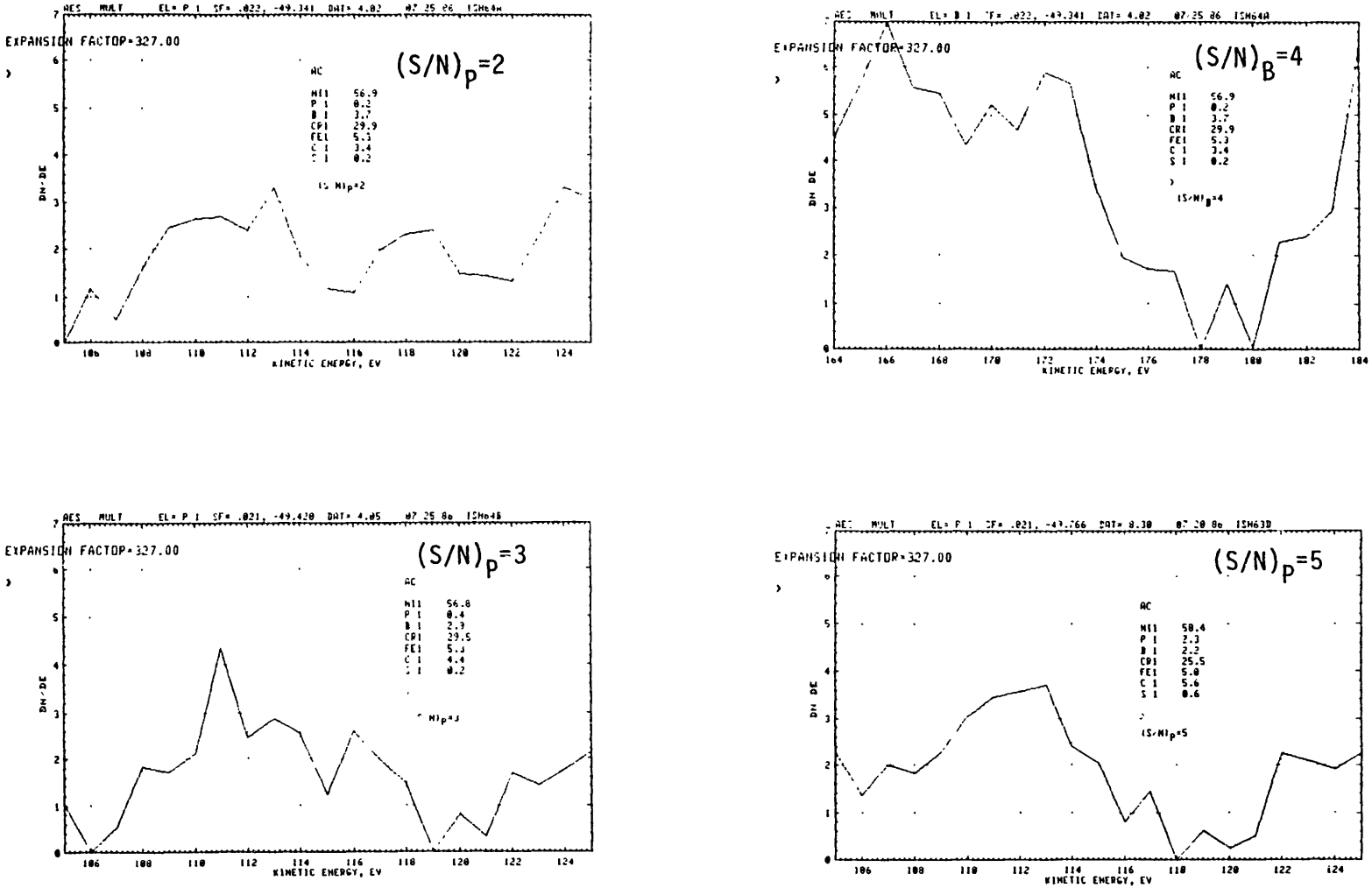

Figure 5.4 Representative AES Multiplex Spectra with a Signal-to-Noise Ratios of 2, 3, 4, and 5.

Scanning Electron Microscopy.

Fracture surfaces were examined using an ISI model DS130 scanning electron microscope at an acceleration voltage of 20 kV. Specimens fractured in the high temperature water environment were coated with about 100^{o}A thick gold layer by a vacuum deposition, in order to minimize charging of surface on surface oxide. The SEM was used primarily to identify the fracture mode of the specimen cross section and side wall. In the case of single-edge notched fatigue specimens, the SEM photographs were taken at a magnification of 28x for the entire cross section. By montage of the micrographs, it was possible to accurately define the transition between one test condition and another.

5.3 ELECTROCHEMICAL CHARACTERIZATION

The electrochemical behavior was examined using potentiodynamic polarization, potential jump, galvanic current measurements and intergranular corrosion tests. A solution of 0.05M sodium sulphate with pH adjusted to 3.00$\pm$0.05 was used as an electrolyte to reduce error from solution resistance. The pH of 3 was selected to simulate the crack tip environment that may develope in the restricted tip region and cause a low pH even with a neutral bulk solution [76]. Sulphuric acid was added to adjust the pH so that no additional species of ions would be introduced. The sulphate ions are considered to be relatively stable at the temperatur range for this work

Potentiodynamic Polarization.

The anodic or cathodic current density was determined as a function overpotential in accordance with guidelines of ASTM Specification G5-82. Specimen designs and the test solution were, however, different from the Specification.

The two different specimen designs used are illustrated in Figure 5.5. For materials with enough thickness, specimens were cut into a rectangular cross section and spot welded to an alloy 600 wire. They

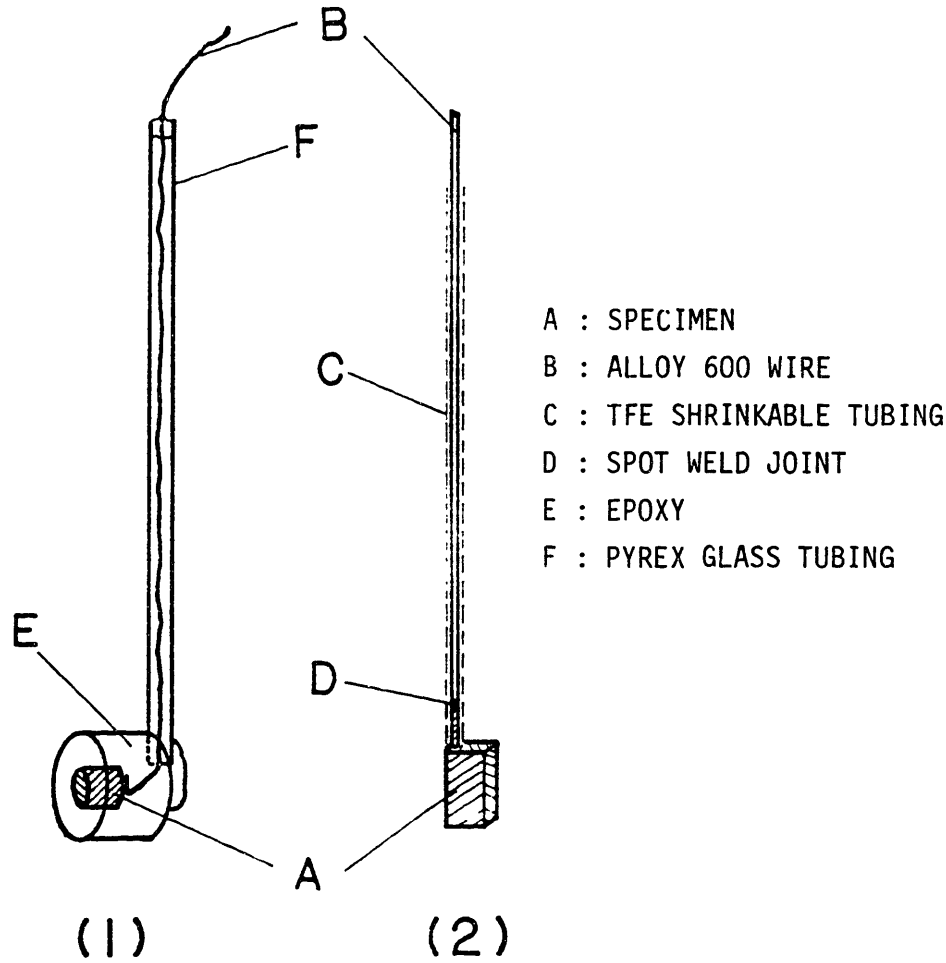

Figure 5.5 Potentiodynamic Polarization Specimen Design for (1) Thick Stock Materials and (2) Sheet Materials.

were then mounted in an EPON828 epoxy resin with 15% of triethylenetetramine (TETA) as a curing agent. Pyrex glass tubing was used to insulate the wire from the solution. A region of joint with back of the specimen was sealed with a patch of epoxy. Curing was complete after 4 hours at 75 C. The second design was used for Ni_3Al in the thin foil geometry. Alloy 600 lead wires were insulated with an Alpha Wire Co. product FIT-500 TFE Heat shrinkable tubing. Specimen surfaces were wet polished using 600 grit SiC paper and rinsed in deionized water. Crevices around the spot weld and the tip of the heat shrinkable tubing was carefully covered with a Michigan Chrome and Chem Co. product Micro Super XP-2000 a chlorine-free stop-off lacquer.

A Pyrex glass cell with six openings was installed with a specimen, a Luggin reference probe, a platinum counter electrode, a thermometer, a gas bubbler and a water-cooled condenser column. After purging the cell with nitorgen gas for at least 15 minutes, the solution was introduced from a 4 liter storage flask which had been bubbled with nitrogen gas for 24 hours. The luggin reference probe was connected to a Saturated Calomel Electrode (SCE) through a saturated KCl salt bridge. A Glasco Co. product external heating jacket and a temperature controlled were used to heat the solution to the desired temeprature within one degree centigrade

A Princeton Applied Research model 173 potentiostat with a model 276 digital interface coupled with HP-85 computer through IEEE-488 general purpose interface bus (GPIB) was used to control the experements. Data acquisition and control was affected using software developed by Hosoya [57]. All polarization experiments were run at the same rate of potential scan which was 0.5mV/min. The scan continued until an anodic peak was observed in anodic direction and until concentration polarization was observed in the cathodic direction. For measurements of electrochemical parameters such as Tafel slope and corrosion current, the scan covered only 150mV from corrosion potential in both directions in order to achieve better accuracy in the measured data. The cell was kept bubbling with nitrogen gas throughout the experiment.

The potential measured with respect to Standard Calomel Electrode (S.C.E) was converted to the Standard Hydrogen Electrode (S.H.E.) scale by the following correlation:

$$E_{S.H.E.} = E_{S.C.E.} + 244 - 1.003\ \Delta T + 1.745X10^{-4}\ (\Delta T)^2 - 3.03x10^{-6}\ (\Delta T)^3 \quad (5\text{-}5)$$

where $T = T - 25^{o}C$, and $E_{S.H.E.}$ and $E_{S.C.E.}$ are in a unit of mV.

Potential Jump Experiments.

The passivation behavior within the active anodic potential region was examined by decay current measurements after a sudden application of anodic overpotential. The relative ease of experiment was the main advantage over other similar experiments such as the scratching electrode test and the load drop experiment. The procedure and apparatus are the same as those used in the potentiodynamic polarization tests discussed in the previous section.

Upon reaching the test temeprature the specimen surface was stripped of any oxide layers by applying a cathodic potential of -1124mV S.H.E. for about 30 minutes. Then an anodic potential of -124 mV S.H.E. was applied and the current measurement began. The data acquisition interval was 5 msec and the experiment lasted for 20 mimutes. All data was transferred to the host computer after the completion of experiment.

Due to the initial cathodic overpotential, there was concern that the measured current might include a significant effect of oxidation of hydrogen atom at the specimen surface. Therefore, the same experiment was run with a specimen made of platinum in order to quantify any background current due to hydrogen oxidization.

Gavanic Current Measurement.

The corrosion potentials of grain boundary precipitates and chromium depleted regions are different, to a varying degree of significance, from that of the surrounding matrix. The significance of gavanic cell formation was quantified by measuring the current of a gavanic couple between the various phases.

The procedures for specimen preparation and experiment were the same as those for the potentiodynamic polarization experiments. Solution annealed X-750 was used as the counter electrode while the other chemistries representing various grain boundary phases were used as the working electrode. The connection of two electrode was instantaneously done by computer controlled internal switching of PAR model 173 potentiostat. By applying a null potential difference between the electrodes, the potentiostat was functioning as a zero resistance ammeter with an arrangement shown in Figure 5.6 [141].

Corrosion Potential Measurements.

Corrosion potentials of various materials were measured in hgih purity water as a function of temeprature. The data were useful in the prediction of the signficance of galvanic coupling on the crack initiation and propagation processes. A Ag/AgCl external reference electrode was used up to 288 C. The reference electrode, developed by Andresen [142] is shown in Figure 5.7.

The zirconia block was made by a procedure, as follows:

1) mixing of ZrO_2 powder with carbowax in water and air dry
2) cold press at 300 MPa to a pellet with 3mm diameter and 7mm length
3) sintering in hydrogen atmosphere at 1600 C for 1 hr
4) Measuring resistance after soaking in AgCl solution to confirm a value of 0.1MΩ

The conversion to S.H.E. was made by McDonald's correlation as follows:

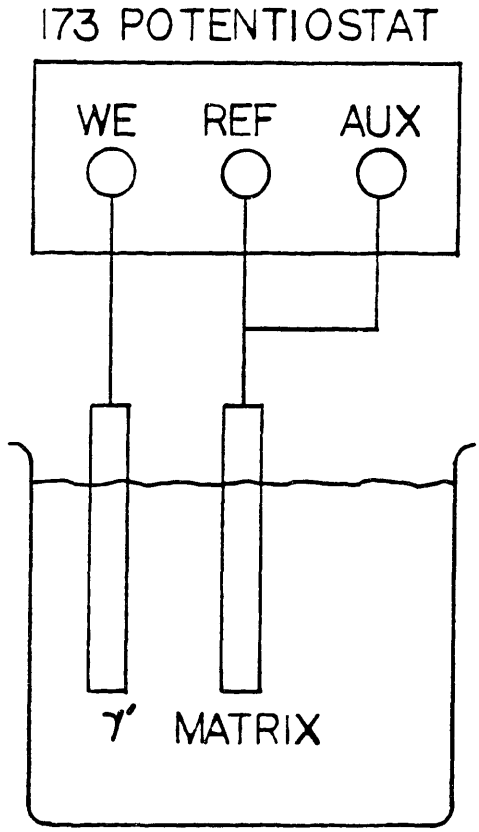

Figure 5.6 Schematic of Galvanic Current Measurement Using the Potentiostat as a Zero-Resistance Ammeter.

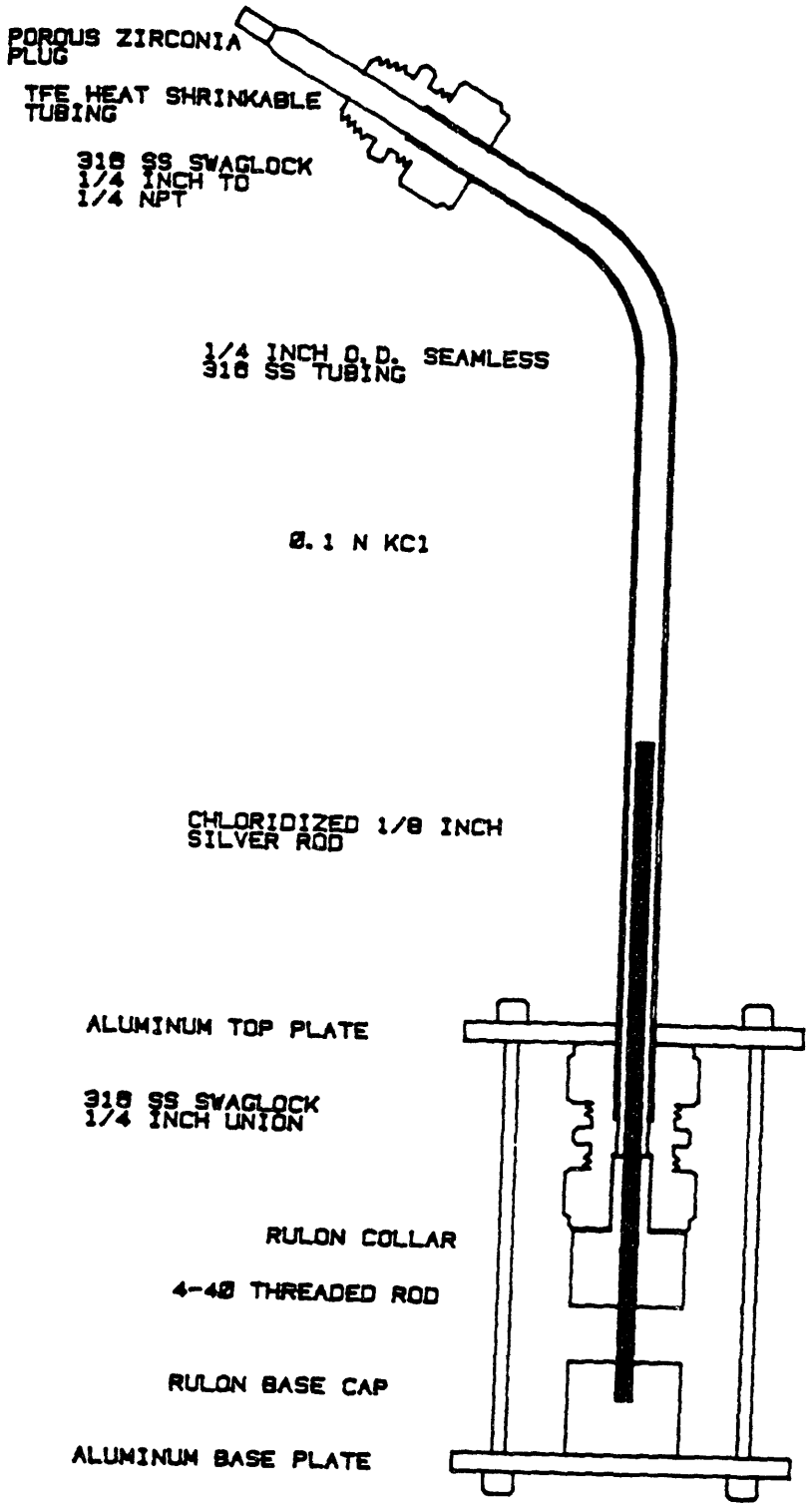

Figure 5.7 Schematic of Ag/AgCl Reference Electrode used for the Electrochemical Potential Measurements in High Temperature Water.

$$E_{S.H.E.} = E_{Ag/AgCl} + 286.6 - 1.003\ \Delta T + 1.745 \times 10^{-4}\ (\Delta T)^2 - 3.03 \times 10^{-6}\ (\Delta T)^3 \quad (5\text{-}6)$$

Where $\Delta T = T - 25$ C

Specimen design was similar to the second one shown in Figure 5.5 except that stop-off lacquer was not applied. One end of specimen was filed into a wire shape so that the spot weld region could be completely covered by shrinking TFE tubing. The alloy 600 lead wire was insulated from the solution by the TFE tubing and a CONNAX compression fitting with a teflon sealant.

To eliminate errors due to variation in autoclave environment, all specimens were placed at the same time and measurement were done differentially by using a digital voltmeter. Resistances between electrodes were also checked before each measurment to guarantee that there was no short circuiting. The temperature of specimens were increased at a rate 60 C/hr by using a computer controlled heater unit.

Intergranular Corrosion Test.

The degree of grain boundary sensitization was measured by a modified Huey corrosion test in a 35% boiling nitric acid for 24 hours. The modification was made to reduce the exposure time and the solution concentration from those in original Huey test (ASTM Specification A262-81, Practic C) which was originally designed for use on austenitic stainless steels.

Specimens were cut using a low speed diamond blade saw and polished with 240 grit SiC paper. For alloy 600 tubings, the ratio of tubing cross sectional area to total surface area was made constant at 0.1. After ultrasonic cleaning in acetone and drying, the surface area was measured. The weight of a specimen was measured immediately before and after the test to an accuracy of ± 0.00005 g.

The test apparatus was set up inside a hood with a 1 liter wide-mouth Erlenmeyer flask, a water cooled condenser of a cold finger type, and a quartz specimen holder. Sufficient flow of cold water through the condenser prevented solution vapors from leaking. A nitric acid solution of 216ml of reagent grade HNO_3 and 384ml of deionized water was boiled gently with the help of a few beads of borosillicate glass. The holder containing the specimen was then suspended in the solutio by a platinum wire for a period of 24 hours. Some tests were terminated after only 12 hours when a serious solution discoloring was evident indicating additional weight loss by grain dislodgement.

After 24 hours, the specimen was softly brushed in flowing water, rinsed in acetone, and dried to measure the final weight. Susceptibility to intergranular corrosion was expressed in terms of weight loss as follows:

$$\frac{\Delta W}{\Delta t} = \frac{W_i - W_t}{A \quad t} \tag{5-7}$$

where $\Delta W/\Delta t$ is the corrosion rate ($mg/cm^2/day$), W_i and W_t are the initial and final specimen weights and t is the exposure time.

5.4 AIR TENSILE TEST

The mechanical properties in the absence of aggressive environment were determined by a tensile testing as a function of temperature and strain rate. The strain rates were fast enough to prevent any significant environmental effect by the laboratory air. The procedure was in accordance with ASTM Specification E8-83. Specimen designs for tensile tests are shown in Figures 4.8 and 5.8.

For alloy 600, the reduced section of specimen was cut by EDM so that the original curvature could be retained. The reduced section was tapered toward center by about 50μm to ensure the final failure within the gage length. The grip section was flattened using a press, but with

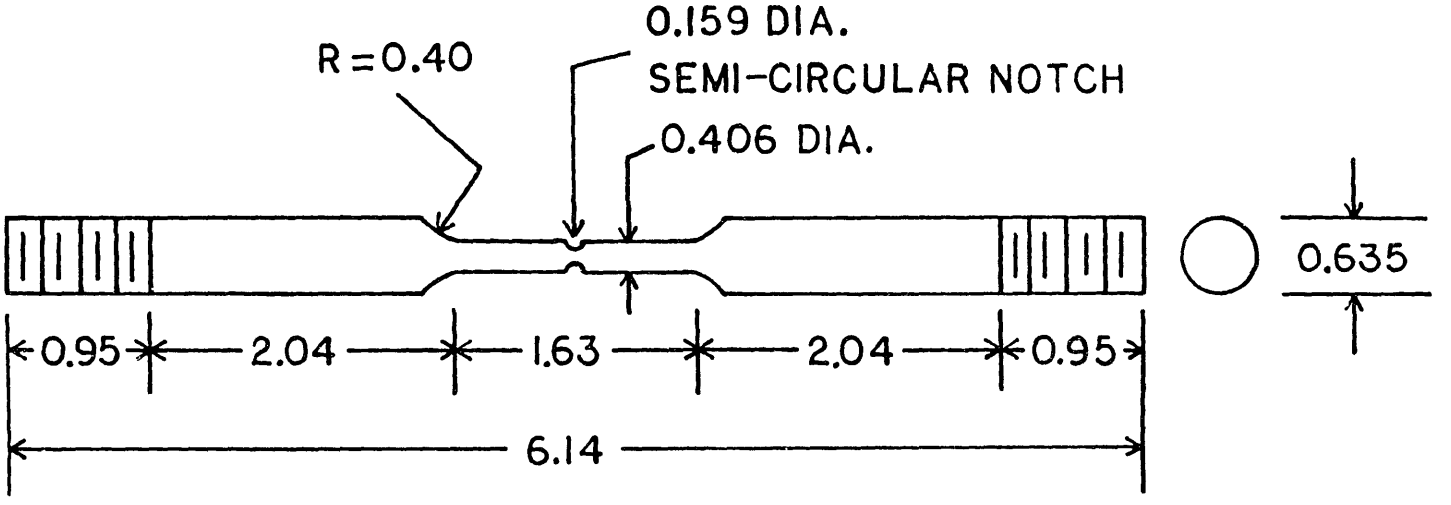

Figure 5.8 Design of Alloys X-750 and 718 Tensile Test Specimens for Tests in Laboratory Air.

care to make a smooth transition the curved reduced section. The holes for loading pins were punched out. All oxide and pits from EDM were removed whereas the surfaces of tubing inner and outer walls were retained as received. Cross sectional area of the specimen ,A, shown in Figure 4.8 can be determined by;

$$A = \left(\frac{\pi - 2\varphi_o}{8}\right) D_o^2 - \left(\frac{\pi - 2\varphi_i}{8}\right) D_i^2 + \frac{WD_o}{4} \sin \varphi_o - \frac{WD_i}{4} \sin \varphi_i \qquad (5\text{-}8)$$

where $\varphi_o = \cos^{-1} (W/D_o)$,

$\varphi_i = \cos^{-1} (W/D_i)$,

in which W is specimen width , D_o and D_i are tubing O.D. and I.D., respectively.

The specimens for alloys X-750 and 718 were of the same design as specimens for the slow strain rates test. The specimens were cut into a long longitudinal orientation. After rough machining, the specimens were heat treated. Then the final machining removed about 500μm of the outer layers. All the surfaces were polished with grit 600 paper.

An Instron Co. model tensile testing machine with an Advanced Testing System model electric furnace were used for the tests. Strain was measured by a SATEC Systems model extensometer with a set of knife edges and extension arms to use in high temperature testing. Once the strain reached about 2% strain, cross head displacement was taken to determine further increase in strain. The temperature of specimen was measured by a type K thermocouple place near the specimen. Maximum temperature deviation during the tests was less than 2 C.

The D.C. output from load cell and A.C. output from the extensometer were connected to HP model 3456 digital voltmeter through a relay multiplexer and transferred to a HP-85 computer. The data was also recorded in a strip chart recorder built-in to the Instron machine. The two sets of data were consistent within relative errors of 3% in load

and 2% in strain.

The load cell was calibrated once every day by a 45.3kg of dead weight. The extensometer was calibrated once every week against a mechanical micrometer with a resolution of 2.5μm.

5.5 STRAINING ELECTRODE TENSILE TEST

The electrochemical behavior at crack tip may be significantly affected by the presence of strain and stress. The mechanical effect was introduced in the electrochemical study by using tensile deformation. Various heat treatment conditions for alloys X-750, 718, and a gamma prime chemistries were used for specimens. In addition to the electrochemical data, the susceptibility of specimens to applied potential could also be obtained.

Specimen design and test apparatus were developed by Lee [94]. The small cylindrical tensile test specimens are shown in Figures 5.9 - 5.10. Straight cylindrical bar with a diameter slightly larger than the final size were machined and heat treated. At least 500μm of outer layer was removed during the final machining. The central reduced section was wet-polished with 600 grit SiC paper, within three hours prior to the beginning of the experiment.

The overall test cell construction is shown in Figure 5.11. The load train except for the test section was insulated from the environment by teflon insulators with O-ring seals. The crevices at the contact area between the specimen and the teflon insulator were sealed by Micro Super XP-2000 stop-off lacquer. Therefore, only the reduced section of about $1cm^2$ of surface was exposed to the environment. The apparatus and procedures for polarization experiment were also used in this experiment. All tests were done at 93 C.

An Instron tensile test machine was used for loading the specimen. Two strain rates including $7 \times 10^{-4} sec^{-1}$ and $7 \times 10^{-5} sec^{-1}$ were used to represent the crack tip strain rate during fatigue testings at

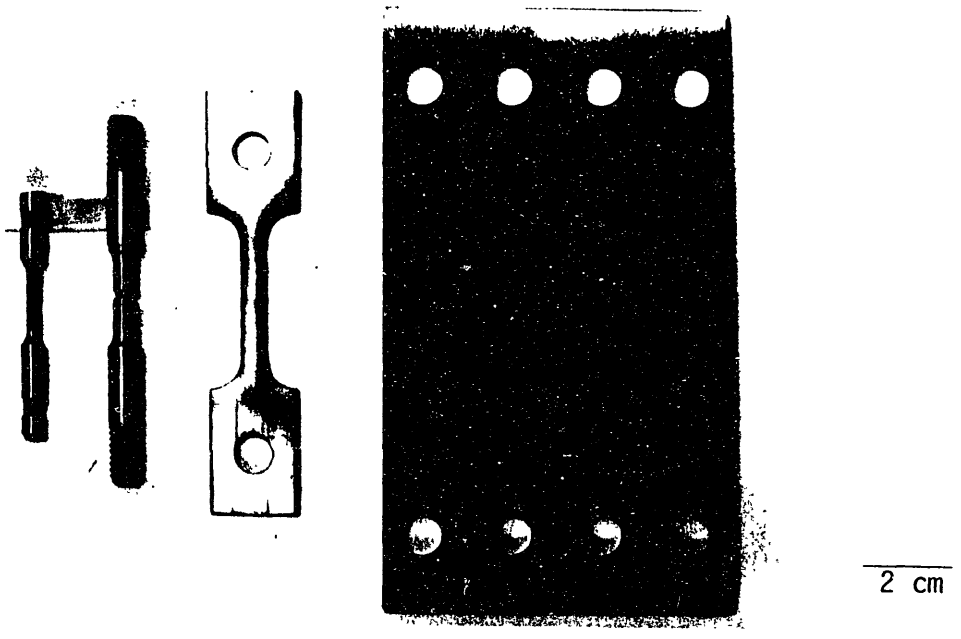

Figure 5.9 Specimens Used in:(1) Straining Electrode Tensile Test, (2) Tensile Tests and Slow Strain Rate Tests of Alloys X-750 and 718, (3) Slow Strain Rate Tests of Alloy 600 Tubing and, (4) Corrosion Fatigue Tests of Alloy X-750.

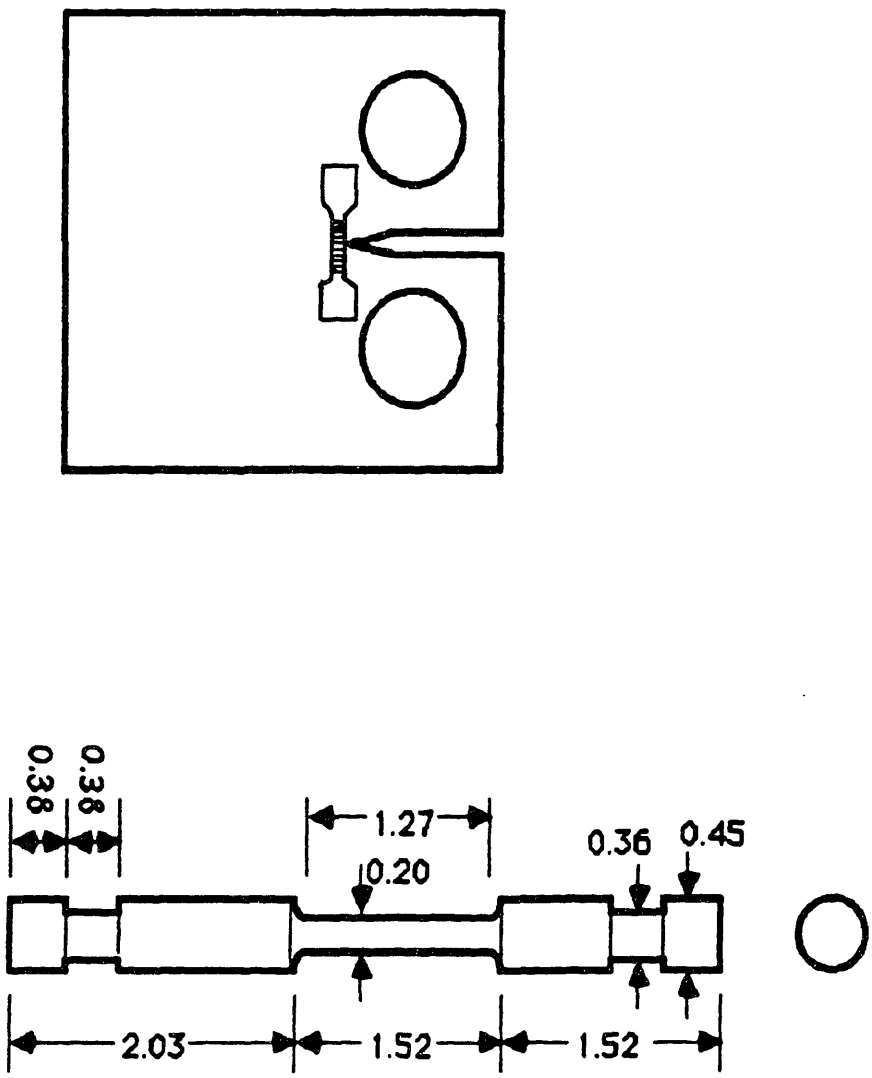

Figure 5.10 Schematic of a Crack Tip Straining Electrode Situation and Design for Straining Electrode Tensile Test Specimen.

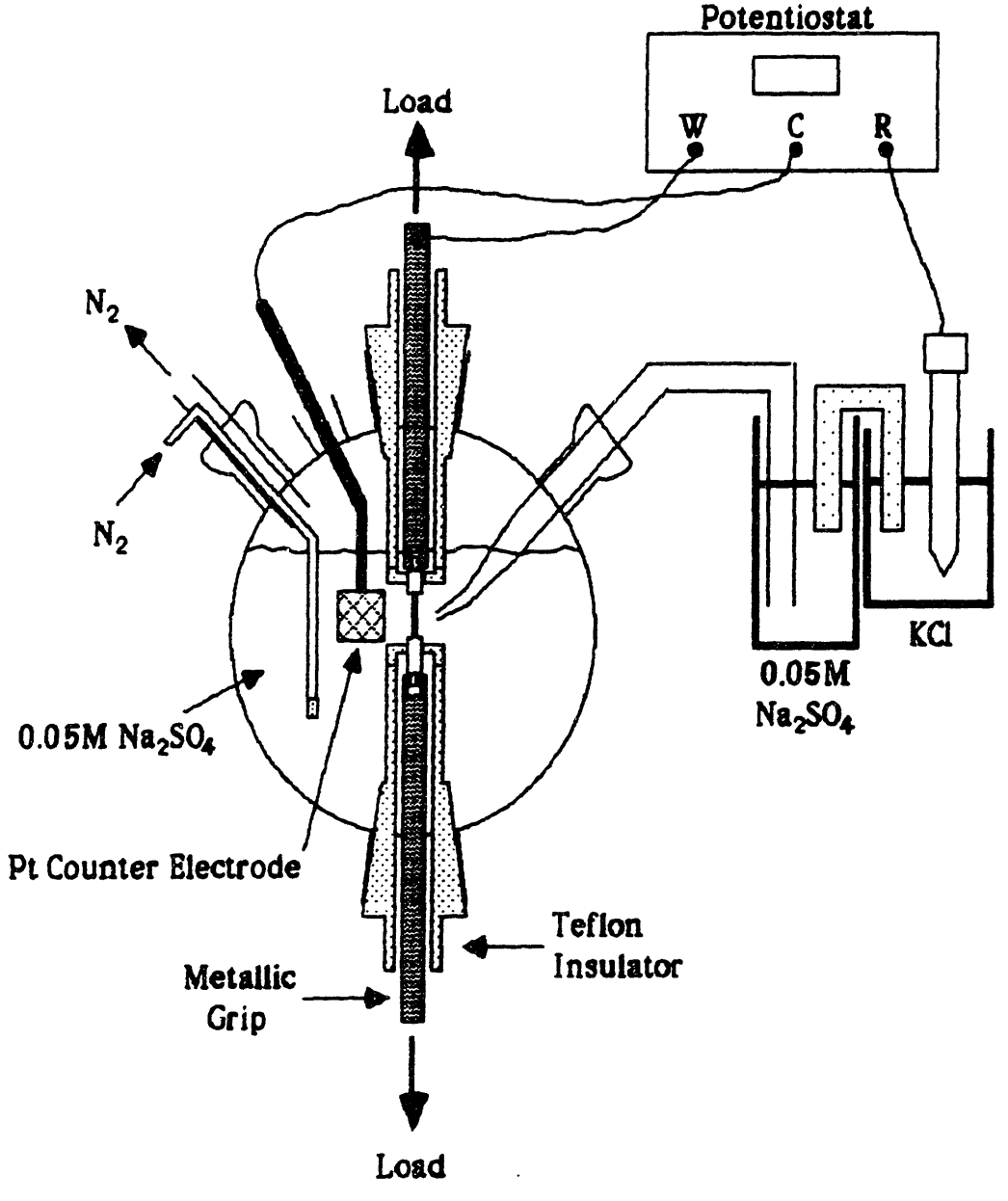

Figure 5.11 Schematic of the Straining Electrode Tensile Test Apparatus.

frequencies of 1 H_z and 10 H_z, respectively. The quantitative basis for determination of the equivalent strain rates was described in chapter 2.

5.6 CORROSION FATIGUE TEST

The specimen design and apparatus used were developed by Was and Ballinger [99]. The single edged notch (SEN) specimen is shown in Figure 5.12. From the 0.318cm thick X-750 plate, specimens were machined to the design, but with a small allowance on each dimension. They were wrapped in stainless steel foil and clamped on a 1.2cm thick block of stainless steel to maintain flatness during heat treatment. The final machining after the heat treatment removed at least 500μm from each dimension. The removal of surface layers on side walls was made only by wet grinding to prevent any heat or deformation. The central strip on both sides was further polished by grit 600 SiC paper to facilitate crack length measurement by optical techniques during the tests. The specimen was then ultrasonically cleaned in acetone.

Inconel wires of 0.038cm diameter insulated with teflon tubing were spot weld to the specimen for use as the electric lead of the working electrode and the D.C. potential drop probes for crack length measurement. All crevices around the spot weld wires and the heat shrinkable tubing were carefully eliminated by the lacquer. The specimen was dried for 24 hours and inserted into a test cell.

The test cell is shown in Figures 5.13 and 5.14. A more detailed design of the cell is described by Was and Ballinger [99]. The narrow gap between the specimen and bottom of the cell was sealed by RTV Silicone rubber. In order to use the cell at a temperature up to 60 C, all the plexiglass joints were reinforced by EPON828 epoxy resin covered with Micro Super XP-2000 lacquer. Hence, the possibility of solution contamination due to bleaching of the plexiglass edges was reduced. The test cell and specimen assembly was then dried for 24 hours.

The specimen was connected to the load train by four-pins on both sides.

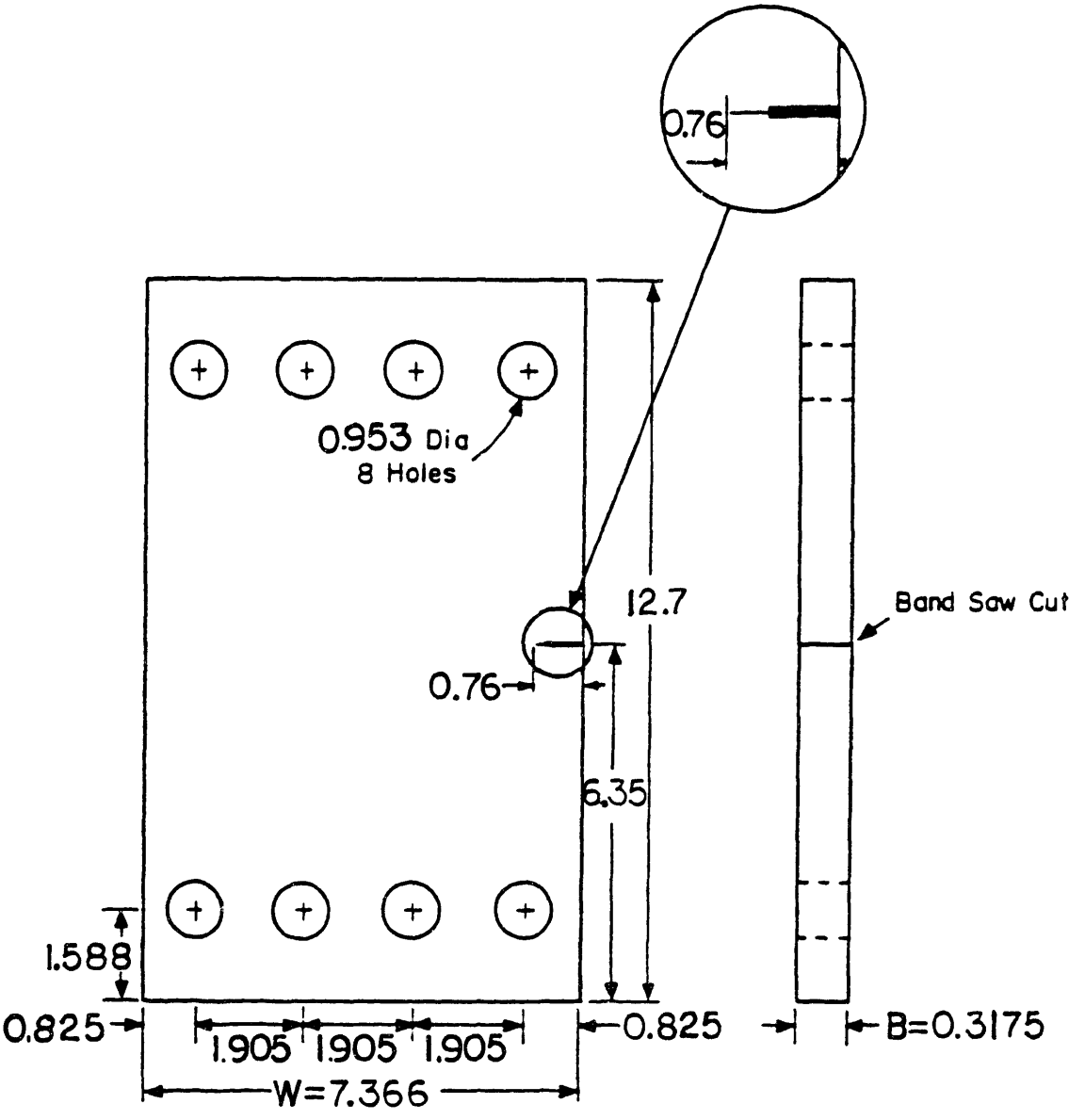

Figure 5.12 Single Edge Notch Specimen Design for Corrosion Fatigue Tests.

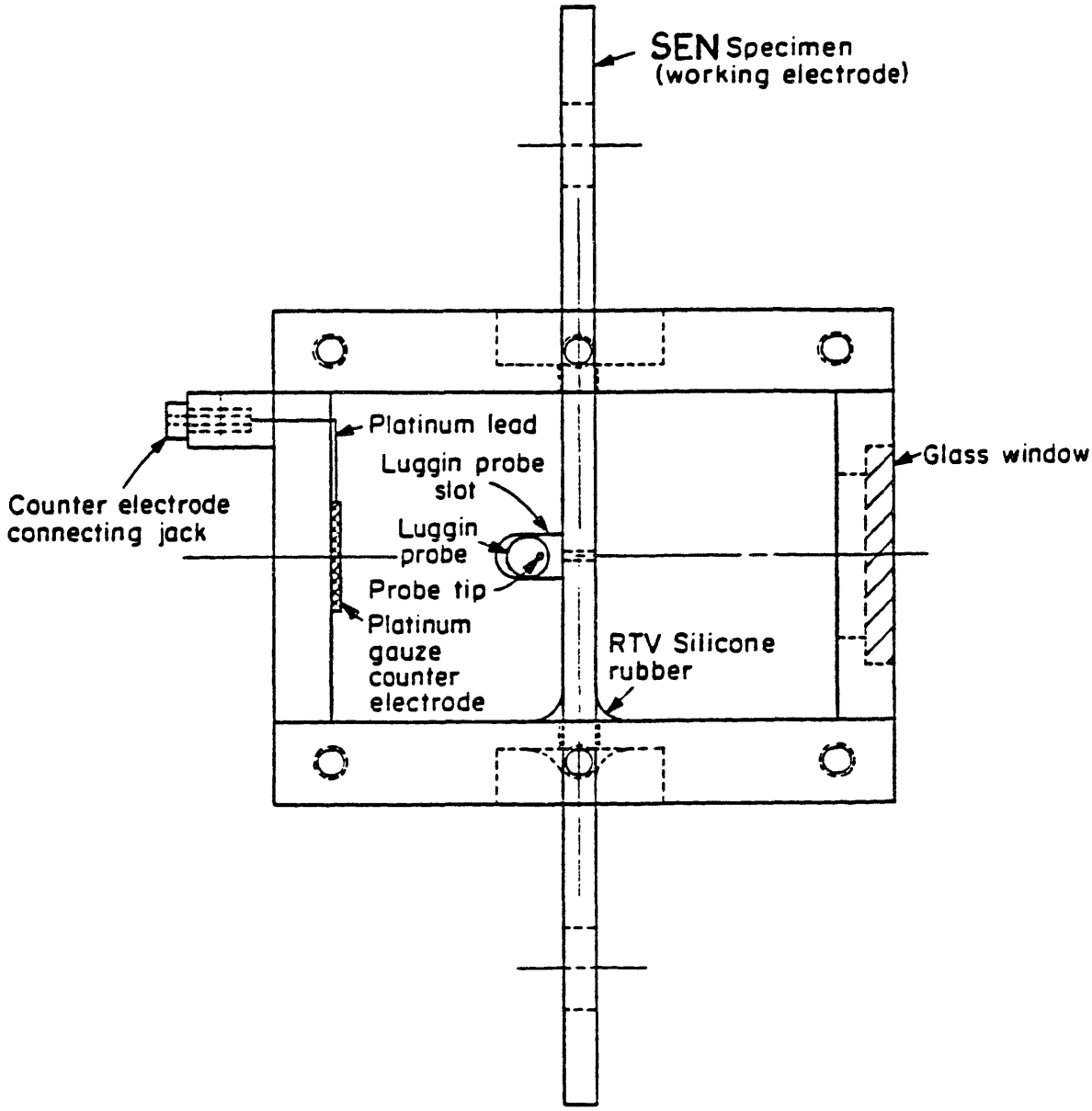

Figure 5.13 Cut-away View of Plexiglass cell for the Corrosion Fatigue Tests.

Clamping was made on the specimen ends by two thick plates which were secured by uniformly torqued bolts. A large pin coupling between the grip and the remaining load train was electrically insulated with tightly fitted plastic washers and teflon sheets on side walls. A servohydraulic fatigue machine of 222 kN capacity with load a cell accuracy of 0.25% was used to apply load to the specimen. To minimize bending moments due to misalignment of the load train, a Wood's metal pot was used as a lower coupling to the machine.

To increase test temperatures, the cell was modified to allow solution circulation between an extenal heater and the cell, as illustrated in Figure 5.14. The heated solution in the middle flask was transferred to the cell through a flow rate control valve by a static head. The effluent solution was pumped back to the heated flask, which could also be filled up from the storage flask on the top in Figure 5.16. The solution flask as well as the cell were purged of oxygen by continuous bubbling with nitrogen gas. The heater was controlled by a Therm-O-Watch model capacitance gage installed on a 76mm long thermometer. The specimen temperature was measured using a type K thermocouple placed in the cell solution within 2mm from the center strip. The system resulted in temperature control within 1 C during the test.

Fracture Mechancial Analysis.

A stress intensity factor correlation of a SEN with multi-pin gripping system is given by Baratta et al. [143] as follows:

$$K = \frac{P\sqrt{a}}{BW}\left[2.181 + 1.957\left(\frac{a}{w}\right) + 7.686\left(\frac{a}{w}\right)^2 - 23.620\left(\frac{a}{w}\right)^3 + 49.812\left(\frac{a}{w}\right)^4\right] \quad (5\text{-}9)$$

where K is the stress intensity factor in $MPa\sqrt{m}$, P is load in Newton, and a is the crack depth in cm measured from the mouth. Dimensions B and W are defined in Figure 5.12. The correlation is valid for an

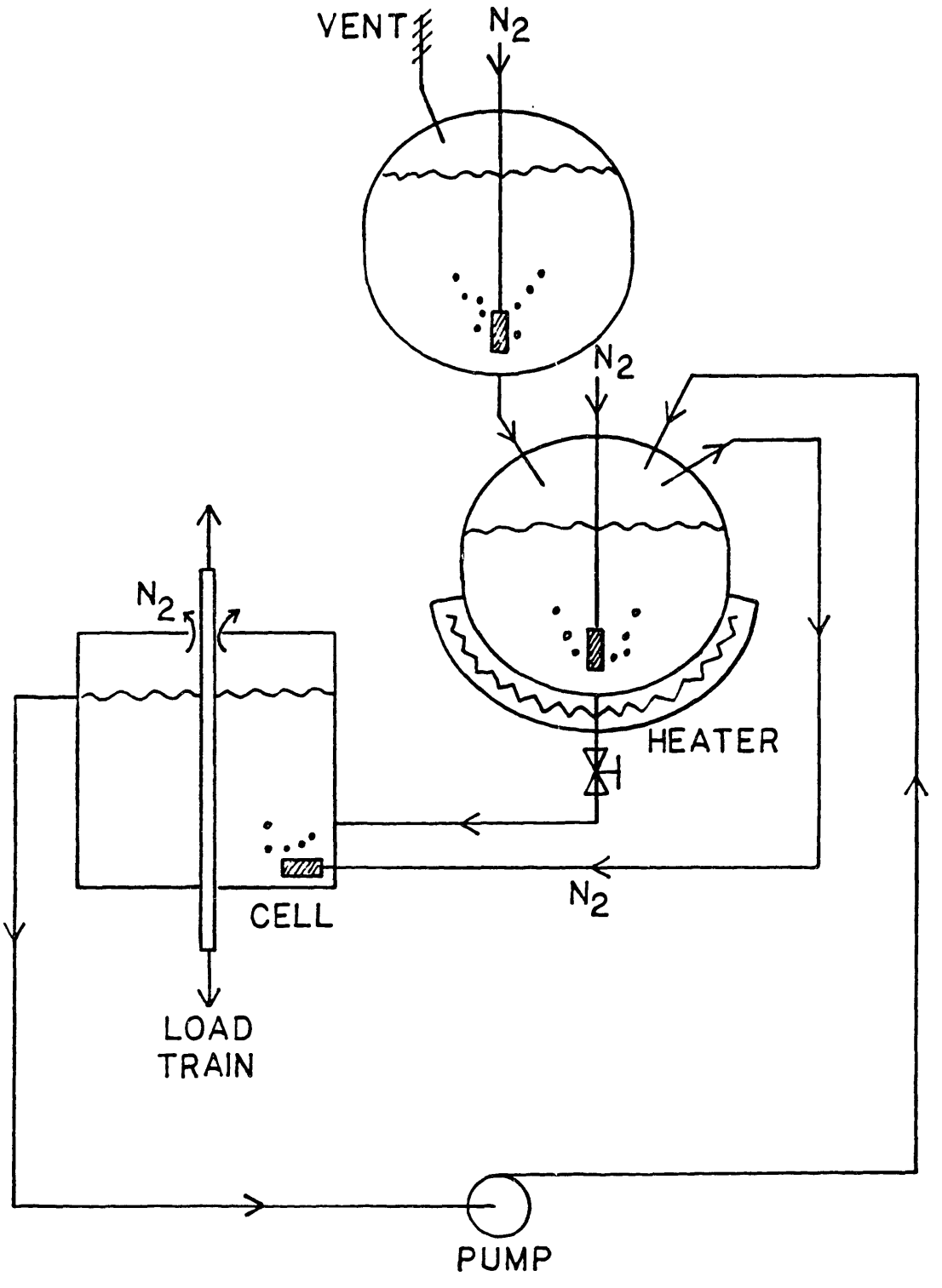

Figure 5.14 Schematic Diagram of the Solution Flow for the Corrosion Fatigue Tests at Temperatures up to 60 C.

experiment a/w up to 0.635 with an error in the fit not greater than 0.75%. A comparison with theoretical calculations suggested the error may have become significant at higher a/w values. Therefore, an a/w value of 0.635 was taken as the upper limit for a valid application of the correlation.

Another limitation on a/w arises from the requirements of linear elastic fracture mechanics which dictate the sepecimen stress should be below its yield strength for most of regions except for a crack tip. This can be translated for the SEN design as follows:

a) The uncracked ligament must have an average length according to

$$w - a \geq \frac{P_{max}}{B\,\sigma_y} \tag{5-10}$$

where P_{max} is the maximum load, and σ_y is the yield strength. The term $P_{max/B}$ can be substituted with relation Eq. (5-9) so that the inequality Eq. (5-10) can be solved for a/w. The result is a condition that a/w be not greater than 0.9983.

b) Any characteristic dimensions of specimen should be at least 25 times the size of a plastic zone at the crack tip. The size of plastic zone, r_p can be approximated, assuming plane stress, by

$$r_p = \frac{1}{2\pi}\left(\frac{K_{max}}{\sigma_y}\right)^2 \tag{5-11}$$

r_p values were caluculated to be about 100μm for AH and 215μm for HTH X-750. For AH conditions, plane strain requirements are expressed as follows:

$$\left.\frac{w-a}{B}\right\} > 25\ r_p = 0.4\text{cm} \tag{5-12}$$

The first condition is satisfied for a/w $\leq$0.987. However, specimen thickness was about 20% lower than the requirement. Therefore, it was expected that an appreciable portion of specimens undergoes plane stress fracture although a majority of the region can be well described by plane strain. It was thus concluded that the maximum a/w value for valid testing was determined to be 0.635 based on accuracy considerations for the strain intensity factor.

Measurement of Crack Depth.

The majority of the data was taken by optical measurement of crack depth by using a traveling microscope with a Strobe light source. By a differential measurement technique, an accuracy of 10μm could be achieved.

During the early stages of a test, a D.C. potential drop technique was used to measure the crack depth. The motivation of its use was complete automation of tests using feedback control for a constant ΔK. A schematic diagram for the D.C. potential drop technique is shown in Figure 5.15. About 5 amperes of D.C.current was passed through the specimen. The potential drop between two probes at the crack mouth was amplified and measured to correlate with the crack depth. Since an A/D converter was used, there was a zero-shift problem in the measured data. The difficulty was solved by averaging two data taken with opposite polarity of current. The polarity was switched by a Douglass-Randall solid state relay.

The measured potential drop was related to crack depth by Johnson's equation [145] as follows:

$$\frac{U(a_1)}{U(a_0)} = \frac{\text{Cosh}^{-1}\left[\frac{\text{Cosh }(\pi L/2W)}{\text{Cos }(\pi a_1/2W)}\right]}{\text{Cosh}^{-1}\left[\frac{\text{Cosh }(\pi L/2W)}{\text{Cos }(\pi a_0/2W)}\right]} \qquad (5\text{-}13)$$

where $U(a_1)$ and $U(a_0)$ are the D.C. potential drop values at a crack

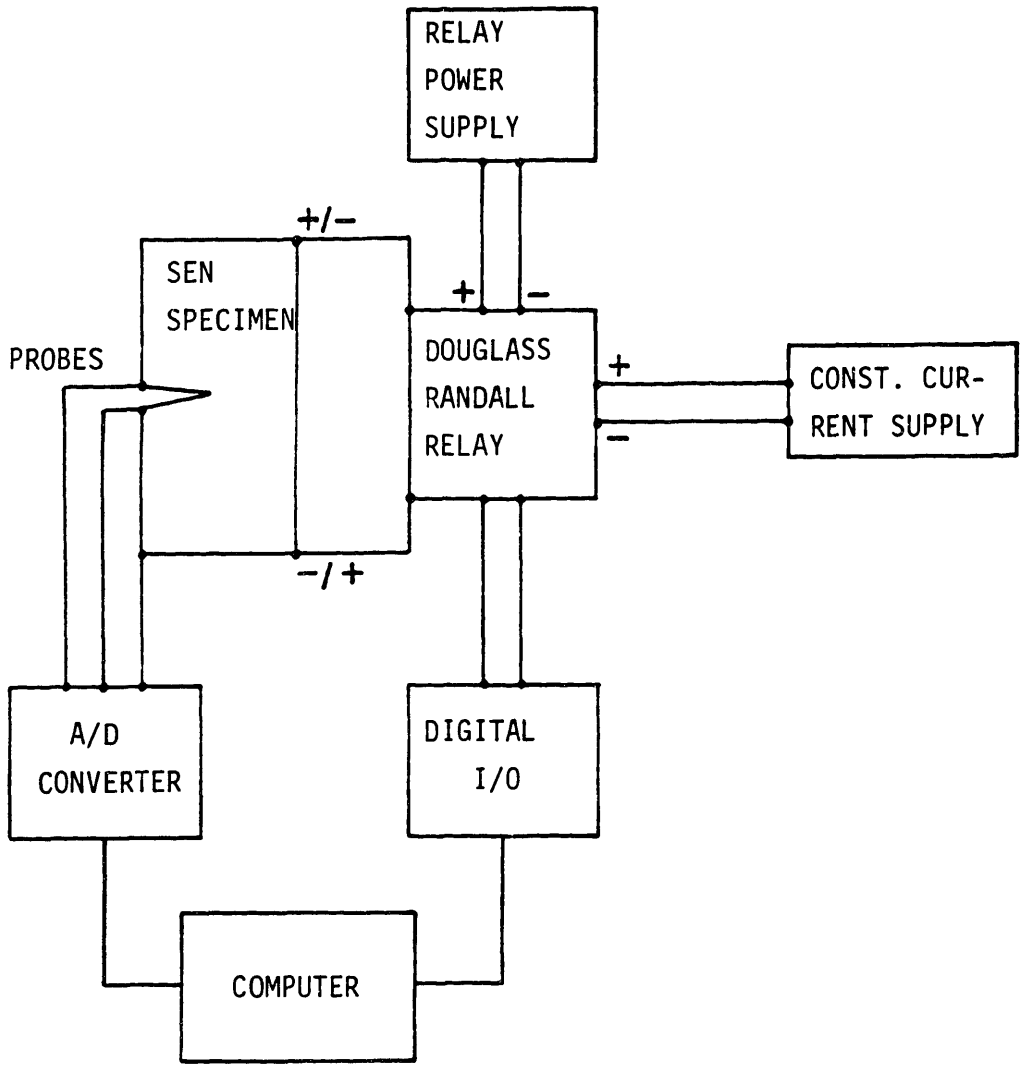

Figure 5.15 Schematic Diagram of the Switched DC Potential Drop Technique Used in Corrosion Fatigue Tests.

depth of a_1 and initial crack depth a_0, respectively. It was necessary to correct the obtain crack depth due to a significant deviation of measured data from the equation. This was done by:

$$a = 0.27\ a_0 + 0.73\ a_1 \qquad (5\text{-}14)$$

where a is a crack depth corrected from a_1 which is obtained by Eq. (5-13).

A constant ΔK of 25 $MPa\sqrt{m}$ with R=0.1 was used for most cases. The control of load to maintain the constant ΔK was achieved by computer control. The feedback process is schematically described in Figure 5.16.

The specimen was precracked at a ΔK of 20 $MPa\sqrt{m}$ with R=0.1 in N_2 gas environment. The experiment was begun when the crack grew by at least 0.1cm from the tip of the sawcut. Three environments used were N_2, 0.05M sodium sulphate solution with pH=3, and deaerated high purity water. In aqueous environments, the specimens were polarized in either the anodic or cathodic direction. Whenever it was necessary, the cell solution was heated by circulating through the external heating flask as described in Figure 5.17.

At an a/w value greater than 0.3, data scatter in the measured D.C. potential drop was significant. It was concerned that there may be a fraction of current short-cutting through the electrolyte near the crack tip. To eliminate the possibility of undesired polarization at the crack tip, ongoing crack measurement was done by optical method using a travelling microscope with a resolution of about 5μm. The measurement interval was such that a crack increment between two measurement did not exceed 50μm. The measure crack depth was manually input to computer so that a constant ΔK was maintained.

5.7 THE SLOW STRAIN RATE TEST(SSRT)

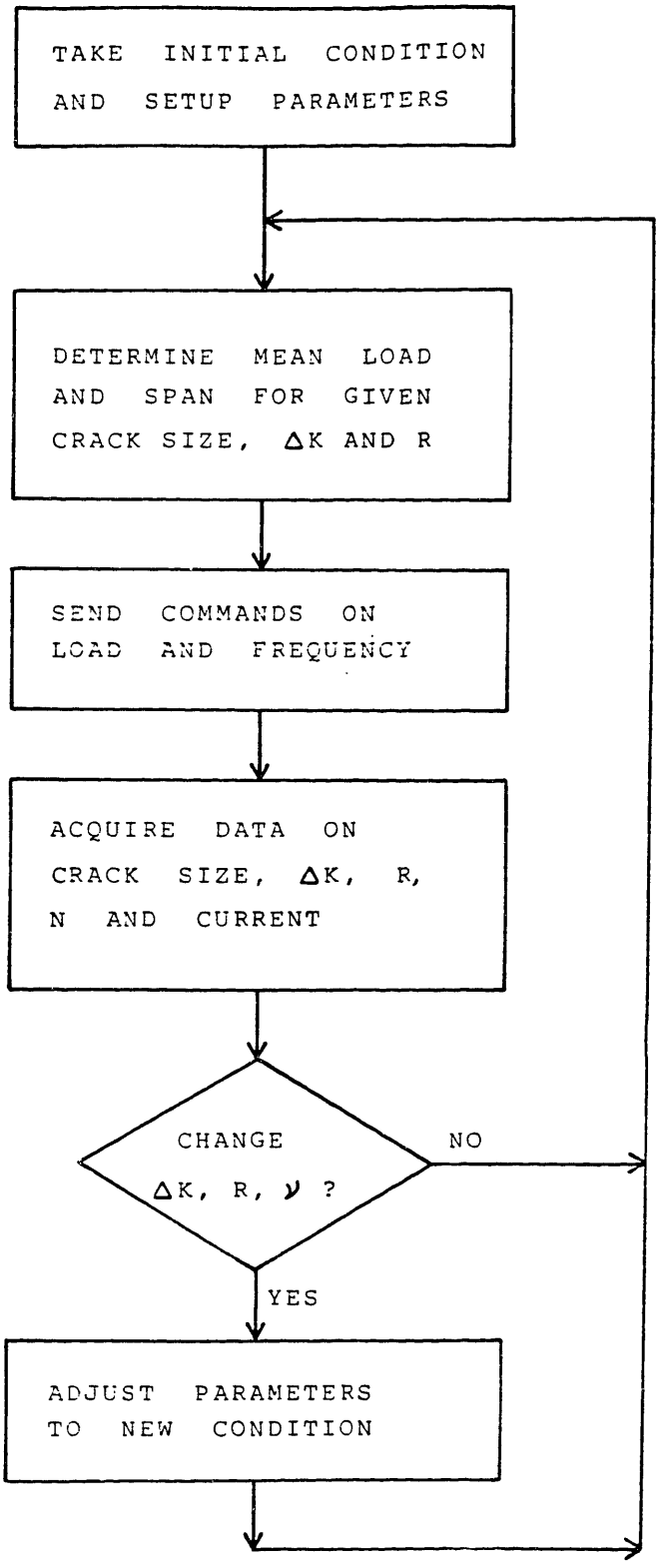

Figure 5.16 Logic Flow of Constant ΔK Control for Corrosion Fatigue Tests.

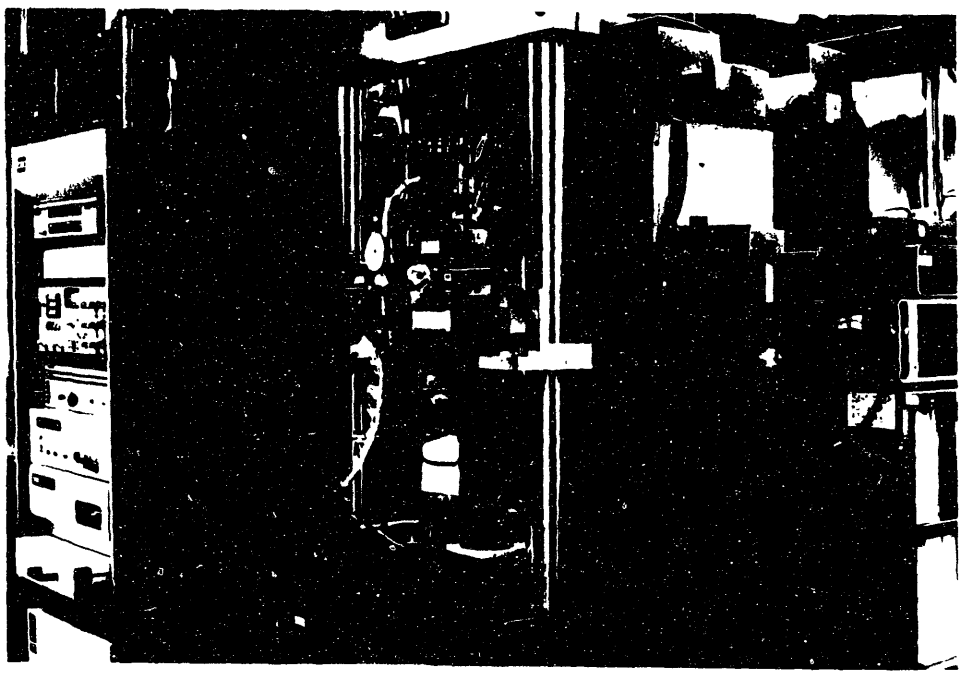

Figure 5.17 Overall View of the Corrosion Fatigue Test System and Assembled Test Cell.

The SSRT specimens were designed based on considerations of the crack detection sensitivity and the shape of stock materials. As a result of theoretical studies on the AC PD system, discussed in chapter 4, it was shown that a round bar geometry has advantages over a rectangular specimen. The round bar specimen is easier to analyze and has a low ratio of skin depth to the smallest dimension which would result in higher sensitivity. In addition, it became necessary to introduce a mild notch on the specimen in order to incresae the AC PD system sensitivity with a reduced probe spacing. Therefore, a round bar design with a mild notch at the center is taken as a standard design for the SSRT system.

For alloy 600 speciemens with a design shoown previously in Figure 4.8, it was not possible to employ the standard design because the stock tubing has a thickness of only 0.14cm. The stress in specimen results from only the hydrostatic force exerted on the pull rod due to system pressure exceeded the ultimate tensile strength of the mateiral when a notch was introduced. The smooth specimen design required a probe spacing of 1.27cm which was determined partly by dimensional requirement of the LVDT knife edges.

For alloys X-750 and 718, the stock materials were big enough to use the standard design, as shown in Figure 5.9. The elastic stress concentration factor for the semi-circular notch was known to be only 1.7. Due to this large notch radius, at it was feet that no environmental perturbation would occur that would affect the crack initiation process.

The preparation of specimens was done in the same way as in previous cases. Alloy 600 tubing was cut by EDM. The grip end sections were flattened and holes were punched. The alloy X-750 and 718 specimens were machined with a small allowance on each dimensions, then heat treated to appropriate final conditions. A surface layer, at least 500μm thick, was removed during the final machining step. The machined specimens were mechanically polished using SiC papers up to grit 600, and ultrasonically cleaned inacetone. Due to a time consuming

preparations for high temperature testing, it took about 16 hours between the specimen polish and the beginning of a test.

The specimens and autoclave internals were handled with gloved hand to minimize undesirable contamination with sodium chloride. After securing the specimen in the load train with appropriate ceramic insulation, the AC PD lead wires and probe wires were spot welded. All electronic devices were electrically disconnected during the spot welding in order to eliminate the chance of damage. The LVDT knife edges were attached and connected to the cores using a Tektronix model 2215A oscilloscope. Any undesirable signals due to abnormal short-circuits and external noises were checked out both before and after closing the autoclave body.

The autoclave was sealed using a stainless steel gasket which was tightened between the body and head of the autoclave using 8 bolts equally torqued to 6 Nm. Then the system was purged of air by flowing a prepurified nitorgen gas into a discharge side of the high pressure pump through a check valve, as shown in Figure 4.2. After at least 30 minutes of purging, the pump was started to pressurize the system to 6 MPa. Unless there was an appreciable leakage in the system, the underpressure interlock was cleared to start heating the autoclave system under the control of computer software described earlier in Chapter 4. A constant heat up rate of 60 C/hr was used up to 320 C above which the heatup rate was lowered to about 20 C/hr. The system pressure was gradually increased from the initial 6 MPa to a desired value when the temperature reached 200 C. A pressure of 6 MPa was used for all tests below 200 C. The data acquisition and control process were fully automated as described in Chapter 4.

Chapter 6

RESULTS

6.1 MICROSTRUCTURAL CHARACTERISTICS

6.1.1 Microstructures of Alloy 600

The two-step etch technique was designed to reveal microstructural distribution of carbides. The first step, the orthophosphoric etch, is known to attack the matrix so that unattacked carbides develop a contrast. The second step, the nital etch, attacks primarily the grain boundaries. Therefore, it was posible to determine the amount of carbides along grain boundaries when two micrographs obtained at the same location are compared. Morphology of intergranular carbide distribution is usually described based on the optical micrographs taken at 500X magnification.

Two-step micrographs are shown for heat NX1638 in Figure 6.1. The heat contains a low level of carbon and received final annael at 1024 C of furnace temperature. The grain boundaries are decorated with morphologies ranging from semi-continuous to discrete. There is a few intragranular MC carbides. There is no evidence of carbide precipitation along prior recrystallization boundaries which normally run in the direction of the tubing axis. The microstructure is bi-modal and consists of coarsensed grains with a size of about 50μm and finer grains with a size of about 25μm. The average grain size was found to be 32μm. There is no significant difference in the grain size between inner and tube outer diameter.

A STEM micrigraph shows grain boundary structure of the heat NX1638 in Figure 6.2. Carbides are widely spaced and dislocations are often associated with carbides. There is an appreciable amount of chromium depletion with an equivalent amount of iron enrichment,as shown in Figures 6.3. The intergranular corrosion test results shows a weight

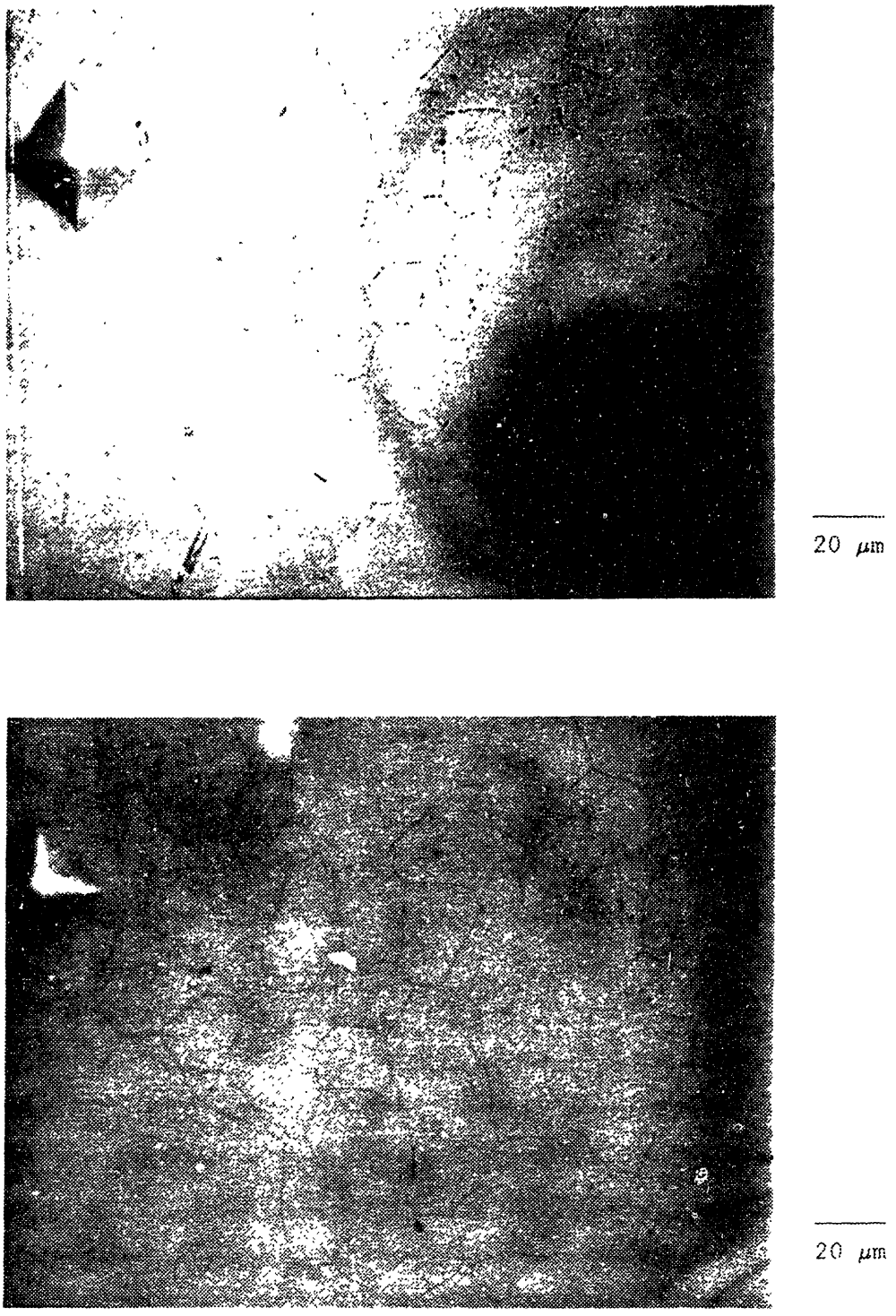

Figure 6.1 Two-step Etch Micrographs of Longitudinal Section of Alloy 600 Tubing Heat NX1638 (upper orthophosphoric and lower nital etch).

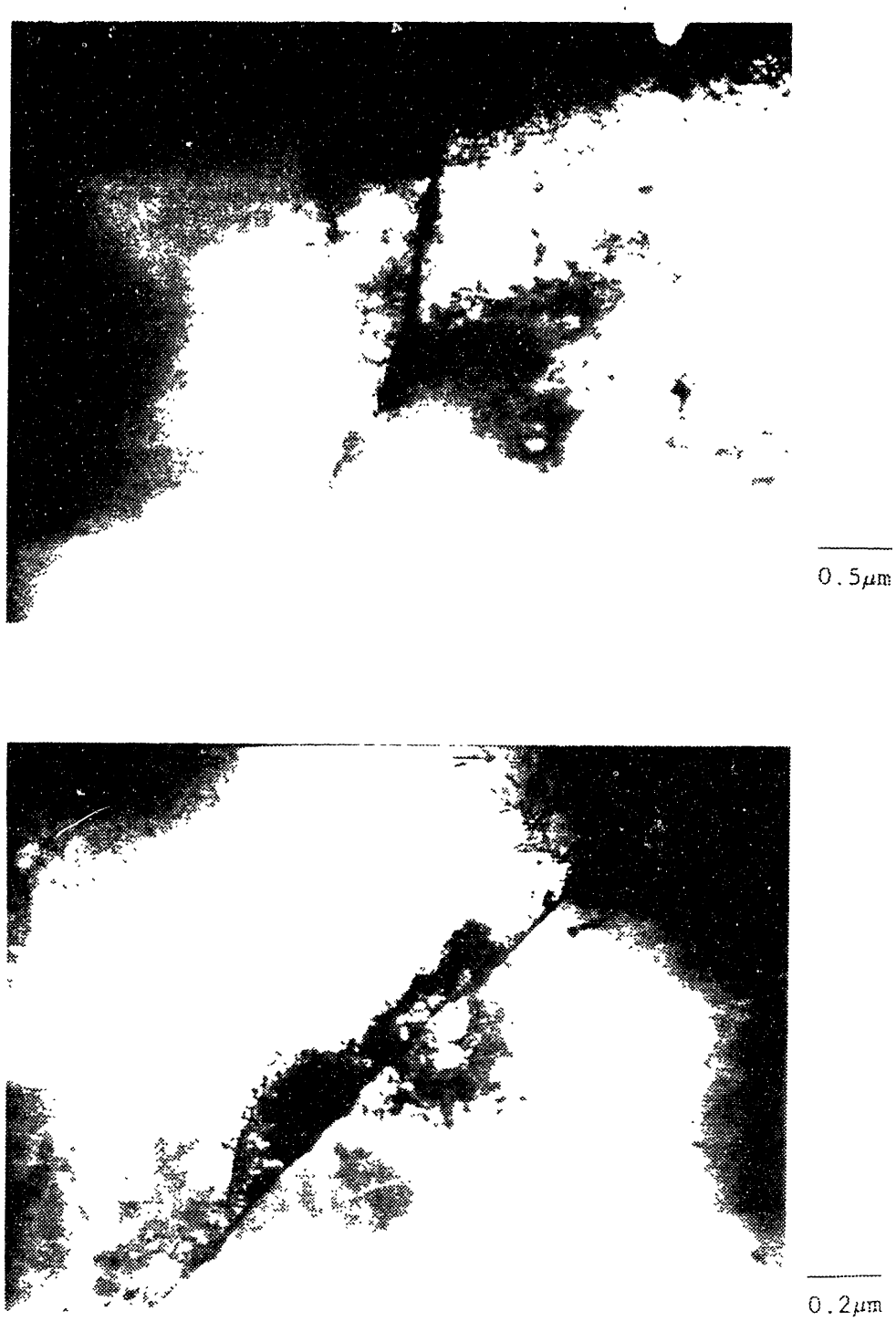

Figure 6.2 The STEM Micrographs for the HTMA Condition of NX1638 (lower micrograph shows dislocations around grain boundary carbide)

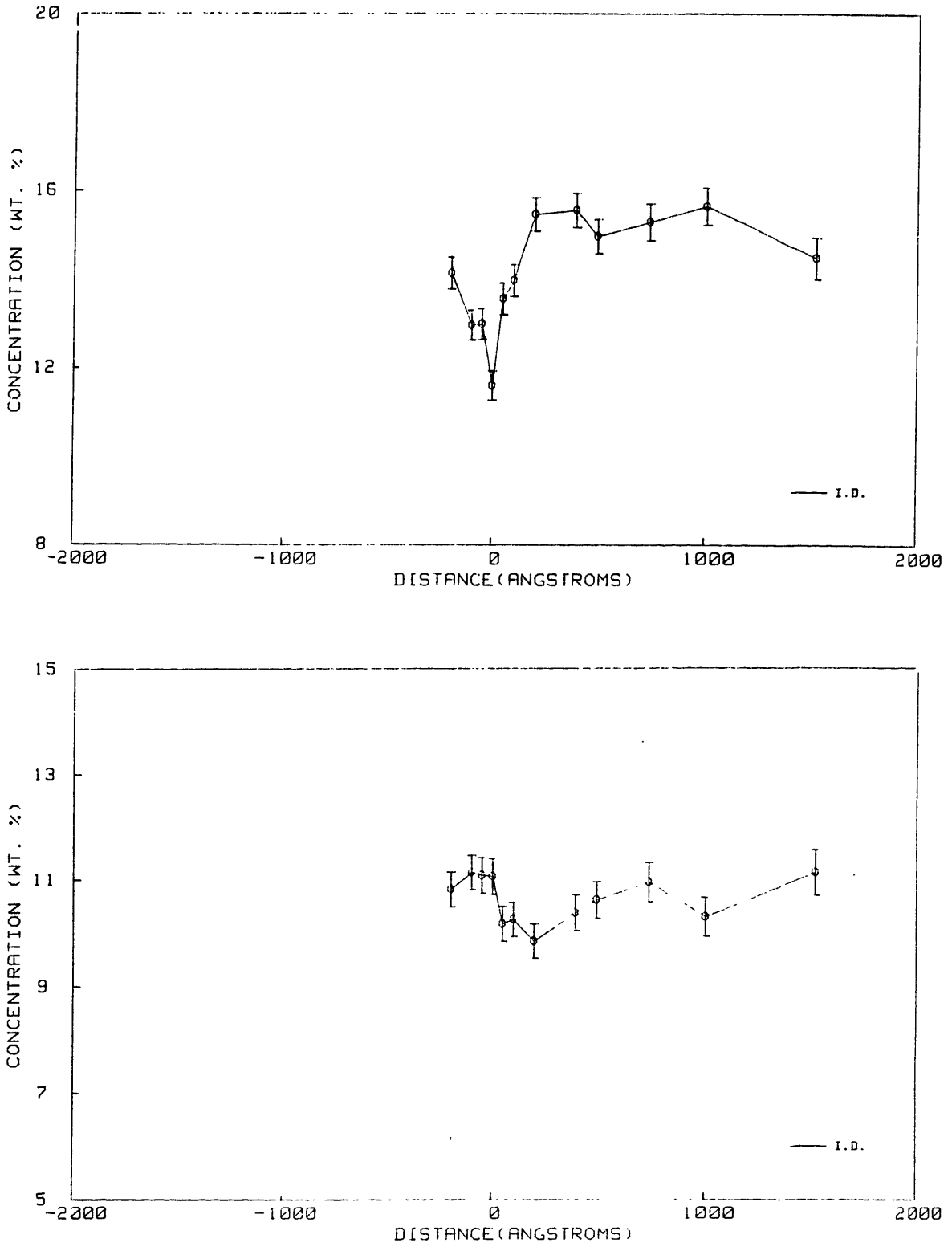

Figure 6.3 Chromium and Iron Distributions as a Function of Distance from a Grain Boundary in an HTMA condition of Heat NX1638 as Determined by the STEM Microchemical Analysis.

loss of 0.35mg/day, indicating that the degree of chromium depletion along grain boundaries is low.

The kinetics of carbide precipitation in heat NX1638 was studied by examining responses of microstructures to aging treatments at 700 C for 0.5 hr, 1 hr, 2 hr, 5 hr, 8 hr, 11 hr, and 15 hr. After 33 minutes of aging, the carbide morphology at the grain boundaries became increasingly continuous, as shown in Figure 6.4. The nital etch in Figure 6.4 does not reveal the grain boundaries with enough contrast. However, by a careful comparison of the micrographs it was observed that most of grain boundaries are decorated with the carbides. Further aging resulted in enhanced grain boundary contrast upon etching, but there was no significant change in the carbide morphology. Therefore, the optical microstructures for conditions aged for more than an hour may be represented by one obtained after 15 hours of aging. The latter condition, designated as thermal treatment(TT), produced nearly continuous carbides along grain boundaries which agrees with microstructures typically obtained from the alloy 600 commercial tubing produced by the same process, as shown in Figure 6.5. The SEM micrographs for the condition are shown in Figure 6.6. The continuous carbides at grain boundaries are, in fact, semi-continuous when observed at the higher magnification.

The results of intergranular corrosion tests for the aged conditions are shown in Figure 6.7. The susceptibility to intergranular corrosion increases, immediately upon aging, to a maximum after 33 minutes of aging, and rapidly decreases to the original level. The maximum weight loss after 33 minutes of aging is low enough to indicate that the amount of solutionized carbon in the HTMA condition is limited due to low bulk carbon content (0.014%). The edges of the Huey test specimen after aging 33 minutes are shown in Figure 6.8. It is to be to be noted that the depth of intergranular attack is higher at the inner surface. This behavior will be further examined later with the STEM results.

The high carbon(0.038%) heat NX2650, after the same HTMA process, produced a microstructure quite different from the heat NX1638, as shown

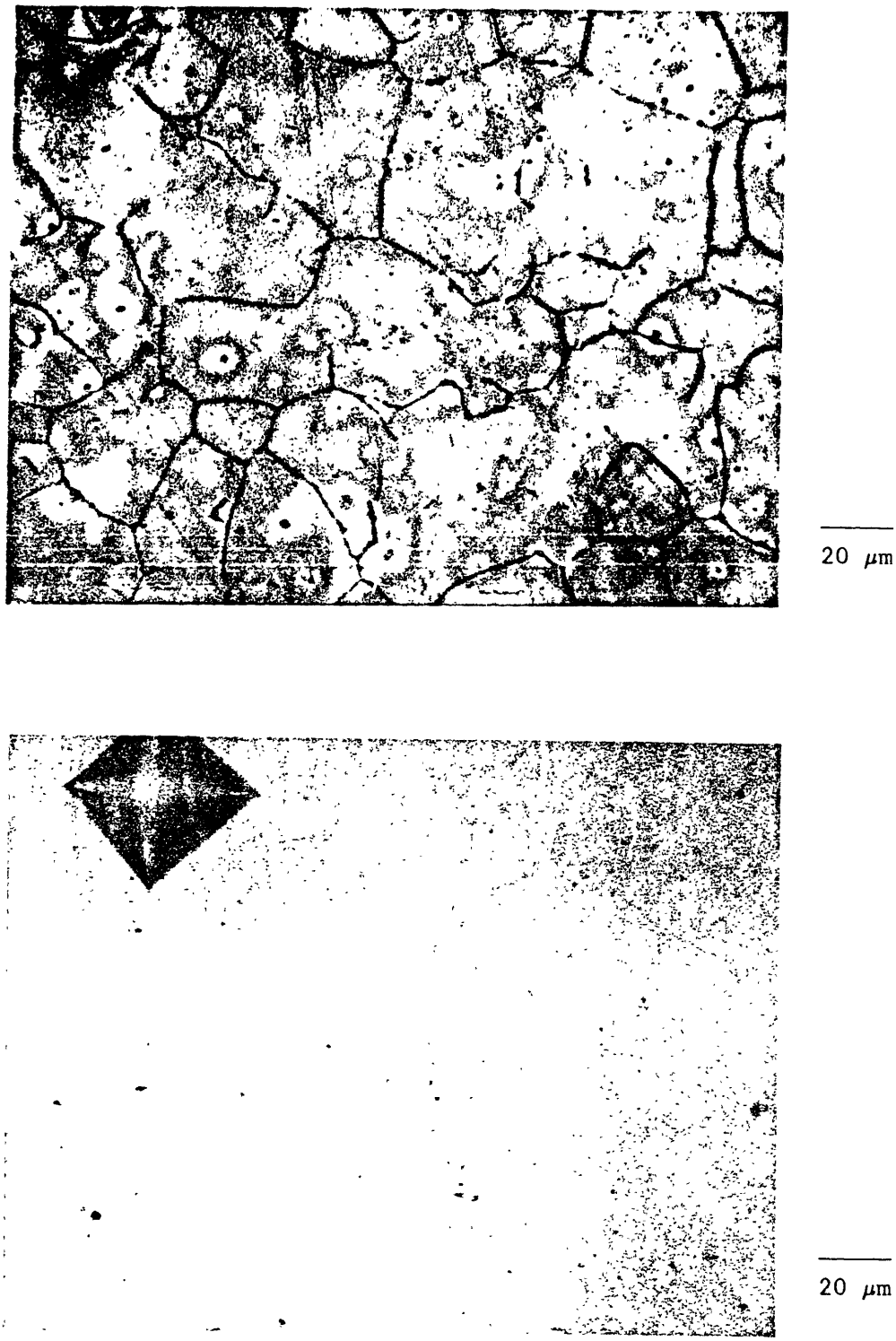

Figure 6.4 Two-step Etch Micrographs of Longitudinal Section of Alloy 600 Tubing Heat NX1638 after an Aging at 700 C for 33 Minutes (upper orthophosphoric and lower nital etch).

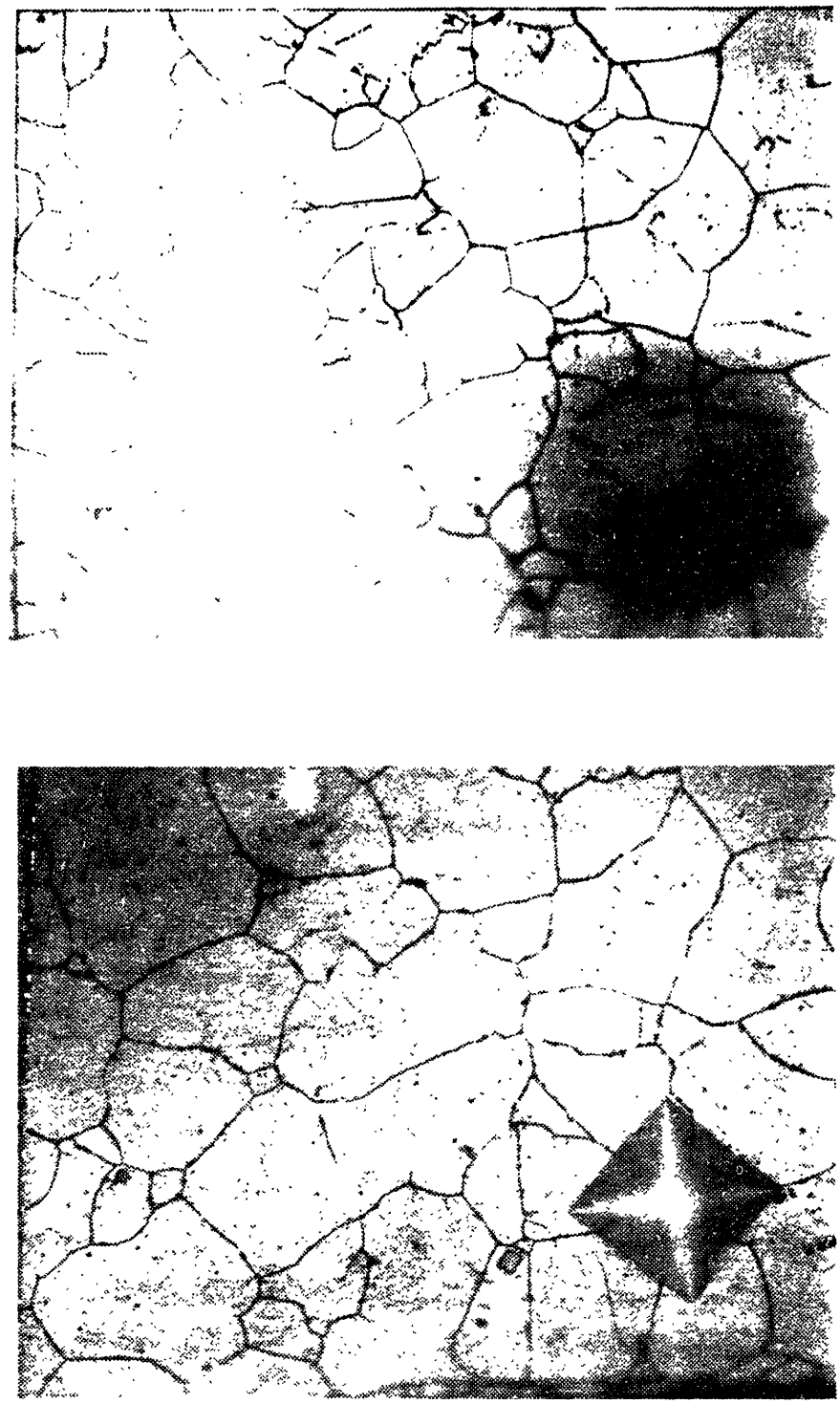

Figure 6.5 Two-step Etch Micrographs of Longitudinal Section of Alloy 600 Tubing Heat NX1638 at 700 C for 15 hours (upper orthophosphoric and lower nital etch).

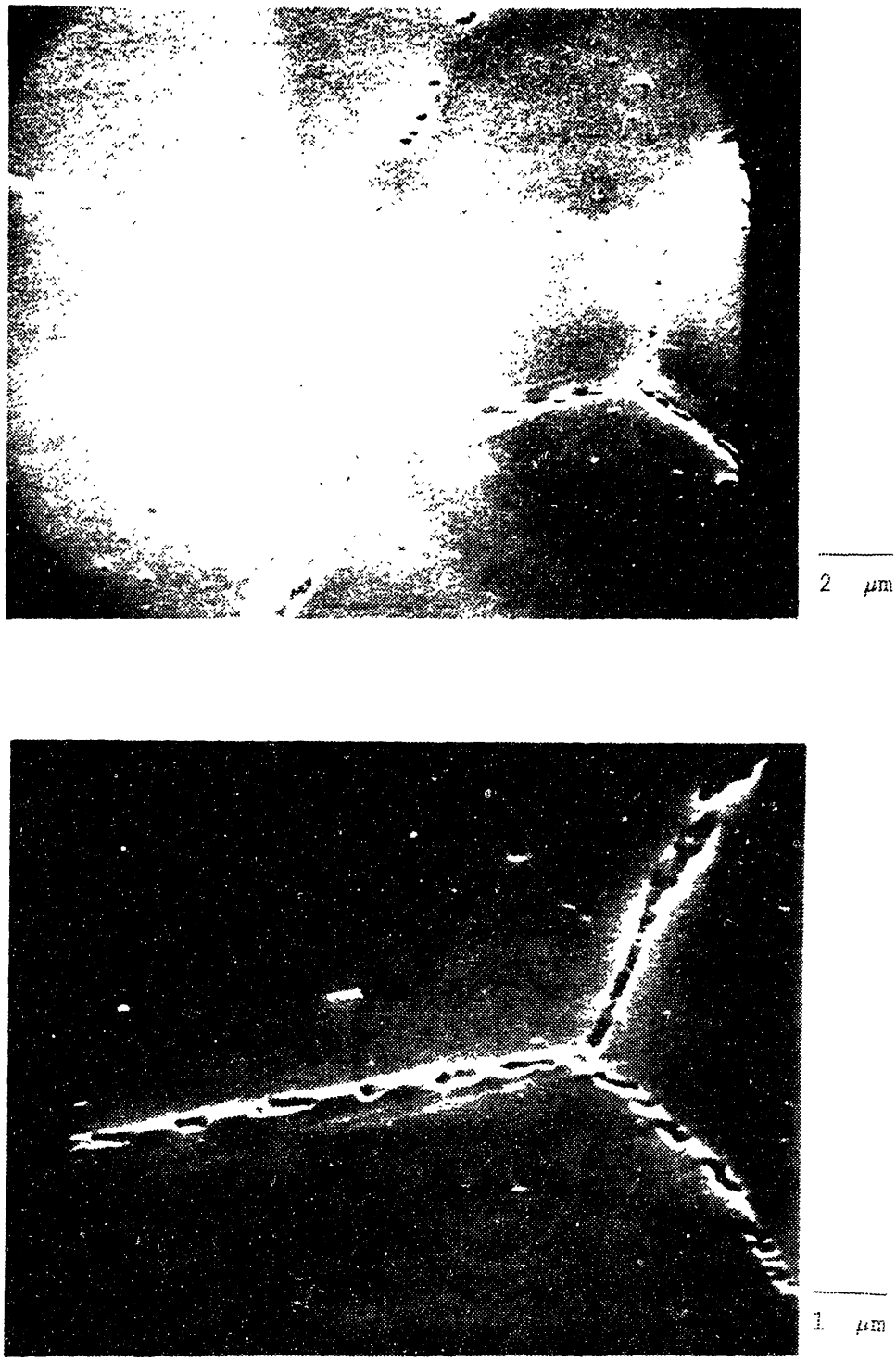

Figure 6.6 The SEM Micrographs of the Longitudinal Section of Alloy 600 Tubing Heat NX1638 after Aging at 700 C for 15 Hours (orthophosphoric etch).

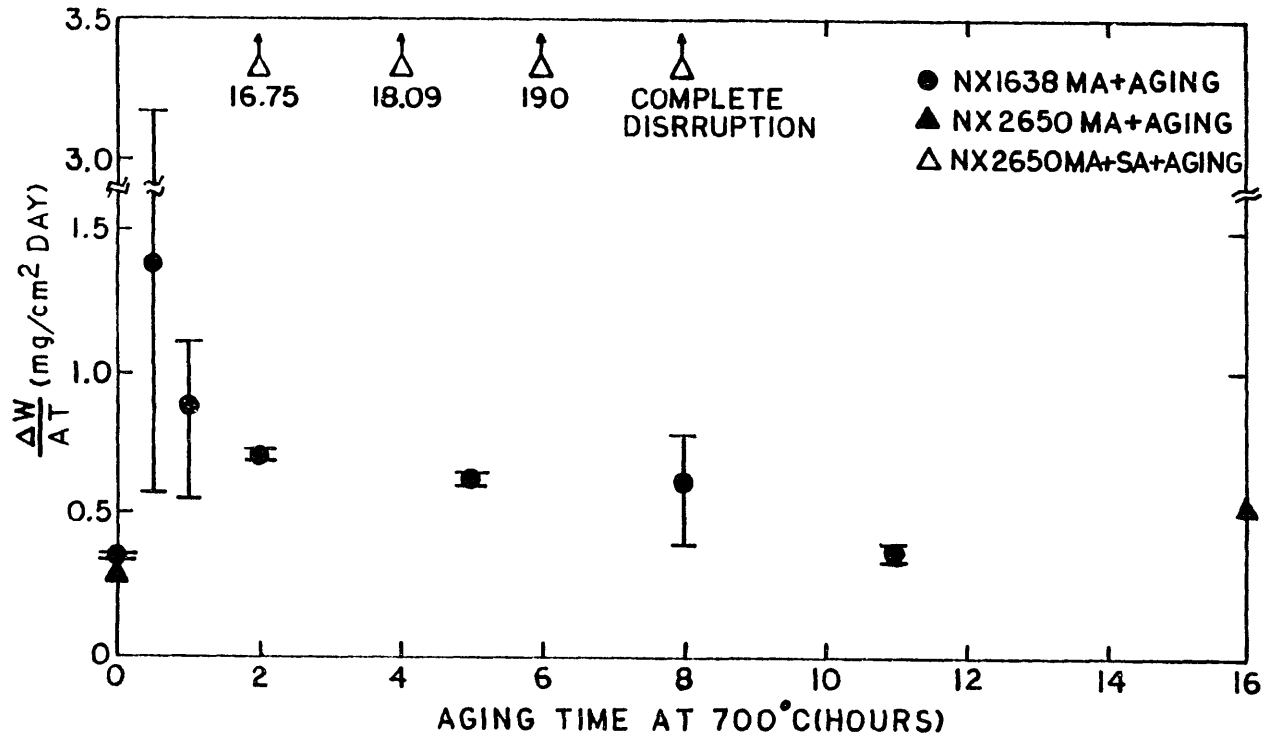

Figure 6.7 Boiling Nitric Acid Test for 25 Hours (Modified Huey) of NX1638 and NX2650 Tubing Specimens after 700°C Aging for Varicus Time.

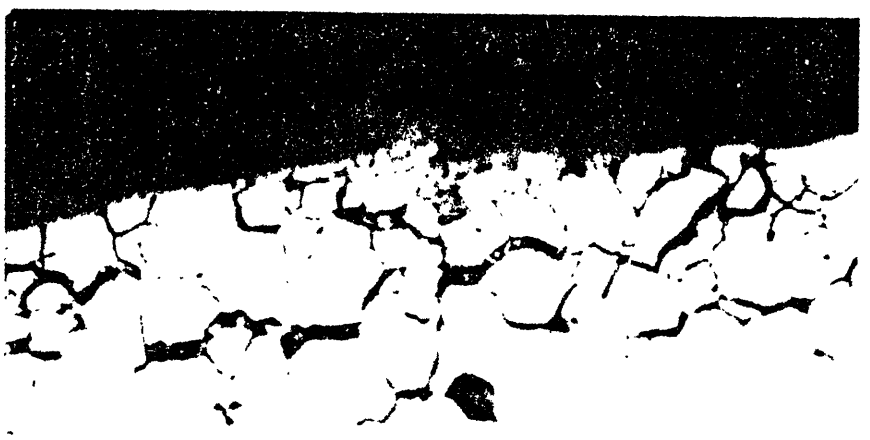

Figure 6.8 Edges near Inner (upper micrograph) and Outer Diameter (lower micrograph) of the Huey Test Specimen of Alloy 600 Tubing Heat NX1638 aged for 33 Minutes at 700C.

in Figure 6.9. It is shown that there are considerable amounts of intragranular carbides lined up in the direction of cold works whereas the grain boundaries are relatively free of carbides. The intragranular carbide are believed to have formed along the elongated grain boundaries after the final drawing during the heatup period since the penultimate anneal at 1066C was a solution treatment. The final anneal time appears to be too short to resolutionize all the intragranular carbides.

The grain size is ranging between about 2μm and 50μm with an average of 15μm. The extensive precipitation of intragranular carbides may have slowed down the kinetics of grain coarsening during the HTMA process. A more detailed microstructure is revealed by the scanning transmission electron microscope (STEM). As shown in Figure 6.10, grain boundaries are essentially free of any form of precipitates whereas coarse intragranular carbides are easily observed. Distributions of chromium and iron at grainboundaries are found to be slightly different from the matrix as shown in Figure 6.11. The Huey test on the heat NX2600 showed that the sensitization is negligible, as shown in Figure 6.7.

The HTMA condition of NX2650 responded to the thermal treatment by significant precipitation of carbides along grain boundries, as shown in the two-step etch micrographs, Figure 6.12. The morphology of intergranular carbides is of a semi-continuous type. The intragranular carbides have also increased when compared with the microstructure of the HTMA condition, Figure 6.9. These additional precipitation of intragranular carbides appear to result from the growth of existing fine carbides since there is no driving force for nucleation of new carbides along the prior boundaries once the recrystallization is completed. The grain size is found to remain unaffected by the aging.

A sensitized microstructure was produced by a solution treatment of NX2650 for 8 minutes at 1100 C followed by a water quench and an aging at 700 C for 8 hours. The solution annealed and sensitized (SAS) material shows a continuous carbide precipitates along grain boundaries of the significantly coarsened microstructure, as shown in Figure 6.13. Most of the intragranular carbides were resolved while remaining

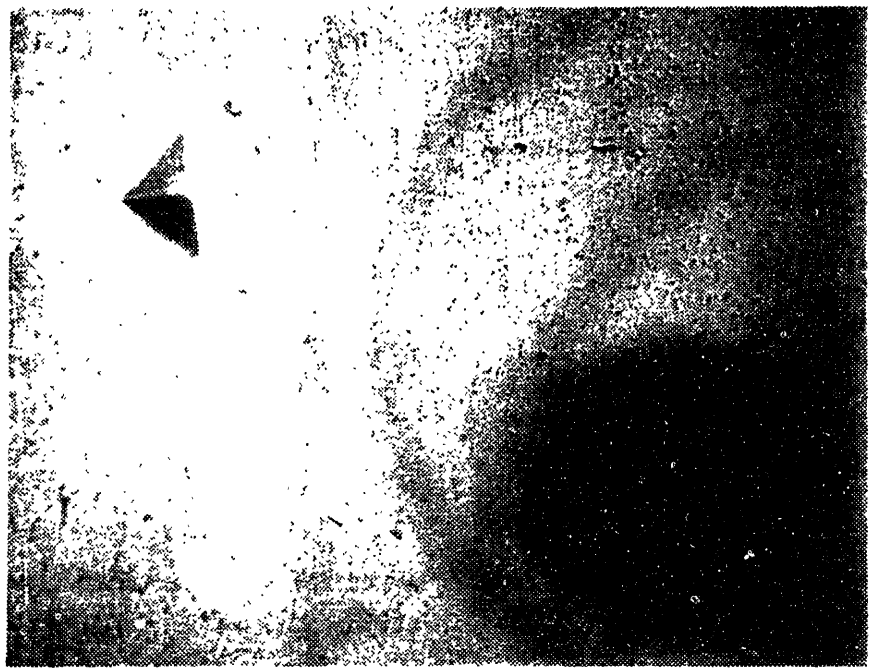

Figure 6.9 Two-step Etch Micrographs of Longitudinal Section of the HTMA Condition of Heat NX2650 (upper orthophosphoric and lower nital etch).

Figure 6.10 The STEM Micrographs of the HTMA Condition of NX2650.

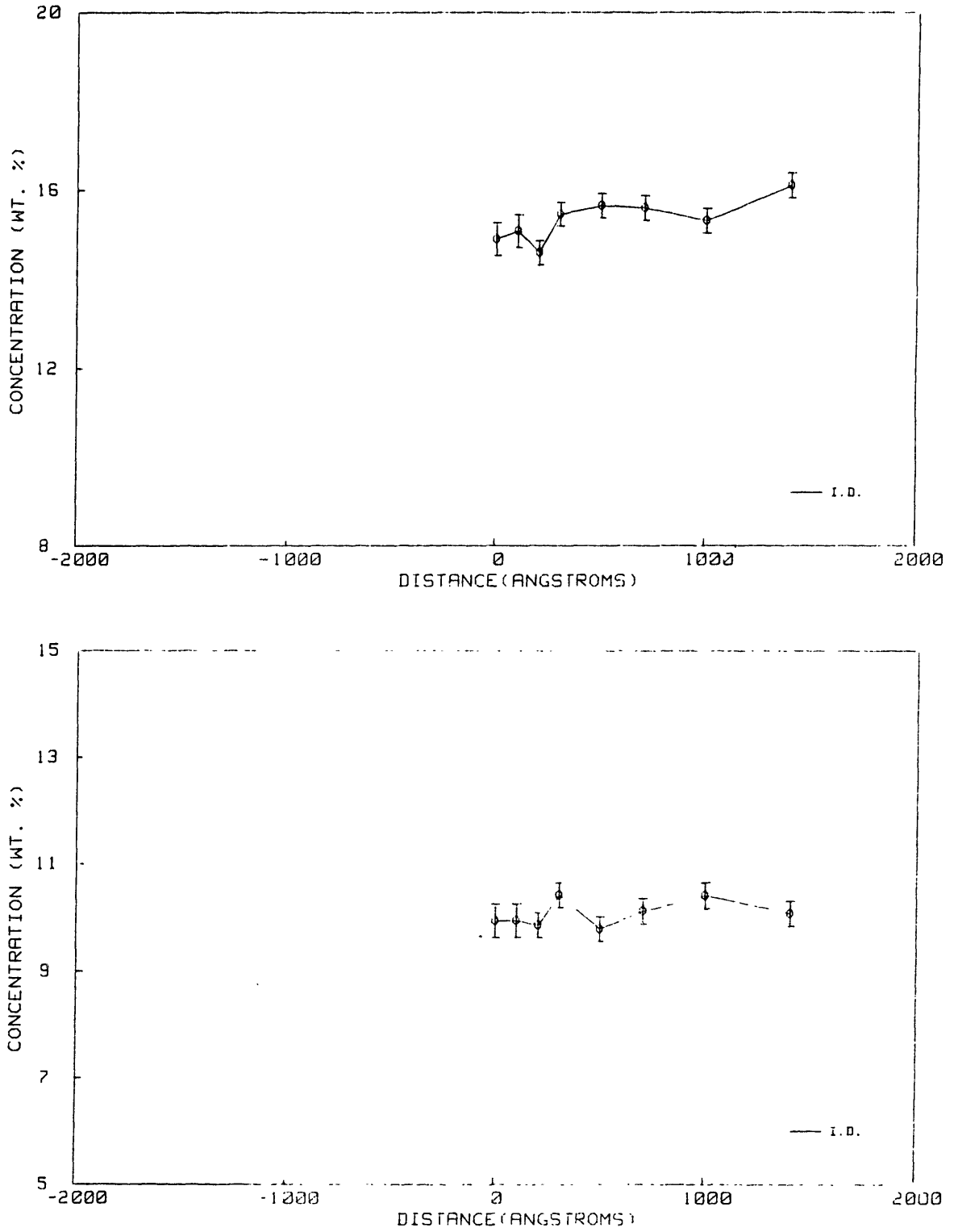

Figure 6.11 Chromium and Iron Distributions as a Function of Distance from a Grain Boundary in the HTMA Condition of Heat NX2650.

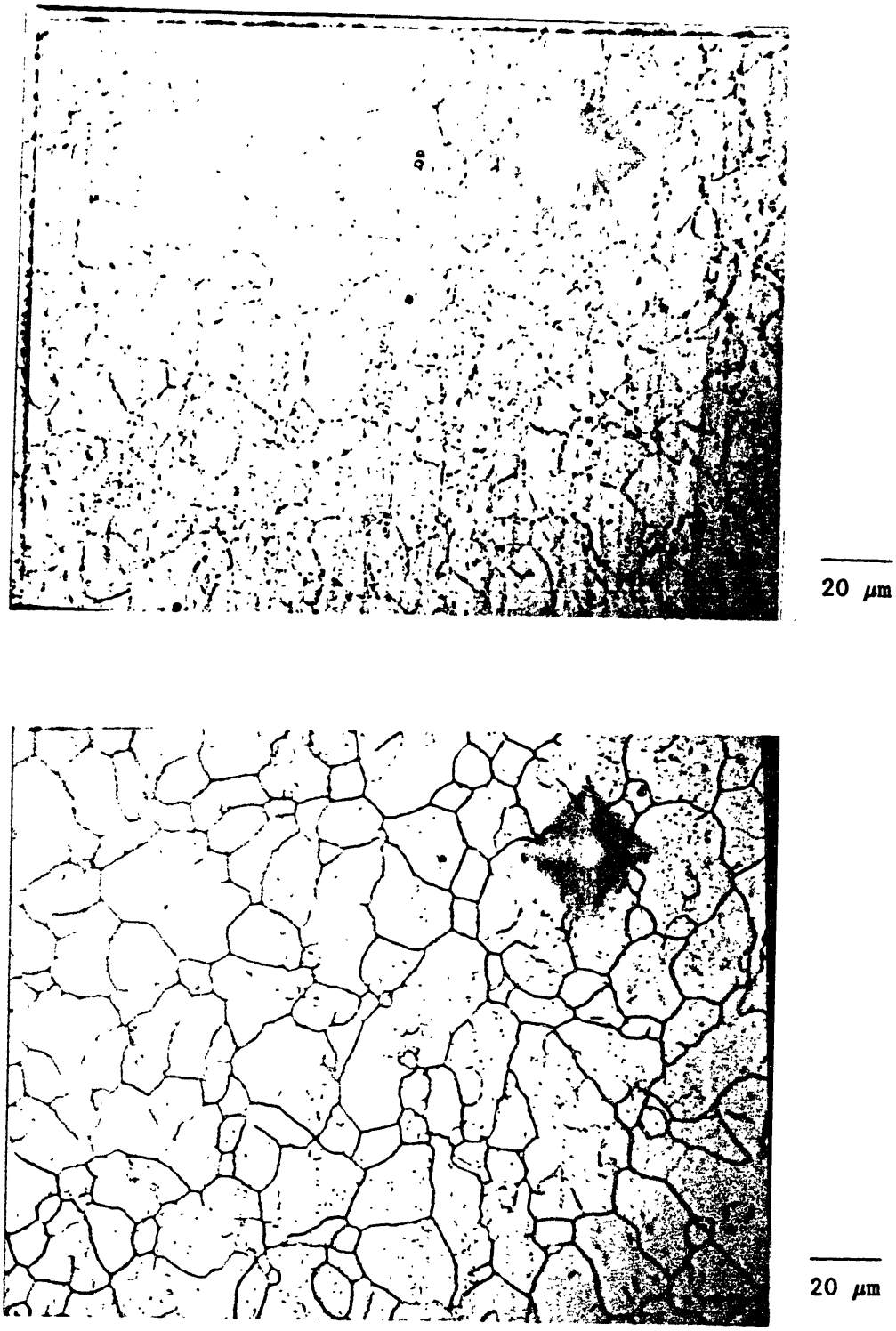

Figure 6.12 Two-step Etch Micrographs of Longitudinal Section of Alloy 600 the Thermally Treated Condition of Heat NX2650 (upper orthophosphoric and lower nital etch).

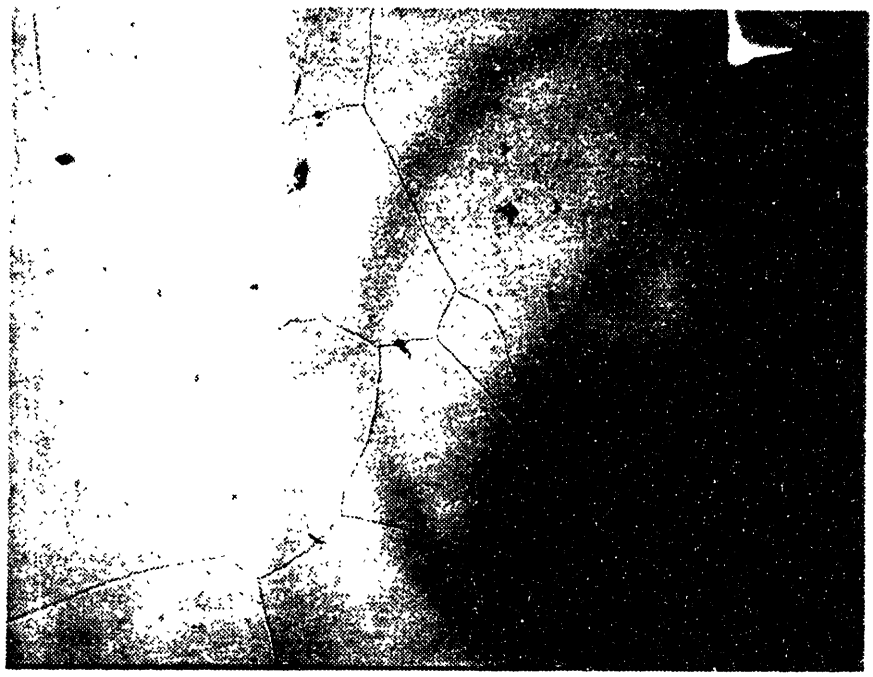

Figure 6.13 Two-step Etch Micrographs of Longitudinal Section of Alloy 600 the Solution Annealed and Sensitized Condition of Heat NX2650 (upper orthophosphoric and lower nital etch).

precipitates are considered to be of an MC-type. The average grain size was measured to be 55μm. The Huey tests were done for the solution annealed conditions of heat NX2650 as a function of aging time at 700°C. The results are summarized in Figure 6.7. The weight loss increases rapidly with aging which can be expected from the high carbon content of the heat. After 8 hours of aging, the SAS condition showed a complete disruption of the sample after about 12 hour of test.

The two-step etch metallography of the EPRI specially processed heats such as 96834, 76375, and NX3857 were done by Takemoto[21]. A part of results are reproduced here for the discusion in conjunction with STEM results. As described in Chapter 5, an HTMA condition denotes 927 C for the anneal.

The heat 96834 has two final tubing diameters; namely, a 2.2cm and a 1.9cm nominal. There is little difference between two in microstructure revealed by both two-step etch and STEM analysis. The two-step etch micrographs for the HTMA condition are shown in Figures 6.14 and 6.15 for the 2.2cm and 1.9cm diameter tubings, respectively. Both have a uniform grain size with an average of 35μm. The grain boundaries are heavily decorated with carbide. Also, intragranular carbides are present in a considerable amount and lined up in the longitudinal direction.

The STEM micrographs are shown for the 2.2cm diameter tubing of the HTMA condition, in Figure 6.16. By the procedure described in Chapter 5, specimens were made from either near inner surface or near outer surface of a tubing. For both inner and outer diameter regions, grain boundaries are decorated with a discontinuous carbides morphology. Near the inner diameter, in general, the carbides are bigger and more closely spaced than the case of the outer diameter. The chromium concentrations and iron are shown in Figure 6.17 for three different locations of the tubing as a function of distance from a grain boundary. There are moderate degrees of sensitization with a minimum chromium concentration of about 12% at the inner diameter whereas the least sensitization occurs at the outer diameter with about 2% higher chromium. The width

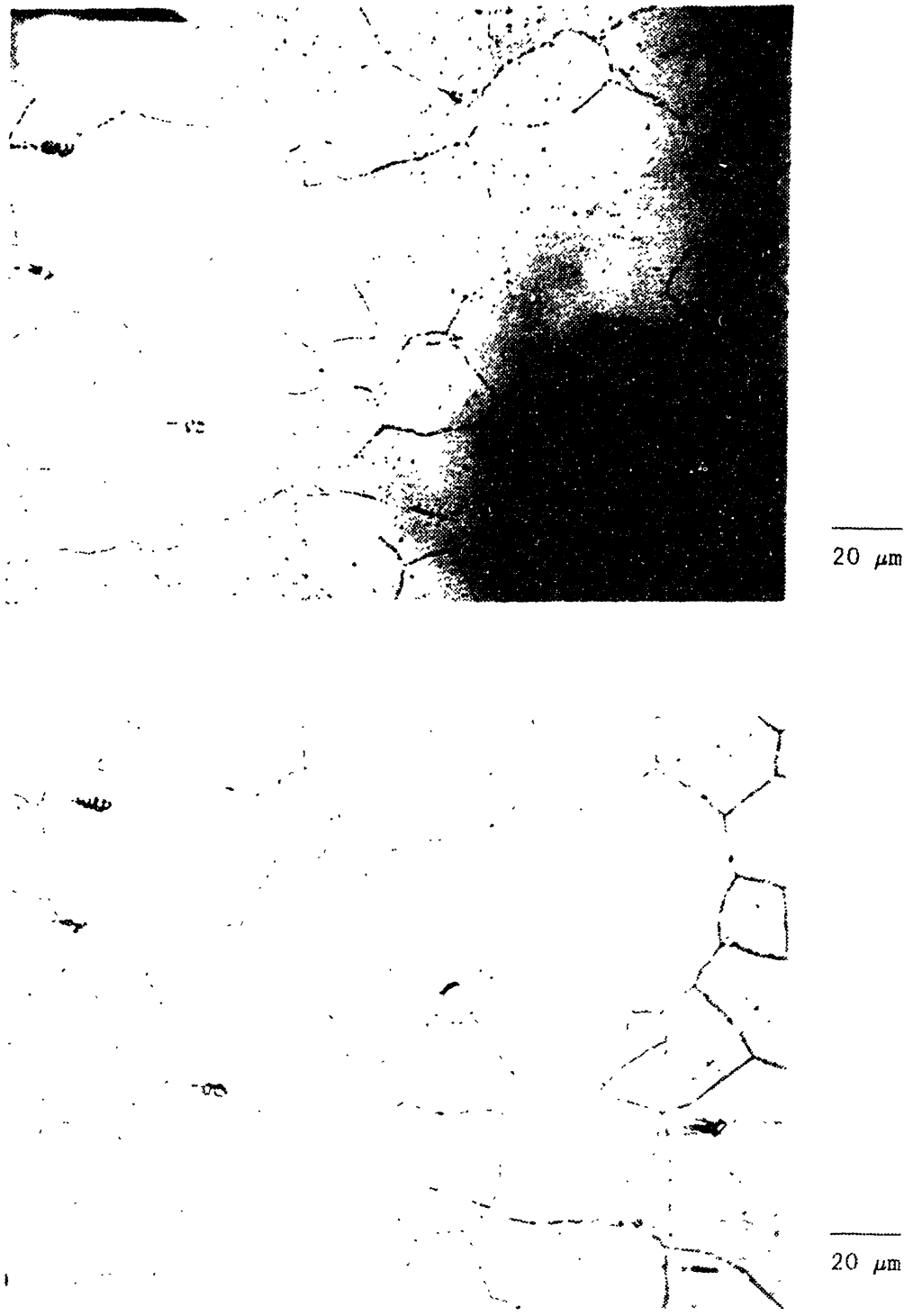

Figure 6.14 Two-step Etch Micrographs of Longitudinal Section of Alloy 600 a HTMA Condition of Heat 96834 with 2.2cm Nominal Diameter (upper orthophosphoric and lower nital etch)[21].

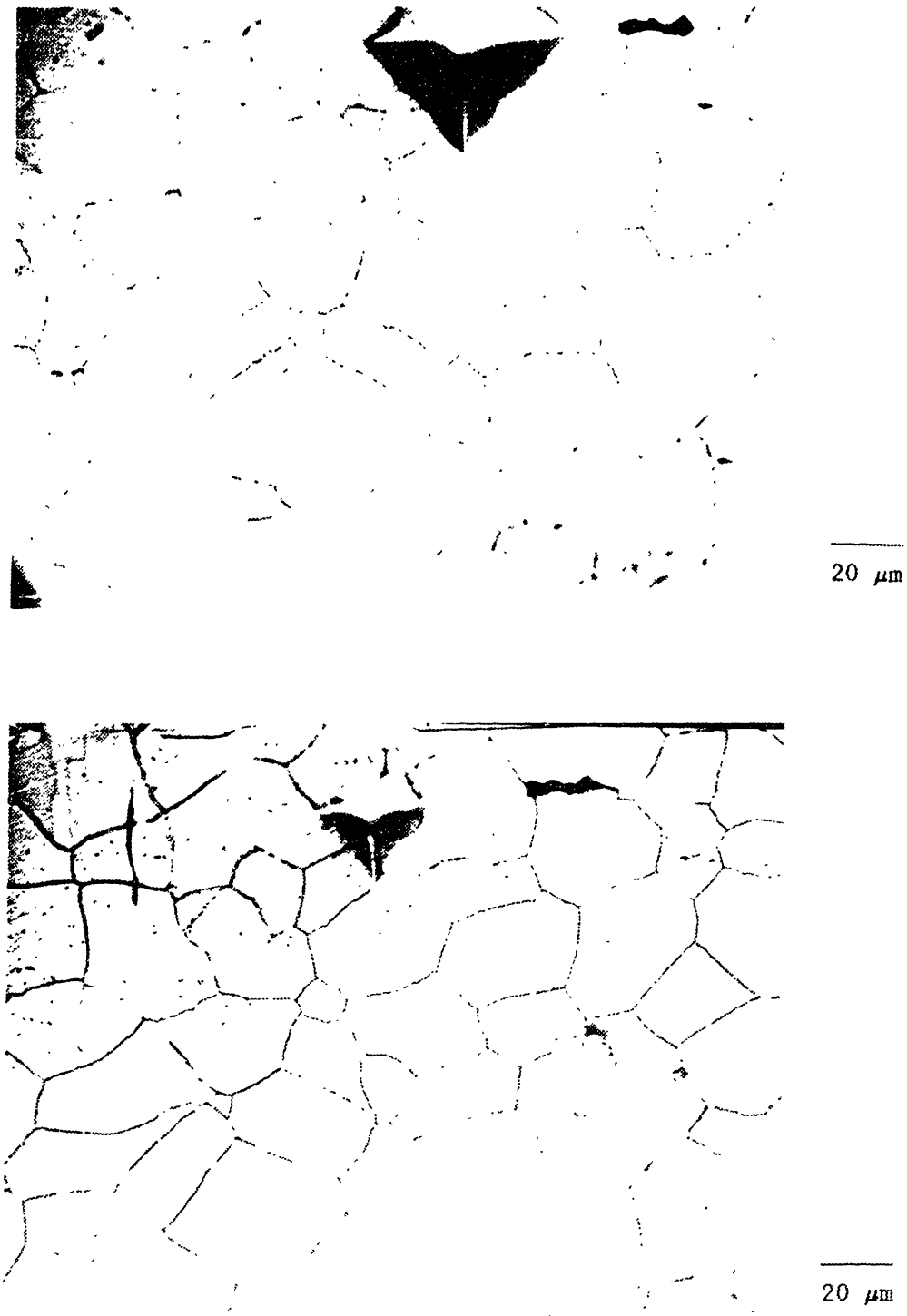

Figure 6.15 Two-step Etch Micrographs of Longitudinal Section of Alloy 600 a HTMA Condition of Heat 96834 with 1.9cm Nominal Diameter (upper orthophosphoric and lower nital etch).

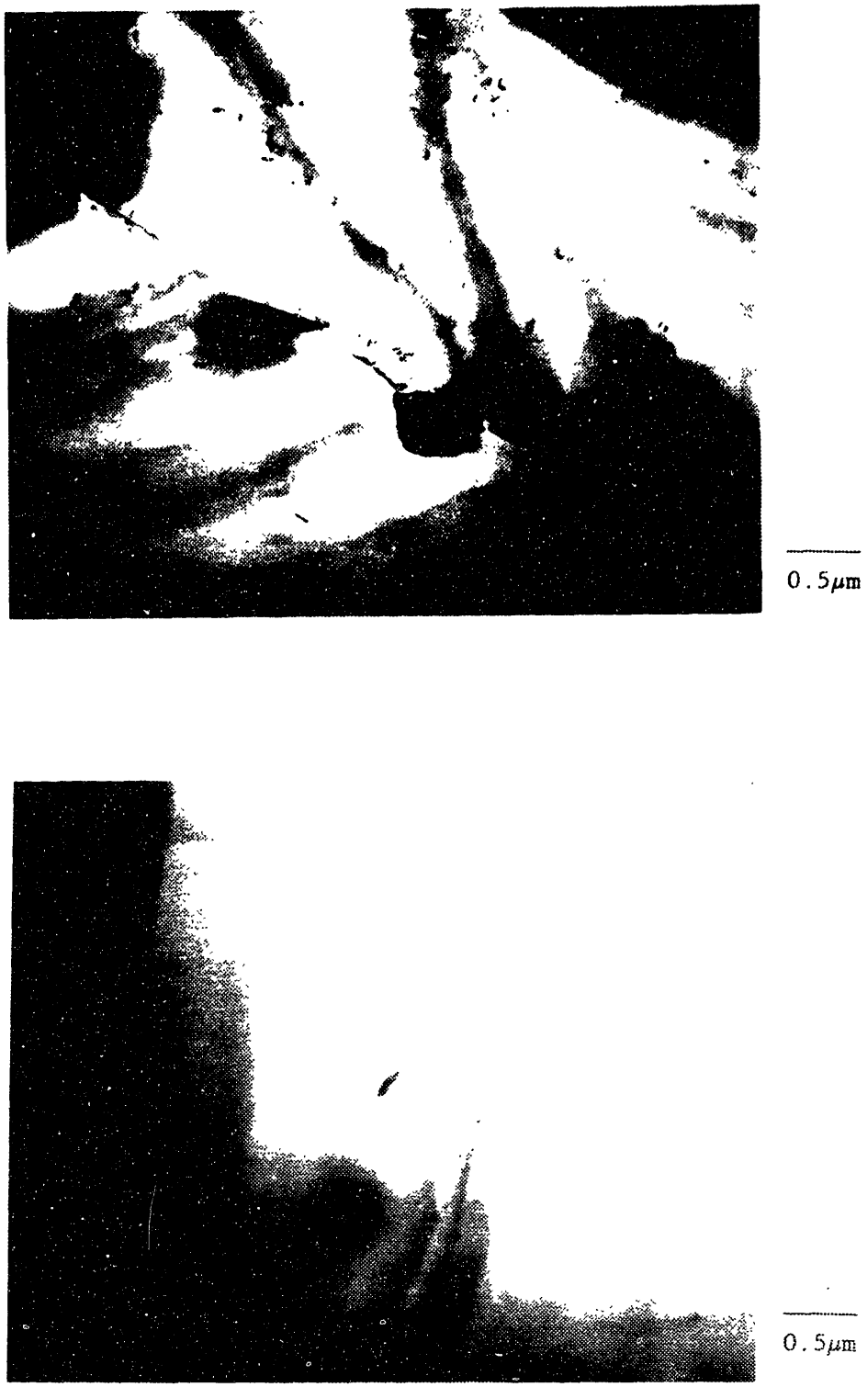

Figure 6.16 The STEM Micorgraphs for a 2.2cm Diameter Tubing of a HTMA Condition of Heat 96834 (upper micrograph at inner diameter region and lower at outer diameter region).

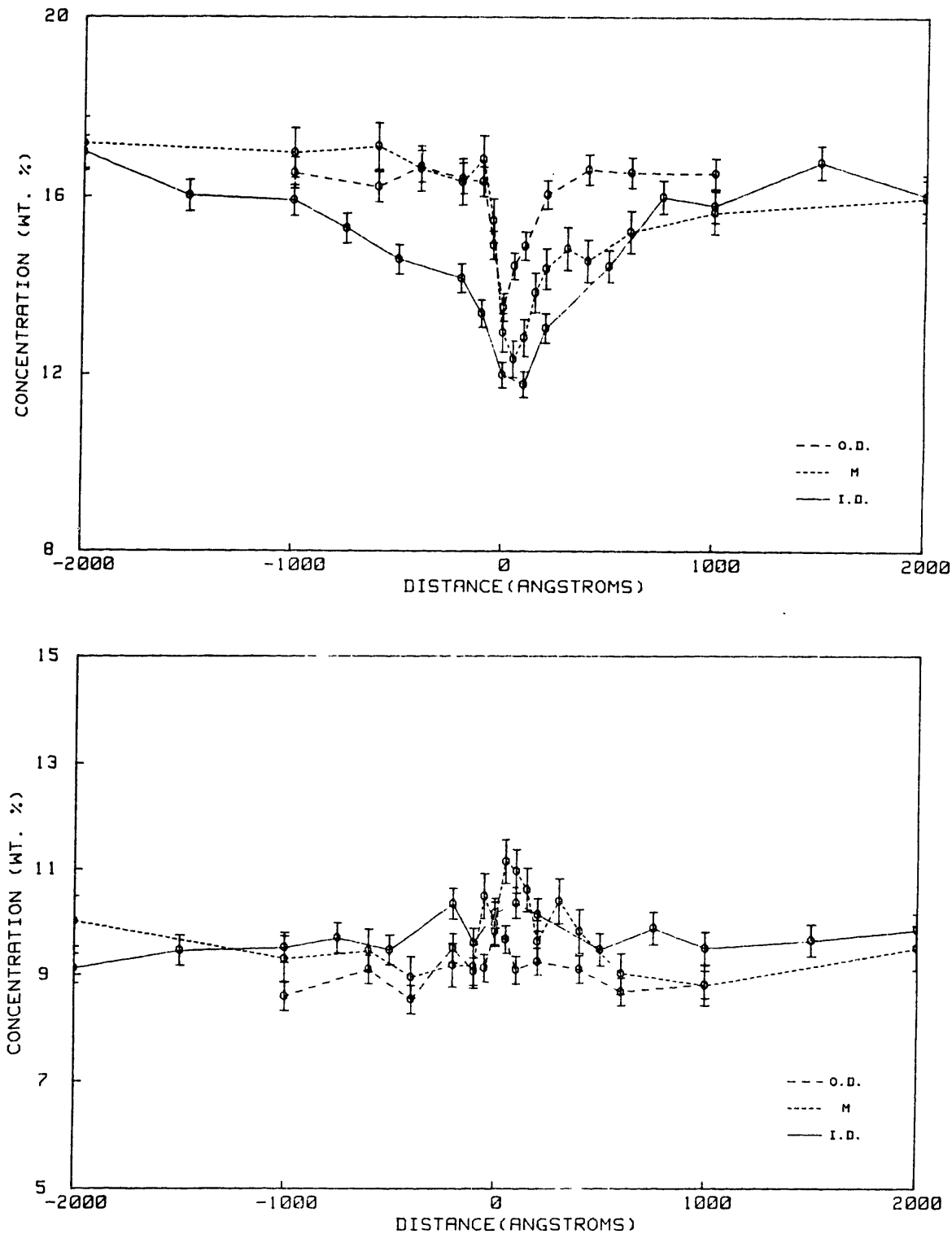

Figure 6.17 Chromium and Iron Distributions as a Function of Distance from a Grain Boundary in a 2.2cm Diameter Tubing of a HTMA Condition of Heat 96834.

of chromium depleted zone increases proportionally with the degree of depletion. The iron concentration is increased by about two percent at the grain boundary where the chromium is depleted by up to 5%. Hence, the remaining 3% is made up by the increase in nickel content.

The STEM micrograph of a 1.9cm diameter tubing for the HTMA condition of heat 96834 is shown in Figure 6.18. Discrete carbides are observed along grain boundaries with the same morphology as that of 2.2cm diameter tubing. The grain boundary carbide is an elongated shape while the intragranular carbides are found to be round shapes. The microchemical analysis was performed only for the inner diameter region where the maximum depletion is expected. There appears no depletion of chromium at the grain boundary as shown in Figure 6.19. The grain boundary analyzed containes apparently no carbides. However, the chromium distribution peak at the grain boundary indicates that there is a vey thin carbide film with a high chromium concentration. The iron distribution in Figure 6.19 shows a small depression at the grain boundary. The minimum chromium level may have occurred at a interface between matrix and the film although the degree of sensitization is insignificant. This HTMA condition of heat 96834 has the same carbon content and the final anneal temperature as the HTMA condition of NX2650. However, the more intergranular carbides is formed at the expense of intragranular carbides in the heat 96834. Since the nominal process conditions and carbon content are indentical t is not determined what exactly caused such a difference. This suggests that the two major process variable, the anneal temperture and carbon content, are inadequate to describe the final microstructure. The entire history of temperature during the final anneal needs to be specified.

The two-step etch micrographs for the LTMA conditions are shown in Figures 6.20 and 6.21 for the 2.2cm diameter and 1.9cm diameter tubing, respectively. Both tubings have an identical carbide morphology. There is little intergranular carbide while an extensive precipitation of intragranular carbides is shown along the drawing direction. The average grain size was measured to be 10μm for both tubing sizes. The dominance of intragranular carbide in the direction of cold work

Figure 6.18 The STEM Micrograph for an 1.9cm Diameter Tubing of the HTMA Condition of Heat 96834.

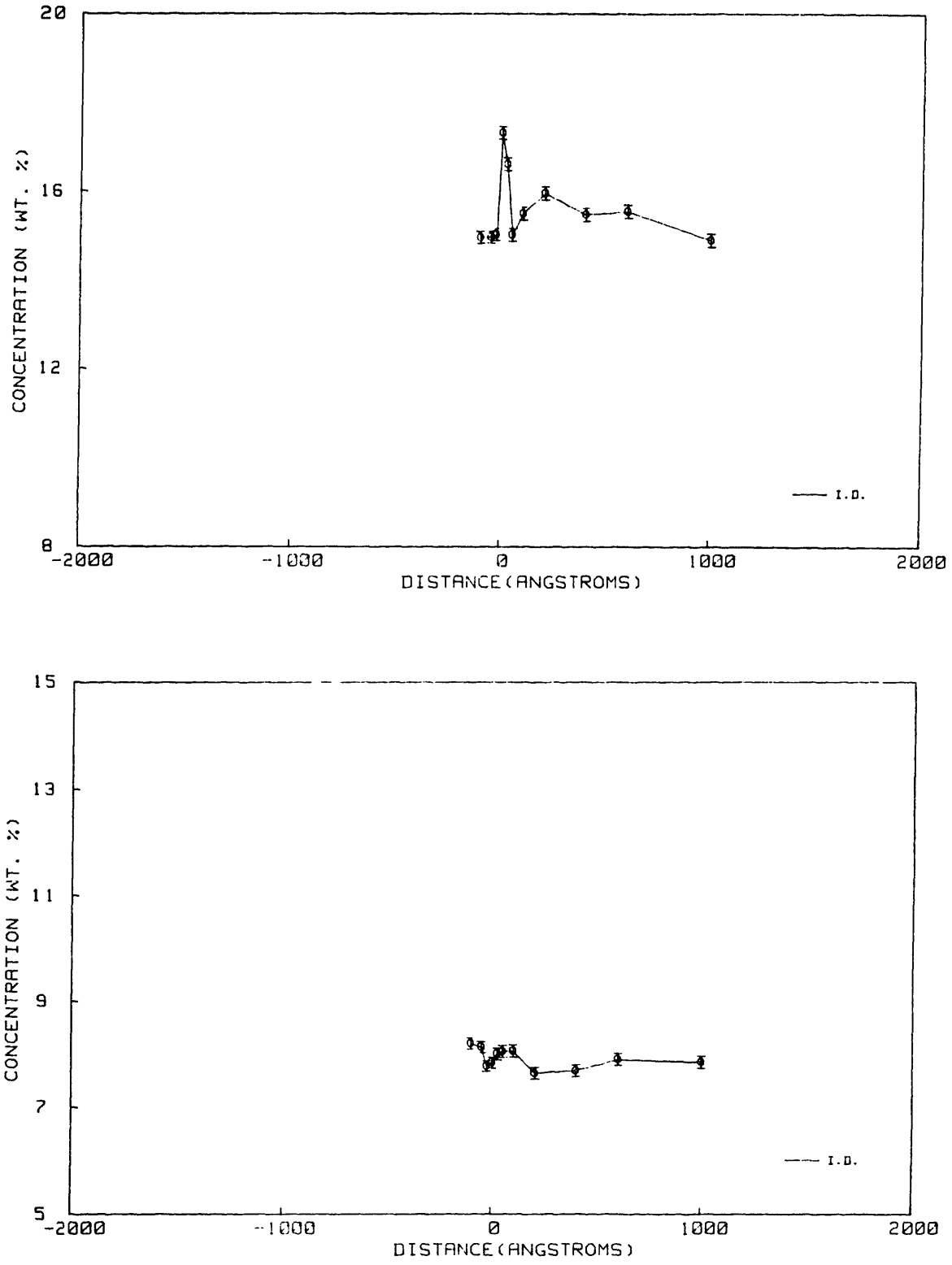

Figure 6.19 Chromium and Iron Distribtuions as a Function of Distance From a Grain Boundary in a 1.9cm Diameter Tubing of a HTMA Condition of Heat 96834.

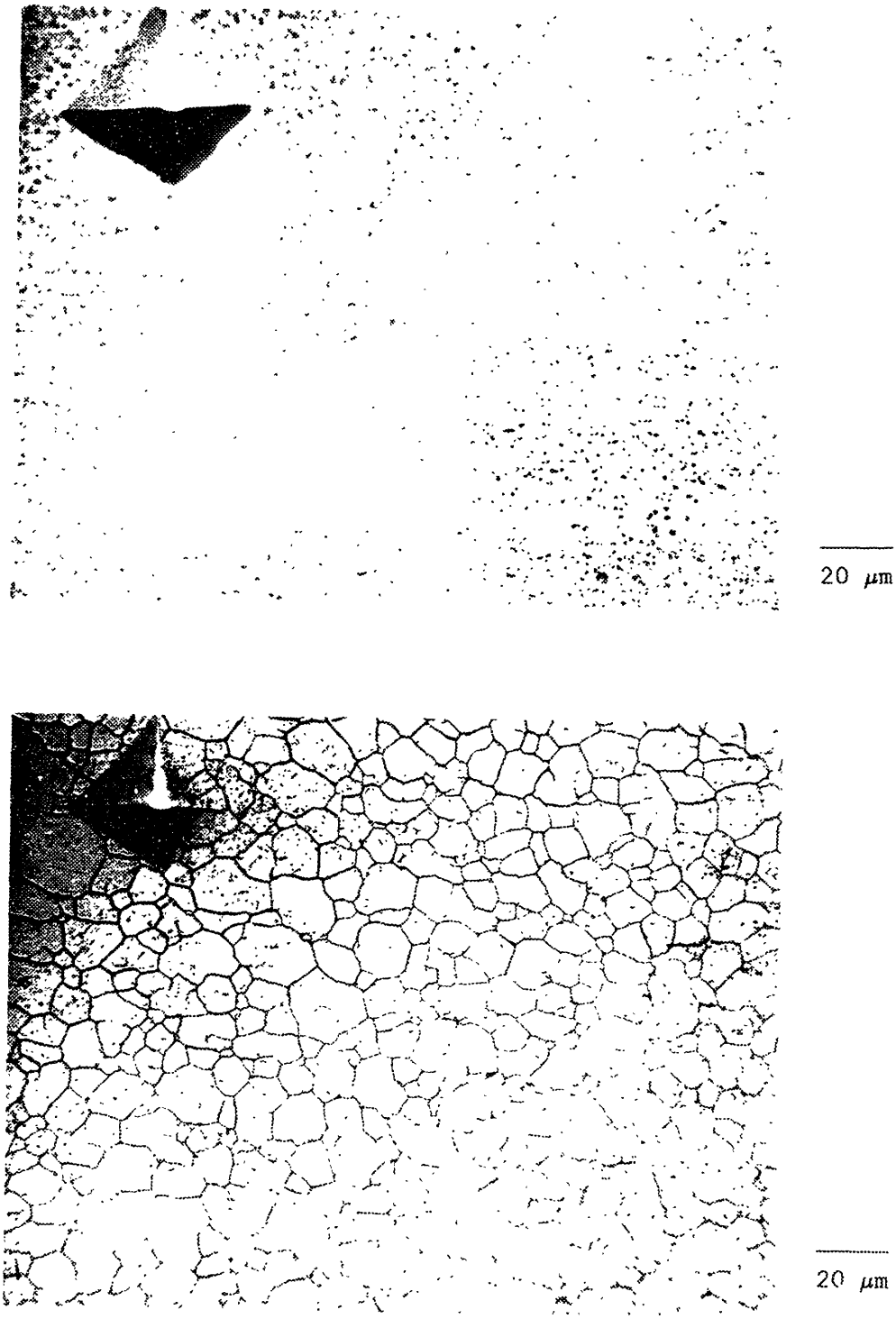

Figure 6.20 Two-step Etch Micrographs of Longitudinal Section of a 2.2cm Diameter Tubing of the LTMA Condition of Heat 96834 (upper orthophosphoric and lower nital etch).

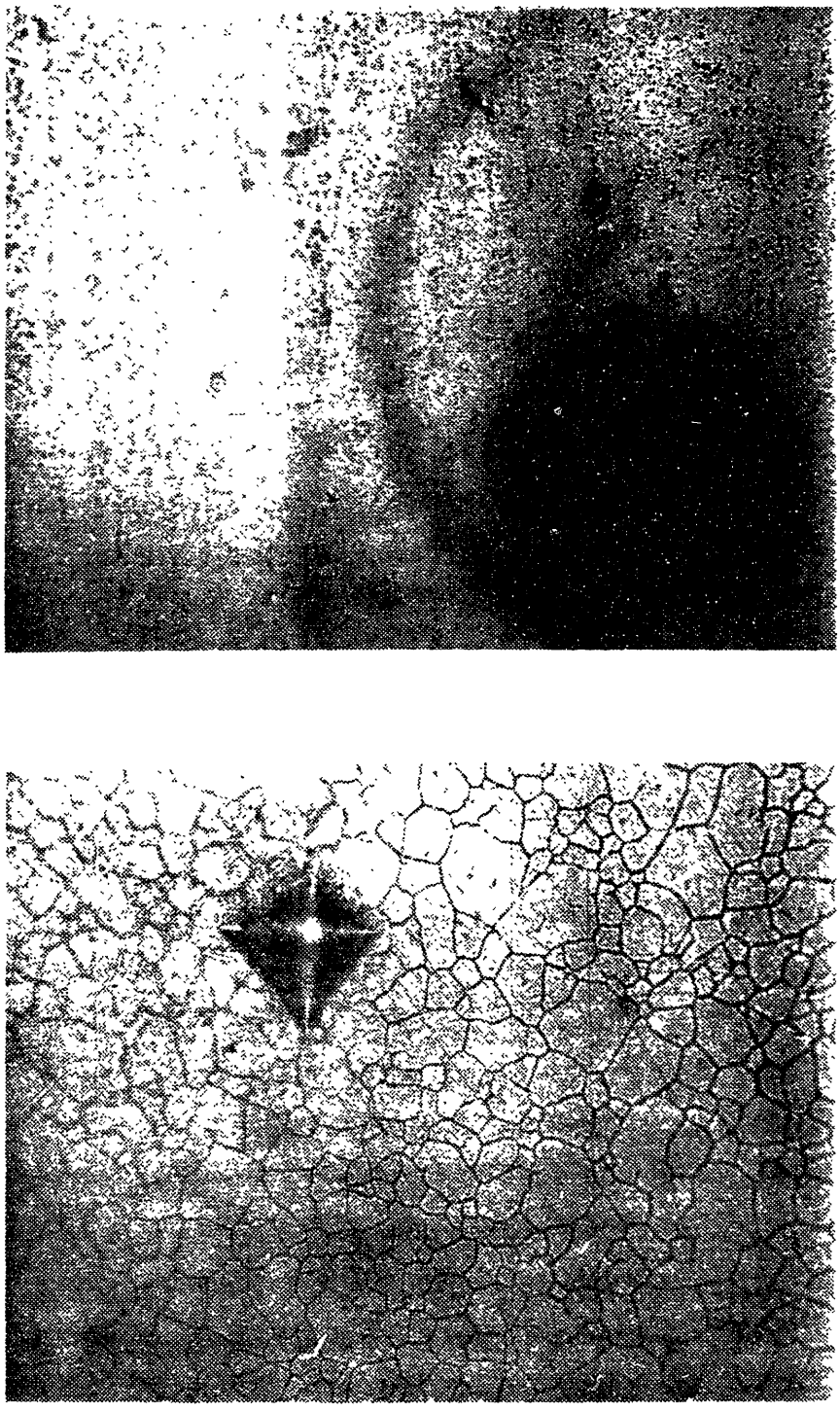

Figure 6.21 Two-step Etch Micrographs of Longitudinal Section of an 1.9cm Diameter Tubing of the LTMA Condition of Heat 96834 (upper orthophosphoric and lower nital etch).

indicates that the extensive precipitation took place before recrystallization the precipitation is believed to have occurred during the final heatup transient. Either the intermediate or the final anneal stage may have been involved such a responsible transient.

The STEM micrographs for the LTMA condition are shown in Figures 6.22 and 6.23, for a 2.2cm diameter and a 1.9cm diameter tubing, respectively. Most of grain boundaries in a 2.2cm diameter tubing are fee of carbides with a heavy intragranular precipitation. There was no significant difference between the inner and outer diameter regions. The microchemical analysis shows only a limited amount of chromium depletion which occurs at the inner diameter as shown in Figure 6.24. The iron was found to be the primary element to compensate the depletion. In the 1.9cm diameter tubing, a considerable amount of carbides are observed along grain boundaries at the inner diameter region, as shown in Figure 6.23. The outer diameter region shows few carbides on the grain boundaries. There are significant amount of intragranular carbides observed in agreement with the optical metallography. Microchemical analysis results are shown in Figure 6.25 There is about 4% reduction in chromium at the inner diameter while about 2% depletion is found at the outer diameter. The iron concentration is increased only by 1% indicating that nickel is the primary element to compensate for the chromium depletion.

Heat 763675

The two-step etch micrographs for a HTMA and LTMA conditions of heat 763675 are shown in Figures 6.26 and 6.27, respectively. This heat containing 0.02% carbon produced microstructures with a few carbide precipitates at the grain boundary and in the matrix. The HTMA condition shows a small amount of grain boundary carbides with virtually no intragranular precipitates. With an average grain size of 30μm, this microstructure resembles closely with that of the HTMA condition of heat NX1638. The same final anneal temperature and comparable carbon content resulted in the similar end products. The STEM micrograph in Figure 6.28 shows a representative grain boundary that is free of carbides.

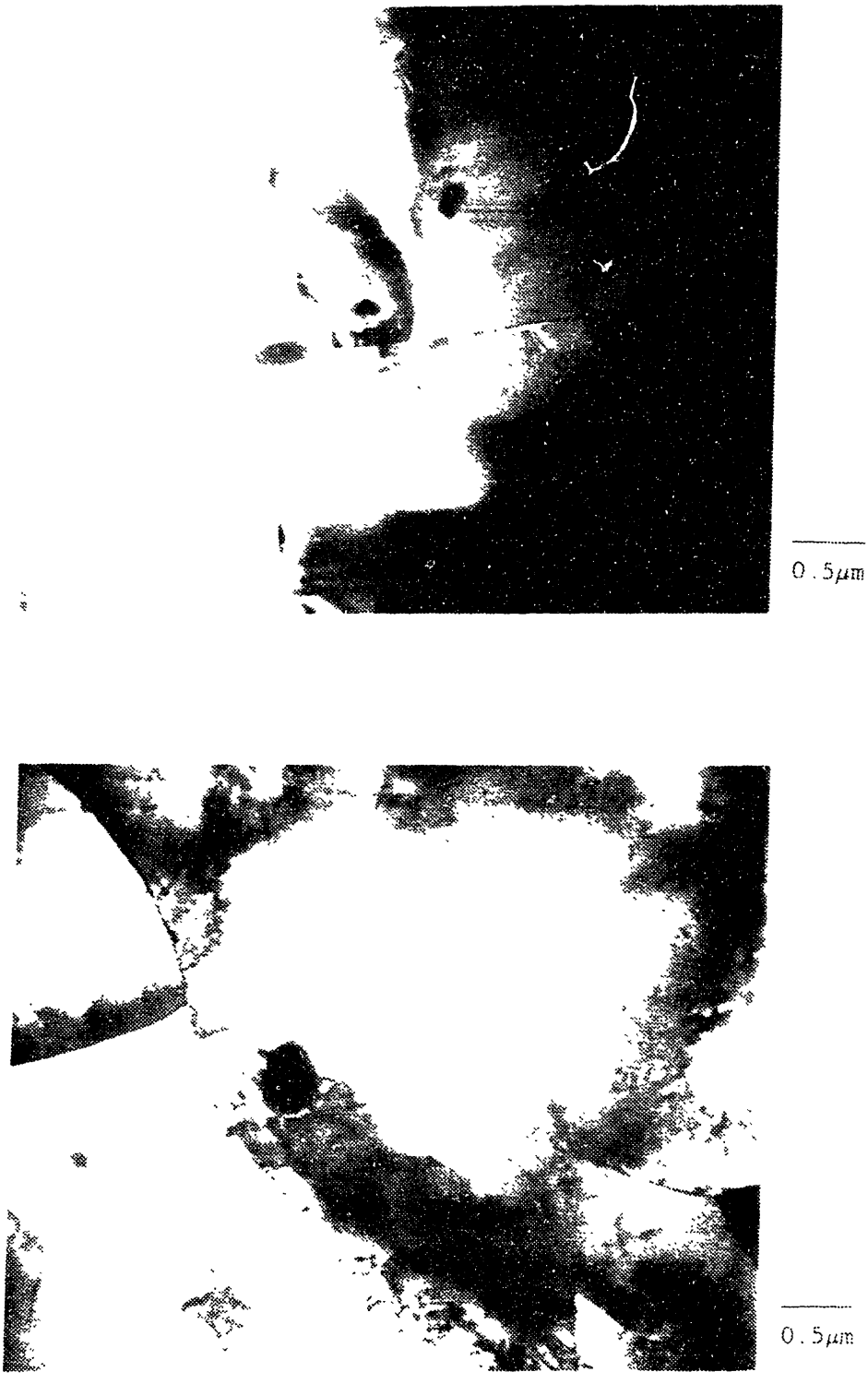

Figure 6.22 The STEM Micrographs for a 2.2cm Diameter Tubing of the LTMA Condition of Heat 96834 (upper micrograph for an inner diameter region and lower micrograph for an outer diameter region).

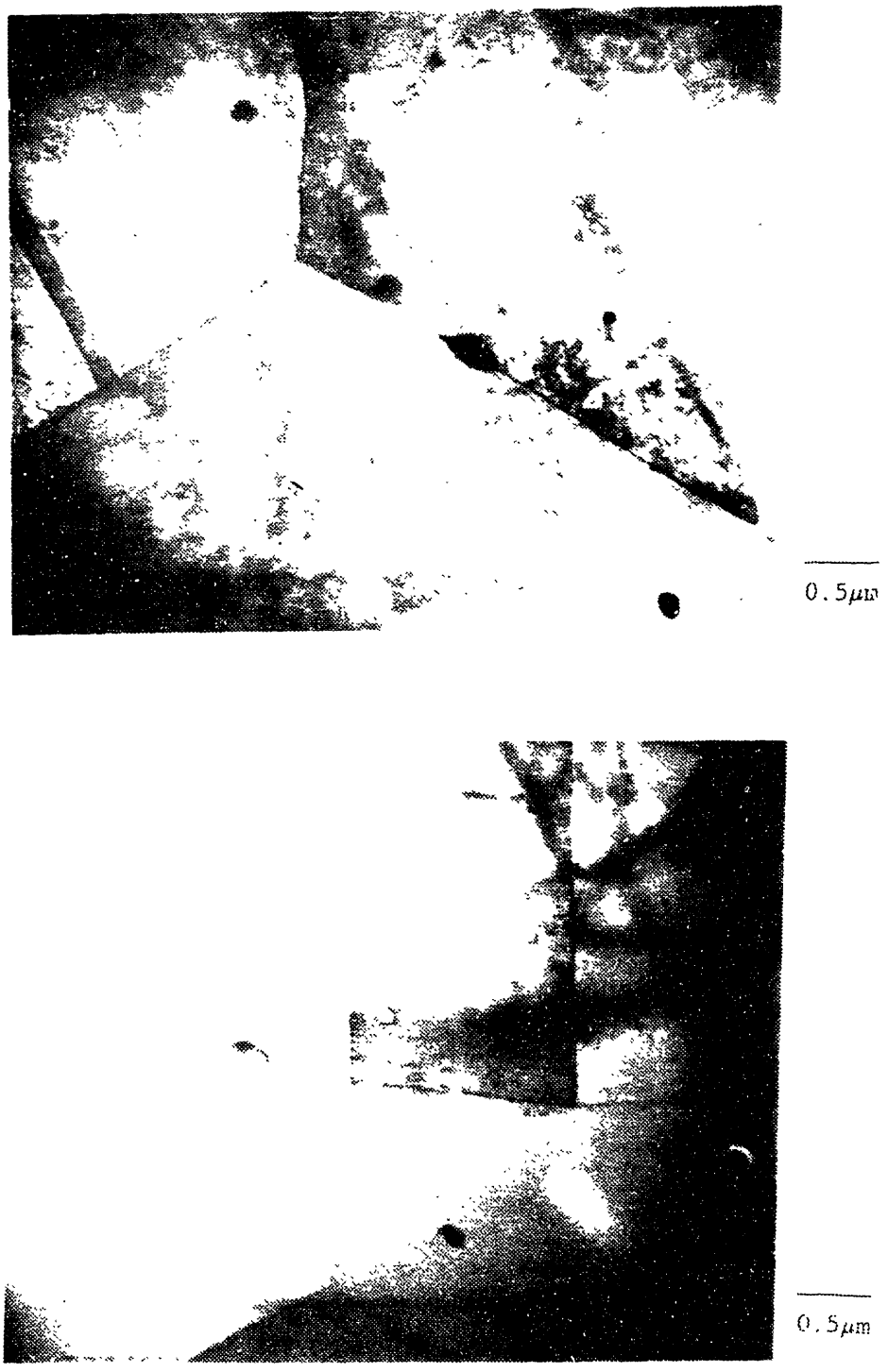

Figure 6.23 The STEM Micrographs for an 1.9cm Diameter Tubing of the LTMA Condition of Heat 96834 (upper micrograph for an inner diameter region and lower micrograph for an outer diameter region).

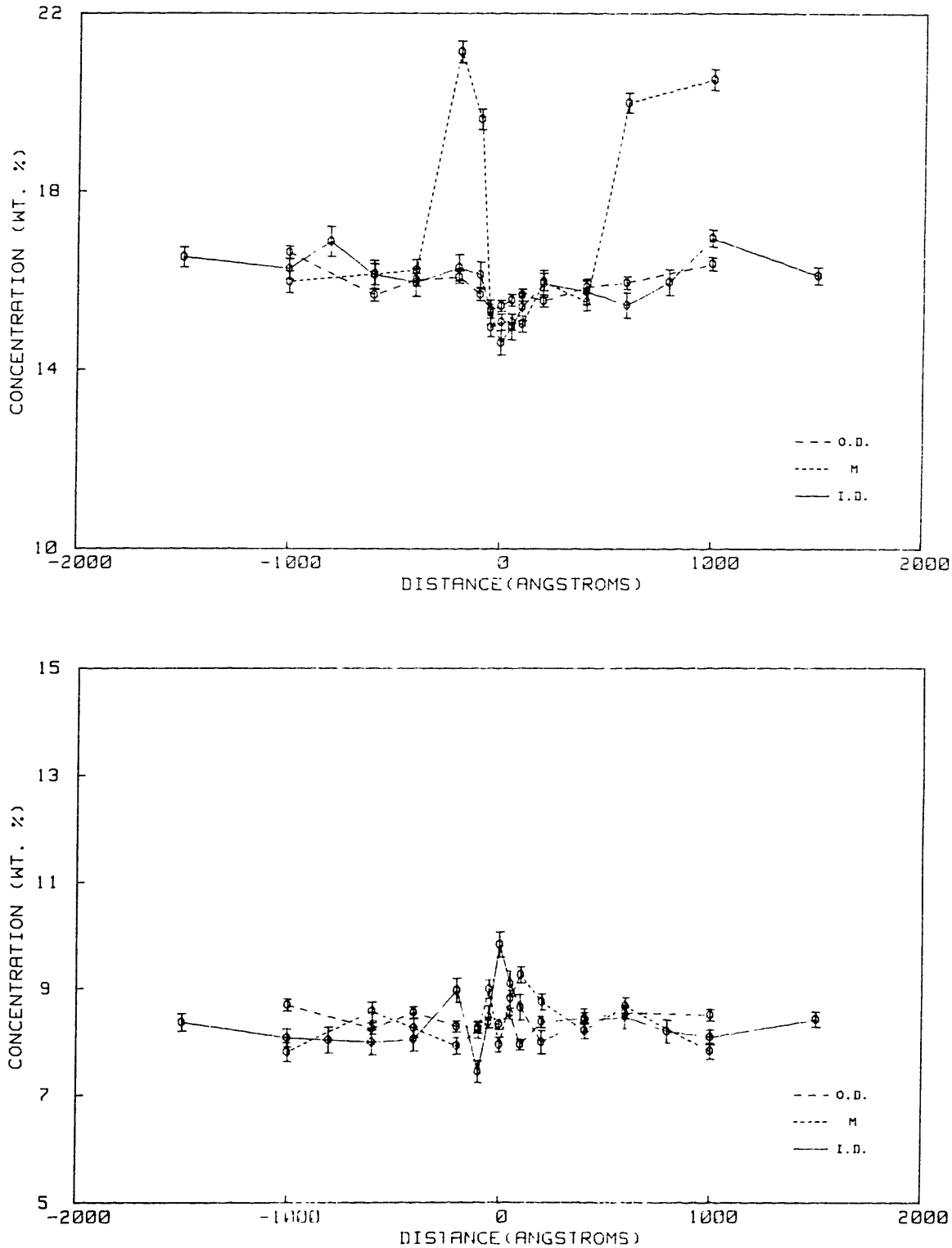

Figure 6.24 Chromium and Iron Distributions as a Function of Distance from a Grain Boundary in a 2.2cm Diameter Tubing of a LTMA Condition of Heat 96834.

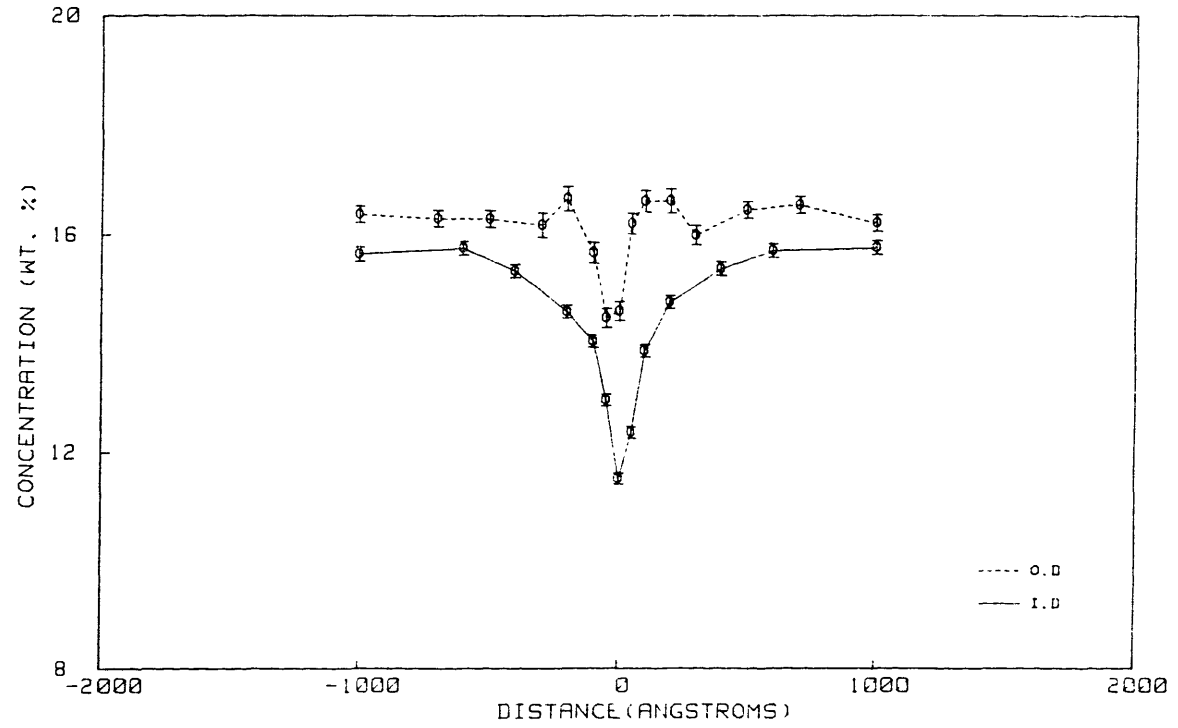

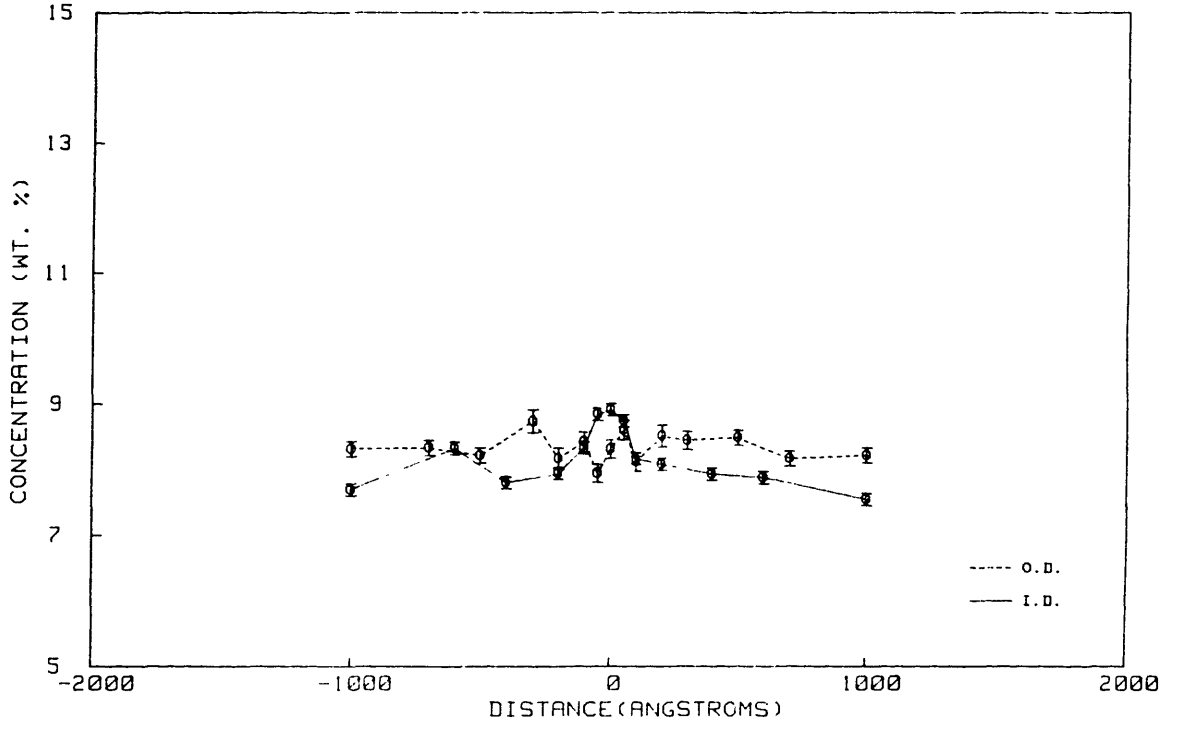

Figure 6.25 Chromium and Iron Distributions as a Function of Distance From a Grain Boundary in a 1.9cm Diameter Tubing of a LTMA Condition of Heat 96834.

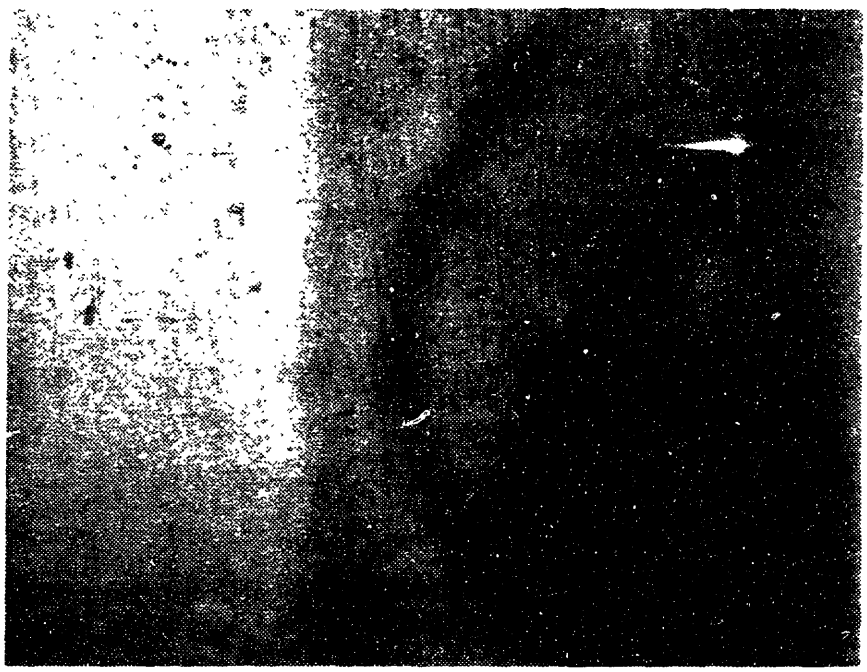

Figure 6.26 Two-step Etch Micrographs of Longitudinal Section of a HTMA Condition of Heat 763675 (upper orthophosphoric and lower nital etch).

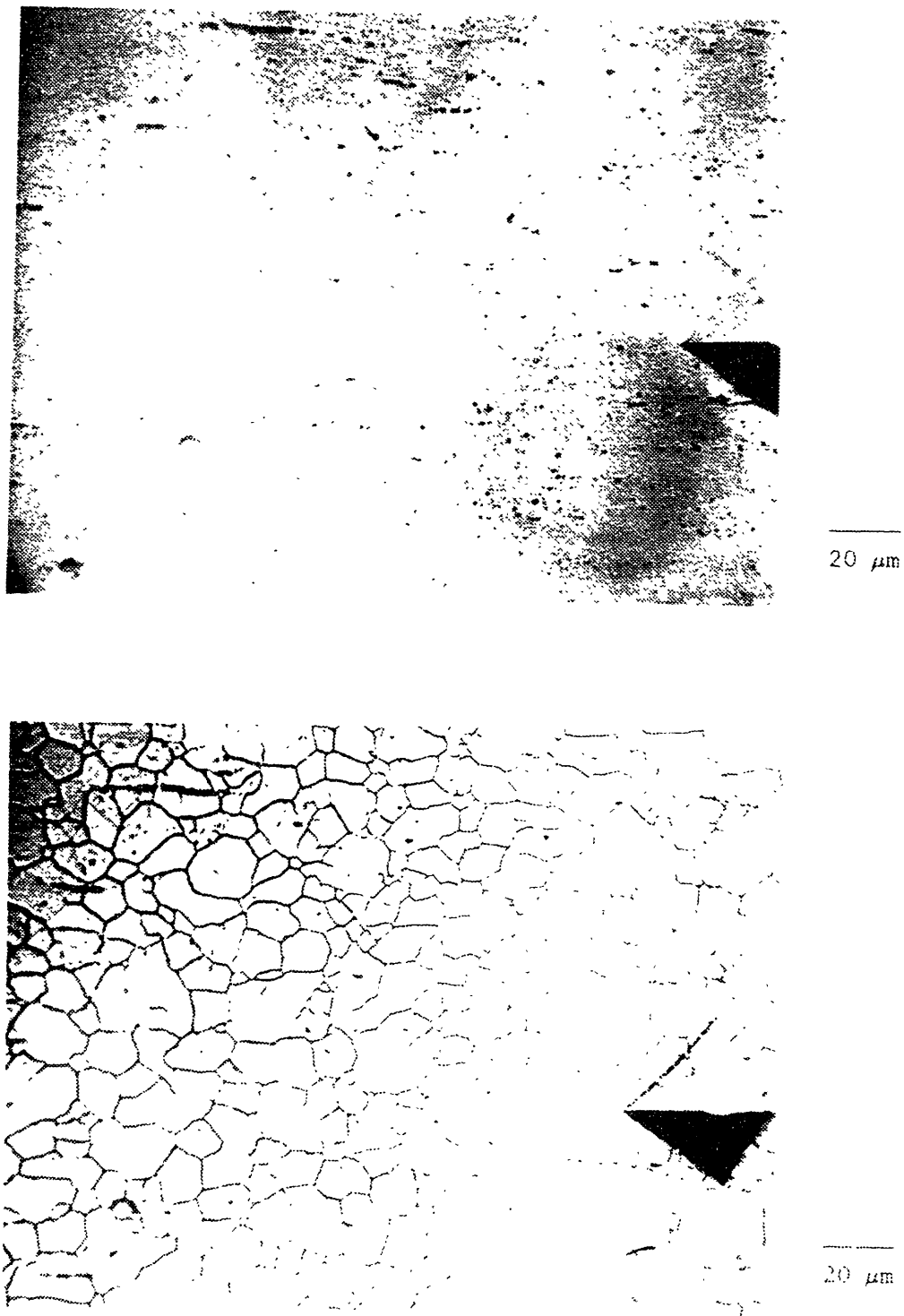

Figure 6.27 Two-step Etch Micrographs of Longitudinal Section of Alloy 600 a LTMA Condition of Heat 763675 (upper orthophosphoric and lower nital etch).

Figure 6.28 The STEM Micrographs for a HTMA Condition of Heat 763675.

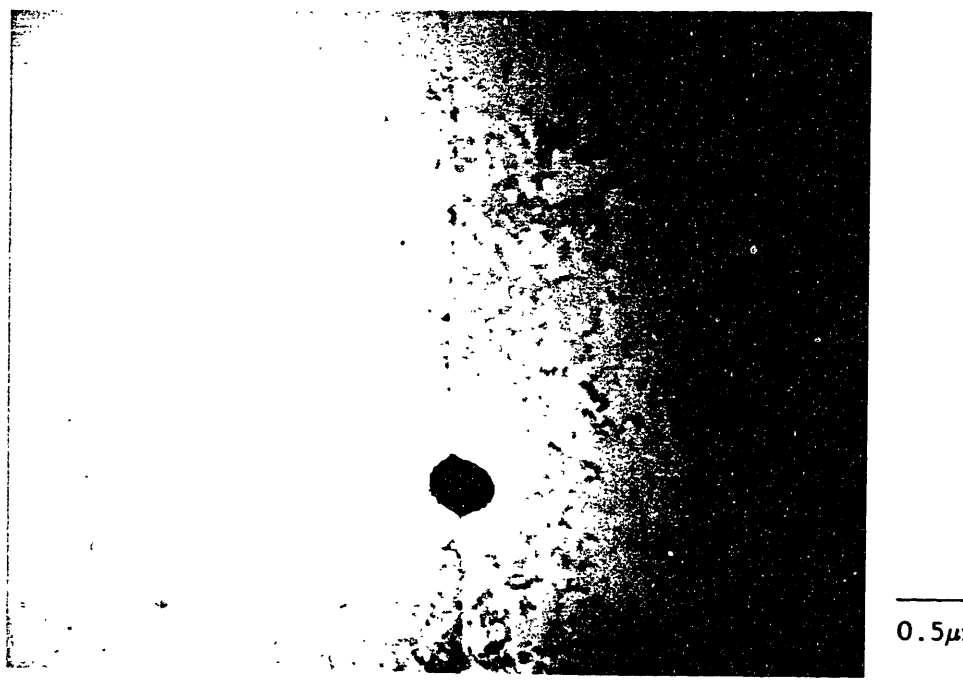

Figure 6.29 The STEM Micrograph for a LTMA Condition of Heat 763675.

Microchemical analysis indicates no significant disturbance in chromium or iron content, as shown in Figure 6.30.

The LTMA condition of heat 763875 produced a microstructure with appreciable amount of intragranular carbides and little intergranular precipitates, as shown in Figure 6.29. The small grain size(11μm) and the preponderous intragranular carbide are the characteristics of the LTMA condition. The STEM micrograph for this condition show virtually clean grain boundaries with occasional carbide precipitates. The grain boundary was found to be depleted of chromium and enriched in iron by an appreciable amount, as shown in Figure 6.31. The minimum chromium level at an inner diameter is enough to maintain the resistance against intergranular corrosion.

Heat NX3857

Microstructure of the heat NX3857 is shown in Figures 6.32 and 6.32 for a HTMA and a LTMA condition, respectively. The heat containing 0.025% carbon reveals an intermediate degree of precipitation among all the heats examined. The HTMA condition produced a grain boundary structure decorated with discrete arrays of carbides. With an average size of 45μm, matrix was essentially free of intragranular precipitates. The STEM micrograph, in Figure 6.34, shows a high density of intragranular carbides with a very small size. The chromium depletion amounts to about 5% for which iron compensates up to 3% , as shown in Figure 6.34.

The LTMA condition of heat NX3857, shown in Figure 6.33, shows a microstructure with heavy intragranular precipitation and almost no grain boundary carbides. The average grainsize was measured to be 15μm. This LTMA microstructure is similar with the LTMA conditions of both heats 96834 and 763675. Intragranular carbides are mostly lined up in the direction of cold work. The STEM observation shows grain boundaries which is essentially free of carbides, as shown in Figure 6.35. Microchemical analysis revealed no disturbance in chromium or iron concentration near the grain boundary, as shown in Figure 6.37.

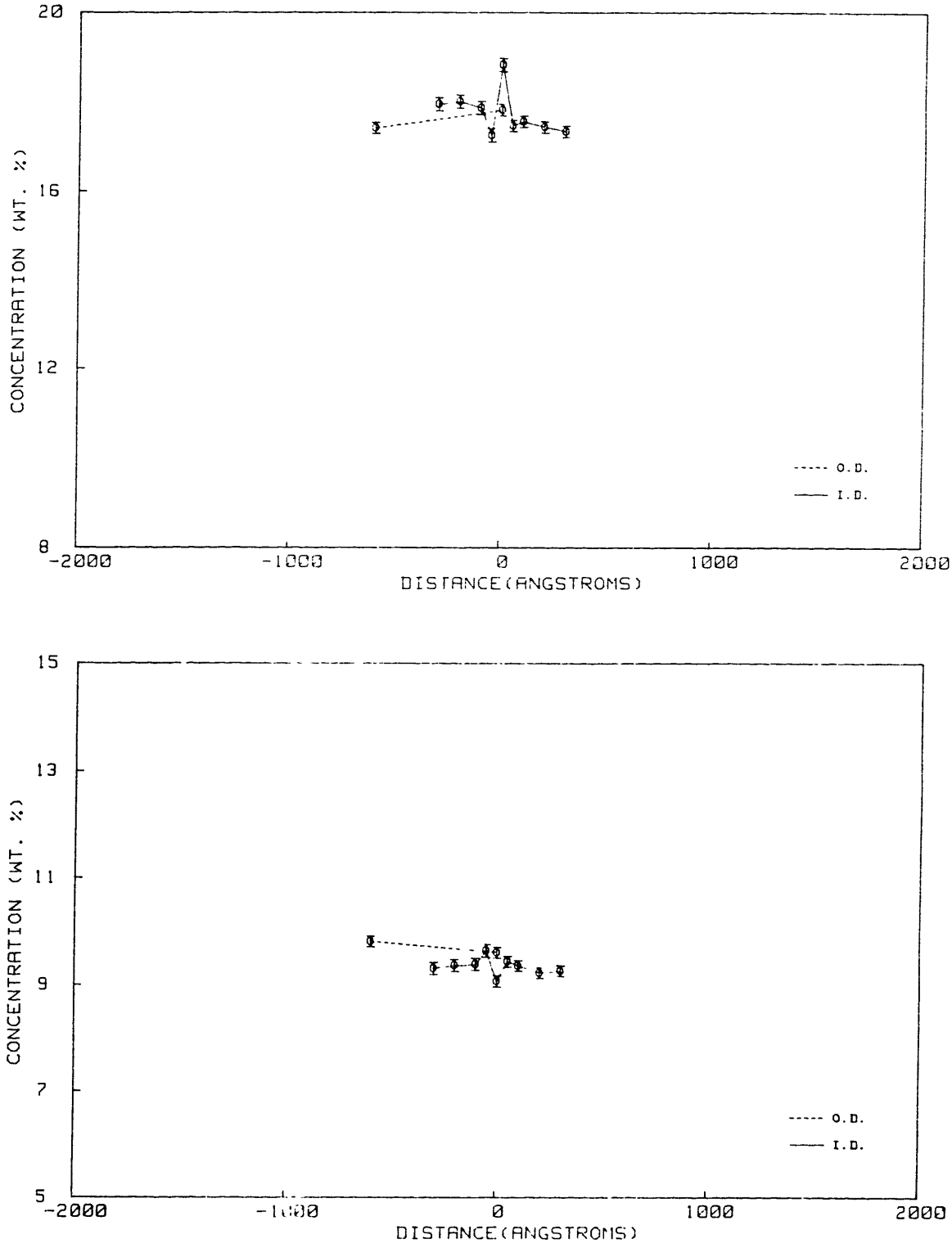

Figure 6.30 The Chromium and Iron Distribtutions as a Function of Distance from a Grain Boundary in a HTMA Condition of Heat 763675.

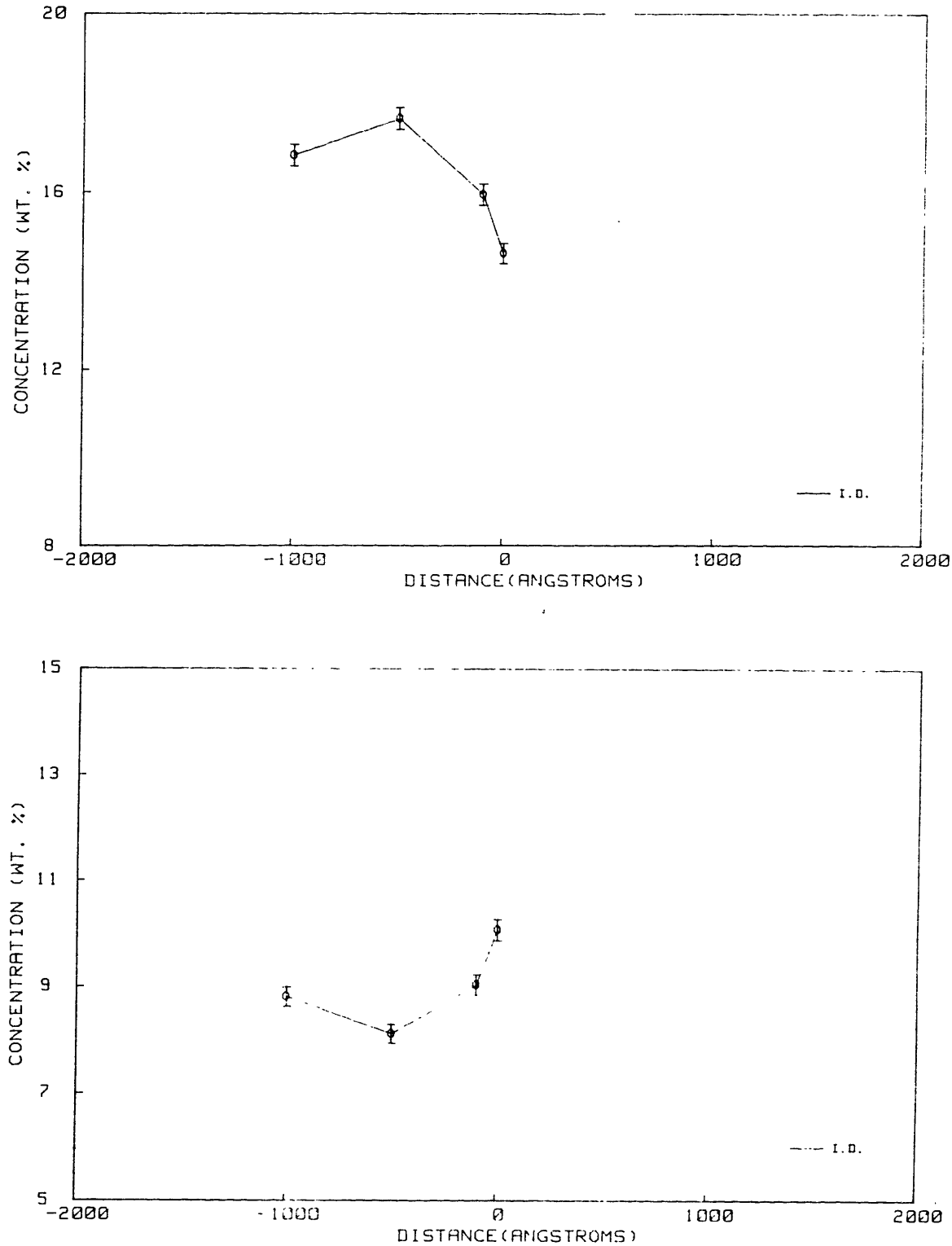

Figure 6.31 The Chromium and Iron Distribtutions as a Function of Distance from a Grain Boundary in a LTMA Condition of Heat 763675.

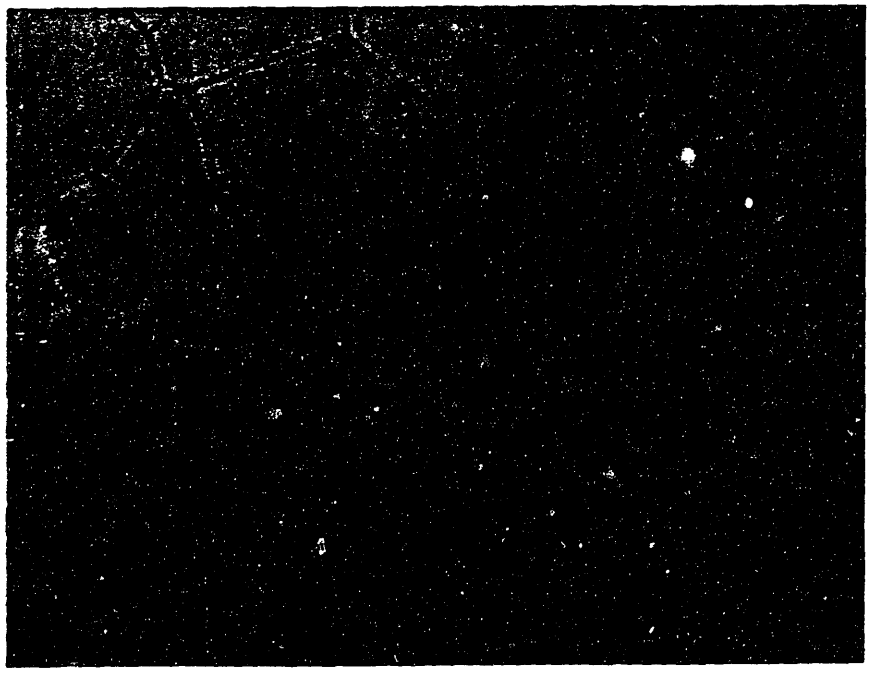

Figure 6.32 Two-step Etch Micrographs of a HTMA Condition of Heat NX3857 (upper orthophosphoric and lower nital etch).

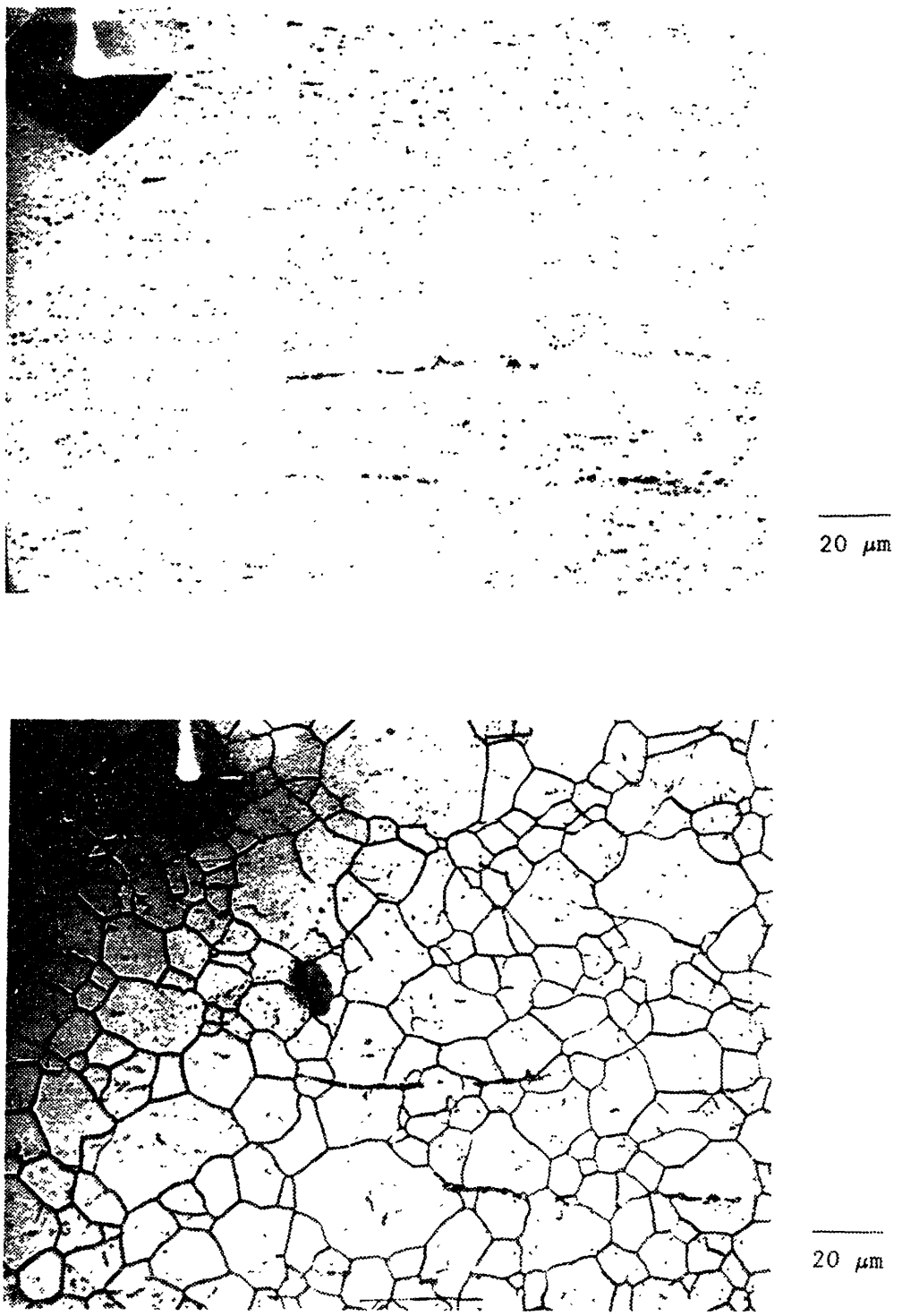

Figure 6.33 Two-step Etch Micrographs of a Longitudinal Section of a LTMA Condition (upper orthophosphoric and lower nital etch).

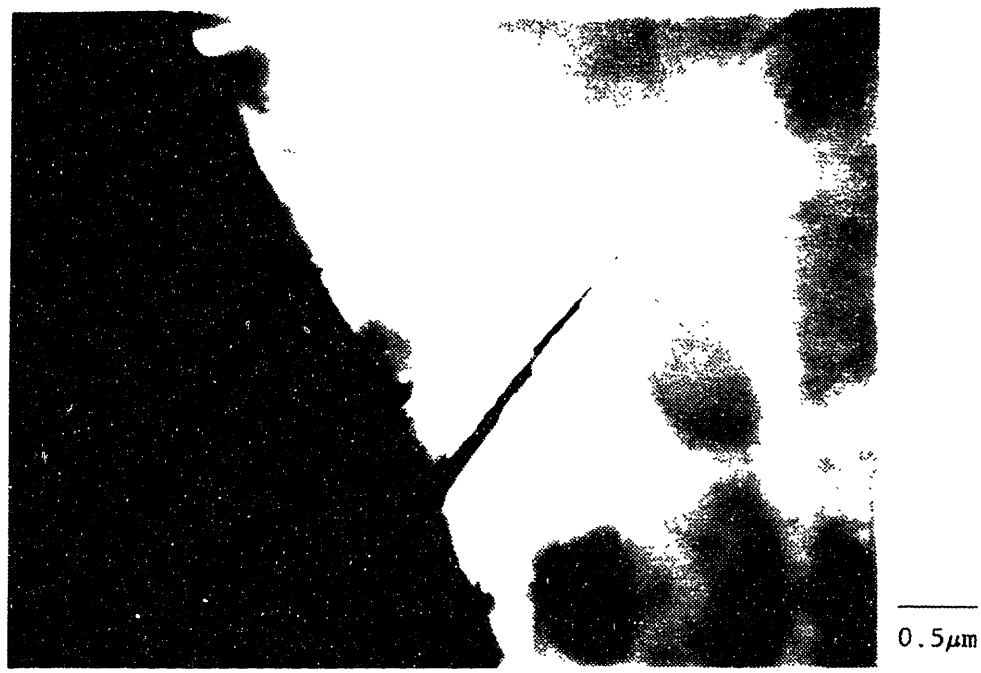

Figure 6.34 The STEM micrographs for a HTMA Condition of Heat NX3857.

Figure 6.35 The STEM micrographs for a LTMA Condition of Heat NX3857.

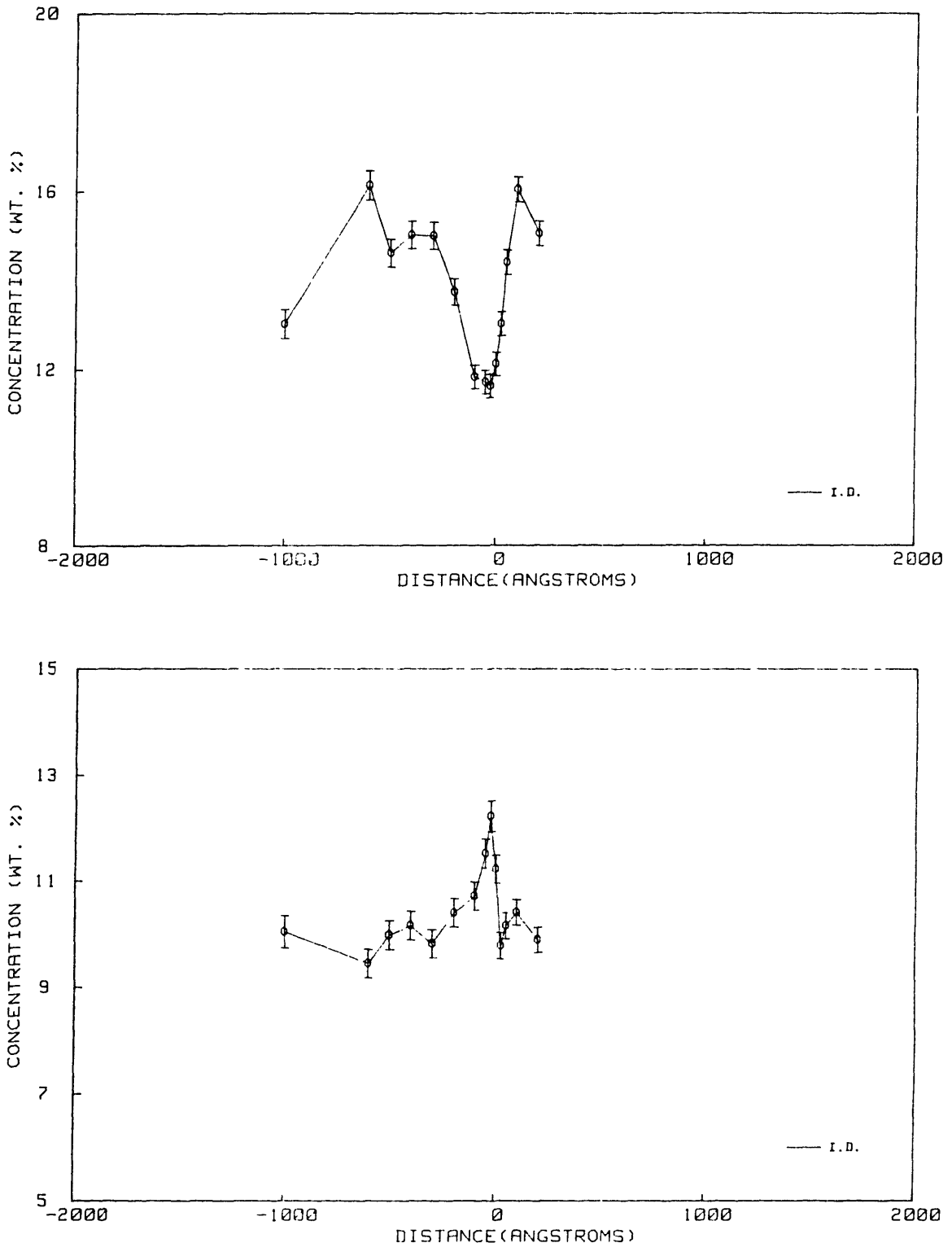

Figure 6.36 Chromium and Iron Distributions as a Function of Distance From a Grain Boundary in a HTMA Condition of Heat NX3857.

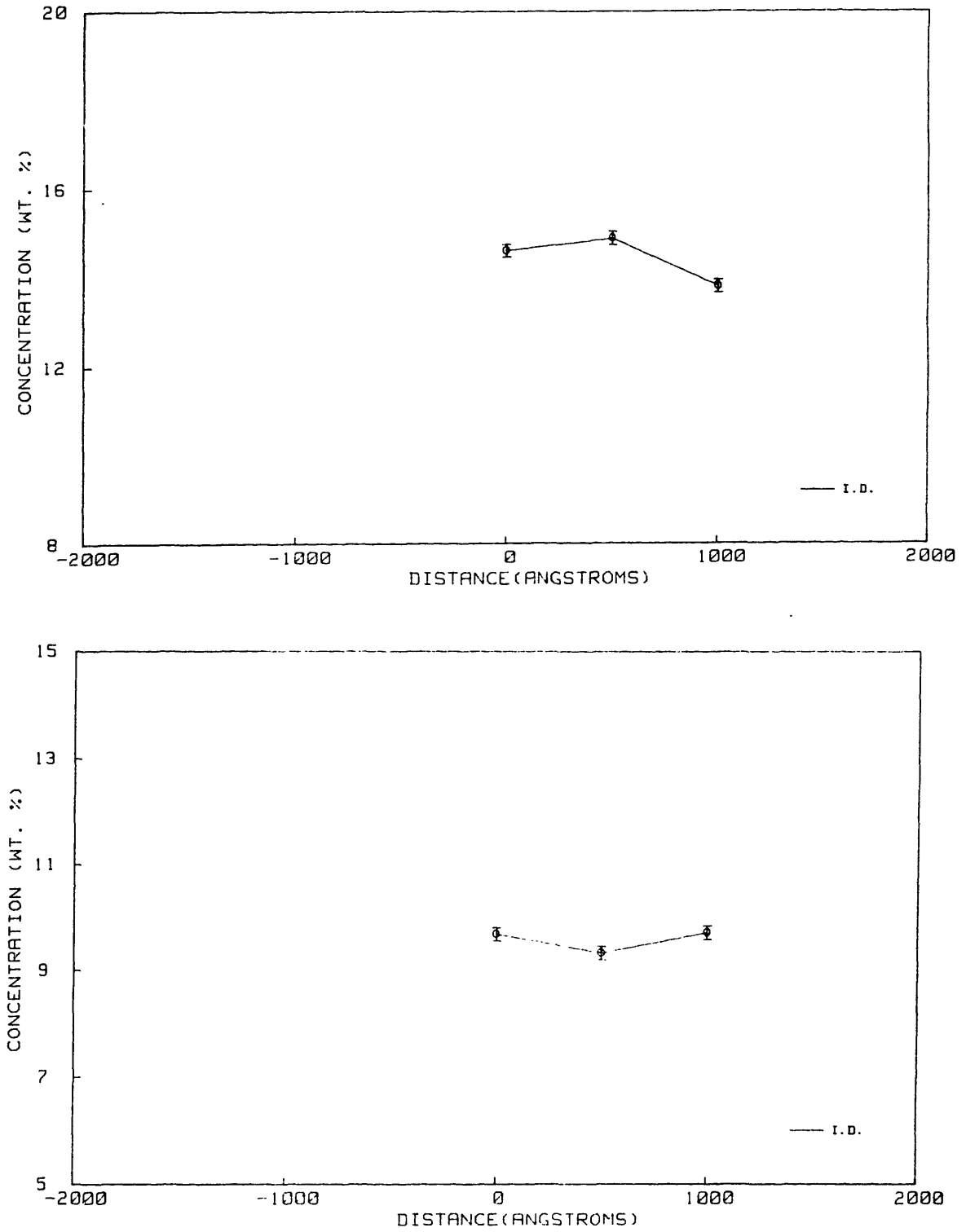

Figure 6.37 Chromium and Iron Distributions as a Function of Distance From a Grain Boundary in a LTMA Condition of Heat NX3857.

Based on the observation made from the two-step etch technique, it is clear that the majority of the HTMA heats produce more intergranular than intragranular carbide while the LTMA heats result in completely intragranular carbide aligned along the longitudinal cold work direction. However, an exception occurs with the HTMA of NX2650 where an extensive intragranular precipitates is retained with marginal grain boundary carbides. Therefore the final anneal process based on furnace temperture can lead to a microstructure which is quite different from that expected by metal temperatyre-based processes.

It is useful to represent the optical metallographic observations in terms of certain quantities. Therefore, two parameters are defined as follows:

f_{GB} = an estimated fraction of grain boundaries decorated with carbide

f_m = an estimated ratio of lengths of intragranular carbide arrays to grain boundary length from the micrographs

Although it is a laborious procedure, a rough estiamtioln of f_{GB} is feasible by careful measurement of a representative area. The estimation of f_m is made based on the optical micrographs as follows. The total length of longitudinal arrays of carbides is approximately calculated by multiplying the number of arrays by the full length shown in the micrograph. The total length of grain boundaries is approximated by assuming that all grains of average size are squares with a side $\bar{d}$. For the standard micrograph at 500x magnification, the total length is approximately,

$$L_{GB} \simeq 8 \times 10^4 / \bar{d} \qquad (6\text{-}1)$$

where L_{GB} is total length of the grain boundaries and $\bar{d}$ is the average grain size in μm.

6.1.2 Microstructures of Alloys X-750 and 718

Comprehensive microstructural characterizations were made on a similar heat of X-750 by Elliott [23] and the same heat of 718 by Prybylowski[26]. A TEM charaterization on the heat 96457E6 was also done by Sheeks [50]. Therefore, the microstructural analysis performed in this thesis is aimed at confirming that all the specimen conditions are in agreement with those results for each heat treatment condition. Precipitates, grain size and morphology are determined primarily by optical metallographic techniques.

Two heats of X-750 including 96457E6 and the plate heat were examined although only AH condition is used in the latter heat. The as-received condition of the heat 96457E6 of alloy X-750 shows a fine grained microstructure with an average size of 10μm, as shown in Figure 6.38. Grain size varies in a range between 2μm and 40μm. The larger grains are elongated and apparently lined up in the rolling direction. An appreciable amount of twin boundaries are revealed by the Kallings reagent etch in the larger grains. This may be an indication for an incomplete time for recrystallization during the hot rolling process.. There is no precipitate observable by the optical method in the matrix or at grain boundaries.

The AH condition of heat 96457E6 was examined by using both Kallings reagent and the standard two-step etches. Kallings reagent revealed the details of twin deformation as well as the general microstructures as shown in Figure 6.39. The microstructure is found to be the same as the as-received materialwith an average grain size of 10μm. Occasionally large and elongated grains are also retained. Figure 6.40 show the two-step etch micrographs for the same condition. The orthophosphoric etch revealed coarse precipitates while the subsequent nital etch produced only minimal contrast for the grain boundaries. The larger precipitates with a needle shape were identified as η phase, an intermetallic compound, Ni_3Ti, with a small aluminum content [23]. The

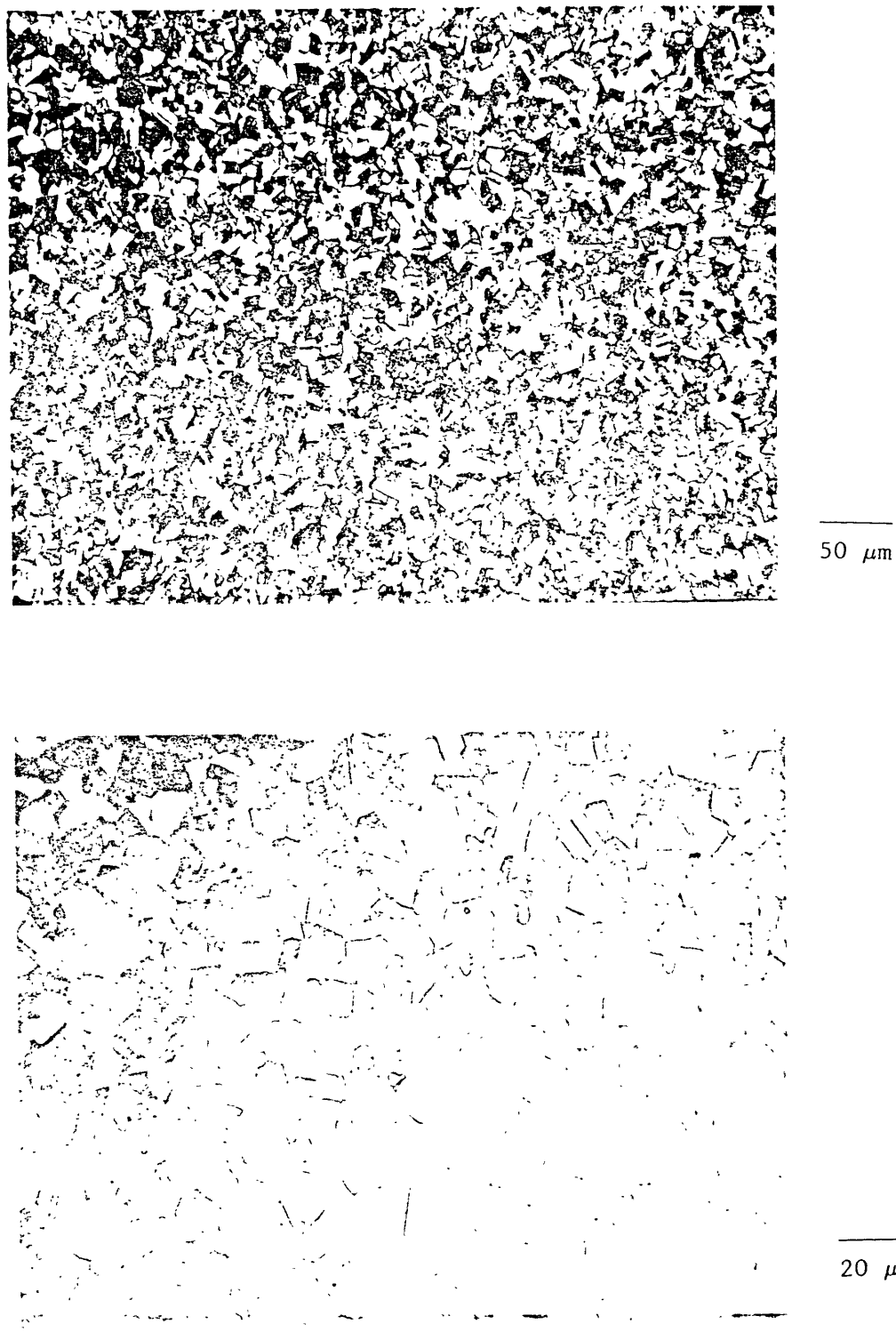

Figure 6.38 Optical Micrographs of the As Received Hot-Rolled Condition of Alloy X-750 Heat 96457E6 (Kalling's Reagent).

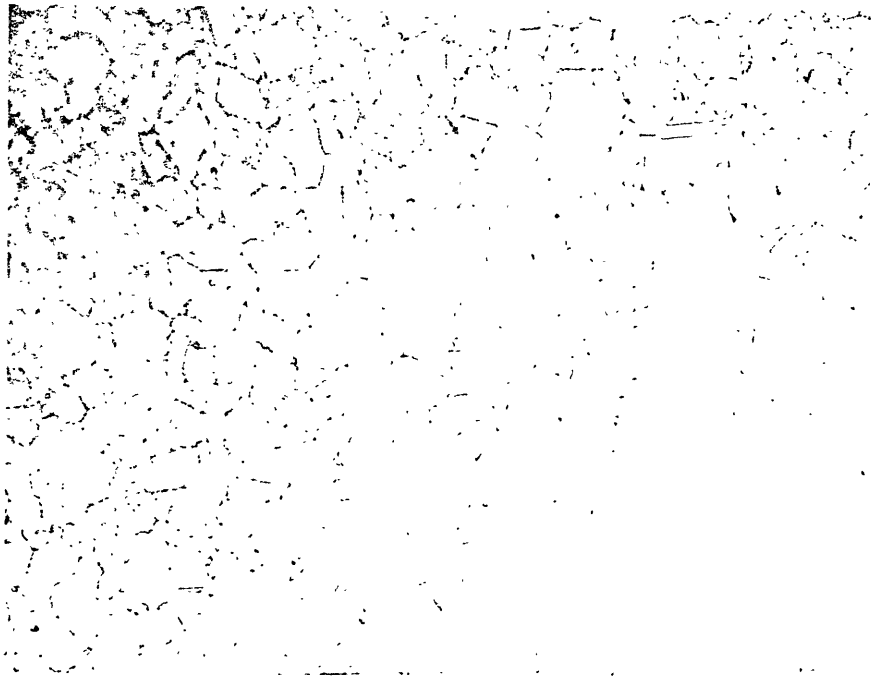

Figure 6.39 Optical Micrographs of the AII Condition of Alloy X-750 (Kalling's Reagent).

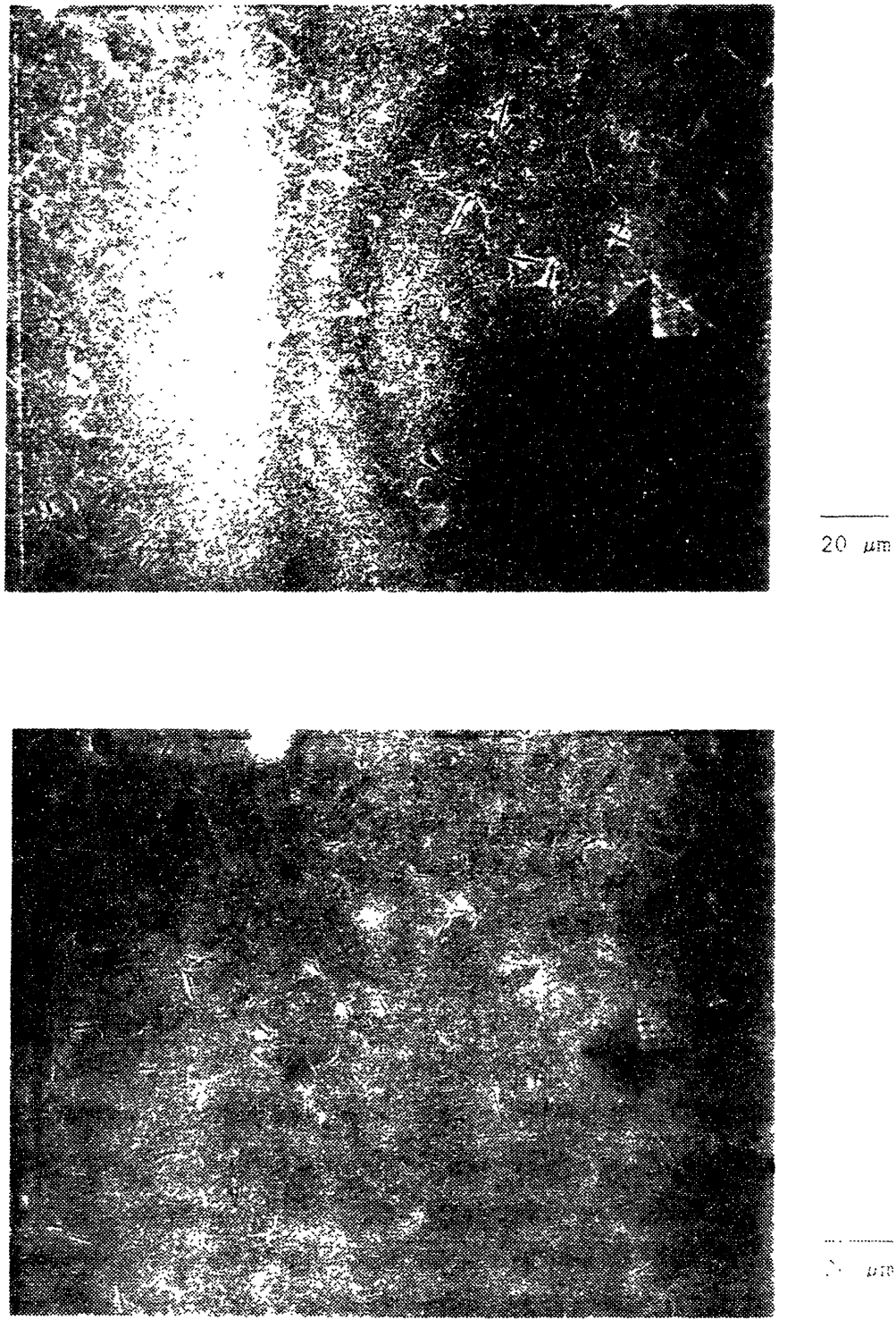

Figure 6.40 Two-step Etch Micrographs of the AH Condition of Alloy X-750 (upper phosphoric and lower nital etch).

η phase is found in localized regions in the AH condition. Narrow regions around the η phase are apparentlt denuded of the round shape of smaller precipitates. The morphology of η phae was examined with EAH condition, as shown in Figure 6.41. It is shown that η phase is evolved during the equalization treatment and its morphology is unaffected by the final at 700 C does not alter The smaller intragranular precipitates revealed by the orthophosphoric etch are coarse γ'. They are not observed in HTH or HOA of the same heat of X-750. A narrow region along gain boundaries is also denuded of coarse γ'. The TEM study showed that fine γ' which can not be resolved in optical micrographs are present in those denuded zones[23].

The plate heat of X-750 was heat treated to the AH condition for corrosion fatigue tests. The microstructure is shown in Figure 6.42. The microstructure is coarse with an average grain size of 50μm. TEM micrographs for both matrix and a grain boundary region are shown in Figure 6.43. The intragranular γ' are shown using a dark field of diffraction pattern shown in the Figure. There are two different sizes of γ' precipitate separated by a narrow interface of γ'-denuded zone. The coarse γ' has an average size of 0.1μm while the fine γ' has about 100^{o}A. The grain boundary structure is shown by the TEM micrographs in Figure 6.43. Much bigger precipitates, found only on the grain boundary, have a lattice parameter exactly three times that of the matrix. Therefore, these are believed to be $Cr_{23}C_6$ carbides with size of about 0.5μm. The extensive presence of carbides makes it difficult to determine the detailed morphology the intergranular γ' precipitates.

Microstructure of BH condition of heat 96457E6 is characterized by a bi-modal grain size, as shown in Figure 6.44. The coarse grains about 100μm in diameter are usually surrounded by the original fine grained structure. The average grain size of the condition is determined to be 30μm. The coarse grains are usually clustered in an isolated area where the grain coarsening took place after the 1 hr anneal at 982 C. The large variation in the microstructure obtained by the treatment can be attributed to the transition nature of microstructure in the BH

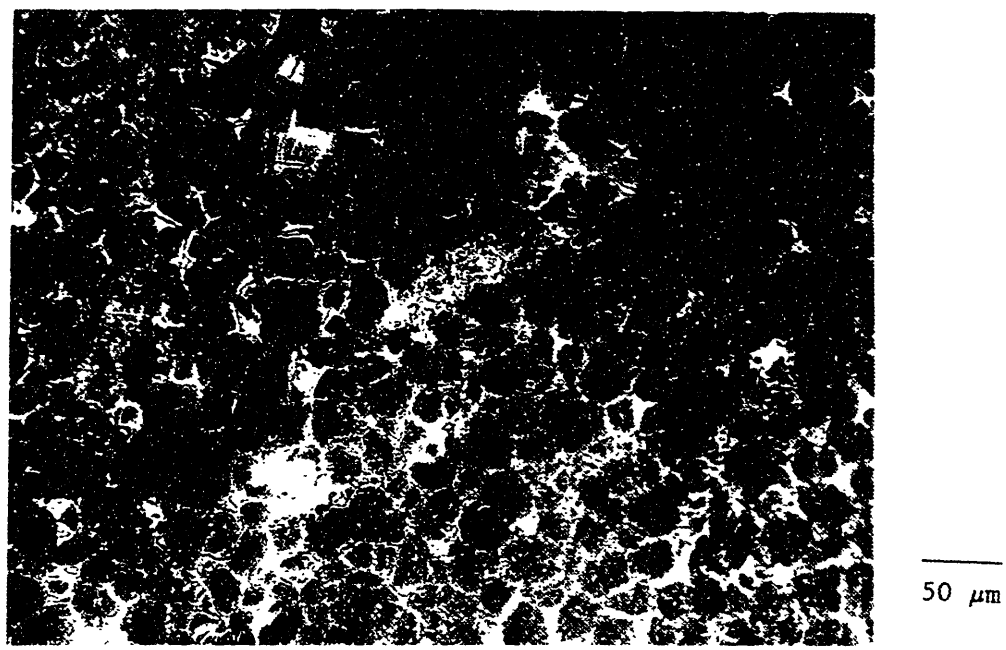

Figure 6.41 Optical Micrographs of the EAH Condition of Alloy X-750 Revealing Needle-Shaped η Phase

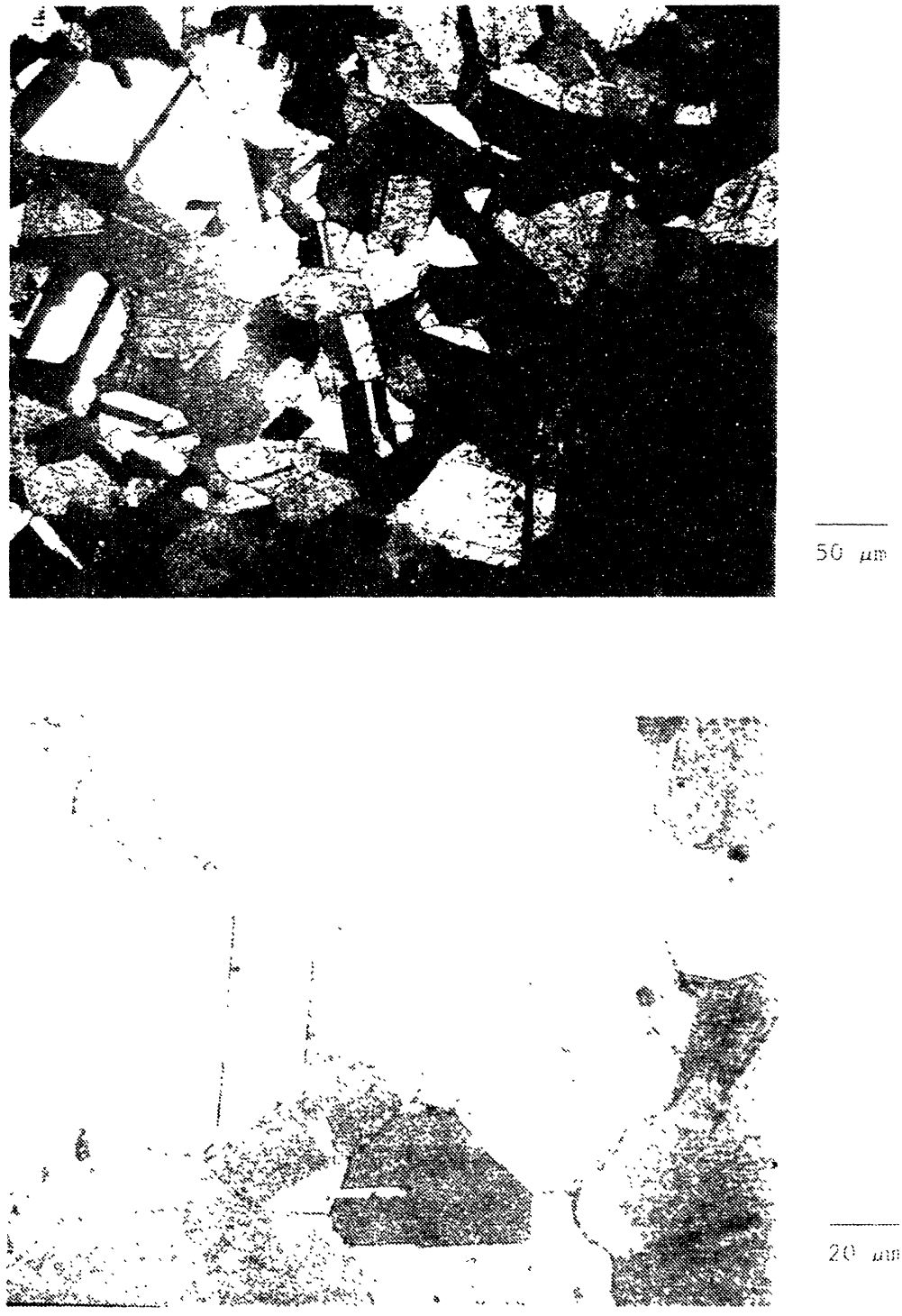

Figure 6.42 Optical Micrographs of the AH Condition of a .28cm thick Plate of Alloy X-750 (Kalling's Reagent).

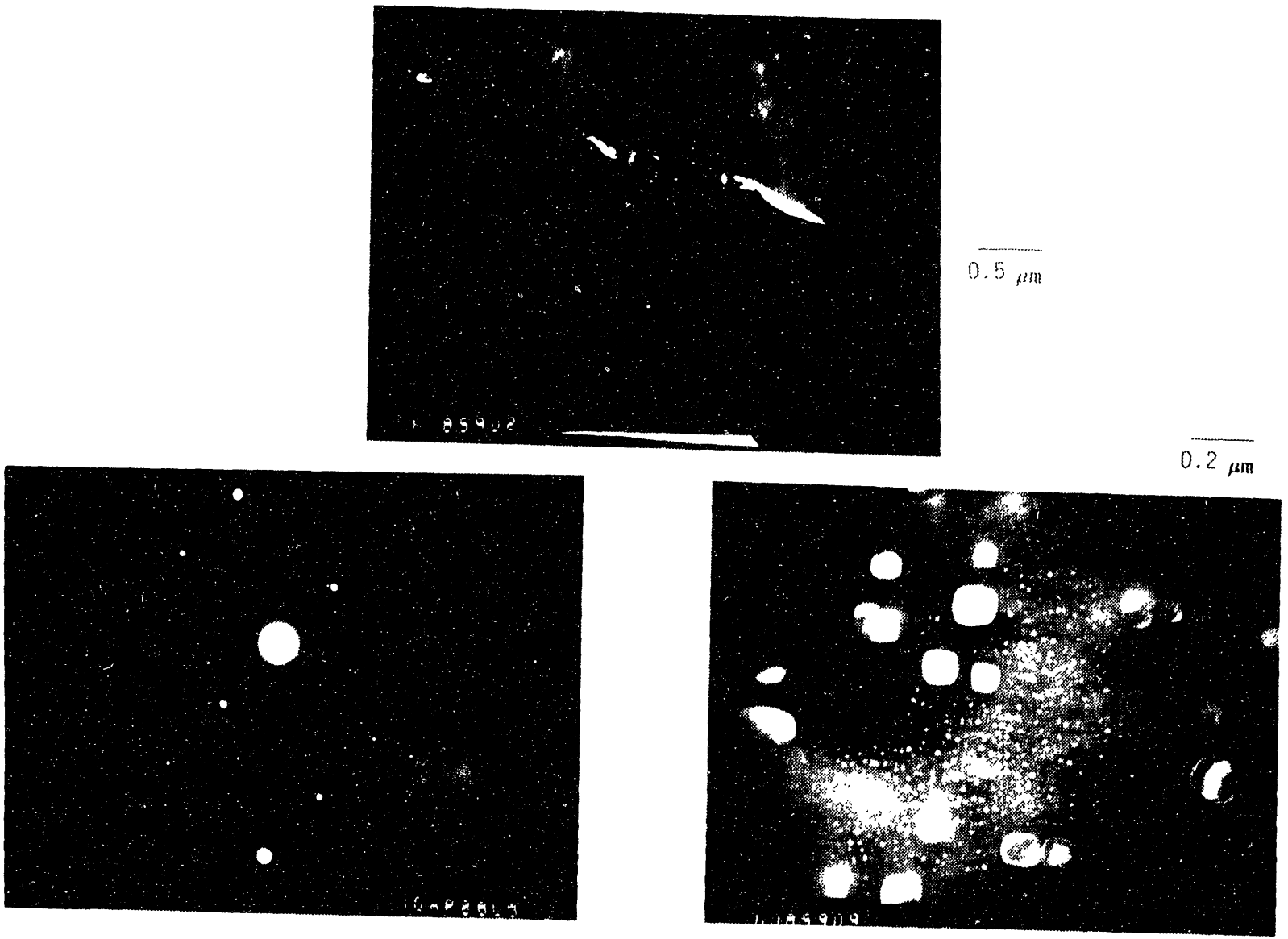

Figure 6.43 The TEM Micrographs of the AH Conditions of a0.28cm thick Plate of Alloy X-750.

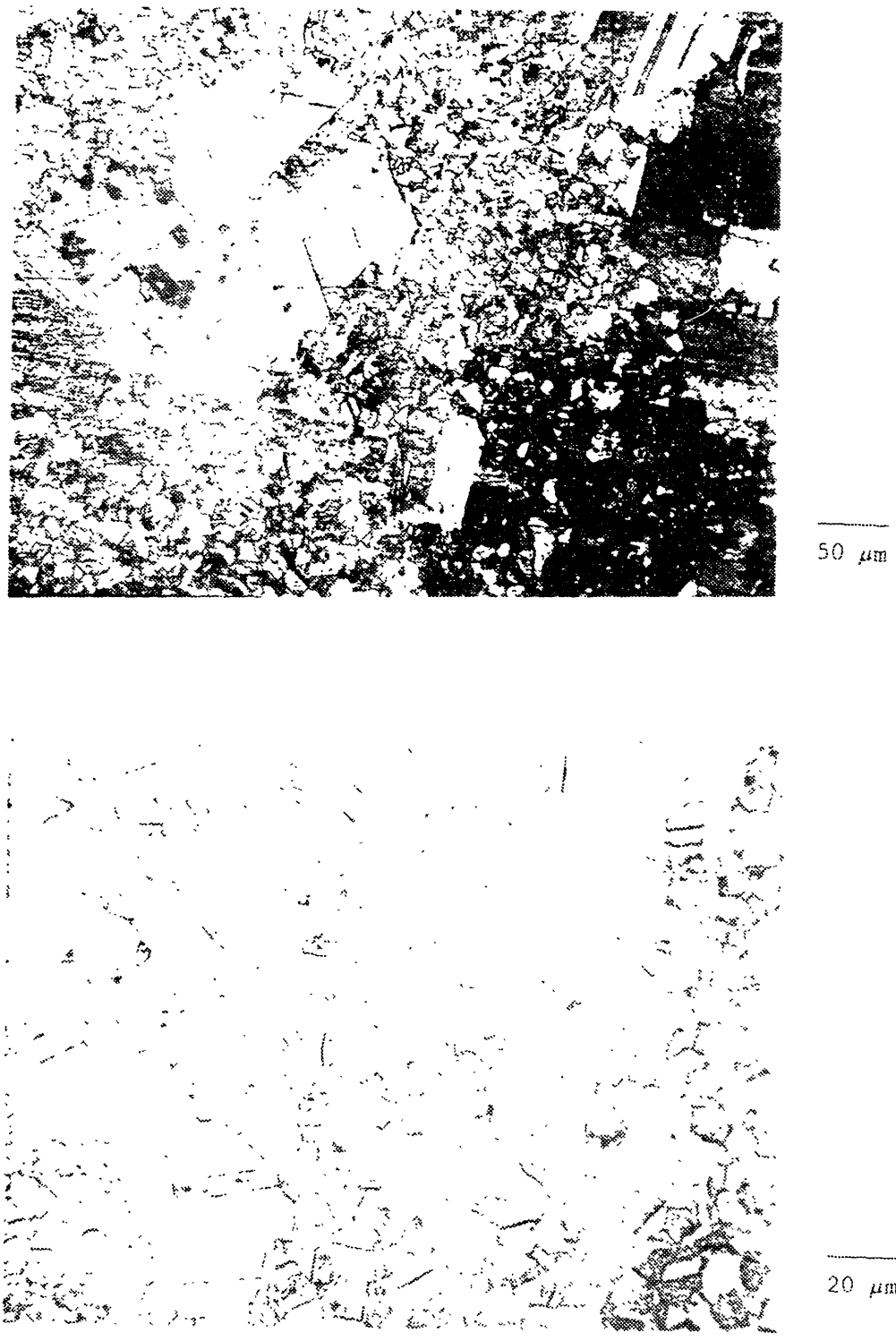

Figure 6.44 Optical Micrographs of the BH Condition of the Alloy X-750.

condition.

The microstructure of HTH condition of heat 96457E6 is shown in Figure 6.45. The coarse grained microstructure has an average size of 70μm. The grain boundaries are decorated with a continuous carbides. Some large intragranualr carbides are observed and aligned in the rolling direction. It is interesting to note that the microstrucutre is very simimar to that of the SAS condition the alloy 600 heat N.2650 with the exception of the presence of γ'.

The HOA condition shows a coarse grained structure similar, with the HTH condition, with an average grain size of 90μm, as shown in Figure 6.46. The AHTH condition shows a microstructure which resembles the HOA condition with the same average grain size and twin deformation structure, as shown in Figure 6.47.

Optical micrographs of the heat 964576E confirm that all the heat treated condition have microstructures in agreement with earlier results with respect to the distribution of γ' and carbide although there are some discrepancies in the measured values of average grain size. The plate heat of X-750 shows the AH condition which is an intermediate microstructure between the AH and AHTH condition of heat 96457E6.

Figures 6.48 and 6.49 show the optical micrographs of alloy 718. Both DA and CHT conditions exhibit a fine grained microstructure with the same average grain size of 15μm. Both condition show intergranular Laves phase (Fe_2Ti) precipitate. Some intragranular precipitates are observed to be lined up in the rolling direction. These were identified as MC carbides[26]. Primary strenthening phase ,γ'', is not resolved under the optical microscope.

A significant difference in the extent of grain boundary precipitate density is visible between the two conditions. The CHT condition has a semi-continuous morphology of Laves phase whereas the DA condition shows a grain boundary structure with a far less precipitates. The fraction

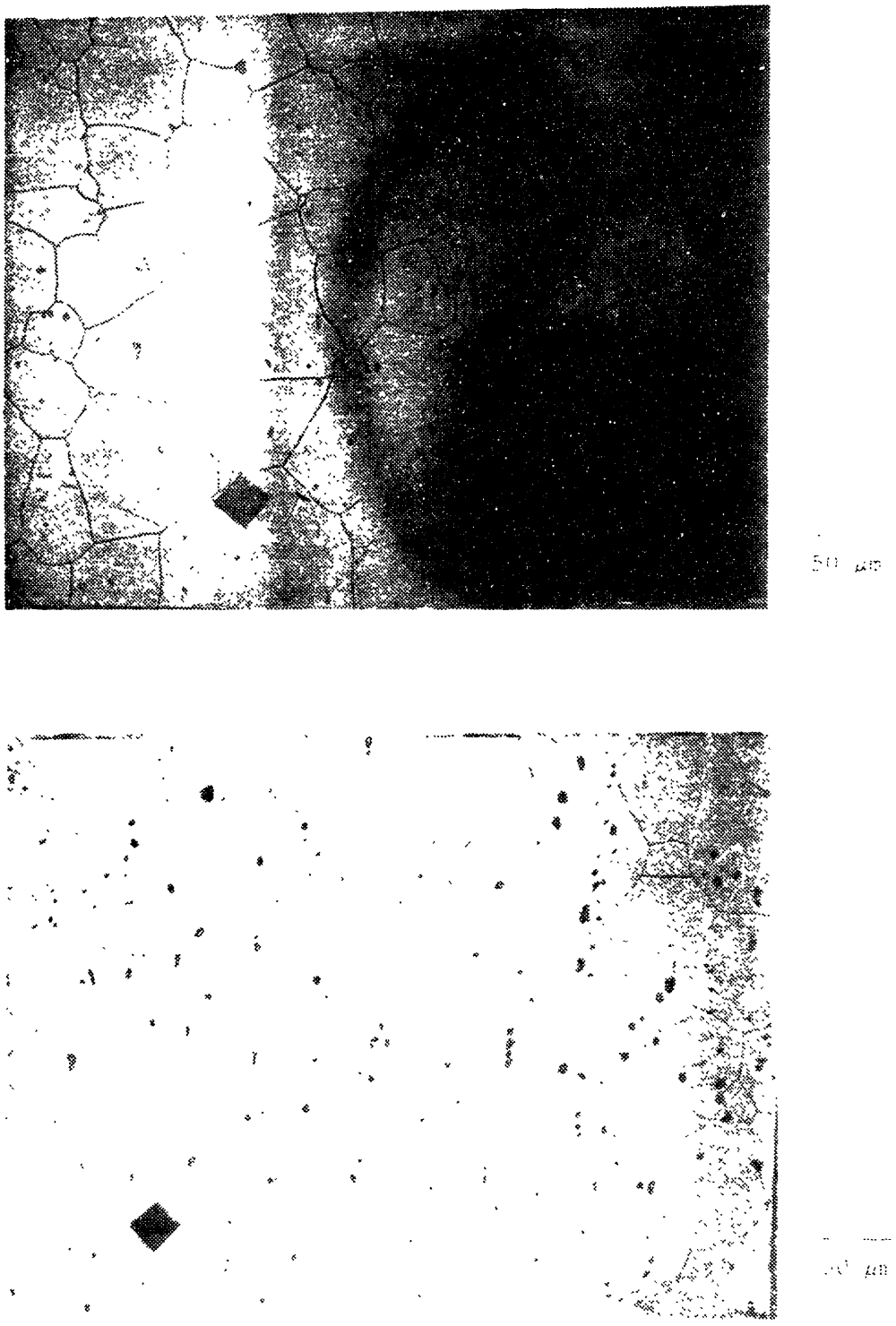

Figure 6.45 Two-step Etch Micrographs of the HTH Condition of Alloy X-750 (upper phosphoric and lower nital etch).

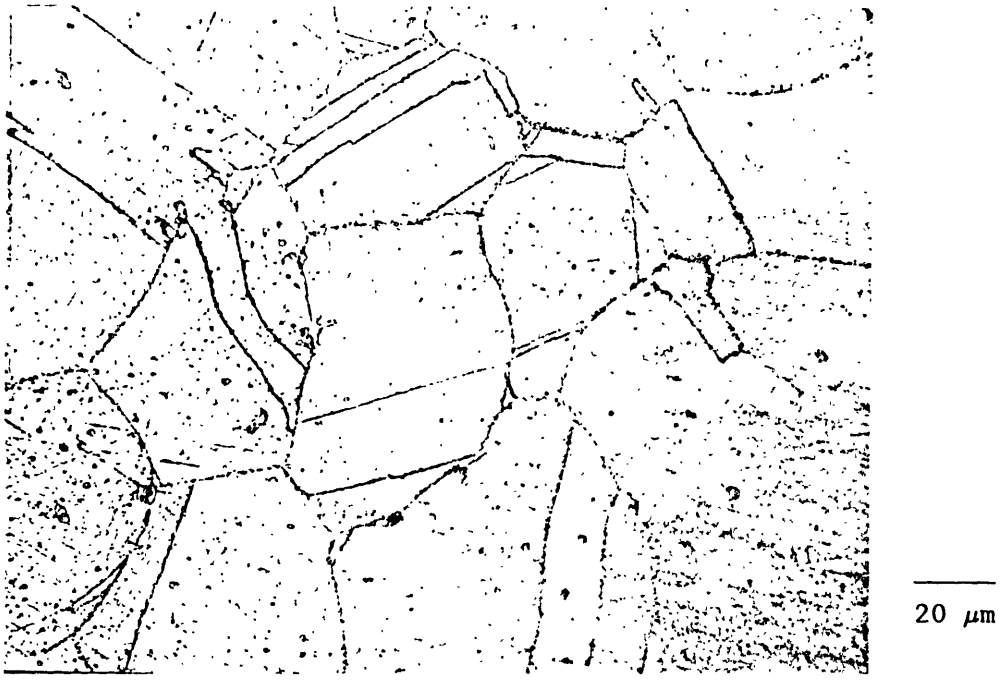

Figure 6.46 Optical Micrograph of the HOA Condition of Alloy X-750 (Kalling's Reagent).

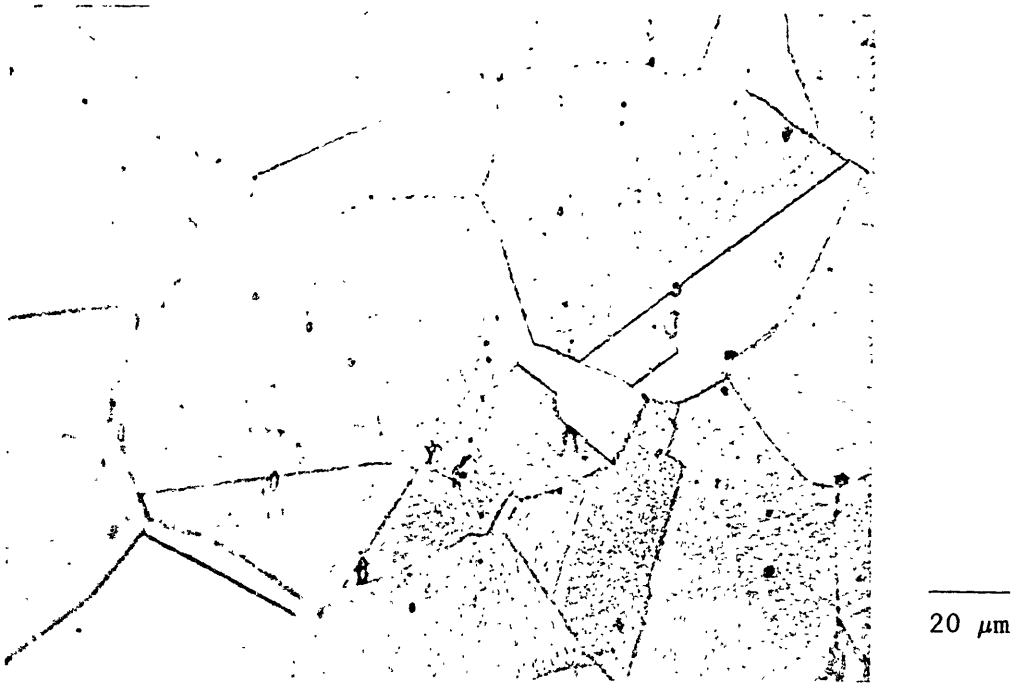

Figure 6.47 Optical Micrograph of the AHTH Condition of Alloy X-750 (Kalling's Reagent).

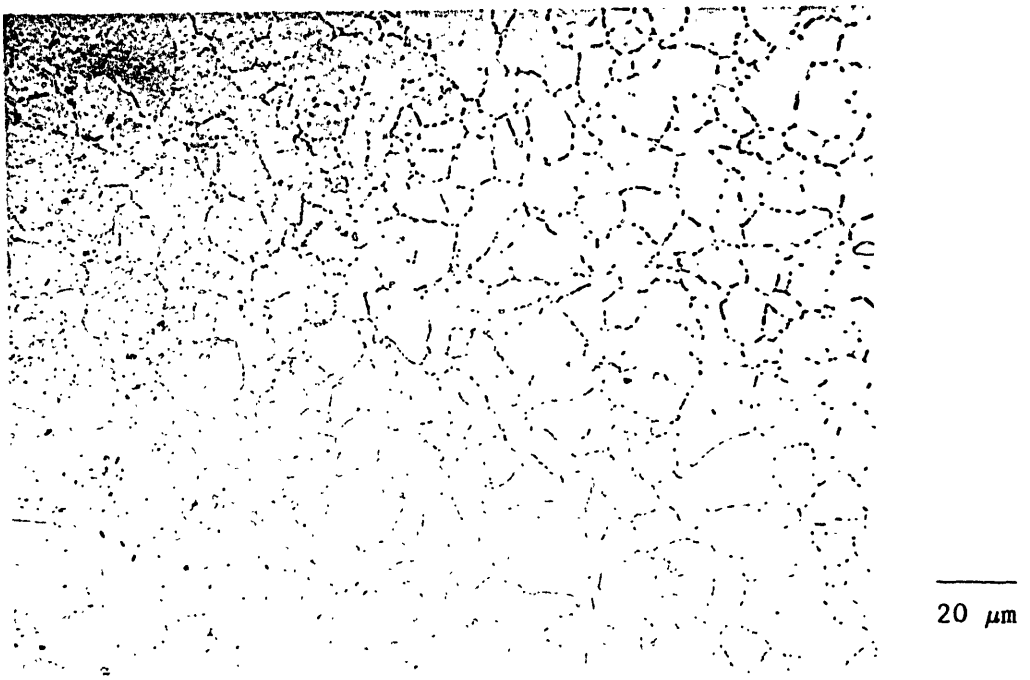

Figure 6.48 Optical Micrograph of the CHT Condition of Alloy 718 (10% hydrochloric acid in methanol).

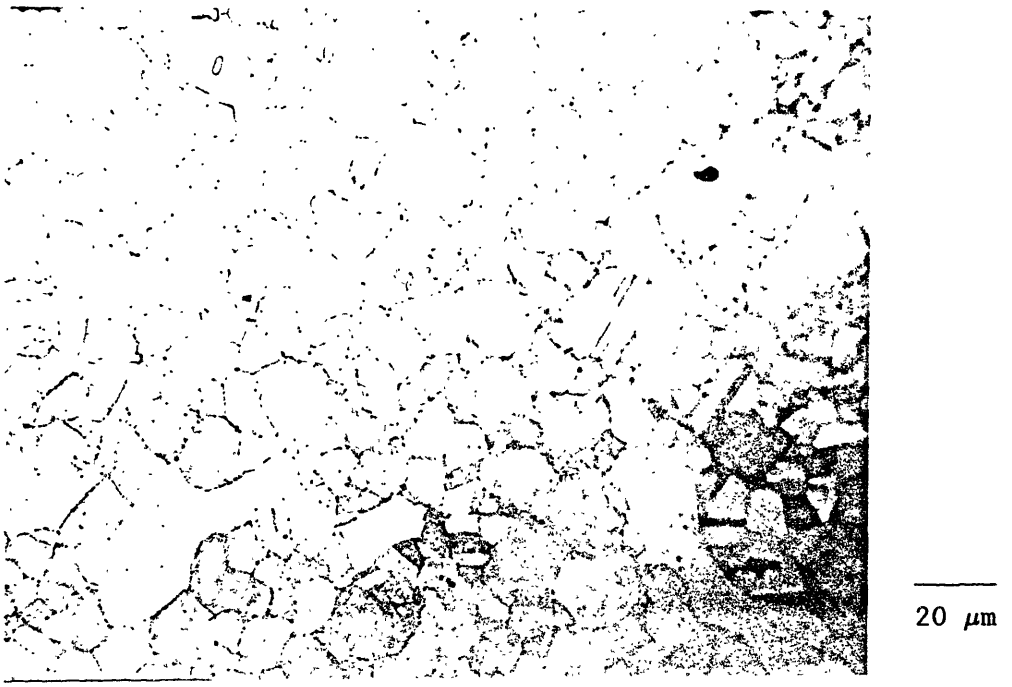

Figure 6.49 Optical Micrograph of the DA Condition of Alloy 718 (10% hydrochloric acid in methanol).

of grain boundaries decorated withthe precipitate is less than 0.1 in the latter condition

6.1.3 Grain Boundary Segregation of Trace Elements

Grain boundary segregation of trace elements such as phosphorus, boron, sulphur, and zirconium were measured by Auger electron spectroscopy (AES). Due to the low level of segregatio and the higher consequence of the surface contamination, it is found that a significant portion of data lie near the practical limit of detectability. Therefore, it is necessary to verify the validity of concentrations determined by Eq. (5-3). The concetrations are expected to be proportional to the signal-to-noise (S/N) ratio when the data are valid. It should be noted that large variation in the mesured concentration is true data scattering provided that the S/N ratio equal to or greater than three. Therefore, all the measured data are plotted against the S/N ratio , as shown in Figures 6.50 through 6.53. The data for phosphorus and boron show positive correlations with repect to the S/N ration, as shown in Figure 6.50 and 6.51. Although there are a few high concentration data with low signal-to-noise ratio, the statistical trend supported by the majority of data confirms that segregation of these elements are real and high enough for the detection technique. Hence a valid data analysis is possible if only data with S/N ratio equal to or greater than three are included. The data on sulphur and zirconium, in contrast, do not show the statistical trend nor have a data group with adequate S/N ratio, as shown in Figures 6.52 and 6.53. Therefore, it is concluded that neither sulphur nor zirconium is present on grain boundaries at a concentration above the practical detectability of the AES system. Hence, data for phosphorus and boron only are presented in this section.

Due to inadequate resolution of the secondary electron image which was used to select areas for AES anaysis, all the fracture surfaces were reexamined later by using a high resolution SEM. For small grained specimens it was not possiblt to locate the AES analysis area due to the difference in detector angle between the two microscopes. Therefore, the final SEM image typical of the secondary electron image for the AES

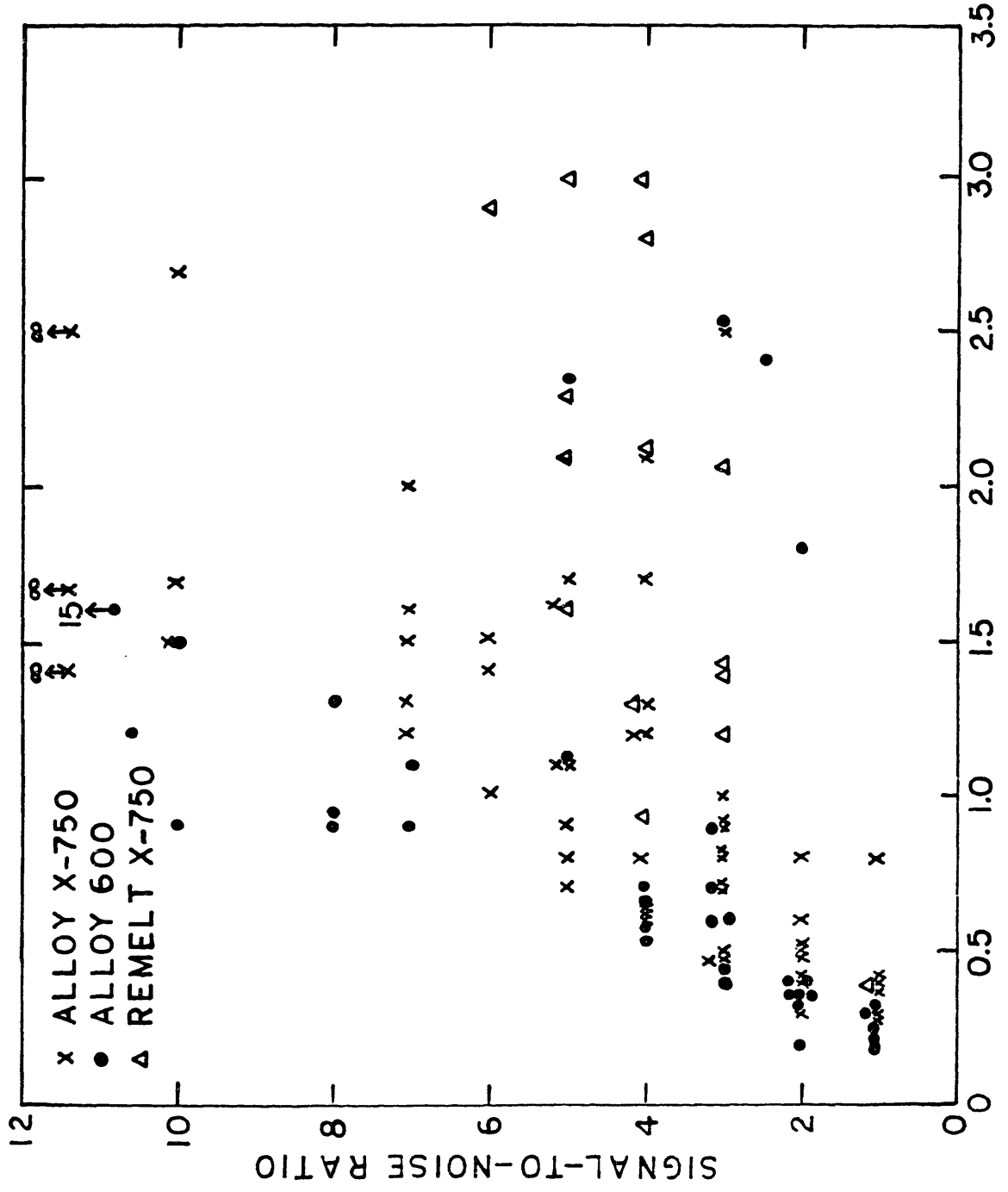

Figure 6.50 The Relation between Signal-to-Noise Ratio and Atomic Concentration of Phosphorus Measured by AES with in-situ Fracture.

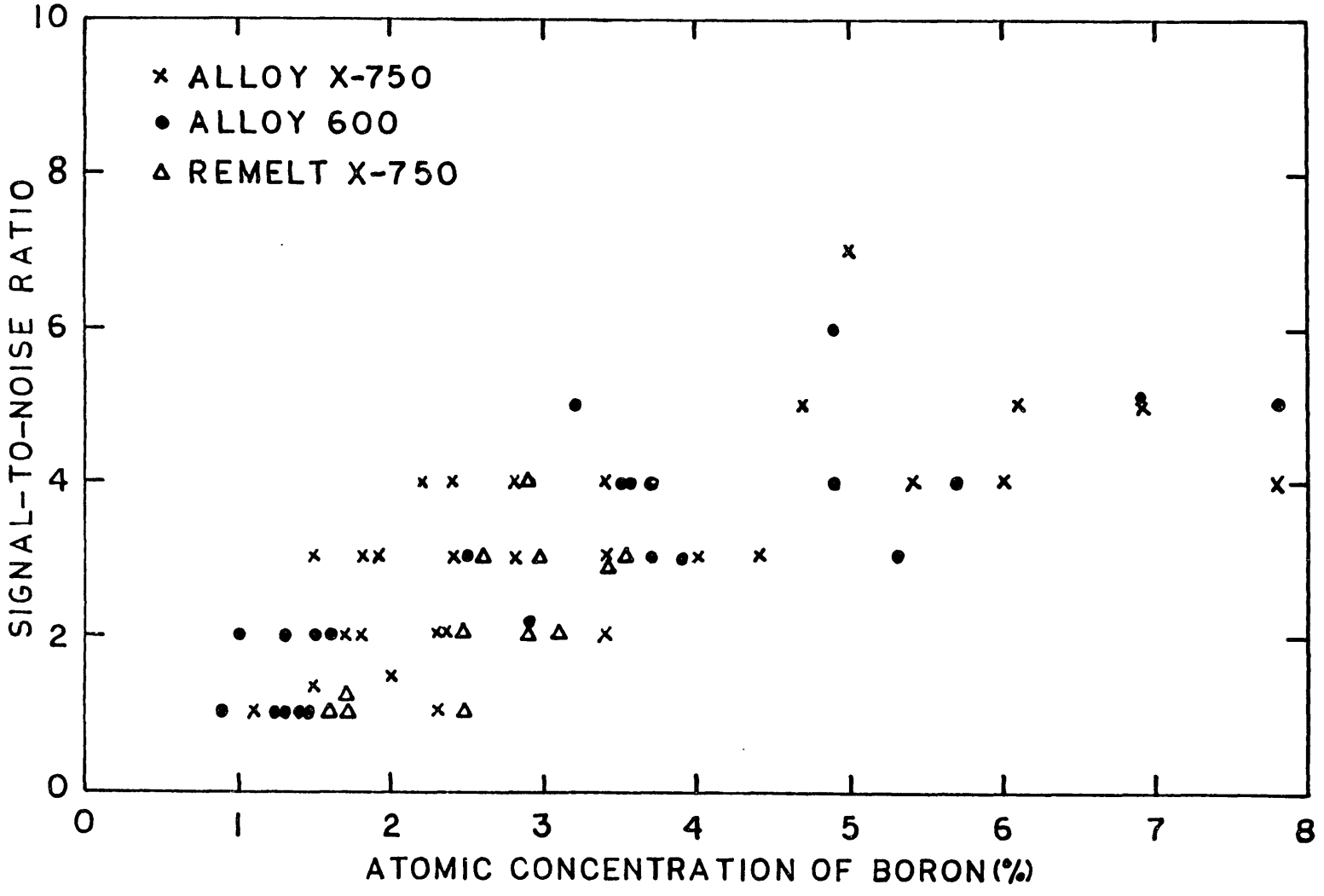

Figure 6.51 The Relation between Signal to Noise Ratio and Atomic Concentration of Boron Measured by AES with in-situ Fracture.

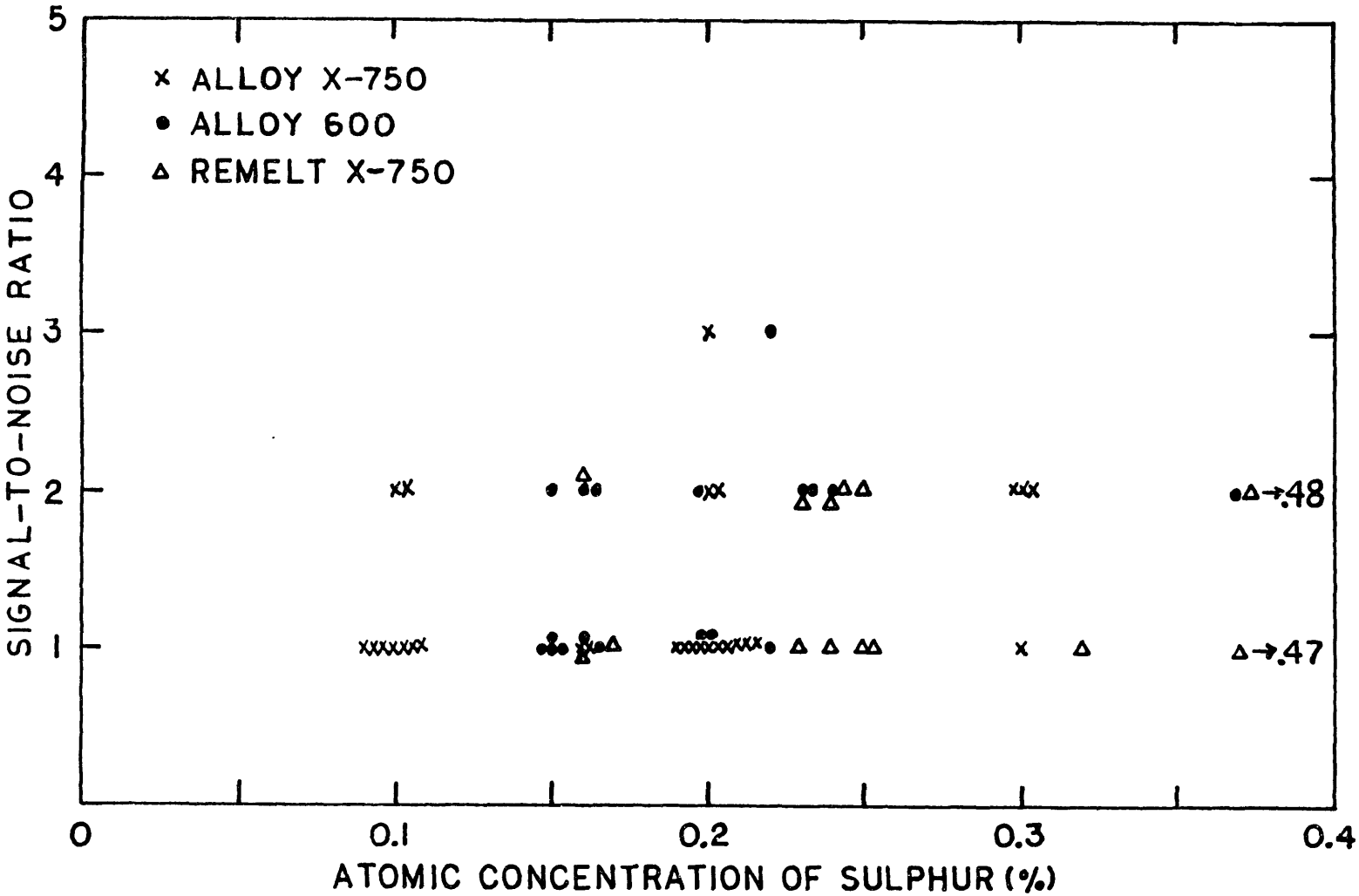

Figure 6.52 The Relation between Signal to Noise Ratio and Atomic Concentration of Sulphur Measured by AES with in-situ Fracture.

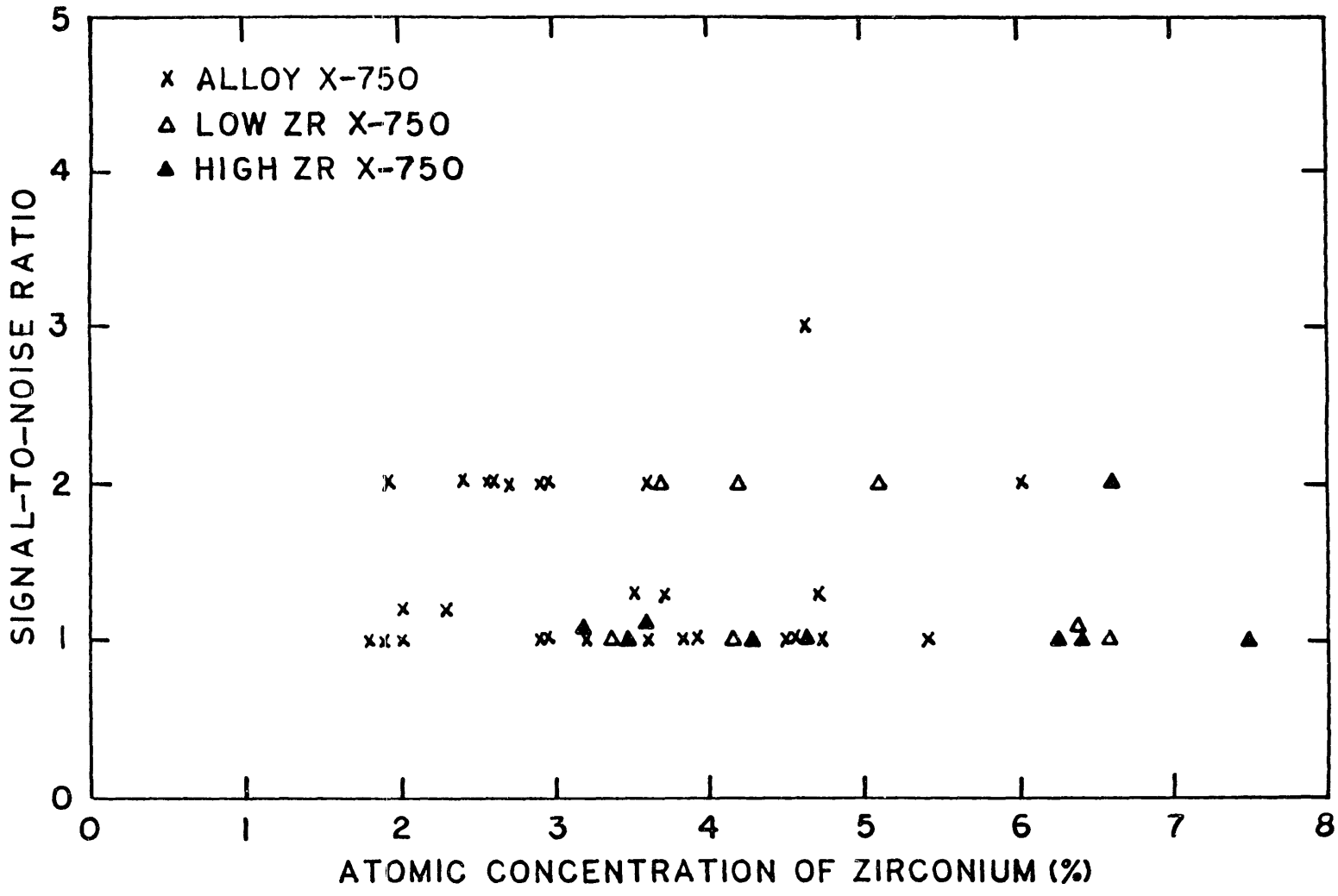

Figure 6.53 The Relation between Signal to Noise Ratio and Atomic Concentration of Zirconium Measured by AES with in-situ Fracture.

analysis was taken to confirm that the analyzed area was a true grain boundary. Most of the fracture surfaces were found to be truly intergranular and all data with the adequate S/N ratio are included in the following analysis.

Alloy 600

Reults of phosphorus analysis is summarized in Figure 6.54 as a function of the final process temperature. Three heats of alloy 600 tubing including NX1638, NX2650, and 96834 were examined for segregation. One specimen of each heat of NX1638 and NX2650 were solution annealed for 20 minutes at 1100°C followed by water quench and fractured without prior hydrogen charging so that base line data could be obtained for bulk matrix composition. The fracture surface of the solution annealed (SA) specimens are completely transgranular with a large reduction of area, as shown in Figure 6.55. No data had the S/N ratio for phosphorus or sulphur greater than or equal to three in the SA condition.

The HTMA condition of NX1638 has a representative fracture surface as shown in Figure 6.56. By judicious selection of the area, six data out of total nine points were obtained with the required S/N ratio. The measured phosphorus concentrations are relatively low with a small scatter band.

The HTMA condition of NX2650 shows a fracture surface with about 30% intergranular areas, as shown in Figure 6.57. The measured concentrations of phosphorous are higher than NX1638 probably due to the higher bulk concentration. The thermally treated (TT) condition of this heat was fractured with up to 90% intragranular surface, as shown in Figure 6.58. Six out of nine data data were obtained with the required S/N ratio. The average concentration of phosphorus is 1.8%. A large variation in the concentration may be attributed by part to an increased topological contrast typical to highly intergranular surfaces. Therefore, the maximum concentration of 2.84% may be a representative value for surfaces with the minimum screening effect. The concentrations of chromium and carbon were measured and found to be

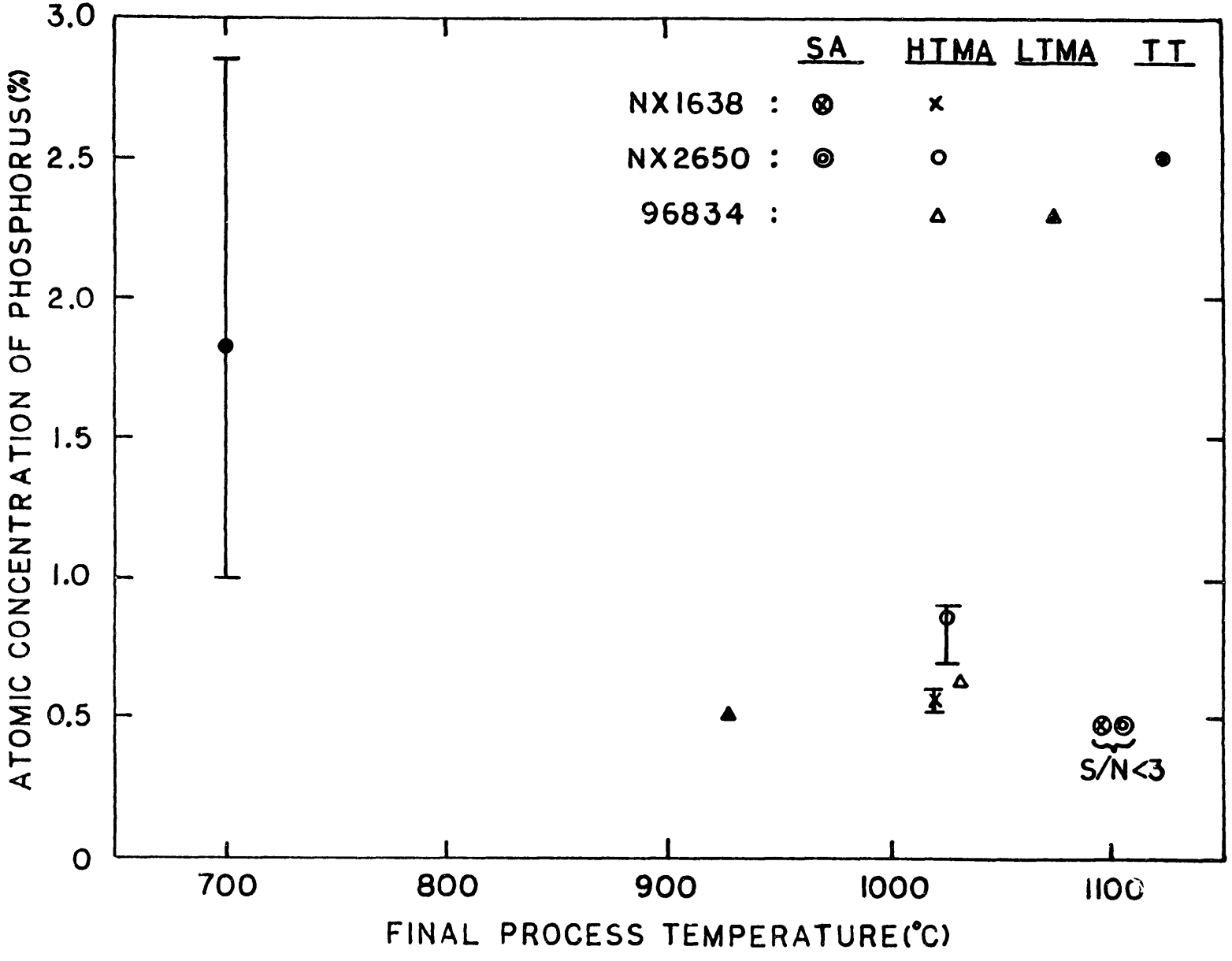

Figure 6.54 The Measured Concentration of Phosphorus on a Intergranular Surface in Alloy 600 as a Function of the Final Process Temperature.

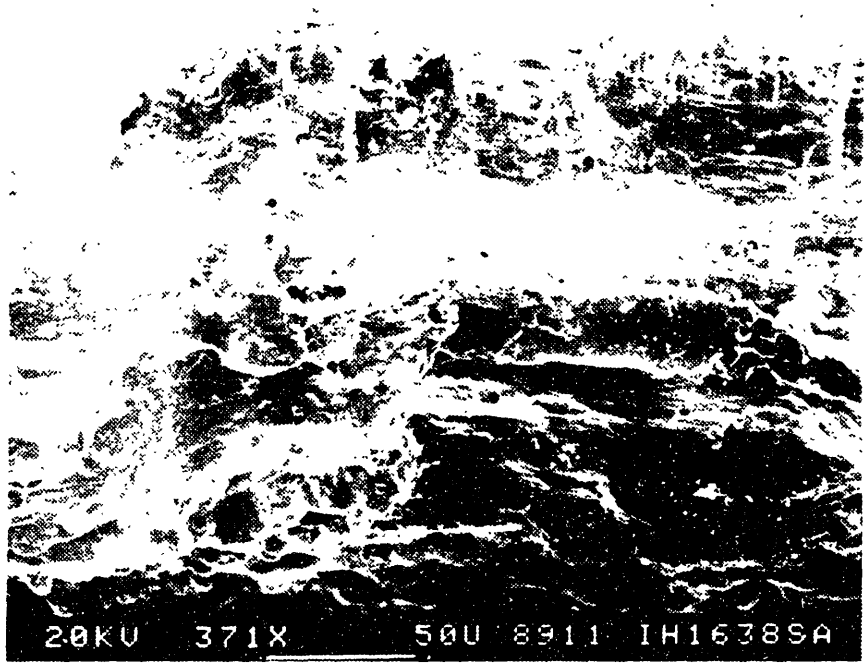

Figure 6.55 Fracture Surface of the AES Specimen for the Solution Annealed (SA) Condition of Alloy 600 Heat NX1638.

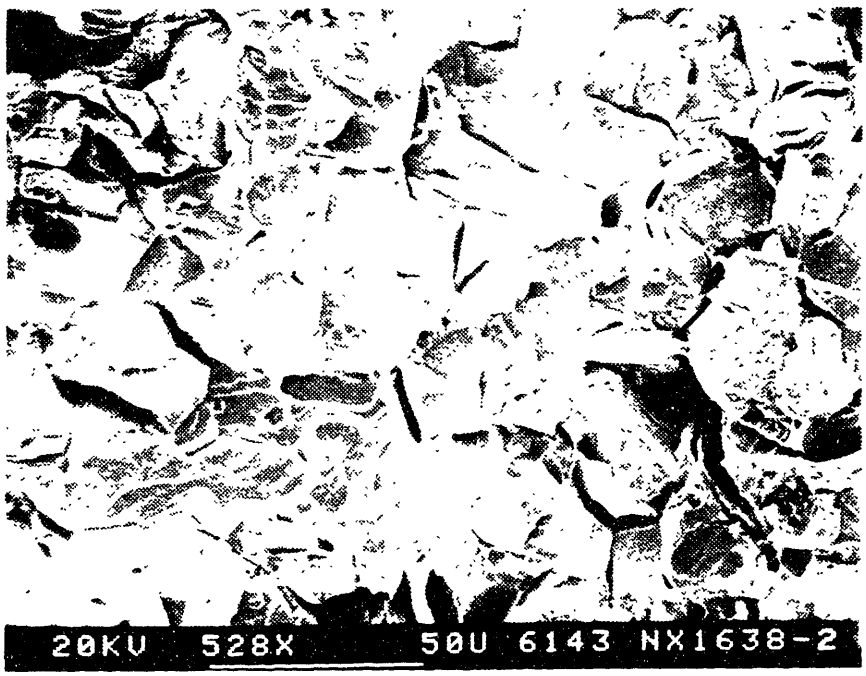

Figure 6.56 Fracture Surface of the AES Specimen for the HTMA Condition of Alloy 600 Heat NX1638.

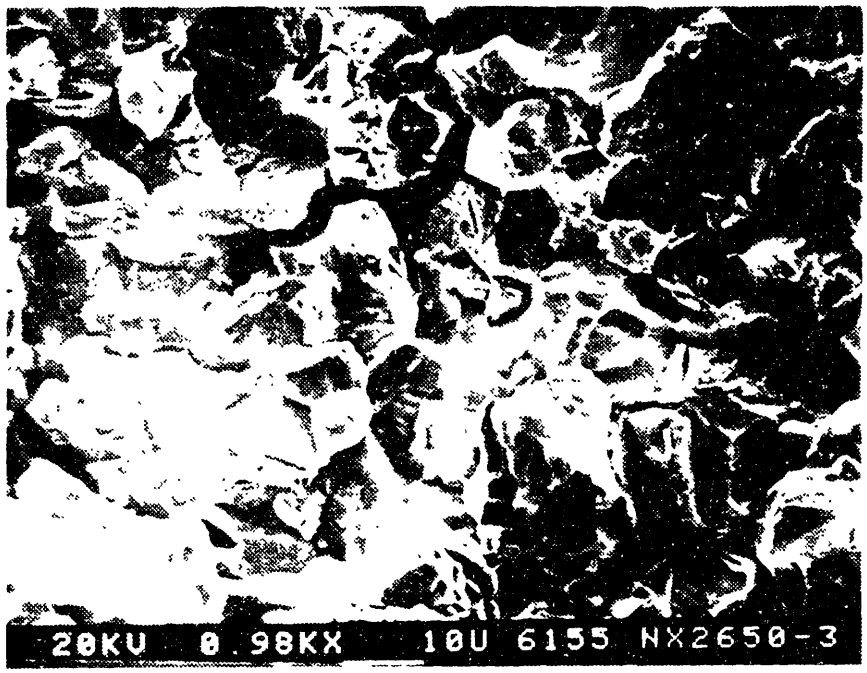

Figure 6.57 Fracture Surface of the AES Specimen for the HTMA Condition of an Alloy 600 Heat NX2650.

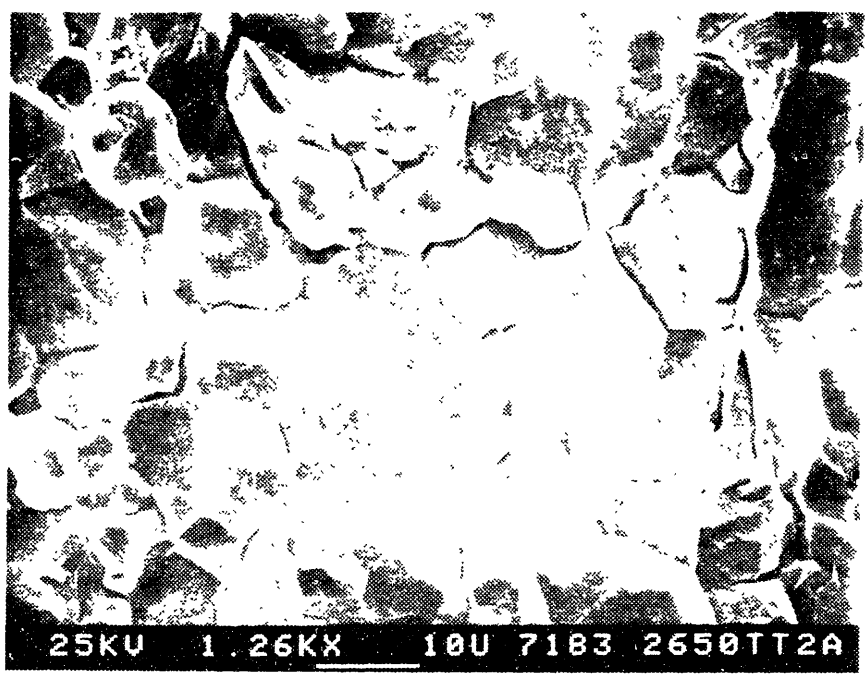

Figure 6.58 Fracture Surface of the AES Specimen for the Thermally Treated Condition of Heat NX2650.

nearly the same as those in the bulk matrix although the fracture surface showed the presence of carbide precipitates at a high number density. This suggests that the fracture after hydrogen charging does not occur through the carbides.

The HTMA condition of heat 96834 with a tubing diameter of 2.2cm shows mostly intergranular fracture, as shown in Figure 6.59. Intergranular precipitates are visible on most grain boundaries. The measured concentration of phosphorus lies between the HTMA conditions of NX1638 and NX2650. The chromium and carbon data, again,do not show the presence of the intergranular carbide. The LTMA condition of the same heat produces intergranular fracture showing the fine grained structure, as given in Figure 6.60. The phosphorus concentraion was measured to be about 0.5%. The fractured grain boundaries are smooth without any carbides in agreement with the micrstructural observation in the previous section.

The concentration of phosphorus increases with decreasing final process temperature. This suggests that the data may be analyzed by using an equilibrium segregation model. McLean's model [146] is widely used for this purpose due to its simplicity. The model suggests that the amount of segregation is determined by assuming a regular solution with a second order chemical interaction between the constituent element. The original model was modified to include the fact that there is a finite saturation level of segregation for a given element at absolute zero K. The model can be expressed for the free energy of phosphorus segregation as follows:

$$\Delta G_p = RT \left[\frac{1}{X_p^M} \cdot \frac{(X_p^{G.B.} / X_{p\ SAT}^{G.B})}{1 - X_p^{G.B.}/X_{p\ SAT}^{G.B.}} \right] \qquad (6\text{-}2)$$

where $X_{p\ SAT}^{G.B.}$ is the maximum value of the intergranular concentration, $X_p^{G.B.}$, at saturation, X_p^M is the matrix bulk concentration of the phosphorus. The free energy of segregation, ΔG_p, is the driving force

Figure 6.59 Fracture Surface of the AES Specimen for the HTMA Condition of Alloy 600 Heat 96834.

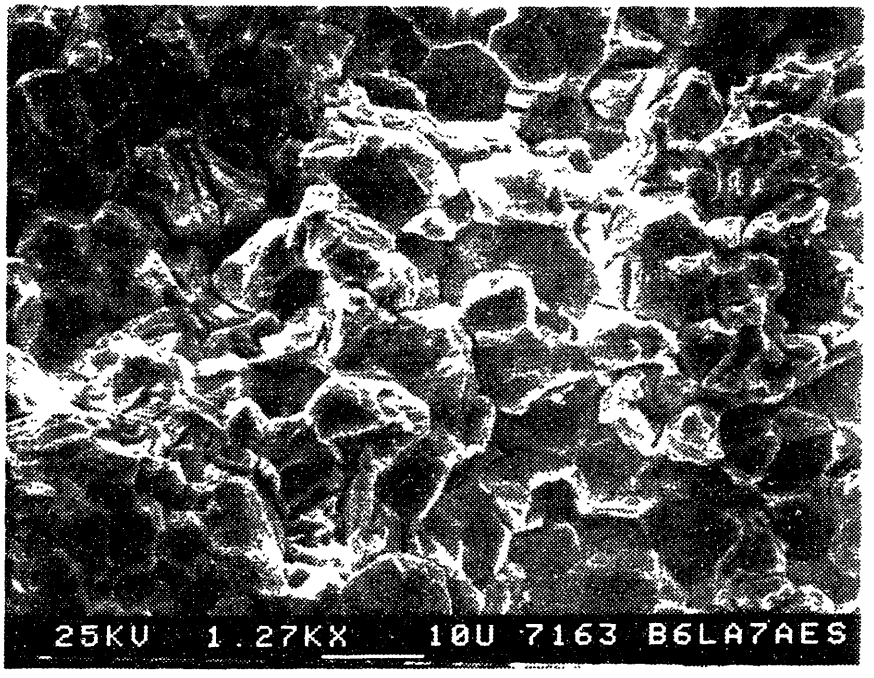

Figure 6.60 Fracture Surface of the AES Specimen for the LTMA Condition of Alloy 600 Heat 96834.

of segregation for phosphorus. A saturation concentration of 0.5 in atomic fraction is assumed for phosphorus, as estimated by Dumoulin et al. [147]. The measured concentration is multiplied by a factor of two to obtain true values for the intergranular concetration since the measurement was made on only one side of the entire grain boundary. The results are summarized in Figure 6.61. The values for heat 96834 were not determined due to lack of bulk composition data. Two heats, NX1638 and NX2650, show a relatively constant value for the free energy over a wide temperature range. At higher temperatures, the data agree well with available data on one alloy 600 with comparable bulk concentration [32] and a Ni-Cr-Fe alloy with about five times higher bulk concentration [35].

The measured concentrations of boron in the alloy 600 tubings are presented as a function of the final process temperature in Figure 6.62. The boron segregation is significant at a temperature around 1000 C and decreased at 700 C.

It is interesting to note the decreased boron concentration in heat NX2650 by the thermal treatment. The concomitant increase in the phosphorus suggests a correlation between segregation of the two elements. The correlaiton is examined by plotting data of phosphorus concentration against boron concentration, as shown in Figure 6.63. In the figure, all the data are selected with a S/N ratio greater than three on any one of the two elements. The statistically significant number of data indicate a negative correlation between the measured concentrations of two elements. Therefore, it is suggested that there is a site competition between phosphorus and boron. Since phosphorus is found to follow the equilibrium model, as shown in Figure 6.61, boron is apparently controlled by the site competition process. Therefore, boron may be displaced from grain boundaries during the thermal treatment of NX2650.

Alloy X-750

The AES study on alloy X-750 was performed on five different heats

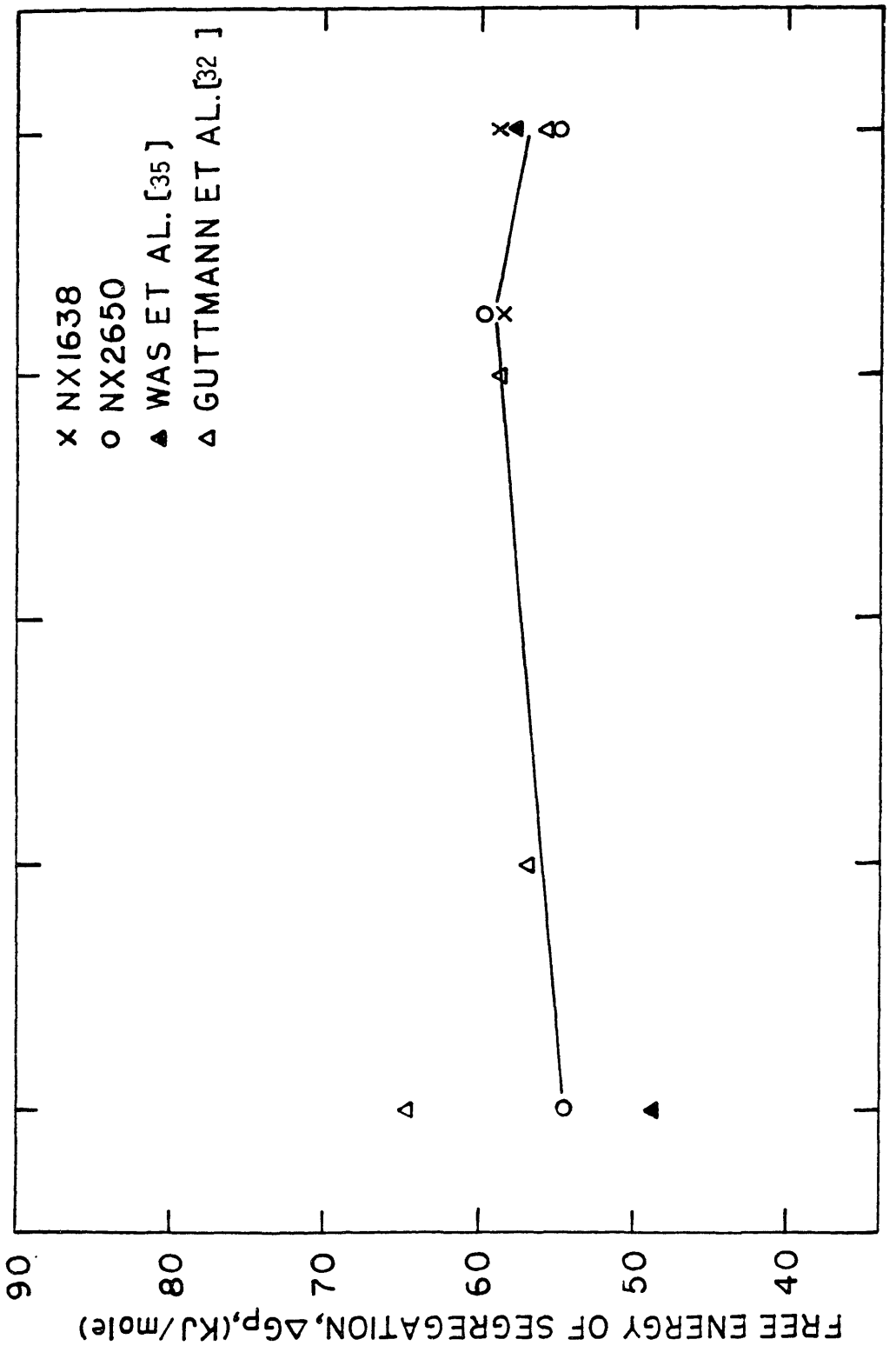

Figure 6.61 Free Energy of Phosphorus Segregation in Alloy 600 as a Function of Final Process Temperature.

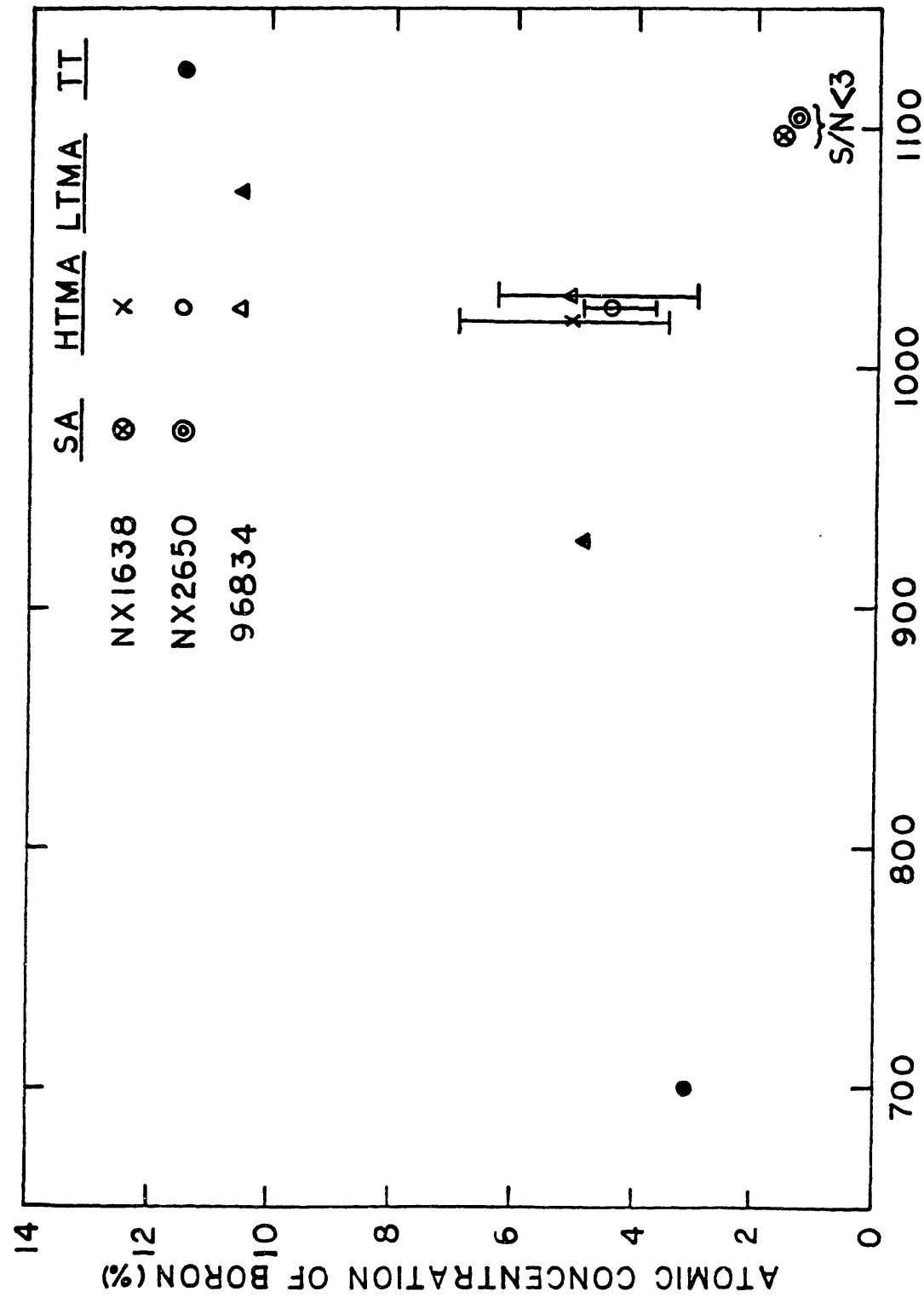

Figure 6.62 The Measured Concentration of Boron in Alloy 600 as a Function of Final Process Temperature.

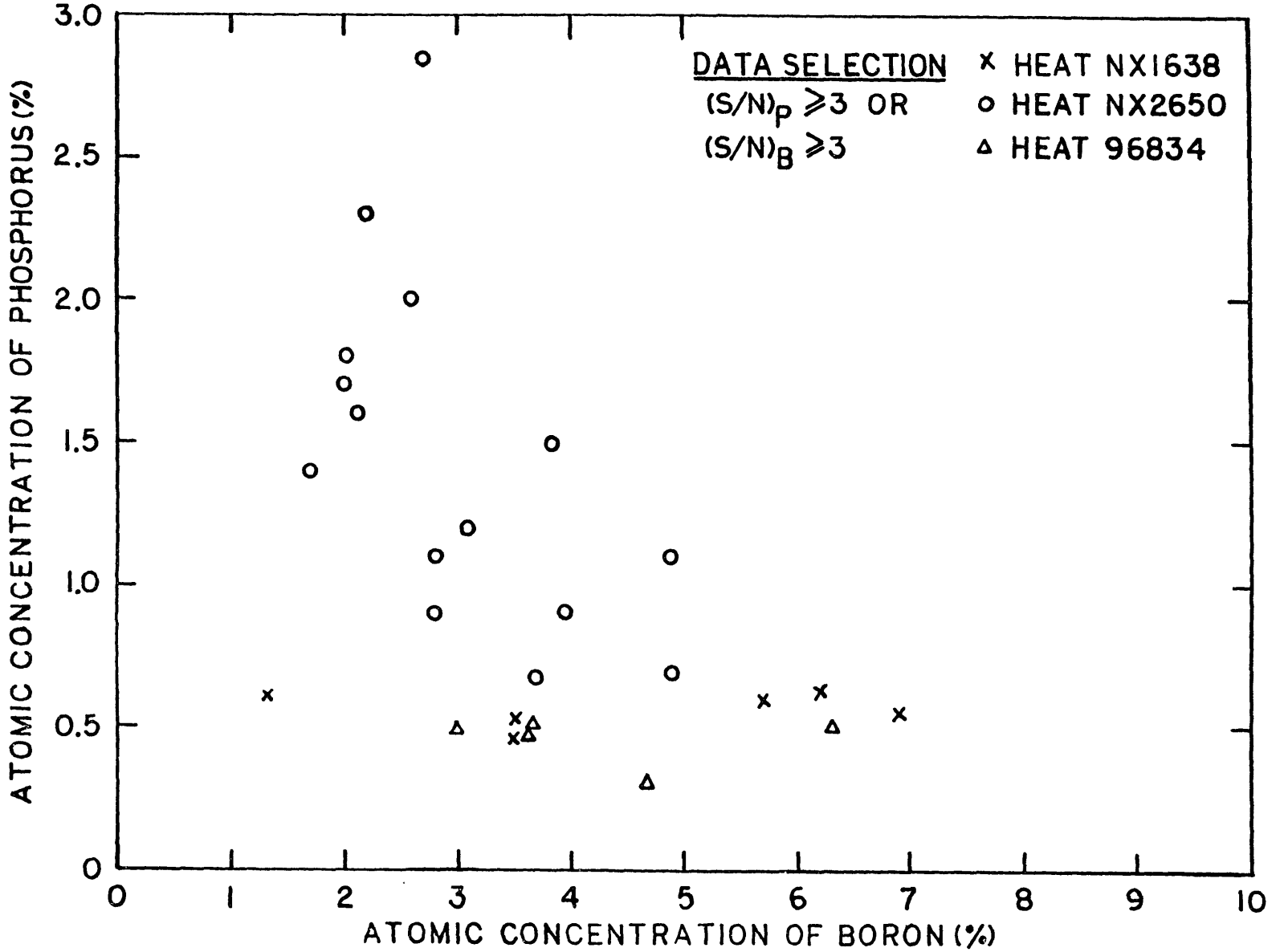

Figure 6.63 The Relation Between the Measured Concentrations of Phosphorus and Boron in Alloy 600.

including 96457E6, a result X-750 with a low zirconium and a high zirconium content, and 90330. The chemical composition of the heat are summarized in Table 5.2. The fracture surfaces were mostly intergranular except for only a few solution annealed specimens used to measure the base line data from transgranular area.

Most complete examination over wide range of heat treatment was made with heat 96457E6. The fractured AH condition is mostly intergranular as shown in Figure 6.64. The grain boundaries contain coarse precipitates with a size of about 0.3μm which are consistent with the size of the intergranular γ' precipitates. A total of five data points out of eight spots examined met the S/N criterion. The average measured concentration of phosphorus is about 1.1%. The HTH condition revealed a large grained structure after fracture, as shown in Figure 6.65. Large MC-type carbides are lined up in the rolling direction. Up to 70% of data were obtained with enough S/N ratio. The average measured concentration of phosphorus is about 1.1%.

The BH condition produced enough intergranualr areas with two different grainsizes in agreement with the optical metallography. The fracture surfaces were decorated with large MC-carbide and coarse $M_{23}C_6$ type carbides, as shown in Figure 6.66. Only about 30% of examined spots met the S/N ratio criterion. The measured phosphorus concentration has an average of 0.9%.

The AHTH condition was fractured in a mostly intergranular pattern and revealed MC carbides on the fracture surface, as shown in Figure 6.67. Five out of eight examined spot produced data with the S/N ratio greater than three. The average measured concentration of phosphorus is found to be about 1.4%.

The fracture surface of the HOA condition is shown in Figure 6.68. A large grained structure shows broken MC-carbides on the fracture surface. Only two outof seven spots meet the S/N ratio criterion. An average of 1.1% was measured as the phosphorus concentration.

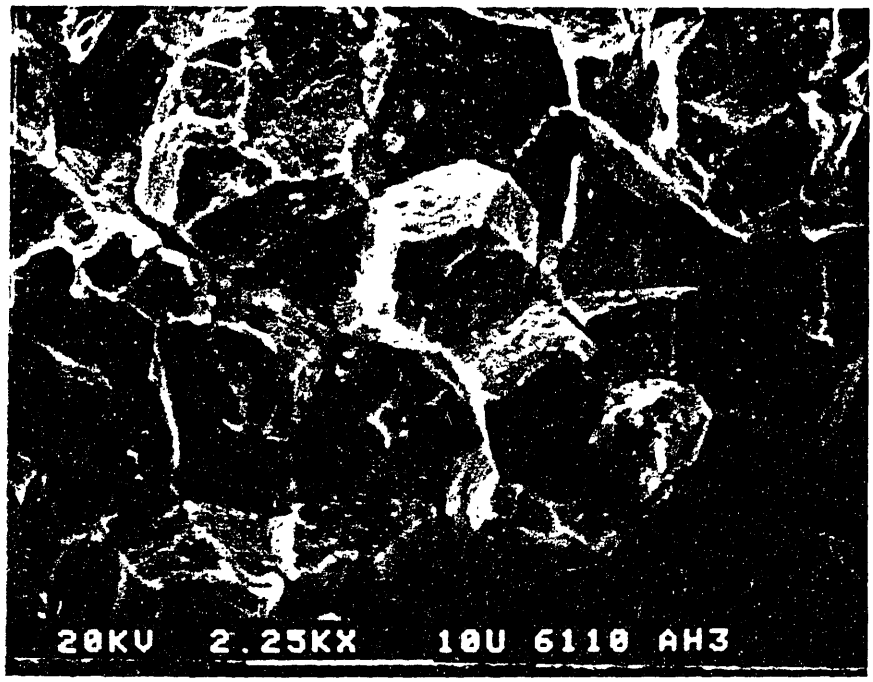

Figure 6.64 Fracture Surface of the AES Specimen for the AH Condition of an Alloy X-750 Heat 96457E6.

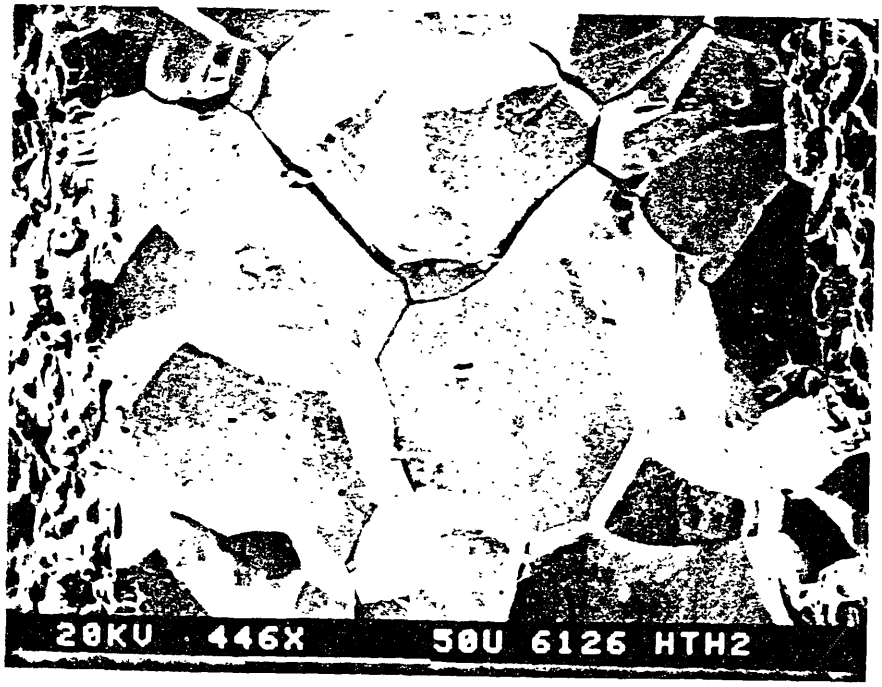

Figure 6.65 Fracture Surface of the AES Specimen for the HTH Condition of an Alloy X-750 Heat 96457E6.

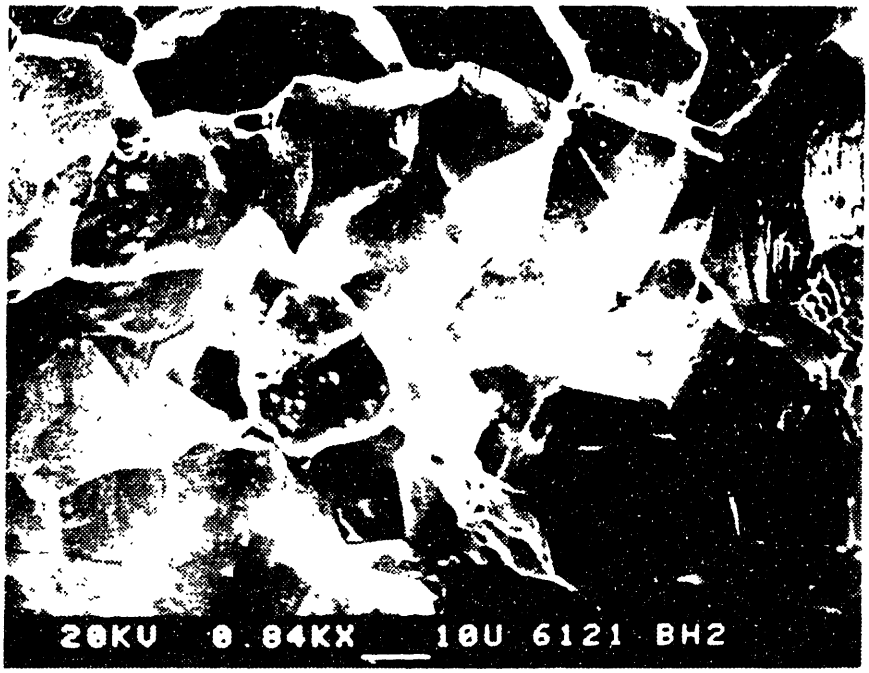

Figure 6.66 Fracture Surface of the AES Specimen for the BH Condition of an Alloy X-750 Heat 96457E6.

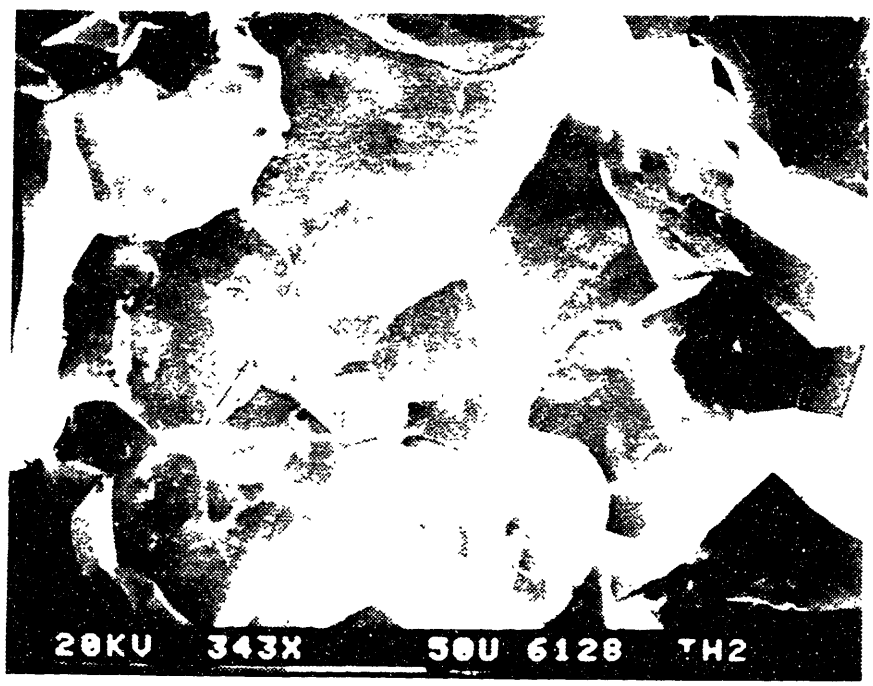

Figure 6.67 Fracture Surface of the AES Specimen for the AHTH Condition of an Alloy X-750 Heat 96457E6.

Figure 6.68 Fracture Surface of the AES Specimen for the HOA Condition of an Alloy X-750 Heat 96457E6.

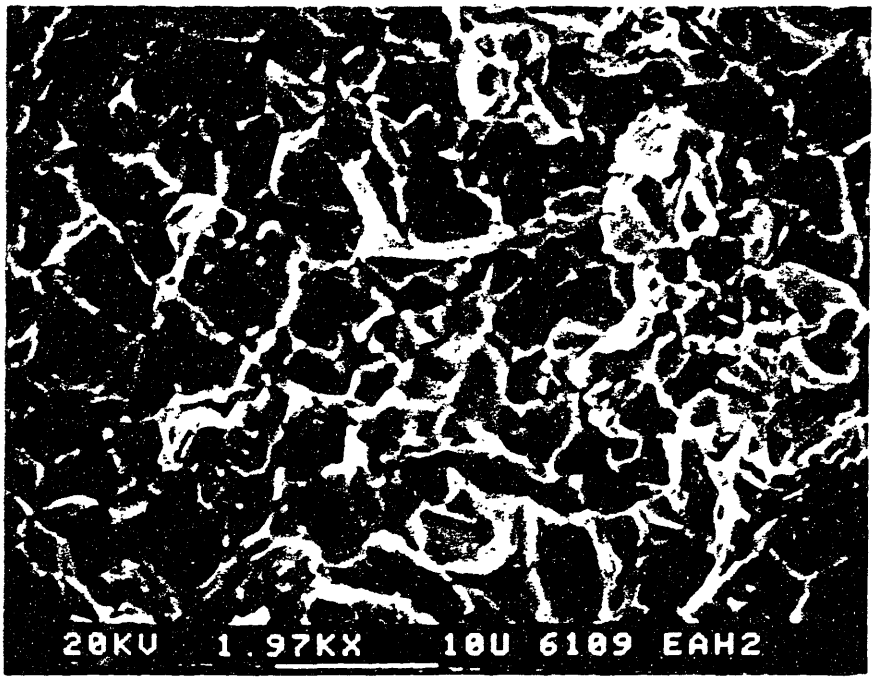

Figure 6.69 Fracture Surface of the AES Specimen for the EAH Condition of an Alloy X-750 Heat 96457E6.

All the unaged conditions such as EAH, EBH, EHTH as well as SA produced a ductile fracture surface even after the same period of hydrogen charging. The EAH condition produced only a small amount of intergranular areas. The fracture surface consists of about 30% intergranular area and the remaining 70% of area characterized by a ductile shear rupture, as shown in Figure 6.69. By careful selection of the intragranular surface, all the data were obtained with a S/N ratio greater than three. The measured concentration of phosphorus is the highest with the EAH among all the standard treatment conditions. Both the low temperature annealed condition (EBH) and the high temperature annealed condition (EHTH) produced intergranular areas, as shown in Figures 6.70 and 6.71, respectively. Three out of six spots for EBH and four out of six spots for EHTH were obtained with enough S/N ratio. An average of 0.7% was measured for phosphorus in both conditions. The solution annealed and water quenched conditon (SA) as well as the as received condition were fractured mostly in transgranular. Nevertheless, there are two data for SA condition and one data for AR with enough S/N ratio. The measured value of the phosphorus concentration are about 0.6%.

All the data with alloy X-750 are summarized in Figures 6.72 and 6.73. For the heat 96457E6, it was found that all the final conditions including AH, HTH, BH, AHTH, and HOA contain approximately the same amount of phosphorus at grain boundaries. The peak values are slightly higher with condition AH and AHTH compared with conditions HTH, BH, and HOA but the difference is insignificant..

The data from remelt X-750 also shows no systematic trend, as shown in Figure 6.73. The HTH condition of the low Zr heat shows the highest concentration of phosphorus. The high Zr heat shows lower segregation of phosphorus for both HTH and HOA conditions while no distinction is made for the AH condition. Therefore, there is a weak effect of zirconium on the reduction of phosphorus segregation for the HTH and HOA conditions. Since the measured zirconium concentration at the fracture surface was below the practical limit of the AES system, the role of

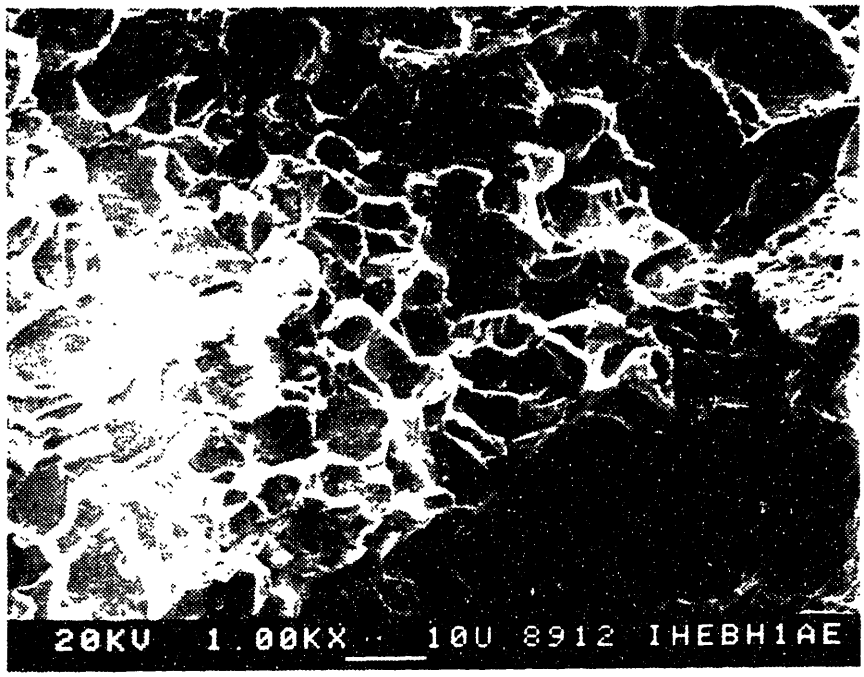

Figure 6.70 Fracture Surface of the AES Specimen for the EBH Condition of an Alloy X-750 Heat 96457E6.

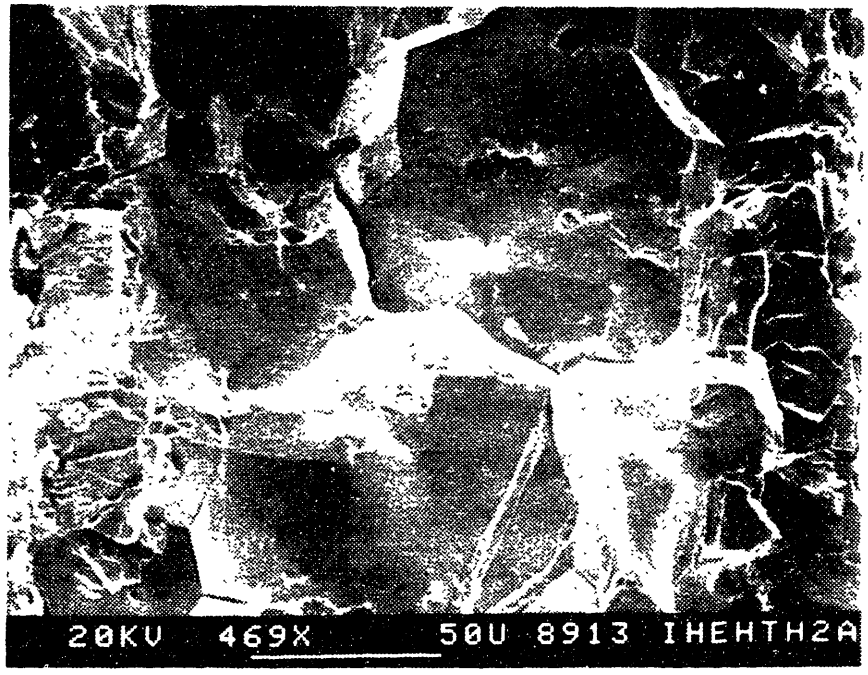

Figure 6.71 Fracture Surface of the AES Specimen for the EHTH Condition of an Alloy X-750 Heat 96457E6.

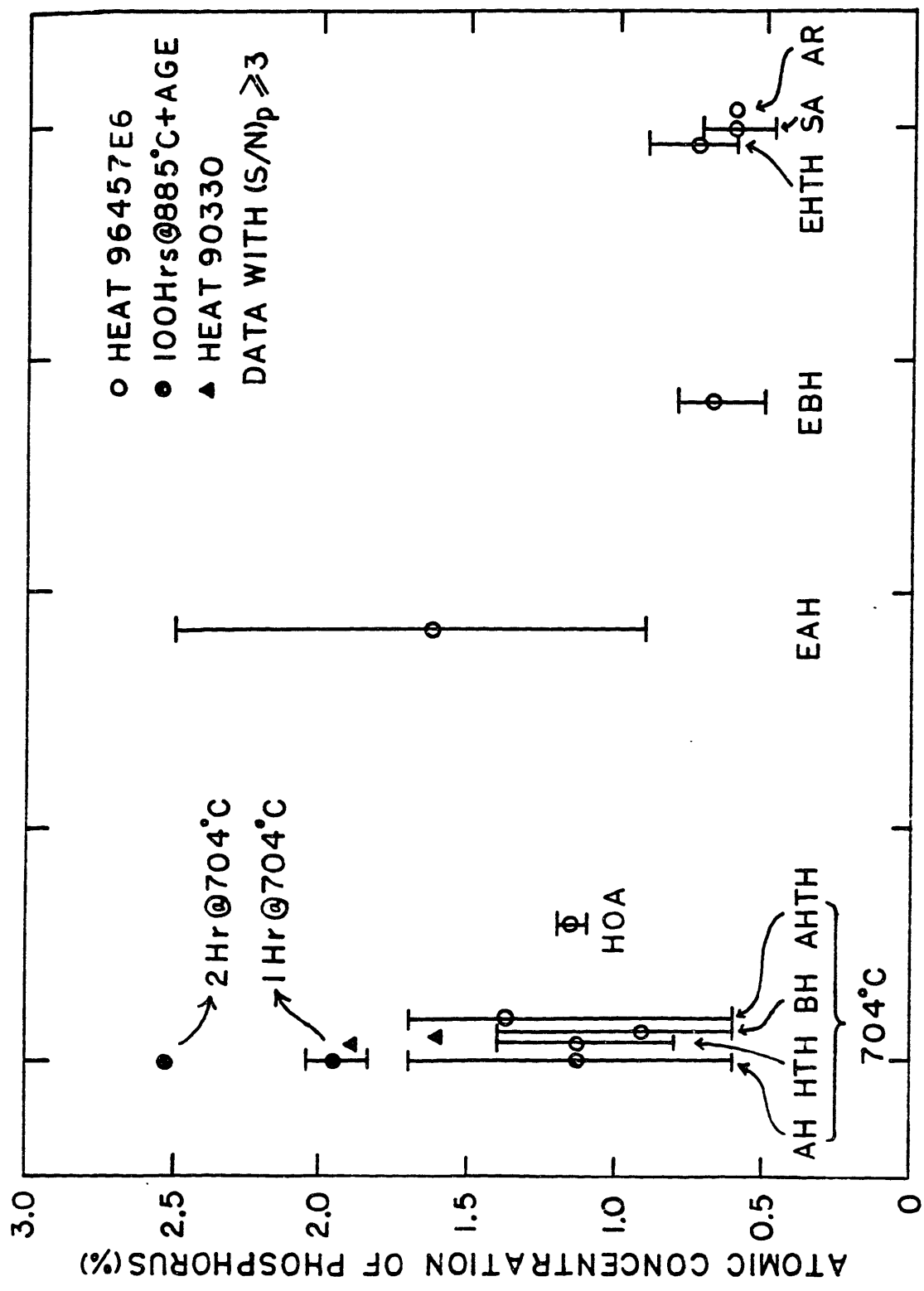

Figure 6.72 The Measured Concentration of Phosphorus on the AES Specimens of Alloy X-750 as a Function of Final Process Temperature.

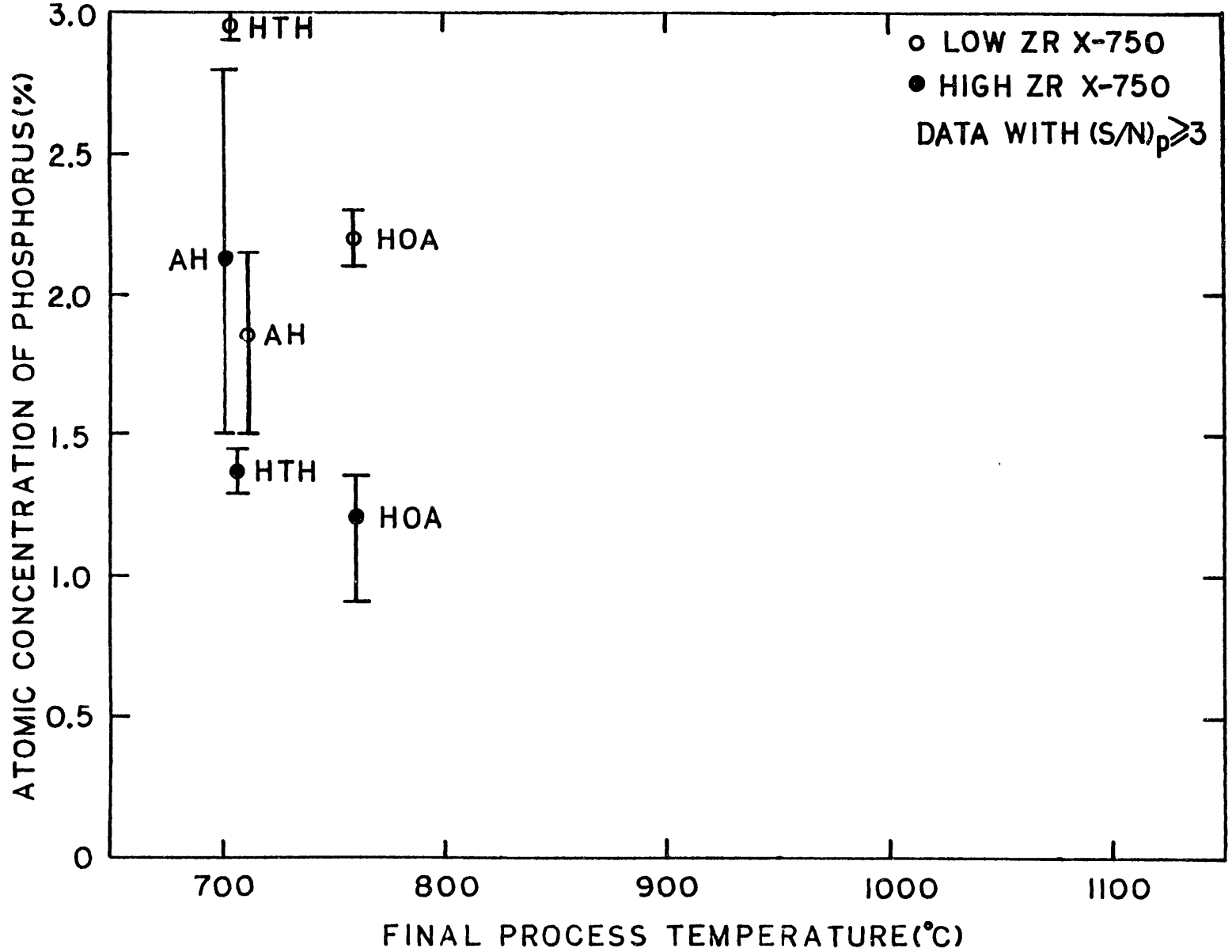

Figure 6.73 The Measured Concentration of Phosphorus on the AES Specimen of the Remelt X-750 as a Function of Final Process Temperature.

zirconium is probably to retain the phosphorus with in the matrix. However, no supporting evidence is available in the literature. The low zirconium heat has the same bulk concentration of zirconium as the heat 96457E6. The higher segregation, on the average, can be explained by the higher bulk concentration of phosphorus in the heat.

Figure 6.74 shows the results of calculated free energy of phosphorus segregation obtained by using the previous McLean model. The free energy is fairly consistent in the high temperature region, with an average value of 70 kJ/mole. At temperatures of the final aging, the free energy is found to to decrease by a significant amounts. The same temperature dependence was observed with a free surface segregation study of X-750 done at the Battelle Pacific Northwest Laboratories [36], as shown Figure 6.75. The segregation at high temperature regions (>900 C) is believed to follow the equilibrium behavior. Therefore, it is postulated that phosphorus segregation is reduced by certain microstructural interaction which is active primarily at temperature below 900 C.

Since the precipitation of fine γ' takes place at a temeprature below 885°C, it may be assumed that the phosphorus is trapped at the fine γ' particles during a diffusion process to grain boundaries. If this is true, more segregation will take place upon aging after most of the γ' are allowed to form extensive coarse γ' precipitates. The idea was tested by equalizing the heat 96457E6 at 885°C for 100 hrs and aging at 704°C. The results show more precipitation of coarse γ' at 885°C indeed allows higher segregation of phosphorus at 704°, as shown in Figure 6.72. Increasing the aging time from one hour to two hours increases phosphorus segregation by an appreciable amount. The case of two hour aging shows about a 4 kJ/mole increase in the free energy, as shown in Figure 6.74. Further work is desirable to confirm the effect of γ' precipitation on the segregation.

Inorder to examine heat-to-heat variation with a comparable bulk concentration of phosphorus, an X-750 heat 90330 was employed. Grove and Petzold[36] observed a systematically higher segregation in BH

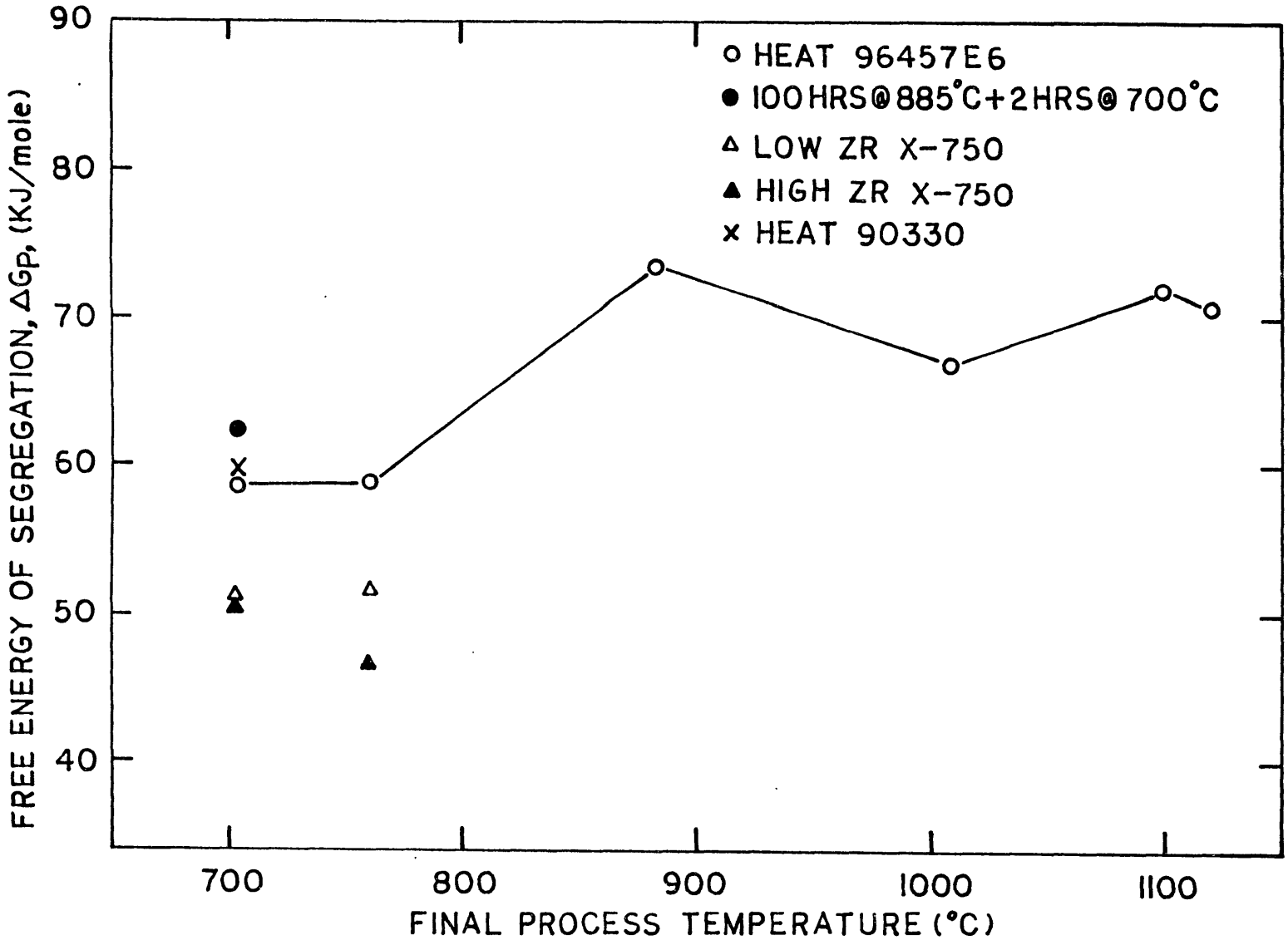

Figure 6.74 **The Free Energy of Phosphorus Segregation as Determined by the McLean Type Equilibrium Model based on the Peak Concentration.**

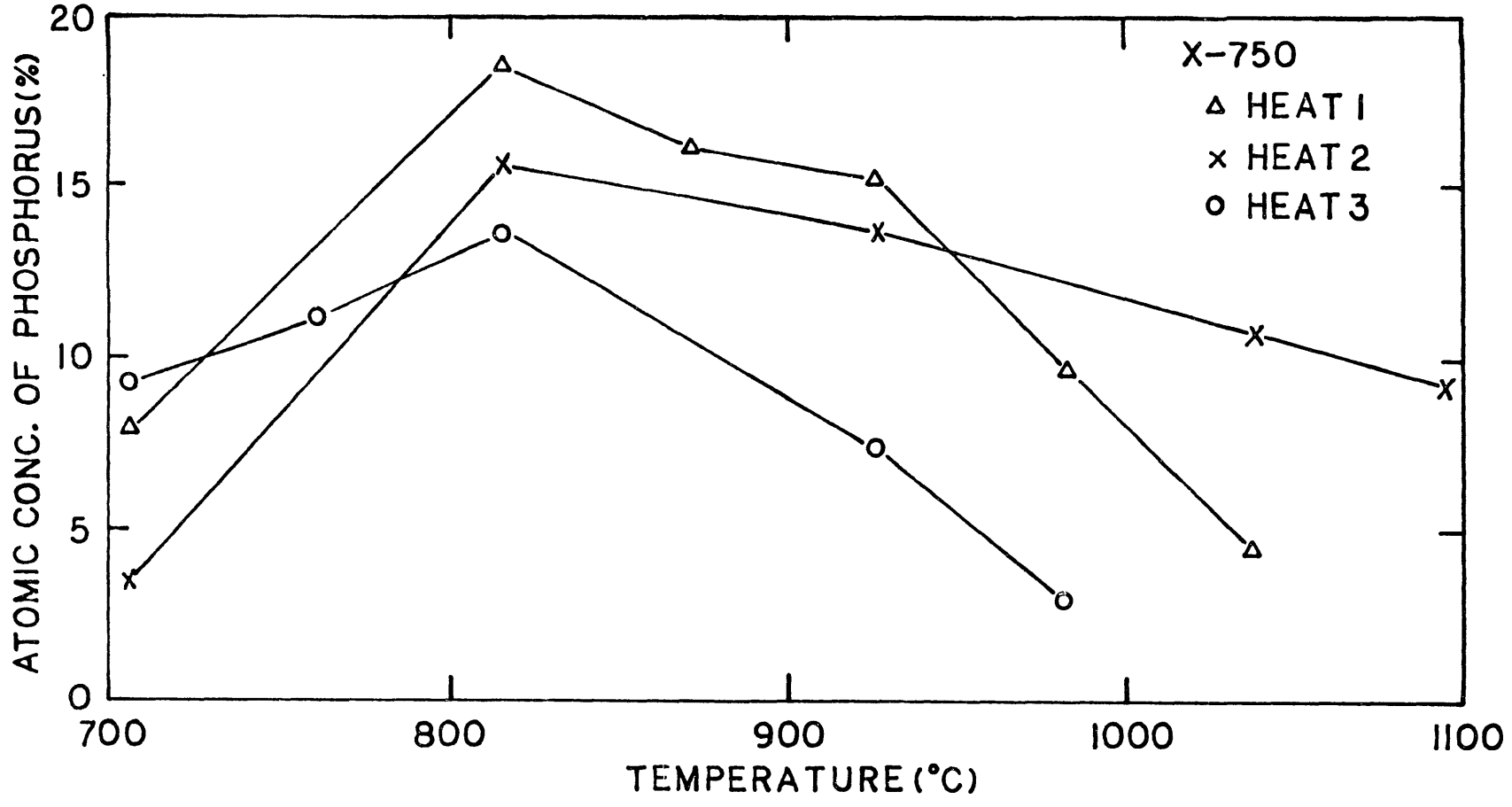

Figure 6.75 The Measured Concentration of Phosphorus on the Free Surfaces as a Function of Temperature [36].

condition compared with HTH condition. Hence use of the material allow to examine any significant difference in segregation data due to variation in analysis technique between laboratories. Each of BH and HTH conditions show peak values of phosphorus concentration higher than the corresponding condition of heat 964576E, as shown in Figure 6.72. The maximum value of free energy of segregation in heat 90330 is higher than the maximum value of heat 96457E6. The number of data was however limited by amount of available material and it was difficult to find any significant difference between BH and HTH.

The concentrations of boron measured with the S/N equal to or greater than three are summarized for heat 96457E6 and the remelt X-750, in Figures 6.76 and 6.77, respectively. In both heats the temperture dependence of boron segregation is not as evident as in the case of phosphorus. The HOA and HTH conditions show more segregations than the BH condition. No data out of three spots examined for each condition of AH and AHTH was obtained with the required S/N ratio criterion. The concentration of boron is, on the average, much higher than the phosphorus concentration.

The relation between the two major segregants are examined also for the case of alloy X-750. Figure 6.78 was obtained using all of the data satisfying the S/N ratio criterion either for phosphorus or for boron. A small number of cases where the boron concentration was not measured could not be included. The results for the four heats of alloy X-750 show as a whole show a negative correlation between phosphorus and boron concentration. This negative correlation is more convincing within heat 96457E6.

By comparing heat 96457E6 with heat 90330, it is observed that the latter has a higher average concentration of phosphorus and a lower average concentration of boron than the former. Since both heats have the same bulk concentration of phosphorus, the higher phosphorus segregation in heat 90330 can be attributed to the lower boron segregation. Since a comparison of the remelt heats with 96457E6 reveals that the boron segregation increases with the bulk concentration

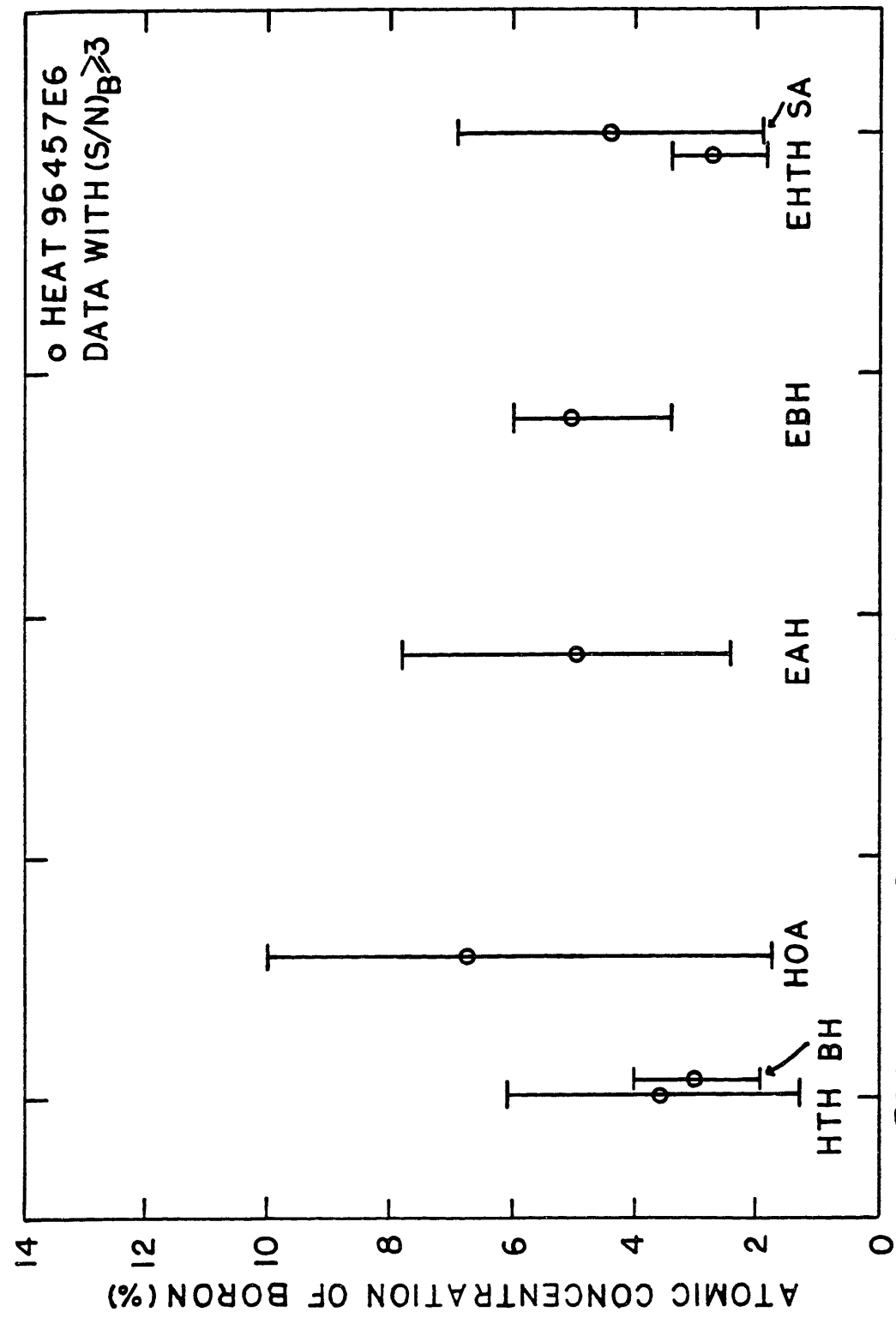

Figure 6.76 The Measured Boron Concentration on the AES Specimen of Alloy X-750 Heat 96457E6 as a Function of Final Process Temperatures.

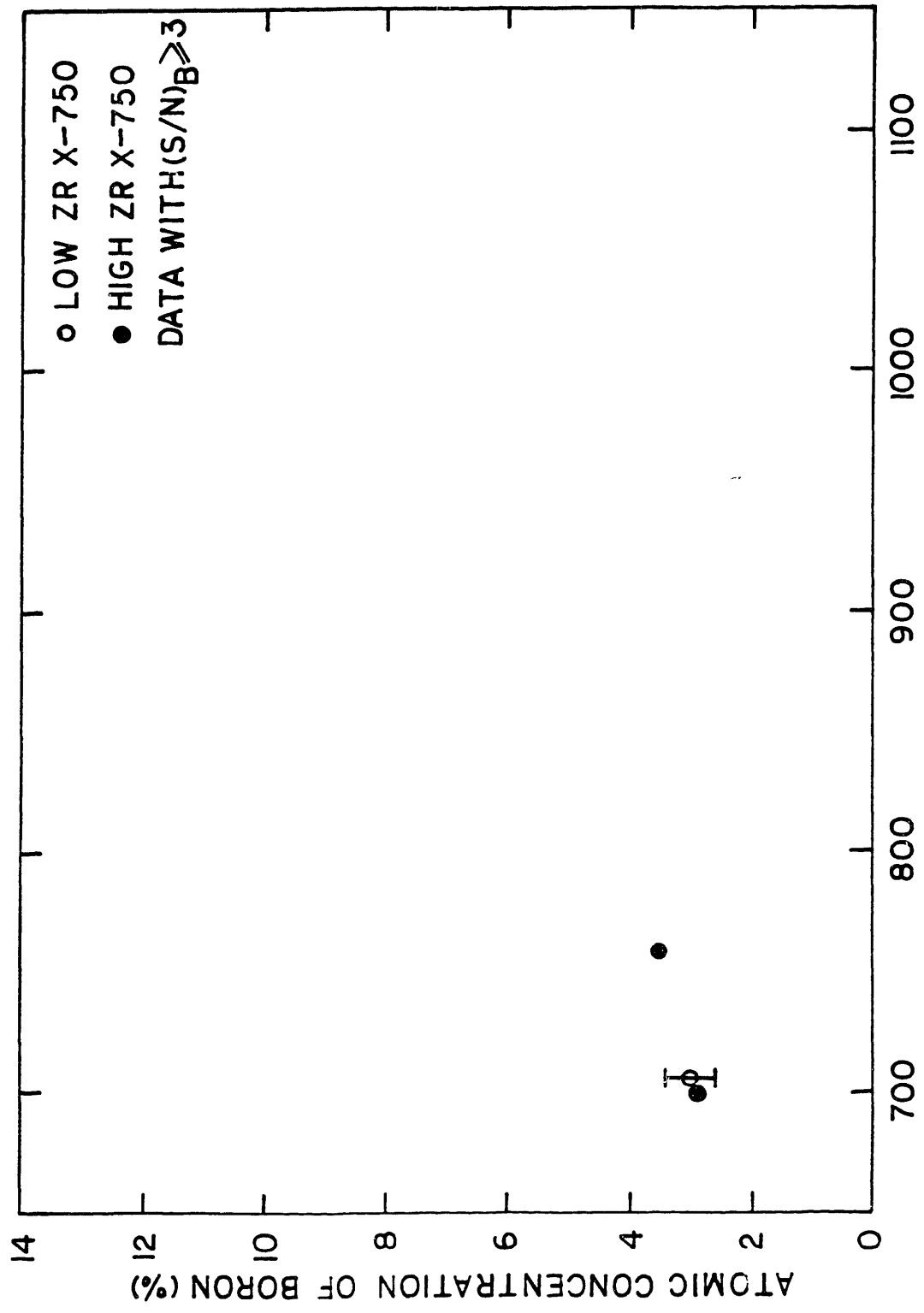

Figure 6.77 The Measured Boron Concentration on the AES Specimens of Remelt X-750 as a Function of Final Process Temperature.

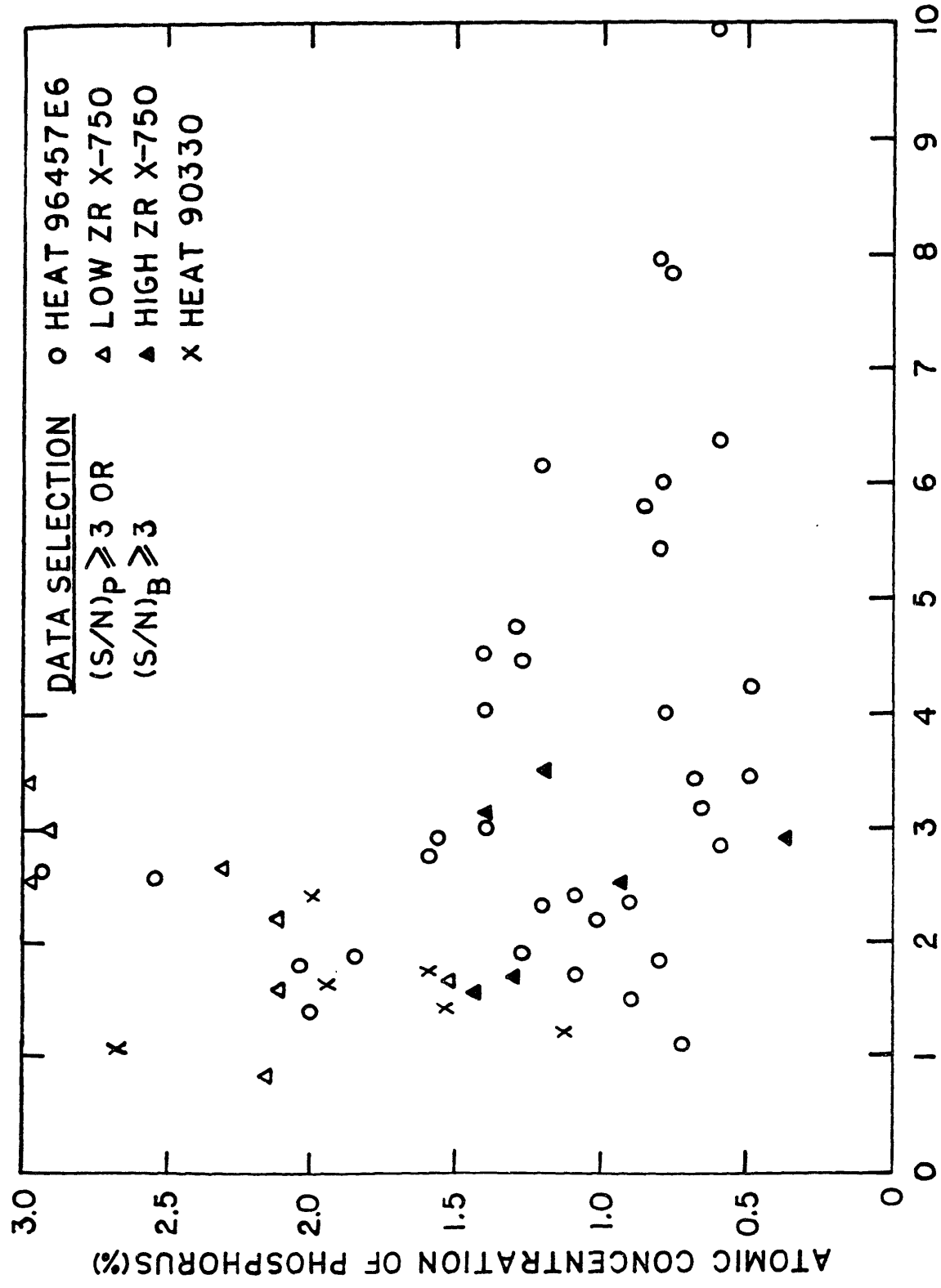

Figure 6.78 The Relation Between the Measured Concentration of Phosphorus and Boron in Alloy X-750.

the bulk concentration of boron in heat 90330 is lower than that of heat 96457E6. The explanation appears reasonable cosidering that the heat 96457E6 contains an unusually high amount of boron. As stated already, it was not possible to dicern any significant difference in phosphorus segregation between BH and HTH conditions of heat 90330. Due to small difference between the two conditions, it would be necessary to perform statistically significant number of analysis to draw any conclusion as to the effect of variation between laboratories. Due to limited amount of material such an extensive work could not be made.

6.1.4 Summary

Microstructures of five heats of alloy 600 tubing were characterized by using the two-step etch technique, STEM and AES as well as intergranular corrosion (Huey) tests. The heat-to-heat variation in the grain boundary chemistry and precipitate distributions as well as the grain sizes were determined. The heats examined have ranges of carbon contents and the final anneal temperatures which envelop most heats in practical applications.

The two-step etch technique revealed the extent of inter-and intragranular carbide distributions as well as grain boundaries. The morphology of intergranular carbide, known as Cr_7C_3, was described by three classes including discrete, semicontinous and continuous. In order for a quantitative description two new variables were defined. The results of the microstructural characterization summarized in Table 6.1.

The HTMA process produced more intergranular carbide at the expense of intragranular carbides in coarse grained microstructures. The opposite charateristics are observed with the LTMA conditions. The HTMA condition of NX2650 showed, however,a typical LTMA microstructure. This is because the final anneal metal temperature for NX2650 was close to that of typical LTMA conditions. The results suggests that a large uncertainty in the microstucture is possible unless true metal temperature is monitored and used in process control.

Table 6.1.

Summary of Two-step Etch Metallography of Alloy 600 Tubings

Material	C(wt %) Content	C(wt %) Solubility*	Grain Size (μm)	G.B.Carbide Morphology	$f_{G.B.}$	f_M
NX1638(2.2cm)	0.014					
HTMA		0.037	32	Discrete	0.7	0
TT			32	Continuous	1.0	0
NX2650(2.2cm)	0.038					
HTMA		0.037	16	Discrete	0.1	2.6
TT			16	Semi-continuous	0.9	2.8
SAS			55	Continuous	1.0	0
96834(2.2cm)	0.039					
HTMA		0.037	38	Semi-continuous	0.9	0.3
LTMA		0.018	10	Sparse	0	3.6
96834(1.9cm)	0.039					
HTMA		0.037	35	Semi-continuous	0.8	0.3
LTMA		0.018	10	Sparse	0	3.6
763675(1.9cm)	0.020					
HTMA		0.037	32	Discrete	0.2	0
LTMA		0.018	11	Sparse	0	1.8
NX3857(1.9cm)	0.025					
HTMA		0.037	45	Discrete	0.3	0
LTMA		0.018	13	Sparse	0	2.0

NOTE: * Based on Scarberry's Data [19] at the final anneal temperature.

Microchemical analysis results by the STEM are summarized in Table 6.2 and compared with the results of intergranular corrosion (Huey) tests. All conditions have chromium concentrations which are high enough to reveal only marginal weight losses in the intergranular corrosion tests. Appreciable difference in the chromium concentration is found between the inner and outer diameter regions of each tubing. A lower cooling rate at the inner surface is attributed to more sensitization. The shape of chromium distribution is identical at both inner and outer diameter regions.

The microchemical analysis by STEM revealed significant vairaiton in the chromium distribution among the heats. The commerically produced heats NX1638 and NX2650 showed no significant chromium depletion at grain boundaries. The specially produced heats were observed to be depleted of chromium depending on the annealing temperature and the tubing size. For larger diameter tubing (2.2cm), significant depletion occurred in the HTMA conditon while little depletion was found in the LTMA counterpart. Exactly opposite results were obtained with a smaller diameter tubing (1.9cm), as shown in Table 6.2. In the latter cases, narrow chromium peaks were observed at grain boundaries of the HTMA conditons indicating that carbide films are present. This suggests that the microstructures have been desensitized upon the HTMA process.

By comparing chromium distributions among different heats, two patterns are observed. The first pattern is found with heats 96834 with 2.2cm tubing diameter and NX3857 with 1.9cm diameter which have measurable amount of chromium depletion in the HTMA conditions while only slight depletions are shown in the LTMA condition. The second pattern involves heats 96834 with 1.9cm diameter and 763675 with 1.9cm diameter which show replensihed chromium distribution in the HTMA condition while measurable chromium depletions are observed in the LTMA conditons. Both patterns can be explained based on the fact that the time at temperature for carbide precipitation is much longer with the HTMA process. The HTMA heat NX2650 can be described by the first LTMA pattern in agreement with optical metallographic observations. The actual metal annealing

Table 6.2

Summary of STEM Analysis on Chromium Distribution at Grain Boundaries of Alloy 600 Tubings.

Material	$(Cr)^{I.D.}_{G.B.}$ (wt %)	$(Cr)_{MATRIX}$ (wt %)	Cr Distribution I.D.	Cr Distribution O.D.	Huey Test (mg/cm^2 day)
NX1638					
HTMA	11.6	15.6	Depleted	*	0.35
TT	*	*	*	*	0.36
NX2650					
HTMA	14.9	16.1	S.D.**	*	0.30
TT	*	*	*	*	0.52
96834(2.2cm)					
HTMA	11.8	17.0	Depleted	Depleted	0.14***
LTMA	14.6	16.9	S.D.	S.D.	0.14***
96834(1.9cm)					
HTMA	17.3	14.9	Replenished	*	0.26***
LTMA	11.5	15.8	Depleted	Depleted	0.12***
763675(1.9cm)					
HTMA	18.8	18.0	Replenished	Uniform	0.09***
LTMA	14.6	17.6	Depleted	*	0.11***
NX3857(1.9cm)					
HTMA	11.6	16.0	Depleted	*	0.11***
LTMA	14.6	15.0	S.D.	S.D.	0.25***

NOTE: * Not measured.
** Slightly Depleted (S.D.)
*** From Ref. 21.

temperature of the heat is expected to be close to that of LTMA. Hence it is suggested to use metal temperature instead of furnace temperature for a more consistent control of both carbide distribution and grain boundary chemistries.

The AES studies on alloy 600 tubings showed that phsophorus and boron segregate to grain boundaries while sulphur and zirconium do not segregate in any detectable amount. The phosphorus concentration is observed to follow a McLean-type equilibrium model with relatively constant values for the free energy of segregation between 700 C and 1100 C. A free energy of 58 ± 2 kJ/mole is found to agree well with ealier studies by Guttmann et al. [32] and Was et al. [34] for temperature between 700C and 1100C. Significant segregation is observed with the TT condition. The present data on the fre energy of phosphorus segregation in the TT condition lies in the middle between the two reported data. A negative correlation was observed between the phosphorus and boron concentration at grain boundaries. This supports the site competition mechanism may be operating in the segregation process.

Optical metallography on alloy X-750 heat 96457E6 was done using Kalling's reagent. The general microstructural chracteristics such as grain sizes and the extent of intergranular precipitates could be determined, as summarized in Table 6.3 Optical metallographs for all the heat treated conditions agree well with earlier works on comparable and the same heats. The distribution of fine precipitate determined by previous works is assumed to be applicable to the present conditions.

Grain boundary phases in the AH condition X-750 plate were identified by TEM in addition to the optical characterization. Primarily γ' and $Cr_{23}C_6$ were present in close proximity. Due to slightly larger grains (30μm), and the presence of $Cr_{23}C_6$ in a significant amount, the AH conditon of the X-750 plate was considered to be an intermediate microstructure between the AH and AHTH of X-750 heat 96457E6.

Table 6.3

Summary of Microstructural Characterization on Alloys X-750 and 718

Material	Grain Size (μm)	G.B. Precipitate Primary	G.B. Precipitate Secondary	Chromium Depletion
X-750(96457E6)				
AR	10	$Cr_{23}C_6$	γ'	none
AH	10	γ'	(Ti,Nb)C,n	none
BH	10 or 100	$Cr_{23}C_6$	γ'	appreciable
HTH	70	$Cr_{23}C_6$	γ'	significant
HOA	90	$Cr_{23}C_6$,γ'	-	none
AHTH	90	γ',$Cr_{23}C_6$	-	none
X-750(Plate)				
AH	30	γ',$Cr_{23}C_6$	-	none
718				
CHT	15	Laves, MC	$Cr_{23}C_6$	-
DA	15	MC, Laves	$Cr_{23}C_6$	-

A detailed study was made on the intergranular segregation of trace elements including P,B,S and Zr on alloy X-750. As with the case of alloy 600, sulphur and zirconium concentrationswere below the detectability limtis of the AES system. Phosphorus segregation in alloy X-750 is found not to follow the McLean type equilibrium behavior; the phosphorus segregation increased with decreasing temperature between 1121 C and 885 while no further segregation was evident with aging at 704 C for 20 hours or at 760 C for 100 hours. The results agree with free surface segregation study on X-750[36]. Hence, it is suggested that precipitation of intragranular γ' may have trapped the phosphorus and thus prevented further segregation. A supporting evidence was obtained by observing systematically increased segregation upon the final aging when the specimens were allowed to precipitate much of γ' by a prolonged treatment at 885 C.

Although phosphorus segregation was correlated with the presence of fine γ', there was no significant difference in the measured phosphorus concentration among the AH, BH, HTH, HOA, and AHTH conditions of X-750 heat 96457E6. Considerable heat-to-heat variation was explained by the different bulk concentration of the segregants. On a statistical basis there was a negative correlation between the phosphorus and boron concentrations at grain boundaries. This suggests that site competition may play an important role. The heat with low zirconium content showed slightly higher segregation of phosphorus although zirconium was not detected in any condition.

Optical metallography on the CHT and DA conditions of alloy 718 showed the presence of Laves phase on the grain boundaries. An extensive precipitation of the Laves phase was observed in the CHT condition while only minimal precipitation occurred in the DA conditioon.

6.2 ELECTROCHEMICAL CHARACTERISTICS

6.2.1 Potentiodynamic Polarization Behaviors

Potentiodynamic Polarization Behaviors of Alloy 600

Potentiodynamic polarization measurements were done for alloy 600 tubing to examine microstructural dependences. In the HTMA conditions, there was no appreciable difference between NX1638 and NX2650 with respect to the corrosion potential, the passivation current density and transpassive behavior, as shown in Figure 6.79 A factor of two difference in the peak current density is considered to be within experimental error due to the specimen surface condition before the experiment and the oxygen concentration in the solution. Hence, the electrochemical behavior of both heats are identical in the solution of 0.05M sodium sulphate adjusted to pH 3 at 25°C.

In Figure 6.80, the polarization behaviors of the three conditons of heat NX2650 are compared at 25°C. All three conditions show approximately the same corrosion potential and the peak current density. The the active-passive transition occurs between 0.2V and 0.3V (SHE) for all the conditions. Both HTMA and SAS conditions exhibit almost identical behavior for the entire range of potentials. The specimen surface of the SAS condition after the experiment shows clear grain boundary etches which is not observed in the HTMA condition. This indicates a significantly a higher dissolution of the grain boundary regions in the SAS condition. However, such a microscopic characteristics is not revealed in the polarization curve which represent an average value for the entire specimen surface.

The TT condition of NX2650 shows no distinct active-passive transition at 93C, as shown in Figure 6.81. Its corrosion potential and corrosion current density consistently indicate a more active behavior. The passivation current density is about 6 times higher than other two conditions. The examination of specimen surface after the polarizaiton revealed a yellow film which was cracked into arrays of about 2μm by 2μm square elements. Such film cracking was not observed with other specimens. Since all polarization measurements of alloy 600 tubing were done with the same batch of solution, it is difficult to attribute the significant difference to the typical due to solution contamination problem. Therefore, the TT condition appears to form quite a differnt

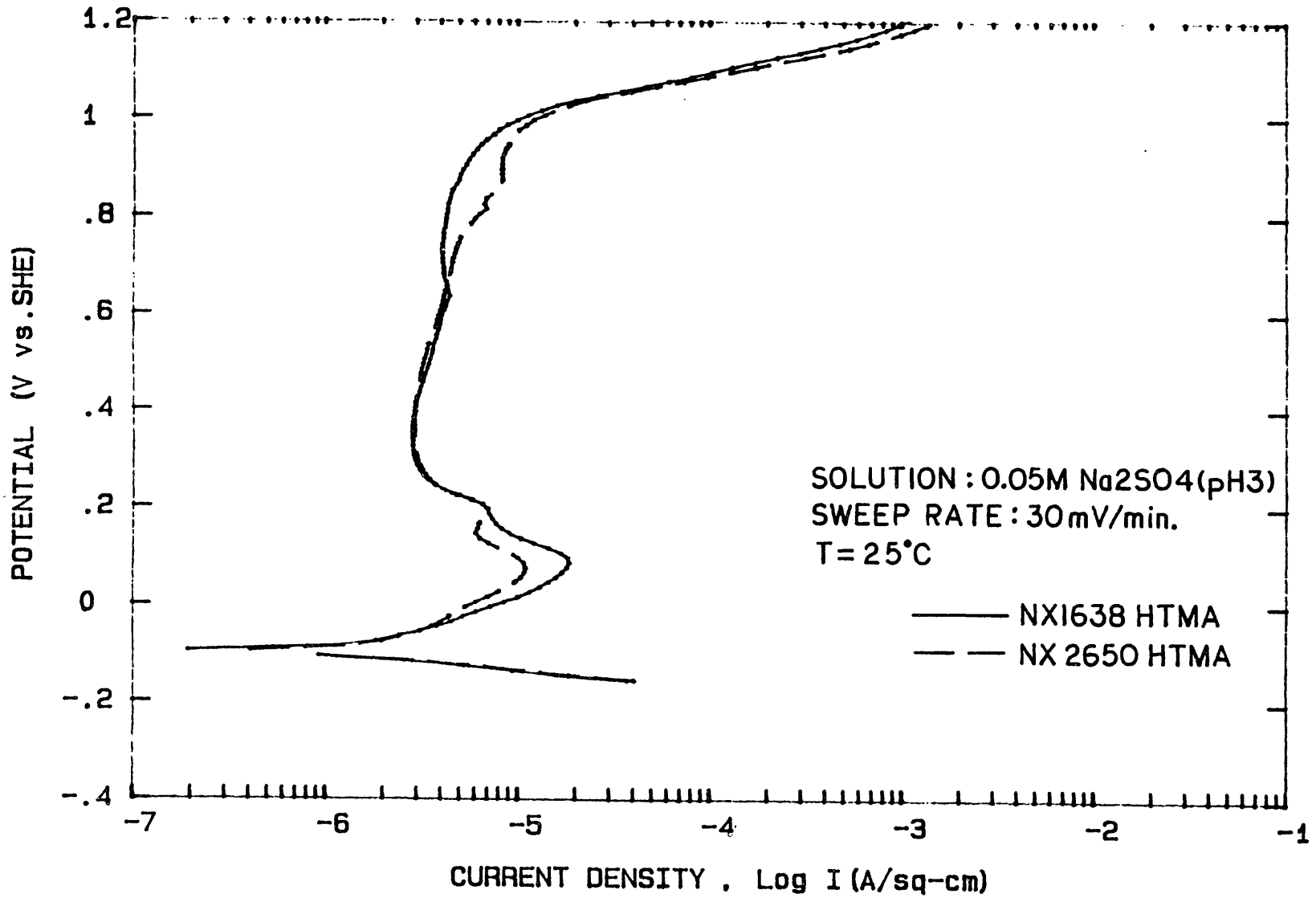

Figure 6.79 Potentiodynamic Polarization Diagrams for the HTMA heats NX1638 and NX2650 in 0.05M Na_2SO_4 (pH=3) Solution at 25 C.

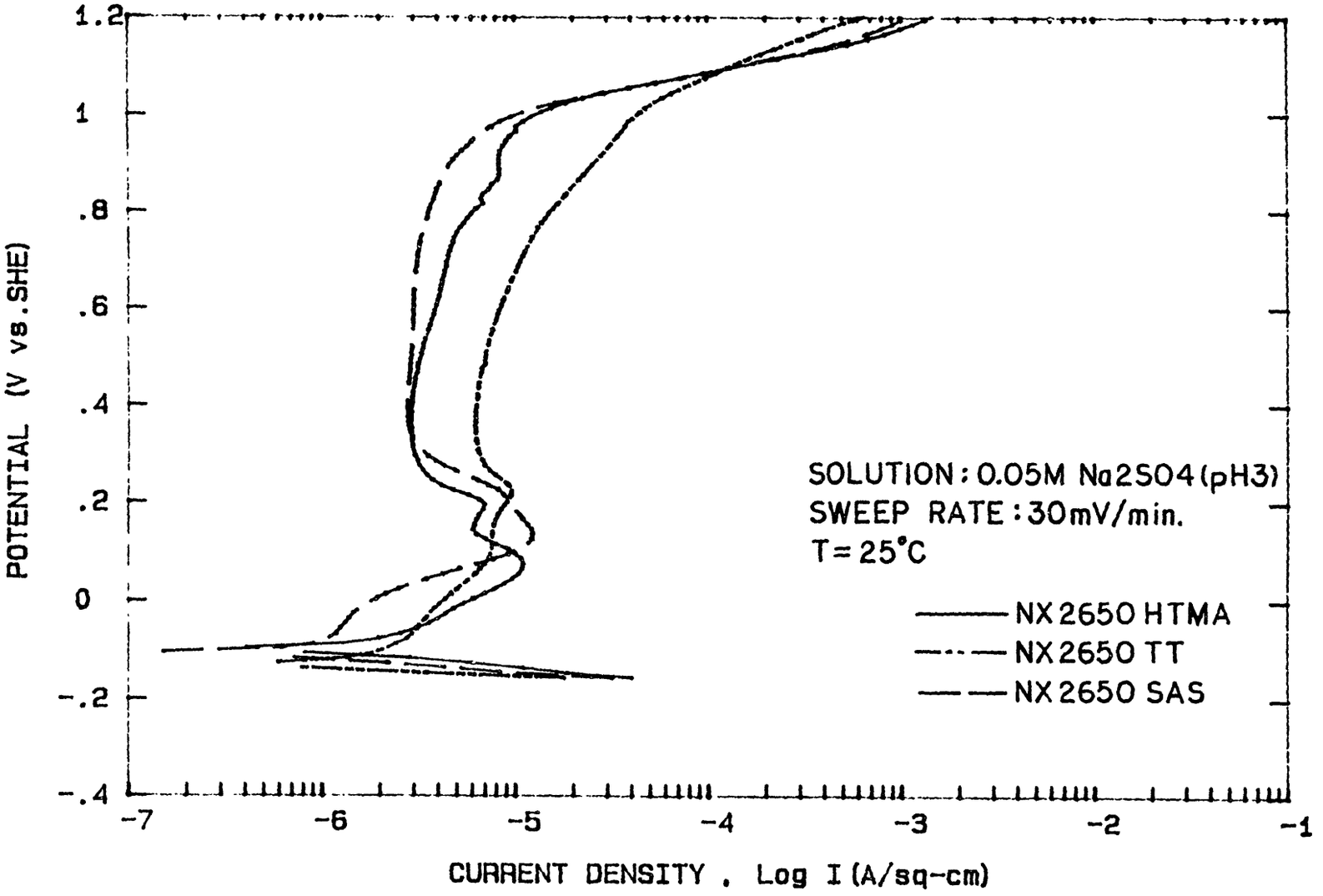

Figure 6.80 Potentiodynamic Polarization Diagram for the TT and SAS Conditions in Comparison with the HTMA in case of Heat NX2650 in 0.05M Na_2SO_4(pH=3) Solution at 25 C.

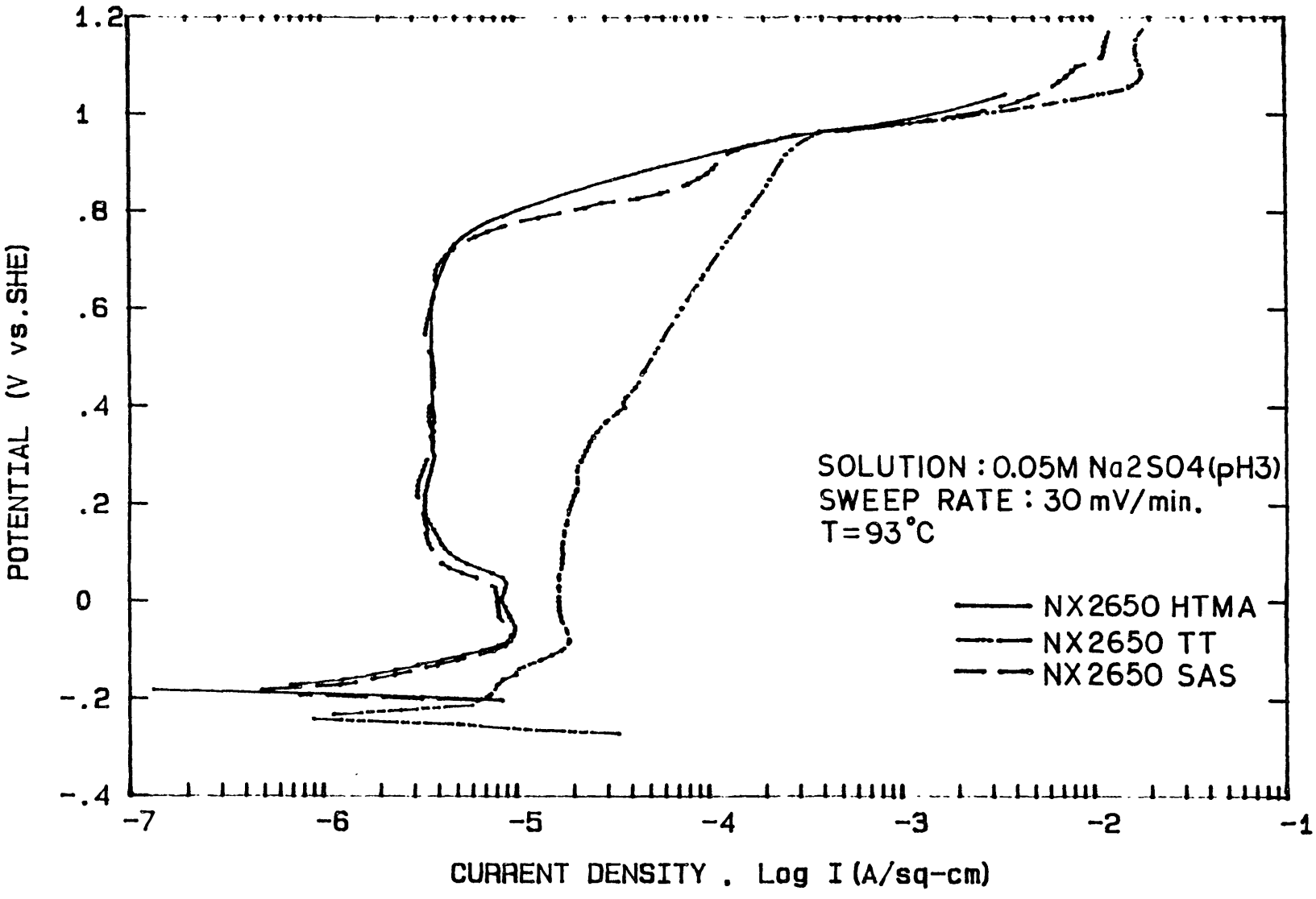

Figure 6.81 Potentiodynamic Polarization Diagram for the TT and SAS Conditions in Comparison with the HTMA Condition of Heat NX2650 in 0.05M Na_2SO_4(pH=3) Solution at 93 C.

type of film which is less protective due to the cracking. Electrochemical parameters measured from the anodic polarization curves are summarized in Table 6.4.

Potentiodynamic Polarization of Alloy X-750

An extensive electrochemical study was made by Hosoya et al. [57] on the alloy X-750 and its representative phases such as γ' and chromium depleted chemistries. The same material and the solution were used in this work for a more detiled characterizaiton. this includes potentiodynamic polarization experiments for electrochemical parametrization and the potential jump tests to describe the passivation kinetics.

Polarization results over 150mV of overpotential in each direction are shown in Figure 6.82. The corrosion potentials are measured each time before the cathodic polarizaiton and the anodic polarization. The values are consistent within 4 mV except for the case of Ni_3Al (T=0.15) where an 11 mV difference is obtained. The anodic and cathodic Tafel slopes were determined by tangent lines intersecting the corrosiuon current and potentials which are determined by the measured Tafel slope in the other side. The hydrogen exchange current densities were also determined by extrapolating the cathodic Tafel lines to 0 V(SHE).

The results are summarized in Table 6.4. The measured corrosion potentials agree well with the previous results by Hosoya et al [57] except for #5051 alloy. The present data are considered to provide a consistent basis since all measurement are made with the same batch of solution. The chromium depleted chemistry shows about 30 mV lower corrosion potential and several times higher peak aondic current density compared with the solution annealed X-750. The γ' chemistries have a range of electrochemical behaviors which depend strongly on the titanium content. With no titanium, the corrosion potential is about 80 mV lower with a 10 times higher current density whereas a γ' with 15 at % titanium shows only a small activity compared with the solution annealed

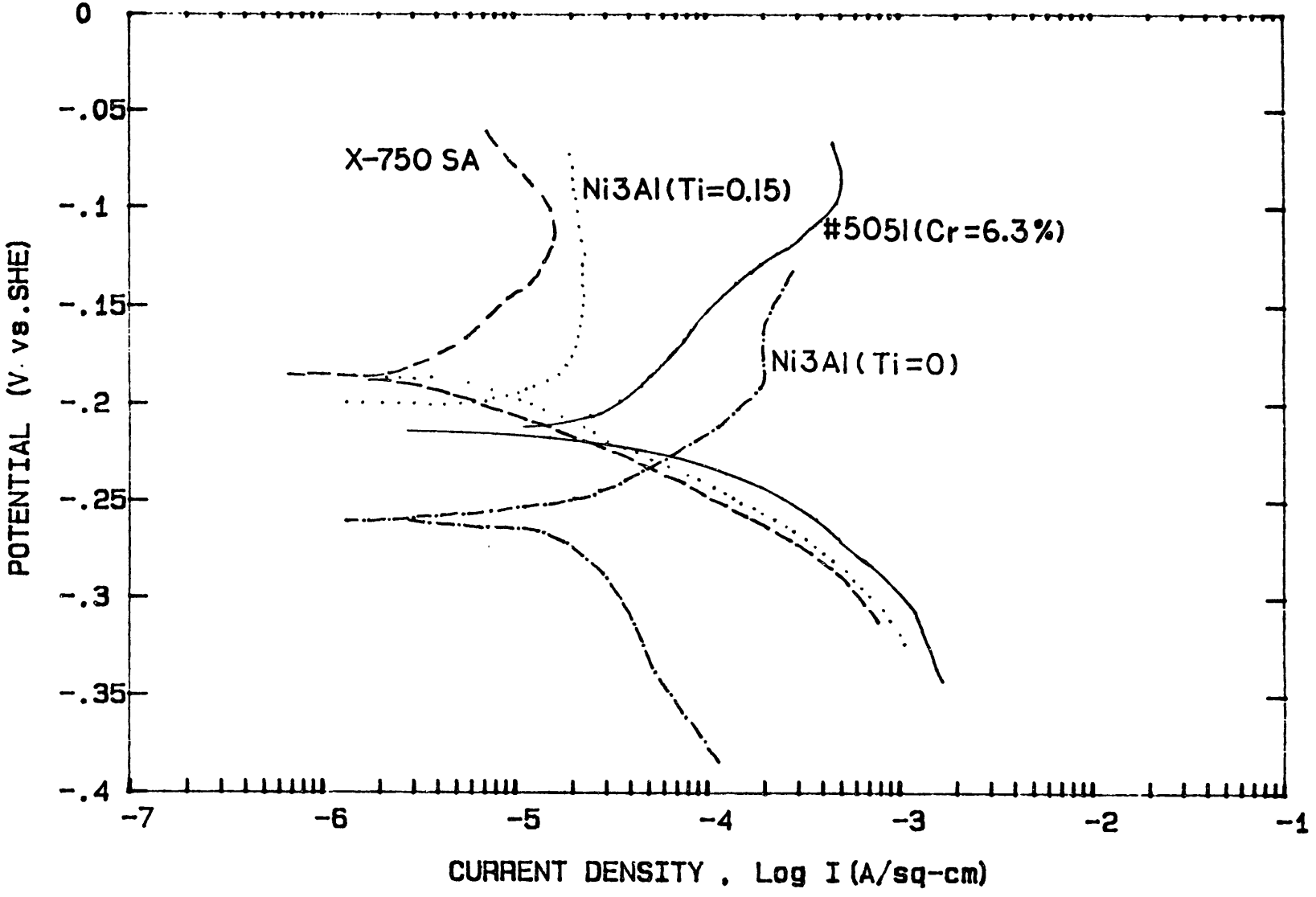

Figure 6.82 Potentiodynamic Polarization of Alloy X-750 and Representative Grain Boundary Chemistries in 0.05M Na_2SO_4 Solution (pH=3) at 93 C.

Table 6.4

Electrochemical Parameters
of Representative Chemistries for Nickel-base Alloys
in 0.05M Na_2SO_4 (pH 3) Solution Measured at 93 C

Material	E_{corr} (mV SHE)	i_{corr} (A/cm^2)	β(V/decade) Cathodic	β(V/decade) Anodic	$i_o H^+/H$ (A/cm^2)
Alloy 600(HTMA)	-182	1.0×10^{-6}	*	0.083	*
Alloy 600 (TT)	-230	4.5×10^{-6}	*	0.190	*
Alloy 600 (SAS)	-185	1.2×10^{-6}	*	0.092	*
X-750 (SA)	-186	2.9×10^{-6}	-0.043	0.089	1.5×10^{-10}
5051(Cr=6.3wt%)	-212	3.9×10^{-5}	-0.050	0.107	2.2×10^{-9}
Ni_3Al(Ti=0)	-262	2.4×10^{-5}	-0.084	0.047	1.7×10^{-8}
Ni_3Al(Ti=0.15)	-196	9.2×10^{-6}	-0.049	0.038	1.2×10^{-9}

NOTE: * Not measured.

X-750.

The estimated hydrogen exchange current density are two to three orders of magnitude lower than the values for pure nickel ($6.3 \times 10^{-6} A/cm^2$) and titanium ($6.3 \times 10^{-7} A/cm^2$). The alloys appear to have lower values compared with the pure elements which may be ,in part, attributed to a increased passivity. Except for the γ' with no titanium, all the material show passive regions which indicates possible effects of passive film forming during the slow polarization studies. In a real situation, however, bare surface exposed by fracture would be free from any such less conductive layer and hence may have much higher hydrogen exchange current density until the passive layer builds up. This limitaion of polarization experiment calls for characterization of rapid passivation transients to complement long term characterization.

6.2.2. Passivation Kinetics of Bare Metals

The kinetics of bare surface passivation were determined by the potential jump experiment. The results are shown in Figures 6.83 and 6.84. The Ni_3Al (Ti=0) shows a completely active behavior, as shown in Figure 6.83. Nearly the same behavior is observed with Ni_3Al (Co=0.1) as shown in Figure 6.84. All other materials show typical passivation kinetics which is characterized by a logarithmic rate of current decay. It is of concern that there may be a contribution of hydrogen oxidation and oxygen evolution reactions to the measured current density because the specimens were cathodically cleaned at a potential of -1.14 V(SHE) before jumping to -0.14 V(SHE). The contribution was measured experimentally by using a polished platinum anode. The measured current was found to amount to up to 50% for the cases of AH, HTH, and SA conditions of X-750. This effect is, however, negligible for all γ' specimens.

Long-term passivation transients revealed a number of noise spikes. These fluctuation in the current can be either purely noise or due to passivity breakdowns. There are two reasons which lead to the former

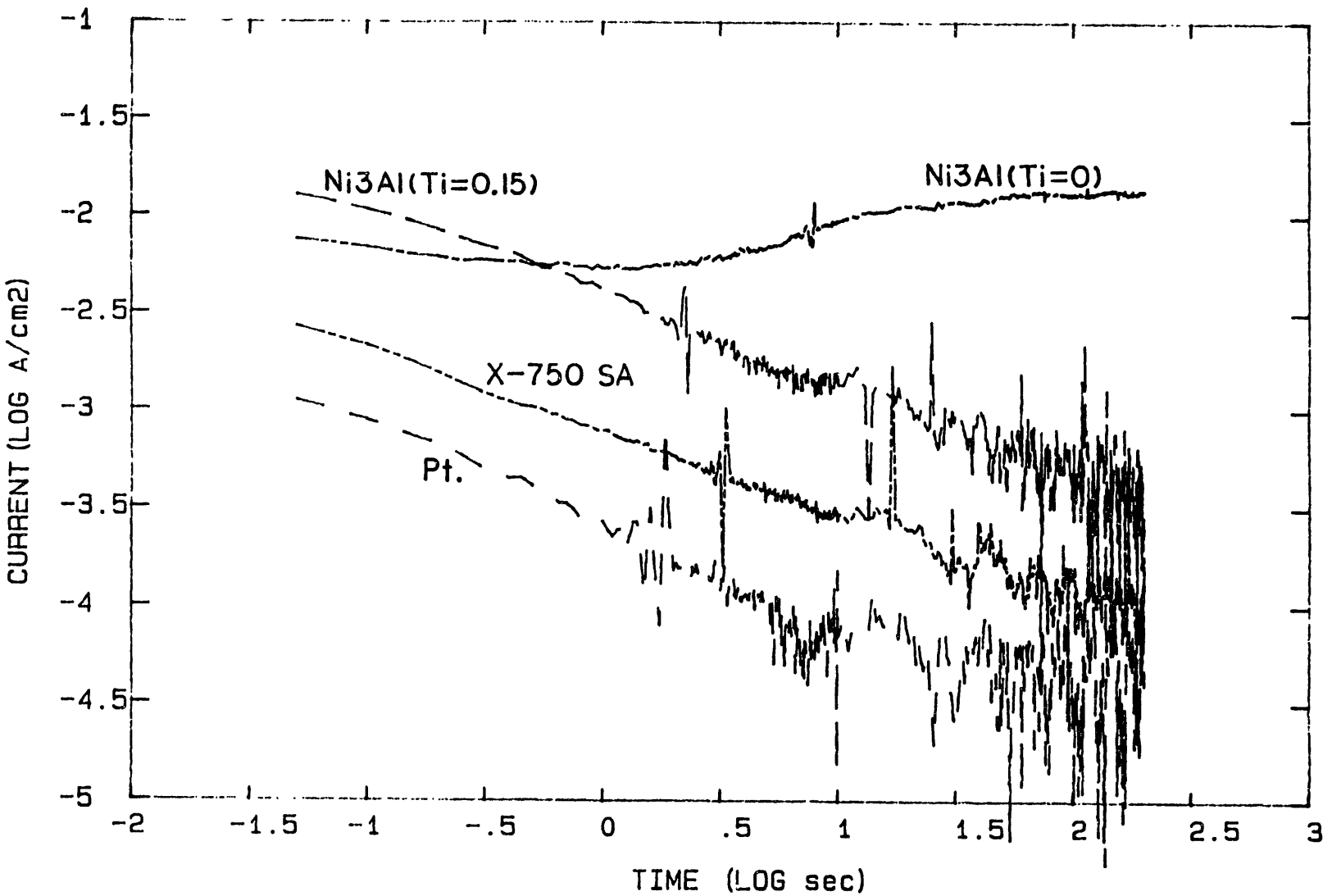

Figure 6.83 Passivation Kinetics of Alloy X-750(SA) and γ' Chemistries as Determined by the Potential Jump Experiments in 0.05M Na_2SO_4 (pH=3) Solution at 93 C.

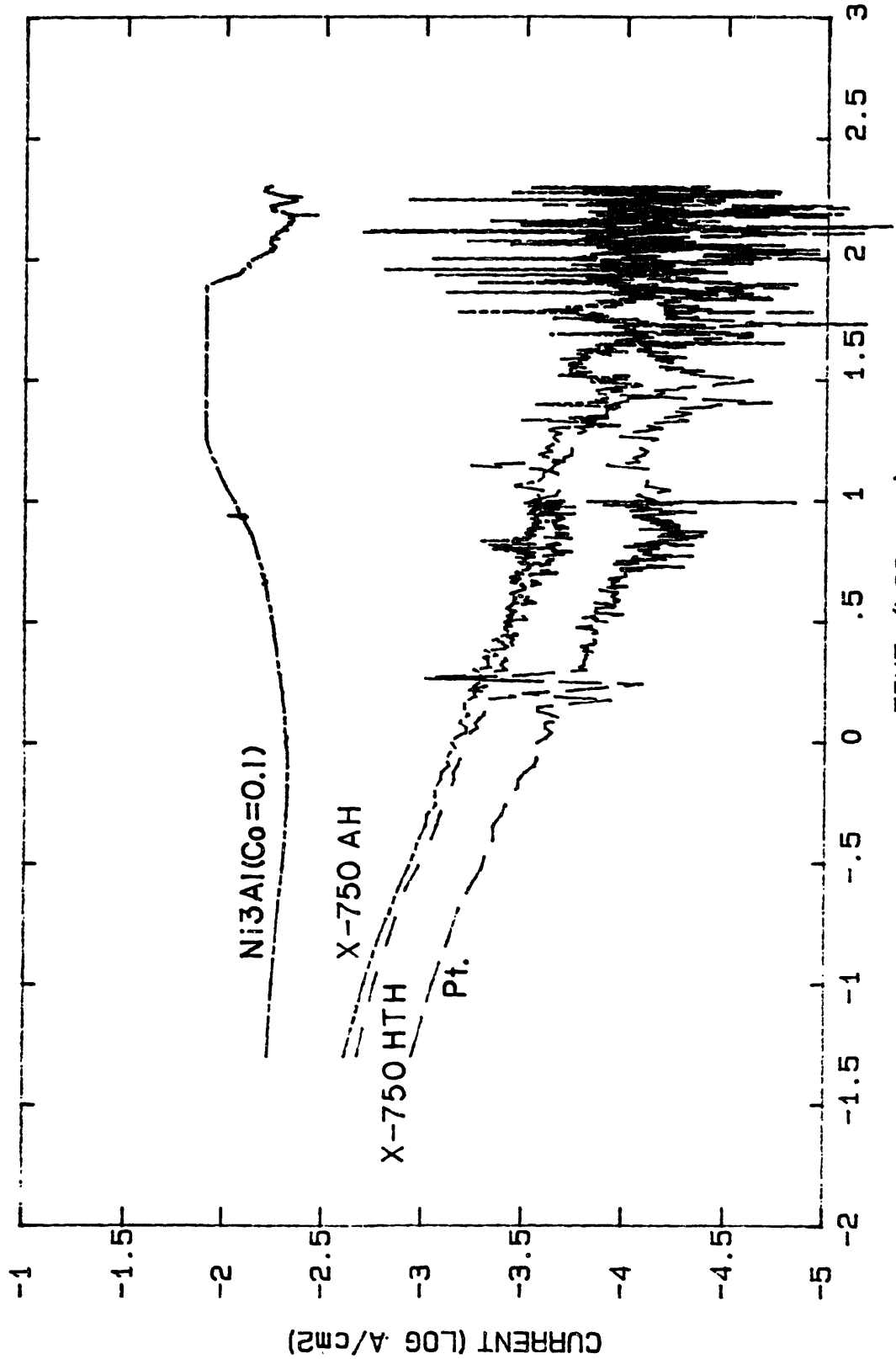

Figure 6.84 Passivation Kinetics of Heat Treated X-750 and a γ' Chemistry as Determined by the Potential Jump Experiments in 0.05M Na_2SO_4 (pH=3) Solution at 93 C.

explanation. The same spikes are observed with platinum specimen despite that its passive film is expected not to break down. Also the spike occurs in both directions from the mean values which is a characteristics of electronic noises in the system. Further confirming clues should be obtained to fully understand the behavior.

The passivation transients are divided into an early activation control period and a later ($t \geq 10$ msec) diffusion control period. Constant current densities are expected during the first period which is not revealed by this study. The curves fit to the best lines for the second period are described by a kinetic equation as follows:

$$i = C_1 \cdot (t^{C_2})$$

where i is the current density in A/cm^2, t is time in seconds. Constants, C_1 and C_2, are measured graphically and summarized in Table 6.5. The constant C_1 for AH, HTH, and SA of X-750 are divided by a factor of two to take into account the effect of the hydrogen oxidation and the oxygen evolution reaction. The exponent, C_2 is found to be close to -0.5. Hence parabolic kinetics may be applied to describe the passivation kinetics. It is assumed that the reaction rate is determined by the water diffusion in the film layer. Then,

$$i = \frac{\Delta E}{R} = \frac{\Delta E}{C\sqrt{t}} = i_a \, (t/t_a)^{0.5} \qquad (6\text{-}3)$$

where ΔE is the imposed overpotential, i_a is activation controlled current density during initial period t_a, and C is a constant.

The peak current densities measured by the polarization study [57] are compared with the potential jump experiment results. The Ni_3Al (T=0) and Ni_3Al (Co=0.1) cases agree well with the peak current density in the polarization. In other cases, however, the peak current densities measured by polarization represent current density values after a considerable period passivation time. The passivation time (t_p) to

Table 6.5

Parameters of the passivation kinetics
for Alloy X-750 in 0.05M Na_2SO_4(pH 3) Solution at 93 C

Material	C_1(A/cm^2)	C_2	i_p(A/cm^2)*	t_p(sec)
X-750 SA	4.0×10^{-4}	-0.40	4.0×10^{-5}	320
Ni_3Al(Ti=0)	6.9×10^{-3}	-0.07	1.0×10^{-2}	0
Ni_3Al(Co=0.1)	5.6×10^{-3}	0	1.0×10^{-2}	0
Ni_3Al(Ti=0.15)	3.9×10^{-3}	-0.43	2.2×10^{-4}	80
X-750 AH	3.3×10^{-4}	-0.47	4.0×10^{-5}	89
X-750 HTH	2.8×10^{-4}	-0.47	4.2×10^{-5}	57

arrive at the peak current density is calculated to be about 100 seconds. This agrees well with the time to reach the potential of -0.14 V(SHE) from the corrosion potentials during the polarization experiment at a sweep rate of 0.5 mV/sec. The calculated time (t_p) to the peak current density (i_p) is listed in Table 6.5.

There is good reason to examine the passivation behavior during the short time period before reaching the peak current densities measured by the polarization method. The time scale of importance in the crack growth process at this low temperature is about one second because the crack growth rate is shown to increase rapidly above a frequency of 1 Hz during the fatigue loading [23]. The current density of Ni_3Al (Ti=0.15) is observed to be as high as that of Ni_3Al (T=0) during the first one second. Therefore it is necessary to use Ni_3Al (T=0) instead of Ni_3Al (T=0.15) in the experiment where the behavior of the latter is to be examined for an extended period. Otherwise, the anodic dissolution of Ni_3Al (Ti=0.15) would be grossly underestimated. There is another benefit from using such active material since the mixed potential theory, useful for galvanic characterization, is valid only for non-passivation anode system, as discussed in detail in the next section.

6.2.3 Galvanic Corrosion

The results in the previous sections imply that active intergranular constituents such as γ' and chromium depleted regions can set up a microscopic galvanic cell with the surrounding matrix. The significance of such a galvanic coupling may be estimated by applying the mixed potential theory based on the electrochemical parameters listed in Table 6.4.

In alloy 600 and the HTH condition of X-750 the representative constituents of a grain boundary region are the chromium depleted chemistry and carbides as well as surrounding matrix. Effect of

galvanic coupling between the chromium depleted region and the matrix is examined. The data for #5051 (Cr = 6.3 wt%) is employed to represent a severely sensitized condition and the solution annealed X-750 is considered to describe the matrix of both alloy 600 and X-750. The mixed potential theory is applied to determine the galvanic current density, as shown in Figure 6.85. Due to a small difference in the corrosion potentials, the corrosion current of a galvanic couple is almost the same as that of #5051 with a value of about 4×10^{-5} A/cm^2. The intergranular dissolution rate in SAS condition of alloy 600 may be described by this value. For most conditions of practical interest, the chromium concentration is at least 12% at the grain boundary. Therefore, the realistic galvanic current density may be significantly lower than the above value for SAS condition. No materials were available for the elctrochemical characterzation of the intergranular carbides such as M_7C_3 and $M_{23}C_6$. Hence a more realistic situation involving carbides, chromium depleted regions and matrix could not be examined in this work.

For the AH condition of X-750 a significant amount of intergranular γ' is in contact with the solution annealed matrix. Figure 6.86 shows the application of mixed potential theory to describe the situation of grain boundary corrosion based on the data of Ni_3Al (Ti=0). The predicted current density is about 6.5×10^{-5} A/cm^2. The galvanic coupling results in an increase in the current density from the corrosion current of Ni_3Al (Ti=0) by about a factor of three. This result with Ni_3Al(Ti=0) is a valid approximation for the case of Ni_3Al(Ti=0.15) during the first second after the exposure of fresh surface by fracture, as discussd earlier.

The predicted galvanic current between Ni_3Al (Ti=0) and the X-750 SA has been experimentally verified with an equal area(1cm^2) of specimens in a pH 3 solution of 0.05M sodium sulphate at 93°C, as shown in Figure 6.87. During the period A, the galvanic current decreases slowly from an initial value of 7.0×10^{-5} A/cm^2 to a stable value of 4.5×10^{-6} A/cm^2.

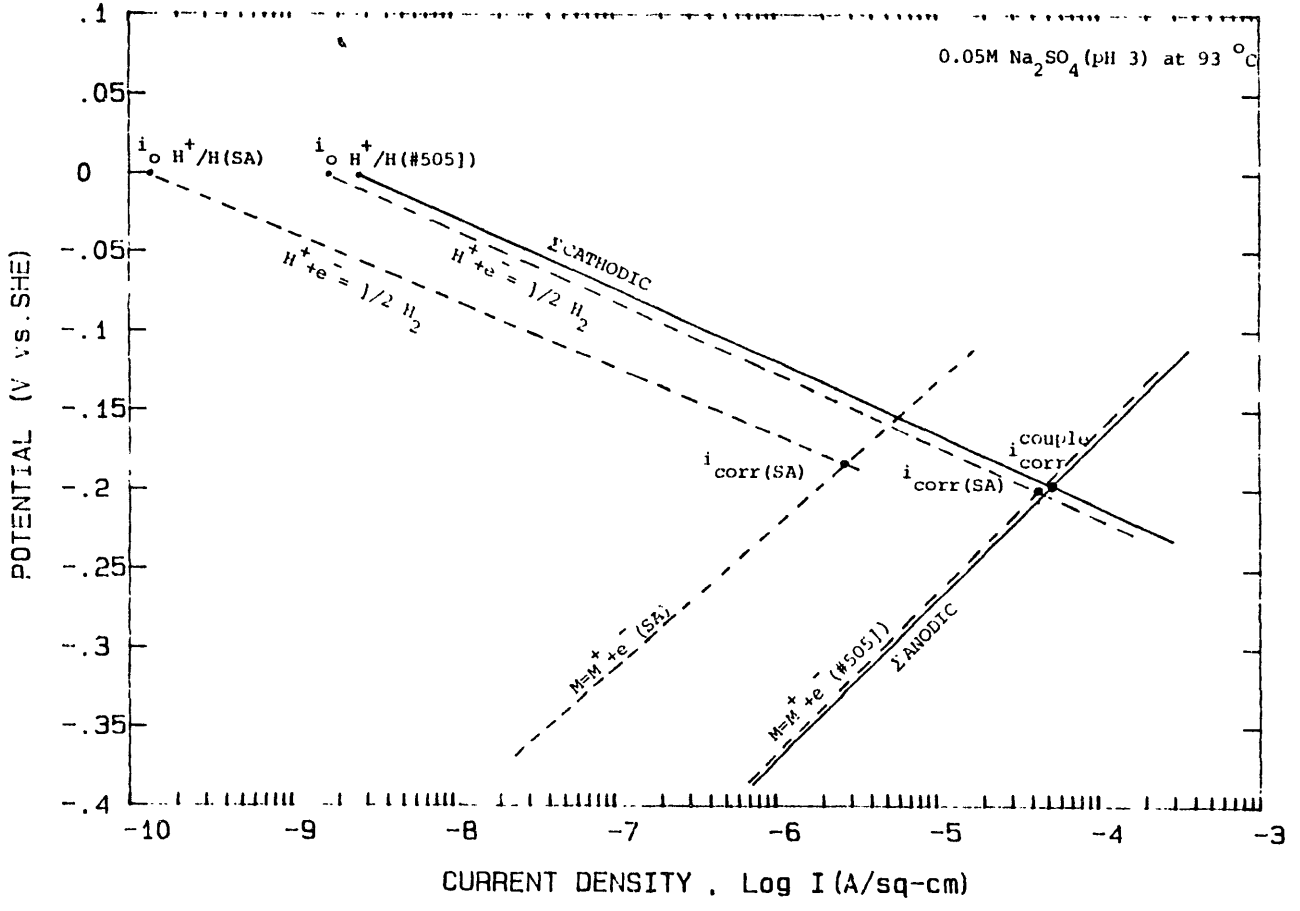

Figure 6.85 **The Prediction of Galvanic Current Density between the Chromium Depleted Zone as an Anode and the Surrounding Matrix as Cathode.**

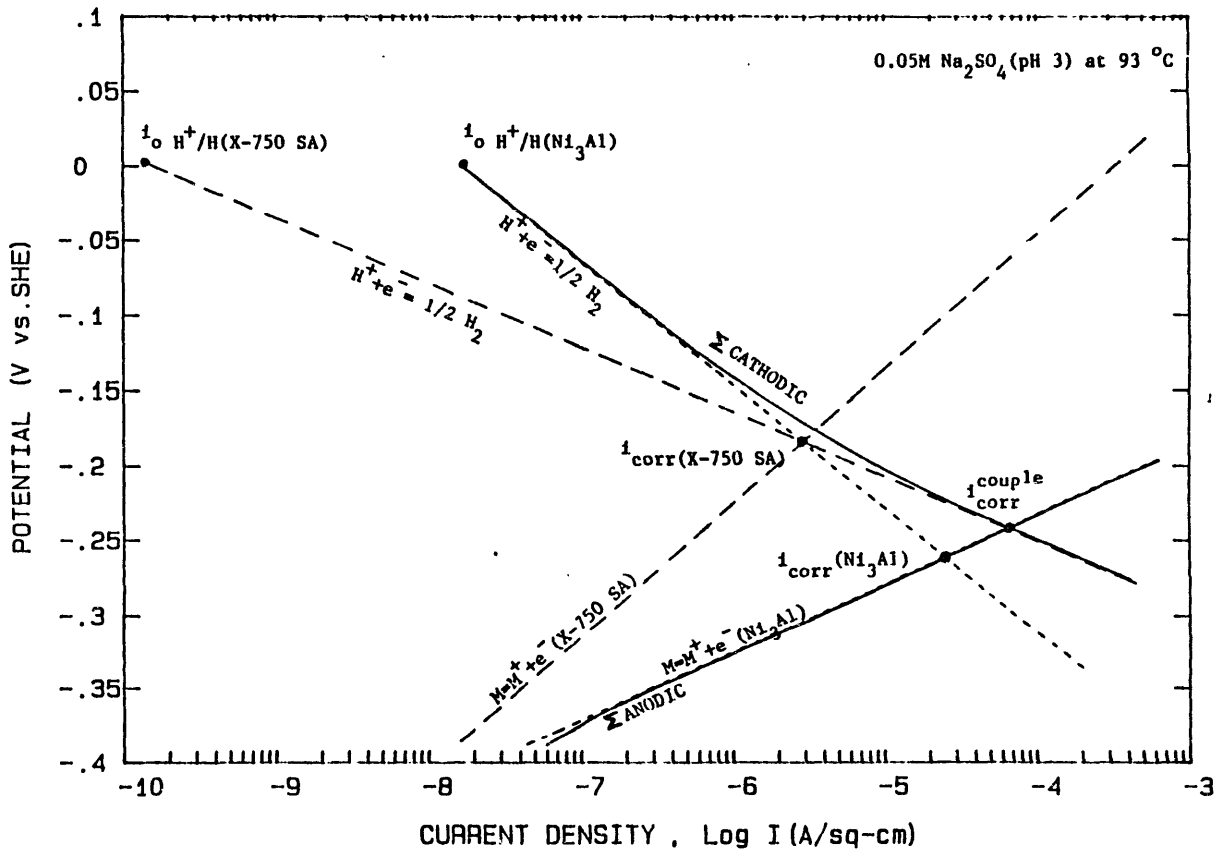

Figure 6.86 The Prediction of Galvanic Current Density between Gamma Prime (Ni_3Al) as an Anode and the Surrounding Matrix as a Cathode.

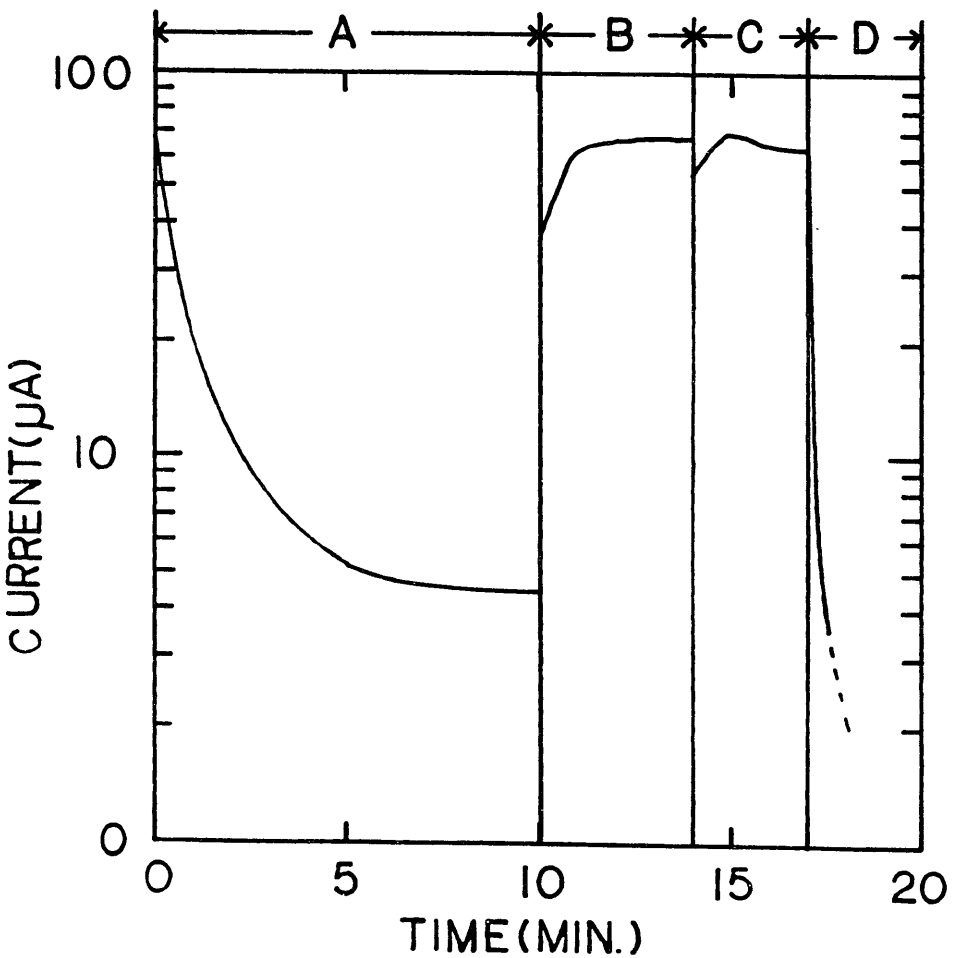

Figure 6.87 Measured Galvanic Current Between the X-750(SA) and NI_3Al (T_i=0) with Initially Equal Surface Area in 0.05M Na_2SO_4(pH=3) Solution with (A) Deaeration (B) Oxygenation (C) Oxygenation with Three-fold Smaller Anode (D) Deaeration.

The rate of the current decay is somewhat slower than parabolic low kinetics. Since the anodic current density of Ni_3Al (Ti=0) is shown by the potntial jump experiment to be constant it is hypothesized that the galvanic current is limited by the cathodic reaction.

The initial transient during the period A is plotted in Figure 6.88 as a function of a square root of time. A linear relation is observed during the first 15 seconds which is of most interest in real fracture processes. Thus cathodic deterioration due to adsorbed hydrogen atoms may be suggested to be responsible for the gradual decay so that total resistance of the galvanic cell can be significantly increased. The observed time dependence of current transient can be explained based on the assumption that;

1) overall reaction rate is controlled by hydrogen diffusion flux in electrolyte and proportional to $1/\sqrt{D_H t}$,
2) all generated hydrogens are adsorbed on cathode and loss by recombination is negligible which leads to accumulated hydrogen concentration with $\sqrt{t}$-dependence,
3) effective driving force i.e., overpotential, of galvanic coupling is reduced due to IR drop across adsorption layer in proportional to accumulated hydrogen concentration.

Then it can be easily shown that the galvanic current density decreases with time due to increased cathodic deterioration, as follows;

$$i_g(t) = i_o \exp(- C \sqrt{t}) \qquad (6\text{-}4)$$

where i_o is an initial value of galvanic current density, i_g, and C is a constant. The agreement in functional dependence on time is assumed to support the validity of above assumptions. It should now be noted that hydrogen recombination is assumed to be negligible. If the recombination takes place to an any significant extent it can be shown that the galvanic current density follows a time dependence which is a higher order than the present case.

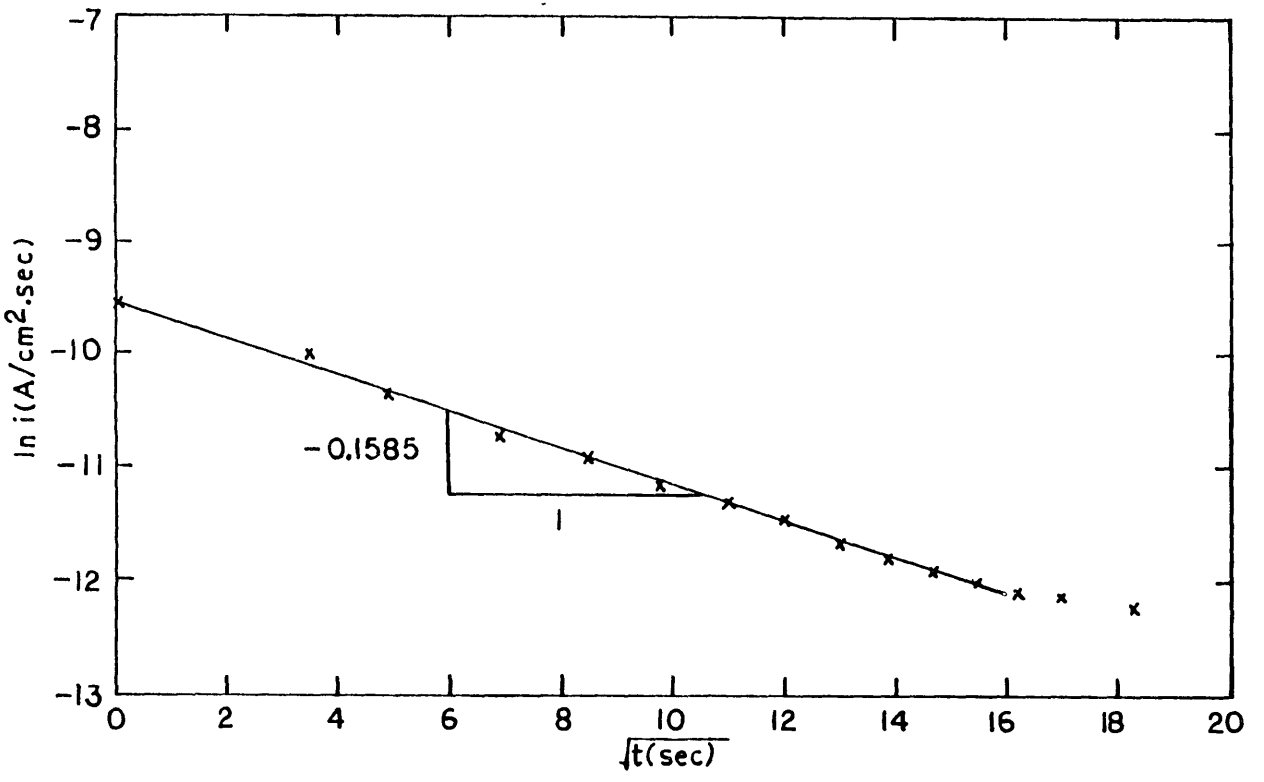

Figure 6.88 Initial Current Transient showing a Linear Dependence of Logarithmic Current on Square-root of Time.

The hypothesis of cathodic rate control was further tested by systematically varying the rate of anodic and cathodic partial process in the subsequent period B and C. During period B, the solution was bubbled with air which can augment the cathodic partial process through the oxygen evolution reaction. The measured galvanic current, indeed, increases rapidly to about $6x10^{-5}$ A/cm^2. During period C, the anodic surface area was cut into one third of the initial area and the same total current was observed. This is a convincing evidence that the cathodic reaction is still rate limiting even with oxygen bubbling. The current density of about $7x10^{-5}$ A/cm^2 appears to be a limitng cathodic current density under the galvanic situation regardless of the type of cathodic reaction involved. The limiting value of the anodic current density is, thus, not determined, but it is shown to be at least three times that of the cathode. During period D, the solution was bubbled with the nitrogen gas. The current decreases rapidly to a level lower than the stable current level during the period A. This can be attributed to an altered surface condition of the cathode which experienced the oxygen evolution reaction over about 7 minutes.

Therefore it is suggested that the cathodic reaction is rate-controlling, specifically, due to hydrogen adsorption effect. This effect is negligible during the cathodic potentiodynamic polarization of the solution annealed X-750 since the time to reach the small overpotential is only about 20 second. Therefore the predicted galvanic current density should be compared with the initial value of the period A. The agreement is found to be excellent.

Galvanic effects are observed to be significant at 93 C. The same study should be repeated for the entire temeprature range of interest in order to understand the temperature dependence. Such a complete study is beyond the scope of this work. However, the corrosion potentials of the specimens were measured as a function of temperature in deaerated high purity water with an 0.18 MPa hydrogen overpressure, as shown in Figure 6.89. Two sets of data are included in Figure 6.89. The first set of data includes the solution annealed alloy 600 and the AH condition of X-750 of which potentials were measured by using the external Ag/AgCl

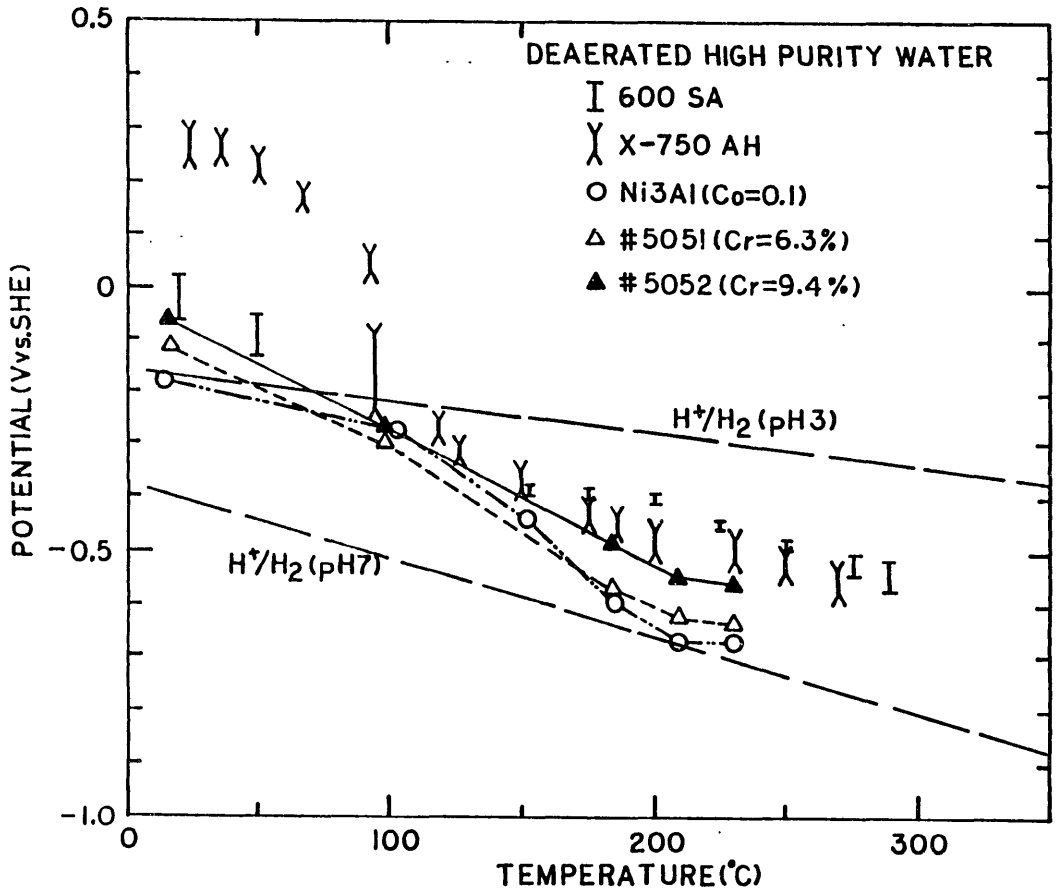

Figure 6.89 Measured Corrosion Potential of Alloys 600, X-750 and Representative Grain Boundary Chemistries in Deaerated High Purity Water.

reference electrode. The others are measured differentially with respect to the solution annealed X-750. The latter values are plotted with a reference to the average potentials of the solution annealed alloy 600 which is almost the same chemistry as the solution annealed X-750. At low temperautres below 100°C, the measured potential varies by a significant amount. It is believed to be affected by different surface conditons at the time of measurement. Since the surface could not be cathodically cleaned in the high purity water, the variation is difficult to eliminate. The hydrogen reduction potentials, E_{H^+/H_2}, are calculated by the Nernst equation as follows:

$$E_{H^+/H_2} = - \frac{2.3\ RT}{F} (pH) - \frac{2.3\ RT}{2F} \log p_{H_2} \qquad (6\text{-}5)$$

where R is the universal gas constant, F is the Faraday constant. The hydrogen pressure, p_{H_2}, of 1 atm is used to represent the hydrogenated water.

Comparison of the measured corrosion potential with the calculated potentials suggests that the hydrogen discharge is not possible in neutral water for the entire range of temperature up to 350°C. The hydrogen discharge is, however, expected to take place for a pH 3 water which may be present at various occluded cells such as the crack tip crevices due to cracked oxide layers and corrosion pits.

The measured corrosion potentials show an appreciable difference between the solution annealed condition and other active grain boundary chemistries such as γ' and the sensitized matrix. In case of γ' represented by $Ni_3Al(Co=0.1)$, the significance of the galvanic effect is believed to exist at higher temperatures at least up to 220 C above which no data is available. The degree of sensitizationis found to be an important variable to estimate the significance of galvanic effects Although data is limited up to 220 C a higher current density isexpected with the more sensitized microstructures. The case of 9.4% chromium,

the potential difference from the solution annealed matrix is about one half of that of the 6.3% chromium.

6.2.4 Summary

Alloys 600 and X-750 were electrochemically characterized in 0.05M Na_2SO_4 (pH=3) solution below 100°C. Potentiodynamic polarization did not reveal the microstructural differences such as carbon content and the localized sensitization in alloy 600. Thermal treatment (TT) was found to result in an appreciable increase in passivation current density compared with other conditions. The surface after polarization showed an extensive network of cracking of oxide layer on the TT specimen.

Electrochemical parameters including the corrosion potential and current as well as Tafel slopes were determined for representative intergranualr phases of alloys 600 and X-750. The SA condition of X-750 behaved in the same way as the HTMA conditons of alloy 600. Ni_3Al(T=0) showed strong activity without passivation and a significantly lower corrosion potential compared with the SA condition of X-750. Use of potential jump experiments revealed that Ni_3Al(T=0.15) is as active as Ni_3Al(Ti=0) in the fresh surface condition. Hence, it is necessary to use Ni_3Al(T=0) to represent Ni_3Al(Ti=0.15) in those experiments where a fresh surface behavior is to be maintained for an extended period. A low chromium (Cr = 6.3 wt.%) specimen also showed a strong activity, but its corrosion potential was lower than the SA condition of X-750 only by about 30mV.

Passivation kinetics were determined using the potential jump experiment. The SA, AH, HTH, and Ni_3Al(T=0.15) exhibited passivation behaviors which can be closely approximated by a parabolic kinectics. Current densities at 50 msec from the potential jump to 0.14 V(SHE) were found to be two to three orders of magnitude higher than values measured by the poalrization experiment.

The galvanic current density was measured between Ni_3Al(T=0) and the SA conditon in deaerated 0.05M Na_2SO_4(pH=3) solutiom at 93C. The initial current density was about $7x10^{-5}$A/cm which is in excellent agreement with a predicted value based on the mixed potential theory. A gradual decrease in the current density was observed. This is explained by the effect of adsorbed hydrogen atoms which limits cathodic reaction rate. The deterioration in cathodic surface was evaluated by varying the cathodic to anodic surface area ratio and solution oxygen content. Localized galvanic corrosion between γ' or low chromium grain boundaries and the surrounding matrix is likely to have a sinificant effect on low temperature behaviors of alloys 600 and X-750.

The temperature dependence of the corrosion potential of the alloys and representative intergranular phases were determined in the high purity deaerated water. The results obtained at temperatures up 220C indicated that galvanic corrosion effects due to interaction between γ' and low chromium phases would be increased at high temperature. Hydrogen discharge was shown to be possible in acidified water (pH=3) whereas the process is unlikely to take place in a neutral water.

6.3 TENSILE PROPERTIES IN LABORATORY AIR ENVIRONMENT

6.3.1 Tensile Properties of Alloy 600

Tensile test data in the laboratory were necessary for use in the SSRT program as reference mechanical properties free of any significant environmental effect. Hence, the strain rates were chosen to be as low as possible, but high enough to minimize oxidation effects at high temperatures. Two strain rates of $2.2x10^{-4}$ sec^{-1} and $2.2x10^{-5}$ sec^{-1} were used for each temperature of 25 C, 320 C and 360 C. For the HTMA conditions of heats NX1038 and NX2650, two specimens were tested for each condition while only one specimen was tested for the TT and SAS conditions of heat NX2650, and the LTMA condition of heat 96834. The results are summarized in Table 6.6. The specific plastic work, W_F, was

Table 6.6

Summary of the Tensile Test on Alloy 600
in a Laboratory Air Environment

Material	ϵ (sec^{-1})	T (C)	0.2% Y.S. (MPa)	U.T.S. (MPa)	Elongation (%)	W_F (MPa)
NX1638 HTMA	$2.2x10^{-4}$	30	377	650	33.2	187
		320	321	635	37.7	201
		360	300	628	40.3	212
	$2.2x10^{-5}$	30	378	646	34.6	195
		320	324	650	38.4	202
		360	308	621	40.8	211
NX2650 HTMA	$2.2x10^{-4}$	30	435	721	28.9	182
		320	393	695	32.1	192
		360	369	688	31.9	186
	$2.2x10^{-5}$	30	442	710	28.1	176
		320	388	716	34.2	208
		360	380	707	32.6	193
NX2650 TT*	$1.7x10^{-4}$	360	319	697	35.9	212
NX2650 SAS*	$1.7x10^{-4}$	360	177	603	53.2	249
96834 LTMA*	$1.7x10^{-4}$	360	335	744	36.1	234

NOTE: * Data from on test each case. All other data are averaged from two test results.

calculated by the numerical integration of the stress-strain curve using a formula as follows:

$$W_F \ (MPa \cdot m^3/m^3) = \int_o^e \sigma \, d\epsilon \qquad (6\text{-}6)$$

where σ and ϵ true stress and strain, respectively. Since the enginerring stress and strain are used in the calculation some error is inevitable. However the error on the difference between materials is expected to be insignificant since these materials exhibit approximately the same elongation and necking behavior.

For each combination of a temperature and a strain rate, two tests were made for heats NX1638 and NX2650 while some other materials were tested for only one specimen for a given condition. Representative stress-strain curves are presented in this section for the discussion on the effects of material condition, temperature and the strain rate. The general dependence of the tensile properties on these parameters are discussed and a more detailed examination is presented in conjunction with the fractography.

Figures 6.90 - 6.94 show a summary of the temperature dependence of tensile properties for heats NX1638 and NX2650. In general, duplicate measurements agree well with each other as shown in Figures 6.90 and 6.91. At all temperatures, heat NX2650 shows the higher yield strength and ultimate tensile strength. As the temperature incresaes, the strengths show monotonous decreases up to 360°C at both strain rates. There is little dependence of the strength on the strain rate. Heat NX2650 shows lower elongation than the heat NX1638 at all temperatures, as shown in Figures 6.92 and 6.93. In case of the HTMA condition of NX2650, there is a small decrease in the elongation at high temperatures which is more evident at the slower strain rate. Heat NX1638 shows monotonous incresae in elongation up to 360°C. The specific plastic work has a temperature dependence which is very similar with that of the elongation, as shown in Figure 6.94. However, the specific plastic work provides more useful information than the elongation by including the

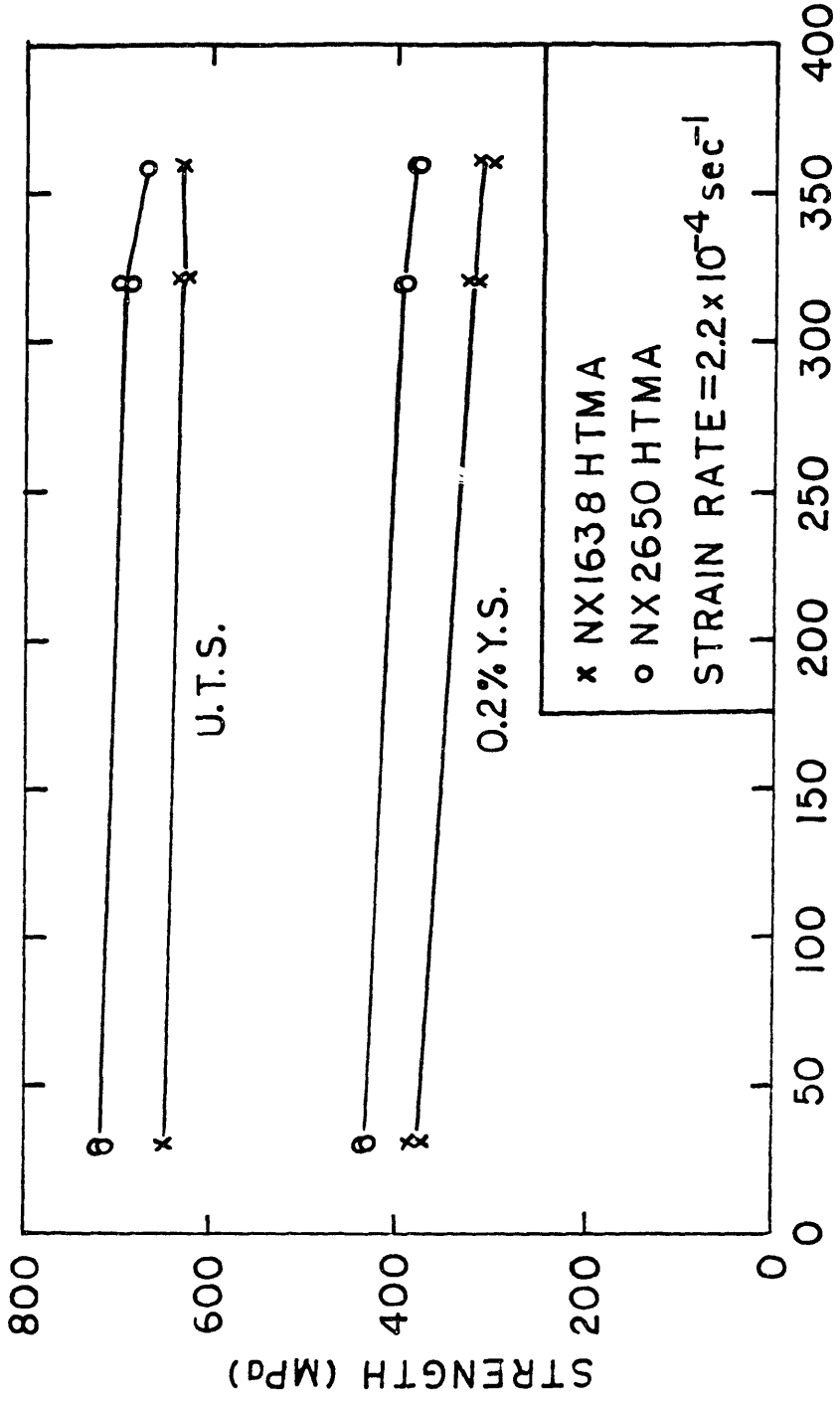

Figure 6.90 The Tensile Strength of the HTMA Conditions of Alloy 600 Heat NX1638 and NX2650 as a Function of Temperature.

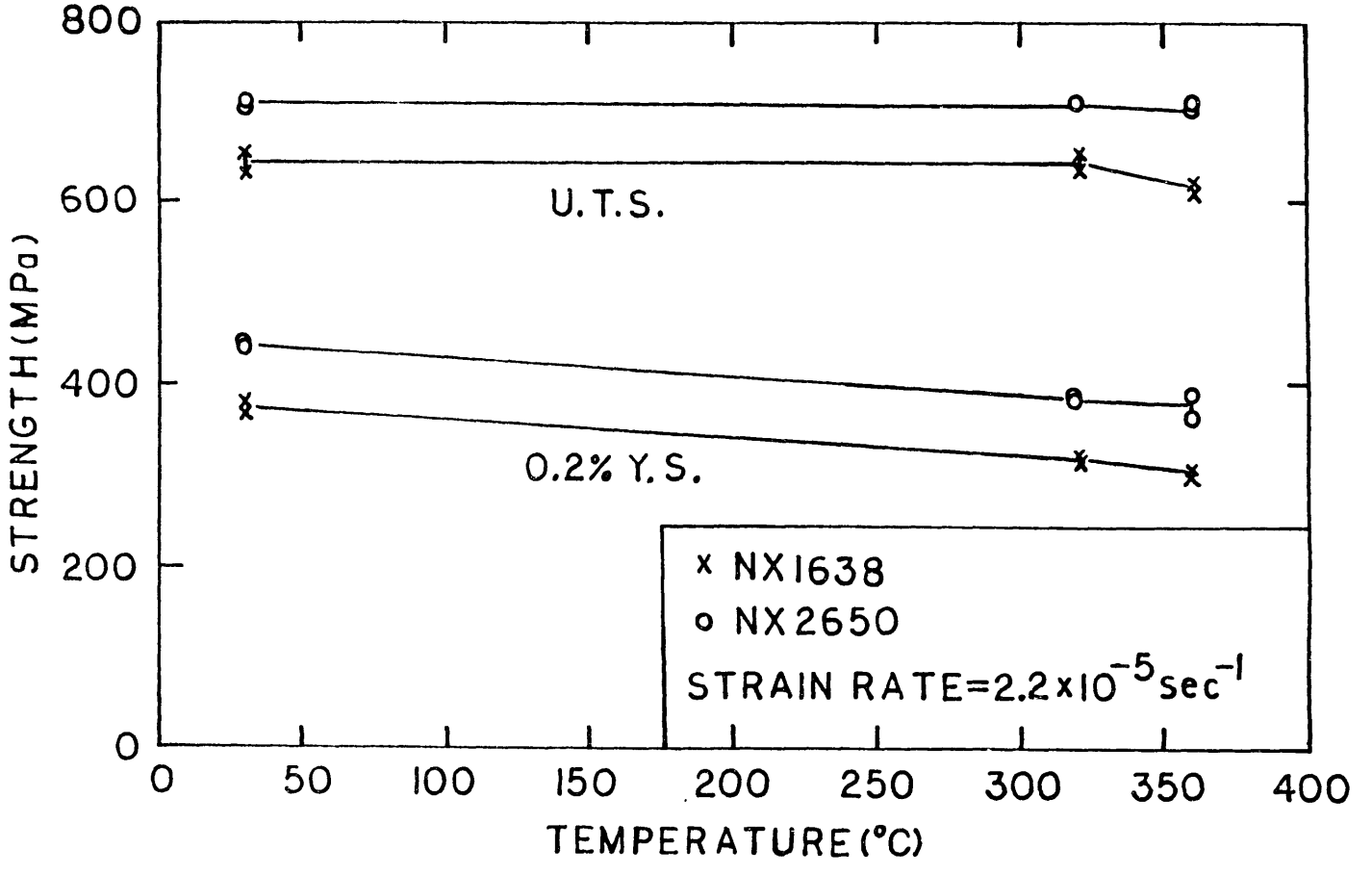

Figure 6.91 The Tensile Strength of the HTMA Conditions of Alloy 600 Heat NX1638 and NX2650 as a Function of Temperature.

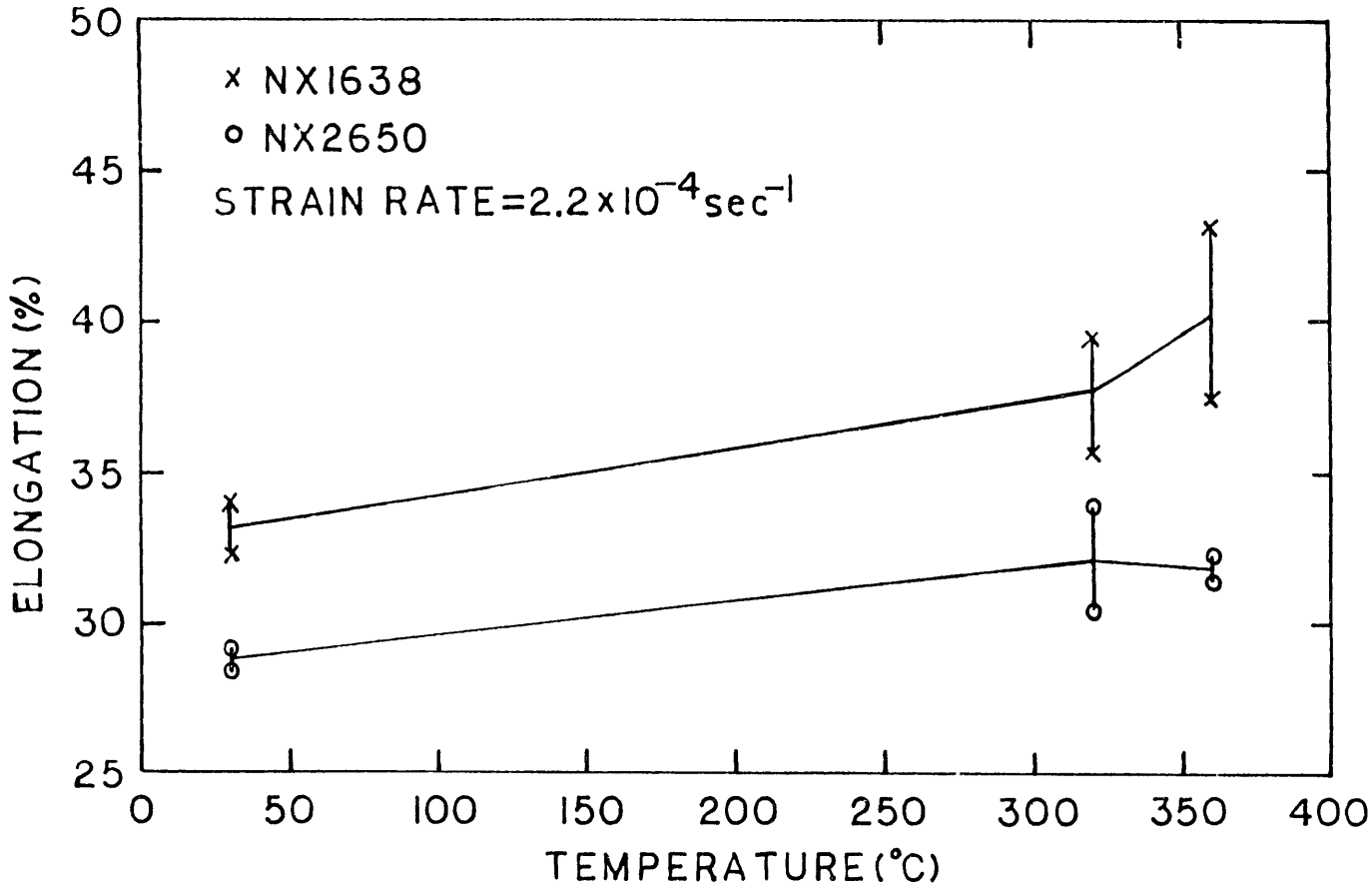

Figure 6.92 The Elongation of the HTMA Conditions of Alloy 600 Heat NX1638 and NX2650 as a Function of Temperature at a Strain Rate of $2.2 \times 10^{-4} sec^{-1}$.

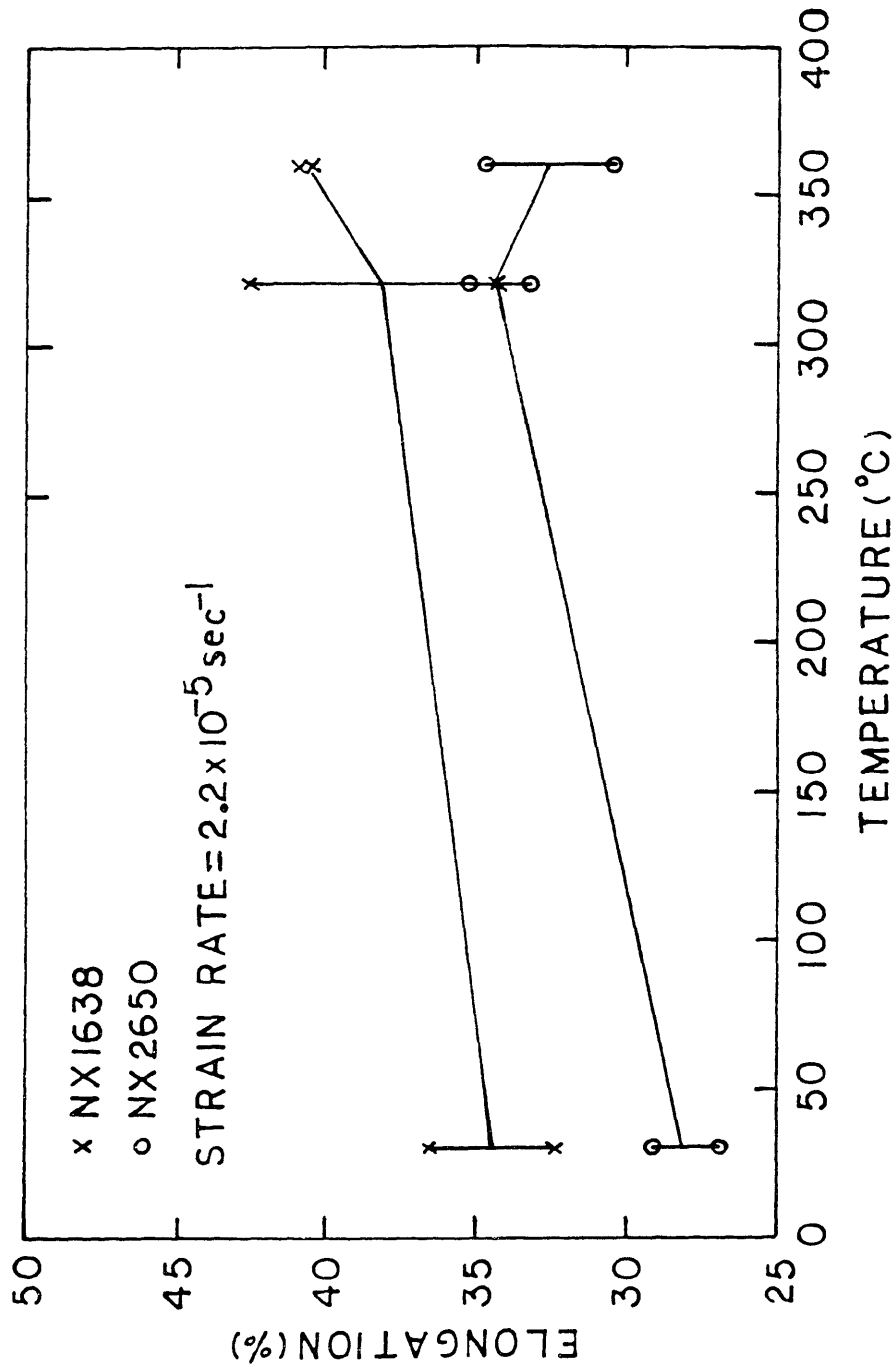

Figure 6.93 The Elongation of the HTMA Conditions of Alloy 600 Heat NX1638 and NX2650 as a Function of Temperature at a Strain Rate of $2.2 \times 10^{-5} sec^{-1}$.

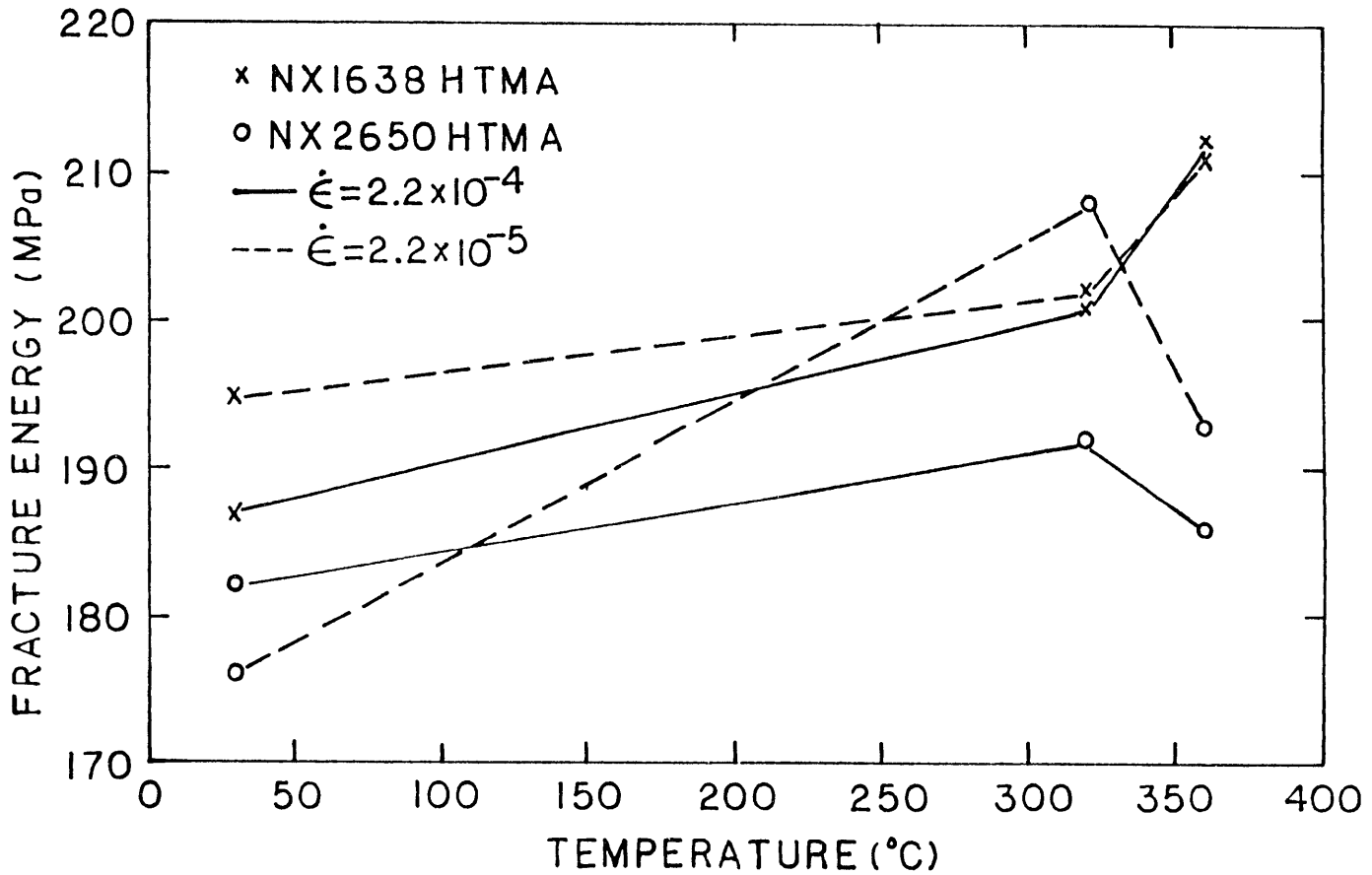

Figure 6.94 The Specific Plastic Work of the HTMA Conditions of Alloy 600 Heat NX1638 and NX2650 as a Function of Temperature at a Strain Rate of $2.2\times10^{-4}sec^{-1}$ and $2.2\times10^{-5}sec^{-1}$.

effect of strength. Heat NX1638 shows a significant increase in the fracture energy with temperature whereas the specific plstic work of heat NX2650 increases up to 320°C followed by a rapid decrease above that temperature.

The stress-strain curves for the two heats are compared at a strain rate of 2.2×10^{-4} sec^{-1} and 30°C, in Figure 6.95. The difference between two heats is nearly the same at the lower strain rate. Heat NX1638 shows about 60MPa lower yield strength and about 70 MPa lower ultimate tensile strength at both strain rates. Elongation is significantly higher with NX1638 resulting in a slightly higher fracture energy. Scanning electron micrographs of the fracture surface and the side walls are shown for NX1638 in Figures 6.96 and 6.97. There is no difference in the fractographs between two strain rates which show predominantly ductile dimpled rupture. The side wall shows slip steps which emerge at 45° with respect to the loading axis. Since the initial scratches made by the grit 400 SiC papers are aligned parallel with the loading axis, all features resembling scratches, but with an angle of about 45° are believed to result from slip deformation. Fractographs for NX2650 are shown in Figures 6.98 and 6.99. The fracture surfaces show ductile dimpled rupture. The side walls show a number of surface cracks at both strain rates. The surface cracks, about 5μm in size, are associated with two different microstructural features; the intersection of slip bands with the surface and the large MC carbide inclusions. When these fractographs are compared with the case of NX1638, NX2650 shows much finer spacing between the microvoid array. Hence, it appears that the morphology of microvoids are associated with the grain size.

At 320°C, the stress-strain curves of both heats indicate frequent occurrence of serrated yielding, as shown in Figure 6.100. The fracture surfaces of both heats are covered with microvoids and shear lips, as shown in Figures 6.101 - 6.104. The size of the microvoids is slightly larger at the lower strain rate which suggests the void nucleation and growth are kinetically controlled by strain rate. Observation of side walls reveals a significant difference between two two heats. In NX1638 specimens, the slip steps emerge from the surface at a higher number

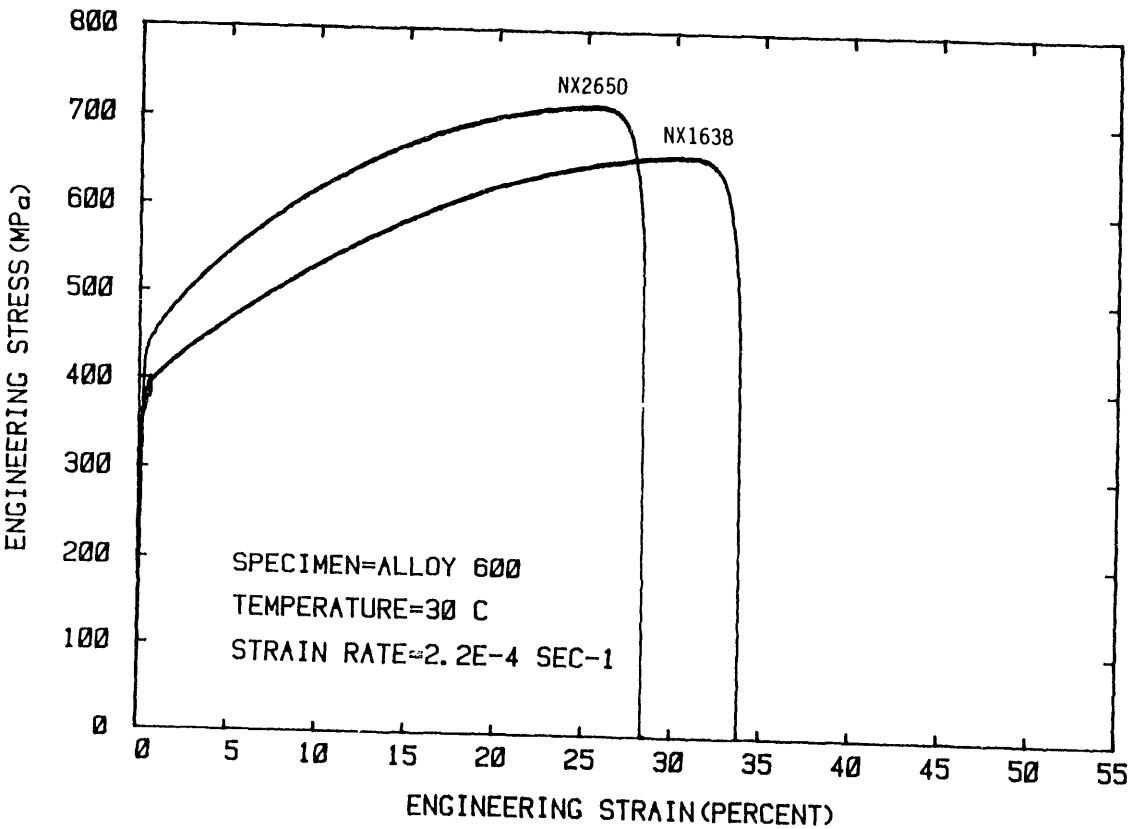

Figure 6.95 The Stress-strain Curves for the HTMA Conditions of Nx1638 and Nx2650 Obtained from the Tensile Test with a Strain Rate of 2.2×10^{-4} sec.$^{-1}$ at 30 C.

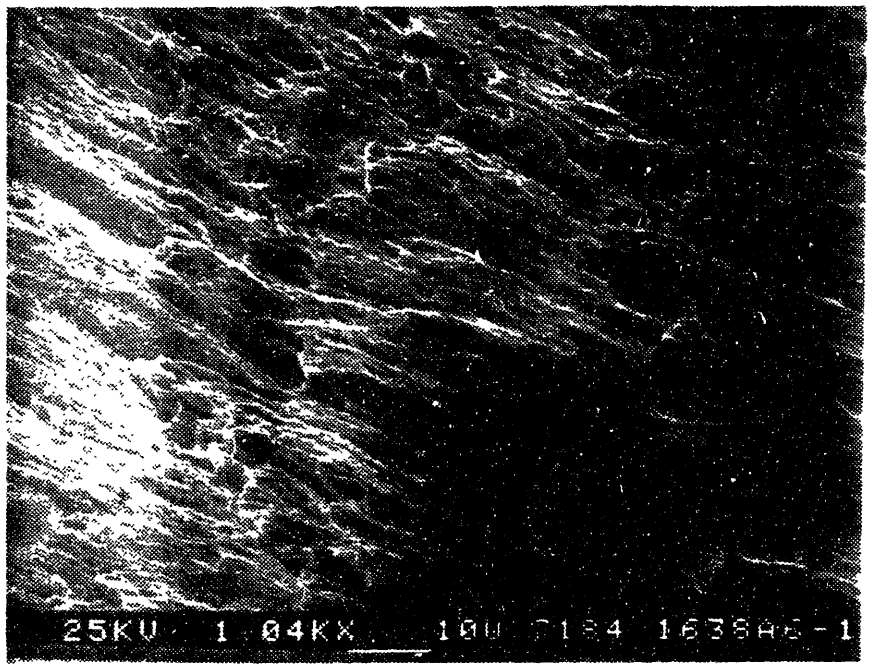

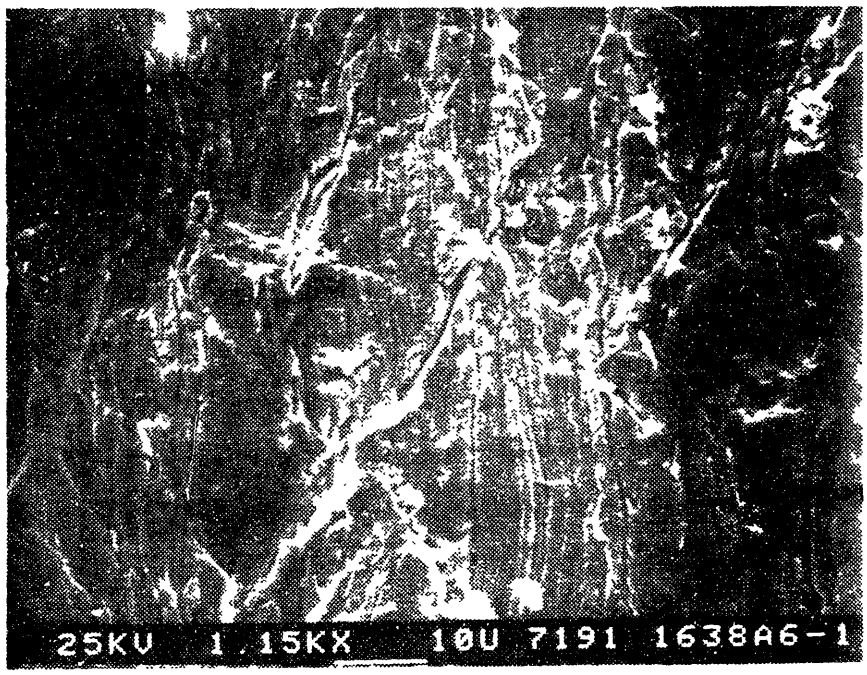

Figure 6.96 The Scanning Electron Micrographs for the Tensile Specimen of The HTMA Condition of Heat NX1638 Tested at a Strain Rate of $2.2 \times 10^{-4} sec^{-1}$ at 30 C (upper fracture surface lower side wall).

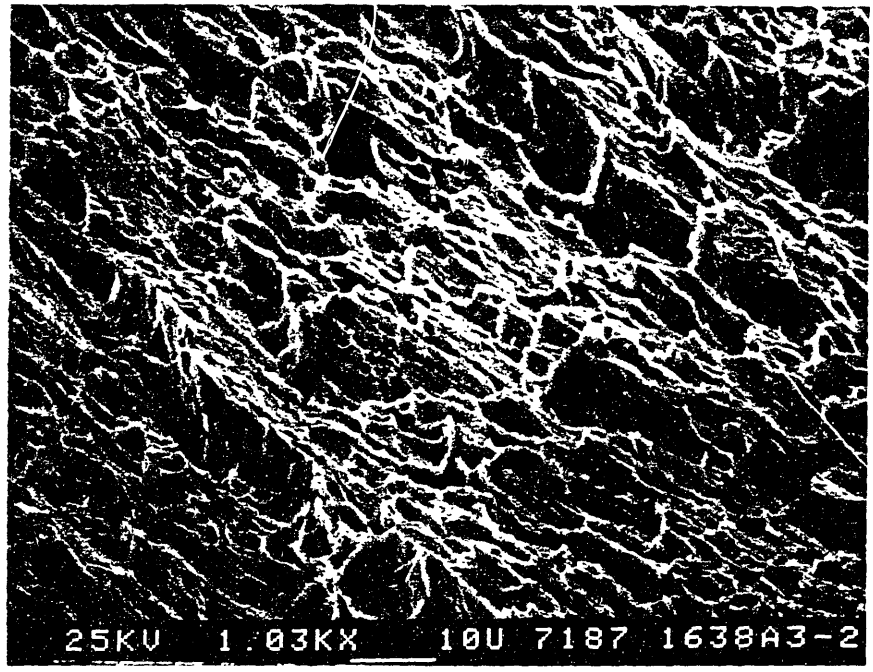

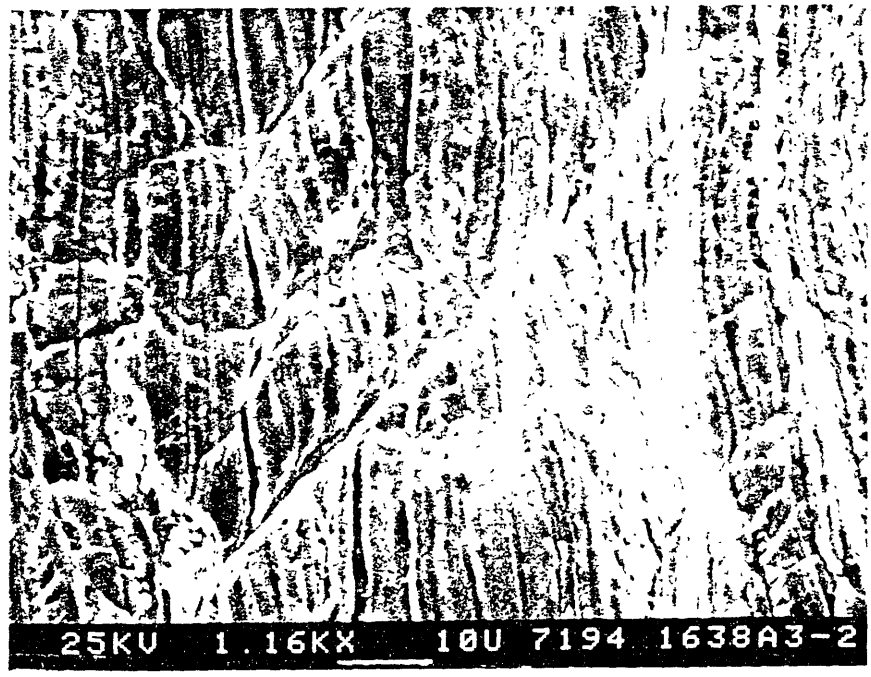

Figure 6.97 The Scanning Electron Micrographs for the Tensile Specimen of The HTMA Condition of Heat NX1638 Tested at a Strain Rate of $2.2 \times 10^{-5} sec^{-1}$ at 30 C (upper fracture surface lower side wall).

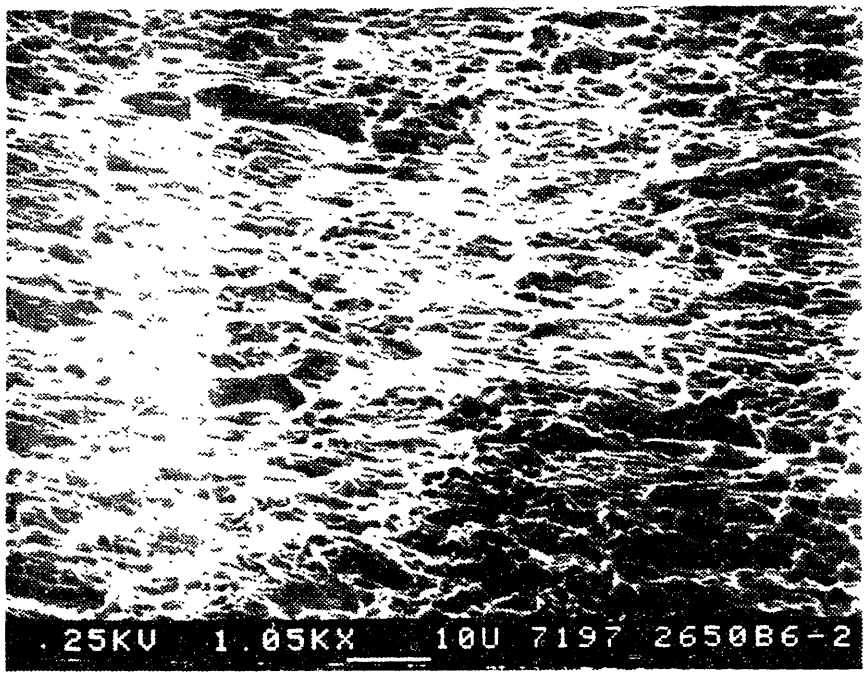

Figure 6.98 The Scanning Electron Micrographs for the Tensile Specimen of The HTMA Condition of Heat NX2650 Tested at a Strain Rate of $2.2 \times 10^{-4} sec^{-1}$ at 30 C (upper fracture surface lower side wall).

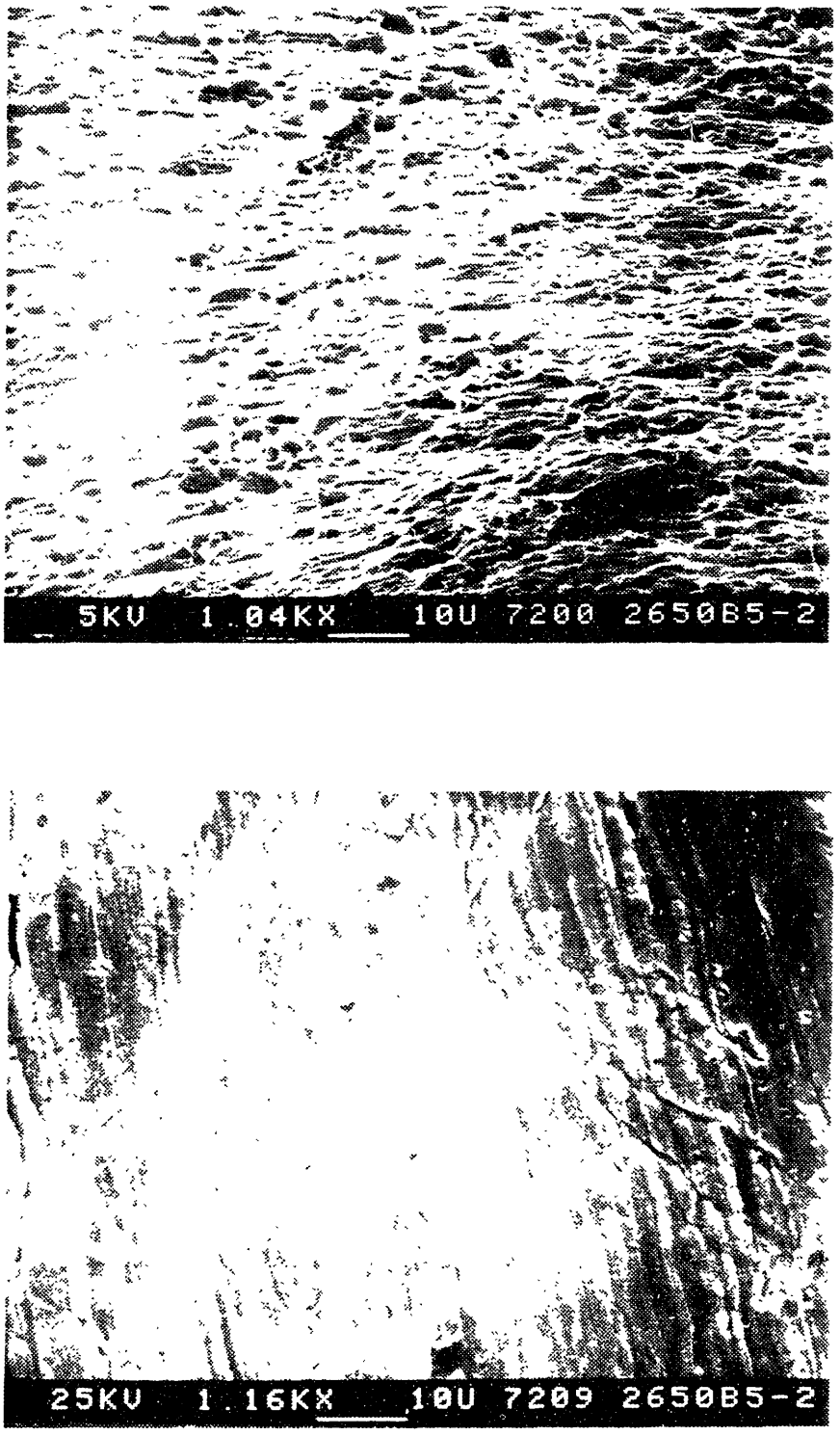

Figure 6.99 The Scanning Electron Micrographs for the Tensile Specimen of The HTMA Condition of Heat NX2650 Tested at a Strain Rate of $2.2 \times 10^{-5} sec^{-1}$ at 30 C (upper fracture surface lower side wall).

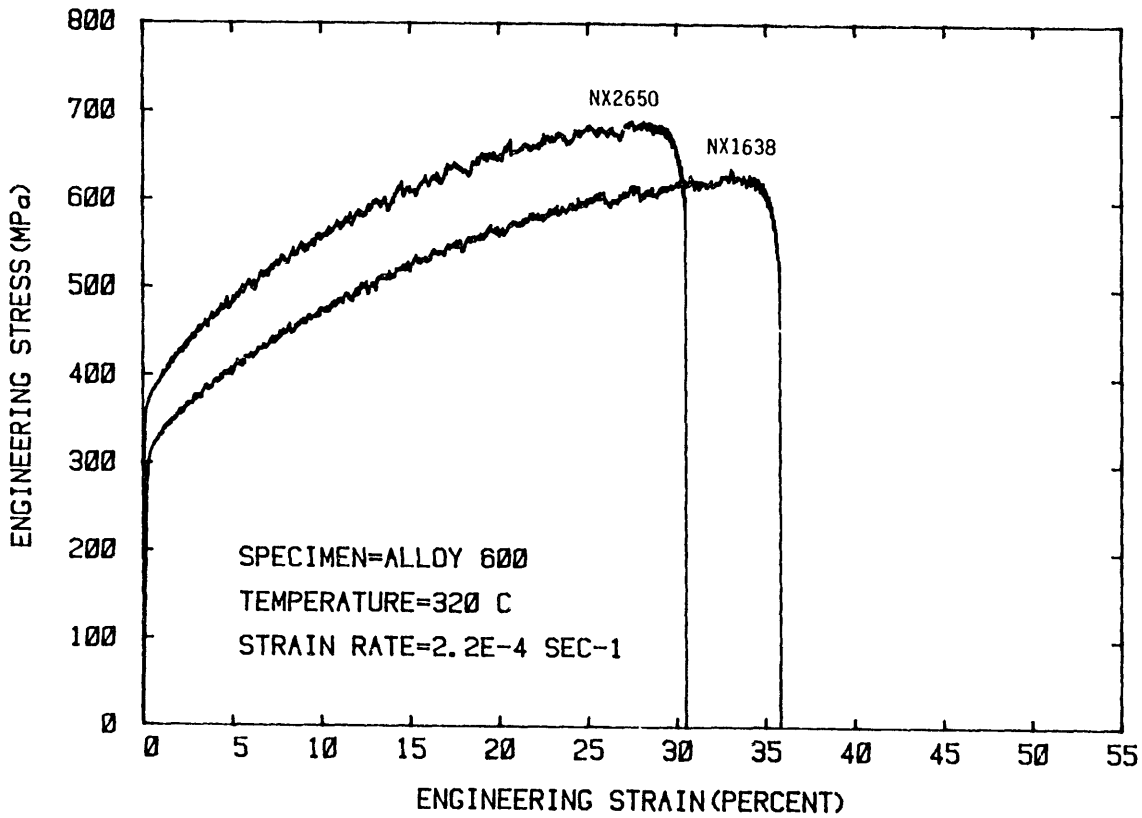

Figure 6.100 The Stress-strain Curves for the HTMA Conditions of NX1638 and NX2650 Obteained from the Tensile Test with a Strain Rate of 2.2×10^{-4} sec.$^{-1}$ at 320 C.

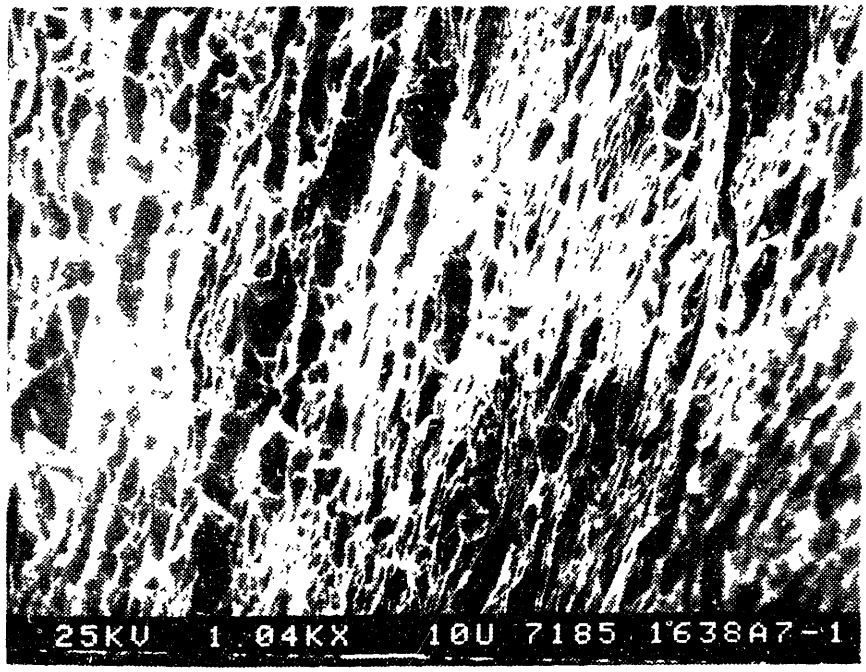

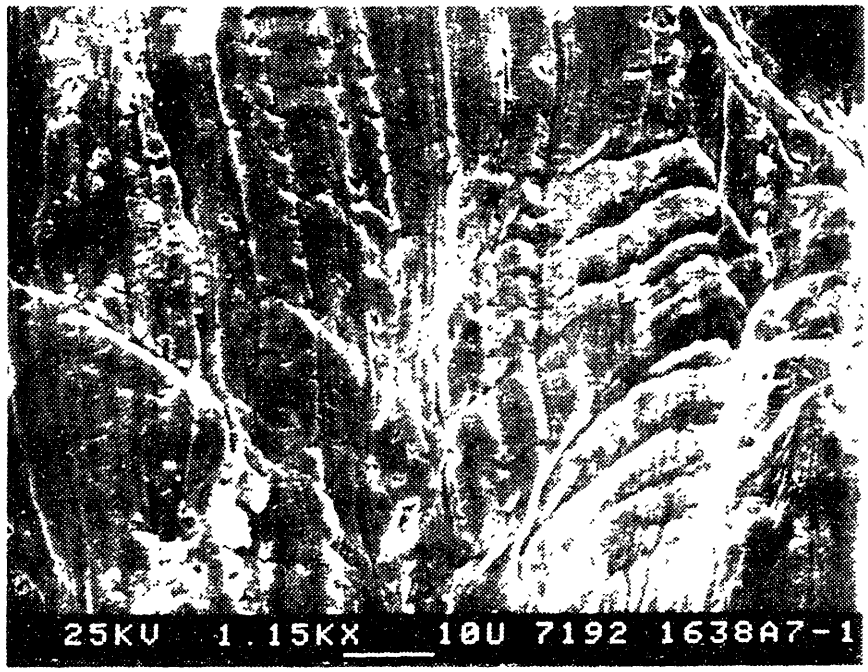

Figure 6.101 The Scanning Electron Micrographs for the Tensile Specimen of The HTMA Condition of Heat NX1638 Tested at a Strain Rate of $2.2 \times 10^{-4} sec^{-1}$ at 320 C (upper fracture surface lower side wall).

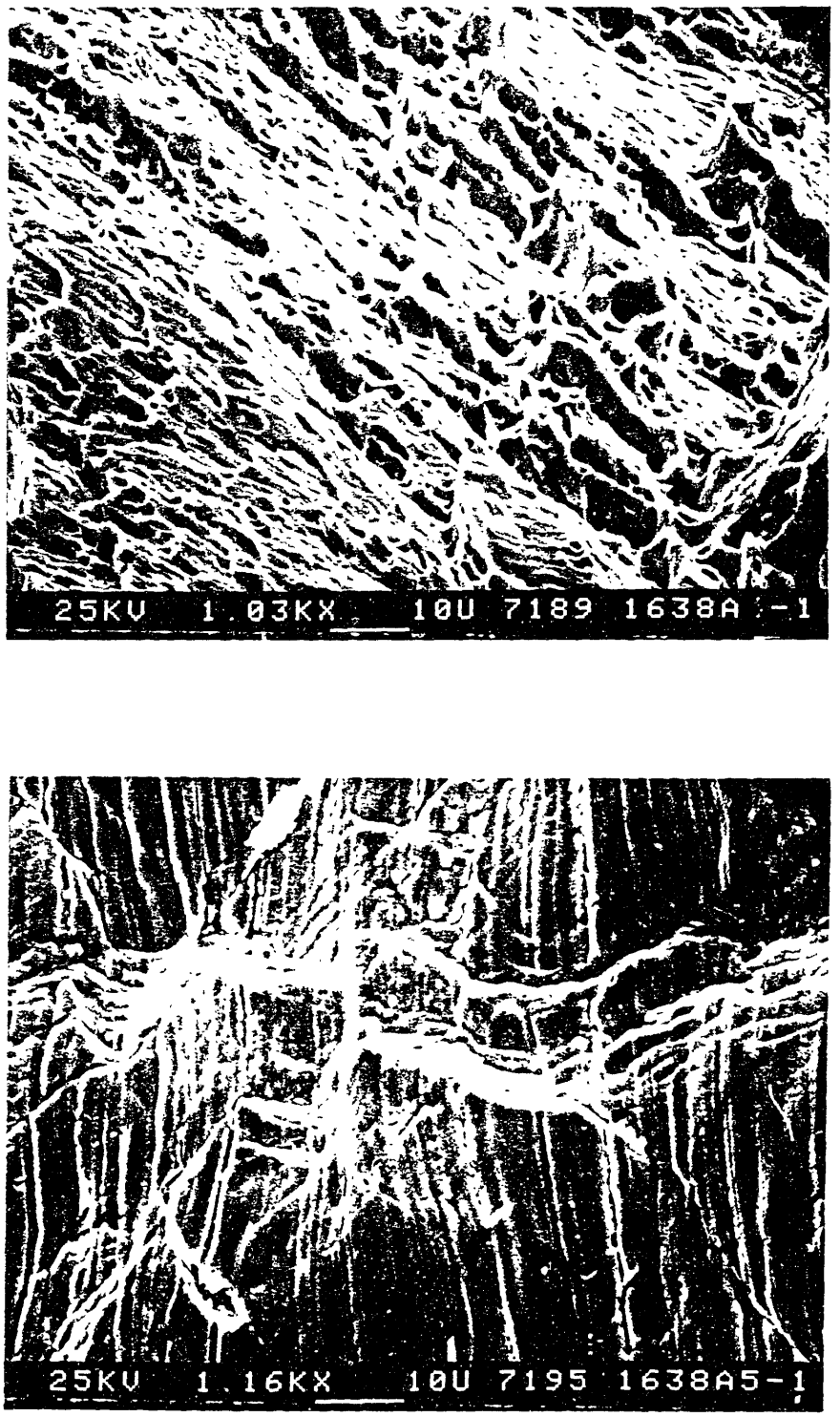

Figure 6.102 The Scanning Electron Micrographs for the Tensile Specimen of The HTMA Condition of Heat NX1638 Tested at a Strain Rate of 2.2×10^{-5} sec^{-1} at 320 C (upper fracture surface lower side wall).

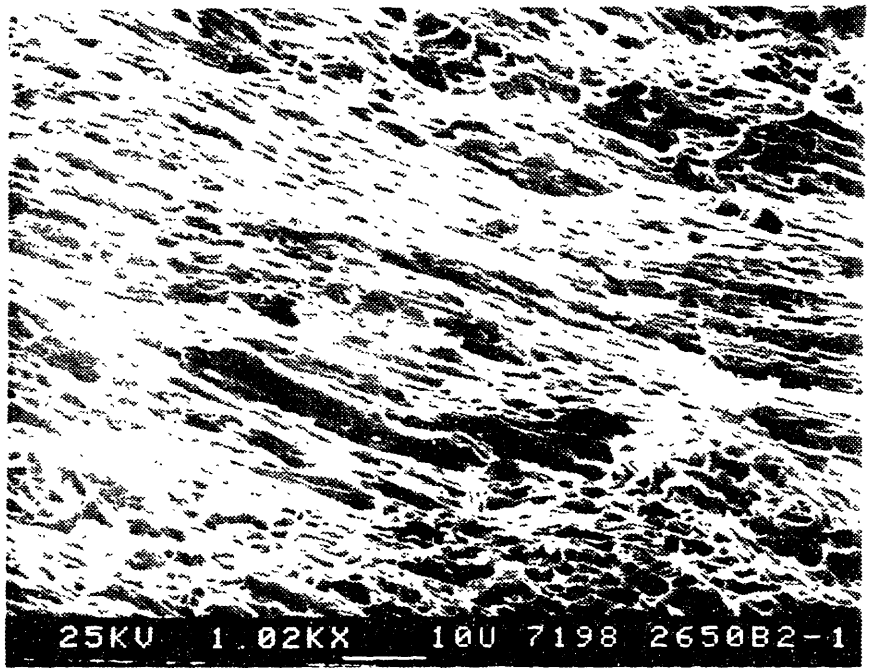

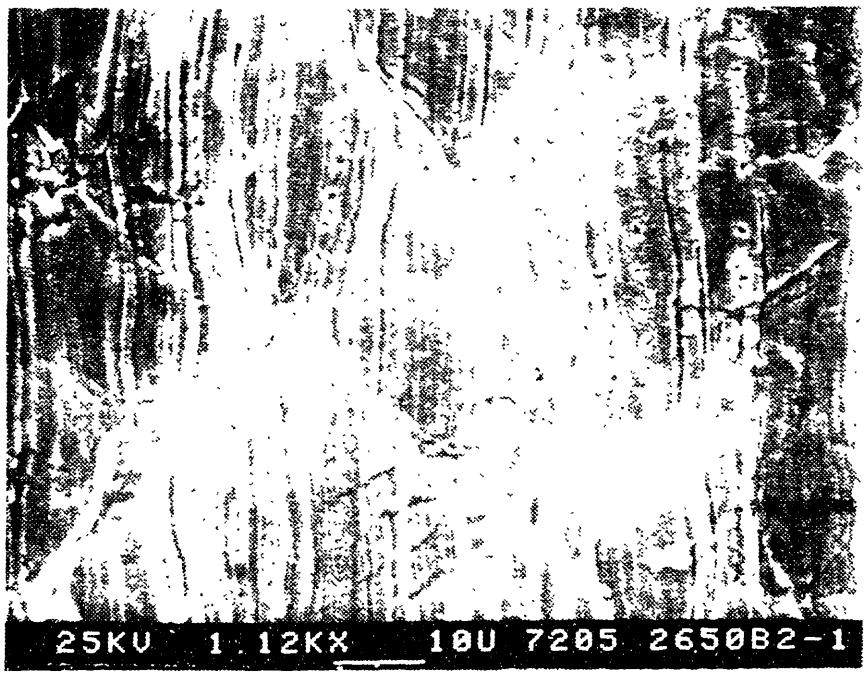

Figure 6.103 The Scanning Electron Micrographs for the Tensile Specimen of The HTMA Condition of Heat NX2650 Tested at a Strain Rate of $2.2 \times 10^{-4} sec^{-1}$ at 320 C (upper fracture surface lower side wall).

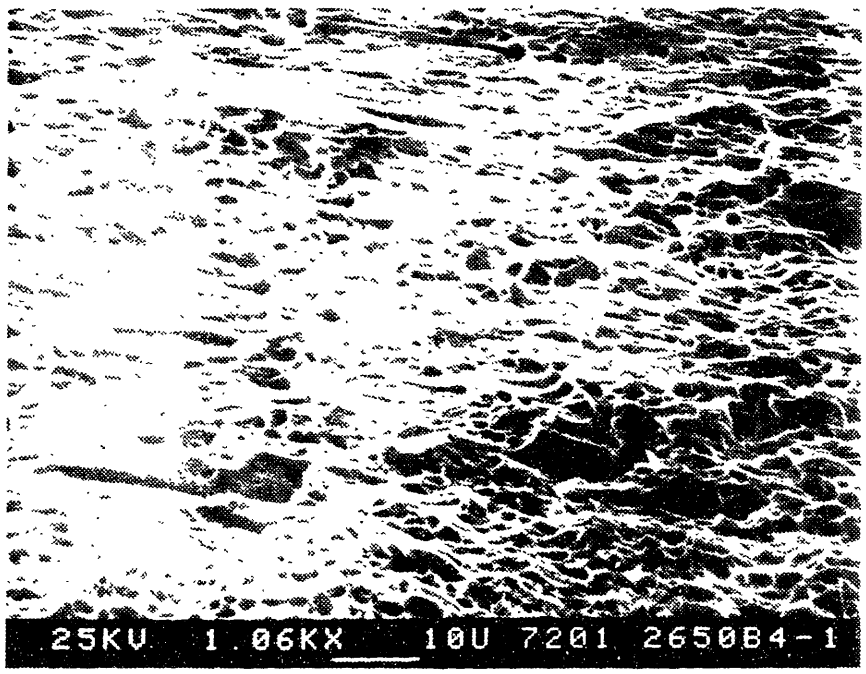

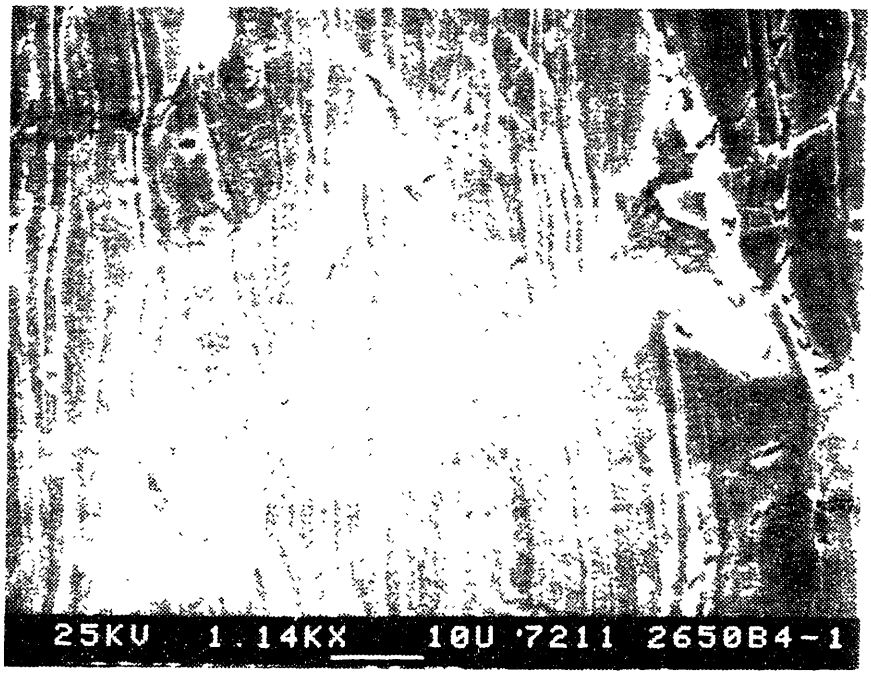

Figure 6.104 The Scanning Electron Micrographs for the Tensile Specimen of The HTMA Condition of Heat NX2650 Tested at a Strain Rate of $2.2 \times 10^{-5} sec^{-1}$ at 320 C (upper fracture surface lower side wall).

density. At the lower strain rate, the slip steps concentrate to form a staircase-type of the localized deformation. Surface deformation at the higher strain rate can be characterized by uniformly distributed slip steps. NX2650 shows a side wall with slip lines rather widely spared compared with NX1638. At the lower strain rate, a number of surface cracks are observed which have initiated from the intersection of slip lines or a large carbide inclusions, as shown in Figure 6.104.

The stress-strain curves at 360°C are shown in Figure 6.105 where the LTMA condition of 96834 is also compared. The yield strength is the highest with NX2650, but only by a small amount from that of the LTMA condition of heat 96834. The ultimate tensile strength is higher for the LTMA condition of heat 96834 by about 60 MPa. Since both heats contain comparable amount of carbon, mostly as intergranular carbides, the higher ultimate tensile strength and the elongation of the LTMA heat 96834 is attributed to the smaller grain size. All the fracture surfaces are similar and can be described as ductile dimpled rupture. The size of the microvoids is not increased at the increased temperture.

The side wall of NX1638 specimen tested at 360°C shows a uniform distribution of fine slip steps at 45° to the loading axis as shown in Figure 6.106. Occasionally, transgranular crystallographic crackings are formed at locations where the slip steps are concentrated. At the lower strain rate, the slip steps are found to be less localized and transgranular crystallographic crackings are replaced by the staircase type damages at surface, as shown in Figure 6.107. The absence of transgranular crystallographic cracking can explain the significant increase in the elongation and the fracture energy of the heat NX1638.

The side wall deformation of NX2650 tested at 360°C are shown in Figures 6.108 and 6.109. There is no distinct change in the deformation charateristics compared with the results at 320C. At the higher strain rate, the slip step are aligned at 45° with a large interspacing which is indicative of slip localization. Some offsets are observed across the slip step which are the beginning of transgranular crystallographic cracking. Therefore transgranular crystallographic crackings due to

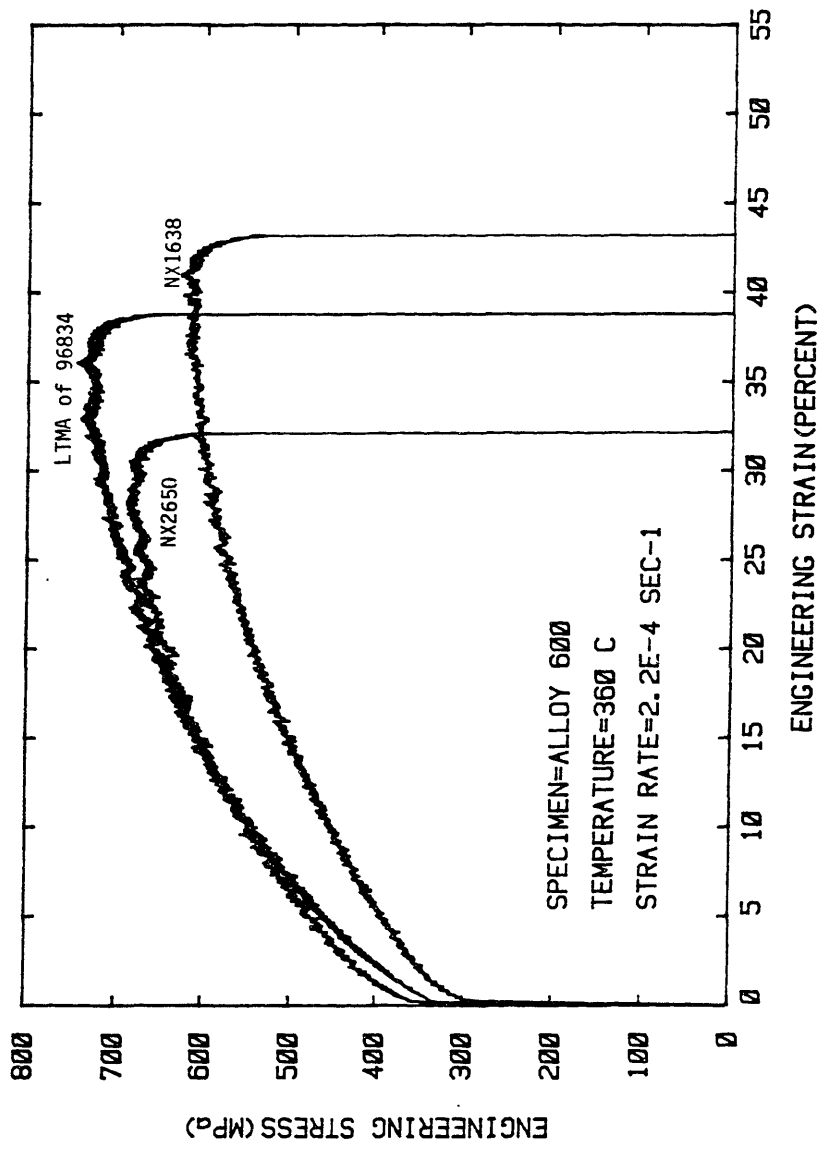

Figure 6.105 The Stress-strain Curves for the HTMA Conditions of NX1638, NX2650 and the LTMA Condition of Heat 96834 Obteained from the Tensile Test with a Strain Rate of 2.2×10^{-4} sec.$^{-1}$ at 360 C.

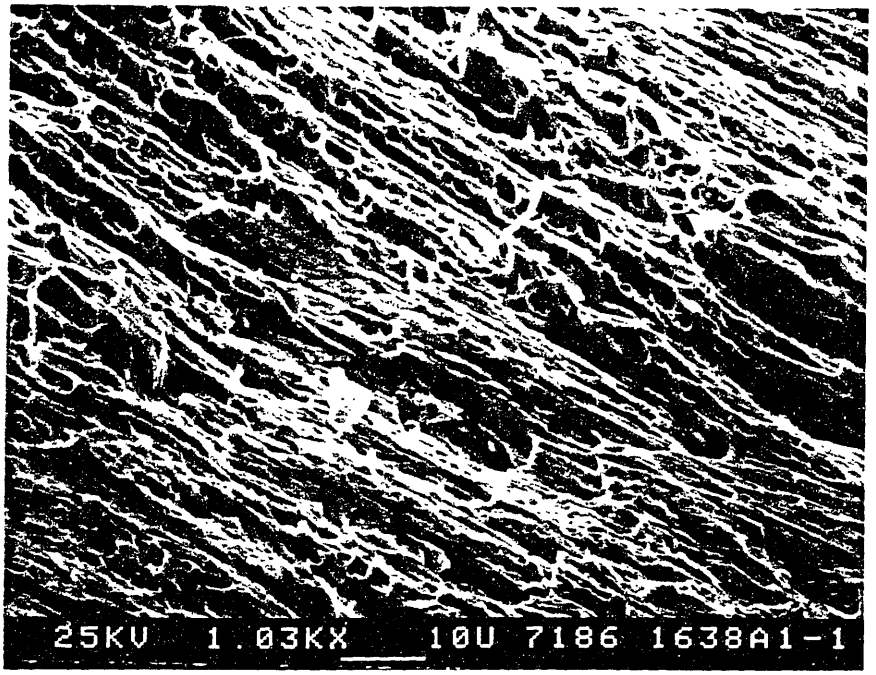

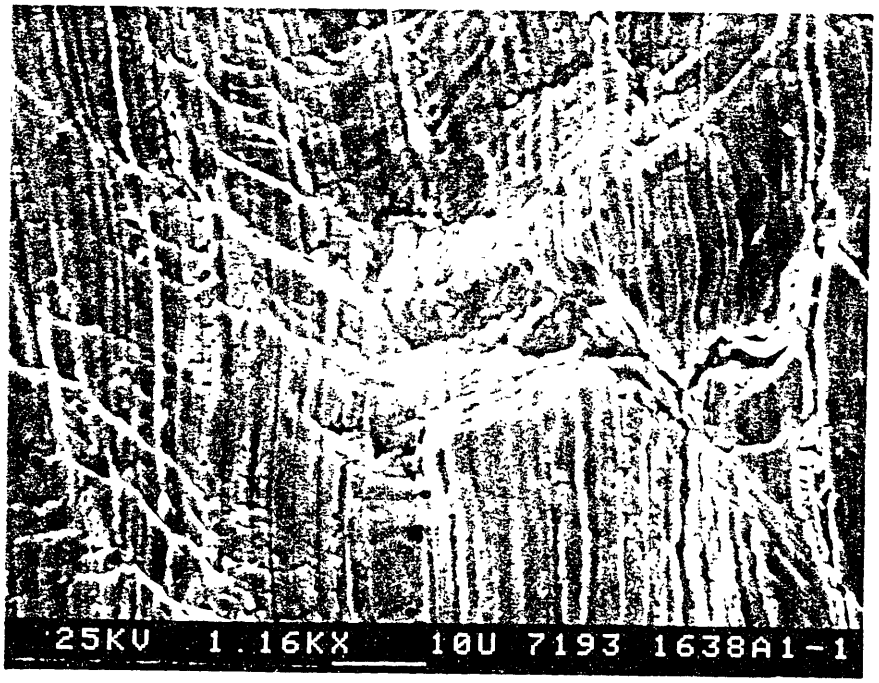

Figure 6.106 The Scanning Electron Micrographs for the Tensile Specimen of The HTMA Condition of Heat NX1638 Tested at a Strain Rate of $2.2 \times 10^{-4} sec^{-1}$ at 360 C (upper fracture surface lower side wall).

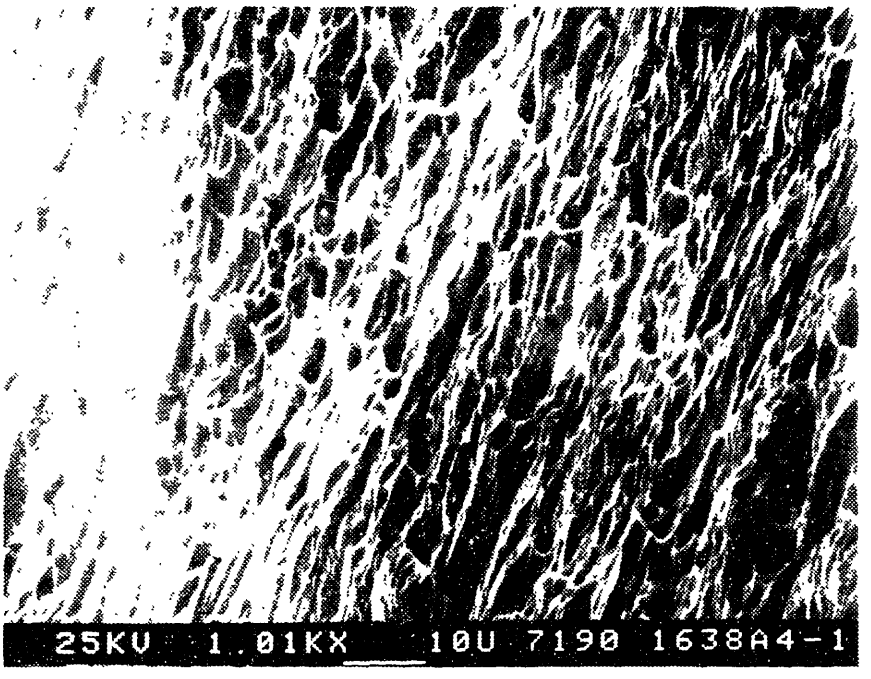

Figure 6.107 The Scanning Electron Micrographs for the Tensile Specimen of The HTMA Condition of Heat NX1638 Tested at a Strain Rate of 2.2×10^{-5} sec^{-1} at 360 C (upper fracture surface lower side wall).

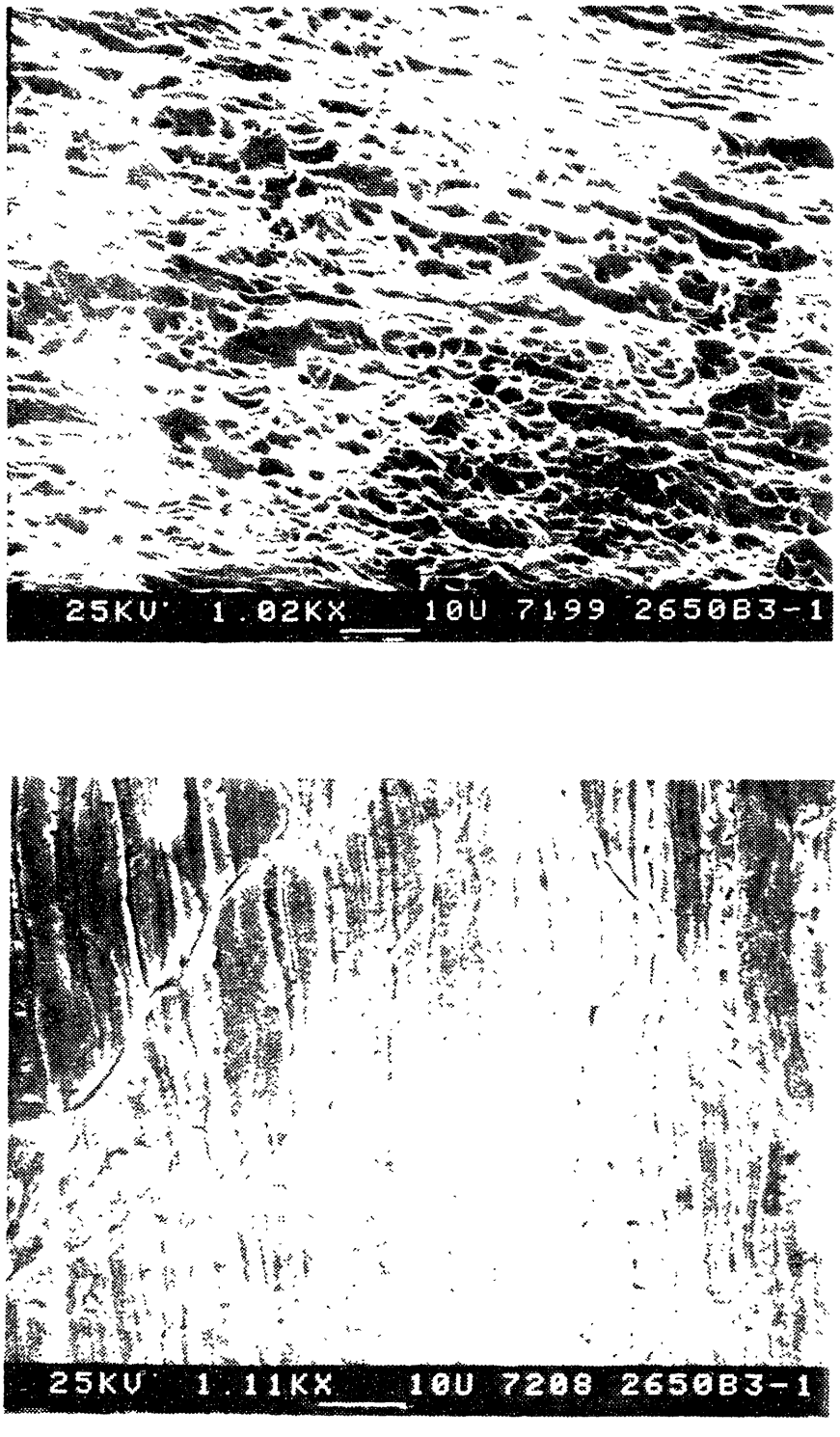

Figure 6.108 The Scanning Electron Micrographs for the Tensile Specimen of The HTMA Condition of Heat NX2650 Tested at a Strain Rate of $2.2 \times 10^{-4} sec^{-1}$ at 360 C (upper fracture surface lower side wall).

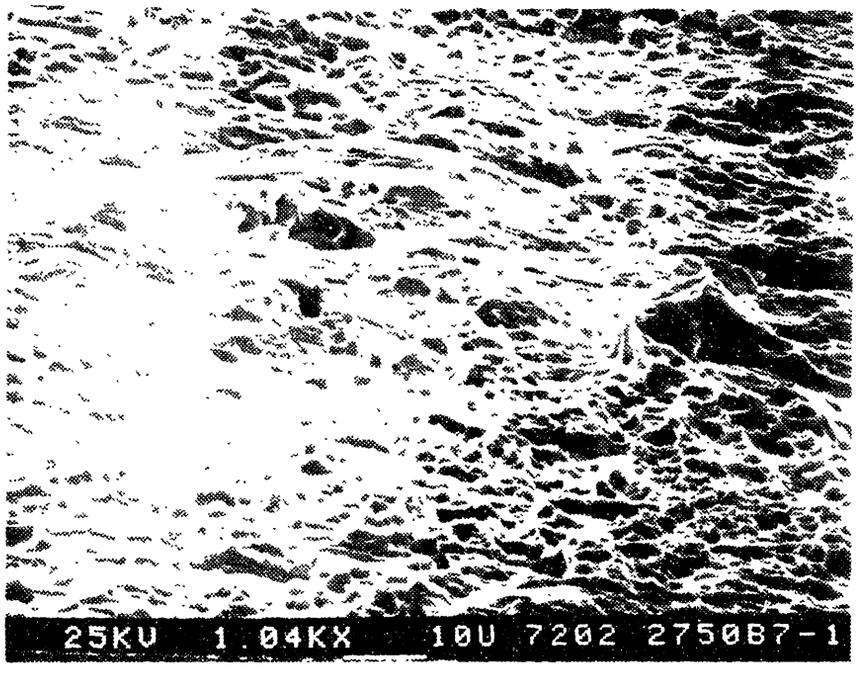

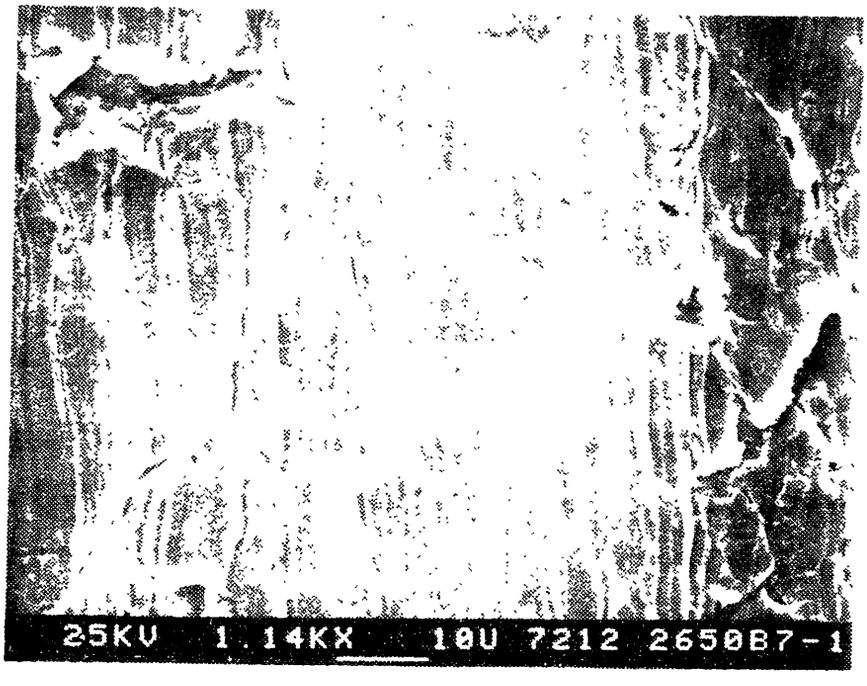

Figure 6.109 The Scanning Electron Micrographs for the Tensile Specimen of The HTMA Condition of Heat NX2650 Tested at a Strain Rate of $2.2 \times 10^{-5} sec^{-1}$ at 360 C (upper fracture surface lower side wall).

slip localization may be responsible for the slightly decreased ductility and fracture energy at the higher strain rate. At the lower strain rate the number of slip steps are increased, as shown in Figure 6.109. Offsets across the slip steps are again found frequently. The most distinguishing feature are the surface cracks initiated from the large carbide inclusions. Surface cracks at inclusions may have caused a significant decrease in the both elongation and fracture energy at the lower strain rate.

The LTMA condition of heat 96834 tested at 360°C shows a side wall with no apparent slip localization as shown in Figure 6.110. There are numerous fine surface cracks which are mostly transgranular crystallographic crackings at 45° to the loading axis. Bigger cracks are also occasionally found at carbide inclusions However the number of large cracks are much lower than in the case of NX2650.

The thermally treated (TT) condition and the solution annealed and sensitzed (SAS) condition are compared with the HTMA condition of NX2650 in Figure 6.111. The TT condition is characterized by an appreciable decrease in the yield strength accompanied by a significant incresae in the elongation with nearly the same ultimate tensile strength. The fracture energy is increased only marginally compared with the average value of the HTMA condition. The side wall shows a number of surface cracks which are more uniformly distributed than those in the HTMA condition, as shown in Figure 6.112. The increased number of intergranular carbides formed in the TT condition appear to lower the stress concentration by generating finer slips.

The SAS condition shows an incresae in both elongation and fracture energy at the expense of strength. The fracture surface of the SAS condition is characterized by patches of shear lips containing much finer microvoids as shown in Figure 6.113. The side wall reveals extensive transgranular transgranular crystallographic crackings which are distributed over entire surface near the fracture site. Although the surface damages is extensive on the fractured specimen, no direct comparison can be be made with other fractographs since the elongation

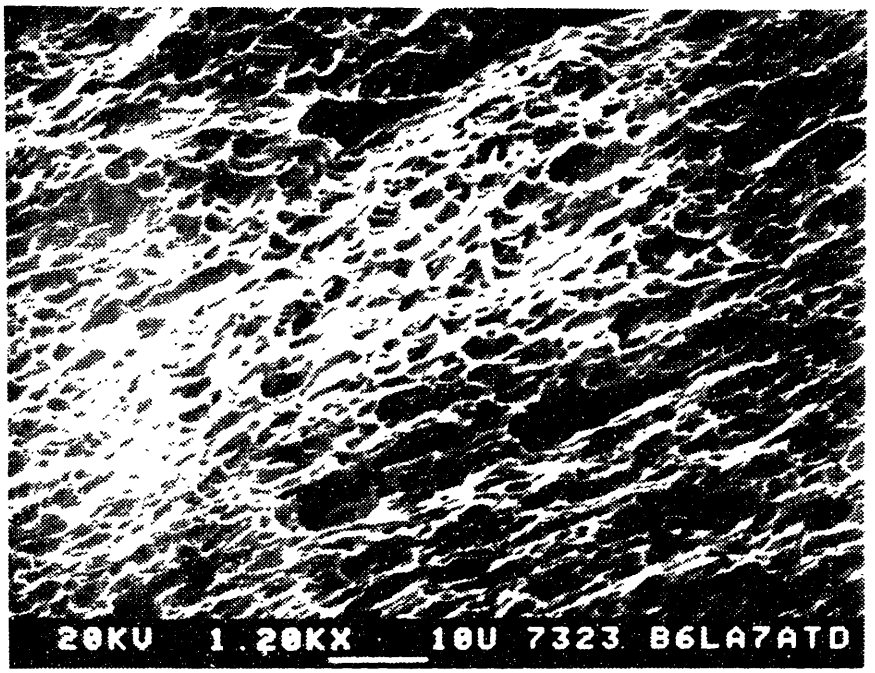

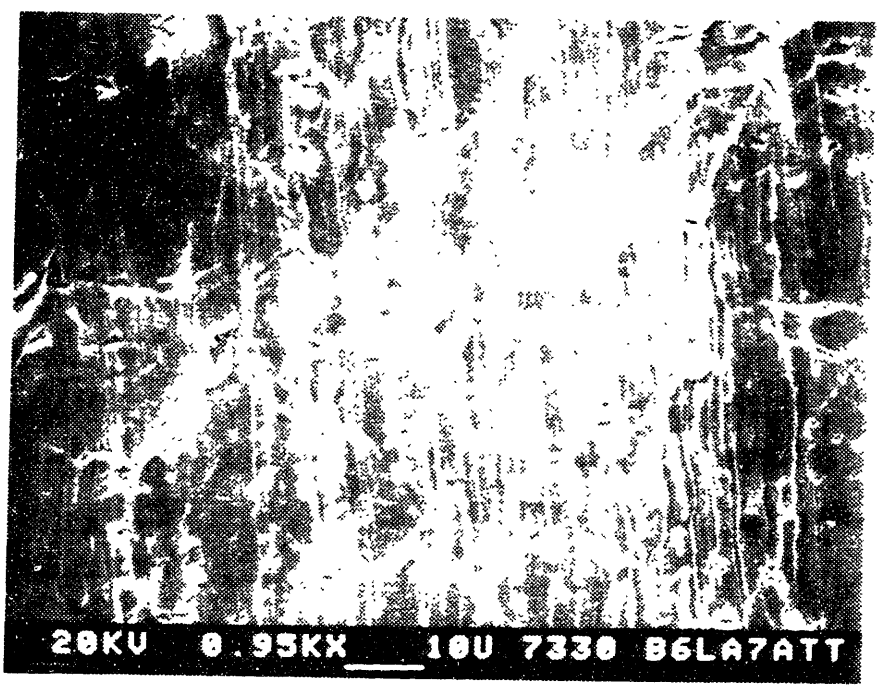

Figure 6.110 The Scanning Electron Micrographs for the Tensile Specimen of The LTMA Condition of Heat 96834 Tested at a Strain Rate of $1.7 \times 10^{-4} sec^{-1}$ at 360 C (upper fracture surface lower side wall).

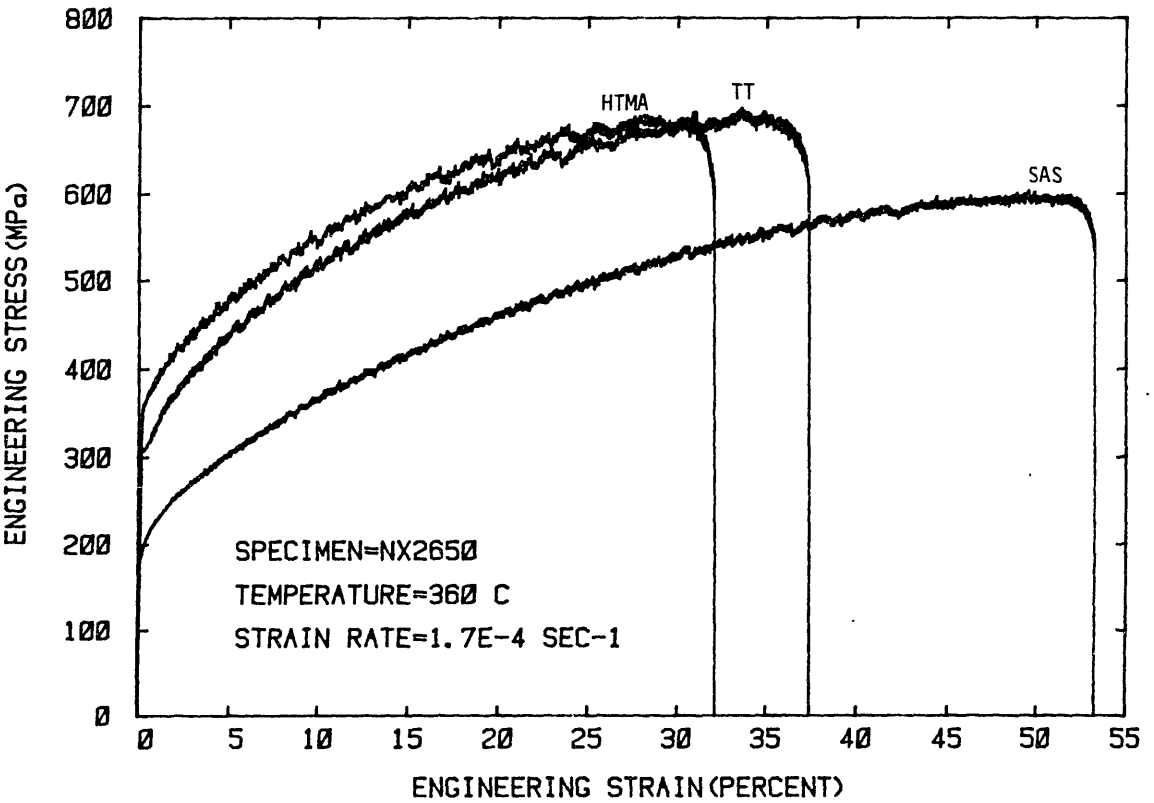

Figure 6.111 The Stress-strain Curves for the TT and SAS Condition of Heat NX2650, Compared with the HTMA Condition, Obtained from the Tensile Test with a Strain Rate of 1.7×10^{-4} sec. at 360 C.

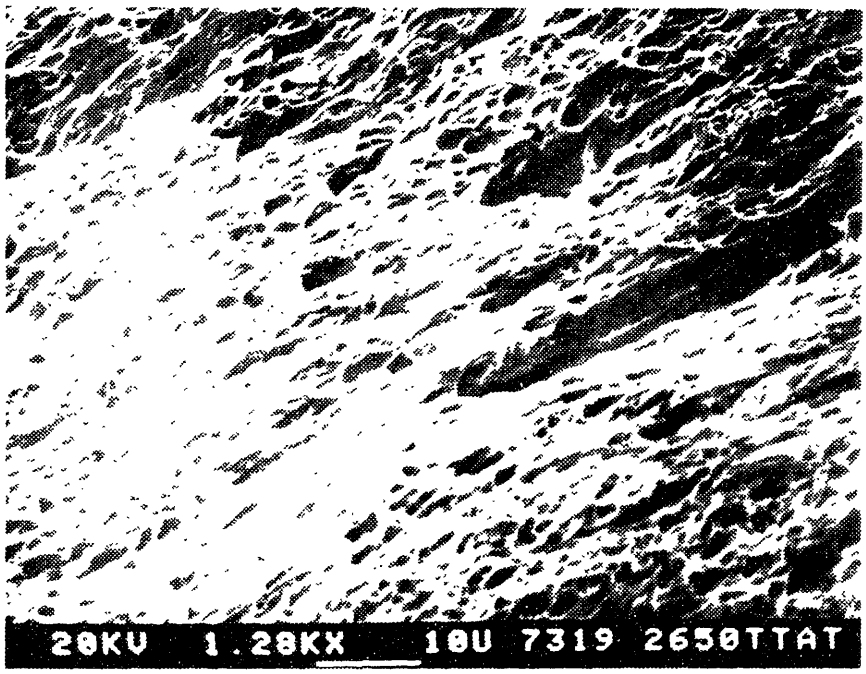

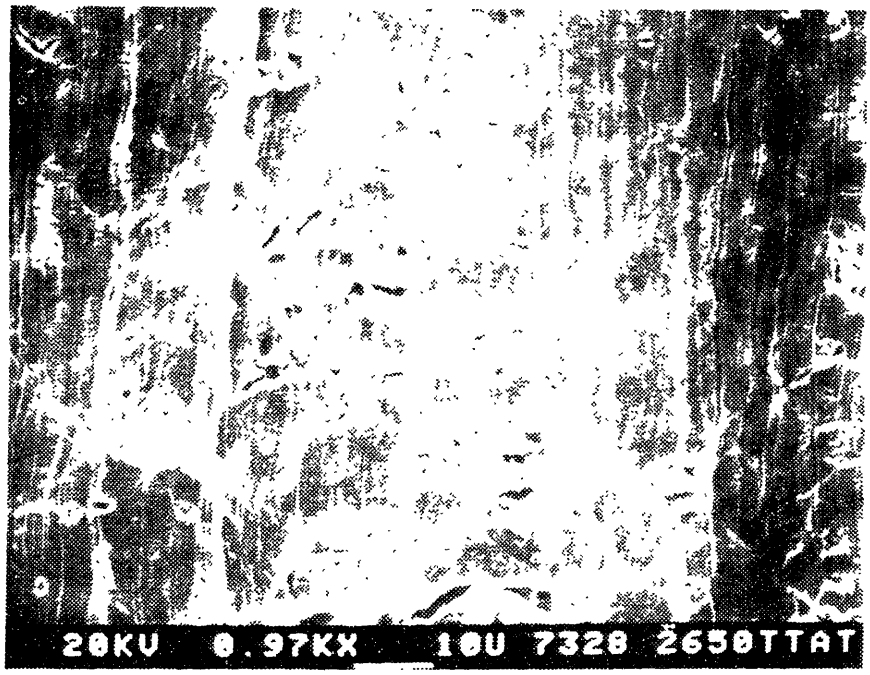

Figure 6.112 The Scanning Electron Micrographs for the Tensile Specimen of the Thermally Treated Condition of Heat NX2650 Tested at a Strain Rate of $1.7 \times 10^{-4} sec^{-1}$ at 360 C (upper fracture surface lower side wall).

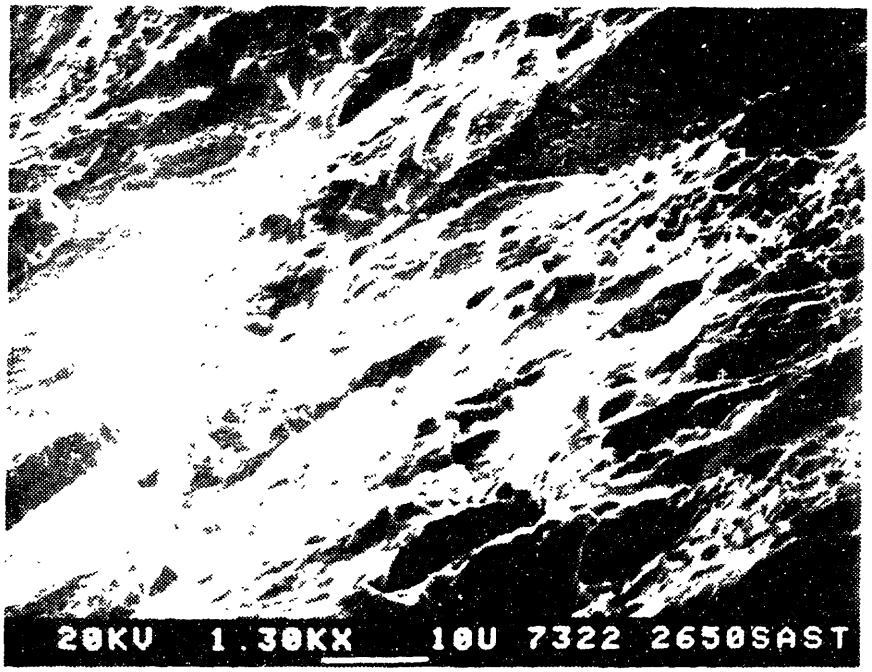

Figure 6.113 The Scanning Electron Micrographs for the Tensile Specimen of the Solution Annealed and Sensitized Condition of Heat NX2650 Tested at a Strain Rate of $2.2 \times 10^{-4} sec^{-1}$ at 30 C (upper fracture surface lower side wall).

is much larger. The increased grain size and intergranular carbide precipitation by the SAS treatment are believed to be responsible for the increased ductility.

6.3.2 Tensile Properties of Alloys X-750 and 718.

The tensile properties of AH, HTH, and HOA conditions of alloy X-750 heat 96457E6 were determined, as a part of another program, by Sheeks [50]. However, a new specimen design with a notch used in the SSRT required knowlege of tensile properties for the specific geometry. Therefore, tensile tests were performed on the alloys at a temperature of 350°C in laboratory air.

The reference tensile data for the AH condition was obtained at 350°C in the high purity water using a higher strain rate so that no environmental effect was introduced. The data is presented later in the discussion of the SSRT results. Hence, only two tests were made for the HTH condition of X-750 and the CHT condition of 718 using a strain rate of $5.3 \times 10^{-4} sec^{-1}$.

The results are compared in Figure 6.114. One striking feature in the stress-strain curve is the absence of a well-defined yield behavior. This is attributed to the notched specimen design which results in a direct transition to the necking process before any significant uniform plastic deformation. It turns out that serrated yielding is the primary process of the plastic deformation at this temperature. Hence, the yield strength is approximated by the stress before the first evidence of serrated yielding. The estimated yield strengths are 992MPa for the HTH condition and 1560 MPa for the CHT condition. The ultimate tensile strengths are found to be 1349 MPa and 1728 MPa for the HTH and CHT condition, respectively. These values for HTH are about 30% higher than the tensile strength obtained using a smooth bar specimen. The strains were measured using a LVDT with knife-edge attachments for the elastic deformation. The plastic strains were measured based on the cross-head displacement. Elongations are found to be 40.4% and 16.3% with a specific plastic work of 672 MPa and 683 MPa for the HTH and CHT

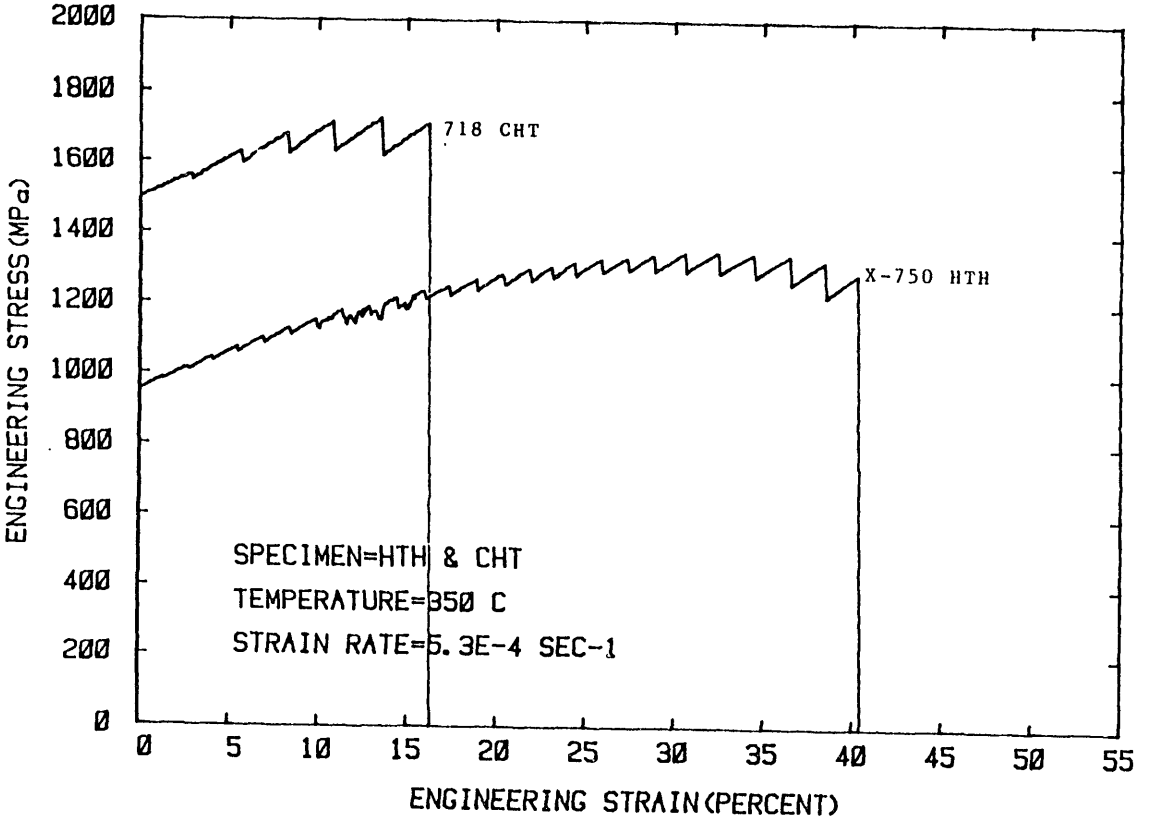

Figure 6.114 The Stress-strain Curves for the HTH Conditions of Alloy X-750 and the CHT Condition of Allot 718 Obteained from the Tensile Test with a Strain Rate of $5.3x10^{-4}$ $sec.^{-1}$ at 360 C.

condition, respectively.

The SEM fractographs are shown for the HTH condition in Figure 6.115. In the typical cone-and-cup fracture surface, the central core contains about 50% intergranular facets. The outer rim shows shear lips with no intergranular fracture. The side wall reveals a roughened surface due to slip deformation, but there are no visible cracks. Therefore, the fracture may be characterized by microvoid coalescence followed by the shear rupture.

The fractographs for CHT condition are shown in Figure 6.116. A cup-and-cone fracture mode is also found in this specimen. The central core region contains a significant amount of intergranular facets which are covered with microvoids. The side wall deformation is less pronounced. However, a few surface cracks are observed. The fracture process is believed to be microvoid coalescence followed by shear rupture.

The observation of serrated yielding requires explanation in connection with the fractographic observation. There was a loud acoustic emission at each load drop. The loudness increased with further deformation which is consistent with increasing load drop with strain. Propagation of Luder's band is believed to be responsible for the phenomenon since the alternative phenomenon of microvoid coalesence does not occur until the end of plastic deformation. Finer serrated yielding in the HTH condition compared with the CHT condition indicates a more homogeneous deformation in the HTH condition.

6.3.3 The Ductility of Hydrogen Charged AES Specimen

Elongation to fracture of the AES specimen was determined from time-to-failure data of the in-situ fracture within the ultra-high vacuum chamber at a constant extnesion rate of 7×10^{-4} cm/sec [139]. This translates to a strain rate of 1×10^{-3} sec^{-1} for the AES specimen with a reduced section length of 0.7cm. Due to lack of load measuring

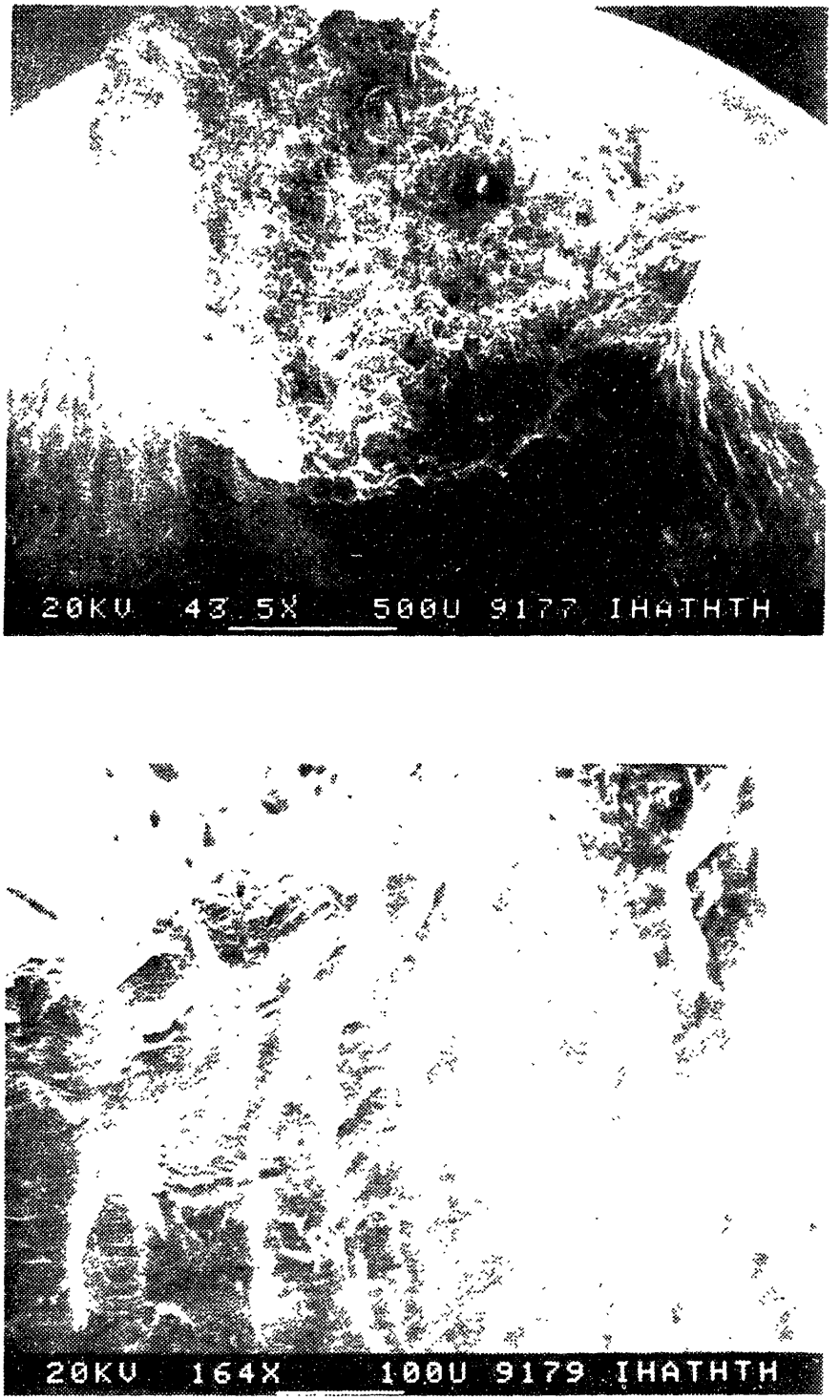

Figure 6.115 The Scanning Electron Micrographs for the Tensile Specimen of the HTH Condition of Alloy X-750 Tested at a Strain Rate of $5.3 \times 10^{-4} sec^{-1}$ at 360 C (upper fracture surface lower side wall).

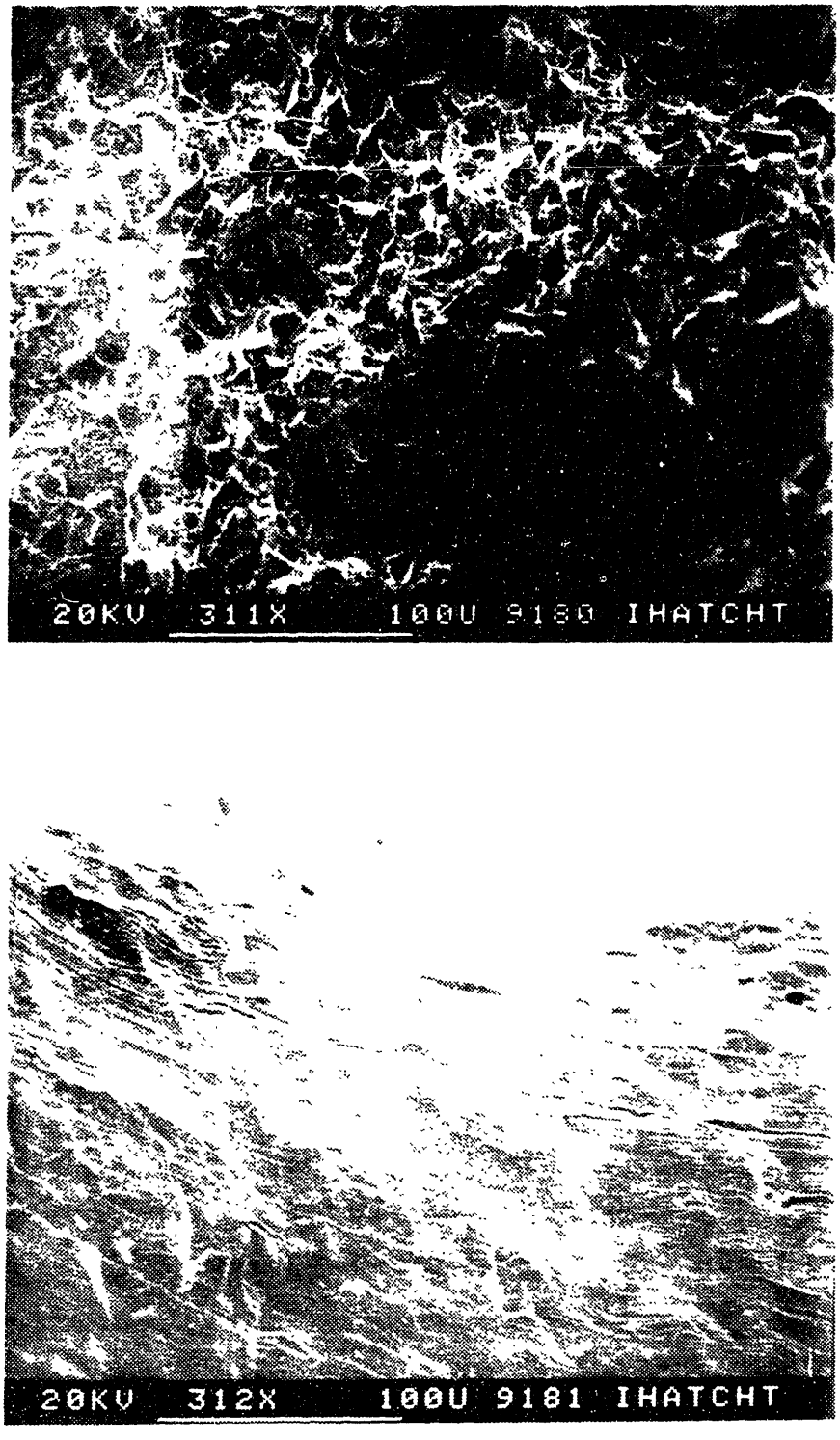

Figure 6.116 The Scanning Electron Micrographs for the Tensile Specimen of the CHT Condition of Alloy 718 Tested at a Strain Rate of $5.3 \times 10^{-5} sec^{-1}$ at 360 C (upper fracture surface lower side wall).

capacity, it was necessary to make sure the specimen was tightened in tension in the loading jig. This was done by finger tightening of the threaded knob of pull rod which extends outside the vacuum seal. A few specimens of alloy 600 were broken during the finger tightening indicating that a significant stress is applied by the process. These specimens are not included in the ductility measurement. Although a large uncertainty exists in the procedure and data, the data is considered to provide a comparative basis on the hydrogen induced ductility loss.

The results with alloy 600 are shown in Figure 6.117. The ductility loss for the mill annealed alloy 600 specimens are insignificant. The TT condition of NX2650 shows, however, a considerable loss in the ductility after the hydrogen charging. This condition showed the highest phosphorus concentration at grain boundaries among the alloy 600 specimens.

The results with alloy X-750 are summarized in Figure 6.118. Except for the as received condition, all the conditions of X-750 show a large degree of ductility loss. When the elongation is compared with the tensile test data obtained at room temperature air, the most significant effect is observed with the HTH and AHTH condition.

It should be noted that the specimens were charged at a high current density of $8mA/cm^2$ and for a time longer than a week. Hence it may be assumed that a hydrogen saturation is achieved for the specimens. Therefore, the ductility loss indicates the susceptibility to hydrogen embrittlement in the environment where the hydrogen supply is sufficient to result in significant accumulation within the material.

6.3.4 Summary

Tensile tests were performed on the heats NX1638, NX2650 and 96834 of alloy 600 tubing. Yield strength was the highest with heat NX2650, and ultimate tensile strength was the highest with the heat 96834. The heat NX1638, having a larger grain size, showed lowest values of both yield

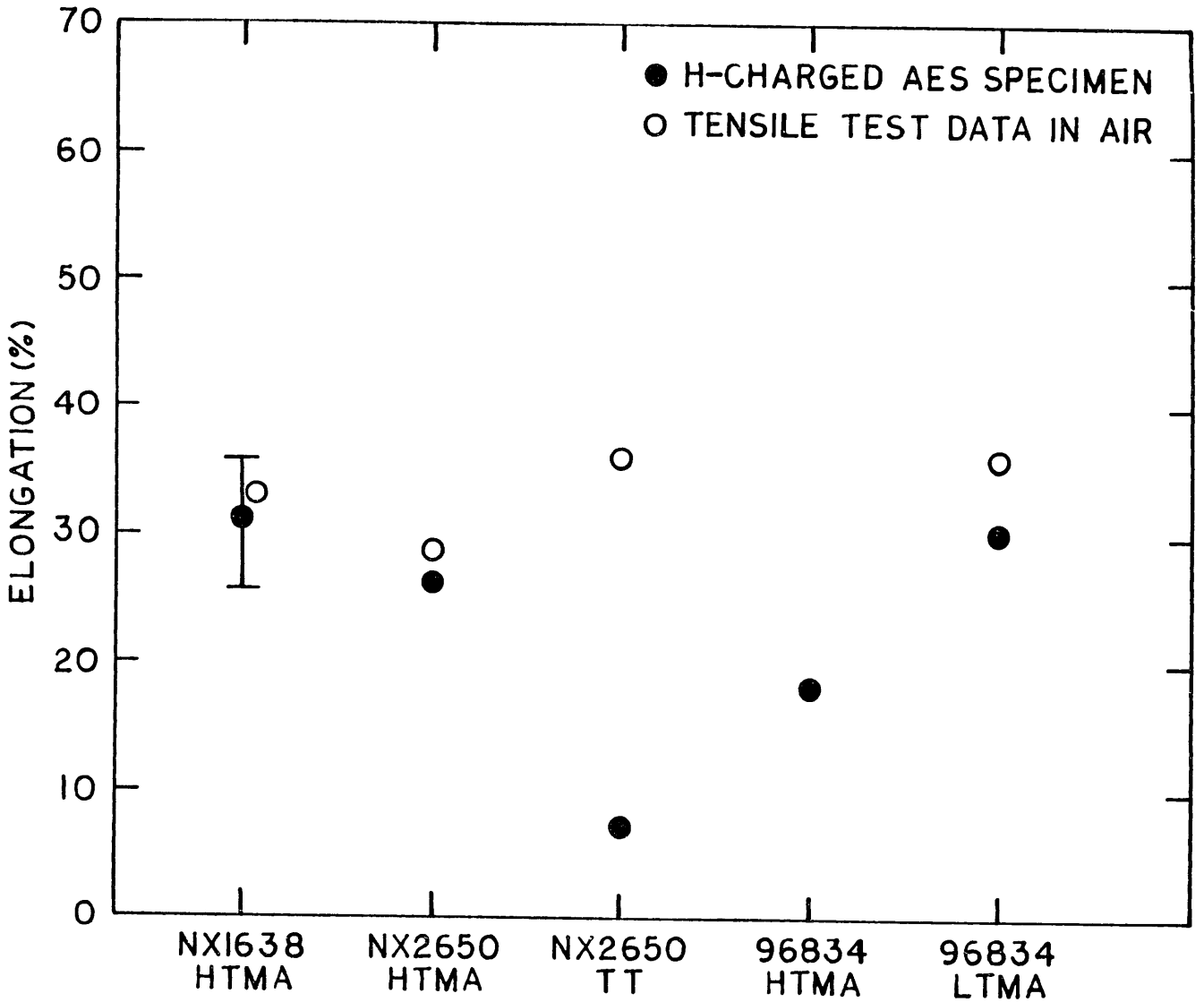

Figure 6.117 The Estimated Elongation of Hydrogen Charged AES Specimens of Alloy 600.

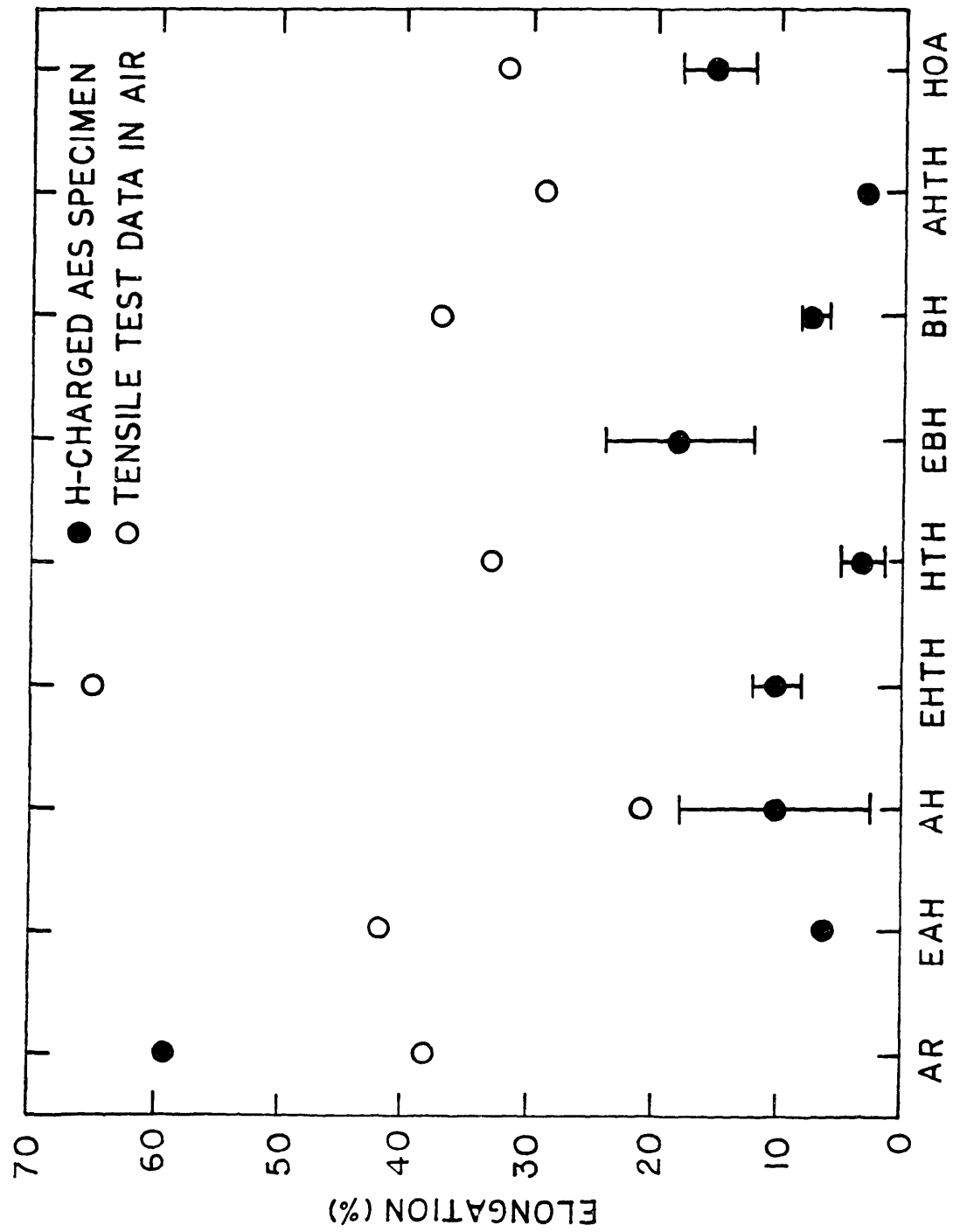

Figure 6.118 The Estimated Elongation of Hydrogen Charged AES Specimens of Alloy X-750.

strength and ultimate tensile strength. The thermal treatment from the HTMA condition of NX2650 resulted in about 15% decrease in the yield strength and change in the ultimate tensile strength but with about a 10% increase in ductility and specific plastic work. The SAS conditon of NX2650 showed a significant increse in ductility and the fracture energy at the expense of strengths as the results of increased grain size. Temperature increase from 30°C to 360°C resulted in about 12% reduction in the yield stregth with only marginal decrease in the ultimate tensile strength. The strengths were insignificantly affected by a 10 times lower strain rate although a consistent increase was observed in ductility.

All the fracutre surfaces were characterized by microvoid coalescence followed by a shear rupture with littel differences in appearance among the conditions. Side wall observation revealed a significant differnce in the nature of the surface as a result of slip step emergence. Relatively homogeneous deformation was evident in NX1638 which showed side walls characterized by numerous and fine staircase type slip steps without formation of surface crack. More localized slip was observed in NX2650 where an intersection of slip steps or carbide inclusions resulted in sharp transgranular crystallographic crackings of a size about 10μm by 10μm. In the specimen of heat 96834, no localized slip steps or intersection was observed despite the same grain size as that of NX2650. There were, however, numerous fine surface cracks with a typical length of 5μm aligned in perpendicular to the loading axis. Similar surface cracks, but about twice the size were found in the TT condition of NX2650. Heat NX2650 showed significant slip localization. The SAS condition showed a distinct fracture surface which was characterized by patches of elongated segments. The side wall observation suggested that the patches may have formed by the intersection of slip bands.

The effect of hydrogen charging on the ductility of alloy 600 was examined based on approximated elongation of the AES in-situ fracture specimens. All the mill annealed conditions of alloy 600 tubing showed insignificant ductility loss after the hydrogen charging. The TT

condition of NX2650 revealed a considerable ductility loss.

Tensile tests on alloys X-750 and 718 were done for the HTH and CHT conditions with a notched bar design. The yield strength was not well defined in the notched bar design. Plastic deformation was discontinuous with characteristics of serrated yielding which emitted acoustic noise at each load drop. The ultimate tensile strength were found to be about 30% higher than those obtained with a smooth bar design. The fracture surfaces for both conditions were characterized by a typical ductile fracture process of microvoid coalescence followed by a shear rupture.

The ductility of alloy X-750 AES specimens is found to decrease significantly with hydrogen charging. No systematic dependence on heat treatment was observed although the HTH and AHTH conditions showed the highest ductility loss. Therefore, all the aged X-750 conditions were believed to be susceptible to a hydrogen embrittlement in an environment where the hydrogen supply is sufficient.

6.4 STRAINING ELECTRODE TENSILE BEHAVIOR

6.4.1 Determination of Test Conditions

The straining electrode tensile tests (SETT) were performed to examine the interaction between electrochemical process and mechanical behaviors Marterials used were the AH, HTH, and HOA conditions for the alloy X-750, the CHT conditon for the alloy 718, and $Ni_3Al(Co=0.1)$. No test was done on the alloy 600 tubing since the thickness was too small to be machined into the required specimen geometry. Two strain rates, 6.7×10^{-4} sec^{-1} and 6.7×10^{-5} sec^{-1}, are selected to simulate the crack tip strain rates of the fatigue cracks at frequency of 1 Hz and 0.1 Hz, respectively. Anodic or cathodic overpotential of about 225 mV in each direction was applied. This overpotential is determined to simulate the effect of galvanic corrosion, based on considerations described as follows.

The amount of galvanic overpotential needs to be measured taking into account the effect of plastic deformation as well as the galvanic coupling. The Ni_3Al(Co=0.1) specimen was coupling with an HTMA condition of Alloy 600 which represents the solution annealed X-750. Since the cathodic reaction may be rate controlling when the surface area is insufficient, a surface area of the cathode used ($50cm^2$) was about 50 times that of the Ni_3Al (Co=0.1). The result is shown in Figure 6.119. A rapid current transition occurs as soon as the couple is made. A steady state value of 0.5 mA is reached before any significant deformation takes place. In short, Ni_3Al(Co=0.1) was found to have a limitng galvanic current density of 0.5mA which is unaffected by deformation.

The initial current increase is attributed to slow cathodic reaction considering that anode, Ni_3Al(Ti=0), is known to be non-passivating, as observed in section 6.2. Since the surface oxide has lower hydrogen exchange current density its gradual reduction by the adsorbed hydrogens would result in faster cathodic reaction. Assuming that surface coverage of the oxide decreases with total amount of hydrogen on the surface, the current can be determinned as follows;

$$i(t)/i_\infty = 1-\exp(a-bt) \qquad (6-7)$$

where i_∞ is the limiting current density, t is time and a and b are constants. The data are plotted based on the derived relation, and shown in Figure 6.120. There is good agreement for the initial transient.

With the galvanic current density of 0.5 mA/cm^2, the overpotential during SETT can be selected based on the results of previous polarization studies. The corresponding overpotentials are found to be about 100mV in the anodic direction for gamma prime and the same in the cathodic direction for the matrix. An overpotential of 100 mV may not be high enough to minimize the influence of test-to test-variation in

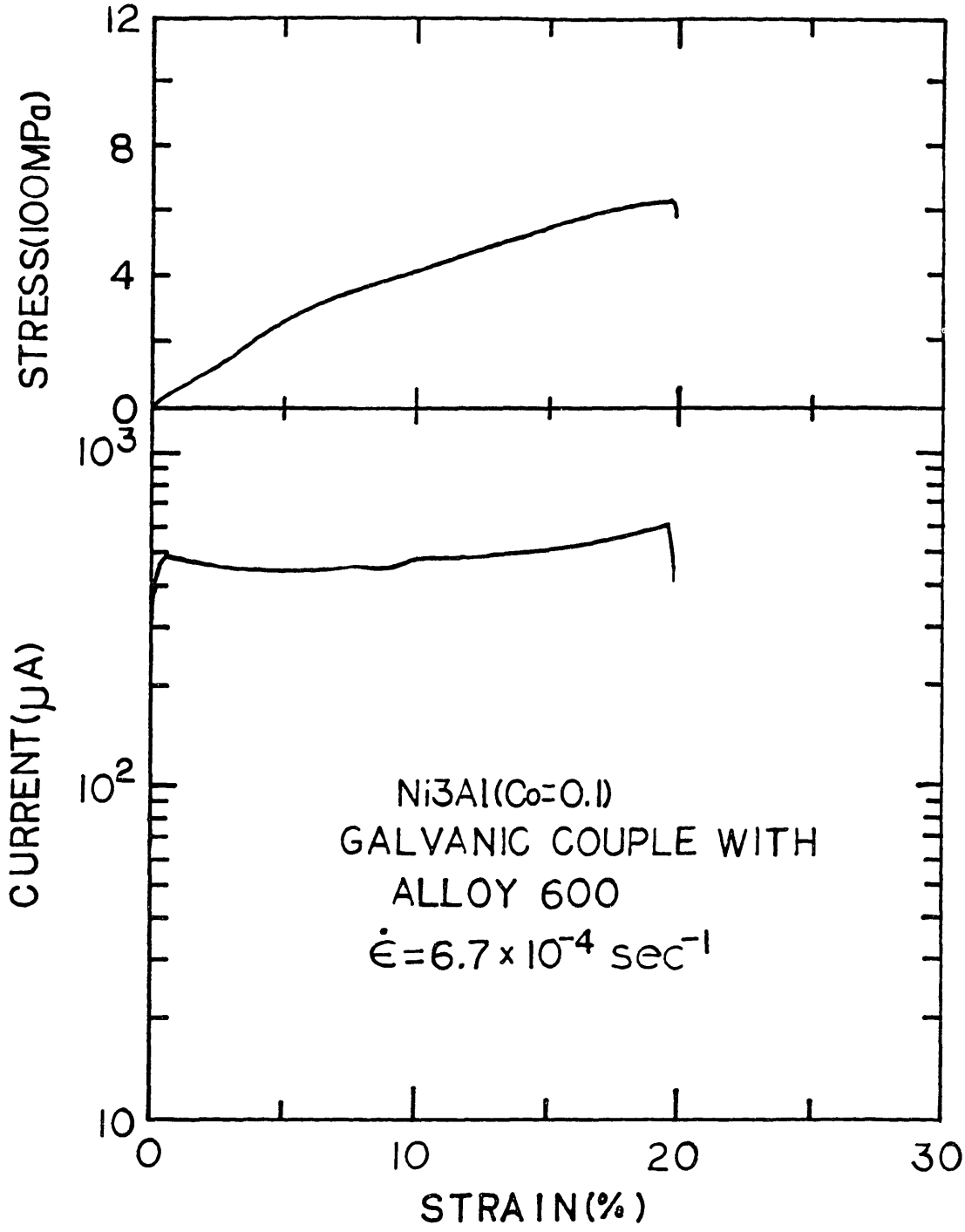

Figure 6.119 The SETT Results of the Ni_3Al(Co=0.1) Galvanically Coupled with Alloy 600 in a 0.05M Na_2SO_4 (pH=3) Solution at 93 C with a Strain Rate of 6.7×10^{-4} sec^{-1}.

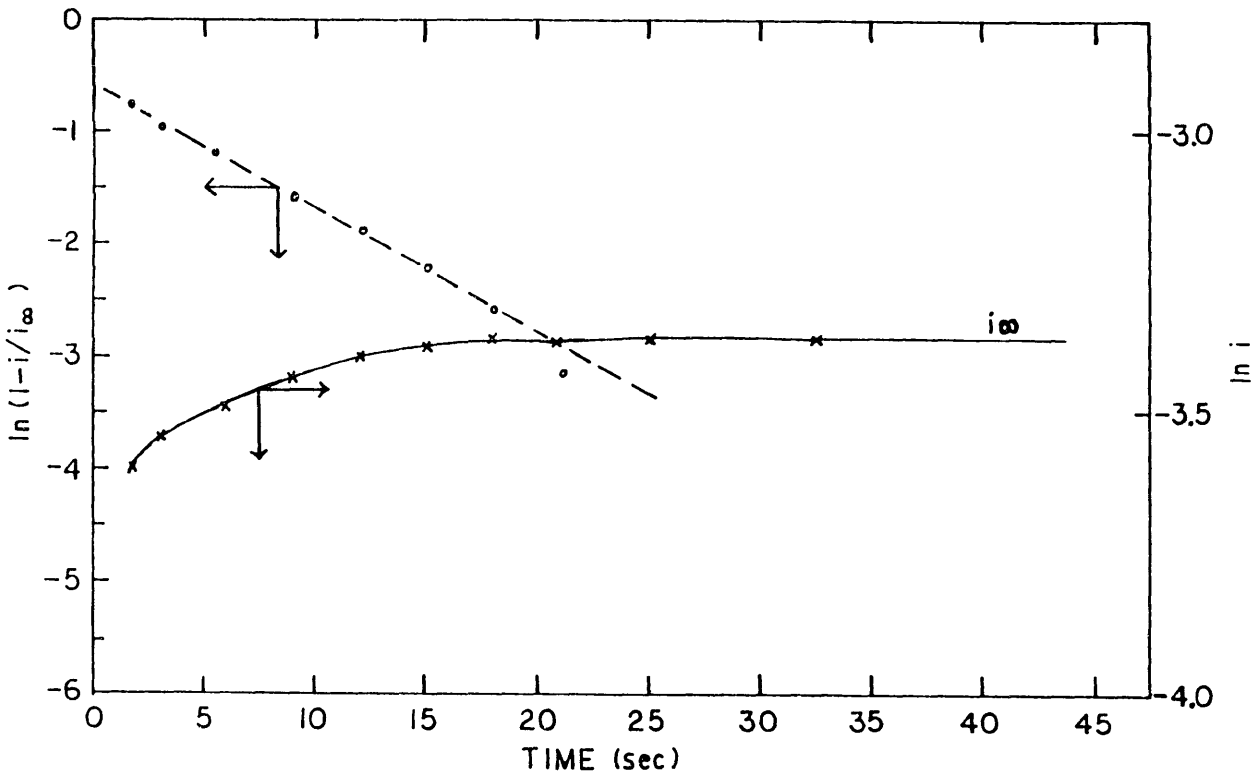

Figure 6.120 Initial Current Transient during the SETT of Ni_3Al(Co=0.1) in Galvanic Couple with Alloy 600.

corrosion potential which is about 10 mV to 50mV. To provide for a more invariant electrochemical conditions about twice the value was taken. This corresponds to an anodic potential of 0 V(S.H.E.) and a cathodic potential of -0.45 V(S.H.E.).

The fractographs for the Ni_3Al(Co=0.1) specimen are shown in Figure 6.121. The fracture surface is mostly intergranular. A small portion near the edge shows ductile rupture with microvoids. The side wall reveals a few intergranular cracks which are aligned perpendicular to the loading axis. However, the intergranular cracking is believed to be a purely mechanical phenomenon since a specimen broken in air also showed similar fracture.

6.4.2 Results at Free Corrosion Potential

Test result at the corrosion potential for the AH condition are shown in Figure 6.122. The current was measured by maintaining the specimen potential at the initial value of -213 mV(SHE). A current transient is observed during the early stage of elastic deformation. A cathodic current density of about $6\mu A/cm^2$ is sustained for subsequent deformation until necking of the specimen. The development of a small cathodic current at the initial corrosion potential suggests that the corrosion potential is perturbed in the anodic direction by deformation. This may be represented by the shifts in both the anodic and cathodic Tafel lines to the right on the Evans diagram in such a way that they intersect at the final corrosion potential. The corrosion potential of the AH condition was decreased by about 10 mV by cathodic cleaning of the surface indicating that the shift of anodic line has greater effect. In addition, the increase in corrosion potential may be due to a greater shift in cathodic Tafel line by the deformation. The explanation should be supported by additional data which show the effects of the strain rate and various techniques of the surface cleaning. The SEM fractographs are shown for the AH specimen in Figure 6.123. The cross section appears to have two different fracture modes. The central region has a fracture surface nearly perpendicular to the loading axis

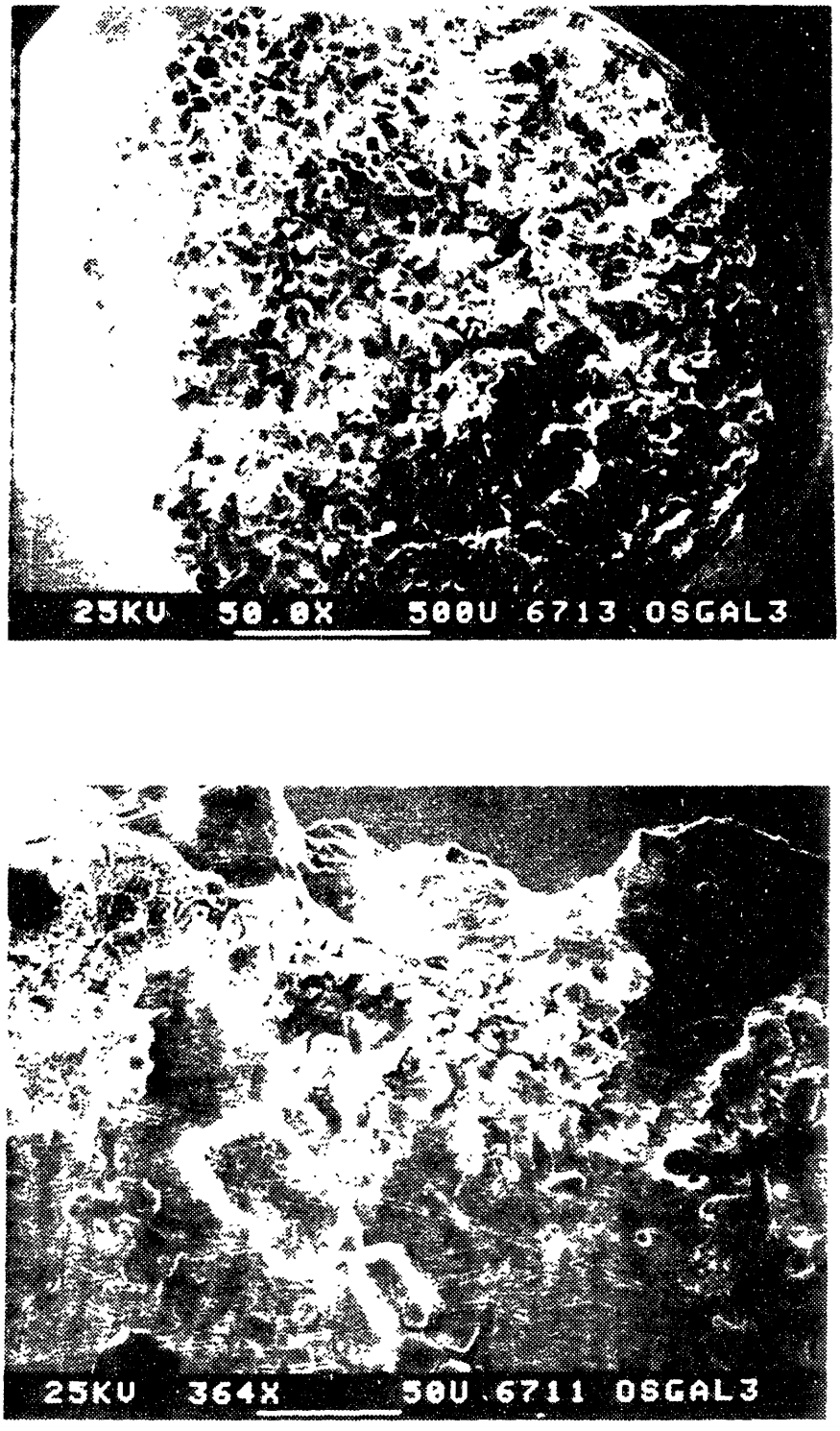

Figure 6.121 The SEM Fractographs of the Ni_3Al(Co=0.1) Galvanically Coupled with Alloy 600 in a 0.05M Na_2SO_4 (pH=3) Solution at 93 C with a Strain Rate of $6.7x10^{-4}$ sec^{-1}.

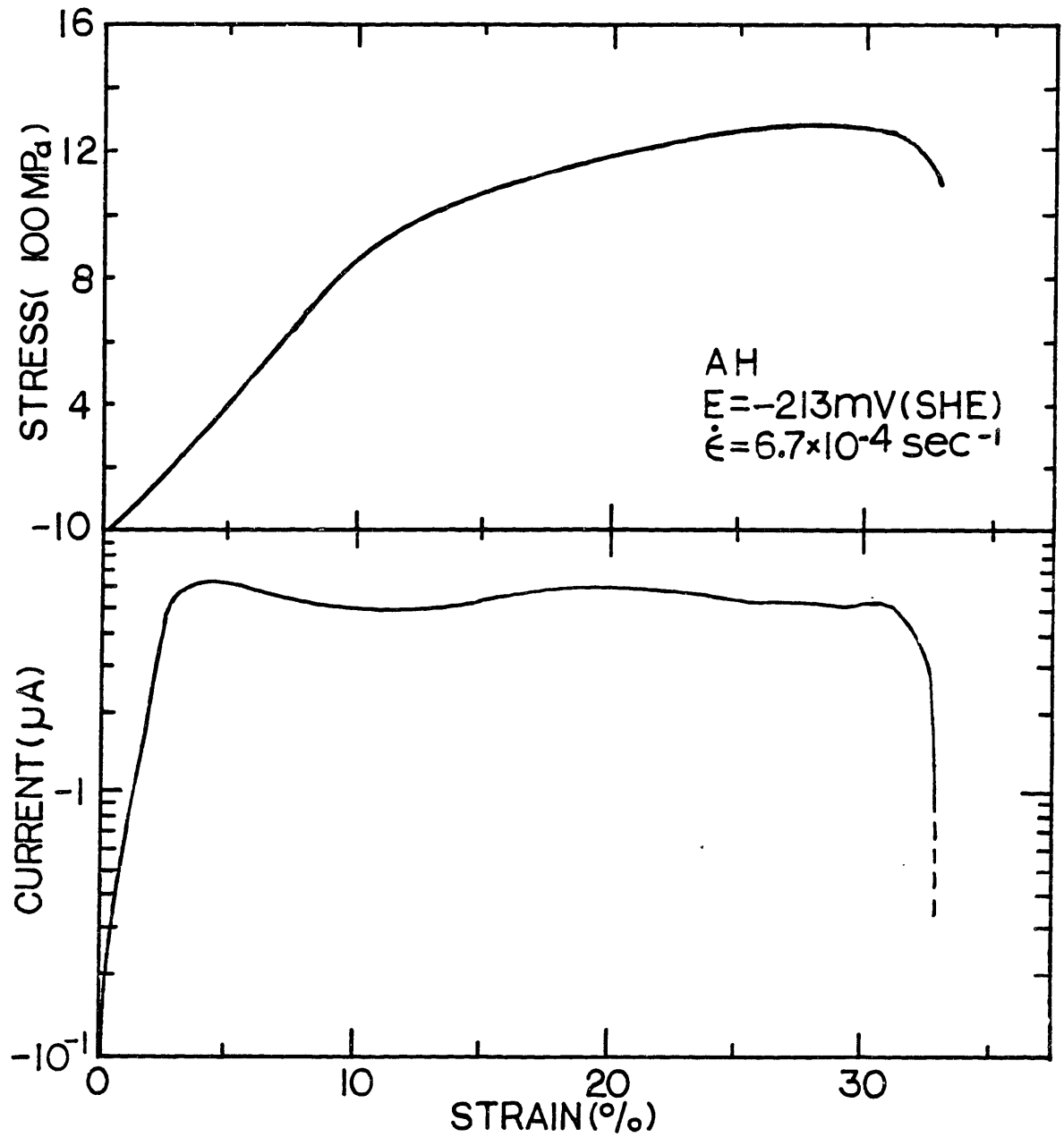

Figure 6.122 The SETT Results of the AH Condition in a 0.05M Na_2SO_4 (pH=3) Solution at 93 C with a Strain Rate of 6.7×10^{-4} sec^{-1} and a Potential of -213 mV(SHE).

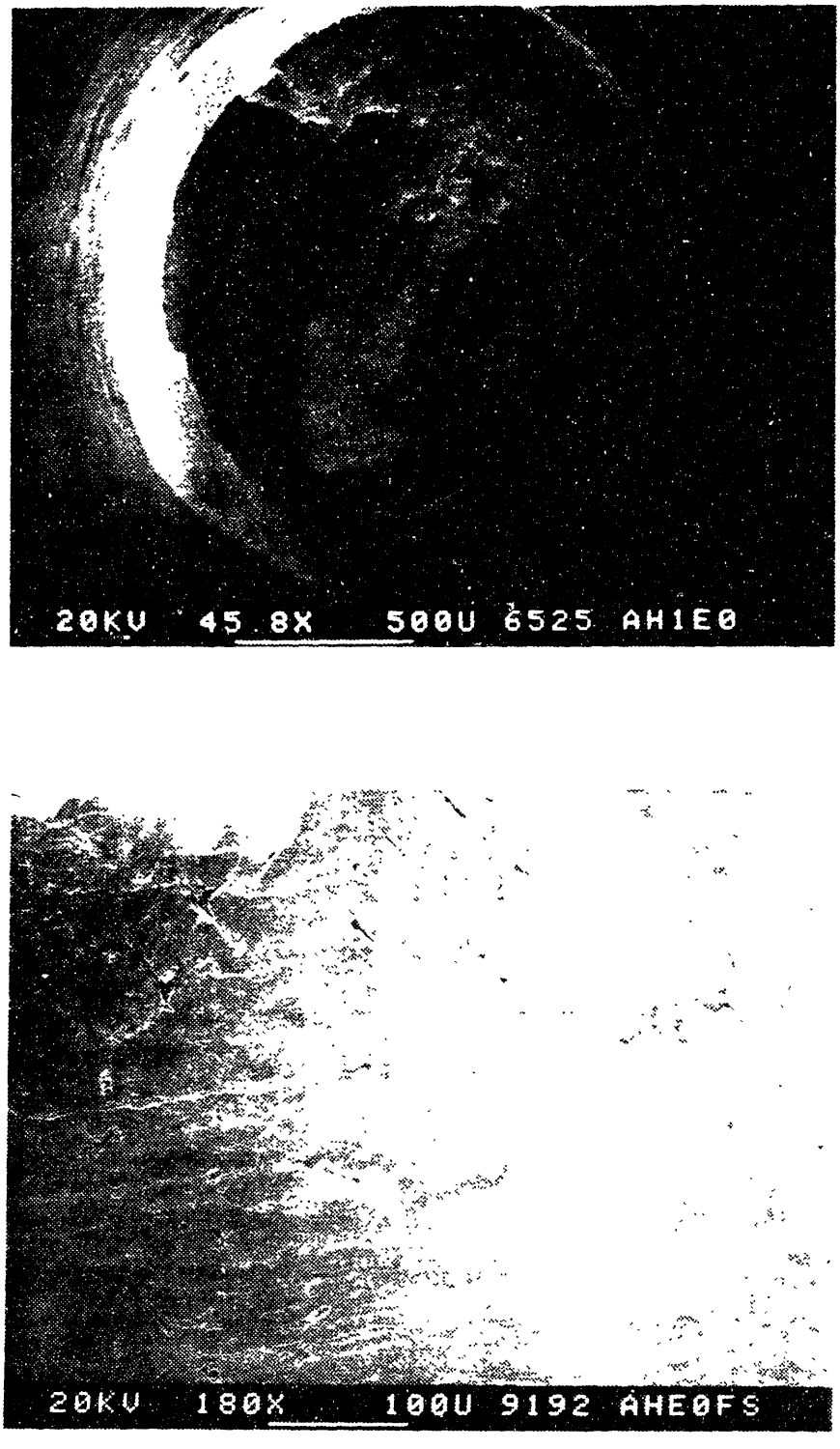

Figure 6.123 The SEM Fractographs of the AH Condition after the SETT in a 0.05M Na_2SO_4 (pH=3) Solution with a Strain Rate of $6.7x10^{-4}$ sec^{-1} and a Potential of -213 mV(SHE).

whereas the peripheral region shows a typical shear rupture at 45° inclination. The difference is mainly due to differnt states of stress depending on the distance from the surface, plane stress state prevailing near the surface and plane strain state in the center. The fracture surface near the specimen surface as well as in the center show ductile rupture type microvoids. There is no secondary crack observed on the side wall of the specimen. All the fractographic observations are consistent with the fact that the measured tensile properties are almost the same as those measured in helium Hence the cathodic current density of $6\mu A/cm^2$ is found to have no effect on the tensile properties.

6.4.3 Results at Anodic Potential

The results with anodic polarization at the higher strain rate are shown for the AH and HTH conditions in Figure 6.124. The anodic current densities show a transition from a low value of $2\mu A/cm^2$ to a steady state value of about $5\mu A/cm^2$ whcih agrees closely with the anodic polarization data of about $8\mu A/cm^2$ [57]. Hence anodic current transients are believed to result from the film rupture during deformation. Although film ductility could not be determined the value appeared to be too small to take any appreciable amount of plastic strain. The current density increases by an order of magnitude until specimen failure. Considering that the surface area of the necking region is only a fraction of entire surface, the effective current density is expected to be as high as the inital current density measured by the potential jump experiments.

The SEM fractographs for the AH specimen at anodic potential are shown in Figure 6.125. The fracture surface is characterized by ductile shear rupture with microvoids. At the edges of shear lips, there is a featureless region which appears to have resulted from anodic dissolution. The side wall ahows a few transgranular crystallographic crackings developed from the slip steps at 45° inclination. Both the yield strength and ultimate tensile strength are decreased by about 5%. The elongation remains unchanged from the value measured at the corrosion potential. Therefore, the surface transgranular

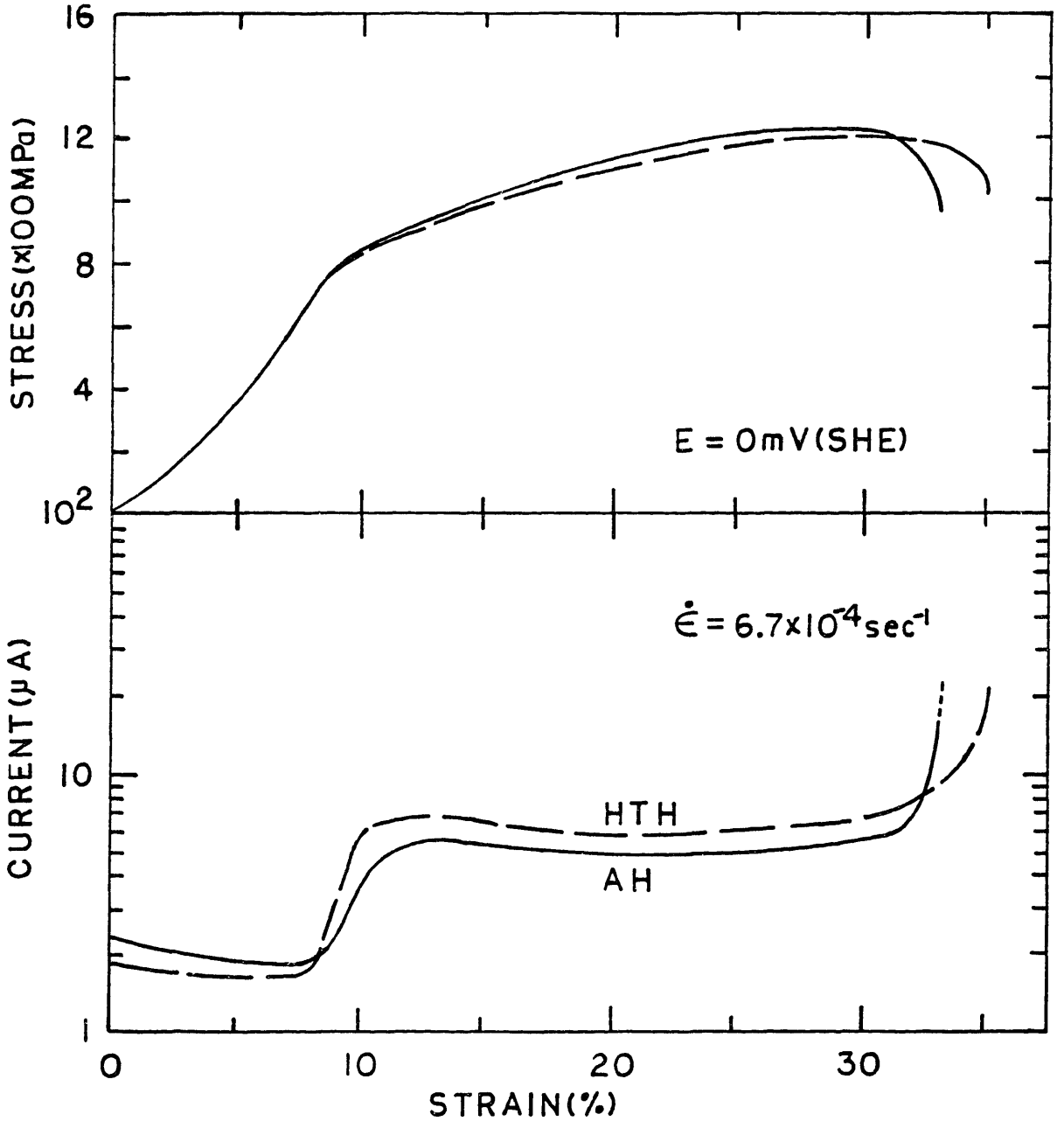

Figure 6.124 The SETT Results of the AH and HTH Conditions in a 0.05M Na_2SO_4 (pH=3) Solution at 93 C with a Strain Rate of 6.7×10^{-4} sec^{-1} and a Potential of 0 mV(SHE).

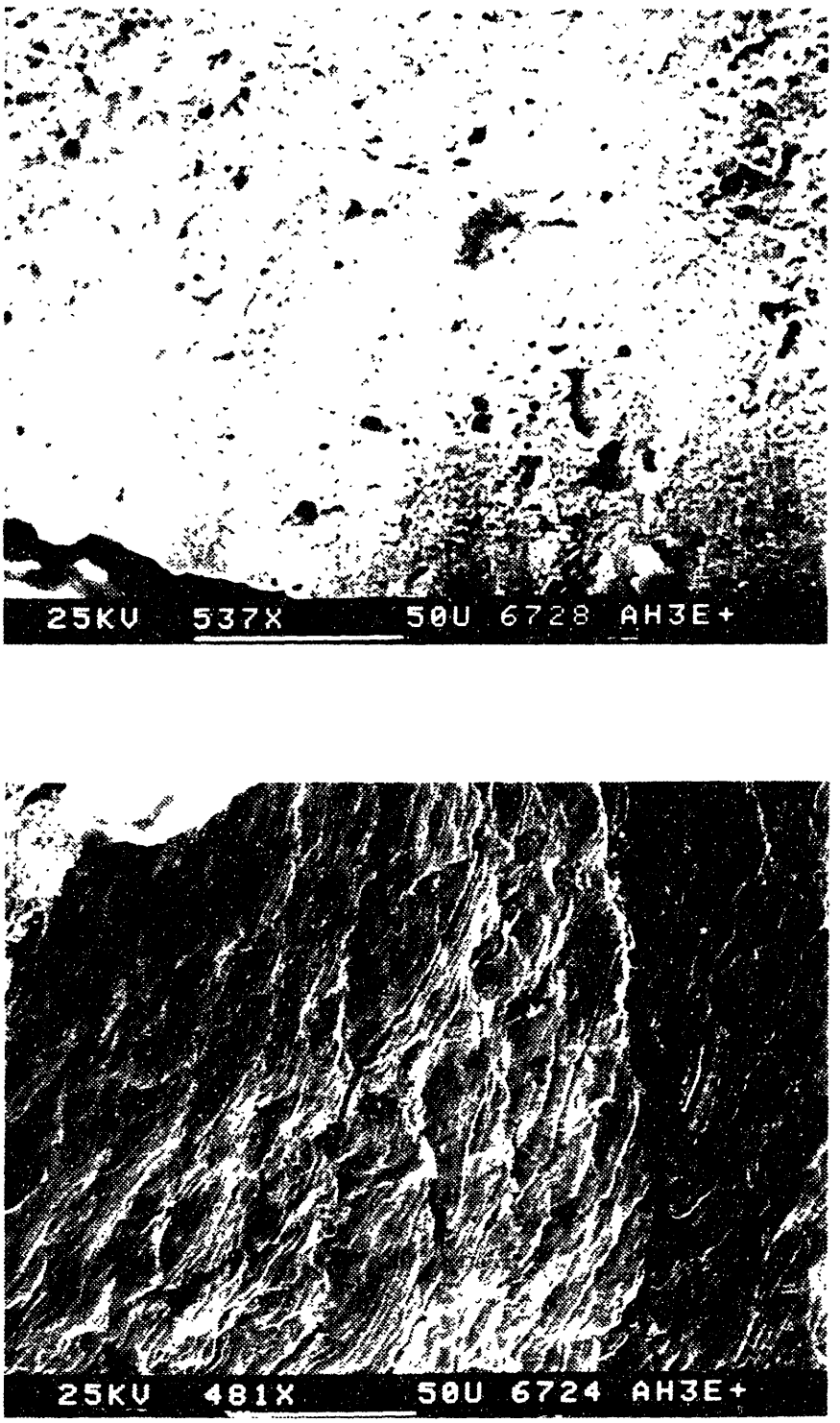

Figure 6.125 The SEM Fractographs of the AH Condition after the SETT in a 0.05M Na_2SO_4 (pH=3) Solution with a Strain Rate of $6.7x10^{-4}$ sec^{-1} and a Potential of 0 mV(SHE).

crystallographic crackings are believed to be too small to affect the tensile properties by any significant degree.

The SEM fractographs for the HTH specimen tested at 0 mV(SHE) and the higher strain rate are shown in Figure 6.126. A ductile rupture mode is predominant over most of the fracture surface except in the central region. The central region shows a small fraction intergranular cracking. This pattern of fracture is also observed in tensile test of the HTH condition [50]. The intragranualr fracture in the specimen center is a purely mechanical phenomenon. The side wall shows no significant damages, but a few transgranular cleaveages at 45^{0} to loading axis. The measured tensile strength is compared with the reference data in Figure 6.138. The small increase in the tensile strength is due to the test-to-test variation. Hence the transgranular transgranular crystallographic crackings on the side wall is believed to be purely mechanical phenomenon. Therefore, it is concluded that there is no effect on the tensile properties due to the anodic polarization.

The test results at the lower strain rate with anodic polarization are presented in Figure 6.127. The AH condition shows an inital current density that is approximately equal to that observed at the higher strain rate. Unlike the higher strain rate case, however, there is no transition to a higher current density with further deformation. As a result, the steady state current density is about $15\mu A/cm^{2}$ which compares well with the passivation current density measured by the polarization. Therfore, the strain rate is believed to be slow enough to allow the continual reformation of the passive film on the deforming surface. The fractographs of the AH condition are shown in Figure 6.128. The fracture surface shows a typical cup-and-cone shape covered with microvoids on most regions. A narrow band of the edge has an evidence of anodic dissolution which resutled in a featureless surface. The side wall shows a small number of transgranular crystallographic crackings at 45^{0} with respect to the loading axis. Hence there is no fractographic difference between this case and the case of higher strain rate for the AH condition. The tensile properties show an appreciable decreases from the reference data. However, the differnce is too small to conclude the

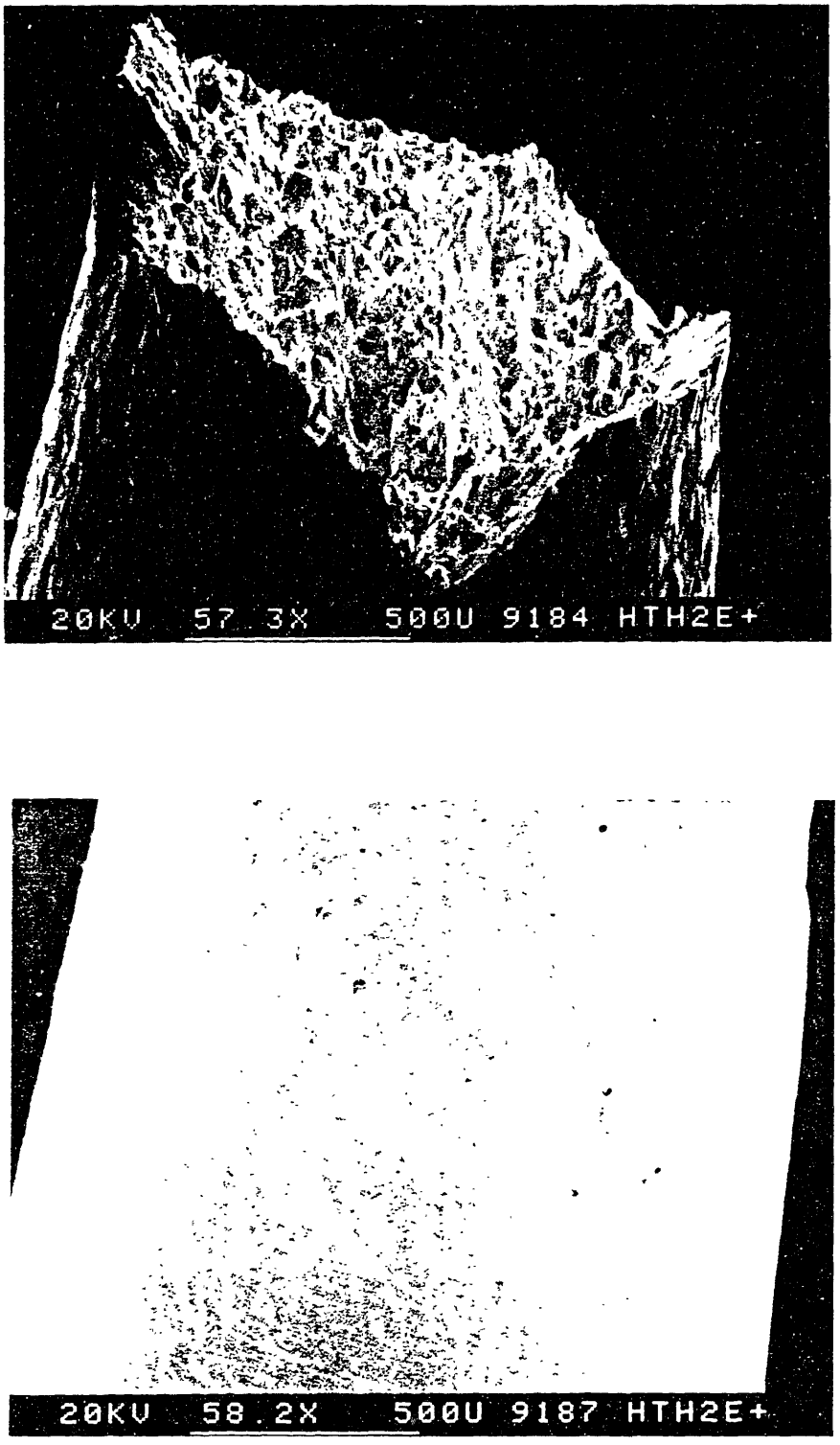

Figure 6.126 The SEM Fractographs of the HTH Condition after the SETT in a 0.05M Na_2SO_4 (pH=3) Solution with a Strain Rate of $6.7x10^{-4}$ sec^{-1} and a Potential of 0 mV(SHE).

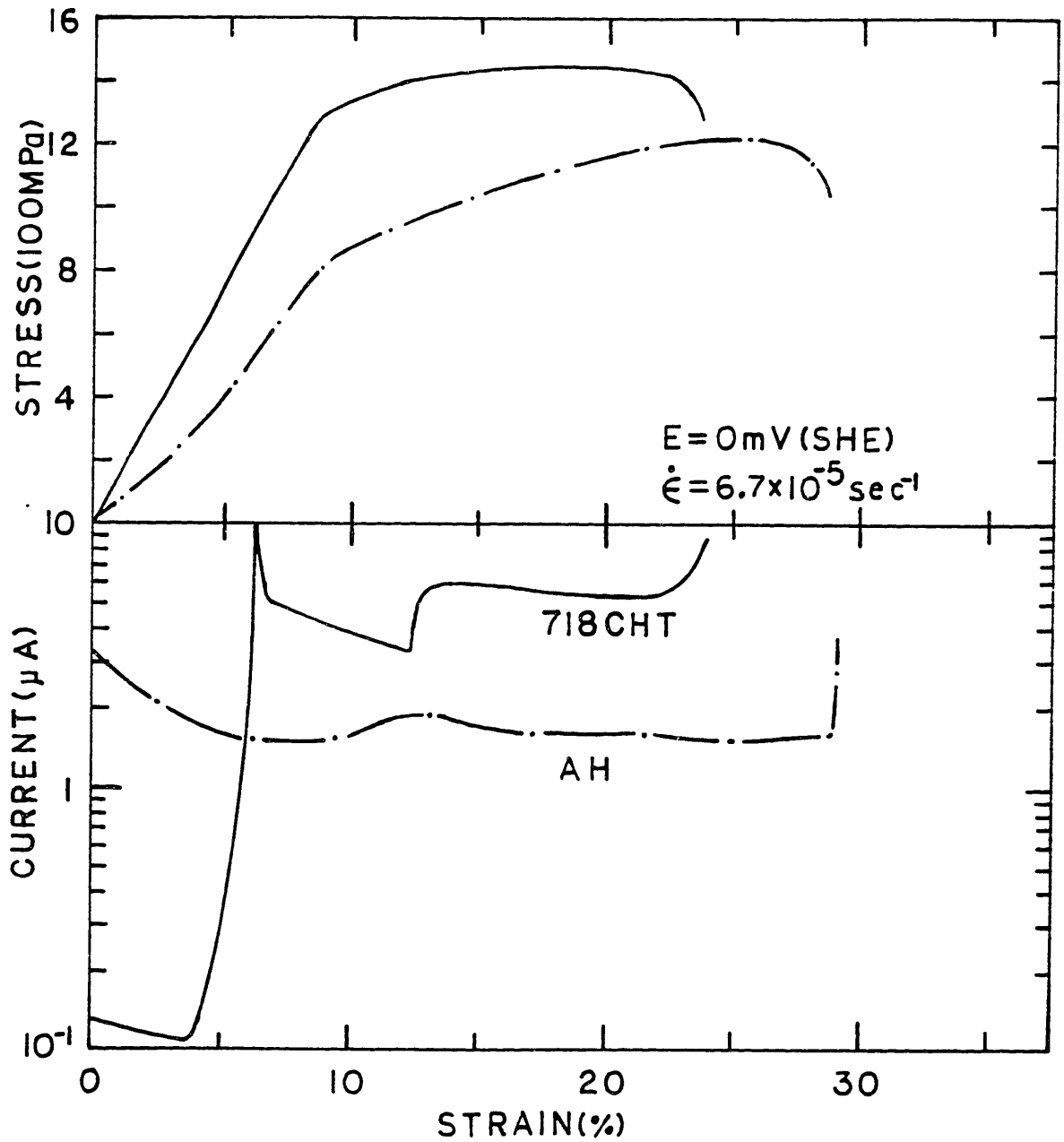

Figure 6.127 The SETT Results of the AH and CHT Conditions in a 0.05M Na_2SO_4 (pH=3) Solution at 93 C with a Strain Rate of 6.7×10^{-5} sec^{-1} and a Potential of 0 mV(SHE).

presence of environmental effects before a statistically significant number of data is obtained.

The CHT condition of the alloy 718 shows a clear transition from an intial low current density to a higher steady state value of about $5\mu A/cm^2$ at the low strain rate. The initial current density is about an order of magnitude smaller than those for the AH and HTH condition. This suggests such a low value for the passivation curernt density. The polarization data in the same environment was, however, not available. The existence of the current transient at the low strain rate suggests that the passive film on the CHT condition may be more brittle than that of the AH condition. There is another current transition at about 12% strain, as shown in Figure 6.127. The strain interval between two transitions, about 6% strain, may be considered as being related to the film ductility at the lower strain rate. SEM fractographs are shown, for the AH and CHT condition, in Figures 6.128 - 6.129. The cup-and-cone fracture surface is characterized by microvoid coalescence followed by ductile shear rupture. There is a small region at the specimen edge which is featureless as a result of anodic dissolution. The side wall shows a moderate number of small transgranular cracks eminating from slip steps. The measured tensile properties indicate no environmental effect under anodic polarization.

6.4.4 Results at Cathodic Potential

The results at the cathodic potential for the AH and HTH conditions are presented in Figure 6.130. The AH material shows a current transition during elastic deformation which suggests the surface film reduces the cathodic current density. The same amount of overpotential in the cathodic direction results in a significantly higher value of the absolute current density during the steady state compared with the anodic polarization case. The SEM fractographs for the AH material are shown in Figure 6.131. When compared with the cases with the anodic polarization and at the corrosion potential, there is clear evidence that the fracture surface consists of several sharp edges of a triangular shape. The side wall reveals a number of cleavages at 45^0 to

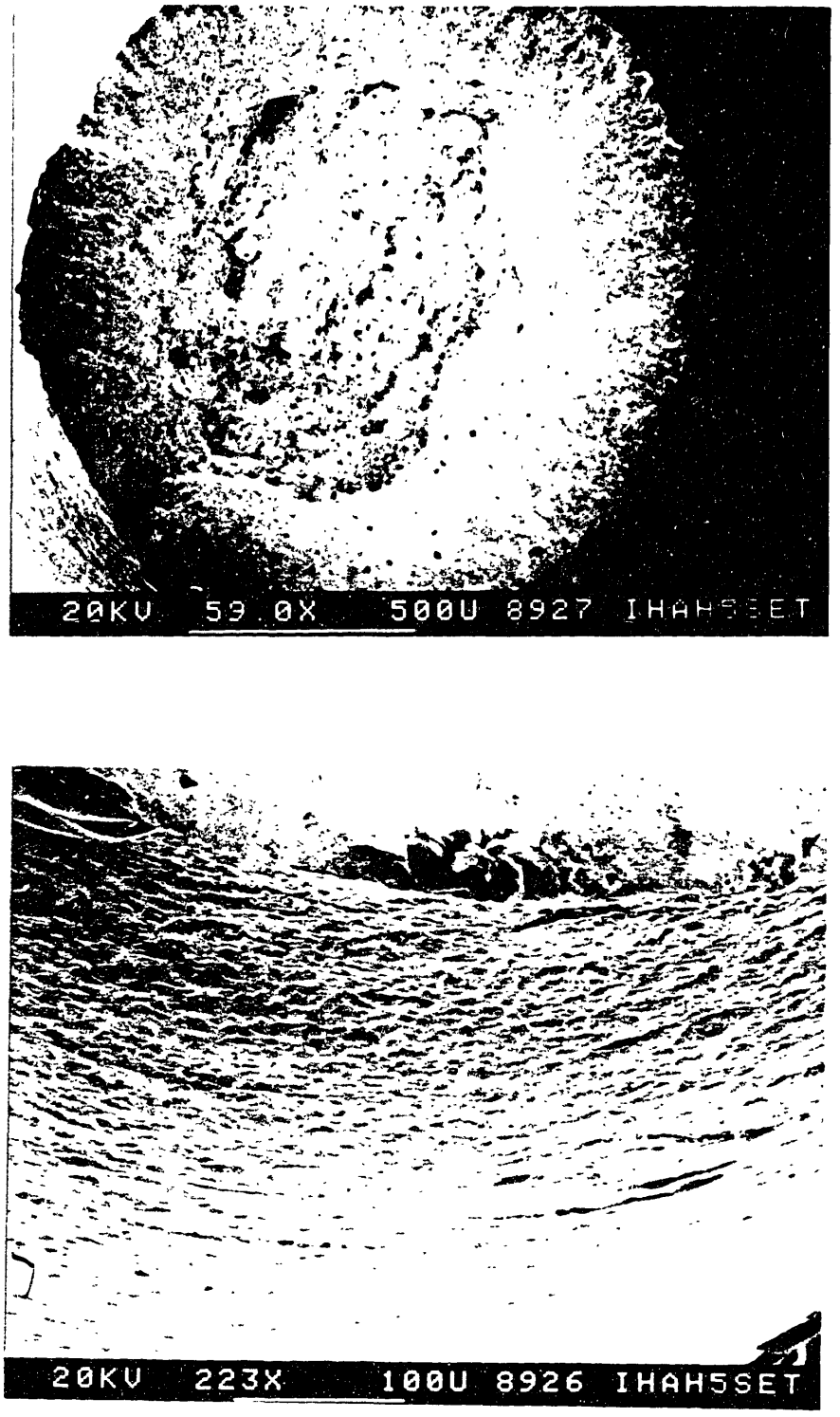

Figure 6.128 The SEM Fractographs of the AH Condition after the SETT in a 0.05M Na_2SO_4 (pH-3) Solution with a Strain Rate of $6.7x10^{-5}$ sec^{-1} and a Potential of 0 mV(SHE).

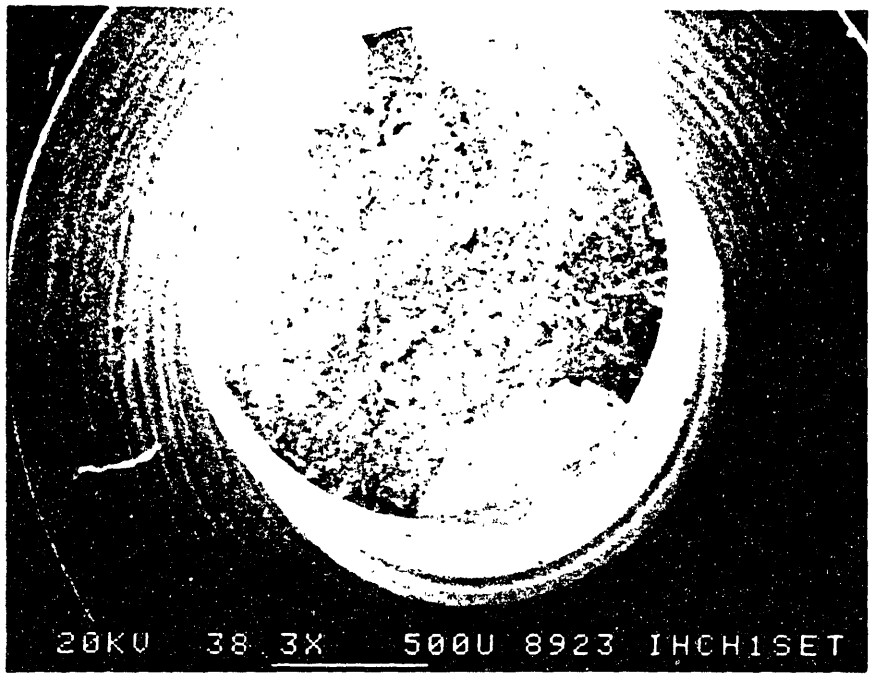

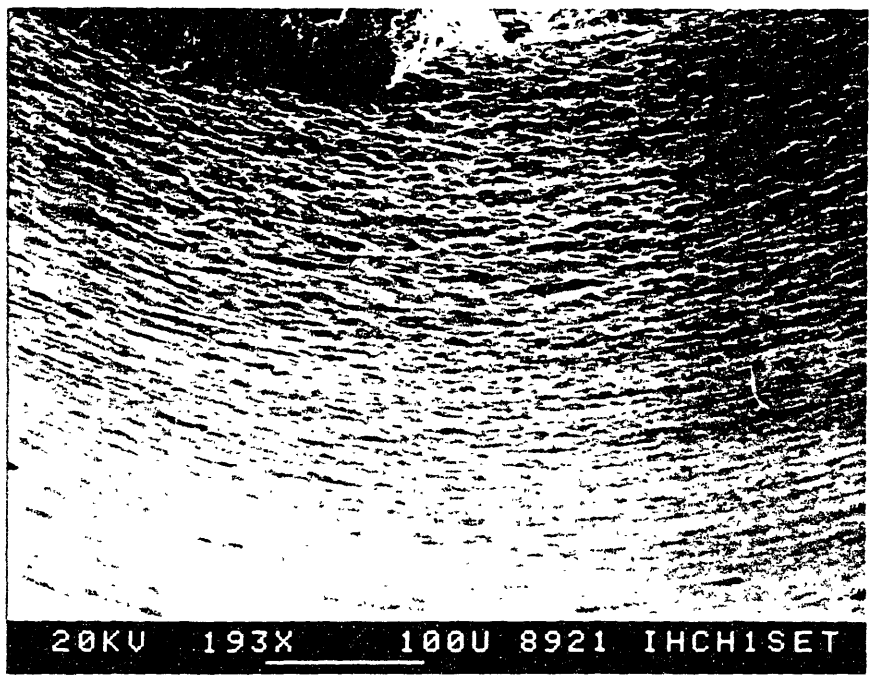

Figure 6.129 The SEM Fractographs of the CHT Condition after the SETT in a 0.05M Na_2SO_4 (pH-3) Solution with a Strain Rate of $6.7x10^{-5}$ sec^{-1} and a Potential of 0 mV(SHE).

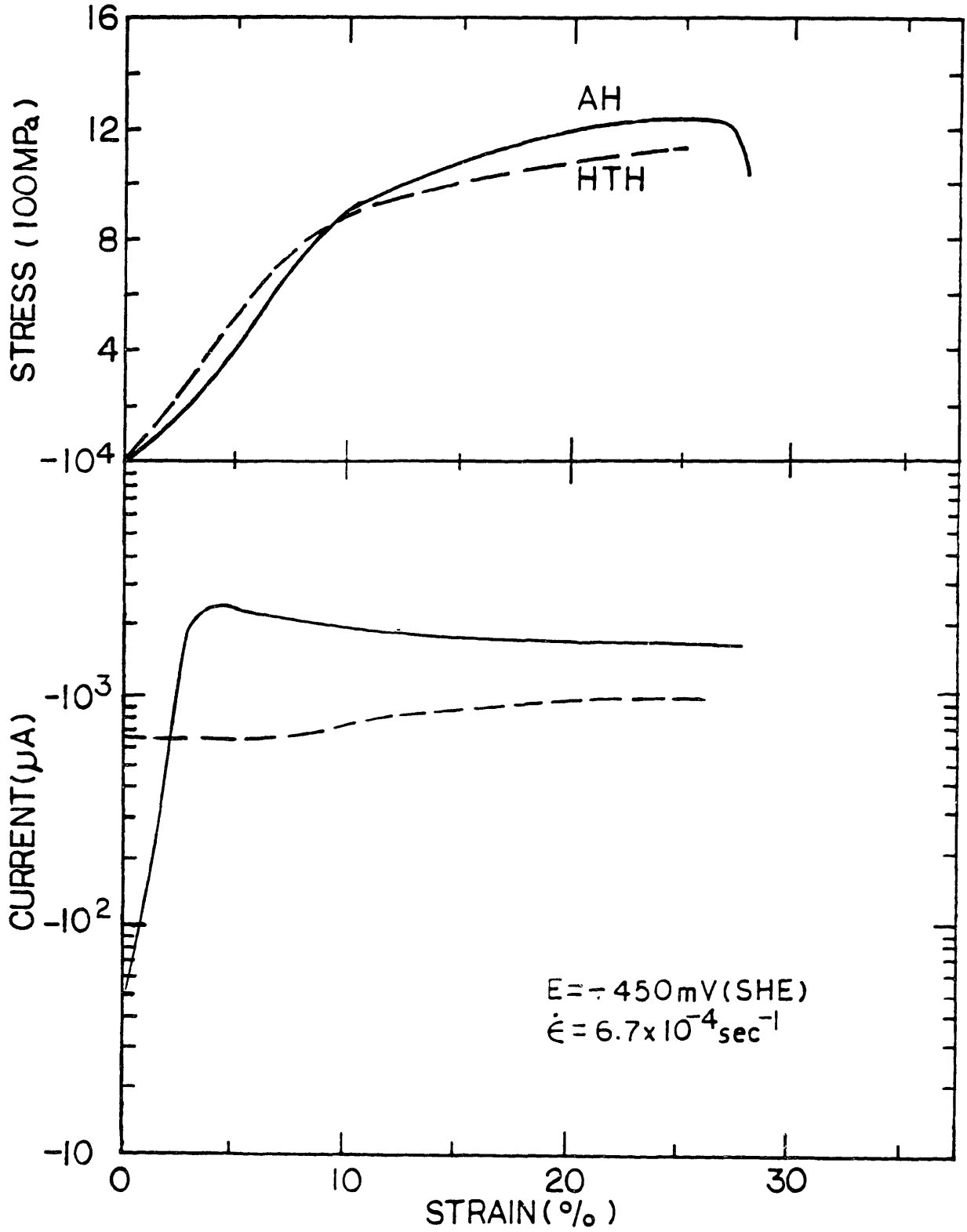

Figure 6.130 The SETT Results of the AH and HTH Conditions in a 0.05M Na_2SO_4 (pH-3) Solution at 93 C with a Strain Rate of $6.7x10^{-4}sec^{-1}$ and a Potential of -450 mV(SHE).

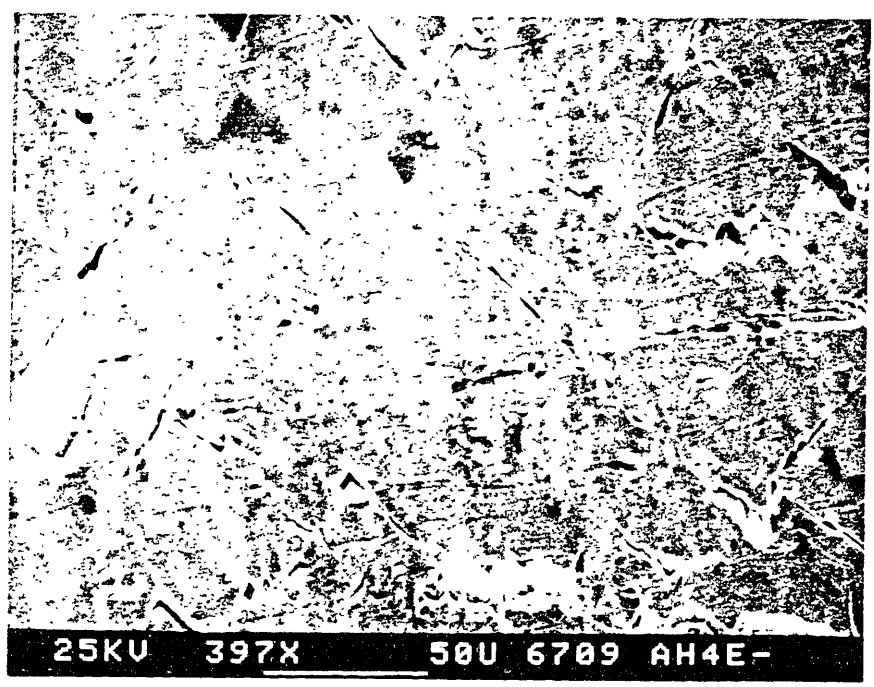

Figure 6.131 The SEM Fractographs of the AH Condition after the SETT in a 0.05M Na_2SO_4 (pH=3) Solution with a Strain Rate of $6.7x10^{-4}$ sec^{-1} and a Potential of -450 mV(SHE).

the loading axis which characterizes the transgranular nature of the surface cracks. Hence the triangular edges on the fracture surface resulted from the growth of these surface cracks. Decreased tensile strengths and elongation provide supporting evidences for embrittlement at the cathodic potential. Therefore, the AH condition is found to be susceptible to the transgranualr cracking at the higher strain rate at the cathodic potential.

The HTH specimen shows mild transition to the steady state current density which occurs near yielding, as shown in Figure 6.132. The steady state current density is about a factor of two lower than that of the AH condition. The fracture surface consists of a central region ofintergranular cracking surrounded by a several acute edges. The intergranular cracking at the center is believed to be purely mechanical phenomenon based on earlier observations. The side wall consists of a continuous array of surface cracks aligned at 45^0 to the loading axis which is the nature of transgranular cracks. Significant decreases in the tensile strength as well as the elongation are confirming evidences for the embrittlement. Therefore, the HTH condition is determined to be susceptible to transgranular cracking at the cathodic potential at the higher strain rate.

The results at the lower strain rate with cathodic polarization are summarized in Figure 6.133. All three conditions of alloy X-750 show no current transition whereas the CHT condition of alloy 718 exhibits a more complex transition to the steady state current density.

The steady state current density of the AH condition is slightly reduced at the lower strain rate although the difference is believed to be within the experimental error. The fractographs for the AH condition are shown in Figure 6.134. The fracture surface is characterized by a ductile shear rupture for most of region except for the edge where the acute crack surfaces are observed. The cracks are found to be transgranular. The side wall shows a moderate number of transgranular cracks which appear to contain a fine structure resembling intergranular cracking. Since the cracks are oriented at 45^0 to the loading axis,

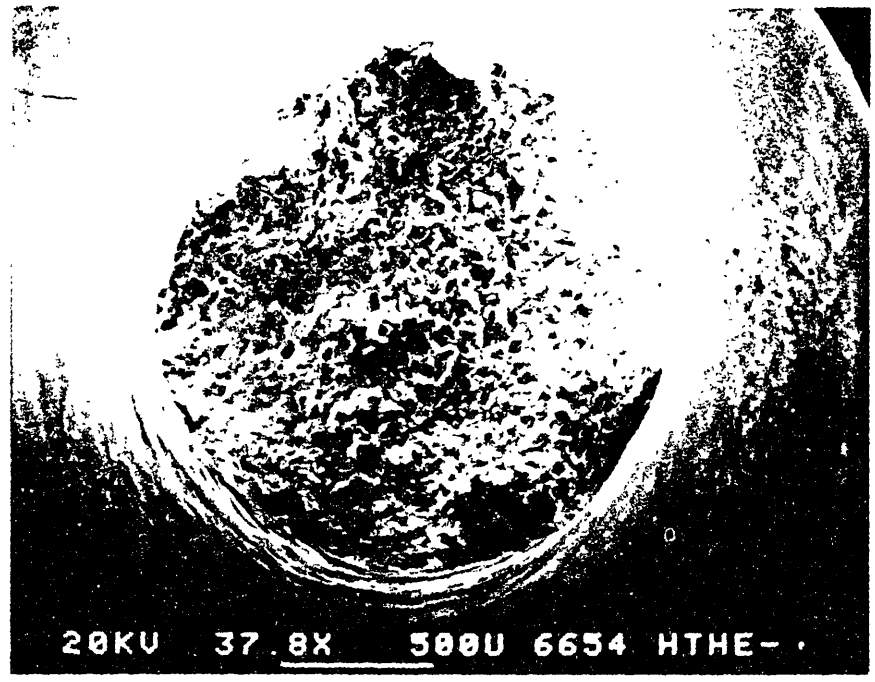

Figure 6.132 The SEM Fractographs of the HTH Condition after the SETT in a 0.05M Na_2SO_4 (pH-3) Solution with a Strain Rate of $6.7x10^{-4}$ sec^{-1} and a Potential of -450 mV(SHE).

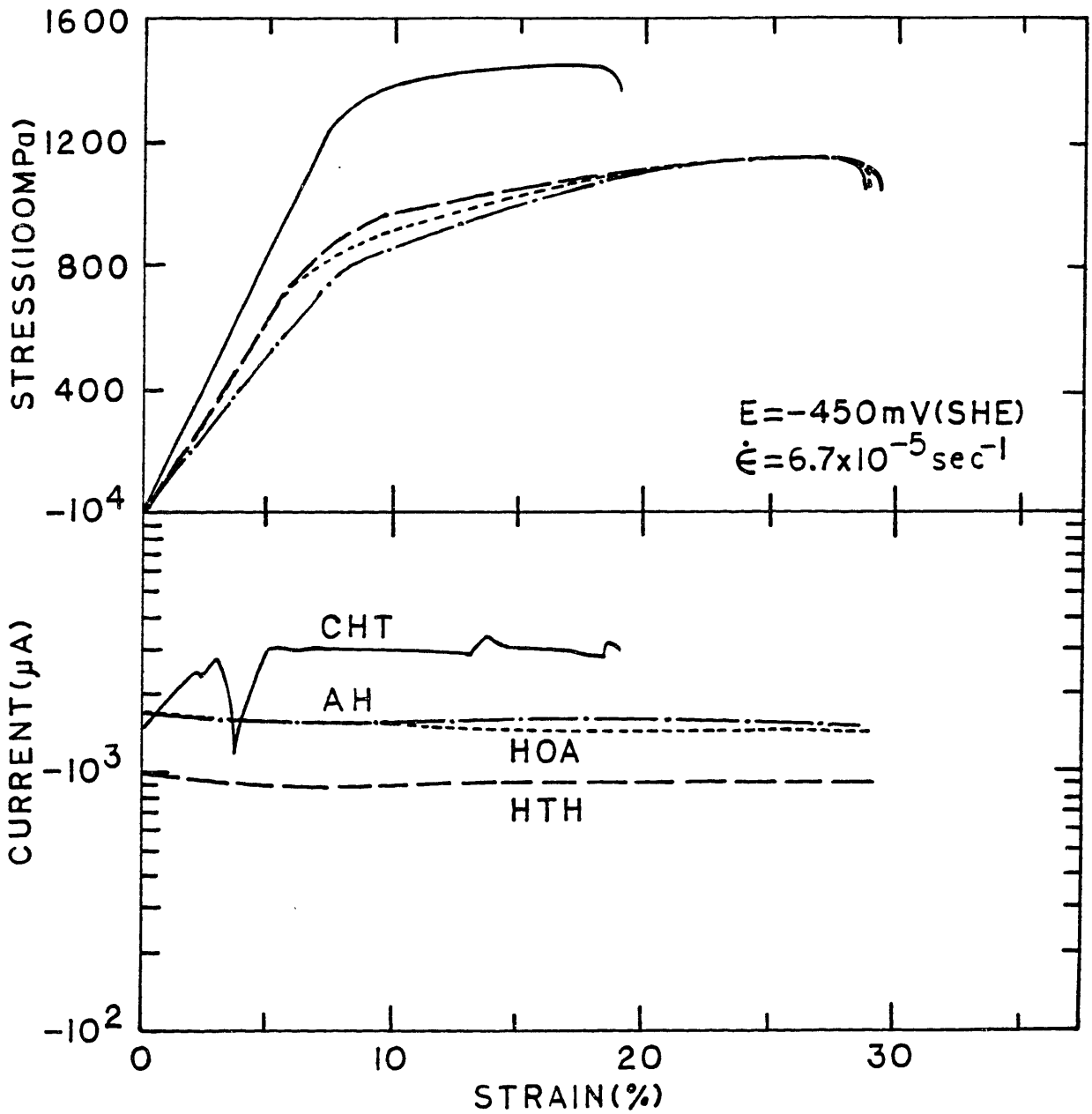

Figure 6.133 The SETT Results of the AH, HTH, HOA, and CHT Conditions in a 0.05M Na_2SO_4 (pH-3) Solution at 93 C with a Strain Rate of 6.7×10^{-5} sec^{-1} and a Potential of -450 mV(SHE).

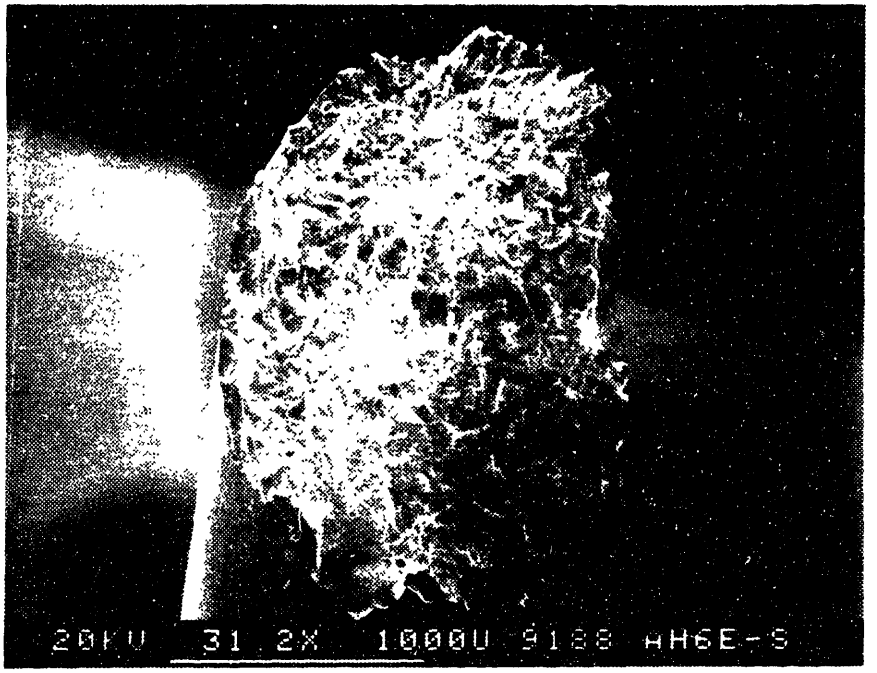

Figure 6.134 The SEM Fractographs of the AH Condition after the SETT in a 0.05M Na_2SO_4 (pH=3) Solution with a Strain Rate of $6.7x10^{-5}$ sec^{-1} and a Potential of -450 mV(SHE).

transgranular crystaloographic cracking is believed to be predominant mode. Decreases in tensile strengths and elongation support the susceptibility of the AH condition to cathodically induced embrittlement at the lower strain rate.

The HTH condition shows a steady state current density equal to the value at the higher strain rate. SEM fractographs for the HTH specimen are shown in Figure 6.135. The fracture surface shows a central intergranular cracking and peripheral transgranular cracks with the triangular edges. Cracking is not as extensive as the case of the higher strain rate. There is an appreciable decrease in the tensile properties which is slightly less significant than the case of the higher strain rate. Therefore, the susceptibility of the HTH condition with the cathodic polarization is believed to be decreased with the lowered strain rate.

The HOA specimen has about the same current density during the steady state as the case of AH condition. The fracture surface shows a central region of intergranular cracking with a surround region of ductile shear rupture, as shown in Figure 6.136. The side wall shows only a few number of cracks localized near the fracture site. The tensile properties are found unchanged from the reference value. Hence the HOA condition is considered to be less susceptible to cathodic embrittlement at the low strain rate.

The CHT condition shows a complex current transition which involves a smmoth undershoot near the end of the transition. The undershoot is too large to be regarded as experimental noise. When the current transition during the anodic polarization in Figure 6.127 is compared, there is a coincidence between the anodic overshoot and this cathodic undershoot. The consistent behavior is not well understood but may be explained by the gradual reduction of the passive surface which can lower the corrosion potential. The resultant decrease in the overpotential is believed to be responsible for the reduced current density. However subsequent current increase to the initial value is not understood. The steady state current density is found to be about twice tha of the AH

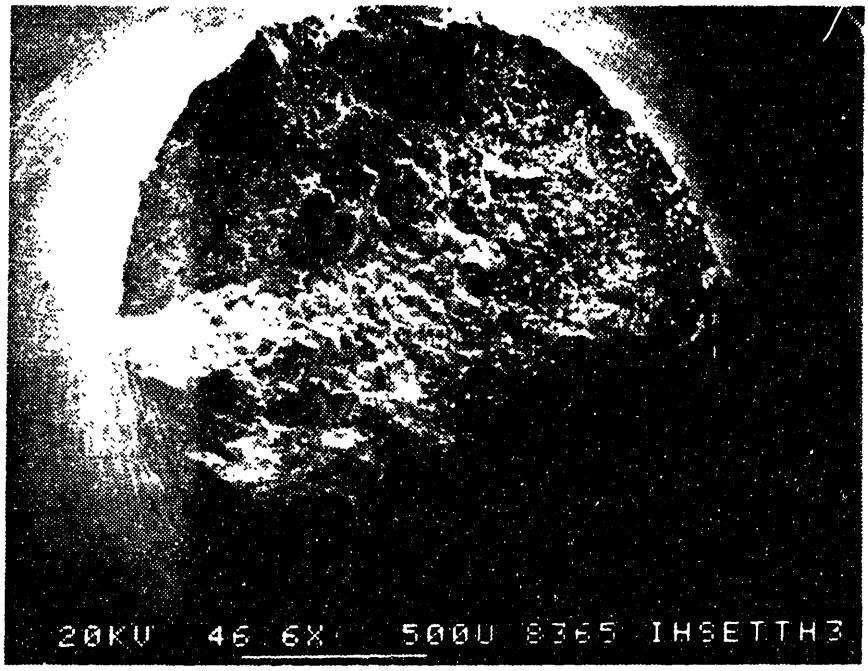

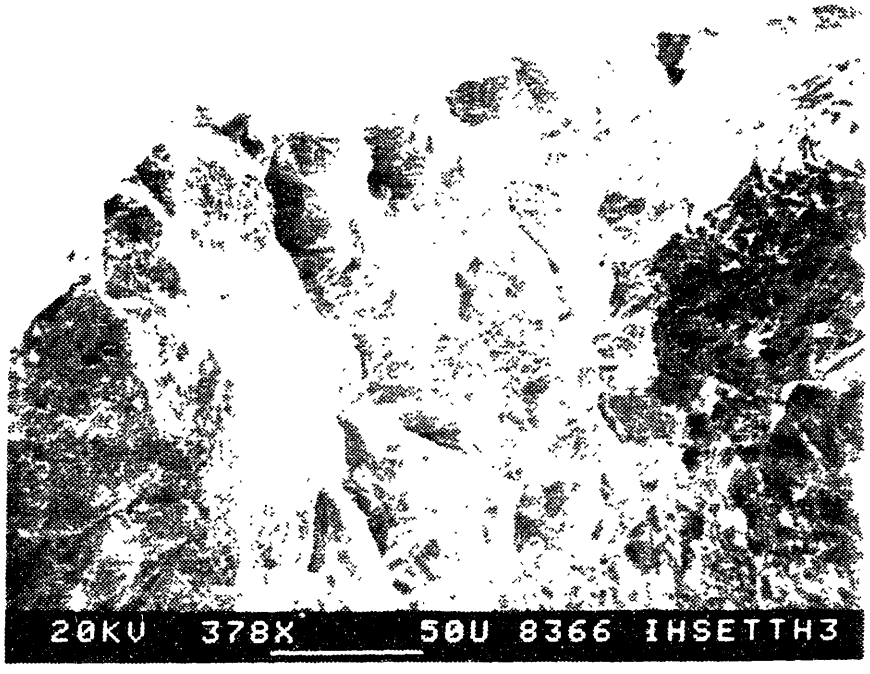

Figure 6.135 The SEM Fractographs of the HTH Condition after the SETT in a 0.05M Na_2SO_4 (pH=3) Solution with a Strain Rate of $6.7x10^{-5}$ sec^{-1} and a Potential of -450 mV(SHE).

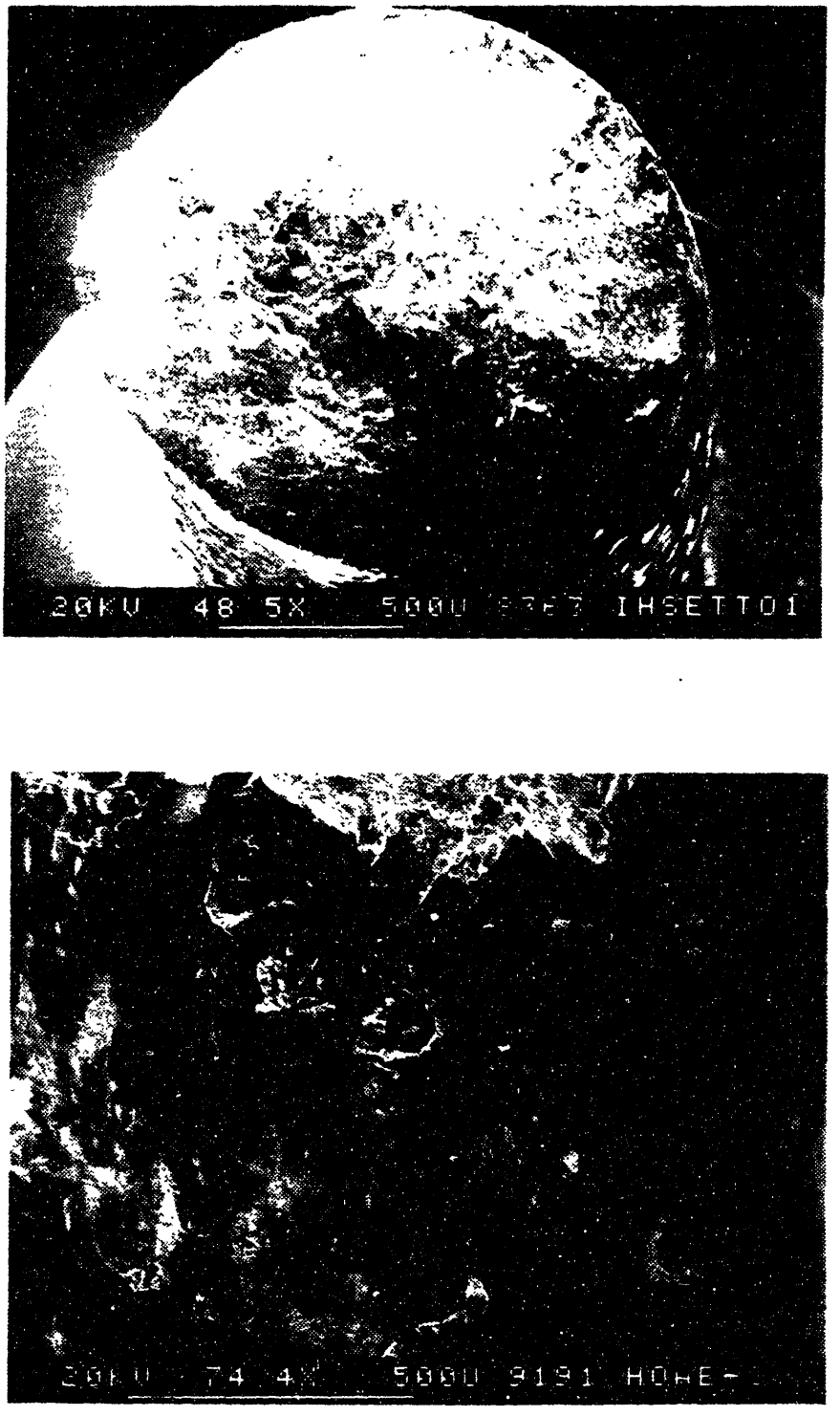

Figure 6.136 The SEM Fractographs of the HOA Condition after the SETT in a 0.05M Na_2SO_4 (pH=3) Solution with a Strain Rate of $6.7x10^{-5}$ sec^{-1} and a Potential of -450 mV(SHE).

condition. SEM fractographs are shown in Figure 6.137. A cup-and-cone fracture shows little evidence of brittle edges. The side wall exhibits a moderate number of transgranular crystallographic cracks. The tensile strengths are unchanged from the reference data although elongation is significantly decreased.

6.4.5 Summary

The results for tensile and transient current properties are summarized in Table 6.7. The tensile strength data are plotted as a function of overpotential for each strain rate, as shown in Figures 6.138 and 6.139. The data in the helium gas environment were obtained at 25°C with a strain rate of 6.7×10^{-5} sec for both alloys X-750 [23] and 718 [26]. The data are employed as the reference values in the absence of the environmental effect for the present test results at 93°C for both strain rates. These reference data are presented in Figures 6.138 and 6.139 by darkened symbols. At the higher strain rate, there is no significant effect of potentiostatic polarization on the tensile strength except for the HTH condition which shows a small decrease in both yield strength and ultimate tensile strength. A similar decrease in the strength at the cathodic potential was found with the AH conditon at the lower strain rate. About a 10% decrease in the strength, in both cases, is beleived to be significant since the measured tensile strength usually shows only a small variation from test to test.

The effect of potential on elongation is shown in Figure 6.140. The elongation of a specimen is determined from the crosshead displacement. not by reconstruction of the failed specimens. The value is, hence, found to be about 10% higher due to a large compliance in the load train. Since the effect of potential on elongation is determined by a change in the value rather than the absolute magnitude, the contribution of the load train compliance is expected to cancel out. Elongation is decreased by the cathodic potential at both strain rates. With the anodic polarization of the AH condition, the elongation is not changed at the higher strain rate, but decreased by about 10% at the lower strain rate.

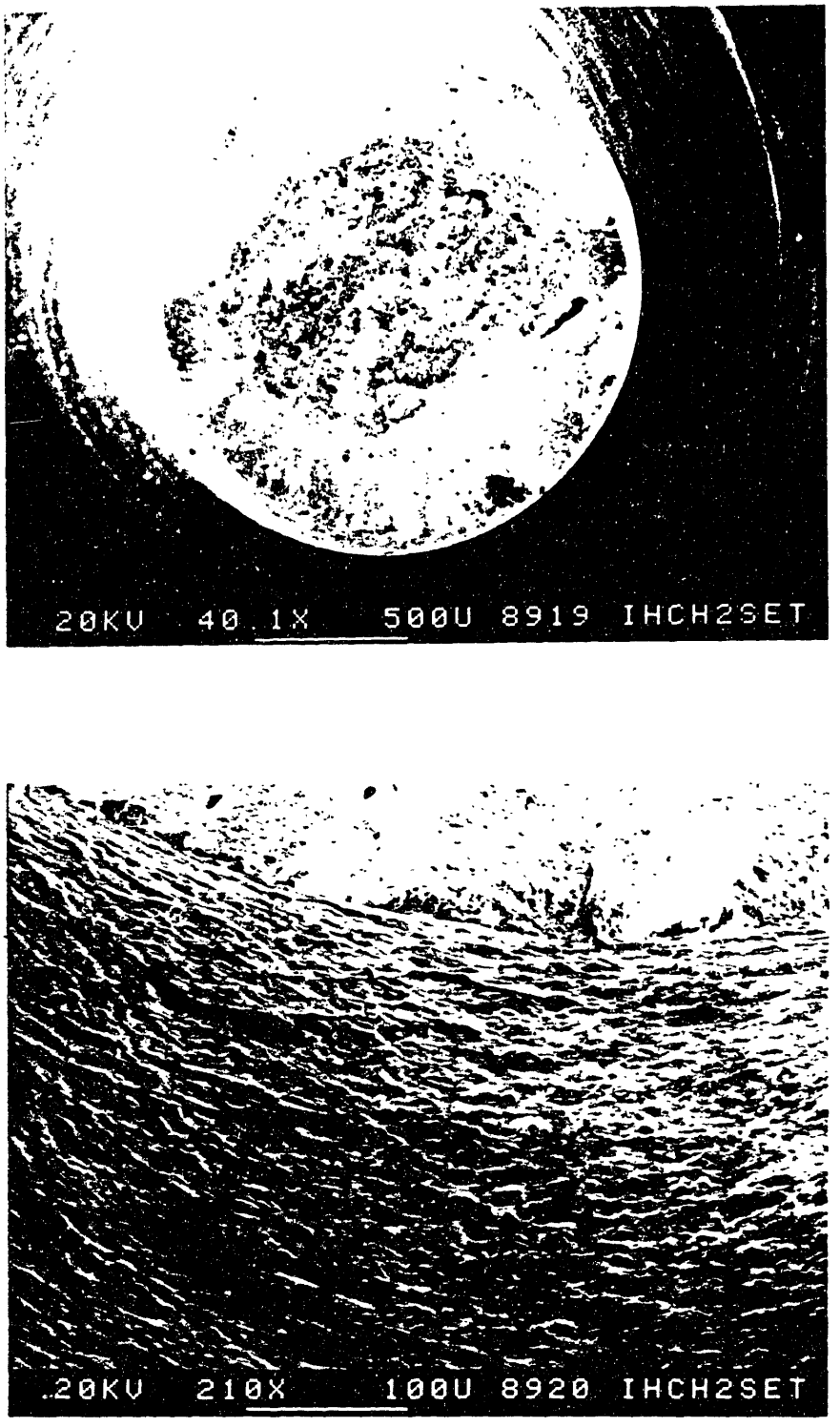

Figure 6.137 The SEM Fractographs of the CHT Condition after the SETT in a 0.05M Na_2SO_4 (pH=3) Solution with a Strain Rate of $6.7x10^{-5}$ sec^{-1} and a Potential of -450 mV(SHE).

Table 6.7

Summary of the Straining Electrode Tensile Test on Alloys X-750, 718 and Ni_3Al (Co=0.1) in a 0.05M Na_2SO_4 Solution (pH=3) at 93C

Material	E (mV SHE)	Y.S. (MPa)	U.T.S. (MPa)	Elongation* (%)	I (mA/cm^2)
X-750 AH					
$\epsilon=6.7x10^{-4}sec^{-1}$	E_{corr}	912	1289	31.1	-0.006
	0	847	1252	30.5	0.006
	-450	878	1256	26.1	-2.0
$\epsilon=6.7x10^{-5}sec^{-1}$	0	864	1245	28.3	0.002
	-450	793	1159	28.7	-1.5
X-750 HTH					
$\epsilon=6.7x10^{-4}sec^{-1}$	0	819	1231	32.6	0.007
	-450	734	1131	26.0	-1.0
$\epsilon=6.7x10^{-5}sec^{-1}$	-450	836	1145	29.2	-0.95
X-750 HOA					
$\epsilon=6.7x10^{-5}sec^{-1}$	-450	747	1160	28.7	-1.7
718 CHT					
$\epsilon=6.7x10^{-4}sec^{-1}$	0	1308	1453	23.9	0.005
	-450	1303	1448	19.0	-2.8
Ni_3Al(Co=0.1)					
$\epsilon=6.7x10^{-4}sec^{-1}$	GALVANIC	288	638	19.5	0.5

NOTE: * The elongation is determined from the crosshead displacement.

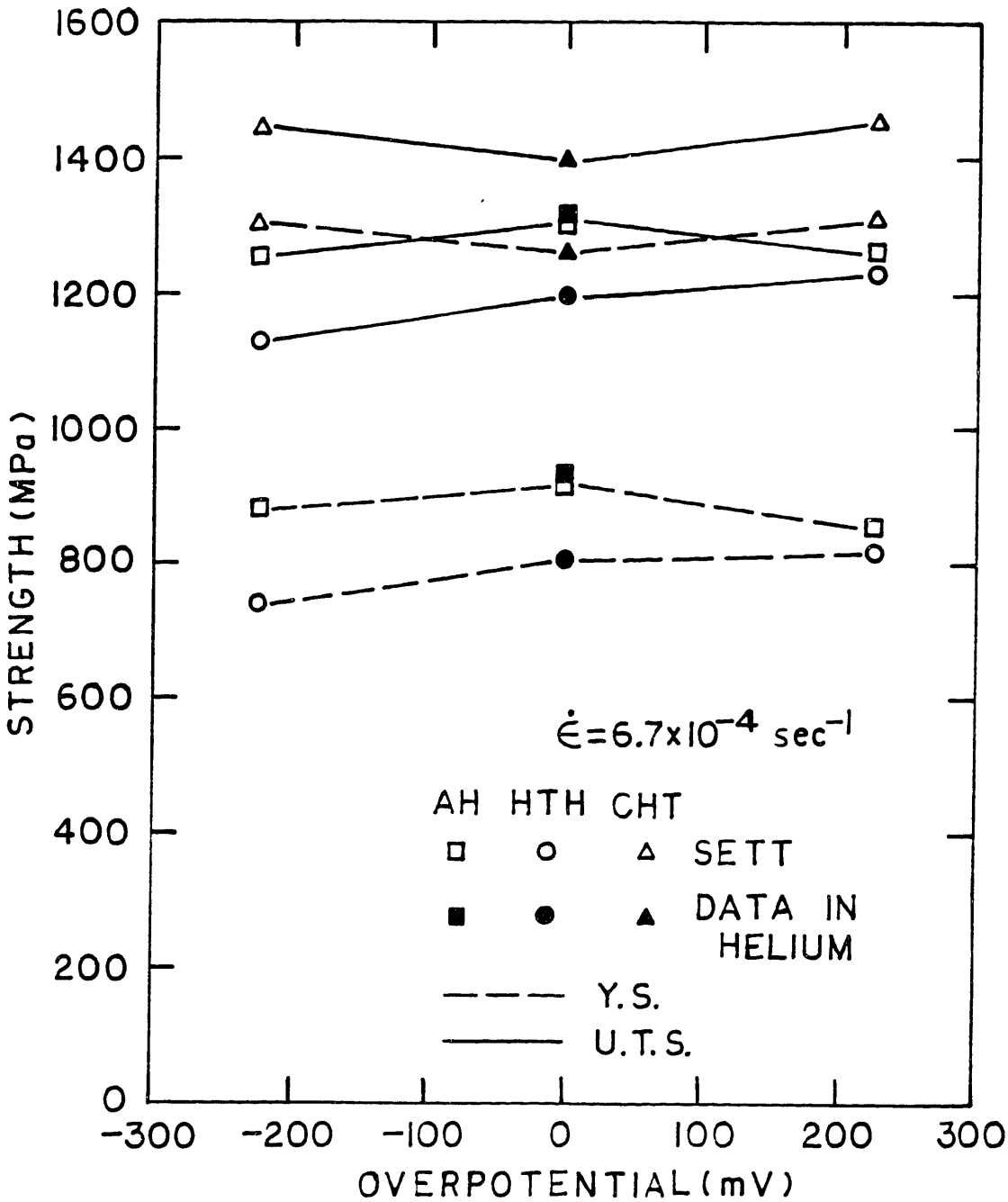

Figure 6.138 Comparison of Tensile Strengths of Alloys X-750 and 718 as a Function of Overpotential during SETT at a Strain Rate of 6.7×10^{-4} sec.$^{-1}$.

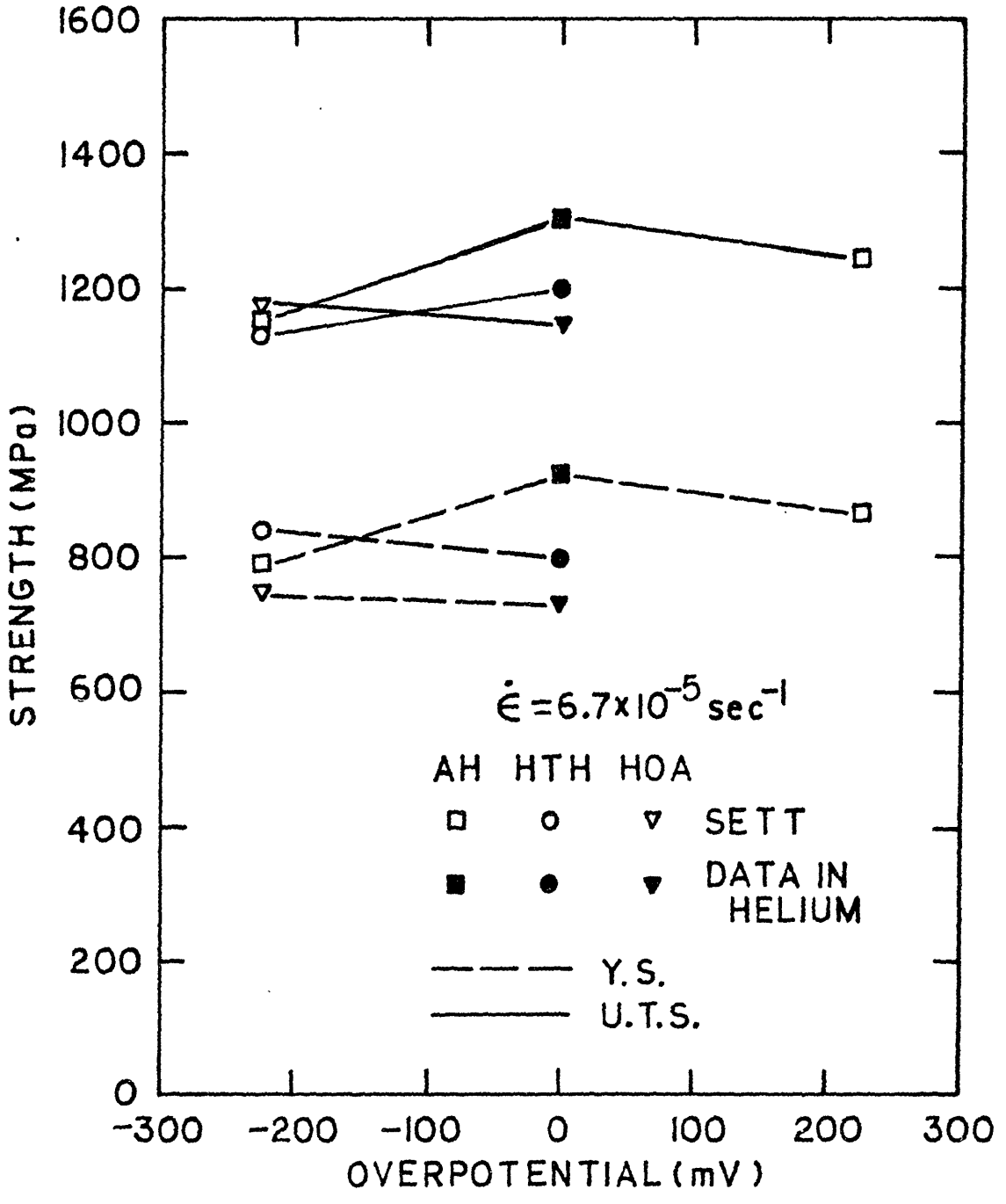

Figure 6.139 Comparison of Tensile Strengths of Alloys X-750 and 718 as a Function of Overpotential during SETT at a Strain Rate of 6.7×10^{-5} sec.$^{-1}$.

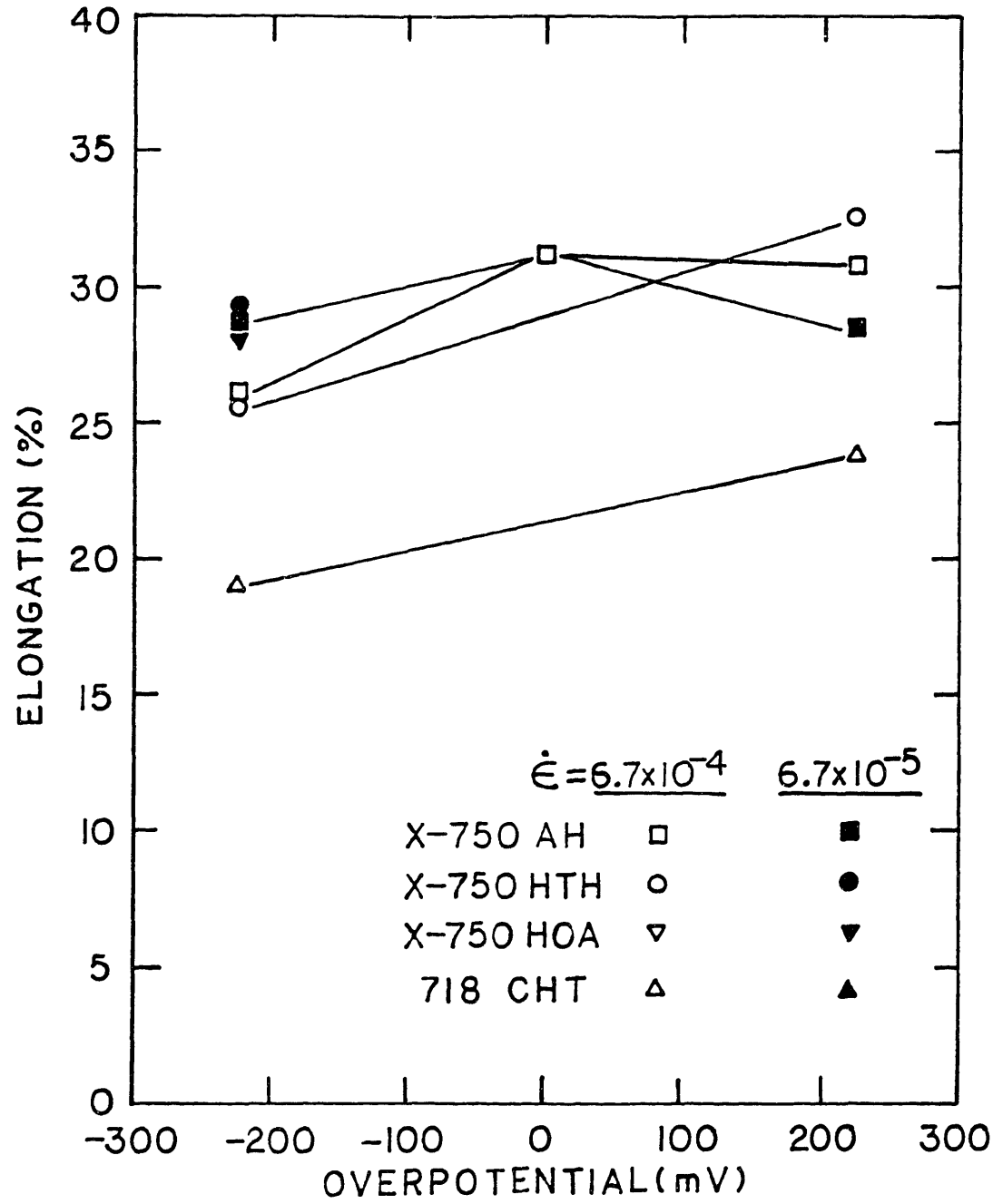

Figure 6.140 Comparison of Elongation of Alloys X-750 and 718 as a Function of Overpotential during SETT.

The measured current density shows a transient during the elastic deformation followed by a steady state value . Since the specimen surfaces were not cathodically cleaned before the test, the current transient during the early deformation is likely to be associated with destabilized surface film. Hence the steady state value can be taken as the representative current density for each test. Figure 6.141 shows the steady state current density for the various conditon of alloy X-750 and 718. The cathodic current densities are about three orders of magnitude higher than the anodic current densities although the overpotential is identical in both direction. This is a direct evidence of passivity maintained at the anodic potential during deformation. The passivity appears to be reduced at a higher strain rate. The higher strain rate results in the higher anodic current density with the AH condition. The higher rate of bare surface exposure is believed to be responsible for the results. More convincing evidences are to be presented during a detailed discussion on each test result. The cathodic current densities show little change due to different strain rates.

The detailed examination is made in conjunction with the fractographic information which helps identify the causes for the observed changes in the tensile and the electrochemical properties. Straining at free corrosion or anodic potential does not introduce significant embrittlement. Cathodic potential introduces embrittlent which is charaterized by transgranular crystallographic cracking.

6.5 CORROSION FATIGUE BEHAVIOR OF THE ALLOY X-750

6.5.1 Fatigue Crack Growth in High Purity Water

Since the AH condition shows the highest crack growth rate among heat treatment conditions of interest at low temperature this condition was selected for a mechanistic investigation. The plate heat of X-750 used for the SEN specimen was found to have a larger grain size and more intergranular carbide precipitation when compared with the heat 96457E6

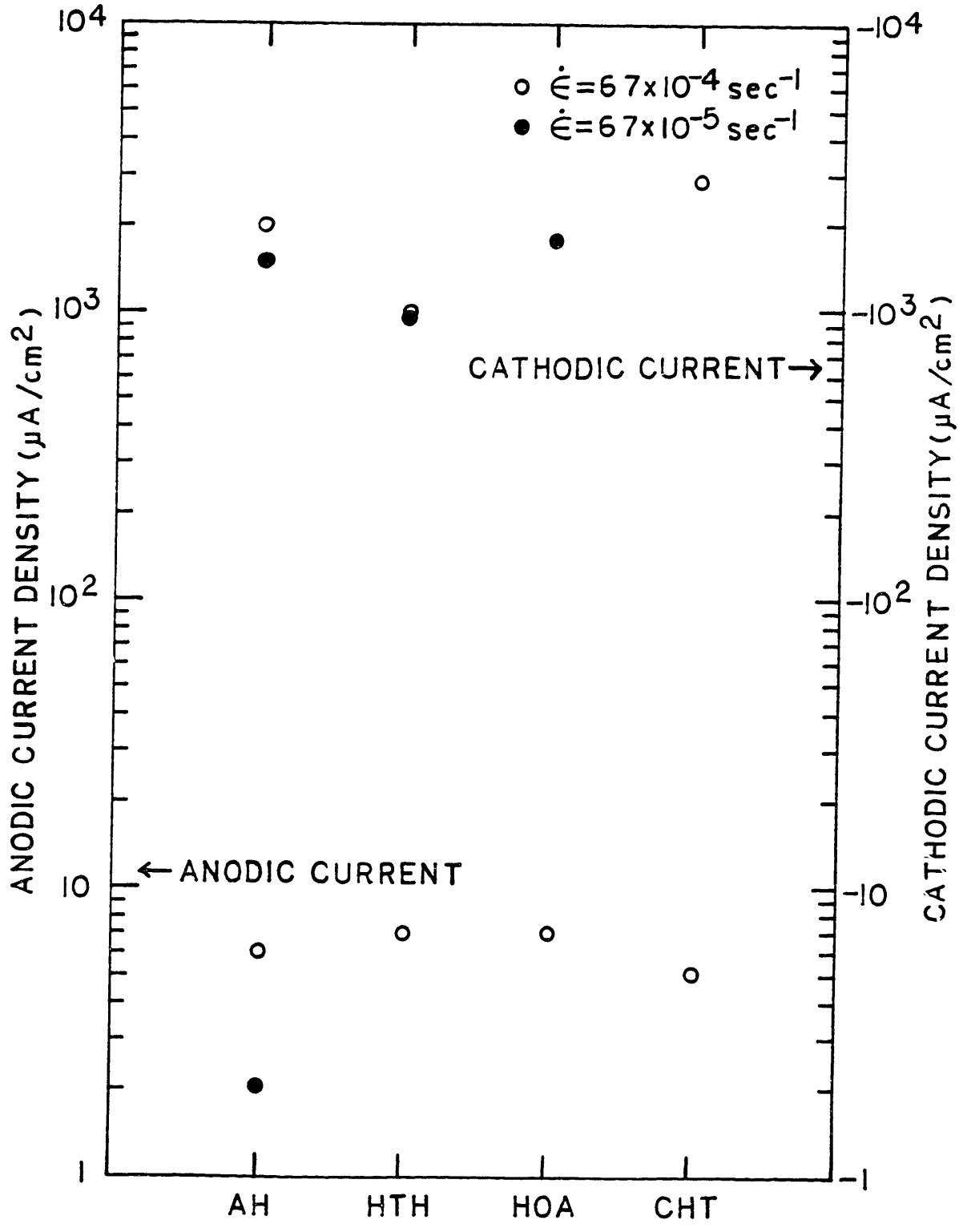

Figure 6.141 Comparison of Steady State Current Density of Alloys X-750 and 718 during SETT as a Function of Heat Treatments.

which was used for all other parts of this work. Also, the SEN specimen design permits the increased degree of plane stress state compared with the compact tension (CT) specimen design used to observe the low temperature embrittlement. Therefore, it is necessary to verify that the test data reproduce the same low temperature embrittlement behaviors as those observed with the reference material.

Fatigue crack growth rates measured in room temperature air agree well with the reference data in 93 C helium. The dependences of the crack growth rate on frequency and temperature measured in deaerated high purity water are compared with the data for the AH condition of heat 94051 which shows the same microstructure and corrosion fatigue behavior as the heat 96456E7 [50]. The frequency dependence of crack growth rate in 60 C water is compared with the refernce data at 93 C, and is shown in Figure 6.142. Due to the plexiglass construction of the test cell further increase in temperature was not practical. The frequency dependece of the two heats of AH condition agrees well with each other for a range of frequency between 0.1 Hz and 10 Hz. The consistently lower crack growth rates of the plate heat may be attributed to the lower temperature, the larger grain size and a smaller amount of γ' at grain boundaries. The temperature dependence up to 60 C is compared with the reference data for heat 94051 in Figure 6.142. Increasing crack growth rate with increasing temperature is consistent with previous results.

Fracture surfaces produced in the room temperature air are shown in Figure 6.143 for two values of ΔK. A transgranular fracture mode is observed with the appearance of slip bands. In high purity water, all the fracture surfaces are found to be intergranular for the range of temperatures investigated, as shown in Figures 6.144 and 6.145. The surfaces are severely damaged by anodic polarization during the later stage of experiment. The fracture mode in two environments is consistent with the earlier observation on the reference material. Therefore, it is evident that the AH condition of plate X-750 shows an identical crack growth behavior as to the frequency and temperature depends at the low temperature.

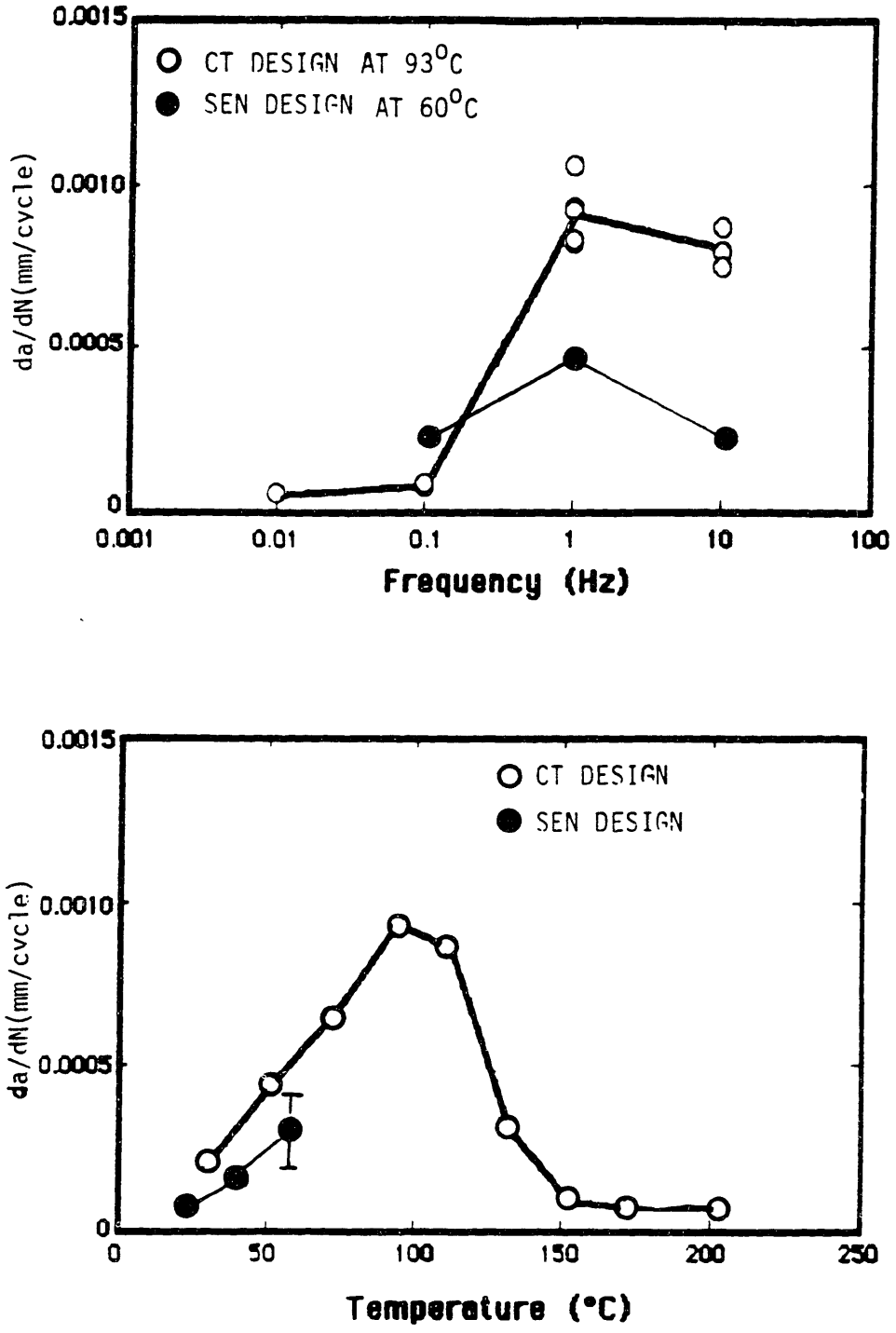

Figure 6.142 Comparison Between the Plate Heat SEN Specimen and the Heat 94051 CT Specimen on the Fatigue Crack Growth Rate at 25 MPa$\sqrt{m}$ and R=0.1 as a Function of Frequency (upper) and Temperature (lower) for the AH Condition in Deaerated Water.

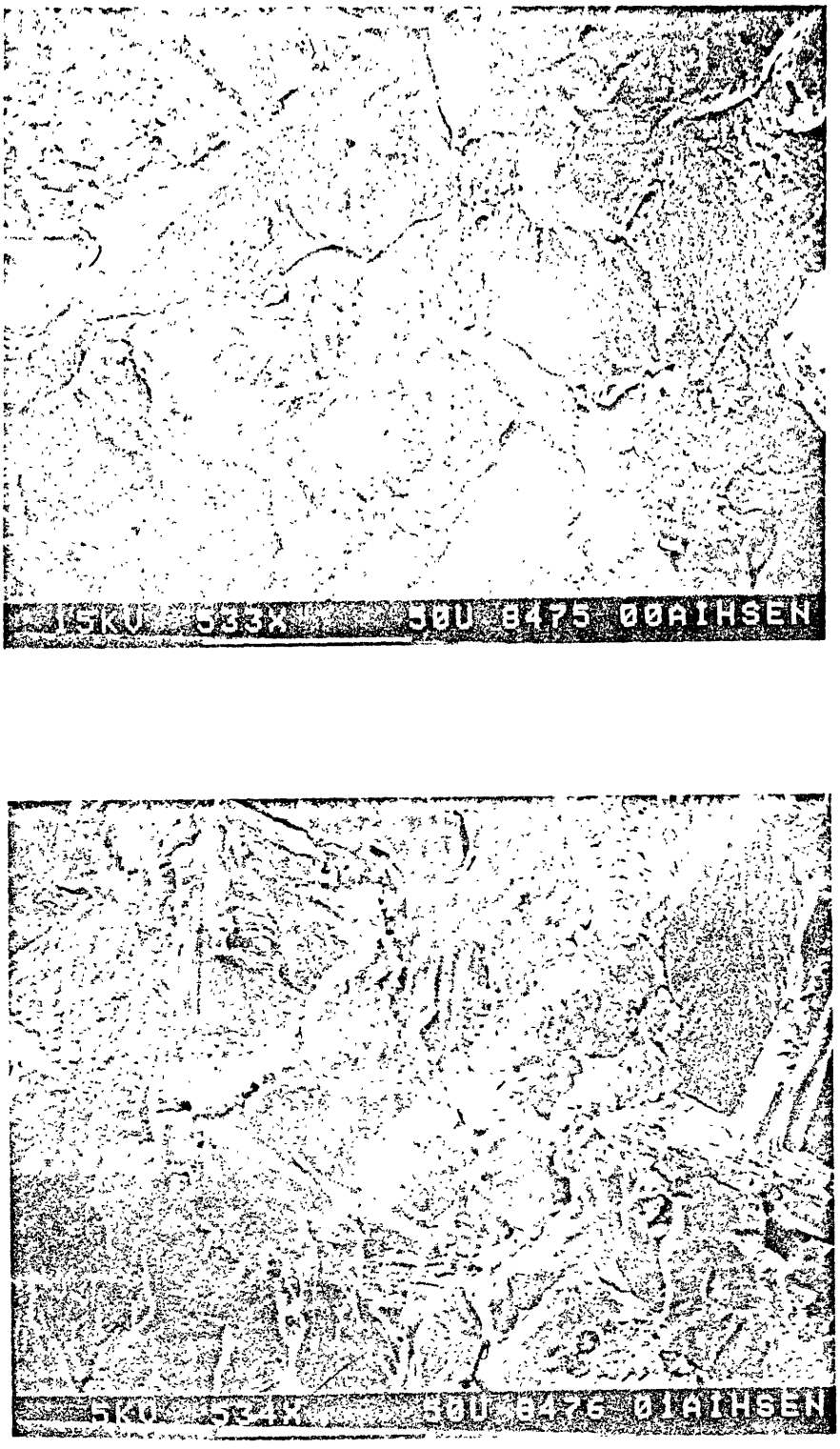

Figure 6.143 The SEM Fractograph of the AH SEN Specimen after a Fatigue Test in the Air with a Frequency of 10 Hz at 20 MPa$\sqrt{m}$ (upper) and 25 MPa$\sqrt{m}$ (lower) and R=0.1.

Figure 6.144 The SEM Fractograph of the AH SEN Specimen after a Fatigue Test in Deaerated Water at 25 C with a Frequency of 10 Hz at 25 MPa$\sqrt{m}$ and R=0.1.

Figure 6.145 The SEM Fractograph of the AH SEN Specimen after a Fatigue Test in Deaerated Water at 43 C with a Frequency of 10 H_2 at 25 MPa$\sqrt{m}$ and R=0.1.

The test results obtained at a ΔK of 25 $MPa\sqrt{m}$ with an R-ratio of 0.1 in 60 C high purity water are summarized as a function of frequency in Figure 6.146. At the free corrosion potential, the crack growth rate shows a maximum at a frequency of 1 Hz. This crack growth rate is about 11 times higher than the growth rate in the room temperature air. Both 0.1 Hz and 10 Hz result in a similar amount of decrease in the crack growth rate. The SEM fractographs for the three frequencies are shown in Figures 6.147 - 6.149. All cases show intergranular cracks for most of the specimen cross section. A small region, about 100μm width, at each side wall shows a transgranular mode of crack growth regardless of frequency. This is illustrated in Figure 6.150. This indicates that transgranular cracking is more favorable under plane stress conditions.

One striking feature of the crack growth in water was that the plastic zone at crack tip estimated by the side wall observation was significantly larger than that in air for the same loading conditions. This is evidence that the crack tip, at least near the side wall, is softened.

The data plotted in Figure 6.146 show results of both anodic and cathodic chargeing at the same current density of 0.5mA/cm. This current density represents the maximum value for galvanic coupling of $Ni_3Al(Co=0.1)$ and surrounding matrix, as determined by straining electrode tests. Cathodic charging showed no significant effect on crack growth rate. Hydrogen bubbles were observed to grow and depart from the side of the surface which faced the platinum counter electrode. However the opposite side of specimen surface did not contain such bubbles. This indicates a high potential difference between the surface layers on the opposite sides of specimen. The resistance of high purity water was measured to be about 3 MΩ cm at 25 C. The resultant IR drop across the distance of specimen thickness (3mm) is large enough to localize the cathodic hydrogen evolution to only one side of the specimen. Fracture morphology is the same as that for free corrosion. The preferentially distributed hydrogen bubbles and coupled with the

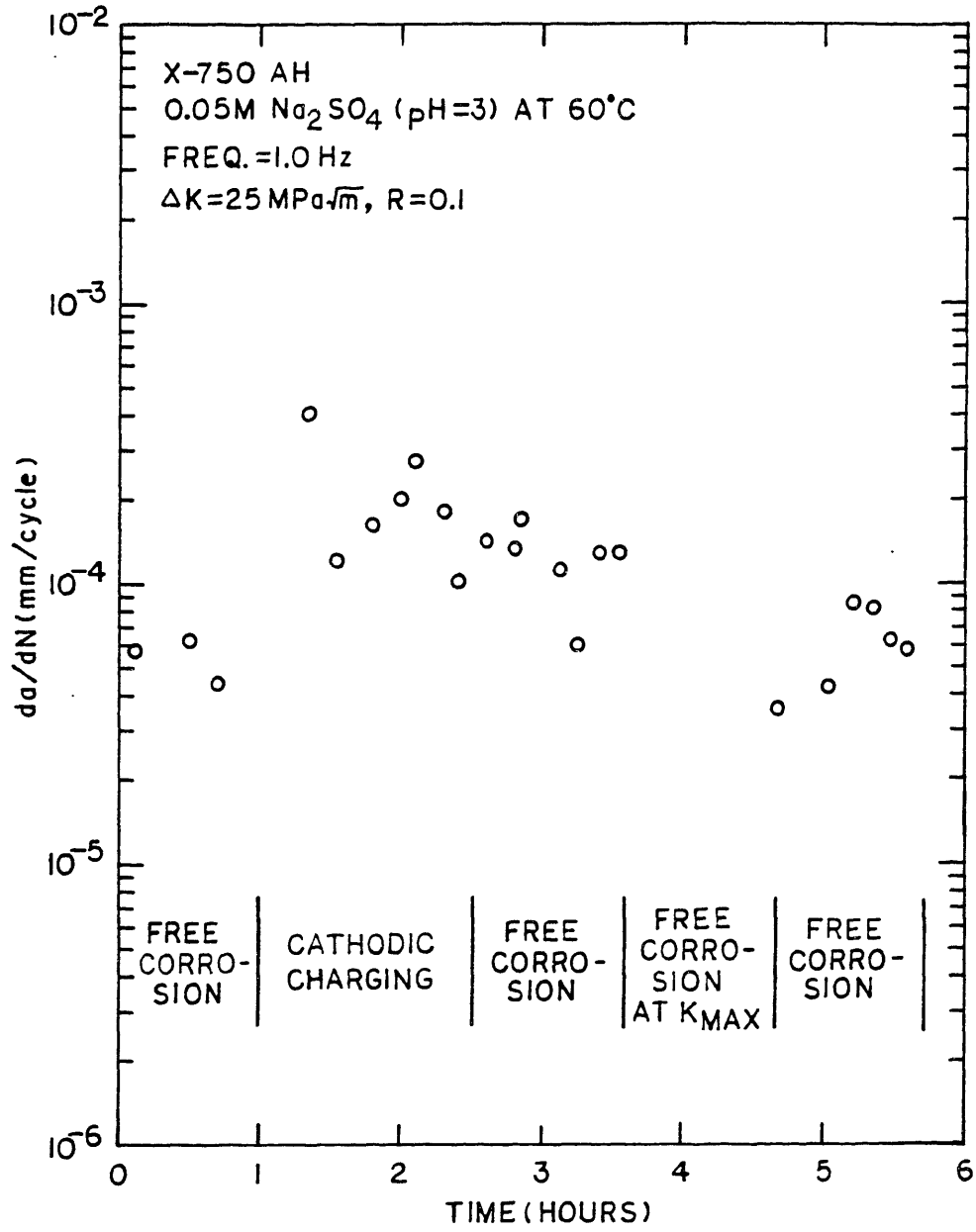

Figure 6.146 Fatigue Crack Growth Rate of the AH SEN Specimen in the Deaerated Water at 60 C under the Cathodic, Anodic Charging and Free Corrosion at $\Delta K = 25\ MPa\sqrt{m}$ and R=0.1 as a Function of Frequency.

Figure 6.147 The SEM Fractograph of the AH SEN Specimen after a Fatigue Test in Deaerated Water at 60 C with a Frequency of 0.1 Hz at 25 MPa$\sqrt{m}$ and R=0.1. during Free Corrosion.

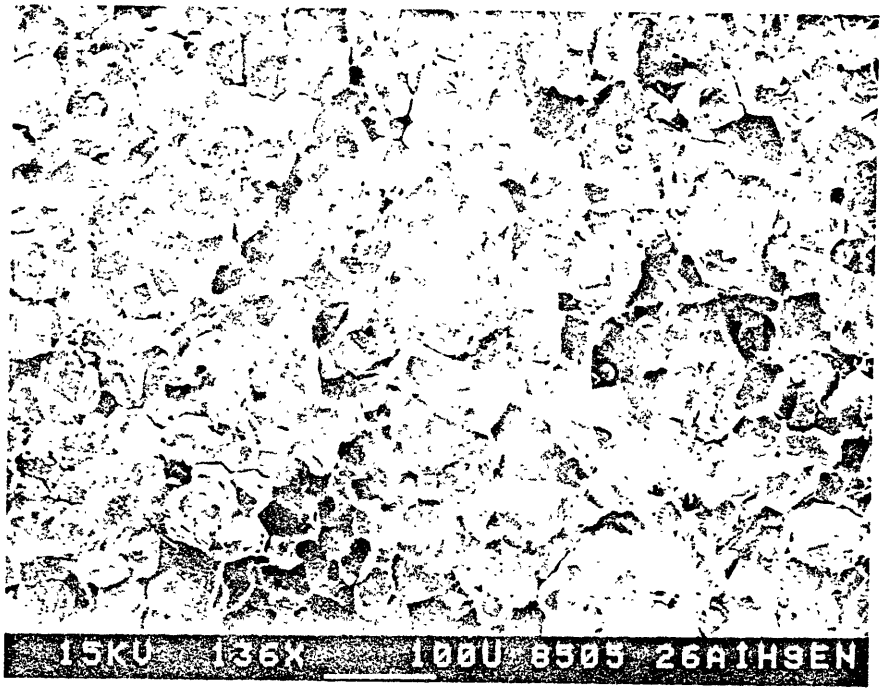

Figure 6.148 The SEM Fractograph of the AH SEN Specimen after a Fatigue Test in Deaerated Water at 60 C with a Frequency of 1.0 Hz at 25 MPa$\sqrt{m}$ and R=0.1 during Free Corrosion.

Figure 6.149 The SEM Fractograph of the AH SEN Specimen after a Fatigue Test in Deaerated Water at 60 C with a Frequency of 0.1 Hz at 25 MPa$\sqrt{m}$ and R=0.1 during the Anodic Charging at 0.5mA/cm^2.

Figure 6.150 The SEM Fractograph of the AH SEN Specimen after a Fatigue Test in Deaerated Water at 60 C with a Frequency of 0.1 Hz at 25 MPa$\sqrt{m}$ and R=0.1 during the Anodic Charging at 0.5mA/cm^2.

observation of no significant in the crack growth rate as well as an identical fracture morphology provide experimental evidence that cathodic charging has no influence on the crack tip. This is probably due to the high solution resistance. Hydrogen evolution appears to have occurred only on the side wall which would not affect the crack tip environment.

Anodic charging at 0.5mA/cm^2 results in no change in crack growth rate in high purity water at 60 C. At a frequency of 0.1 Hz a prolonged period of charging is required to obtain a significant number of crack growth data. For this case the high purity water was gradually contaminated and turned to light yellowish color. This was accompanied by a significant decrease in crack growth rate as is shown in Figure 6.151. The crack growth rate was slowed to about the same as that in air at room temperature. The yellowish contaminant is believed to be hexavalent chromate ions which is known to be an inhibitor of the stress corrosion cracking [148]. The test was then stopped to take a solution sample and clean the test system. A resistivity of the solution is found to be 25kΩ cm at 60 C which is about 100 times lower than the inital value. It was not determined whether the decreased crack growth rate was due to decreased resistivity or by the inhibiting effect of the chromate ions. Thus, a second experiment was performed using low resistivity solution but with chemically stable ions.

The SEM fractograph for the region with the decreased crack growth rate is shown in Figure 6.150. An intergranular crack path is substantially retained but decreased embrittlement is evidenced by the absence of secondary cracks and an increased number of transgranular patches between intergranular facets. Since the crack growth rate was decreased to the value in air the embrittlement is considered to be lowered by the chromate contamination.

6.5.2 Fatigue Crack Growth in a Sodium Sulphate Solution

Since extensive electrochemical data are available and the sulphate ion is chemically stable at temperature below 200 C, a solution of 0.05M

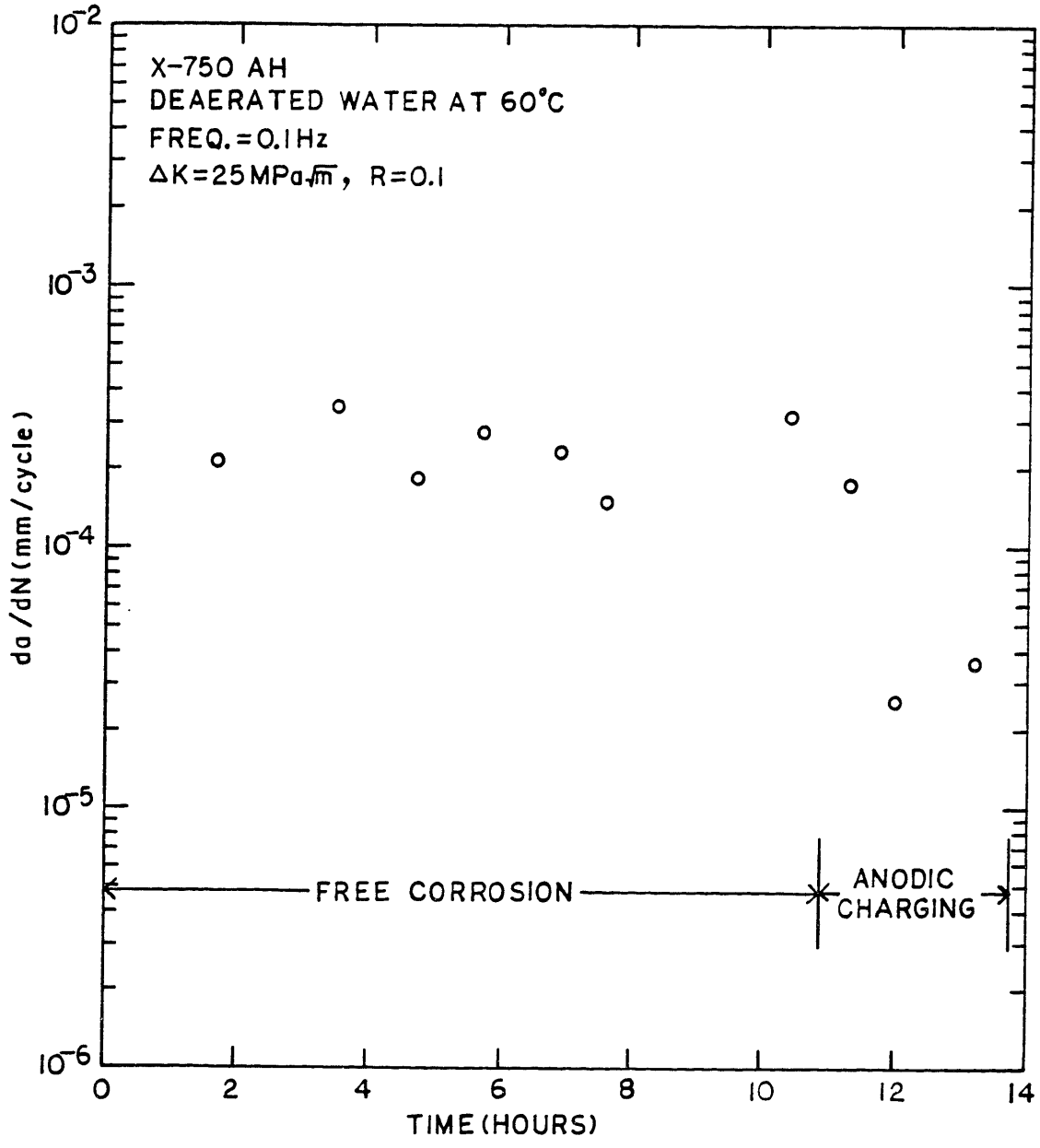

Figure 6.151 The Decreased Fatigue Crack Growth Rate of the AH SEN Specimen by Anodic Charging at 0.5 mA/cm^2 and Subsequent Solution Contamination with a Frequency of 0.1 Hz at 25 MPa$\sqrt{m}$ and R=0.1 in the Deaerated Water at 60 C.

Na_2SO_4 (pH = 3) is selected for the electrolyte. The resistivity of the electrolyte is measured to be 120Ω cm at 25 C and 60Ω cm at 60 C. The previous study in the high purity water showed final crack growth rate of $1.8x10^{-4}$mm/cycle at 25MPa$\sqrt{m}$ and R=0.1 with a frequency of 10 Hz under free corrosion. Upon replacing the solution with the 0.05M Na_2SO_4 (pH=3), the test was continued at the same ΔK and R-ratio with a frequency of 1 Hz under free corrosion at 60 C. The crack growth rate in sodium sulphate solution is found to be as low as $5.1x10^{-5}$mm/cycle. The result is attributed to the effect of increased conductivity since the sulphate solution is known as chemically inert electrolyte.

The effect of cathodic charging was examined based on the response of the crack growth rate. A cathodic current of $0.5mA/cm^2$ was applied to the specimen after a stable crack growth rate was established under the free corrosion state. The cathodic charging restored the high crack growth rate observed in the high purity water which agrees precisely with the fractographic observations, as shown in Figure 6.152. The intergranular fracture mode established in high purity water shifts to a transgranular pattern under free corrosion in sodium sulphate solution. Subsequent cathodic charging clearly reproduced the same intergranular mode.

Through the use of a traveling microscope with a strobe light source, it was possible to examine the detailed behavior of the hydrogen bubbles around the crack tip. Bubbles were uniformly distributed on both side of the specimen and pumped out during each unloading cycle. The plastic zone size during the cathodic charging was significantly increased over that of the previous free corrosion potential at which the plastic zone size was similar to that in air. These observations allow us to draw the following conclusions; 1) the embrittlement mechanism of the X-750 AH at low temperature water is the same as that in the sodium sulphate solution with cathodic charging at a realistic galvanic current density. 2)the embrittlement mechanism is inoperable at the free corrosion potential if the conductivity is high enough. 3) the mechanism enhances the plasticity ahead of crack tip.

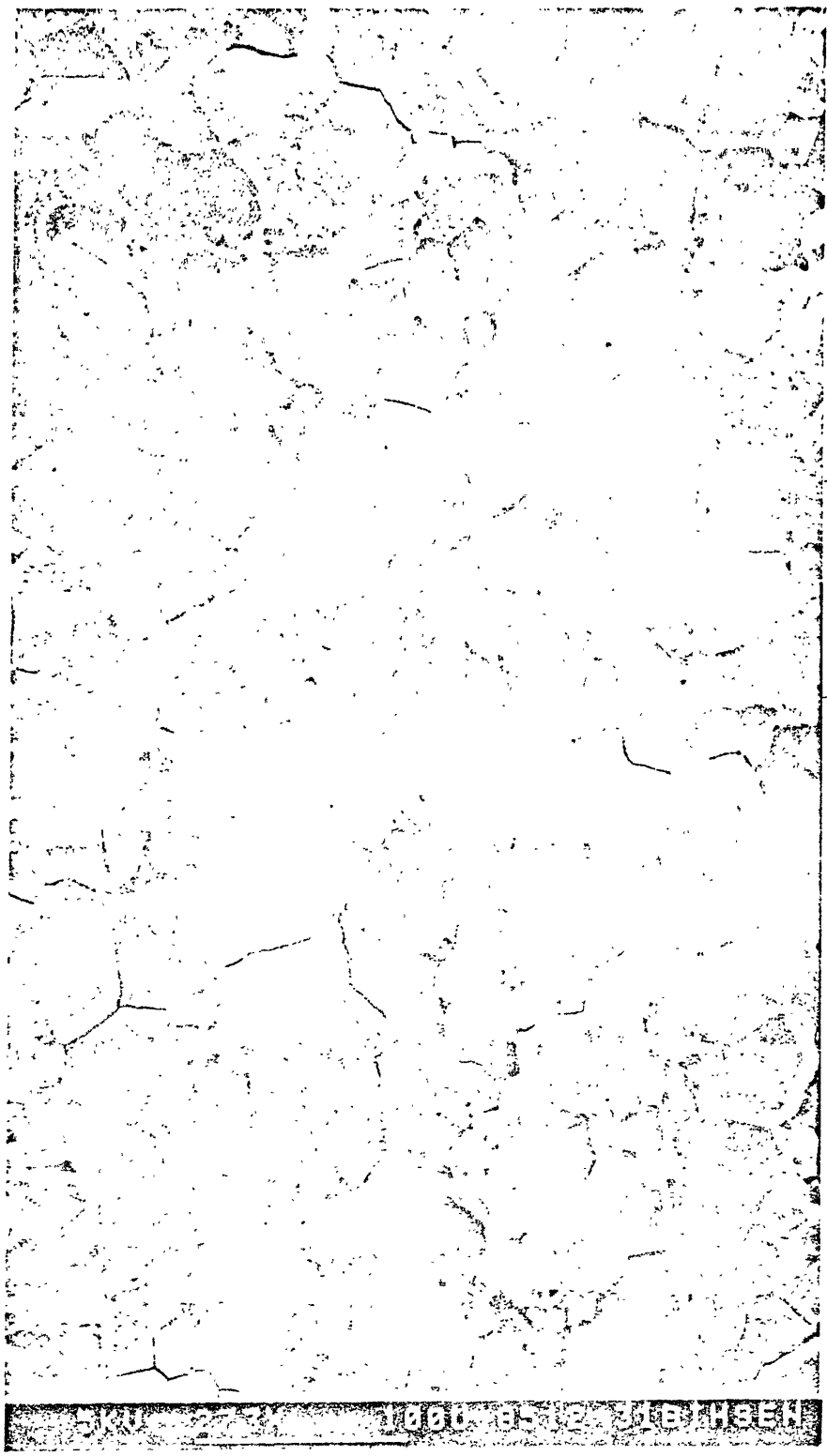

Figure 6.152 Transitions in the Fracture mode in Response to Environmental Changes from Deaerated Water to 0.05M Na_2SO_4 (pH=3) solution and finally to Cathodic Charging at 0.5 mA/cm^2 in the latter Solution at 25 $MPa\sqrt{m}$ and R=1 for the AH Condition at 60 C.

A more detailed observation was made in the same electrolyte with a second specimen of the same condition. The results are summarized in Figure 6.153. Under free corrosion, the crack growth rates were as low as those in air for a frequency range between 0.1 Hz and 10 Hz at both temperatures of 25 C and 60 C. All the fracture surfaces at the free corrosion potential show a transgranular morphology. A representative micrograph is shown in Figure 6.154 for the case of 10 Hz at 25 C.

At 25 C the crack growth rate at 0.1 Hz was increased by a factor of 20 with cathodic charging at 0.5mA/cm. The high crack growth rate was reproduceable by repeated steps of charging and free corrosion potential as illustrated in Figure 6.155. The fracture surface under cathodic charging is completely intergranular while that at the free corrosion potential is transgranular. Figure 6.156 shows such transitions in fracture mode by alternation of cathodic charging and free corrosion at 0.1 Hz.

As the frequency was increased the cathodic charging effect gradually decreased. SEM fractographs are shown in Figures 6.157 and 6.158 for frequency of 1 Hz. The transgranular mode during a free corrosion was changed into an intergranular at 1 Hz with cathodic charging. Although the change in crack growth rate with cathodic charging is not as large as that at 0.1 Hz the difference is measurable,as shown in Figure 6.159.

Data for R=0.5 were obtained at 1Hz to examine the effect of different R-ratios. These results are compared with the case of R=0.1 in Figure 6.159. There was no significant effect due to the increased R-ratio when the maximum stress intensity factor was kept the same. The test at R=0.5 was continued with subsequent anodic charging. The crack growth rate decreased below the value in air at R=0.1.

During cathodic charging under potentiostatic control, the current history was measured during each load cycle. The results are shown in Figure 6.160 for two R-ratios. In this figure the currents are normalized to average values. The normalized amplitude of the current

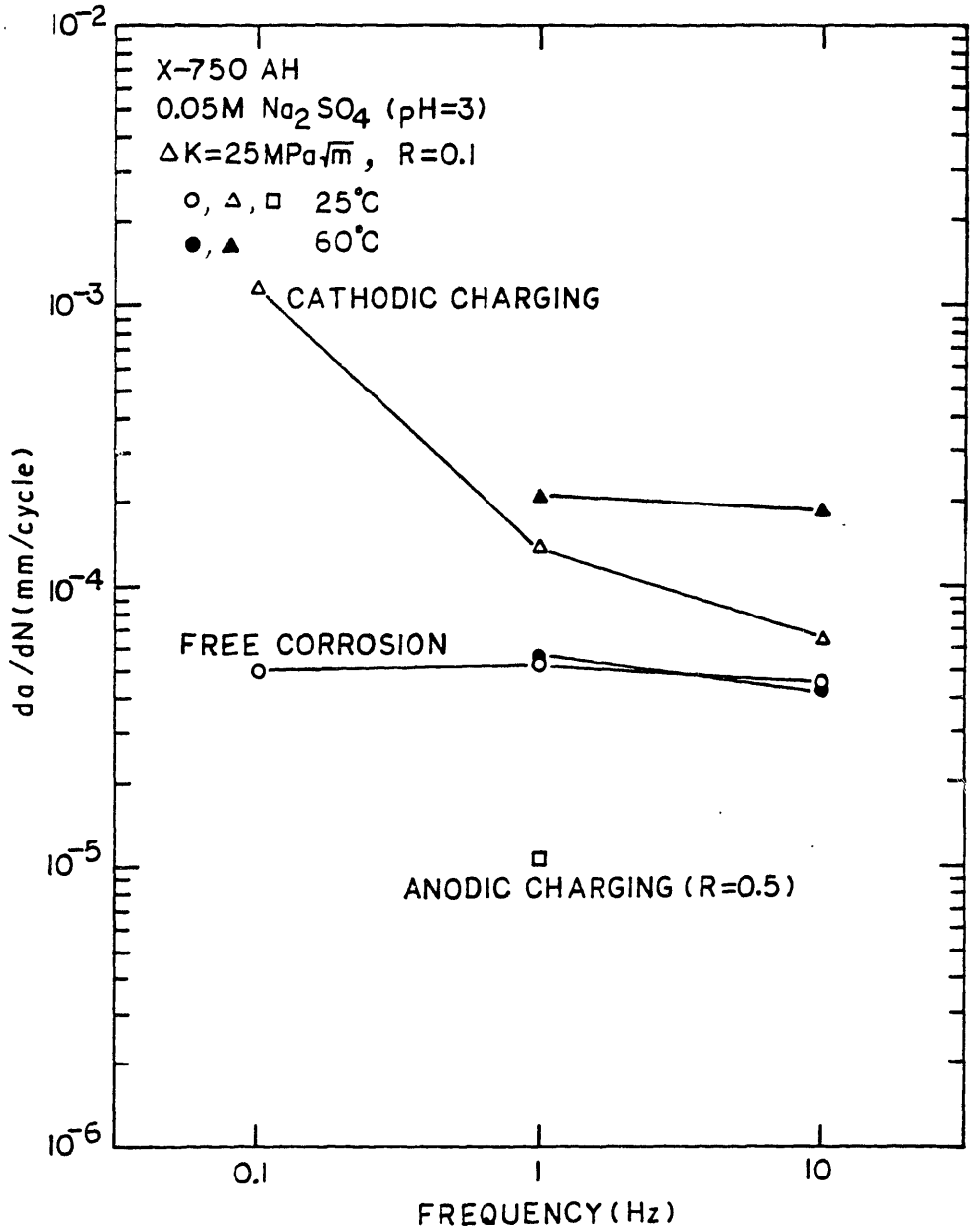

Figure 6.153 The effects of Cathodic and Anodic Charging at 0.5mA/cm^2 on the Fatigue Crack Growth Rate of the AH SEN Specimen in 0.05M Na_2SO_4(pH=3) Solution at 25 MPa$\sqrt{m}$ and R=0.1 as a Function of Frequency.

Figure 6.154 The SEM Fractograph of the AH SEN Specimen after a Fatigue Test in 0.05 M Na_2SO_4 (pH=3) Solution at 25 C with a Frequency of 10 Hz at 25 MPa$\sqrt{m}$ and R=0.1 under Free Corrosion.

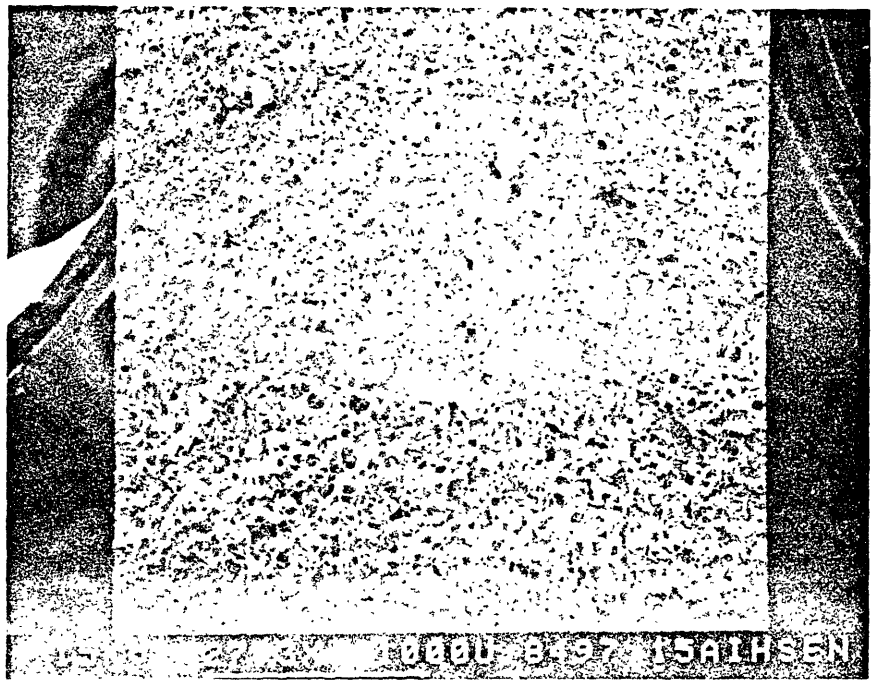

Figure 6.155 The SEM Fractograph of the AH SEN Specimen after a Fatigue Test in 0.05 M Na_2SO_4 (pH=3) Solution at 25 C with a Frequency of 0.1 Hz at 25 MPa$\sqrt{m}$ and R=0.1 with Potential Shifts in a Sequence of Cathodic Charging, Free Corrosion and Cathodic Charging at 0.5 mA/cm^2.

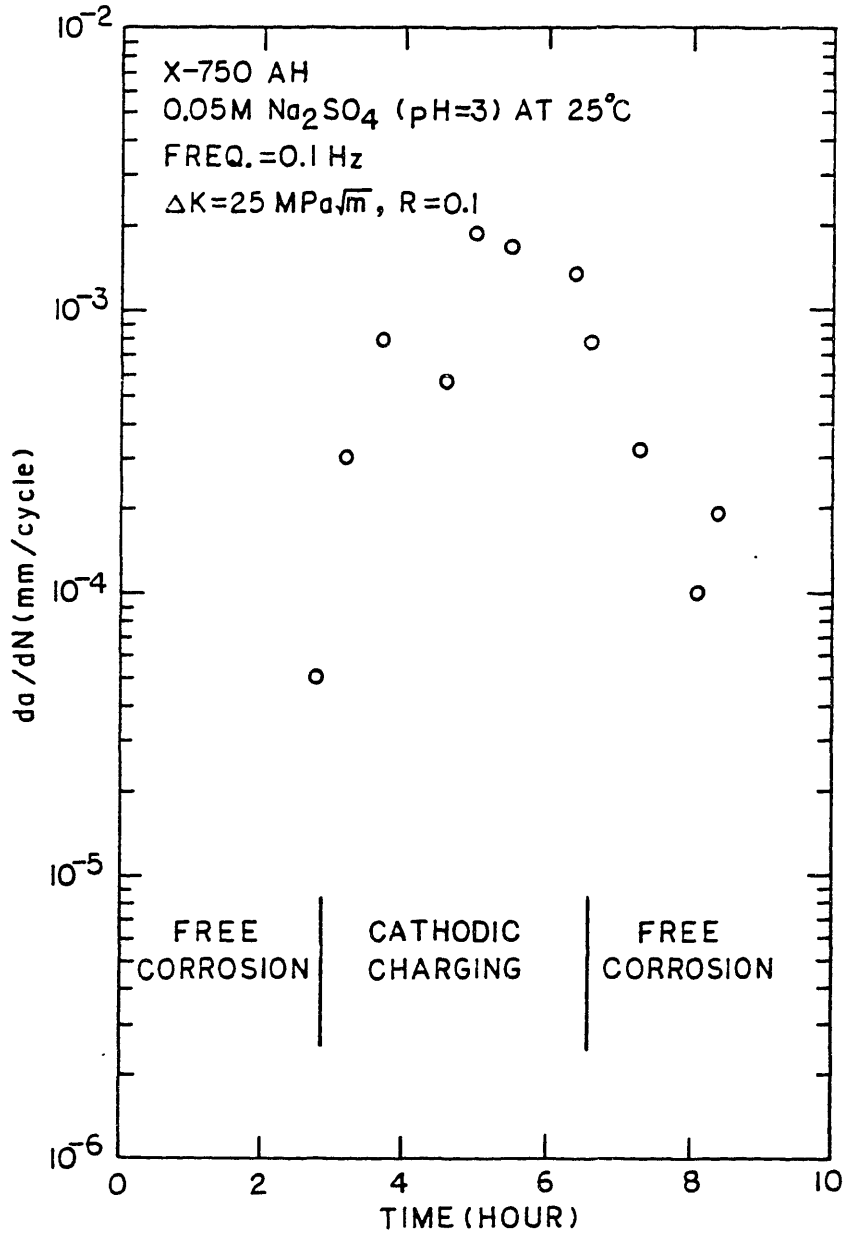

Figure 6.156 Responses in the Fatigue Crack Growth of the AH SEN Specimens to Cathodic Charging at 0.5 mA/cm^2 with a Frequency of 0.1 Hz at 25 MPa$\sqrt{m}$ and R=0.1 in 0.05 M Na_2SO_4 (pH=3) Solution at 25 C.

Figure 6.157 The SEM Fractograph of the AH SEN Specimen after a Fatigue Test in 0.05 M Na_2SO_4 (pH=3) Solution at 25 C with a Frequency of 1.0 Hz at 25 MPa$\sqrt{m}$ and R=0.1 during Initial Free Corrosion and Subsequent Cathodic Charging.

Figure 6.158 The SEM Fractograph of the AH SEN Specimen after a Fatigue Test in 0.05 M Na_2SO_4 (pH=3) Solution at 25 C with a Frequency of 1.0 Hz at 25 MPa$\sqrt{m}$ and R=0.1 under Cathodic Charging at 0.5 mA/cm^2.

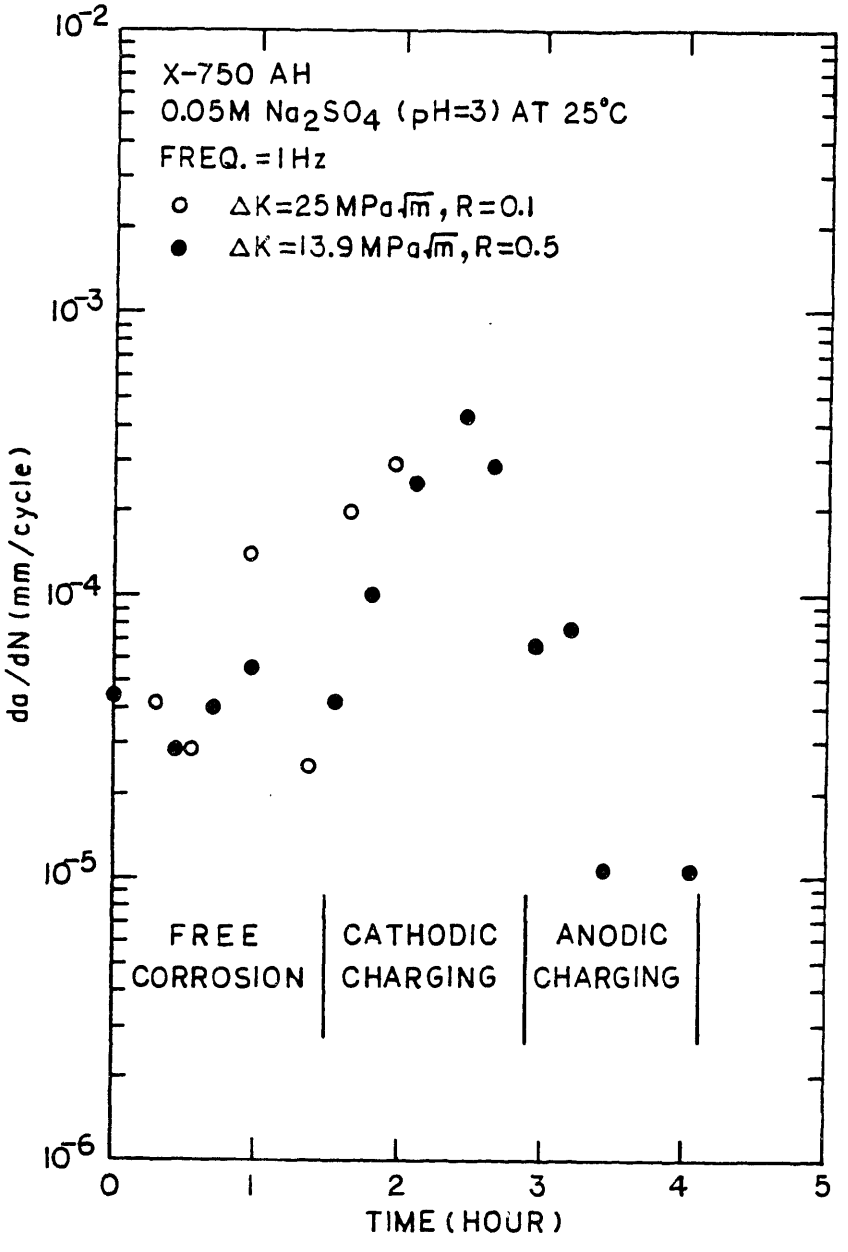

Figure 6.159 The Effect of Cathodic Charging at 0.5 mA/cm^2 on the Fatigue Crack Growth Rate of the AH SEN Specimen in the 0.05 M Na_2SO_4 (pH=3) Solution at 25 C with a Frequency of 1.0 Hz and at a K_{max} of 27.8 $MPa\sqrt{m}$ for two different R-ratios.

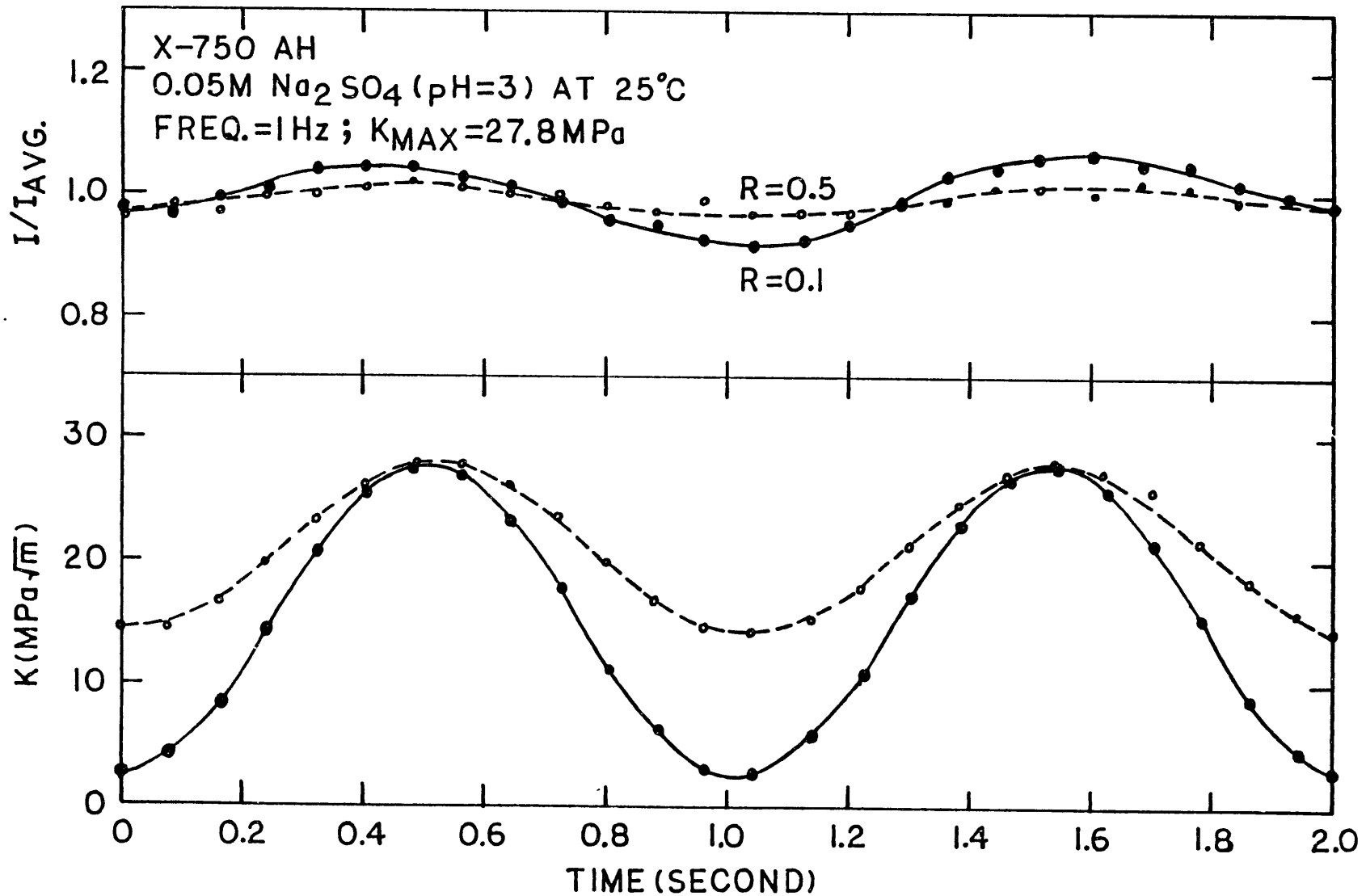

Figure 6.160 The Oscillation in Cathodic Currents during Load Cycles as Measured under Potentiostatic Controls of the AH SEN Specimen at a K_{max} of 27.8 MPa$\sqrt{m}$ and two different R-ratios in 0.05 M Na_2SO_4 (pH=3) Solution at 25 C.

fluctuation at R-ratio of 0.1 is approximately equal to the ratio of fracture surface area to the total exposed area of the specimen. Since the solution has a high conductivity, it is unlikely that the current will be blocked by the unloading as long as the electrolyte is in contact with the fracture surfaces. Hence the decrease in the current may be attributed to hydrogen bubbles trapped on the fracture surface. The squeezed bubble layer during the unloading may act as insulation. The fracture surface is expected to be replenished with solution by the restored spherical shape of the trapped hydrogen bubbles which results in the recovery of the current path. The higher R-ratio would allow less change in the shape of the surface gas bubbles resulting in the smaller current fluctuation.

The result at 60°C and 1 Hz is shown in Figure 6.161. The crack growth rate is increased by a factor of 4 with cathodic charging at 0.5mA/cm^2. In contrast with the relatively fast response observed at 25 C, there is a delayed effect of accelerated crack growth of about two hours after the cathodic charging is discontinued. The SEM fractograph for the transition region is shown in Figure 6.162. The fracture mode is observed to change more gradually than the transitions during tests in the high purity water or the lower temperature case in the sodium sulphate solution, as shown in Figures 6.152 and 6.155. The cases of the delayed effect is not identified. However, it may be postulated that the prolonged charging and transport may have led a significant accumulation in the plastic zone to hydride formation.

The results at 10 Hz, shown in Figure 6.163, show a considerable temperature dependence of the crack growth rate under cathodic charging. At the same current density, a factor of four increase in the crack growth rate is observed at 60 C while the increase at 25 C is found to be marginal, as shown in Figure 6.163. The fracture surfaces at 10 Hz are shown in Figures 6.164 and 6.165 at 25 C and 60 C, respectively. A slight increase in the amount of transgranular fracture is visible on the fracture surface at 25 C.

The effect of current density was also studied for a range between

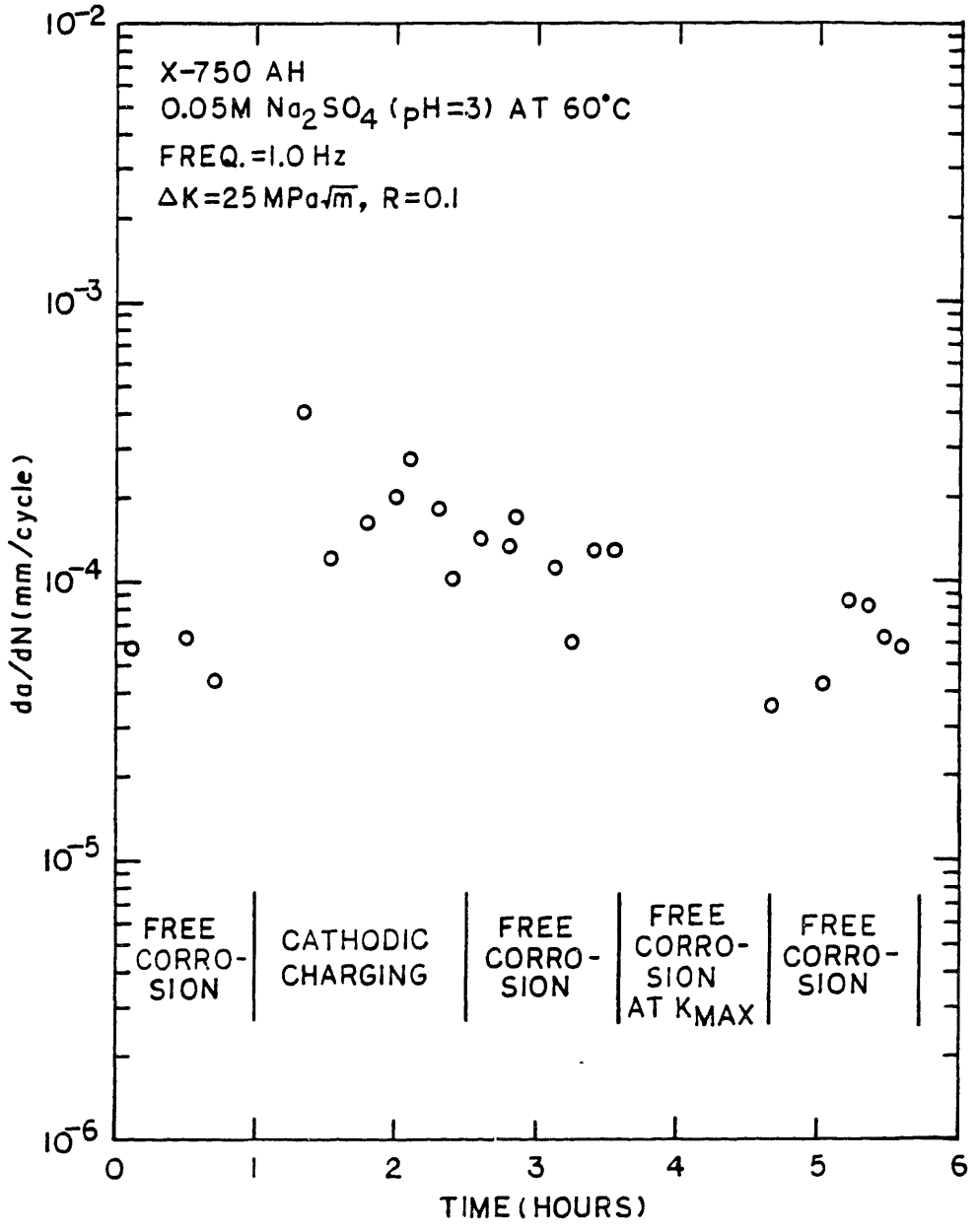

Figure 6.161 The Delayed Effect of Previous Cathodic Charging on the Fatigue Crack Growth Rate of the AH SEN Specimen in 0.05 M Na_2SO_4 (pH=3) Solution at 60 C at 25 MPa$\sqrt{m}$ and R=0.1 with a Frequency of 1.0 Hz.

Figure 6.162 The SEM Fractograph of the AH SEN Specimen after a Fatigue Test in 0.05 M Na_2SO_4 (pH=3) Solution at 60 C with a Frequency of 1.0 Hz at 25 MPa$\sqrt{m}$ and R=0.1 during Free Corrosion following Cathodic Charging and Test Holding at K_{max} for 1 hour.

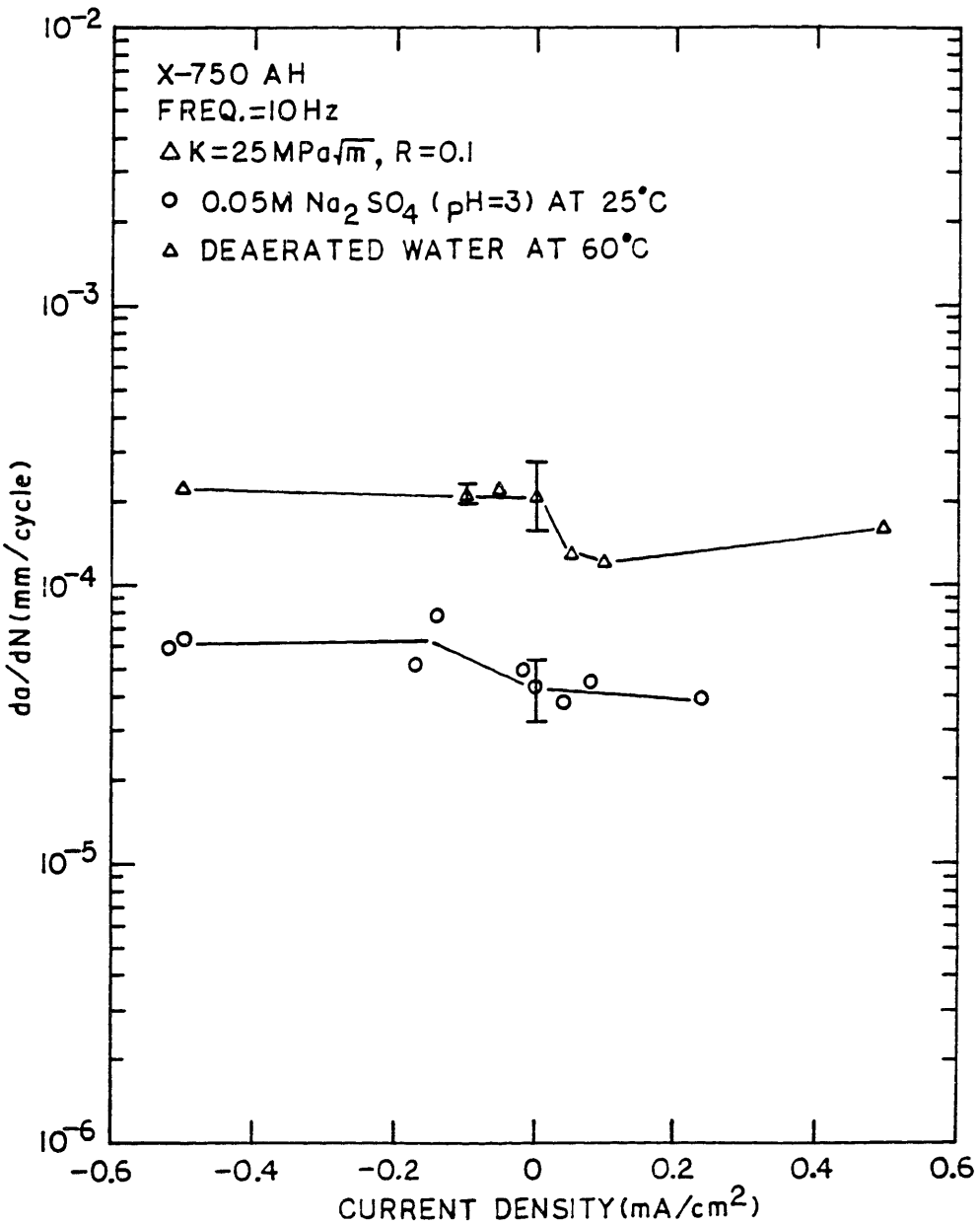

Figure 6.163 The Fatigue Crack Growth Behaviors of the AH SEN Specimen at 60 C in Comparison with that at 25 C at 25 MPa$\sqrt{m}$ and R=0.1 with a Frequency of 10 Hz in 0.05 M Na_2SO_4 (pH=3) Solution.

Figure 6.164 The SEM Fractograph of the AH SEN Specimen after a Fatigue Test in 0.05 M Na_2SO_4 (pH=3) Solution at 25 C with a Frequency of 10 Hz at 25 MPa$\sqrt{m}$ and R=0.1 during Cathodic Charging at 0.5 mA/cm^2.

Figure 6.165 The SEM Fractograph of the AH SEN Specimen after a Fatigue Test in 0.05 M Na_2SO_4 (pH=3) Solution at 60 C with a Frequency of 10 Hz at 25 MPa$\sqrt{m}$ and R=0.1 during Cathodic Charging at 0.5 mA/cm^2.

$5\mu A/cm$ and $0.5mA/cm^2$ at frequencies of 1 Hz and 10 Hz at 25 C. The results are compared with the data in the high purity water, as shown in Figures 6.166 and 6.167 for 1 Hz and 10 Hz, respectively. At 1 Hz in the sodium sulphate solution, the crack growth rate increases sharply with increasing cathodic current density. A saturation current density is observed to be about $-0.5mA/cm^2$ at which time the crack growth rate is comparable with that in the high purity water at 60 C. At 10 Hz, there is a measurable effect of a change in current density. But the change in crack growth rate is only marginal with charging in either directions. The smallest cathodic current density observed with the intergranular mode is found to be about 0.14 mA/cm^2. The fracture surfaces at cathodic current densities of 0.01 mA/cm^2 and 0.14 mA/cm^2 are shown in Figures 6.168 and 6.169. The fracture surfaces under the cathodic charging at $0.4mA/cm^2$ is found to include about 50% intergranular region which is shown in the micrograph. Hence the threshold current density for the intergranular mode appears to lie between 0.1 mA/cm^2 and 0.4 mA/cm^2. It should be noted that the intergranular mode is accompanied with only a slightly increased crack growth rate at current density near the threshold value.

In order to confirm the visually observed increase in plasticity near crack tip during intergranular crack growth, side walls of specimens were examined under optical microscope. Optical micrographs in Figure 6.170 reveal the wider region of plastically roughened surface in high purity water compared with that in 0.05M Na_2SO_4 (pH=3) solution. The plastic zone size was estimated from the size of roughened surfaces and plotted versus the corresponding crack growth rate, in Figure 6.171. The data clearly support the correlation between the high craack growth rate and the laarge plastic zone size. It should be emphasized that the behavior of increased plasticity is observed both in high purity water and in the sodium sulphate solution with cathodic charging. This behavior supports the postulation that a fracture mechanism in both environmental conditions involves crack tip a softening behavior.

6.5.3 Summary

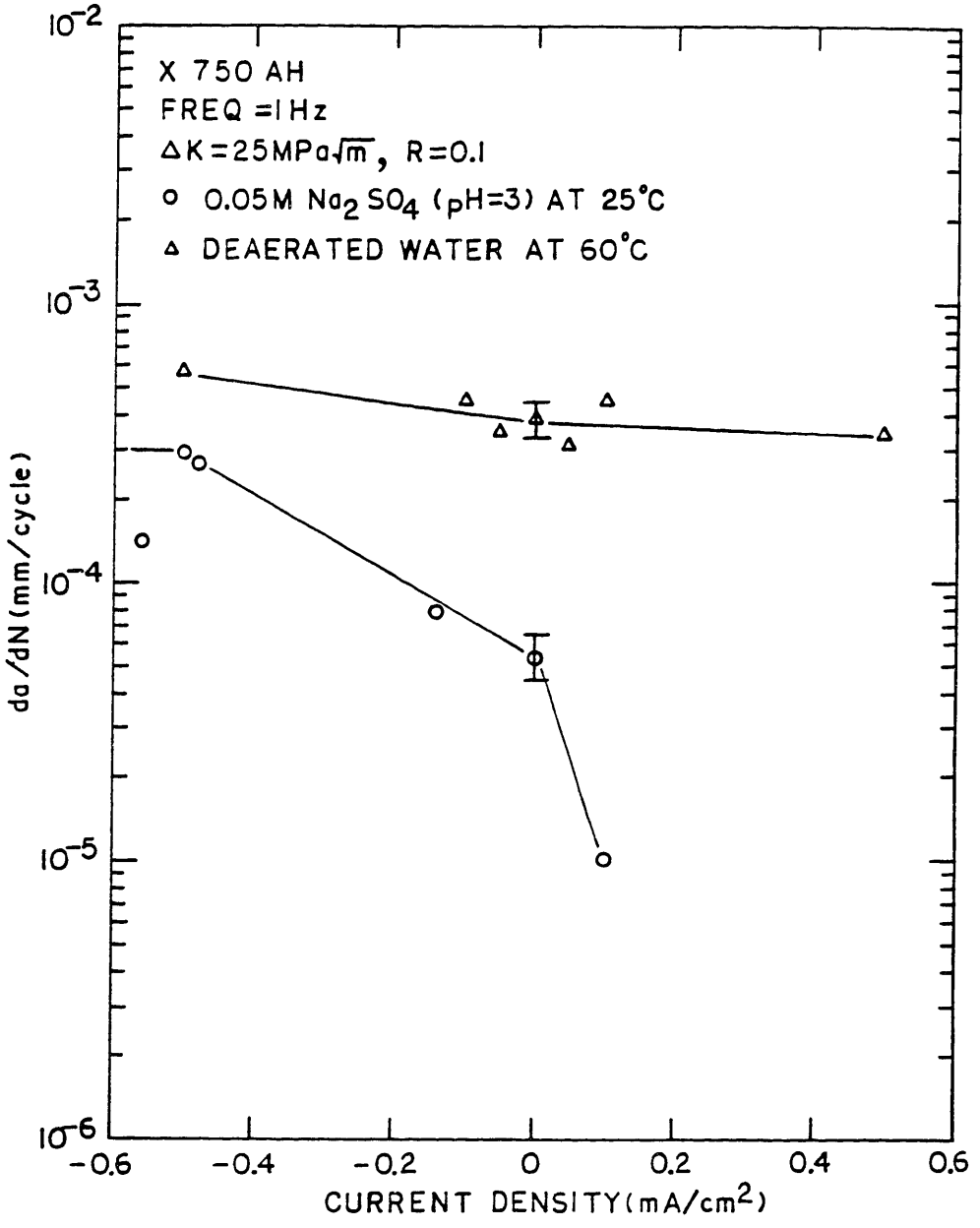

Figure 6.166 Fatigue Crack Growth Rate of the AH SEN Specimen as a Function of Charging Current Density in Two Different Environments at 25 MPa$\sqrt{m}$ and R=0.1 with a Frequency of 1.0 Hz.

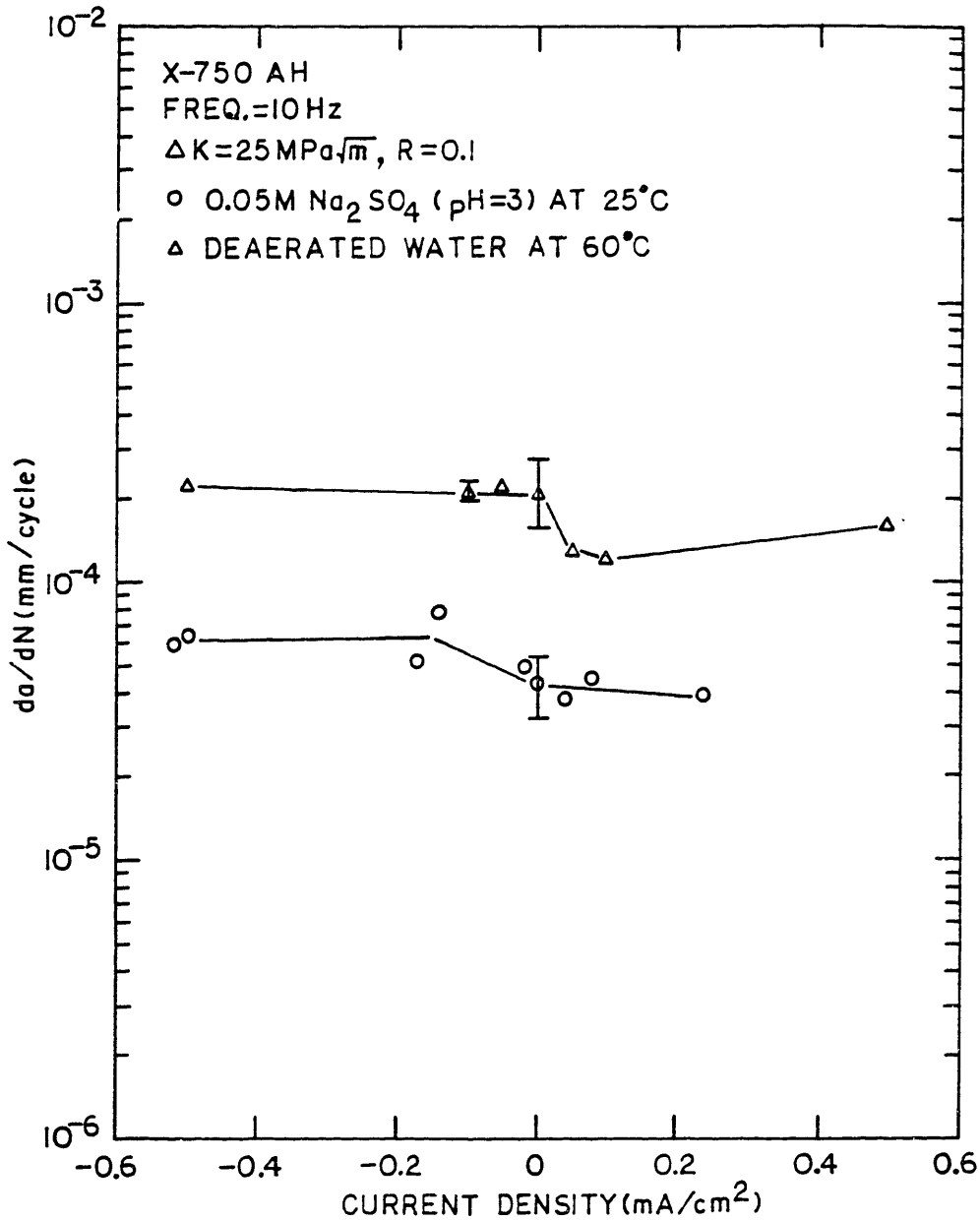

Figure 6.167 Fatigue Crack Growth Rate of the AH SEN Specimen as a Function of Charging Current Density in Two Differnt Environments at 25 MPa$\sqrt{m}$ and R=0.1 with a Frequency of 10 Hz.

Figure 6.168 The SEM Fractograph of the AH SEN Specimen after a Fatigue Test in 0.05 M Na_2SO_4 (pH=3) Solution at 25 C with a Frequency of 10 Hz at 25 MPa$\sqrt{m}$ and R=0.1 during Cathodic Charging at 0.01 mA/cm^2.

Figure 6.169 The SEM Fractograph of the AH SEN Specimen after a Fatigue Test in 0.05 M Na_2SO_4 (pH=3) Solution at 25 C with a Frequency of 10 Hz at 25 MPa$\sqrt{m}$ and R=0.1 during Cathodic Charging at 0.14 mA/cm^2.

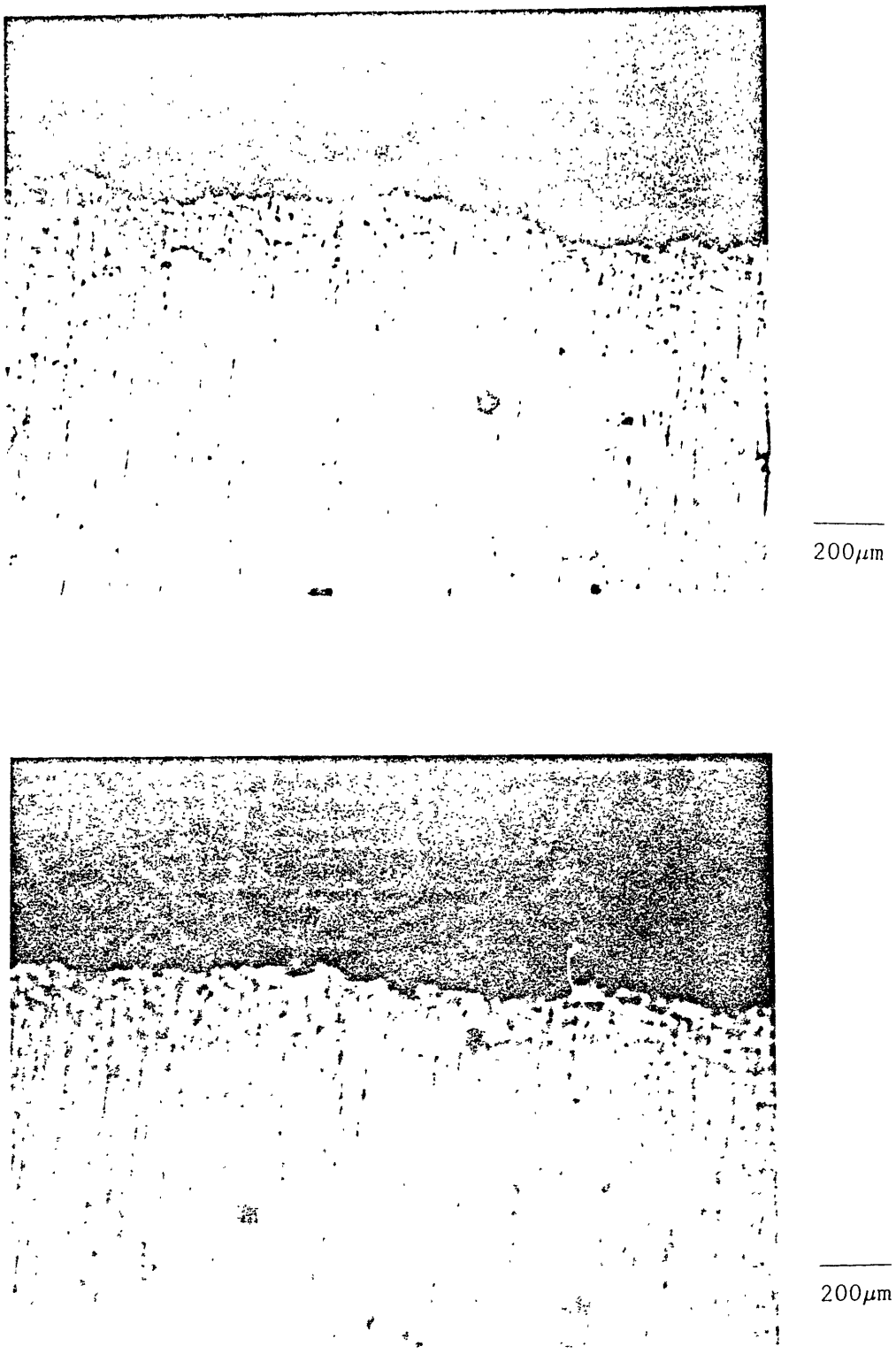

Figure 6.170 Optical Micrographs for Side Walls of SEN Specimens showing Increased Plastic Zone in High Purity Water (upper) Compared with that in 0.05M Na_2SO_4 Solution (lower).

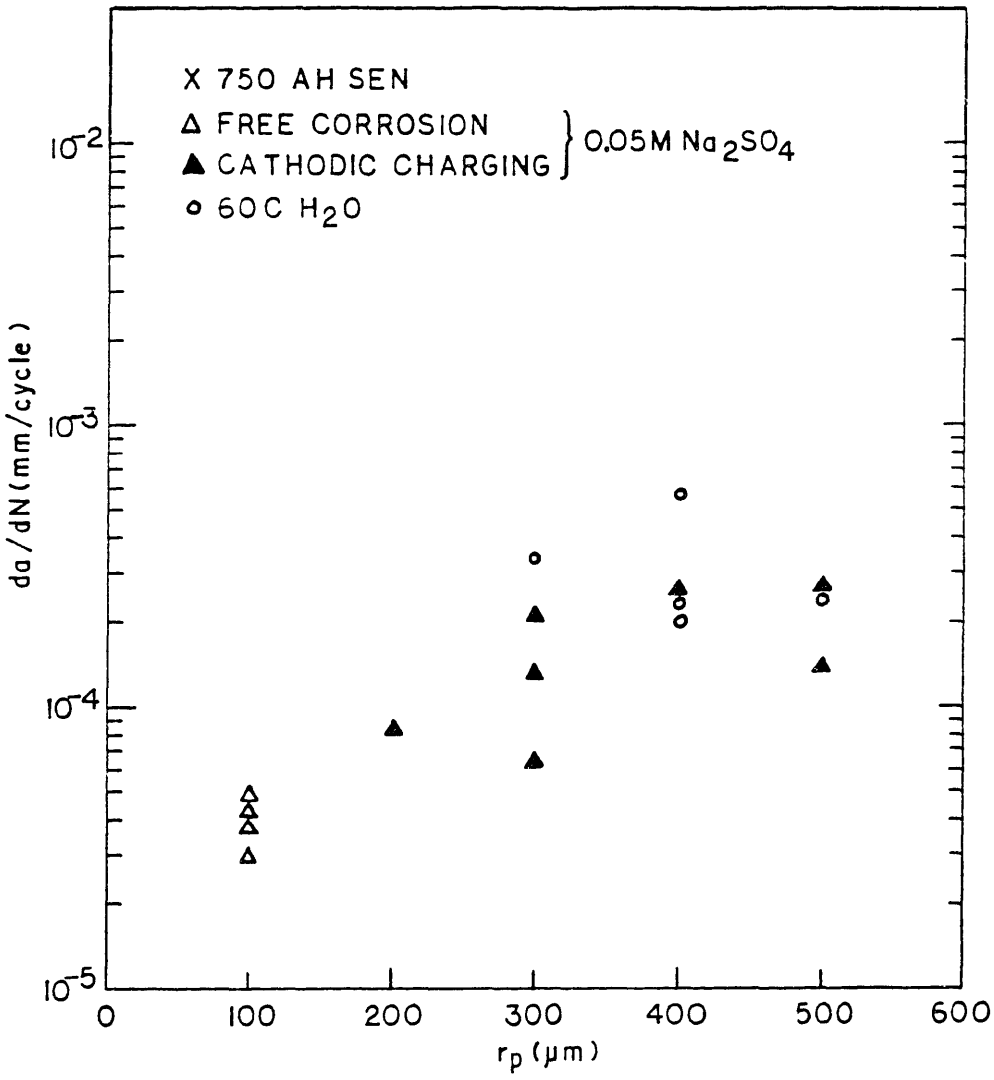

Figure 6.171 Relation between the Crack Growth Rate and Plastic Zone Size as Estimated from Side Wall Examination.

The corrosion fatigue tests were performed on the AH SEN mateiral of alloy X-750 plate at temperatures between 25 C and 60 C. The AH SEN material was shown to behave in the same manner as the CT specimen of heat 94051 as to the crack growth rate dependence on the temperature and frequency as well as the mode of fracture. The crack growth rates of the AH SEN specimens were consistently lower than those of the CT specimen which could be explained by about three times larger grain size of the former condition.

In deaerated water, the fracture mode was always intergranular and the crack growth rate was up to 11 times higher than that in air. Cathodic charging at a current densities of up to 0.5mA/cm^2 did not change the crack growth rate or fracture mode for frequencies between 0.1Hz and 10Hz. Anodic charging at current densities of up to 0.5 mA/cm^2 showed no effect on fatigue behavior in the deaerated water at both 1 Hz and 10 Hz.AT 0.1 Hz, there was initially no effect by the anodic charging during the first hour. The prolonged anodic charging resulted in a solution contamination with yellowish hexavalent chromate ions and a concurrent decrease in the crack growth rate. This is attributed primarily to the effect of increased solution conductivity by a factor of 100.

The tests were repeated using a 0.05M Na_2SO_4 (pH=3) solution so that the solution conductivity was increased by a chemically stable sulphate ions. The crack growth rate was decreased to a value comparable to that in air with a transgranular fracture mode. The intergranular fracture at the high crack growth observed in the deaerated water was reproduced in the sodium sulphate solution by cathodic charging at a realistic galvanic current density.

The plastic zone size was increased by about a factor of four during cathodic charging. The same behavior was observed during crack growth in water. Therefore it is suggested that the two embrittlement observations share an identical mechanism.

The acceleration in crack growth by cathodic charging increases with decreasing frequency in the range between 0.1 Hz and 10 Hz. Hence, the severity of embrittlement is correlated with the amount of hydrogen introduced to the crack tip by cathodic charging in the conducting solution. At 25 C, the crack growth rate showed no delayed effect after cathodic charging. A significant effect of previous cathodic charging was observed on the crack growth rate during a subsequent test under free corosion at 60°C. This is attributed to the increased hydrogen diffusion into specimen at the temperature.

6.6 RESULTS OF THE SLOW STRAIN RATE TESTS IN HIGH PURITY WATER

6.6.1 Results with Alloy 600

Among the five heats of alloy 600, heats NX1638, NX2650 and the LTMA condtion of 96834 were used for the slow strain rate tests (SSRT) in high purity water. The effect of carbon content was examined by comparing heat NX1638 and NX2650. The effect of final annealing temperature was included by comparing the results of heats NX2650 and the LTMA condition of 96834. The effects of sensitized microstructure is also studied by using the SAS conditon of heat NX2650.

It was necessary to drastically reduce the number of tests due to experimental difficulties. Tests at high temperatures were unsuccessfully terminated due to frquent failure of the high pressure pump which exhibited an average time to failures of 2-3 weeks. Hence, the use of high test temperatures was limited to comparison of the low-carbon HTMA condition with the high-carbon LTMA condition. The second problem was a gradual deterioration of the radial seal for the pull-rod which futher limited the maximum test temperature to 344 C during the period of alloy 600 testings. Strain range used were between $1x10^{-4}$ and $2x10^{-7}$ sec^{-1}.

The HTMA condition of NX1638 and NX2650, and the SAS condition of NX2650 were tested in deaerated water which has a measured resistivity of 8MΩ

cm, pH of 6.5 and oxygen content of 90+20ppb at room temperature. The heat 96834 was tested with a hydrogen overpressure at 0.18 MPa in order to accelerate the embrittlement. As mentioned in Chapter 4, a reasonable correciton was made for the pull rod seal force. The corrected data are shown in Table 6.8. The corrected ultimate tensile strength values are found to agree well with the values expected from the fractographs and the tensile data which will be discussed herein.

The ACPD technique was used with a probe spacing of 1cm. At the time of the alloy 600 testing the highest frequency possible was 113kHz. Hence, a frequency of 105 kHz was used for all SSRT testing of alloy 600. The sensitivity was expected to deteriorate to 70μm due to the factor of two lower frequency compared with that used in the sensitivity study, in Chapter 4. The primary goal of the ACPD application in the tests was aimed at verificaiton of the detection sensitivity. The approach used for the sensitivity study, presented in Chapter 4, was adopted.

Low Temperature Behaviors

Two tests at 93 C were made with the HTMA condition of NX2650. This heat was selected for the highest yield strength and small grain size which was the most likely to support low temperature embrittlement compared with other conditions.. The stress-strain and stress-time curves are shown in Figure 6.172 at a strain rate of $1x10^{-5}sec^{-1}$. The elongation and corrected UTS are compared with the tensile test data in Table 6.9. No appreciable change in the tensile properties suggests the environmental effect is negligible. The fractographs are shown in Figure 6.173. The fracture surfaces are characterized by microvoid coalescence followed by ductile rupture. The fracture surface showed the same ductile failure as in the air tensile test indicating no environmental effect. The normalized ACPD is observed to be fairly linear with the true strain before the necking point. The lack of environment assisted cracking allows use of this result as the reference ACPD. A least square fit leads to the following relationship;

Table 6.8

The Correction of the Strength Data for Friction Force due to Two-seal Arrangement for SSRT on Alloy 600.

Material	T (C)	P (MPa)	Y.S.(MPa) SSRT	Y.S.(MPa) AIR	Y.S.(MPa) Δ	U.T.S.(MPa) SSRT	U.T.S.(MPa) Corrected
NX2650 HTMA							
	93	3.0	483	426	57	767	710
	93	3.0	483	430	53	767	714
	330	16.5	452	386	74	800	726
NX2650 SAS							
	150	2.4	307	207	100	*	*
	288	11.7	362	191	171	*	*
NX1638 HTMA							
	344	18.1	498	308	190	*	*
	344	17.9	498	308	190	788	598
96834 LTMA							
	340	17.9	543	335	208	*	*
	344	17.2	431	335	96	825	729

NOTE: * Test stopped before reaching the U.T.S.

Table 6.9

Summary of the Slow Strain Rate Tests on Alloy 600
in a Deaerated High Purity Water

Material	T (C)	ϵ (sec^{-1})	U.T.S (MPa) SSRT	U.T.S (MPa) AIR	Elongation(%) SSRT	Elongation(%) AIR	t (hr)	A_{max} (μm)
NX2650 HTMA								
	93	1E-4	697	715	29.0	29.6	0.8	0
	93	1E-5	710	711	28.5	29.4	8.6	0
	330	2E-6	726	714	33.0	33.8	52.0	0
NX2650 SAS								
	150	1E-5	*	624	*	47.2	7.0	0
	288	1E-5	*	617	*	51.2	11.2	0
NX1638 HTMA								
	344	5E-7	*	621	*	39.7	154	0
	344	2E-7	598	621	*	39.7	405	10
96834 LTMA**								
	340	2E-7	*	744	*	36.1	390	15
	344	2E-7	729	744	25.5	36.1	435	32

NOTE: * Test stopped before reaching the U.T.S.
** A hydrogen overpressure of 0.18MPa is used.

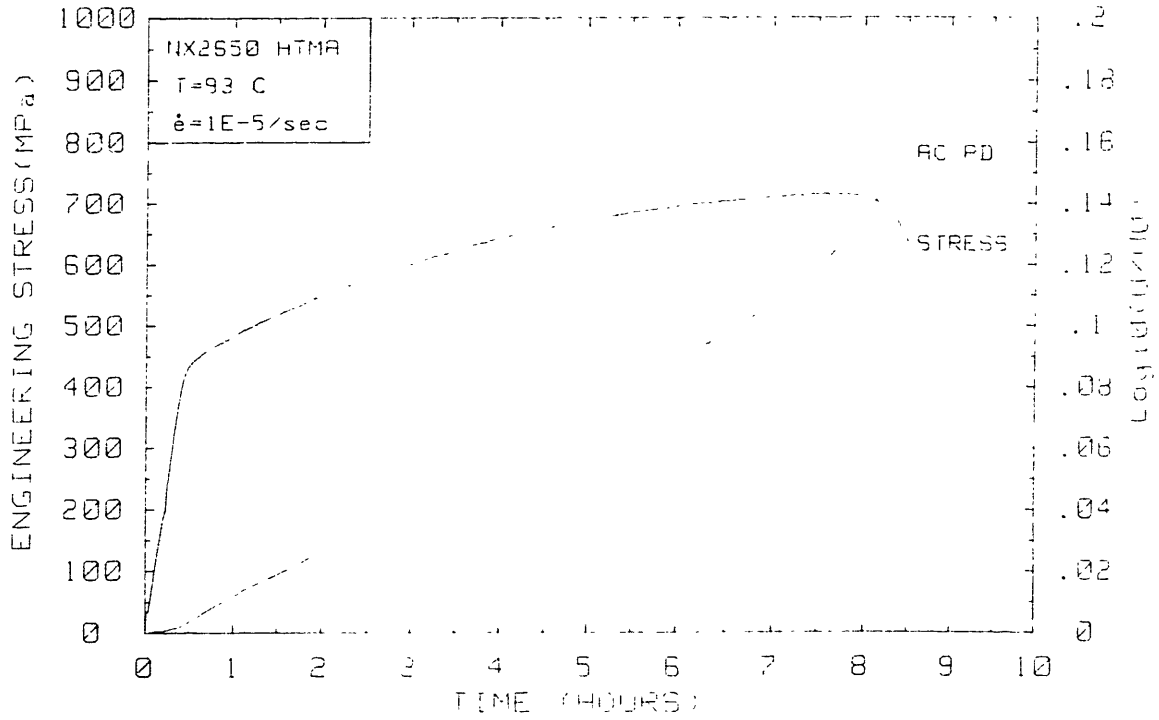

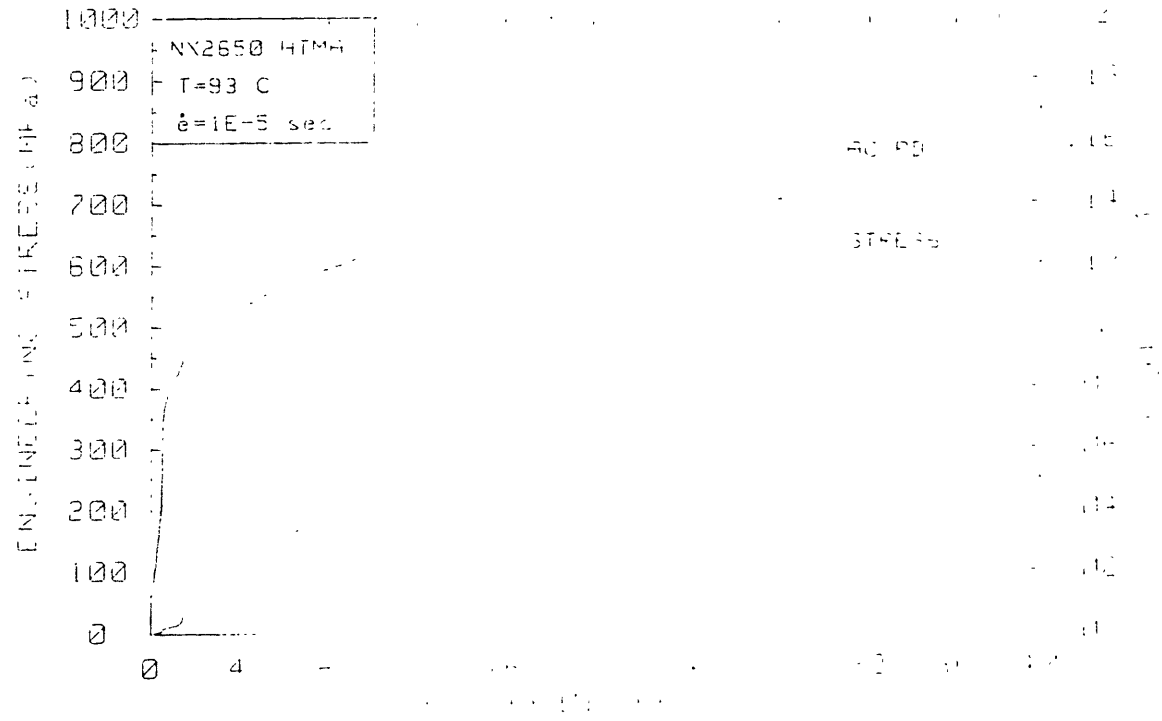

Figure 6.172 Stress and ACPD versus Time (upper) and Strain (lower) for HTMA Condition of NX2650 During a SSRT at a Strain Rate of 1 x 10^{-5} sec^{-1} in a High Purity Deaerated Water at 93 C.

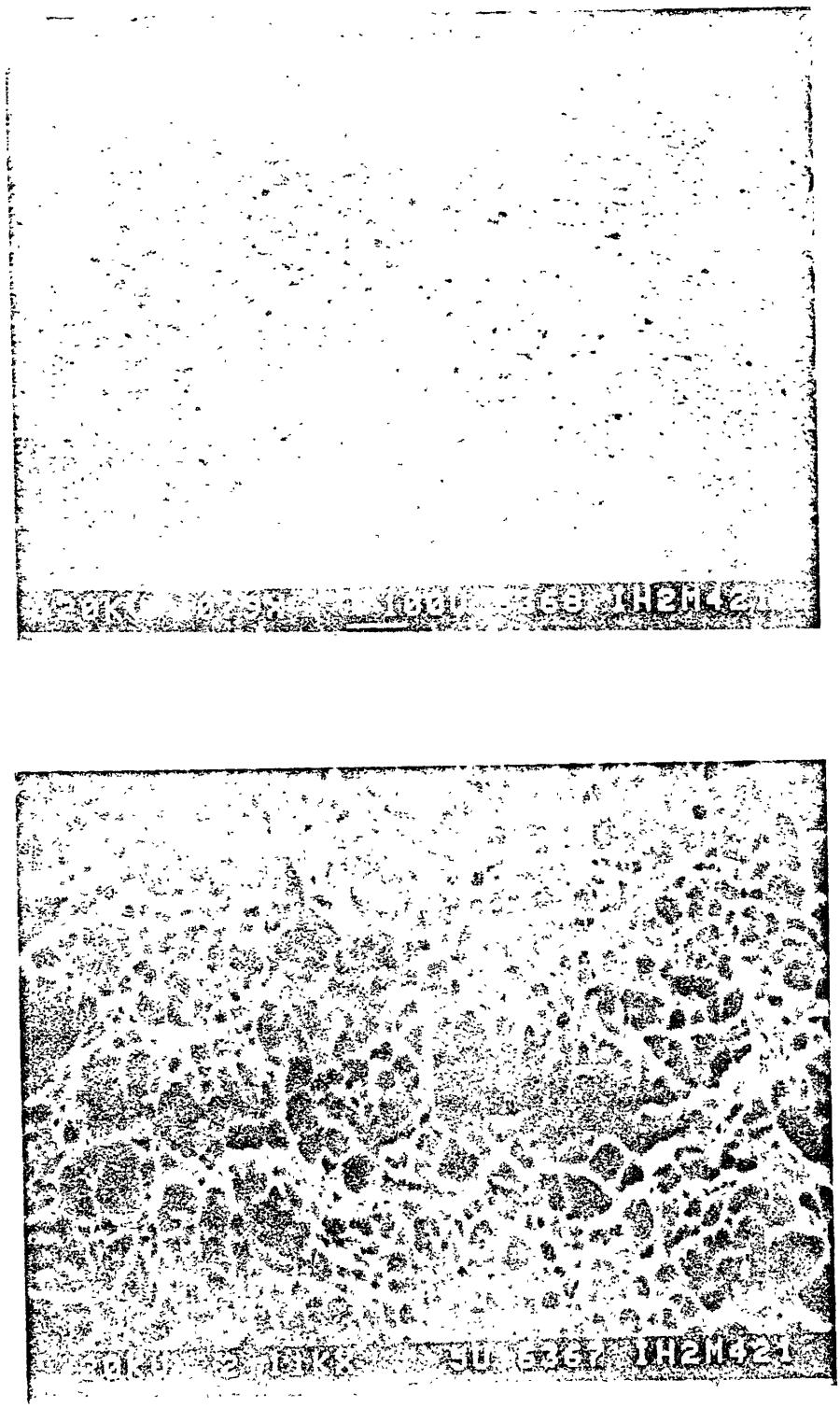

Figure 6.173 SEM Fractographs for the SSRT Specimen of HTHA Condition of HX2050 Tested at a Strain Rate of 1×10^{-5} sec^{-1} in a High Purity Deaerated Water at 93 C.

$$\log_{10}\left(\frac{U}{U_o}\right) = 0.002 + 0.465\ \epsilon \qquad (6\text{-}8)$$

where U_o and U are the ACPD's at zero strain and at a strain of ϵ, respectively. The slope 0.465 is lower than the theoretical value of 0.651 by about 30%. This is attirubted to the perturbation of the potential field by the presence of the probe wire. In a practical sense the difference does not present any problem since it can be compensated for by using the same spacing for all subsequent tests.

The result at 93 C for a strain rate of $1x10^{-4}sec^{-1}$ is shown in Figure 6.174. The tensile properties agree well with the tenisle test data. The fracture surface are characterized by exactly the same micrographs shown in Figure 6.173, indicating that environmental effects ars absent. Thus no environment assisted cracking was found with alloy 600 in the low temperature water. The ACPD data was obtained only upto 13% strain after which failure of the lead wire weld joint caused signal loss.

High Temperature Behaviors

The tests for a range of temperature between 150 C and 344 C were performed to study the behavior at high temperature. The results for the HTMA condition of NX1650 are shown in Figure 6.175. Comparison with the tensile test data indicates that no environmental effect is present. The SEM fractographs are shown in Figure 6.176. Microvoids are found all over the fracture surface including regions near the edges. The side wall shows a number of transgranular cracks oriented at 45° with respect to the loading axis. A comparison with the tensile specimen surface in Figure 6.104 indicates that there is no appreciable differnce in the fracture surface. Therfore, it is believed that no environmental effect is introduced with a strain rate of $2x10^{-6}sec^{-1}$ at 330 C. Further test on this material at lower strain rate was unsuccessfully terminated due to pump failure.

With the SAS condition of NX2650 a test was performed at a strain rate

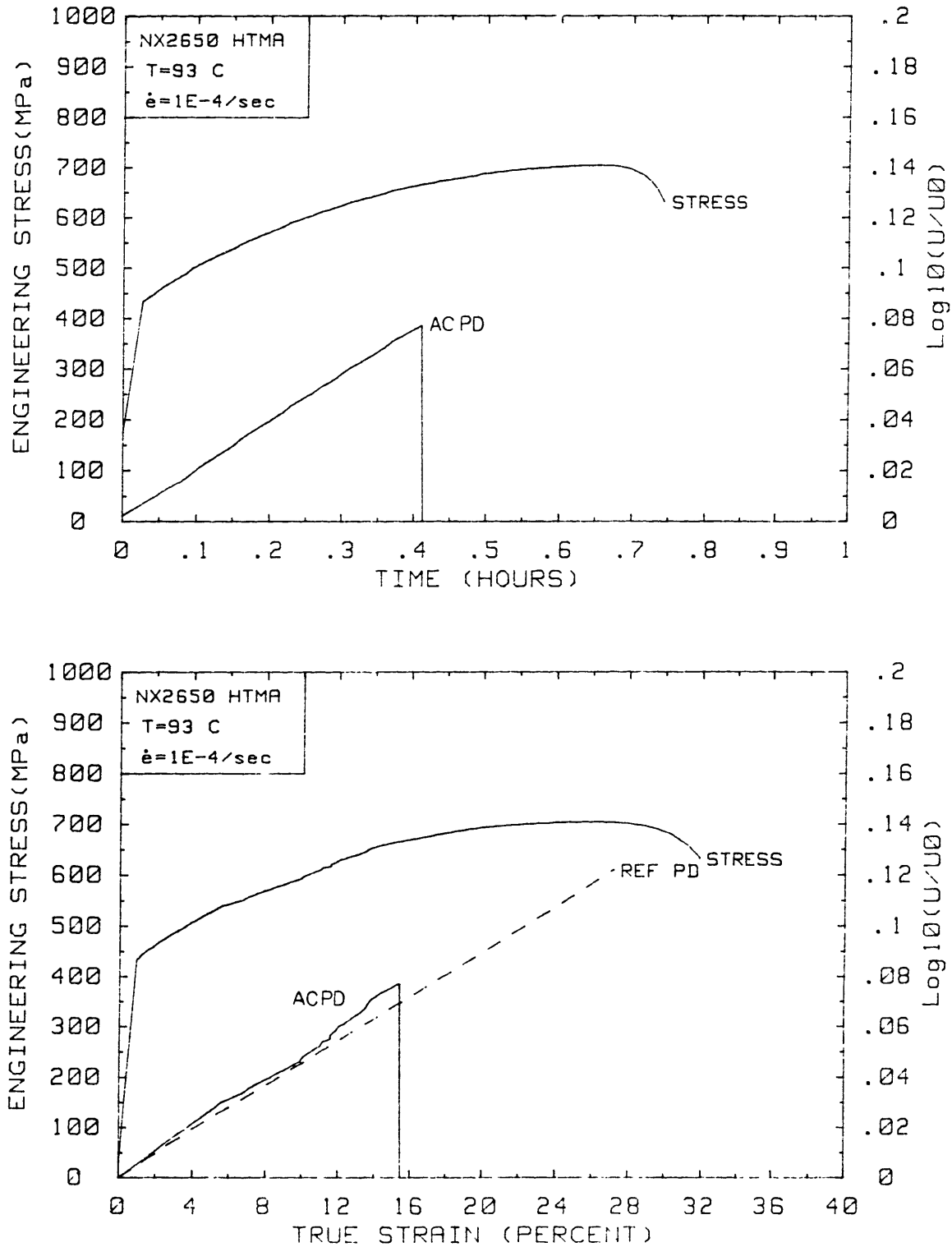

Figure 6.174 Stress and ACPD versus Time (upper) and Strain (lower) for HTMA Condition of NX2650 during a SSRT at a Strain Rate of 1 x 10^{-4} sec^{-1} in a High Purity Deaerated Water at 93 C.

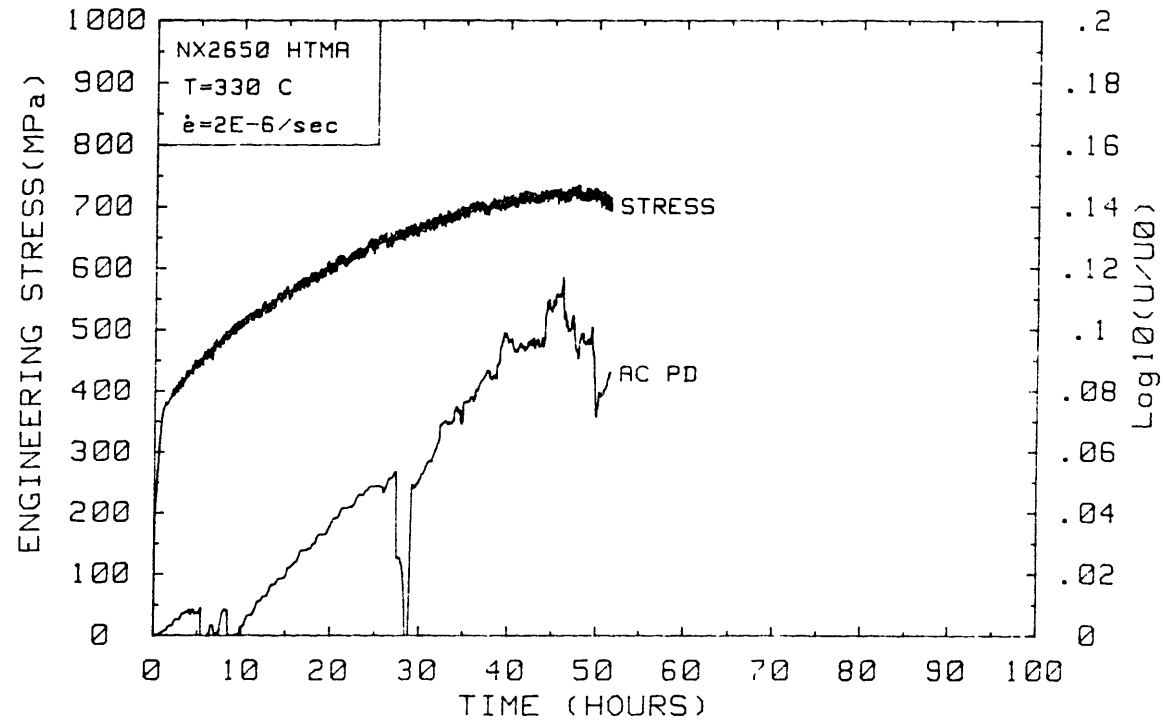

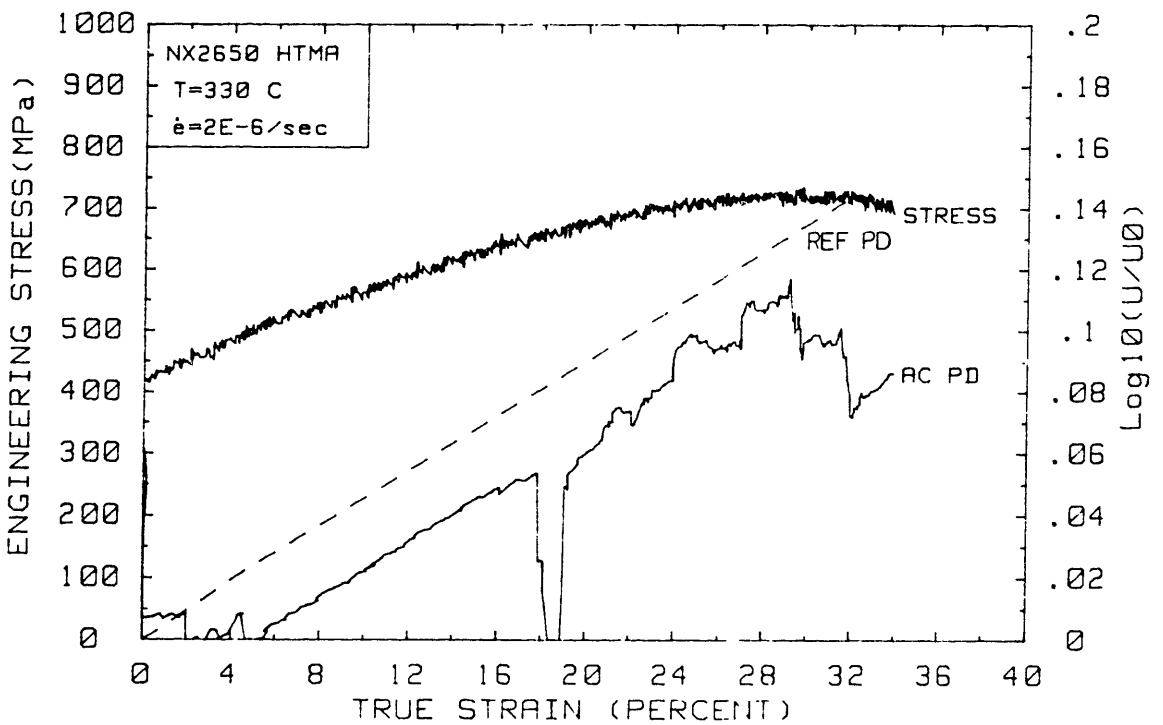

Figure 6.175 Stress and ACPD versus Time (upper) and Strain (lower) for HTMA Condition of NX2650 During a SSRT at a Strain Rate of 2 x 10^{-6} sec^{-1} in a High Purity Deaerated Water at 330 C.

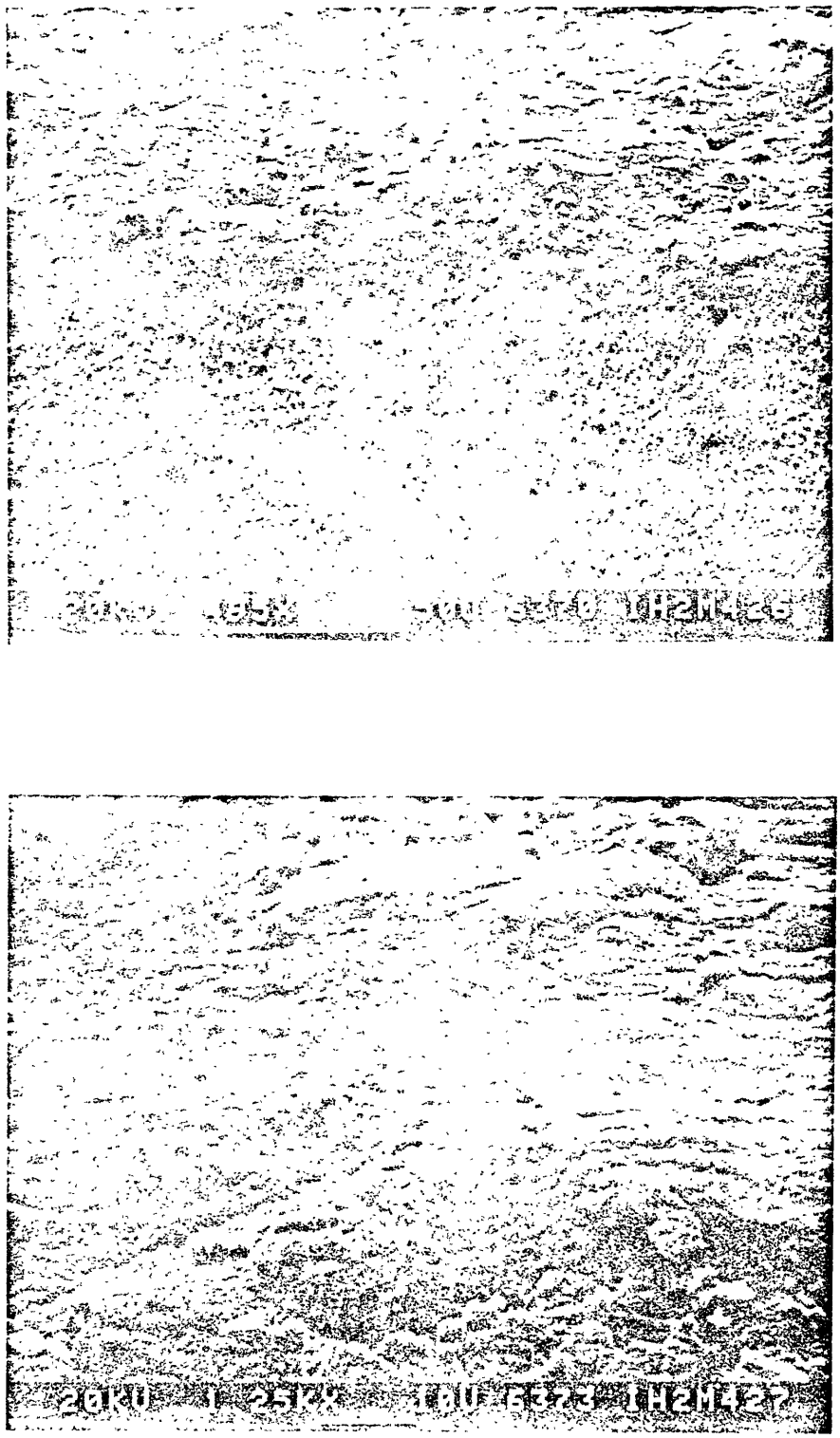

Figure 6.176 SEM Fractographs for the SSRT Specimen of HTMA Condition of NX2650 Tested at a Strain Rate of 2×10^{-6} sec^{-1} in a High Purity Deaerated Water at 330 C.

of $1x10^{-5}sec^{-1}$ at 150 C. The test was intentionally stopped to examine the fracture surface at about 18% strian. No side wall cracks were visible using the SEM. The specimen was pulled to failure in room temperature air. The fracture surfaces are shown in Figure 6.177. There are patches of shear lips which have an average size equal to the grain size of this mateial. The detailed examination of the patches shows fine slip lines mixed with microvoids. Side wall revealed that the transgranular crystallographic cracks typically observed in air tensile tests. The second test on the SAS condition was made at 288 C at the same strain rate. The test was intentionally stopped after an unusual transient in the ACPD signal, as shown in Figure 6.178. The surface examination revealed no evidence of cracking. The specimen was pulled to failure in air to observe the fracutre surface near the edges. The SEM fractographs are shown in Figure 6.179. The inner regions show the patches of shear rupture with an average size equal to the grain size which is the characteristics of tensile deformation of the SAS condition. The side wall shows some grooves due to ductile deformation. No crack is found on the side wall. The unusual transient in ACPD signal is thus attributed to noise with undetermined origin. Its occurrence was repeated during later experiments when the probe attachment had deteriorated after a large deformation. The resultant increase in the overall uncertainty in the ACPD signal was a critical problem with alloy 600 tests in which the probe spacing was as much as 1cm.

It became evident that a higher temperature and a lower strain rate was required to introduce any environmental effect. A temperature of 344 C was used for further testing with the HTMA condition of heat NX1638 and the LTMA condition of 96834. The results at 344 C at a strain rate of $5x10^{-7}sec^{-1}$ are shown for the HTMA condition of NX1638 in Figure 6.180. The test was stopped to examine the specimen after the ACPD increase. There were no significant surface cracks suggesting that the ACPD increase was attributed unstable probe attachement. The specimen was broken open in air and the fracture surface is shown in Figure 6.181. No crack was observed from the edge of the fracture surface. The side wall shows surface damages from the slip defromation which compares well

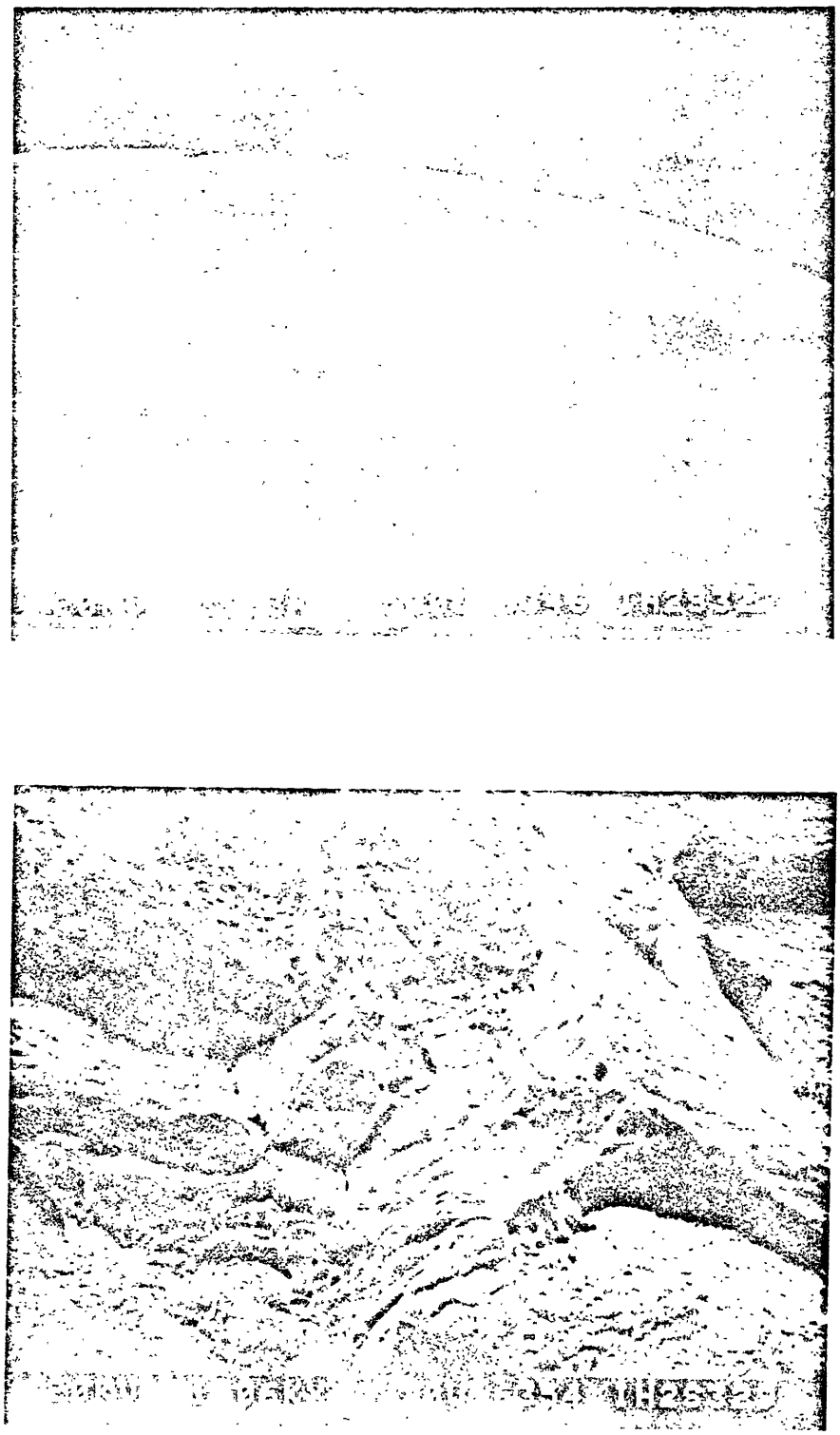

Figure 6.177 SEM Fractographs for the SSRT Specimen of SAS Condition of NX2650 Tested at a Strain Rate of 1×10^{-5} sec^{-1} in a High Purity Deaerated Water at 150 C.

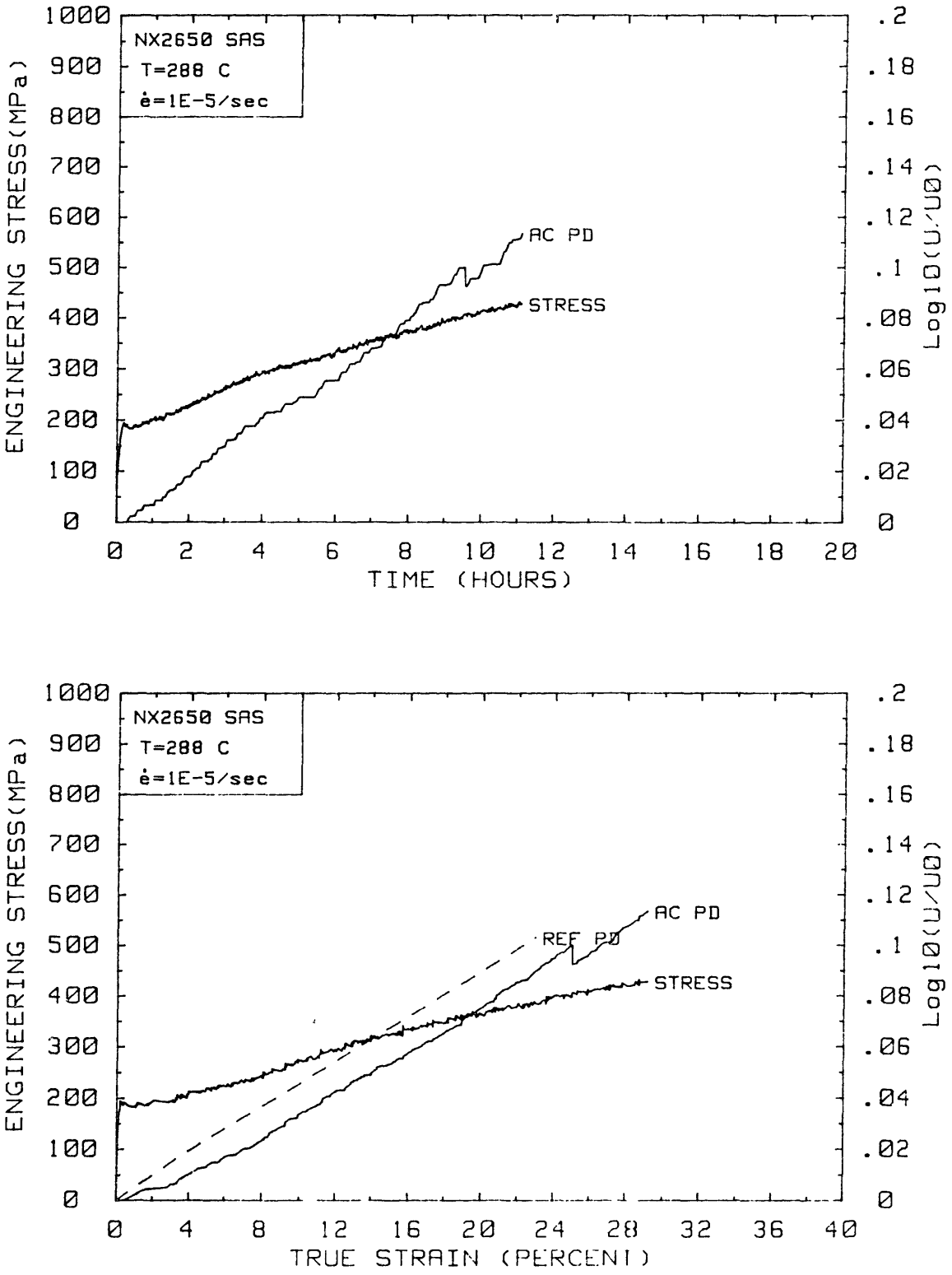

Figure 6.178 Stress and ACPD versus Time(upper) and Strain(lower) for the SSRT Specimen of SAS Condition of NX2650 Tested at Strain Rate of 1 x 10^{-5} sec^{-1} in a High Purity Deaerated Water at 288 C.

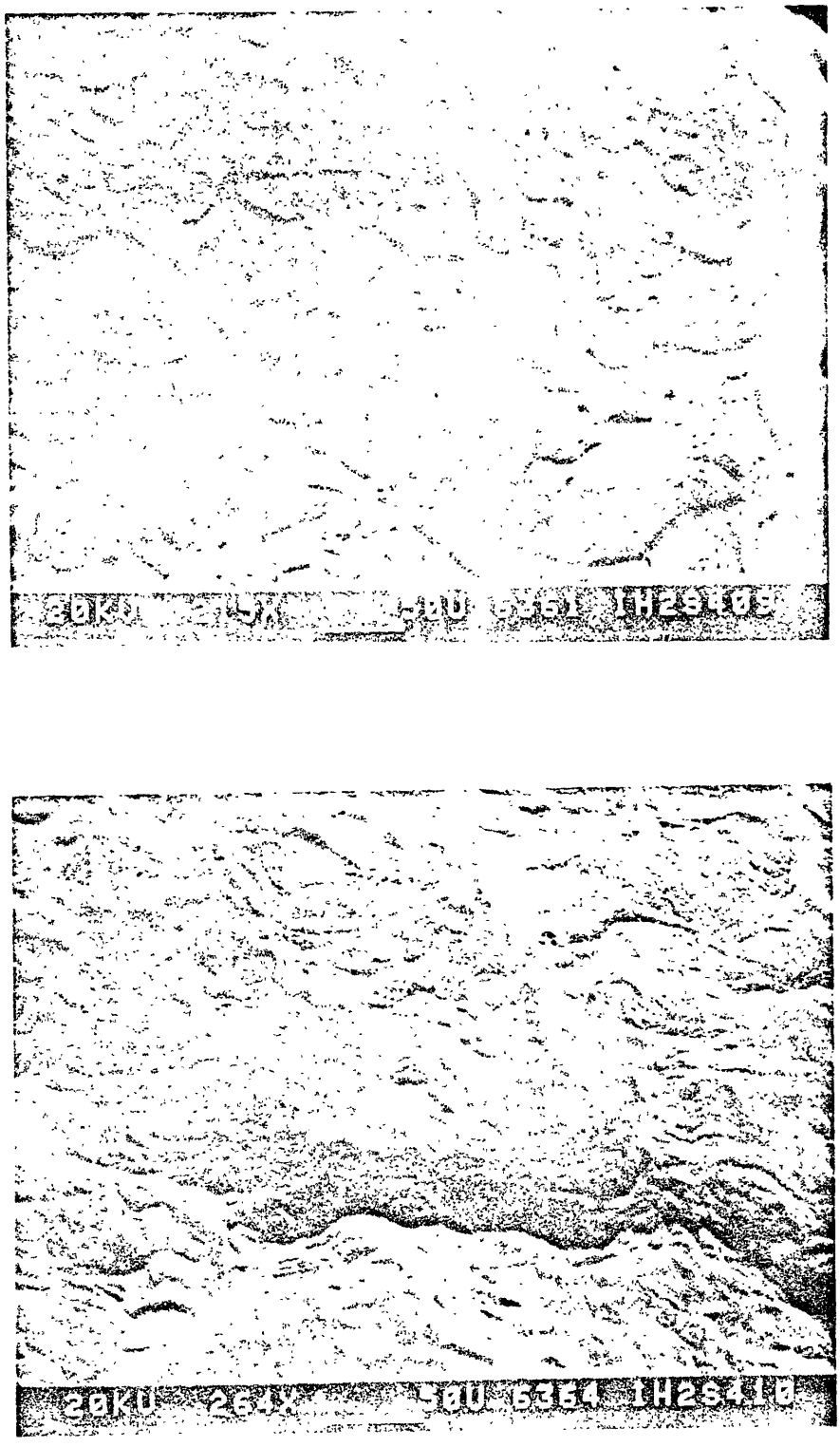

Figure 6.179 SEM Fractographs for the SSRT Specimen of SAS Condition of NX2650 Tested at a Strain Rate of 1×10^{-5} sec^{-1} in a High Purity Deaerated Water at 288 C.

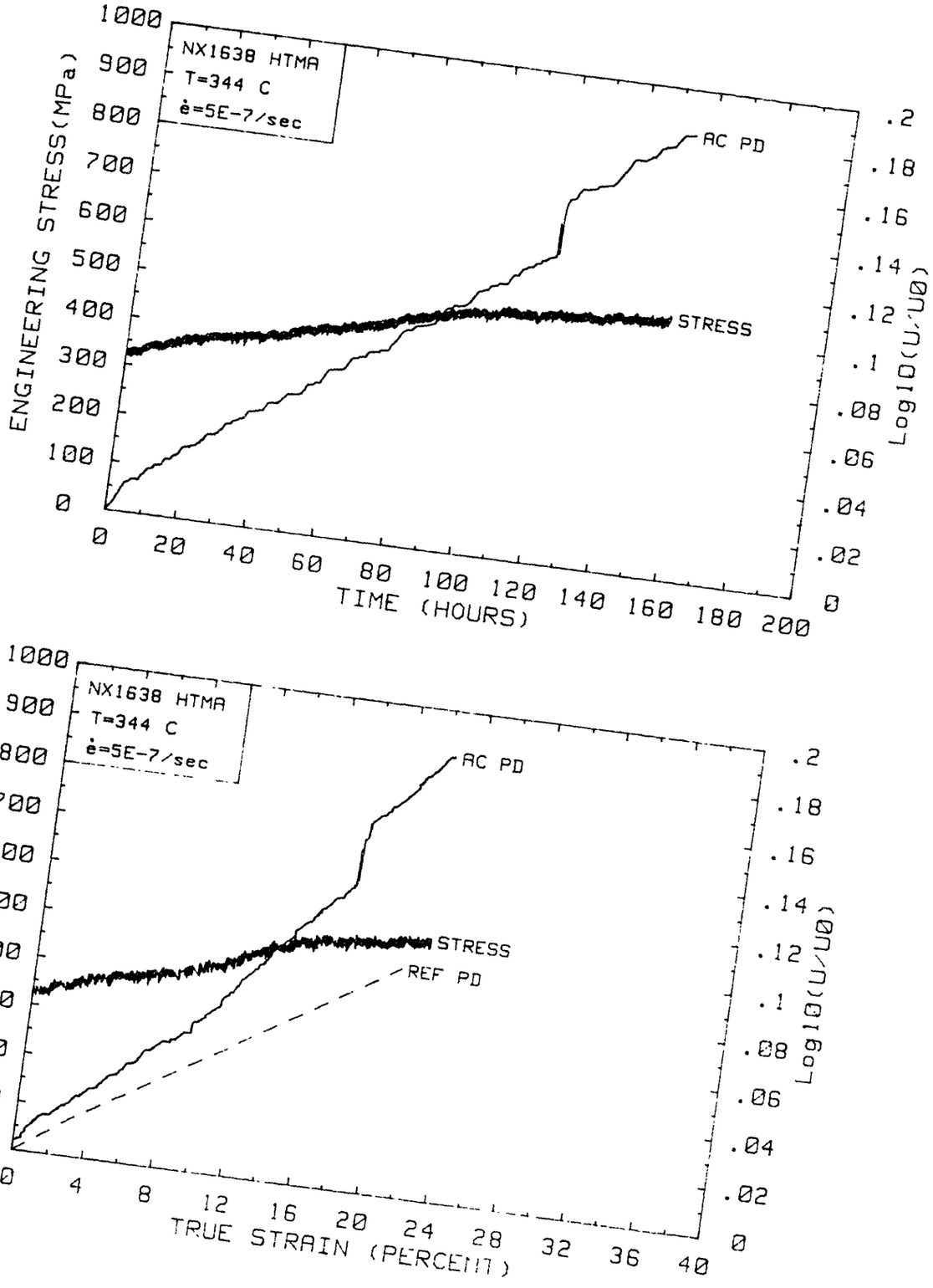

Figure 6.180 Stress and ACPD versus Time (upper) and Strain (lower) for HTMA Condition of NX1638 During a SSRT at a Strain Rate of 5×10^{-7} sec^{-1} in a High Purity Deaerated Water at 345 C.

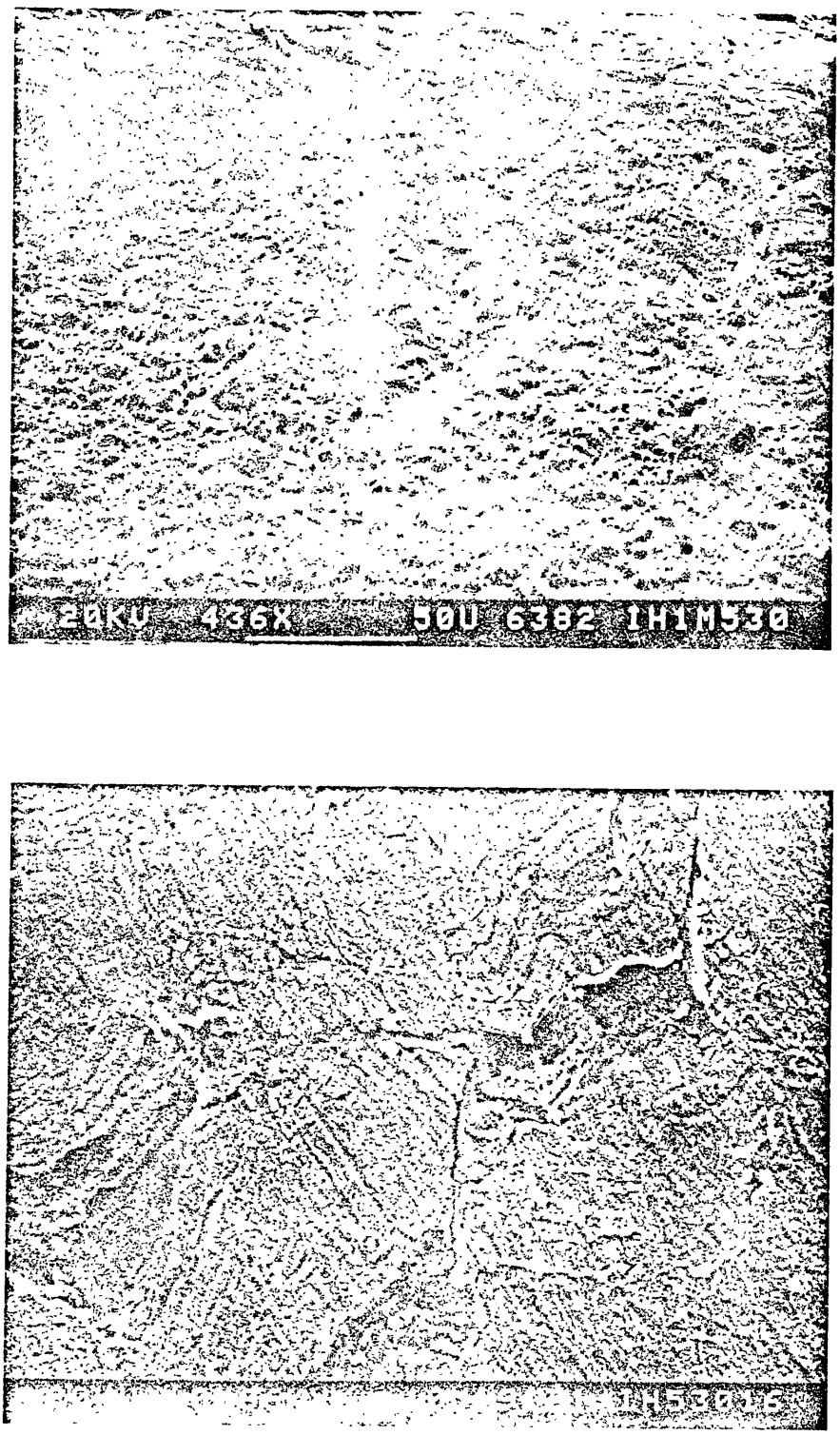

Figure 6.181 SEM Fractographs for the SSRT Specimen of HTMA Condition of NX1638 Tested at a Strain Rate of 5×10^{-7} sec^{-1} in a High Purity Deaerated Water at 345 C.

with that of tensile test speciemns, as shown in Figure 6.107. Therefore, no environmental effect is observed with the strain rate of $5x10^{-7}$ at 344 C for plastic strains up to 18%.

The strain rate was reduced to $2x10^{-7}sec^{-1}$ for subsequent tests of the HTMA condition of NX1638. The results are shown in Figure 6.182. Since the ACPD signal was lost due to probe failure, the test was stopped just before necking. Multiple initiation of the surface cracking is observed uniformly over the gage length as shown in Figure 6.183. The specimen was pulled to failure in air no evidence of cracking was observed at the edges of the fracture surface. Hence, the observation of side surface; instead, was believed to be a more effective way to determine the environemtnal attack. The side wall micrographs, shown in Figure 6.184, reveal that the surface cracks are brittle in nature. This is quite different from the mild surface grooves typically observed from the tensile test of this condition, as shown in Figure 6.107. However, all the cracks are emerged from the slip steps at 45^{0} with respect to the loading axis. The UTS is insignificantly decreased from the tensile test data. Transgranular multiple cracking is believed to be represent a low but finite embrittlememt effect. The maximum crack depth was measured to be about 10 μm based on longitudinal sectioning the specimen, as shown in Figure 6.184.

The failure to produce intergranular crack initiation in the previous tests suggests the need for a more aggressive environment or further reduction in the strain rate. Due to experimental difficulties, further acceleration of the environmental effect was achieved by using hydrogen overpressure. The use of hydrogen can be well justified by the fact that the primary water of the PWR's contain about 3ppm of hydrogen gas during normal operation. Solubility analysis based on Henry's Law shows similar amount of hydrogen can be dissolved at 25 C with an overpressure of 0.18 MPa [149]. The hydrogen pressure was applied to the top of the water storage tank after the completion of normal deaeration procedure with nitrogen bubbling.

The results with the LTMA condition of heat 96834 at 340 C in the

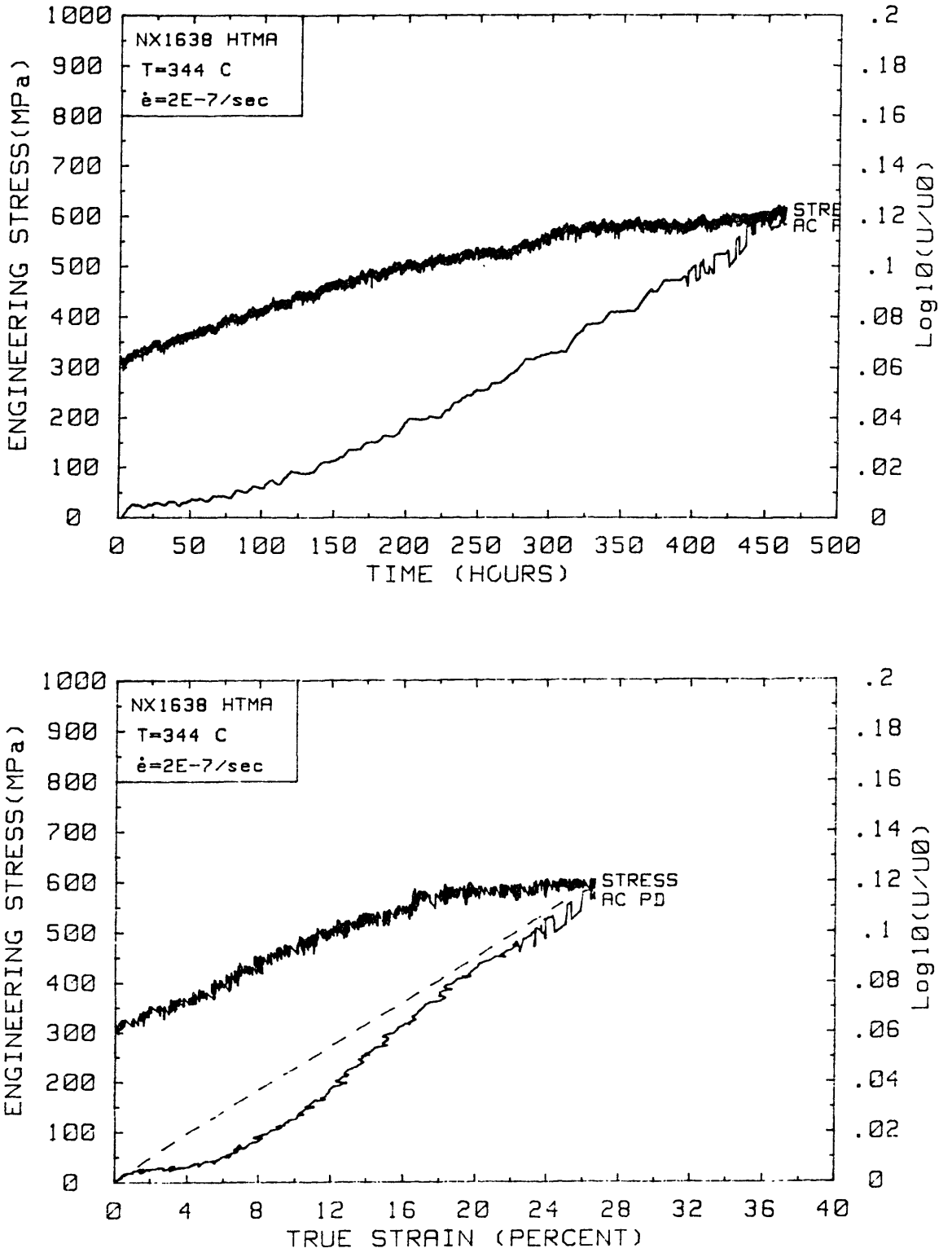

Figure 6.182 Stress and ACPD versus Time (upper) and Strain (lower) for HTMA Condition of NX1638 During a SSRT at a Strain Rate of 2 x 10^{-7} sec^{-1} in a High Purity Deaerated Water at 344 C.

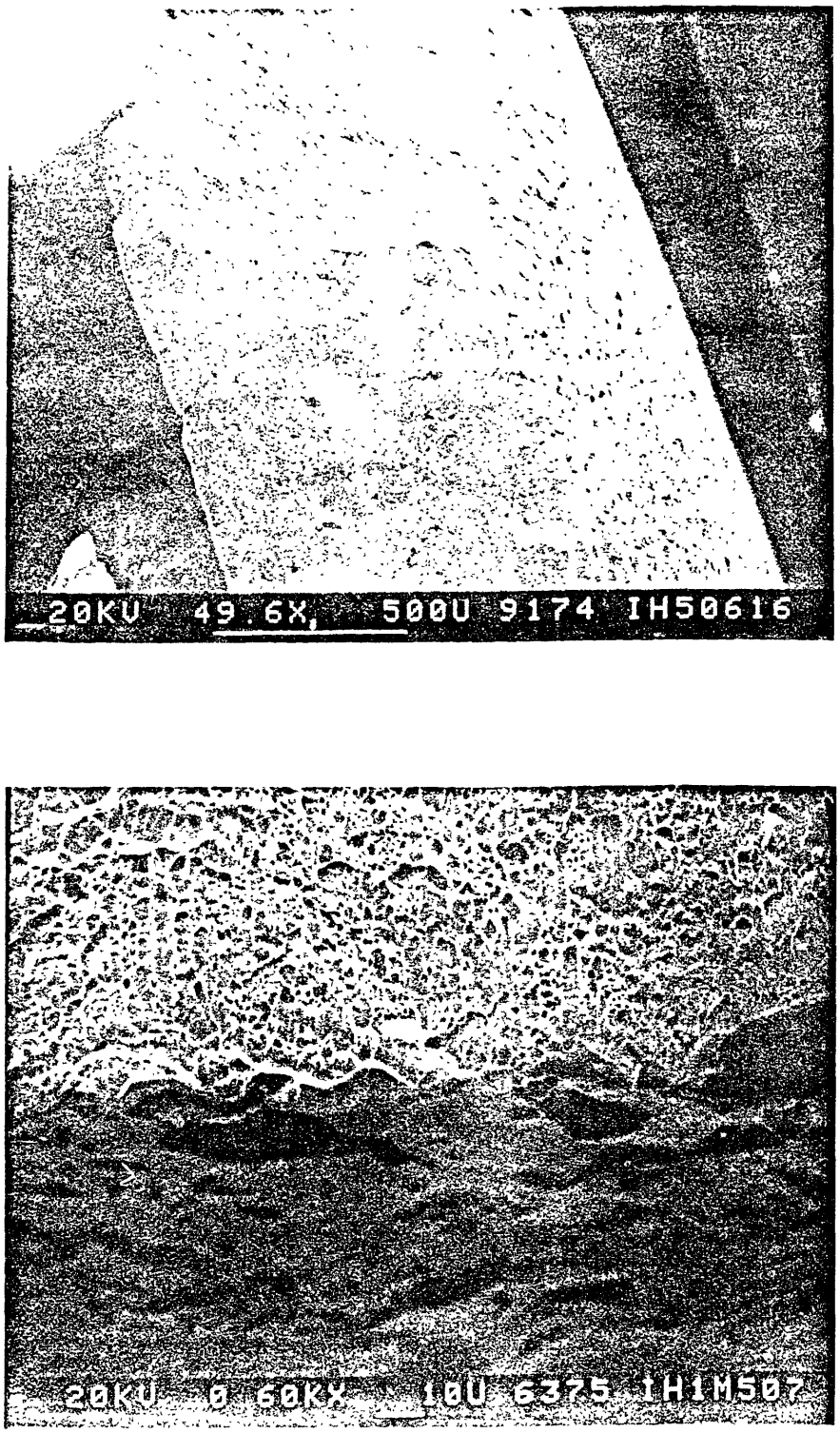

Figure 6.183 SEM Fractographs for the SSRT Specimen of HTMA Condition of NX1638 Tested at a Strain Rate of 2×10^{-7} sec^{-1} in a High Purity Deaerated Water at 344 C.

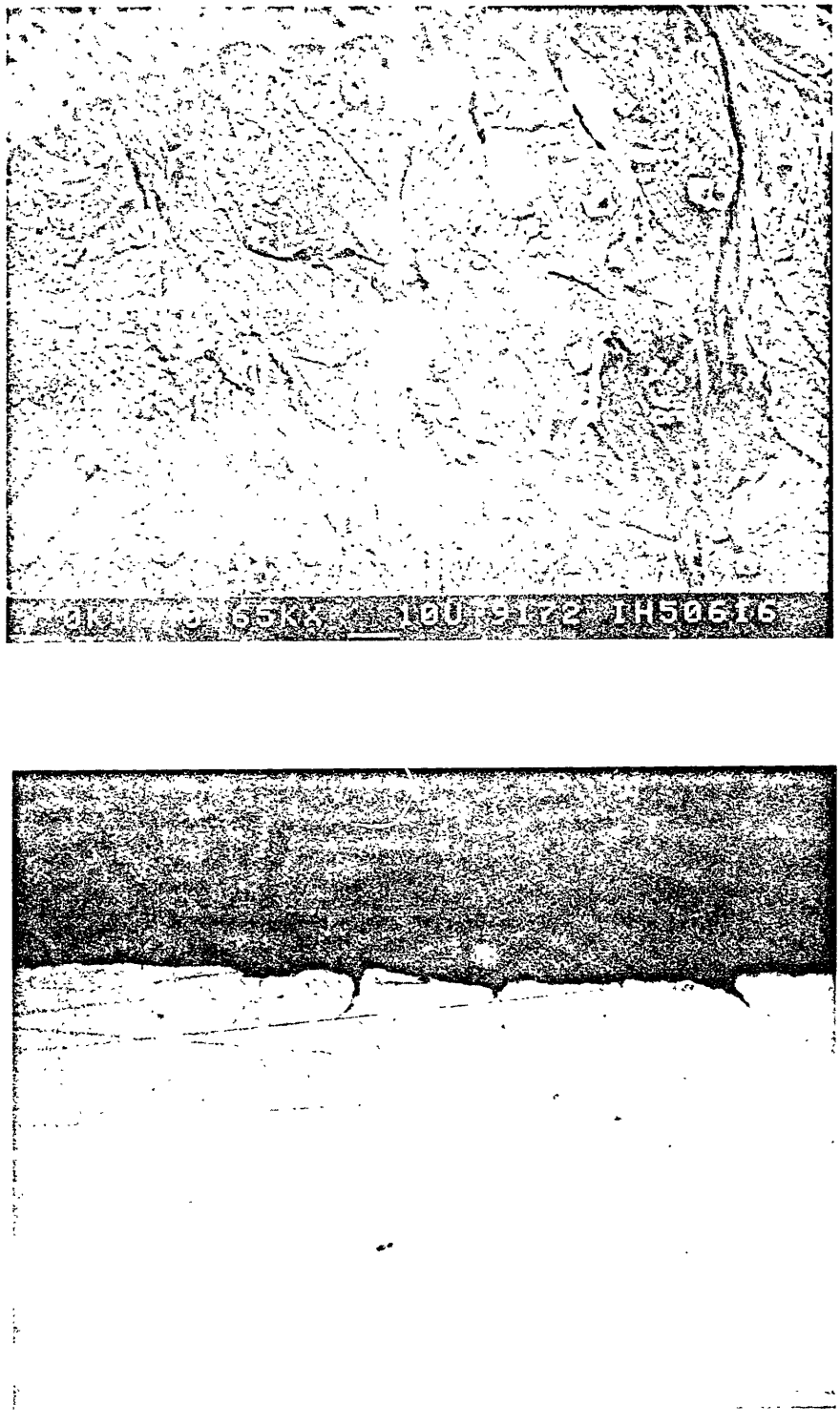

Figure 6.184 SEM Fractographs for the SSRT Specimen of HTMA Condition of NX1638 Tested at a Strain Rate of 2×10^{-7} sec^{-1} in a High Purity Deaerated Water at 344 C (upper side wall and lower longitudinal section optical micrographs).

hydrogenated water with a strain rate of $2x10^{-7}sec^{-1}$ are shown in Figure 6.185. The test was unintentionally stopped due to a loss of electric power. SEM examination of the side wall, in Figure 6.186, reveals surface cracks that are perpendicular to the loading axis. Surface cracks are uniformly distributed over entire gage length distinguishing themselves from localized fine transgranular fissures observed from the tensile test specimen in Figure 6.110. The gage length was cut in the axial direction to determine the mophology of the cracks. The longitudinal section in Figure 6.187 shows an average depth of about 15μm which corresponds to one grain. The ACPD output was not available since the current lead wires failed about 100 hours earlier.

The second specimen of the LTMA condition was tested in the same condition without interruption until fracture. The result is shown in Figure 6.188. The step increase in the load after about 110 hours resulted from a temperature reduction by 2 C as the flow rate was adjusted. The current lead wires failed during the transient. The measured UTS is not reduced significantly from the reference value, but the elongation is decreased by a considerable amount which indicates some the embrittlement. SEM fractographs are shown for the LTMA specimen in Figures 6.189 and 6.190. Extensive surface cracking is revealed with a uniform distribution all over the gage length. The cracks are intergranular and aligned perpendicular to the loading axis. There is confirming evidence for an environmental effect when compared with the fractographs for the tensile test specimens of the same condition, in Figure 6.110. Multiple crack penetrations are fairly uniform with a very small ratio of depth to width, as shown in Figure 6.190. The morphology is consistent with intergranular crack initiation reported earlier by other investigators. The bottom of the Figure 6.190 shows that the fracture mode changed from intergranular to the ductile shear within a grain. The transition to ductile fracture at small crack depth is an evidence that lower strain rate and/or a higher temperature is necessary for stable crack growth. The maximum crack depth is 32μm which corresponds to three grains of penetration, shown near the edge of the fracture surface as shown in Figure 6.191. The outer diameter region showed slightly deeper penetration.

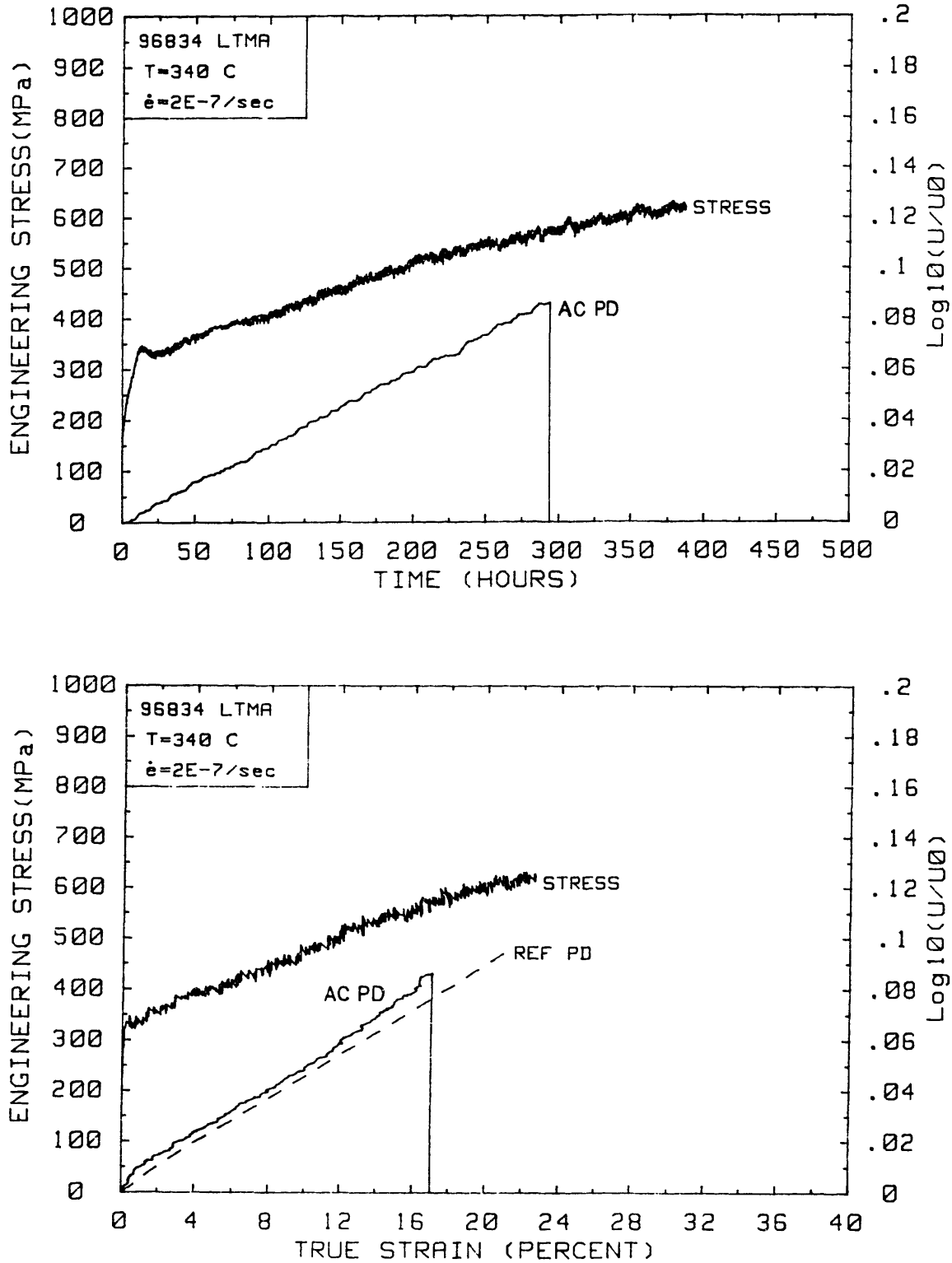

Figure 6.185 Stress and ACPD versus Time (upper) and Strain (lower) for LTMA Condition of Heat 96834 During a SSRT at a Strain Rate of 2 x 10^{-7} sec^{-1} in a High Purity Deaerated Water at 340 C.

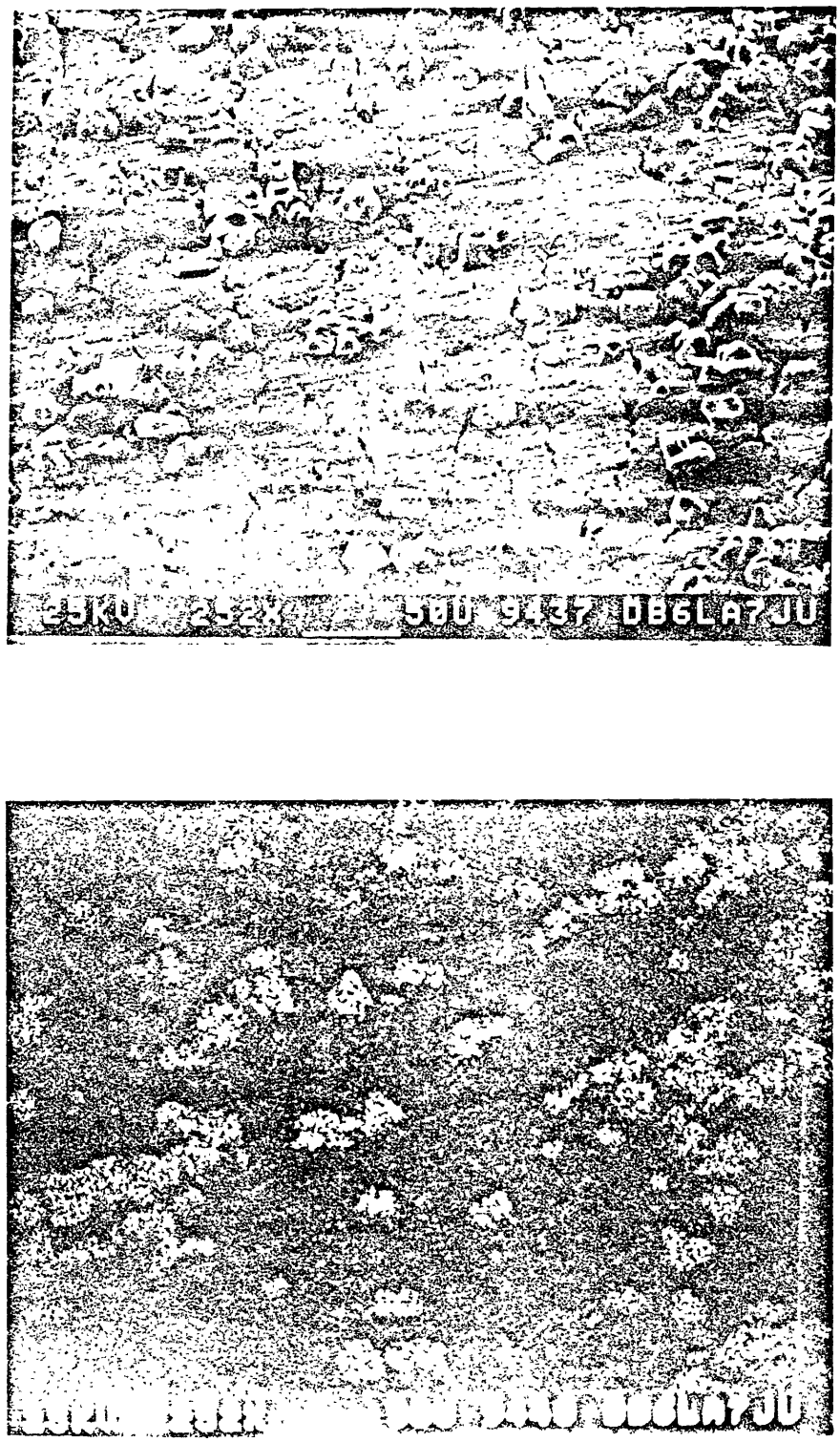

Figure 6.186 Multiple Cracks Initiated on the Inner Wall of LTMA Condition of Heat 96834 Tested at a Strain Rate of 2×10^{-7} sec^{-1} in a High Purity Deaerated Water at 340 C (Lower X-ray map shows recrystallized alumia originated from electrical insulations).

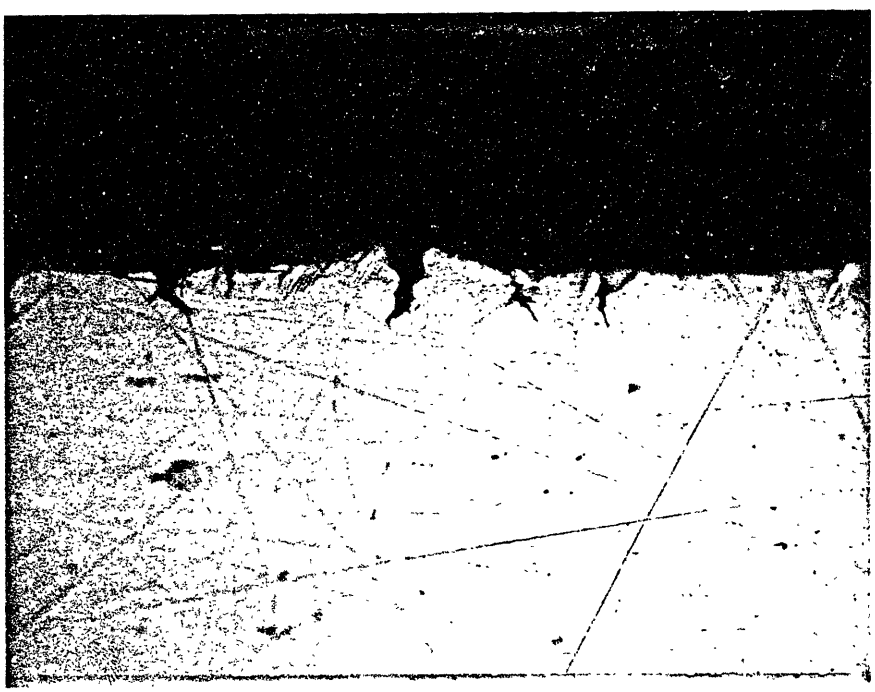

Figure 6.187 Optical Micrograph of Longitudinal Section for Inner Wall of LTMA Condition of Heat 96834 Tested at a Strain Rate of 2 x 10^{-7} sec^{-1} in a High Purity Deaerated Water at 340 C.

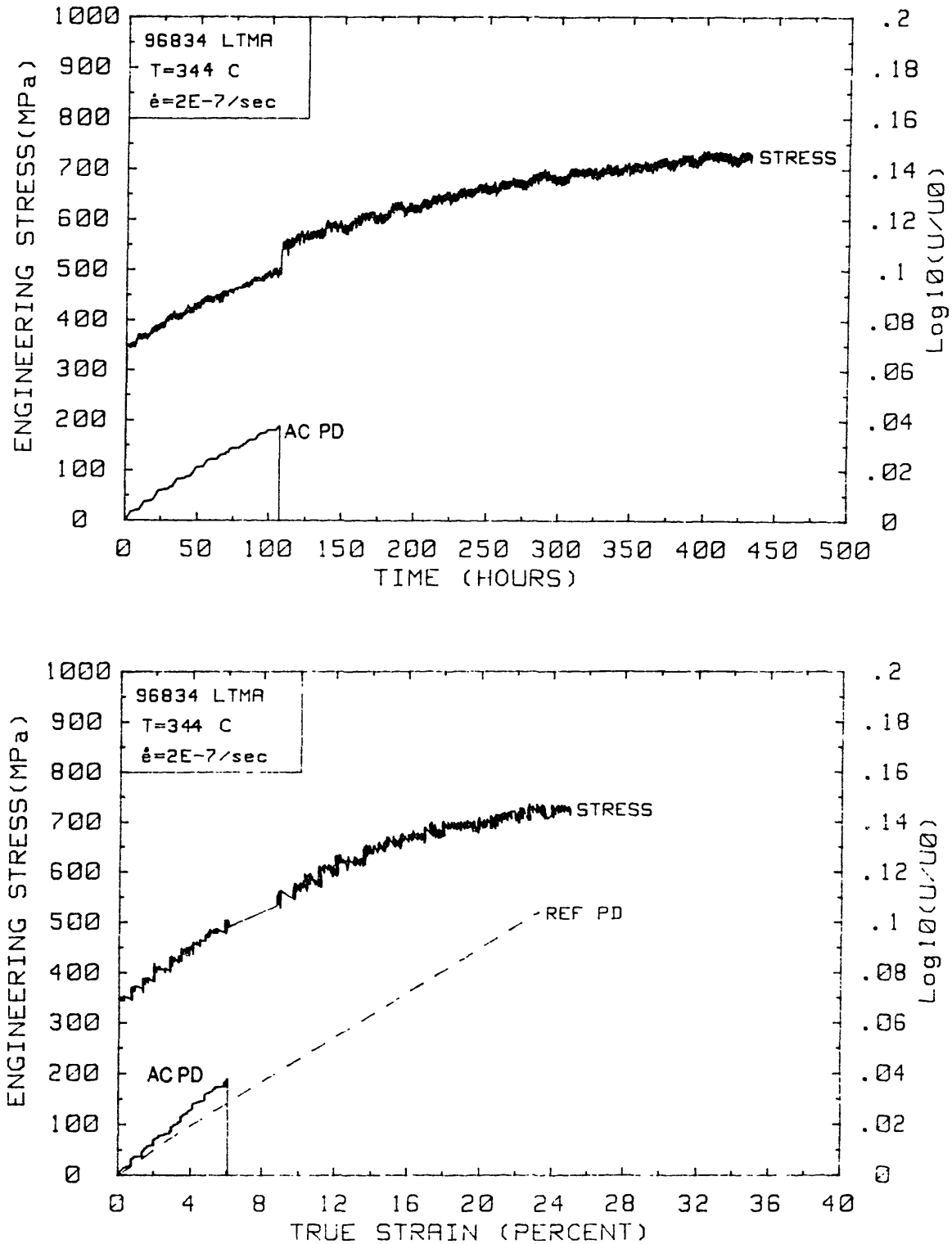

Figure 6.188 Stress and ACPD versus Time (upper) and Strain (lower) for LTMA Condition of Heat 96834 During a SSRT at a Strain Rate of 2 x 10^{-7} sec^{-1} in a High Purity Deaerated Water at 344 C.

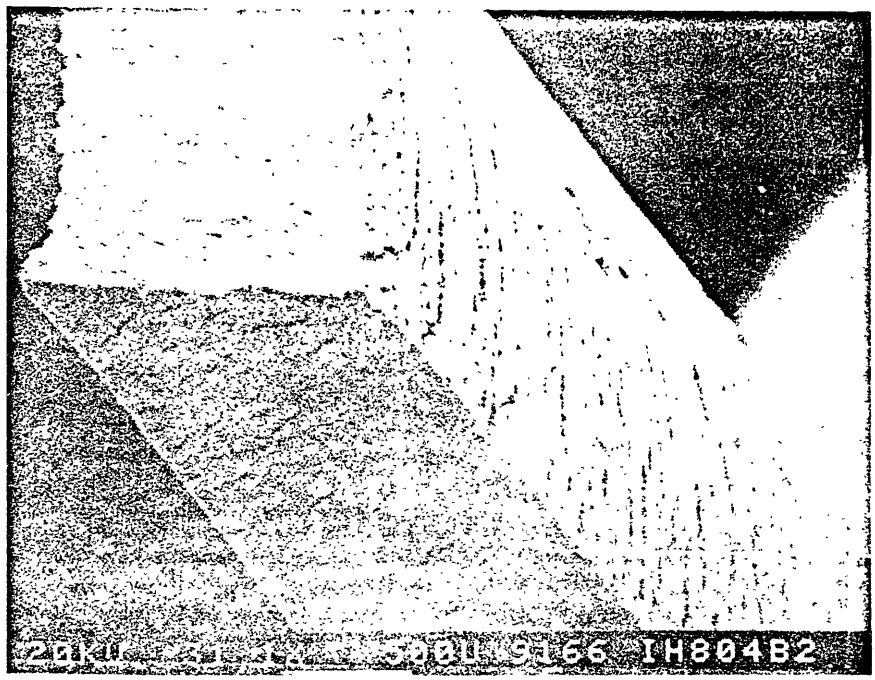

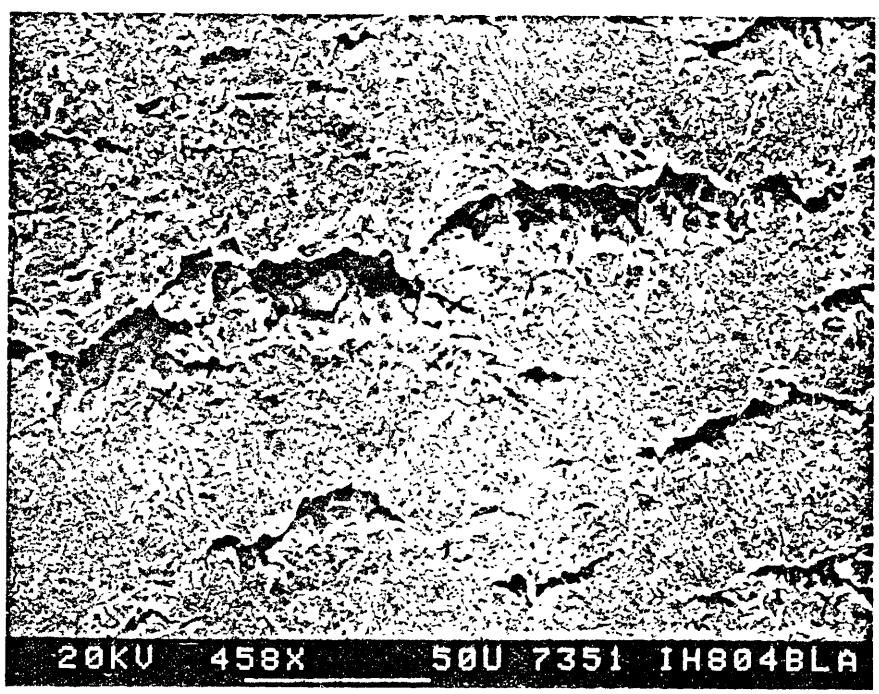

Figure 6.189 SEM Fractographs for the SSRT Specimen of LTMA Condition of Heat 96834 Tested at a Strain Rate of 2×10^{-7} sec^{-1} in a High Purity Deaerated Water at 344 C.

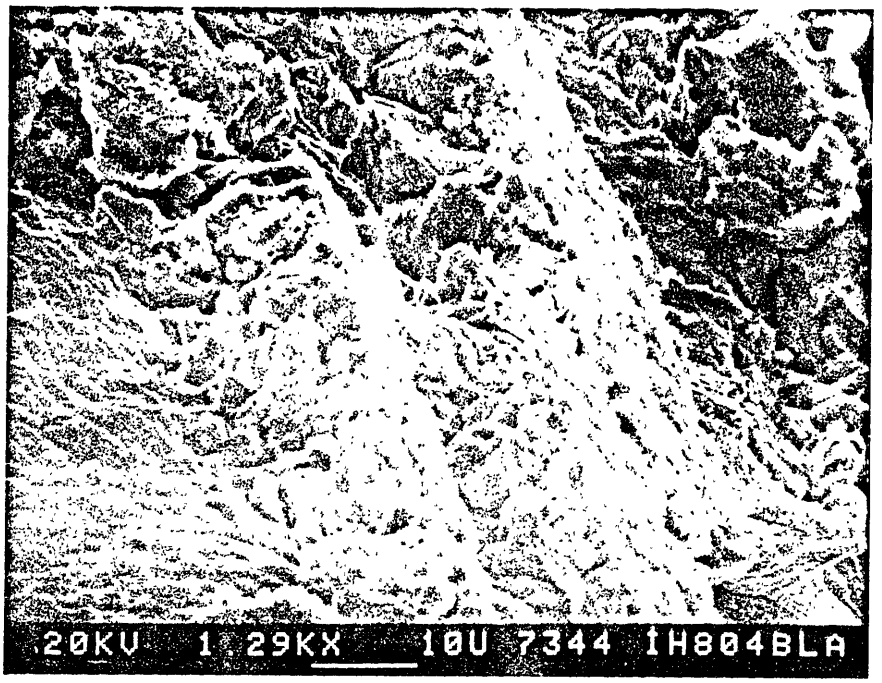

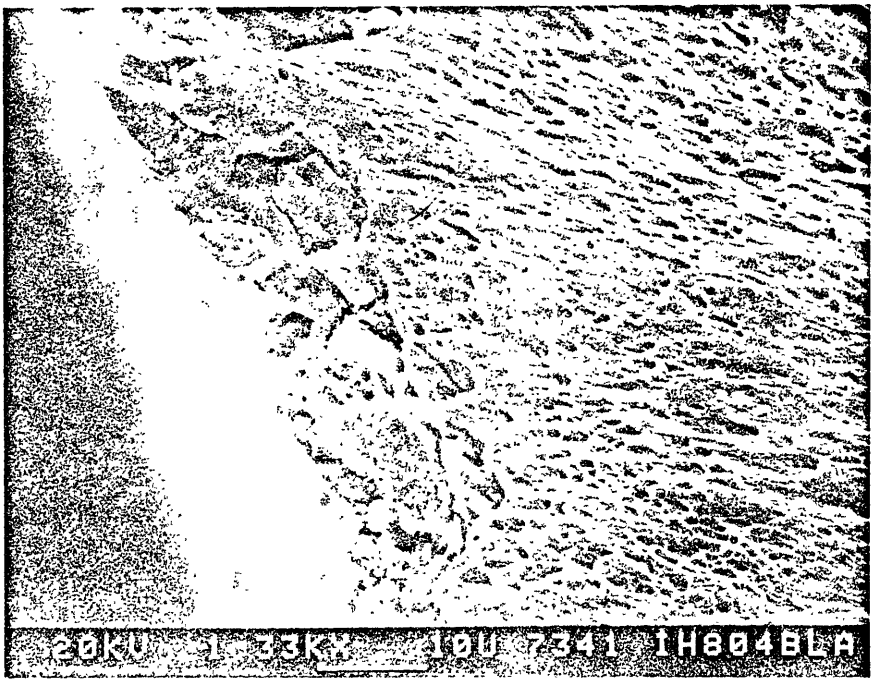

Figure 6.190 SEM Fractographs for the SSRT Specimen of LTMA Condition of Heat 96834 Tested at a Strain Rate of 2×10^{-7} sec^{-1} in a High Purity Deaerated Water at 344 C (upper outer diameter region and lower inner diameter region).

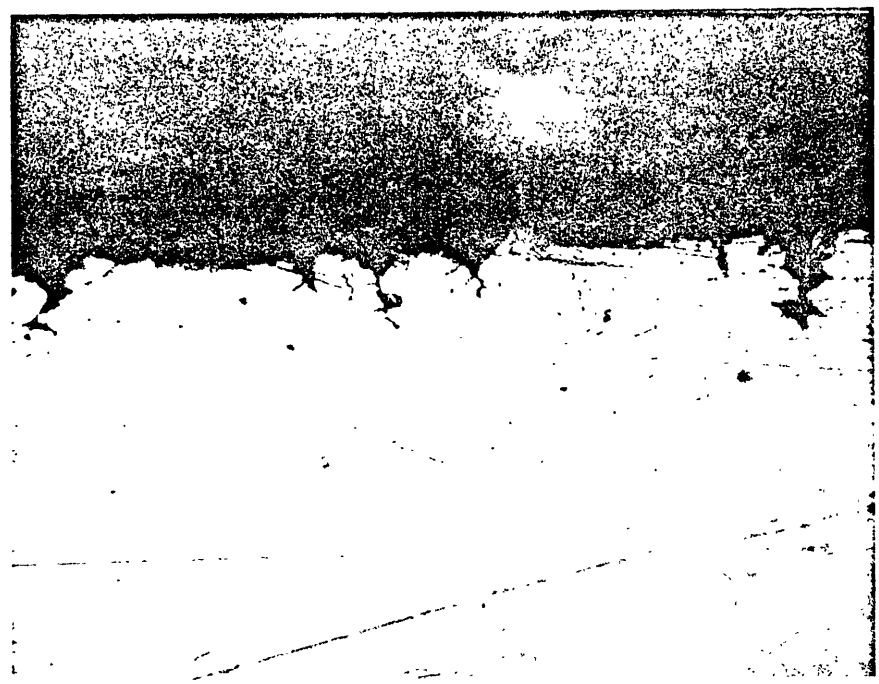

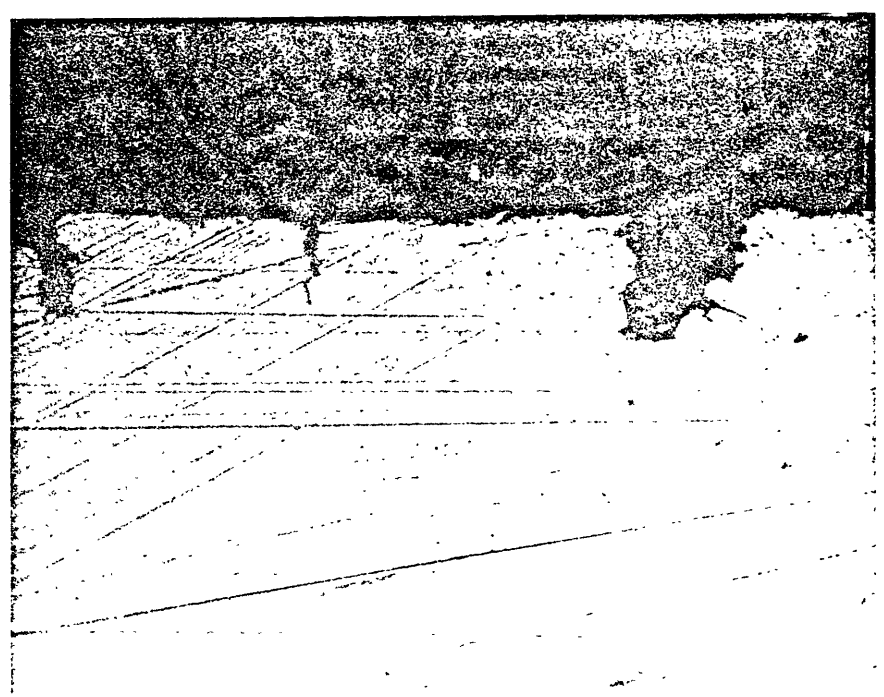

Figure 6.191 Optical Micrographs for Longitudinal Section of LTMA Condition of Heat 96834 Tested at a Strain Rate of 2×10^{-7} sec^{-1} in a High Purity Deaerated Water at 344 C (upper inner diameter region and lower outer diameter region).

These results with alloy 600 in high temperature water confirm several important observations made by earlir researchers as follows; 1) the initiation time was about the same for both HTMA and LTMA condtion while the latter showed about three times deeper cracks. 2) the higher temperature leads to an increased susceptibity. 3) a strain rate lower than $2x10^{-7}sec^{-1}$ are required for a stable crack growth in the hydrogenated water at 344 C.

6.6.2 Results with Alloy X-750

Three conditions including AH, HTH, and HOA were selected for SSRT in high purity water. The smooth round bar specimen design was initially used with an ACPD, probe spacing of 0.76cm. An ACPD frequency of 200kHz was used for the entire test program. As the test progressed, it turned out to be necessary to further improve the ACPD sensitivity by reducing the probe spacing. Hence, the majority of tests involved a semi-circular notch with 1.6mm diameter which represents a stress concentration factor of 1.7. Except for the AH condition which was tested at low temperature as well., all testings were performed in the high temperature water environment with the hydrogen overpressure of 0.18 MPa aiming at the comparison of SCC susceptibility as a function of heat treatment. The measured stresses were corrected for the friction force at the seal by using the data obtained from a previous smooth specimen test at 337 C. A linear dependence on pressure is assumed to determine the correction data for other pressures. The procedure and values used in correction are shown in Table 6.10. The summary of test results with corrected strength are presented in Table 6.11 for both specimen designs.

Results with Smooth Bar AH Specimems

The tests with smooth bar AH specimens were made at 288 C, and 350 C. A specimen was tested at 288 C with a strain rate of $5X10^{-7}$ but was accidentally preloaded to the stress level above the yield strength. Hence, the yield strength data required for the friction calculation was

Table 6.10

The Correction of the Strength Data for Friction Force due to the Pull Rod Seal for the SSRT on Alloys X-750 and 718.

Material	Specimen Design	T (C)	P (MPa)	Y.S.(MPa) SSRT	Y.S.(MPa) AIR	Δ	U.T.S.(MPa) SSRT	U.T.S.(MPa) Corrected
X-750 AH								
	Smooth	288	10.5	*	831	*	1302	1260
	Smooth	337	17.4	867	819	48	1194	1146
	Notched	93	3.9	*	*	21	1614	1593
	Notched	350	18.0	*	*	49	1531	1482
	Notched	350	18.3	*	*	49	*	*
	Notched	350	17.9	*	*	49	*	*
	Notched	350	18.0	*	*	49	1347	1298
	Notched	350	17.9	*	*	49	1364	1315
X-750 HTH								
	Notched	240	3.9	*	*	21	1459	1438
	Notched	350	18.1	*	*	49	1403	1354
X-750 HOA								
	Notched	350	18.2	*	*	49	1467	1418
718 CHT								
	Notched	350	18.1	*	*	49	1604	1555
718 DA								
	Notched	350	18.0	*	*	49	1807	1758

NOTE: * Data not available.

Table 6.11

Summary of the Slow Strain Rate Test on Alloys X-750 and 718 in a Deaerated High Purity Water with 0.18MPa of H_2 Overpressure.

Material	Specimen Design	T (C)	ϵ (sec^{-1})	U.T.S.(MPa) SSRT	U.T.S.(MPa) AIR	Elongation(%) SSRT	Elongation(%) AIR	A_{max} (μm)	t (hr)
X-750 AH									
	Smooth	288	5E-7	1260	1247	*	32	0	108
	Smooth	337	5E-7	1146	1237	14.0	32	500	80
	Smooth	350	**	*	*	*	32	700	354
	Notched	93	7E-5	1593	*	22.0	*	0	1.4
	Notched	350	2E-5	1482	*	19.5	*	0	3.1
	Notched	350	5E-7	*	*	*	*	30	44
	Notched	350	5E-7	*	*	*	*	300	56
	Notched	350	5E-7	1315	*	0.2	*	450	71
	Notched	350	5E-7	1298	*	2.3	*	410	55
X-750 HTH									
	Notched	240	7E-5	1438	*	22.0	*	0	1.2
	Notched	350	5E-7	1354	1349	24.0	40	0	158
X-750 HOA									
	Notched	350	5E-7	1418	*	20.5	*	0	141
718 CHT									
	Notched	350	5E-7	1556	1728	10.0	16	20	103
718 DA									
	Notched	350	5E-7	1758	*	14.3	*	0	111

NOTE: * Data not available.
** Constant load test with a LASER pit.

lost. The test was interrupted after about 108 hours of exposure. The specimen showed no evidence of envirnment assisted cracking.

A second smooth bar test was conducted using the same strain rate, but in deaerated water at 337 C. The results are shown in Figure 6.192. The yield strength is 48 MPa, higher than that of the tensile test made on the same heat of AH using a round bar specimen design [50]. Serrated yielding occurs with a stress drop of about 50 MPa. Each load drop is accompanied with a step increase in the strain and ACPD. Several intergranular fracture regions are shown in Figure 6.193. An interconnection between the cracks appears to have occurred during the final fracture step as indicated by the transgranular mode of fracture between the intergranular cracks. The crack depth is, on the average, about 300μm with a maximum of 500μm. A detailed examination on the edge reveals an oxide layer at the surface with about 1μm thickness beneath which intergranular cracking is believed to have been initiated. The side wall shows only a few secondary cracks which are widely separated. The oxide layers except at the cracks remain intact. This suggests that cracking of the oxide layer may play an important role in initiation.

The oxide compositions of the intergranular and the transgranular surface of the AH specimen tested at 337 C were determined as a function of depth using Auger electron spectroscopy with argon ion sputtering. At an ion current density of 50μA/cm^2 and an acceleration voltage of 4kV, the depth profile of the oxide compositions are compared for the two differnt modes of fracture, in Figure 6.194. Although no precise calibration exists, approximately 0.015μm is assumed to be removed every minute of sputtering [70, 150]. The transgranular surface retained the bulk chemistry with only slight increase in the oxygen level. In contrast, intergranular region shows a significant deficiency in major elements including nickel, chromium and iron near the surface which is enriched in oxygen. This indicates that exposure time of the transgranular surface was substantially shorter than that of the intergranular region. The depth of the oxide layer was compared with the study by Elliott [23] on the intergranualr fracture an AH condition obtained at 93 C. The oxide layer at 337 C appears to be about three

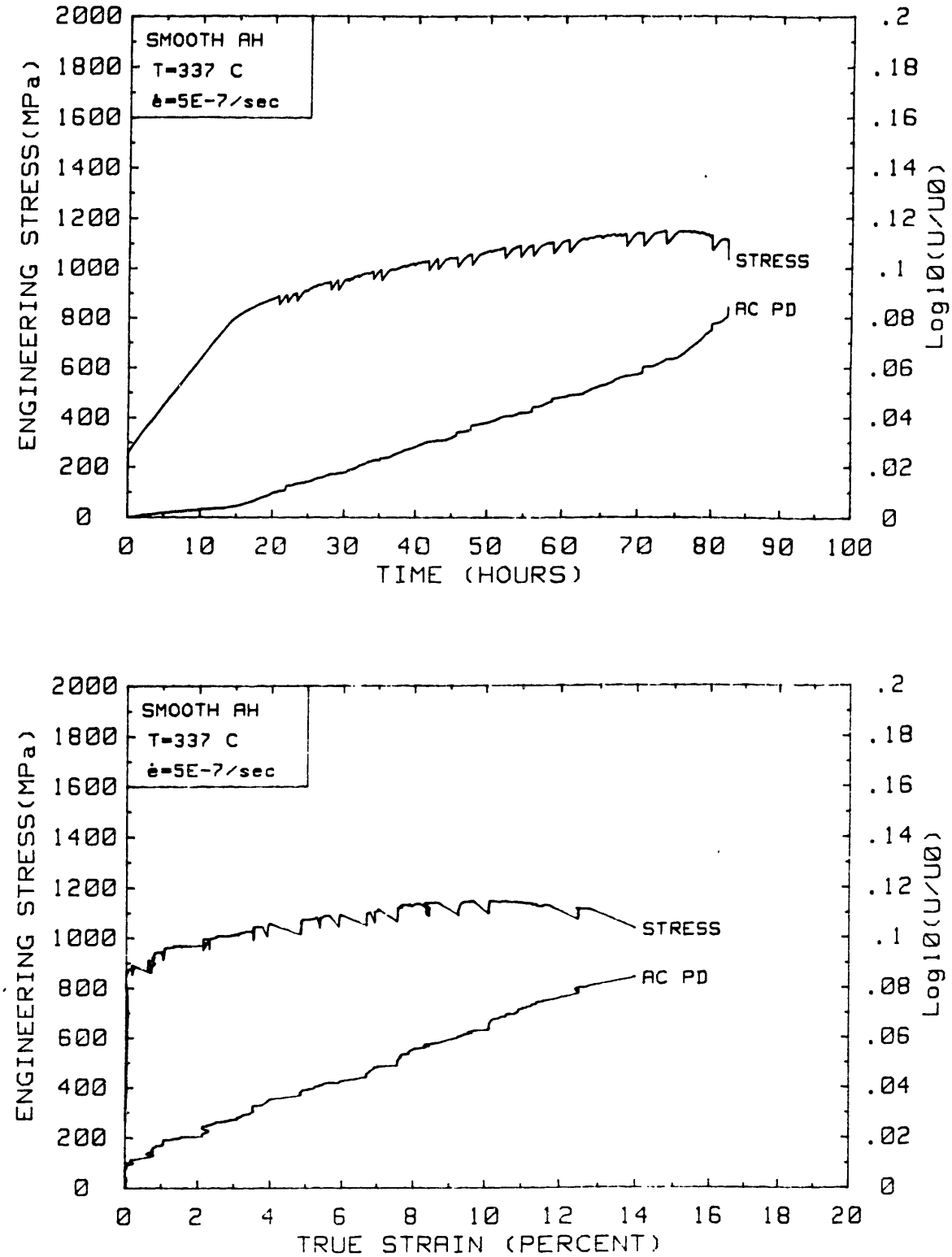

Figure 6.192 Stress and ACPD versus Time (upper) and Strain (lower) for AH Condition of Alloy X-750 During a SSRT at a Strain Rate of 5 x 10^{-7} sec^{-1} in a High Purity Deaerated Water at 337 C (unnotched specimen).

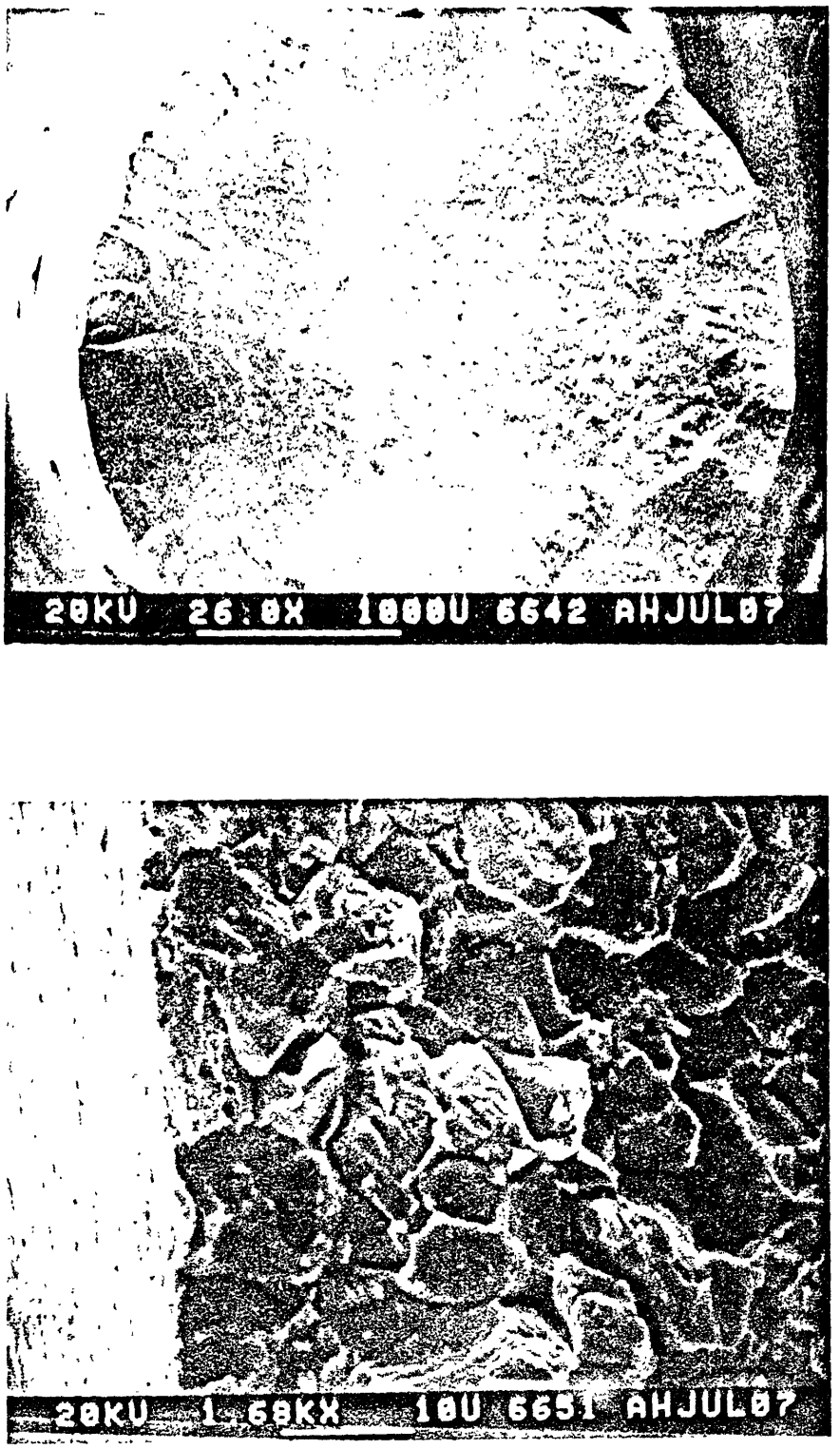

Figure 6.193 SEM Fractographs for the SSRT Specimen of AH Condition of Alloy X-750 Tested at a Strain Rate of 5×10^{-7} sec^{-1} in a High Purity Deaerated Water at 337 C (unnotched specimen).

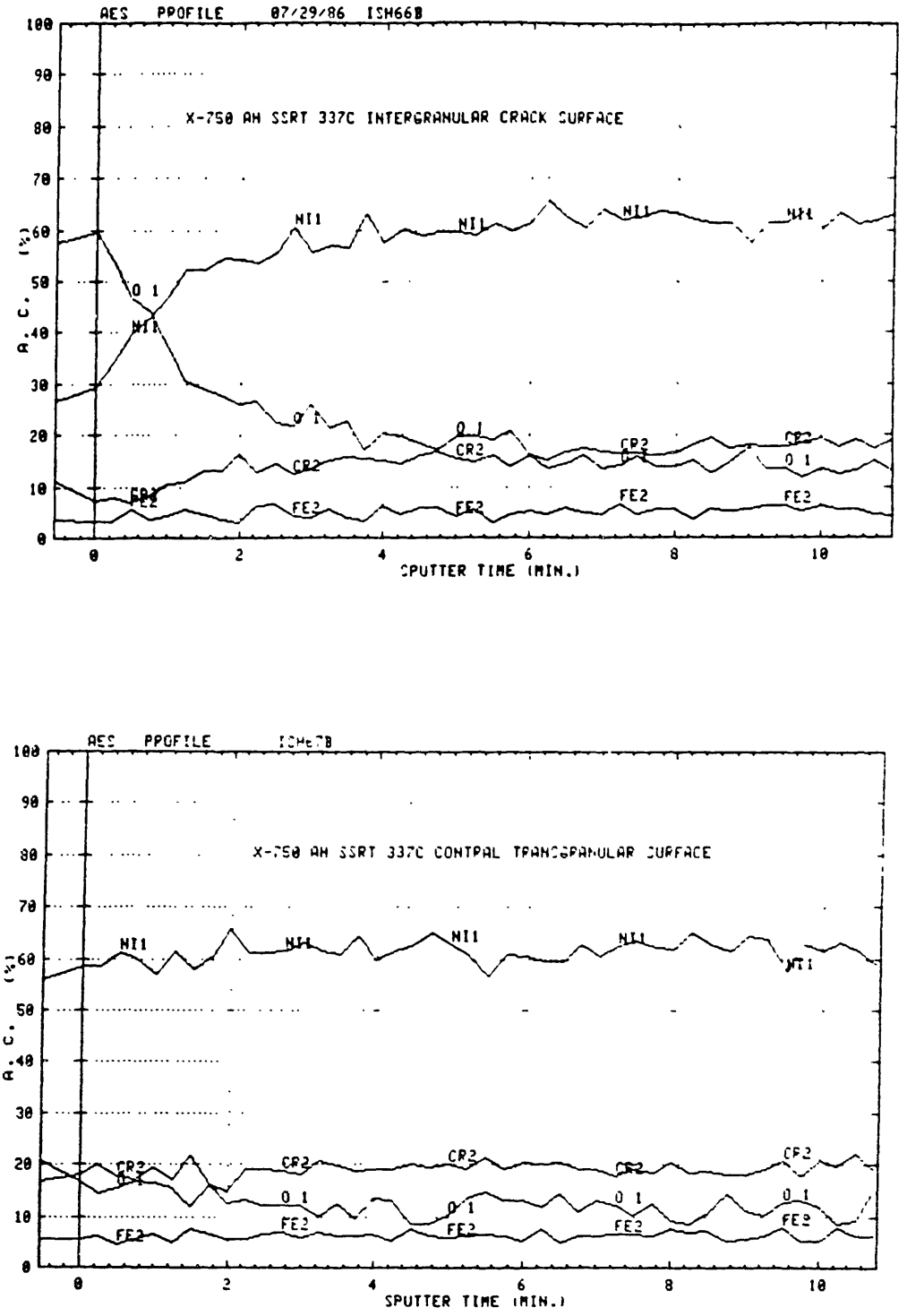

Figure 6.194 Surface Film Composition as Function of Argon Sputtering Duration of the Intergranular Crack Surface (upper) and Transgranular Surface (lower) in the SSRT Specimen in AH Condition of Alloy X-750 Tested at a Strain Rate of 5 x 10^{-7} sec^{-1} in a High Purity Deaerated Water at 337 C (unnotched specimen).

times the thickness at 93 C.

Several large step increases in strain by up to 1% were observed due to serrated yielding. This strain increment translates to 70μm on the displacement of gage length. The displacement is significantly larger than the grain size indicating that a large scale slip occurs during each serrated yielding.The specimen failed after about 80 hours with an elongation of 14% and an UTS of 1146 MPa which represents a significant degree embrittlement.

The ACPD output correlates well with the serrated yielding as well as the final crack opening. However, the magnitude of the ACPD change with the true deformation in the specimen is obscured due to comparable magnitude of noises associated with fluctuation in the measured strains, as shown in Figure 6.192. These noise effects and low crack number density caused a significant deterioration in the sensitivity of the system. The probe spacing had to be reduced to maintain sensitivity.

The benefit of using a smaller probe spacing was verified using about 1200μm for the spacing. To ensure crack initiation within the probe spacing a laser pit of about 60μm diameter was introduced on a smooth bar AH specimen. A constant load at the yield strength was used to eliminate the effect of the serrated yielding. After about fourteen days of exposure at 350 C, a crack was detected, as shown in Figure 6.195. Fracture surface showed about 700μm deep intergranular crack. The ACPD increase at the end of test is about 120% based on the previous steady state value. Considering the electronic instability, it is estimated that 1% increase in the signal is significant. Assuming a linear relationship between the ACPD and crack depth [132] a sensitivity of about 60μm is obtained. The reduced probe spacing thus retored the sensitivity despite the low crack number density. The crack growth rate was estimated to be 2×10^{-5} mm/sec.

Tests with the Notched Specimens

Although a better sensitivity is expected at the smaller probe spacing,

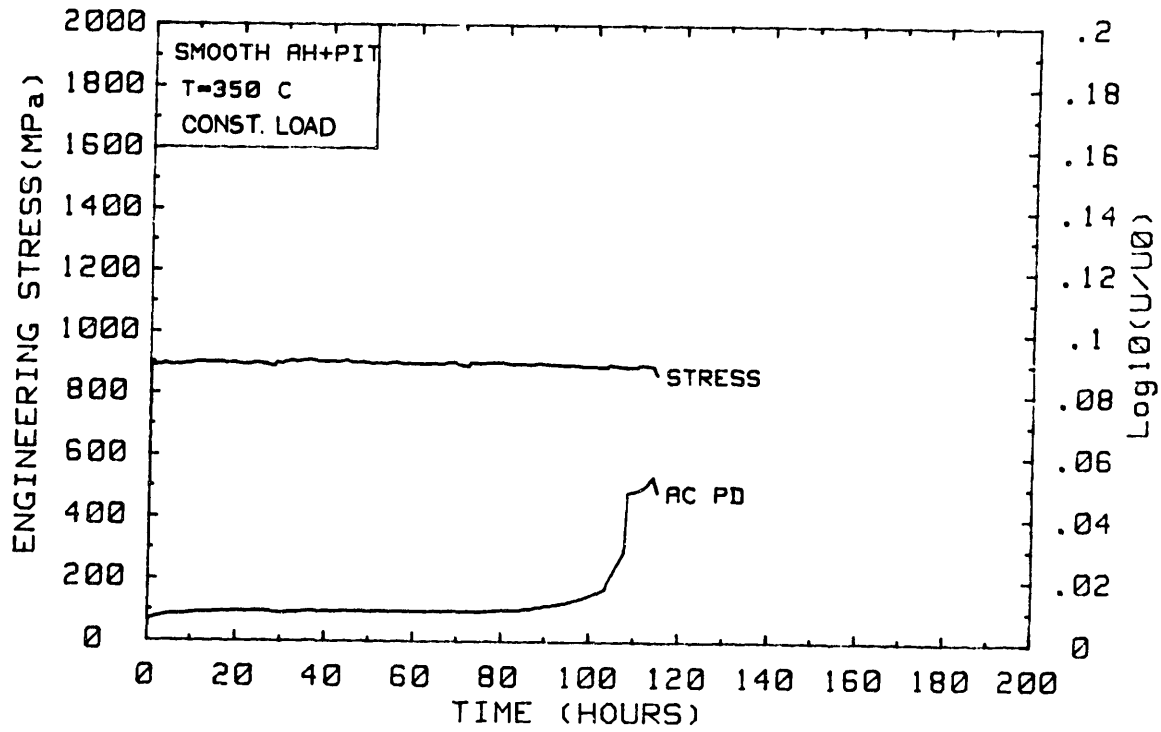

Figure 6.195 Stress and ACPD versus Time for the AH Condition of Alloy X-750 with a LASER Pit During a Constant Load Test at 110% of Y.S. in a High Purity Water at 350 C.

the use of small defects such as a laser pit can eliminate the true initiation process by either environmental or metallugical changes. A compromised design involved an 1.6mm diameter notch introduced in the middle of the gage length.

Results with Notched AH Specimens

An AH specimen was tested at 93 C with a strain rate of $7x10^{-5}sec^{-1}$ to examine the low temperature behavior. The result is shown in Figure 6.196. The yield strength is not well defined due to the notched design. No serrated yielding is observed at 93 C. An SEM fractograph is shown in Figure 6.198. The fracture surface was typical cup-and-cone. The ACPD is linear with strain before the necking point occurs at about 17%. Since no embrittlement was involved this is taken as the reference ACPD to describe the effect of strain. A least square fit up to the necking point leads to:

$$\log_{10}\left(\frac{\Delta U(\epsilon)}{\Delta U(\epsilon=o)}\right)_{a=o} = 2.3x10^{-3} + 4.26x10^{-3}\,\epsilon \qquad (6\text{-}9)$$

where ϵ is the true strain in percent. The standard error of fitting is determined to be $8x10^{-4}$ in the normalized logarithmic value or 0.2% on a relative error scale.

AH specimen with the notch was tested at 350 C with a strain rate of $2x10^{-5}sec^{-1}$, as shown in Figure 6.197. Serrated yield is observed at this temperature. Hence, the mechanism of the serrated yielding is operative only at high temperatures. The ACPD output was not obtained due to a mistake in the grounding scheme. The fracture surface, shown in Figure 6.198, is ductile and transgranular. Therefore, the UTS and elongation are assumed to represent reference values to compare with other tests with the notched AH specimen.

All the high temperature slower strain rate tests were made at 350 C with a strain rate of $5x10^{-7}sec^{-1}$. The first AH test at this strain rate was stopped after 45 hours at which the plastic strain was still

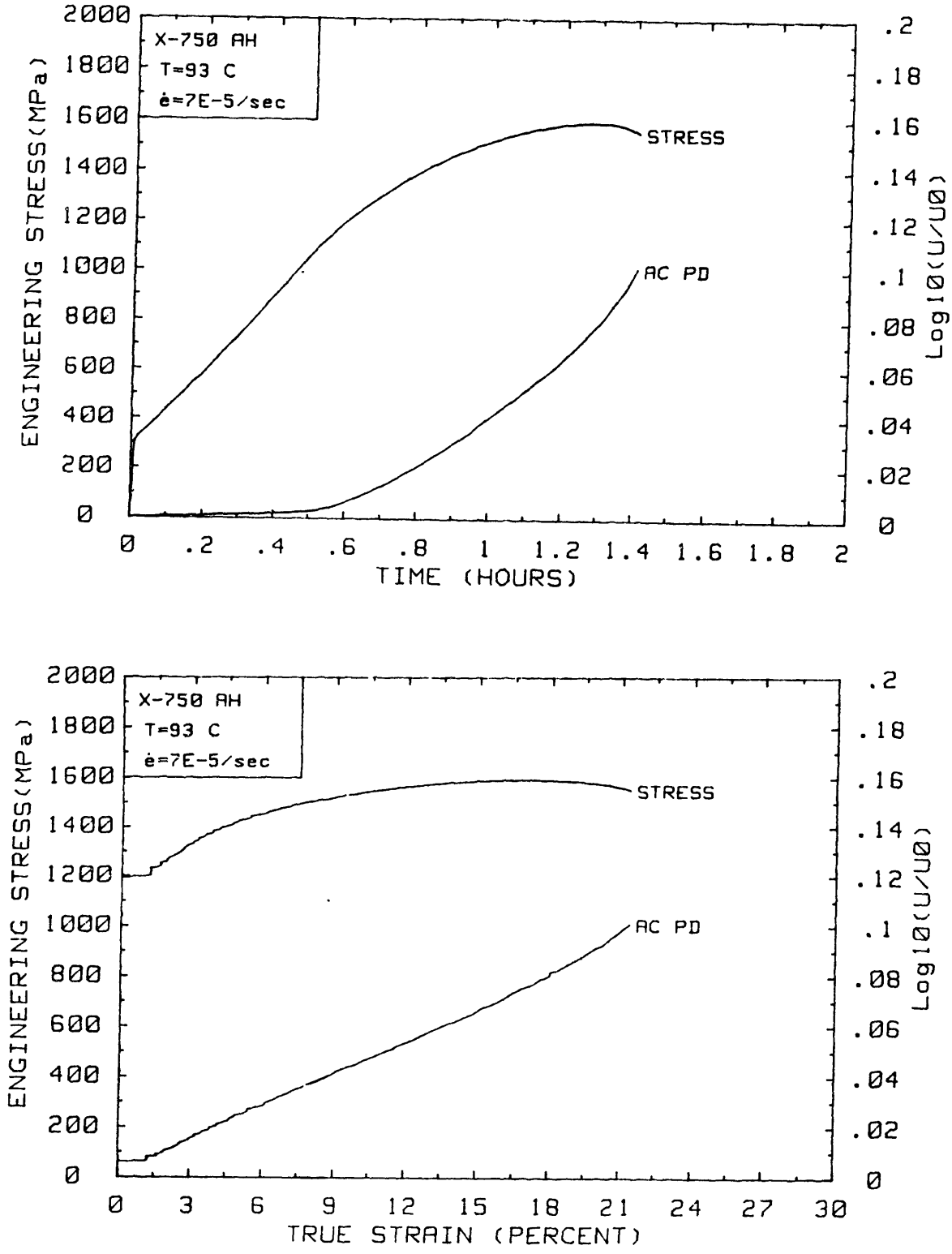

Figure 6.196 Stress and ACPD versus Time (upper) and Strain (lower) for AH Condition of Alloy X-750 During a SSRT at a Strain Rate of 7 x 10^{-5} sec^{-1} in a High Purity Deaerated Water at 93 C.

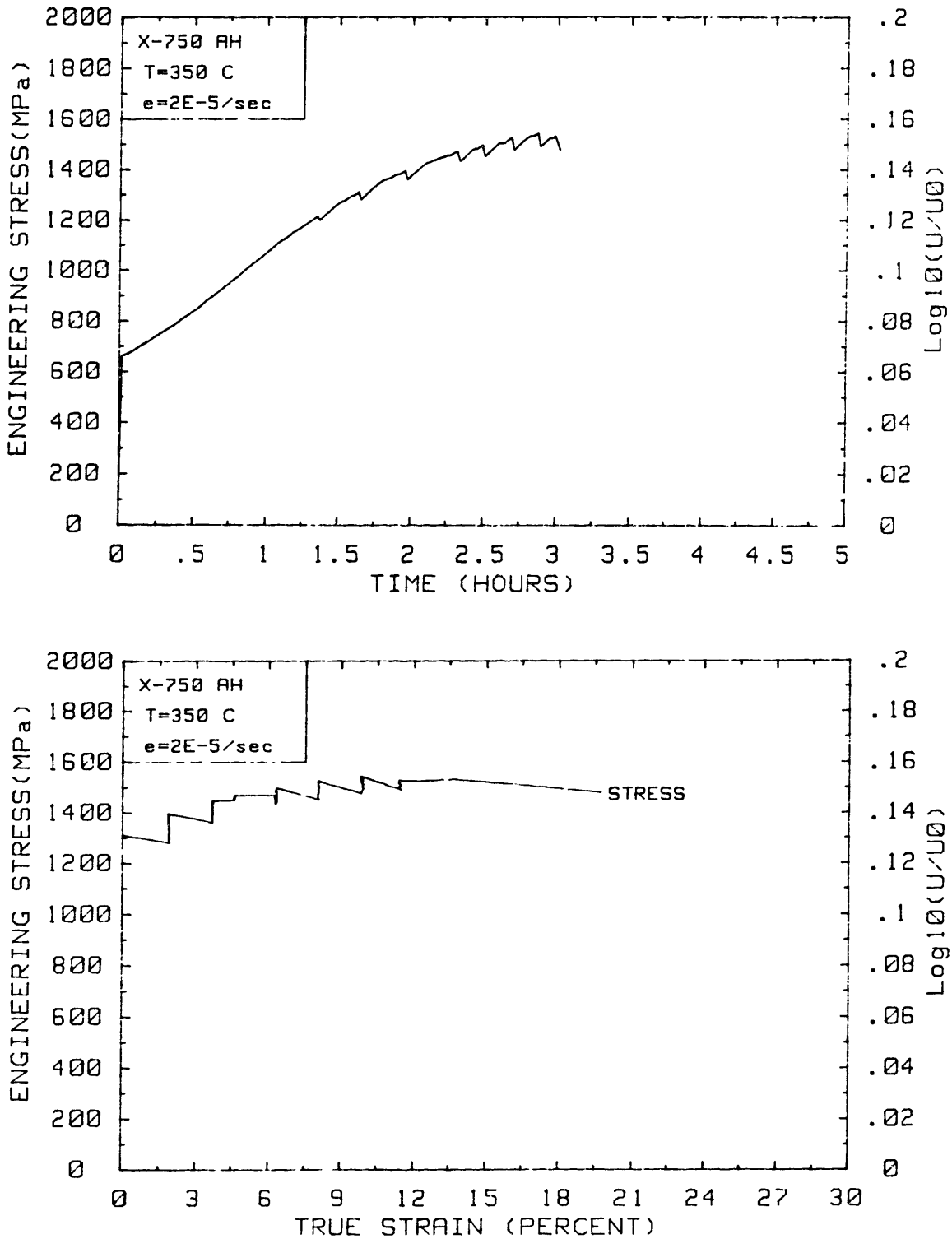

Figure 6.197 Stress versus Time(upper) and Strain(lower) for the SSRT Specimen of AH Condition of Alloy X-750 Tested at a Strain Rate of 2 x 10^{-5} sec^{-1} in a High Purity Deaerated Water at 350 C

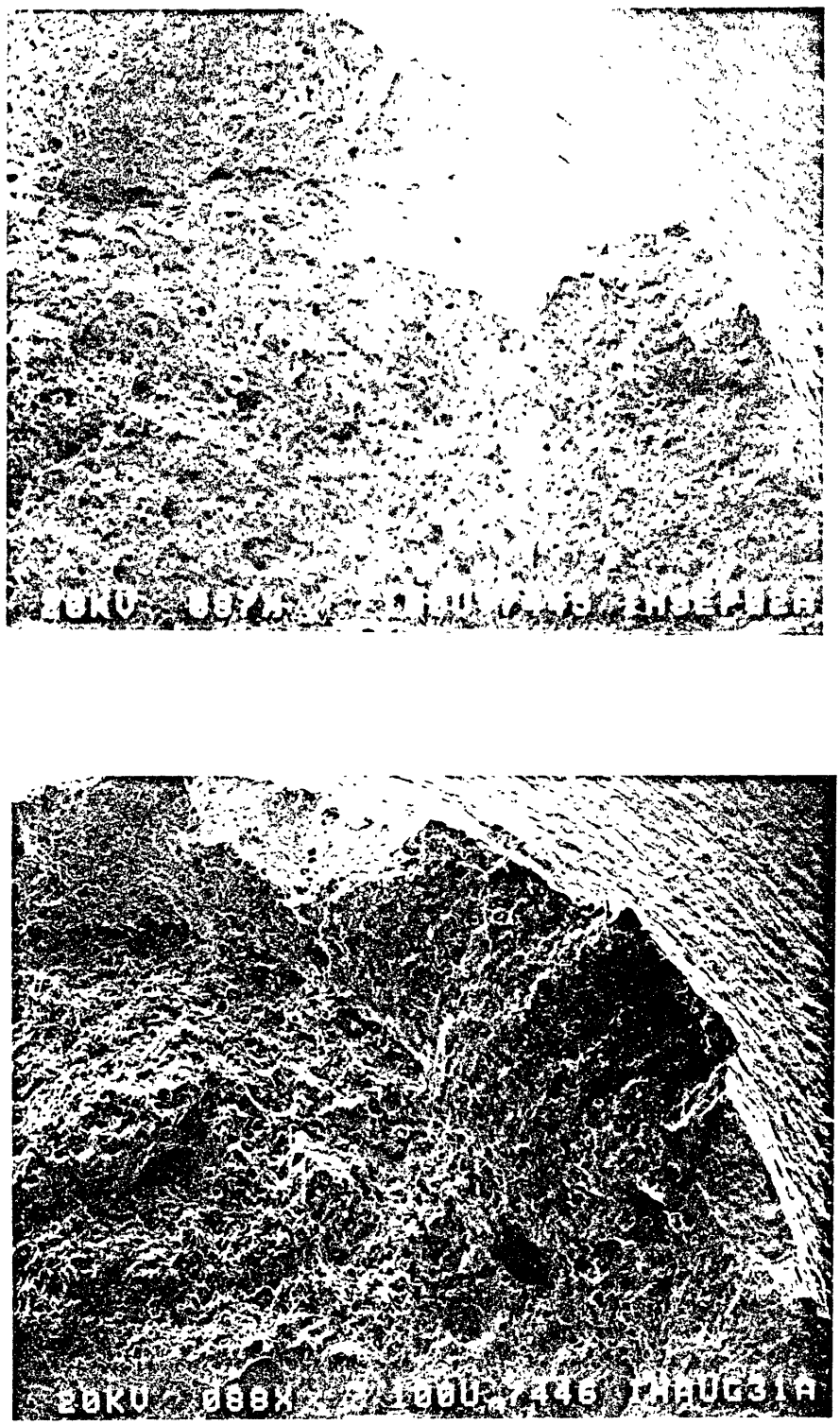

Figure 6.198 SEM Fractographs for the SSRT Specimens of AH Condition of Alloy X-750 Tested in a High Purity Deaerated Water at High Strain Rates ; 7 x 10^{-5} sec^{-1} at 93 C (upper) and 2 x 10^{-5} sec^{-1} (lower) at 350 C.

small. The results are shown in Figure 6.199. The true strain was not determined due to a malfunction of the LVDT. The SEM examination of side wall showed no surface cracks. However, three small cracks including a secondary one were observed on fracture surface, as shown in Figure 6.200. The smaller crack has a semi-circular shape with a size of 10μm by 30μm. The larger one has a longer shape apparently due to the interconnection of two adjacent cracks each with a size of 30μm by 30μm. The secondary crack has a length of 150μm. All the cracks are observed with outer oxide blanket which appears to have been cracked prior to the initiation. The ACPD cannot be compared with the reference data due to invalid strain measurements.

The result of the second AH test is shown in Figure 6.201. The test was stopped after a significant increase in the ACPD. The ACPD increase at 7% strain is about six times the overall standard error. The specimen was broken open and total six semi-circular cracks were obsreved, as shown in Figure 6.202. The cracks have a maximum depth of 300μm and total area of 5% of entire cross section. The side wall reveals a number of fissures in the surface oxide layer formed on scratches made during specimen polishing. A correlation exists between the observed shape and size of cracks. All the smaller cracks are semi-circular while the larger cracks have a greater width than depth as shown in Figure 6.202. The surface oxide layer is shown in Figures 6.203 and 6.204 beneath which the intergranular cracks initiated. A detailed examination of intergranular surfaces reveals evidences of selective dissolution of grain boundary precipitates. The size and density of pits are consistent with those of γ' in the AH condition. It is evidence of galvanic corrosion of γ' in the higher temperature water.

A comparison of the stress-strain curve with the serrated yielding behavior shows that each load drop is accompanied with a step increase in strain. The gradual recovery in the load is made with little change in strain. The step increase in ACPD on time the scale is, in fact, caused by sudden plastic strain as evidenced by its slope, which is identical to the reference curve. During the following load increase, the ACPD increases with little plastic deformation. Hence, the latter

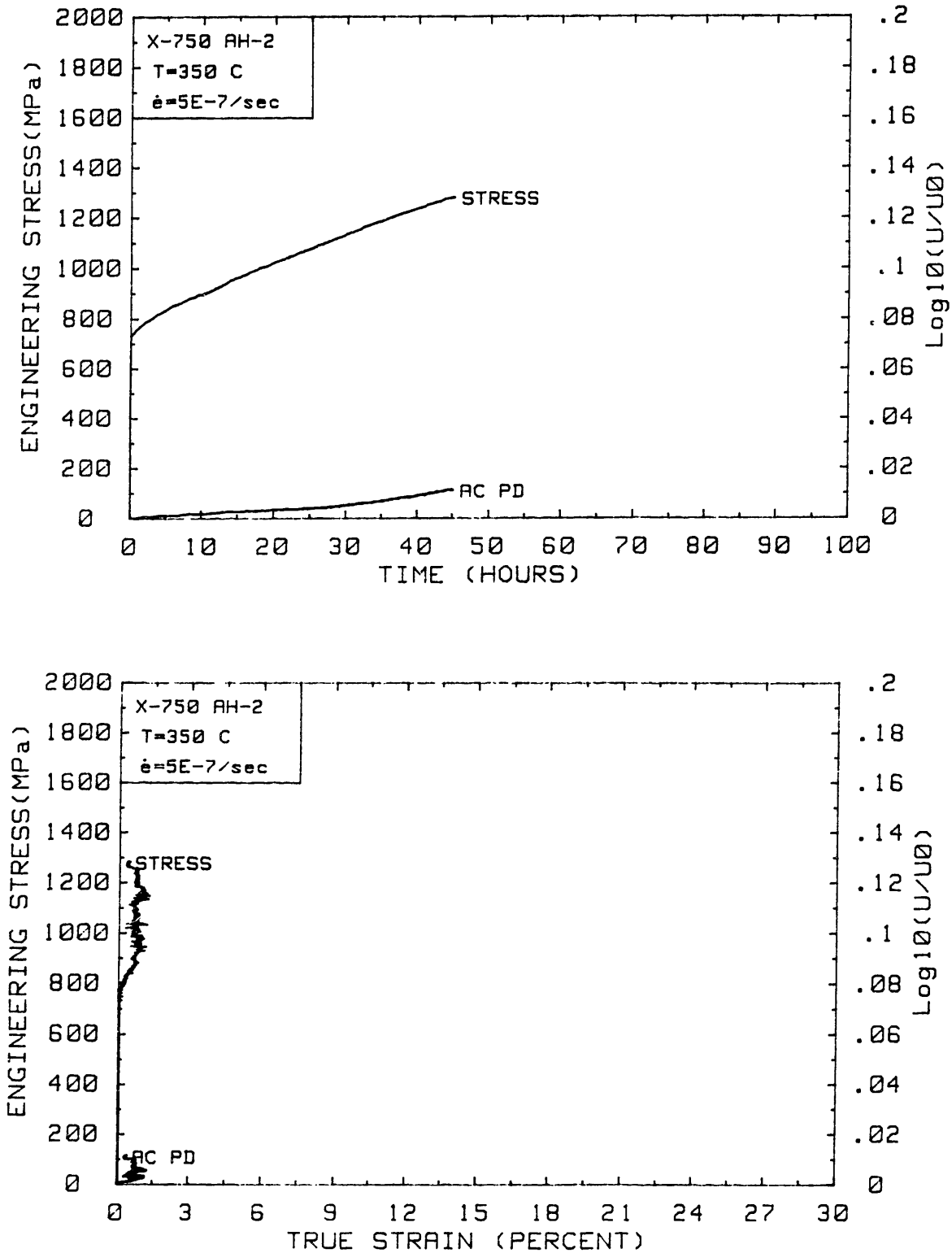

Figure 6.199 Stress and ACPD versus Time (upper) and Strain (lower) for AH Condition of Alloy X-750 During a SSRT at a Strain Rate of 5 x 10^{-7} sec^{-1} in a High Purity Deaerated Water at 350 C (stopped after 44 hours).

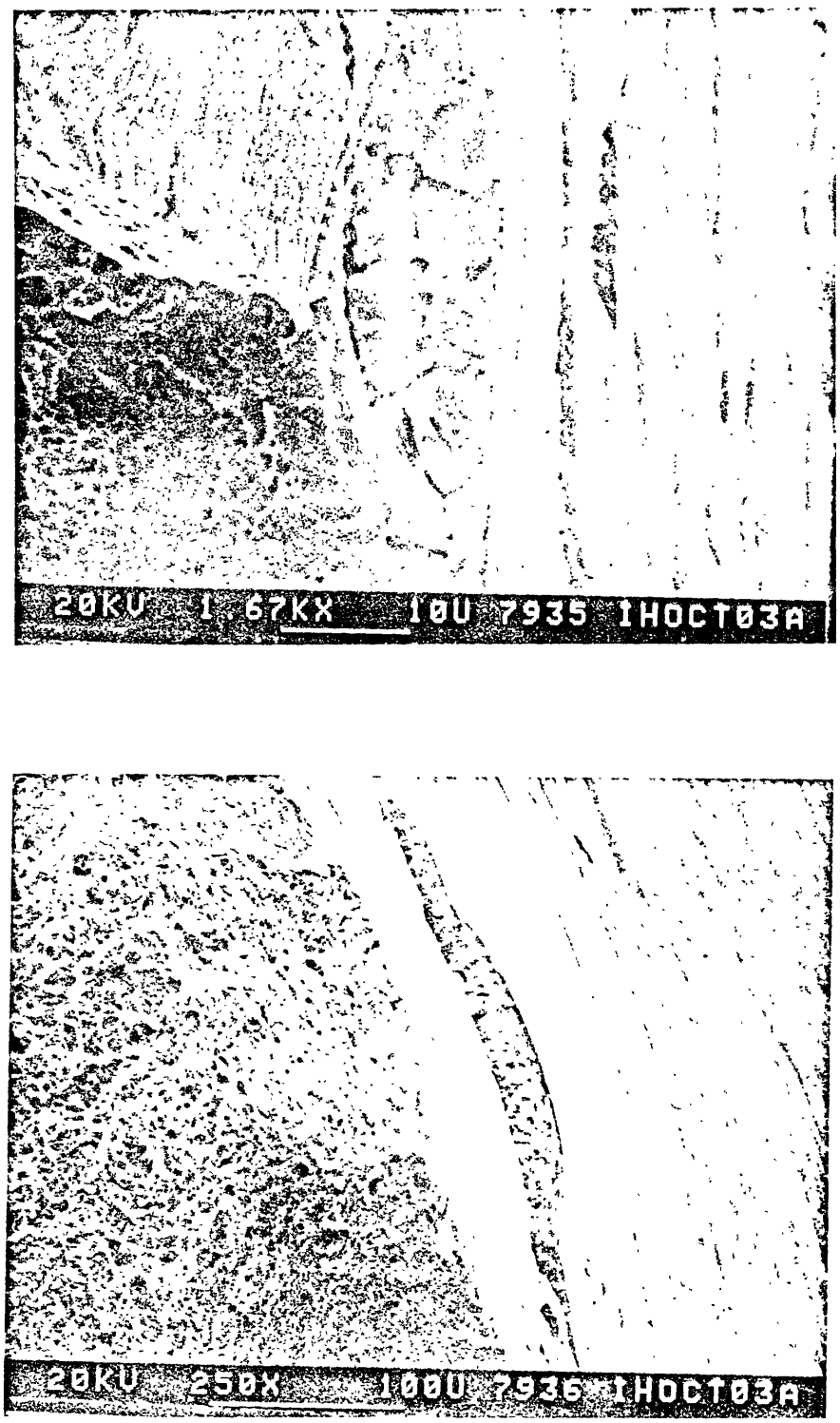

Figure 6.200 SEM Fractographs of Initiating Cracks after 44 Hours of SSRT on AH Condition of Alloy X-750 at a Strain Rate of 5×10^{-7} sec^{-1} in a High Purity Deaerated Water at 350 C.

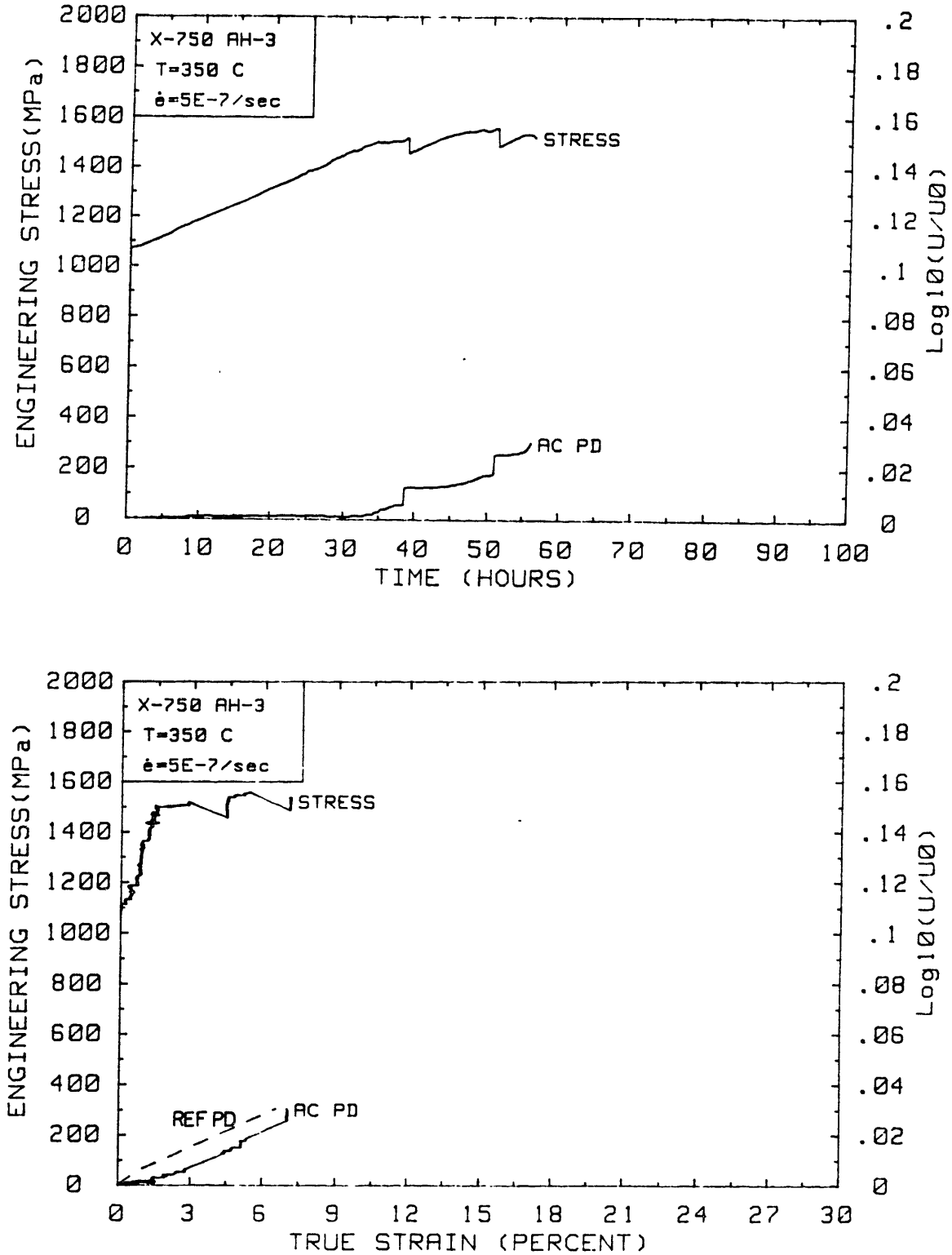

Figure 6.201 Stress and ACPD versus Time (upper) and Strain (lower) for AH Condition of Alloy X-750 During a SSRT at a Strain Rate of 5 x 10^{-7} sec^{-1} in a High Purity Deaerated Water at 350 C (stopped after 55 hours).

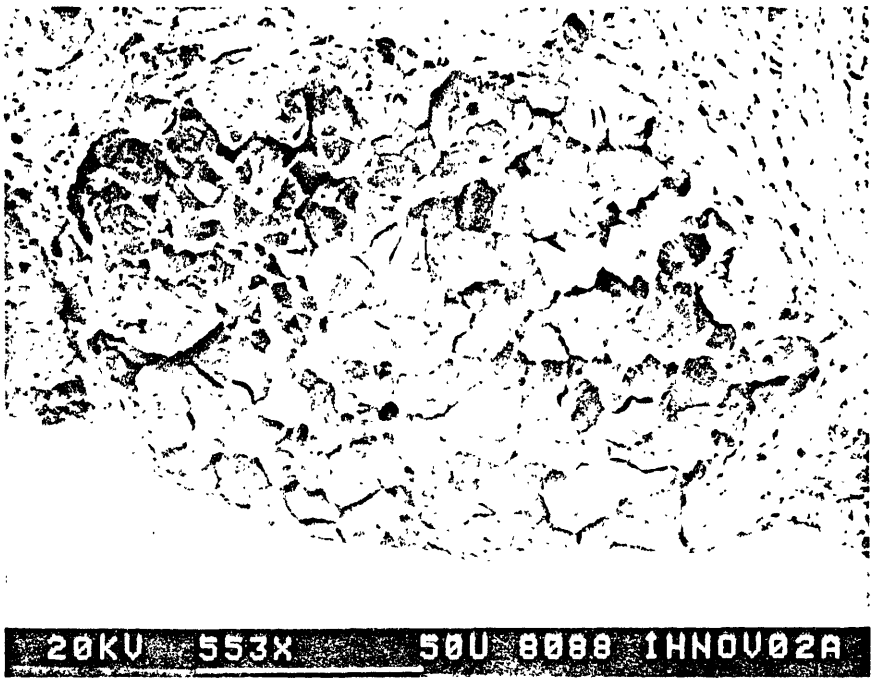

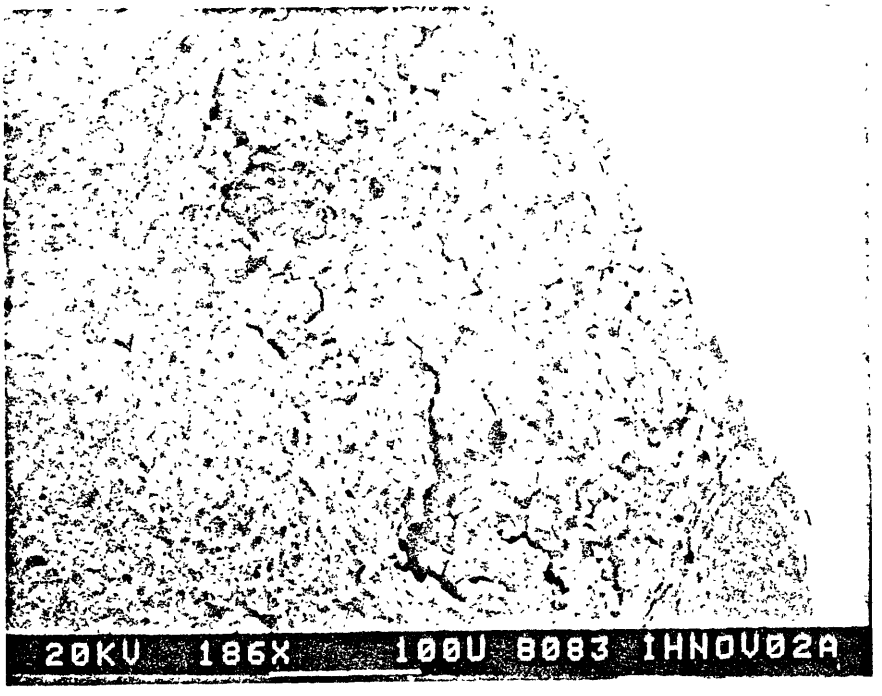

Figure 6.202 SEM Fractographs of Initiating Cracks after 55 Hours of SSRT on AH Condition of Alloy X-750 at a Strain Rate of 5×10^{-7} sec^{-1} in a High Purity Deaerated Water at 350 C.

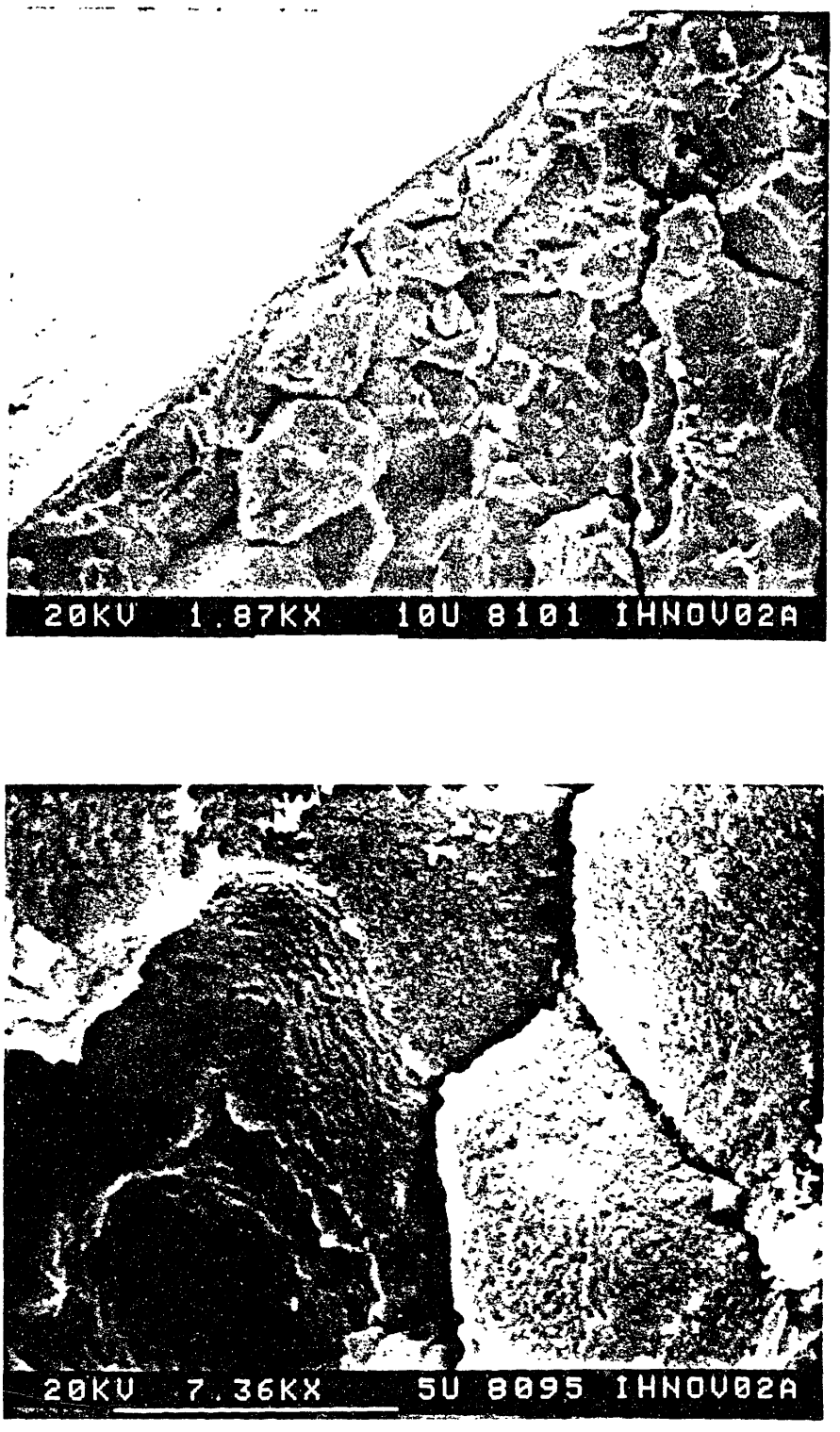

Figure 6.203 SEM Fractographs of Initiating Cracks after 55 Hours of SSRT showing Surface Oxide Layer (upper) and Pits due to γ' Dissolution (lower).

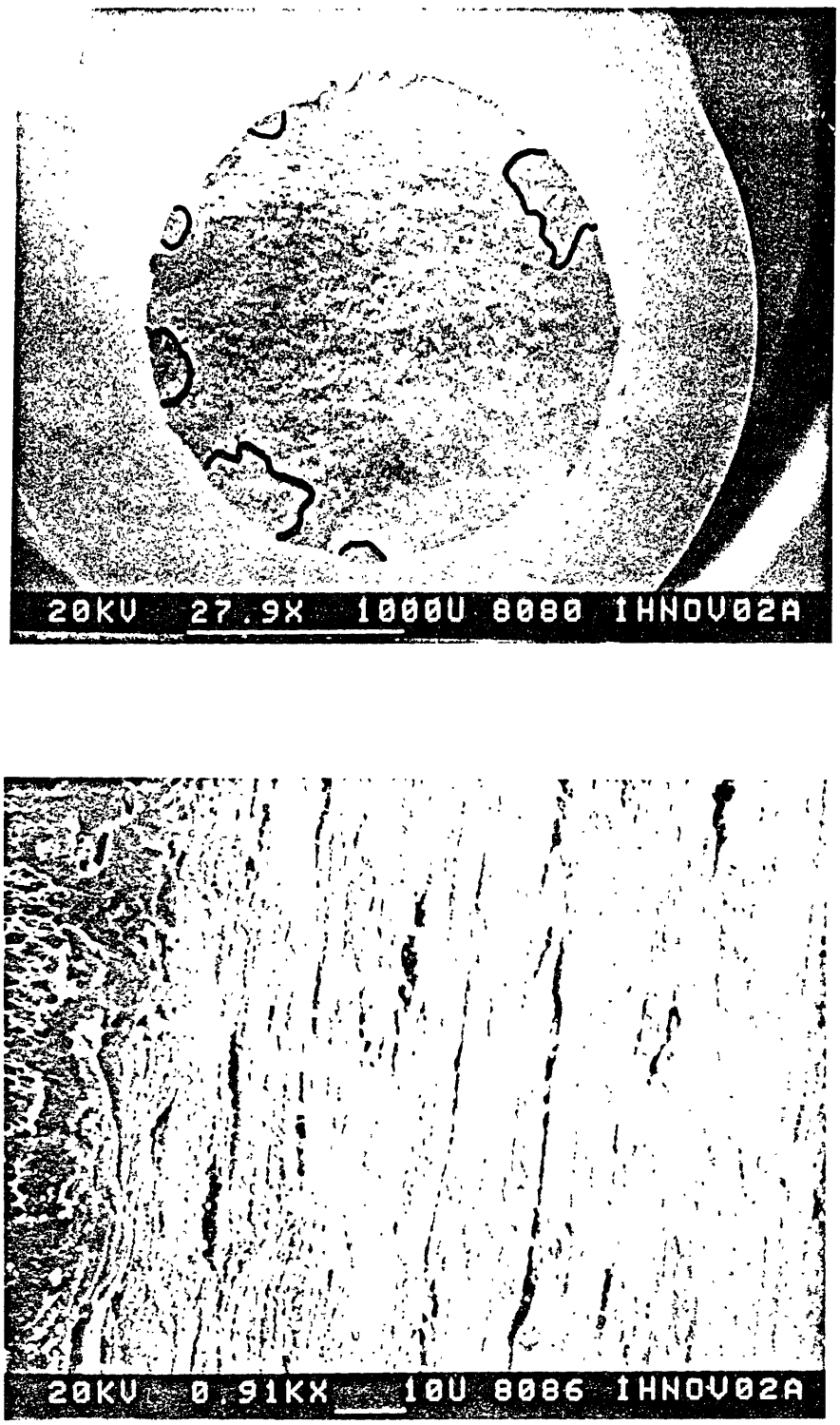

Figure 6.204 SEM Fractographs for the SSRT Specimen of AH Condition of Alloy X-750 Tested at a Strain Rate of 5×10^{-7} sec^{-1} in a High Purity Deaerated Water at 350 C (after 55 hours).

increase in the ACPD represents an increased in impedance of the specimen. The fractographic observation suggests two possible causes; the environmental intergranular cracks and the internal mechanical cracking at slow strain rate. It seems very likely that both contributed to the ACPD. Therfore, the detection of environmental cracking at high temperatures is more complicated due to the effect of mechanically induced cracking during the SSRT. The ACPD-strain plot, though useful for low temperature studies, is no longer helpful since both contributions occur without any change in strain. Instead, information from the ACPD-time plot turns out to be helpful.

A pattern of ACPD increase is observed which involves a plateau, a gradual increase or ramp and final step increase. The slope of the ramp increases as the environmental cracks grow. The validity of the approach must be checked during the examination of other results.

Two more AH specimens were tested at the same temperature and strain rate but without interruption until final fractures. One specimen failed after 71 hours, as shown in Figure 6.205. An early load drop is followed by the final fracture. The UTS is 1315 MPa with 0.2% elongation which represents an 11% decrease in strength and a 99% decrease in ductility. The ACPD clearly shows the crack growth with the load decrease. The step increase in ACPD on the time scale is caused by a serrated yielding as evidenced by a lower slope of ACPD on the strain scale. If this increase was due to rapid cracking, the slope would be much higher. The SEM fractographs are shown in Figure 6.206 where extensive embrittlement is apparent with a maximum crack depth of 450μm. Examination of the side wall reveals a few secondary intergranular cracks. A detailed examination shows intergranular cracks with widely open branches. The surface oxide layer is separated from the subjacent intergranular cracks.

Another AH specimen failed after 54 hours, as shown in Figure 6.207. An UTS of 1298 MPa and an elongation of 2.3% were measured which represent a 12% decrease in strength and a 88% decrease in ductility. The ACPD indicates the crack growth from 1% strain by its increasing slope on the

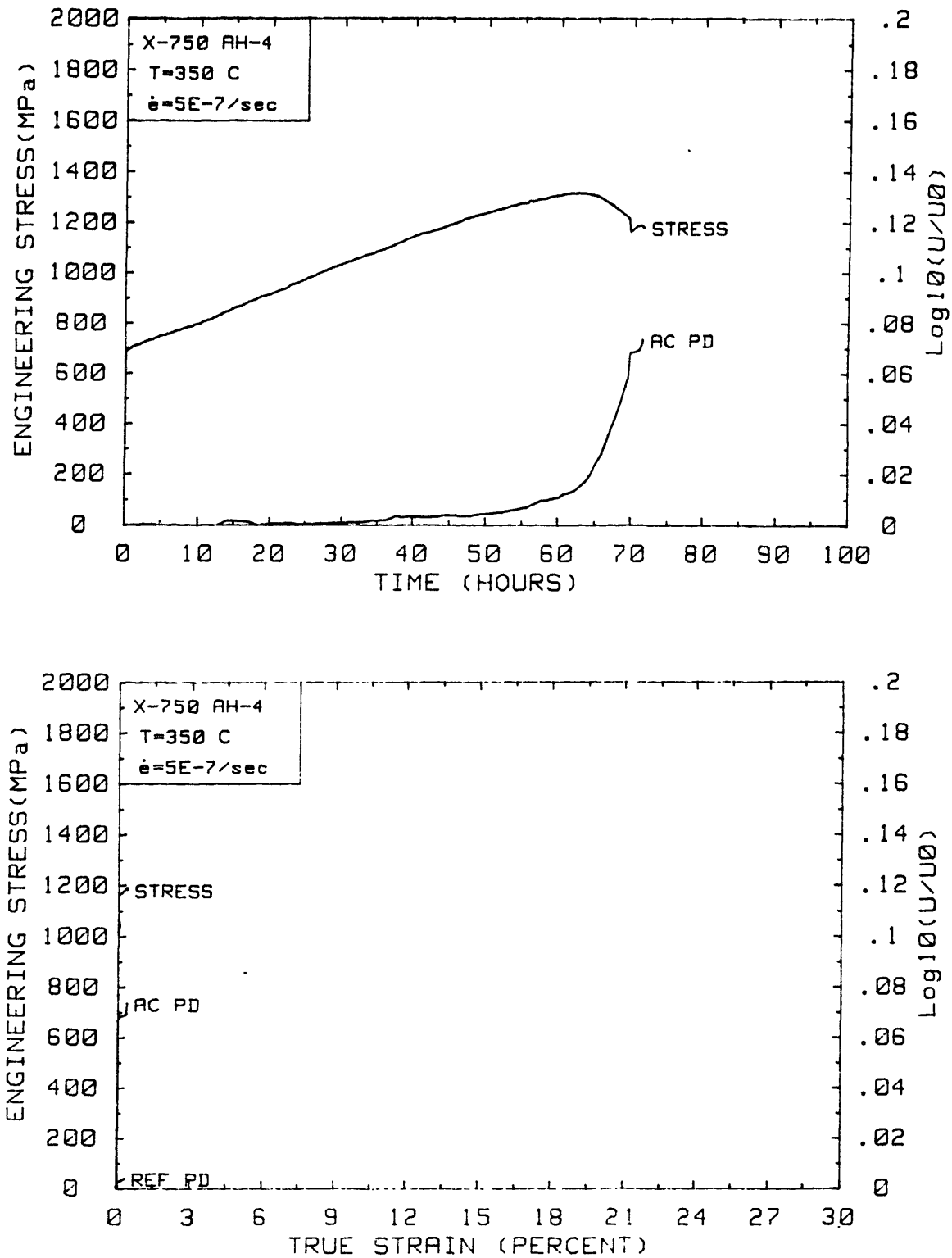

Figure 6.205 Stress and ACPD versus Time (upper) and Strain (lower) for AH Condition of Alloy X-750 During a SSRT at a Strain Rate of 5 x 10^{-7} sec^{-1} in a High Purity Deaerated Water at 350 C (test continued until fracture).

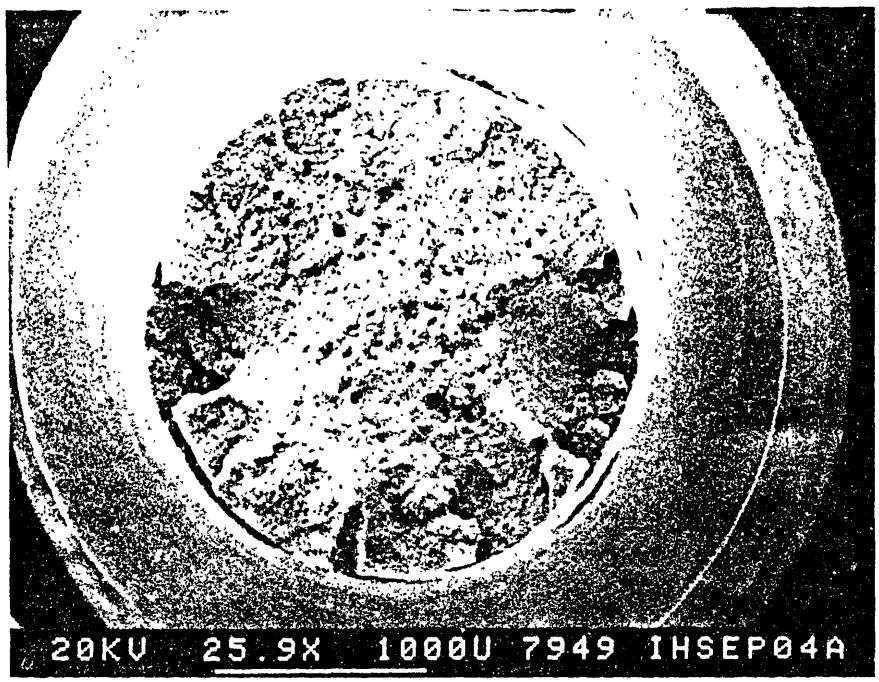

Figure 6.206 SEM Fractographs for the SSRT Specimen of AH Condition of Alloy X-750 Tested at a Strain Rate of 5×10^{-7} sec^{-1} in a High Purity Deaerated Water at 350 C (lower micrograph shows surface oxide layer).

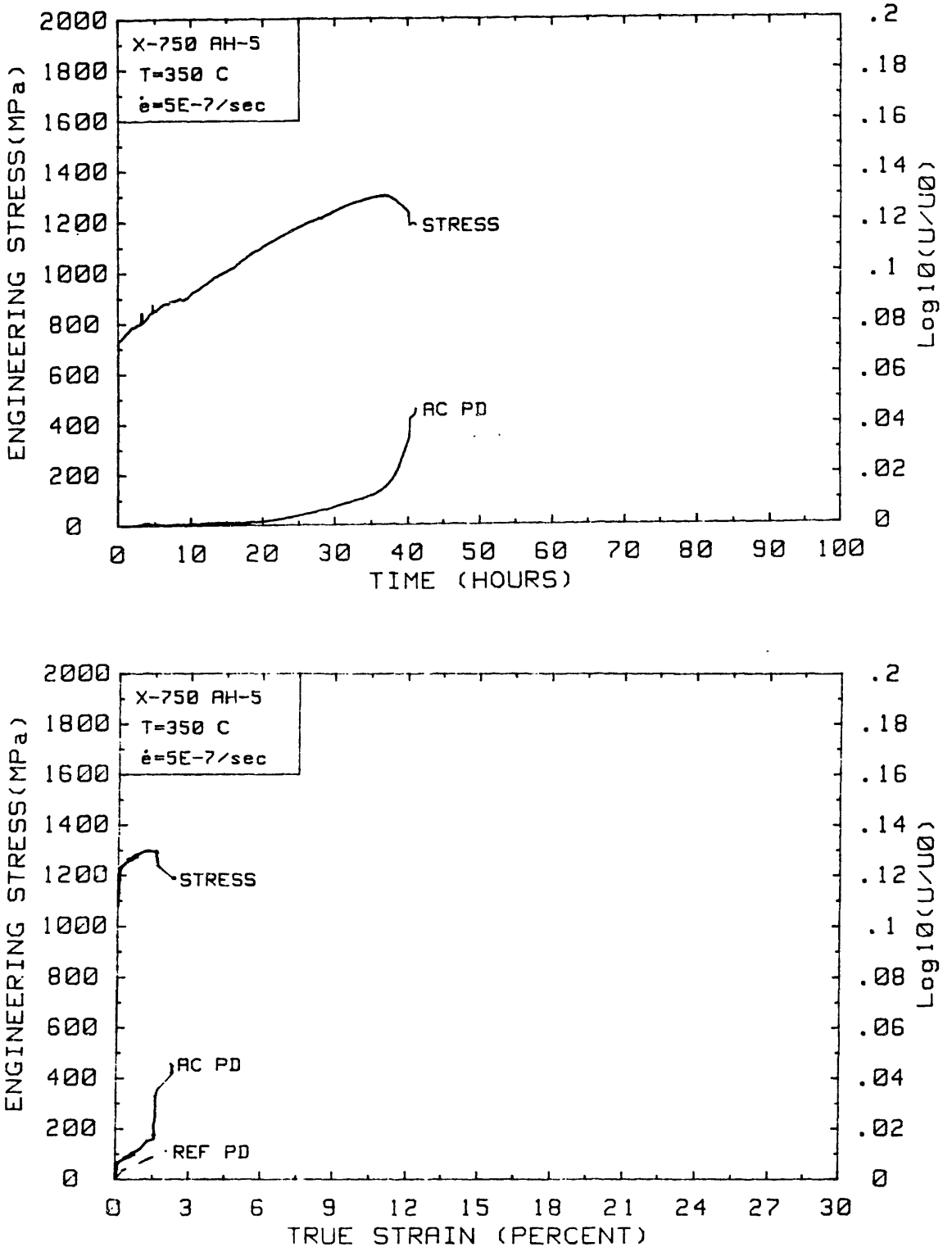

Figure 6.207 Stress and ACPD versus Time (upper) and Strain (lower) for AH Condition of Alloy X-750 During a SSRT at a Strain Rate of 5 x 10^{-7} sec^{-1} in a High Purity Deaerated Water at 350 C (test continued until fracture).

strain scale until the failure. The fracture surfaces are shown in Figure 6.208. Extensive intergranular cracking is visible with a maximum depth of about 410μm. A smaller crack is shown to be at a transition from the semi-circular shape to a wide crack which tends to occur at a crack size of about 120μm. The larger cracks changed the direction of growth toward the loading axis. Increasing degree of the triaxial stress state and resultant change in the direction of principal stress are believed to be responsible for the tendancy towards wider shape for the larger cracks. This suggests the importance of a normal stress as opposed to a shear stress.

Results with X-750 HTH

Two HTH specimen with a notched design were tested the hydrogenated high temperature water. The first test was made at 240^{o}C with a high strain rate of $7x10^{-5}sec^{-1}$ in order to obtain reference data for the HTH condition. The result is shown in Figure 6.209. The specimen failed after 1.2 hour with an UTS of 1438 MPa and an elongation of 22.0%. There is no evidence of serrated yielding. The SEM fractographs, shown in Figure 6.210, is an intergranular mixed with transgranular regions. The intergranular fracture is predominant in the central region while only a few locations of intergranular fracture are found near the edge. The intergranular surfaces are observed to be covered with ductile microvoids which distinguishes this fracture from the environmentally produced intergranular cracks in AH. The side wall reveals a number of small cracks that appear to have been formed from slip steps. The presence of microvoids on the intergranular surface at the edges is consistent with purely mechanical deformation of the HTH for a temperature range between 25 C and 300 C [23]. Therefore, no significant effect of environment is believed to be present. When ACPD is compared with the reference data for the AH condition, it is evident that the ACPD of HTH conditon has appreciably higher slope than the AH reference data. Since the AH condition undergoes ductile transgranular fracture at the high strain rate, the increase in the ACPD slope of HTH condition is attributed to mechanical intergranualr cracking. The tensile test results on the notched HTH specimen at 350 C also showed

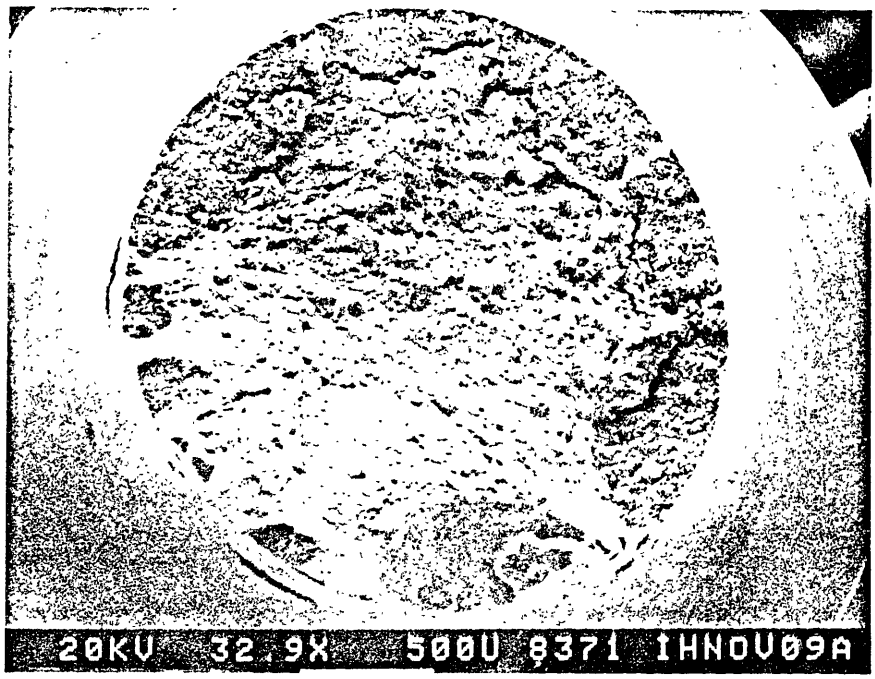

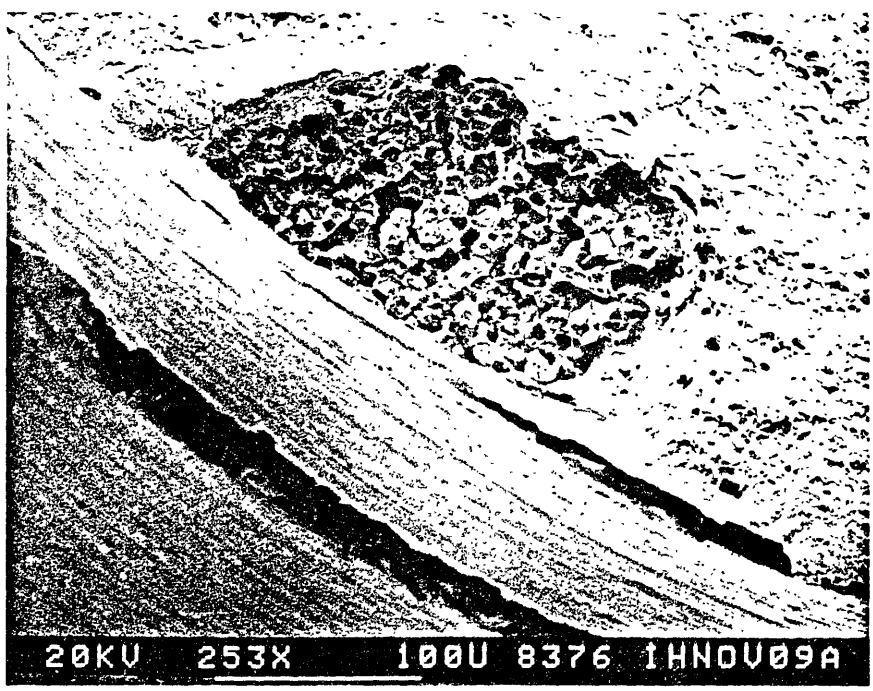

Figure 6.208 SEM Fractographs for the SSRT Specimen of AH Condition of Alloy X-750 Tested at a Strain Rate of 5×10^{-7} sec^{-1} in a High Purity Deaerated Water at 350 C (test continued until fracture).

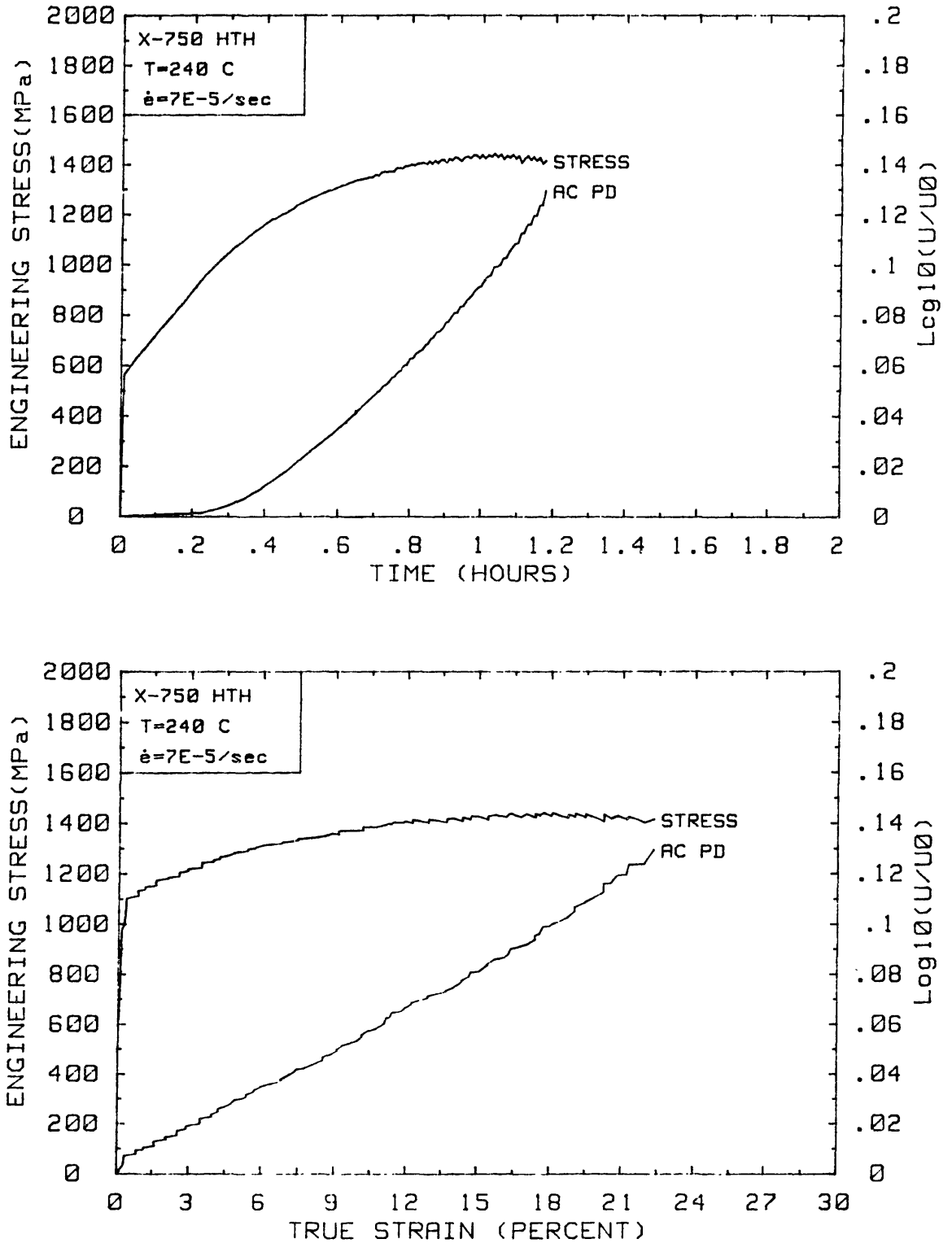

Figure 6.209 Stress and ACPD versus Time (upper) and Strain (lower) for HTH Condition of Alloy X-750 During a SSRT at a Strain Rate of 5 x 10^{-7} sec^{-1} in a High Purity Deaerated Water at 240 C.

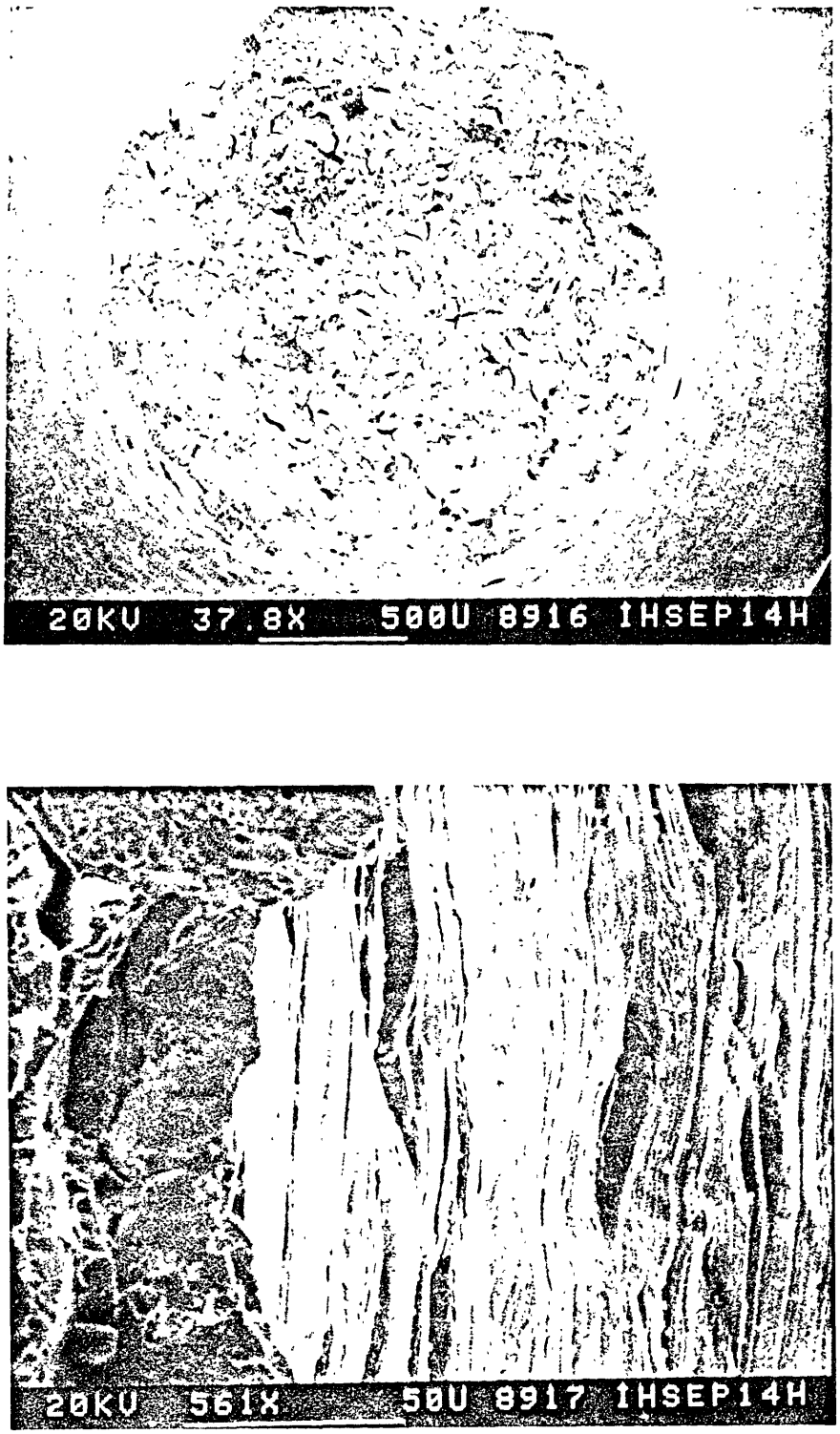

Figure 6.210 SEM Fractographs for the SSRT Specimen of HTH Condition of Alloy X-750 Tested at a Strain Rate of 5×10^{-7} sec^{-1} in a High Purity Deaerated Water at 240 C.

the presence of such intergranular cracking. Hence, the present ACPD data is taken as the refernece data for the SSRT at 350 C.

The results in 350 C water at a strain rate of $5x10^{-7}sec^{-1}$ are shown in Figure 6.211. There is nearly continuous serrated yielding which was also observed in the tensile test in air, shown in Figure 6.3.2.1. The UTS in the SSRT and the air tensile test at 350 C agree with each other within 0.4% indicating that the environmental effect is insignificant. The elongation is considerably lower than that measured by the tensile test. Since direct measurements with LVDT's used in the SSRT are believed to be more accurate, the elongation measured at 240 C is taken as the reference value. The elongation at 350 C is slightly higher than that of 240 C as shown in Table 6.11. The SEM fractographs for the HTH specimen are shown in Figure 6.212. Compared with the results at 240 C, the fraction of intergranular fracture is significantly reduced. The predominance of transgruanular crystallographic cracking, shear lips and the central region with overgrown voids are similar with those observed from the air tensile test specimen, shown in Figure 6.115. The small increase in ductility, with the increase in temperature from 240 C to 350 C, may be attributed to a decreased amount of intergranular fracture. The edges of the specimen are often found to be intergranular, as shown in Figure 6.212. The ACPD, shown in Figure 6.211, increases in a complicated way, but in a typical pattern observed with the AH condition at 350 C. The three-step pattern of ACPD including a plateau, a ramp and a step is clearly evident on the ACPD-time plot. As assumed earlier in the presentation on AH, the slope of a ramp is used to distinguish the effect of internal cracking from environment assisted cracking. In contrast with the earlier case with AH shown in Figure 6.6.33, there is no significant increase in the slop of ramp throughout the test which correctly indicating the absence of environmental cracks. Thus the use of the slope of the ramp in the ACPD-time plot as an indication of the surface cracks is applicable also for the HTH condition. The results with HOA condition at 350 C with a strain rate of $5x10^{-7}sec^{-1}$ is shown in Figure 6.213. The stress and ACPD are very similar with those observed with HTH condition at the same temperature. The time and strain to fracture shown in Figure 6.214, are

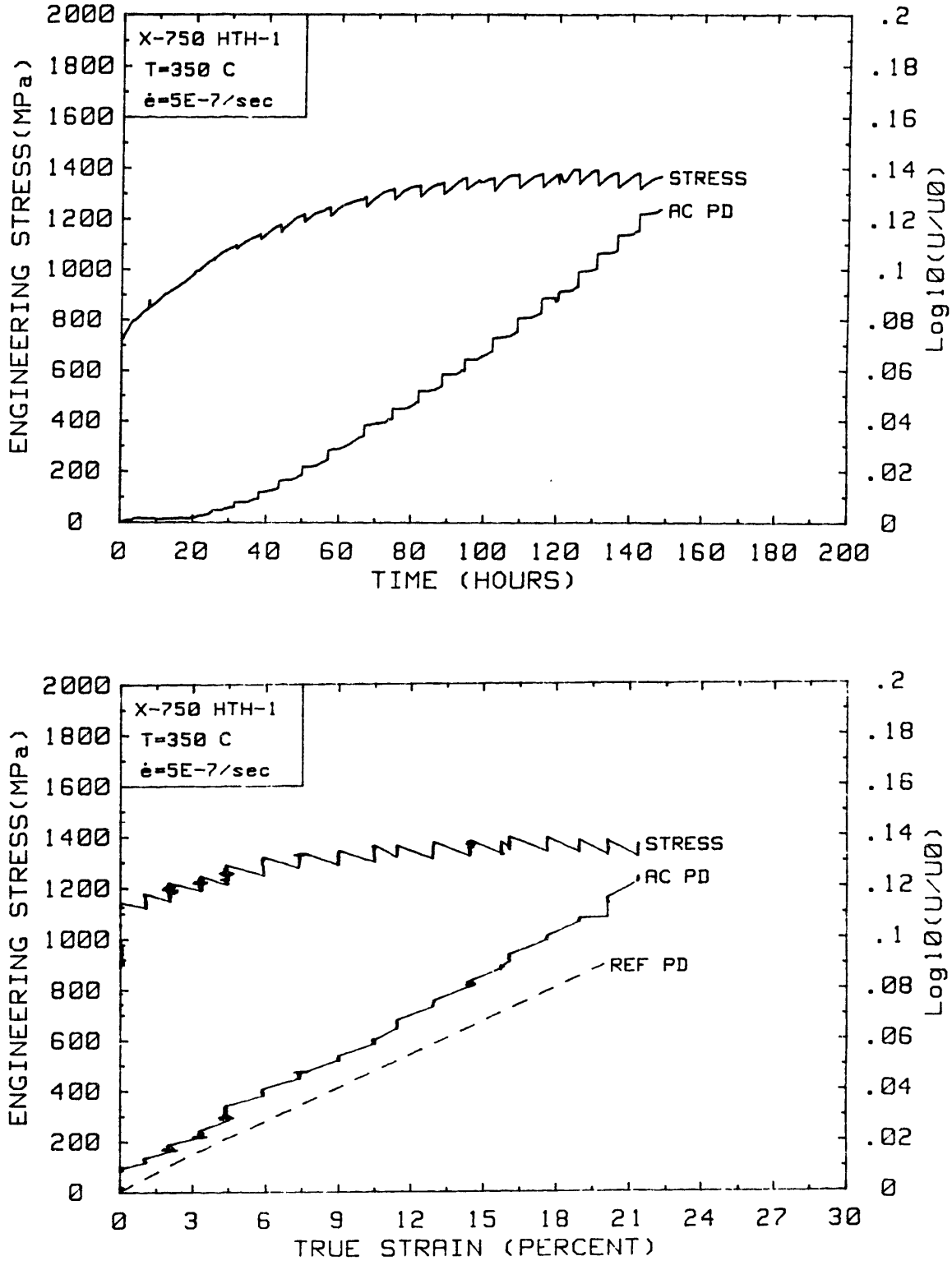

Figure 6.211 Stress and ACPD versus Time (upper) and Strain (lower) for HTH Condition of Alloy X-750 During a SSRT at a Strain Rate of 5 x 10^{-7} sec^{-1} in a High Purity Deaerated Water at 350 C.

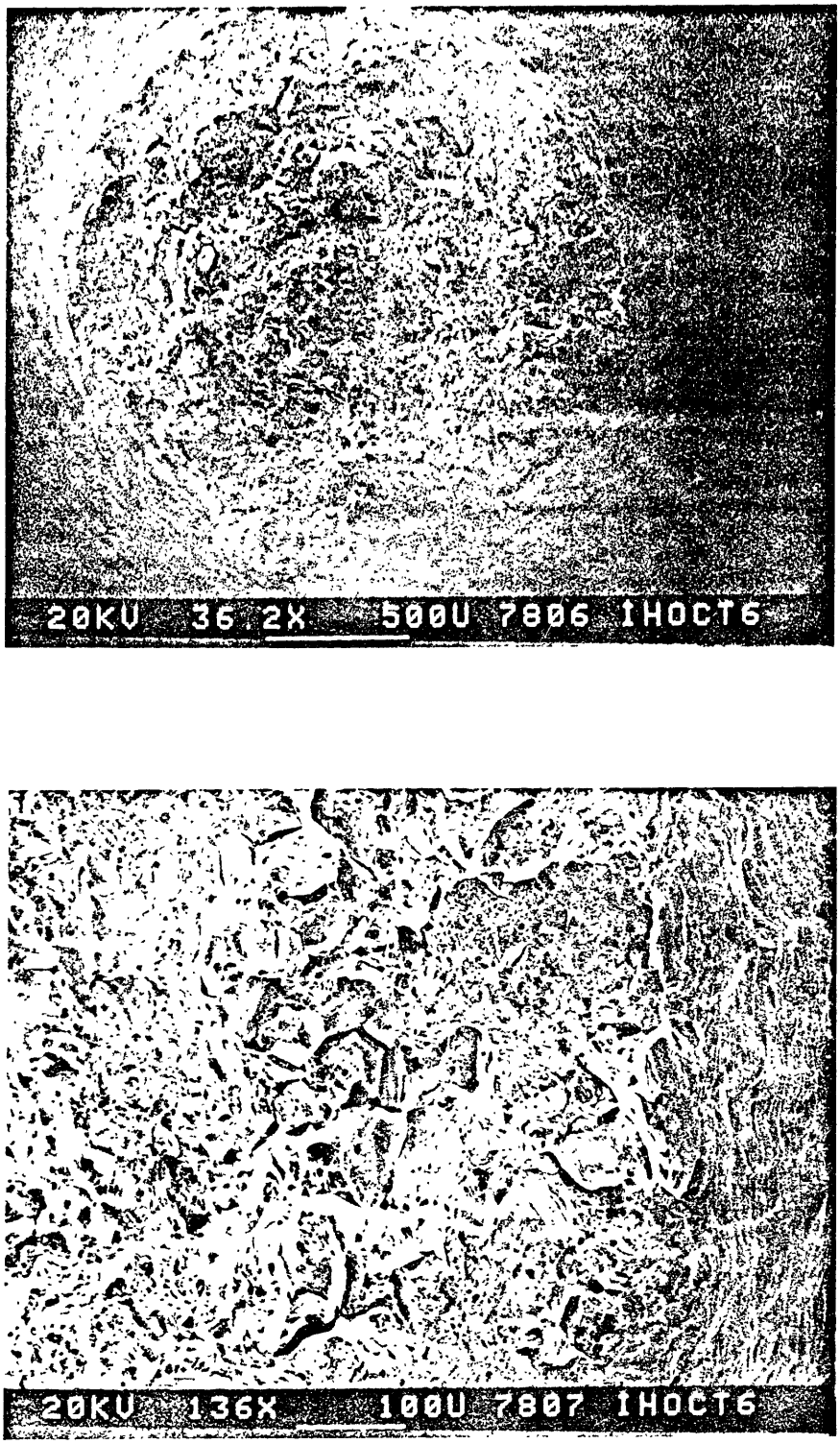

Figure 6.212 SEM Fractographs for the SSRT Specimen of HTH Condition of Alloy X-750 Tested at a Strain Rate of 5×10^{-7} sec^{-1} in a High Purity Deaerated Water at 350 C.

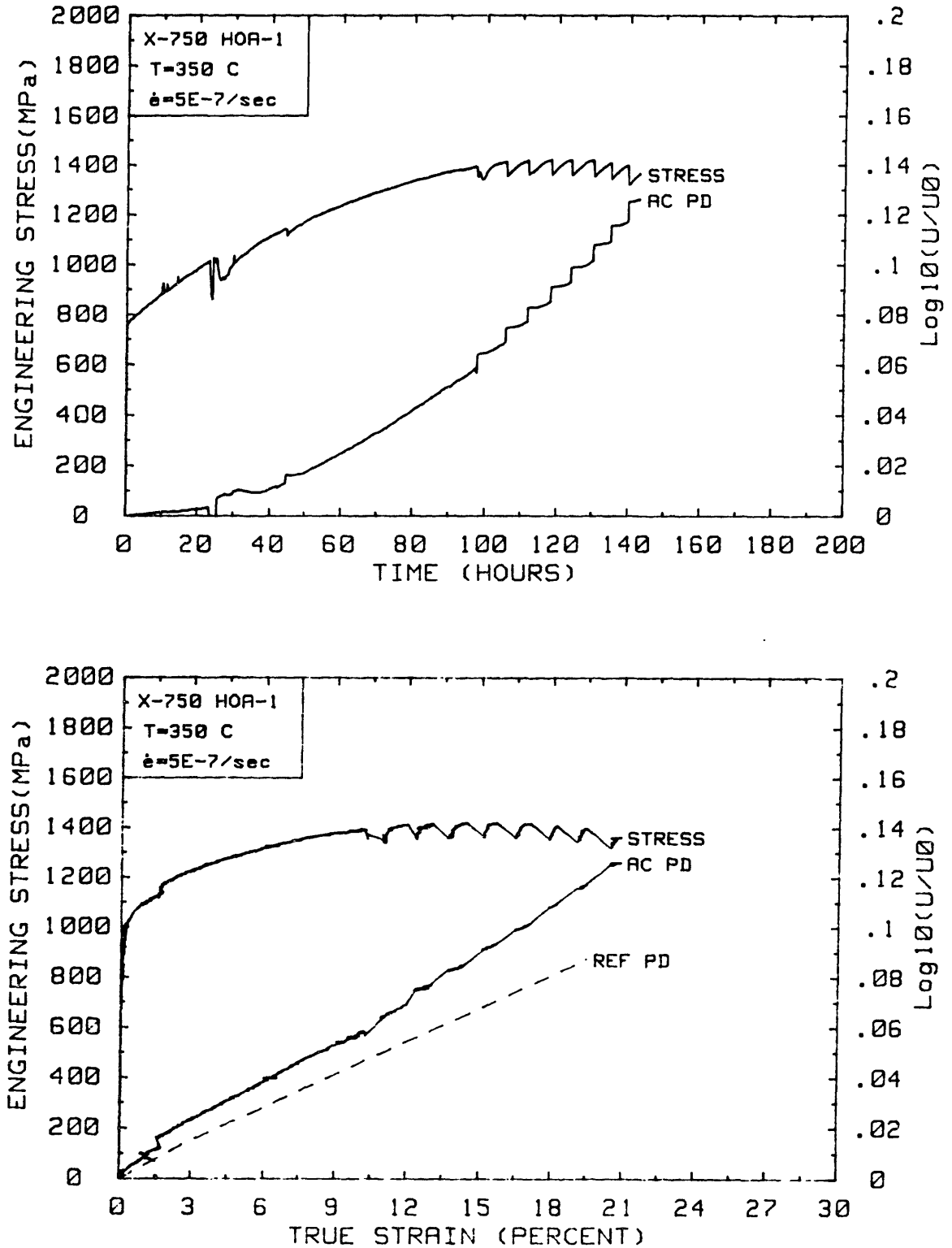

Figure 6.213 Stress and ACPD versus Time (upper) and Strain (lower) for HOA Condition of Alloy X-750 During a SSRT at a Strain Rate of 5×10^{-7} sec^{-1} in a High Purity Deaerated Water at 350 C.

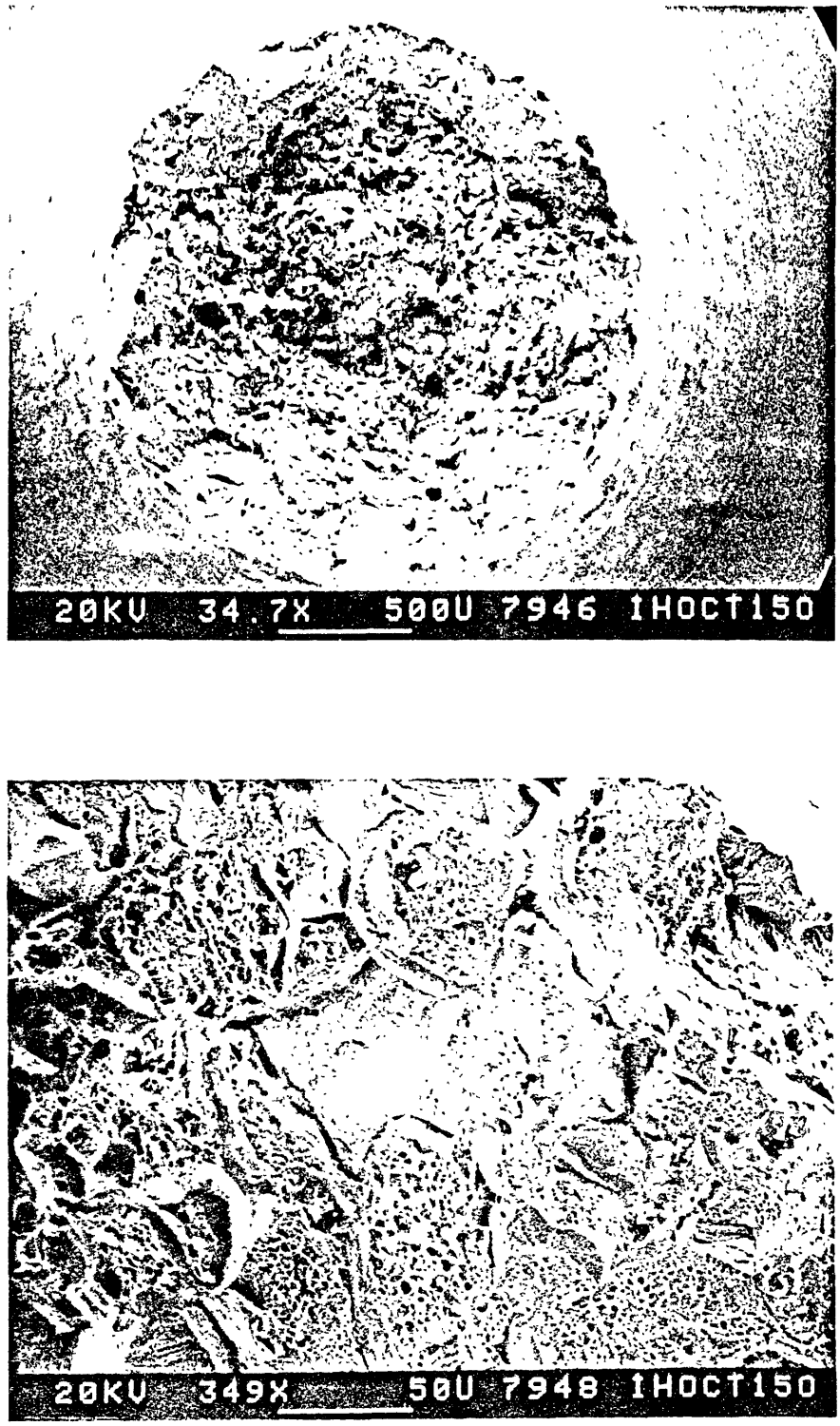

Figure 6.214 SEM Fractographs for the SSRT Specimen of HOA Condition of Alloy X-750 Tested at a Strain Rate of 5×10^{-7} sec^{-1} in a High Purity Deaerated Water at 350 C.

also very similar. No environmental effect could be observed.

6.6.3 Results with Alloy 718

Two conditions, including CHT and DA, were tested in hydrogenated high temperature water with a strain rate of $5x10^{-7}sec^{-1}$. The result with CHT condition is shown in Figure 6.215. Serrated yielding was observed for the entire period of deformation. The load drops increase with time while the associated step in strain remained constant at about 1.5% or 23μm. An UTS of 1556 MPa and an elongation of 10% measured during the SSRT represents a 10% decrease in the strength and a 38% decrease in the ductility. This suggests there may be environmentally assisted embrittlement. The SEM fractographs are shwon in Figures 6.216 and 6.217. A cup-and-cone type fracture surface reveals an intergranular cracks even in some area of the shear lips as well as the central region. Intergranular fracture with grain boundary cavities is believed to be associated with the intergranular preicpitation of Laves phase. The fractographs after a tensile test at a higher strain rate, in Figure 6.116, shows a similar intergranular nature, but to much lesser extent. The increased cavitation is thus understood as the result of about three orders lower strain rate used in SSRT which allows for the slow kinetic process of grain boundary cavitation. There is one location at the edge where an intergranular area is not covered with the microvoids, as shown in Figure 6.217. It is believed that this were formed a significant time before the final fracture since such microvoids are usually not dissolved after a few hours of exposure to the environment. In addition, the semi-circular feature is consistent with the observed shape of initiating cracks. Therefore, the CHT condition deserves a detailed study at various strain rates. The semi-circular feature has a size of only 20μm by 20μm. This is too small to explain the significant deterioration in the mechanical properties. The increased cavitation is, therefore, a purely mechanical phenomenom believed to be responsible for the reduced ductility. Detailed ACPD data were not obtained for the CHT test in favor of multifrequency experiments. Nevertheless the ACPD at 200 kHz does not deviate from the reference data of the HTH condition. The three-step pattern analysis is, however, not possible

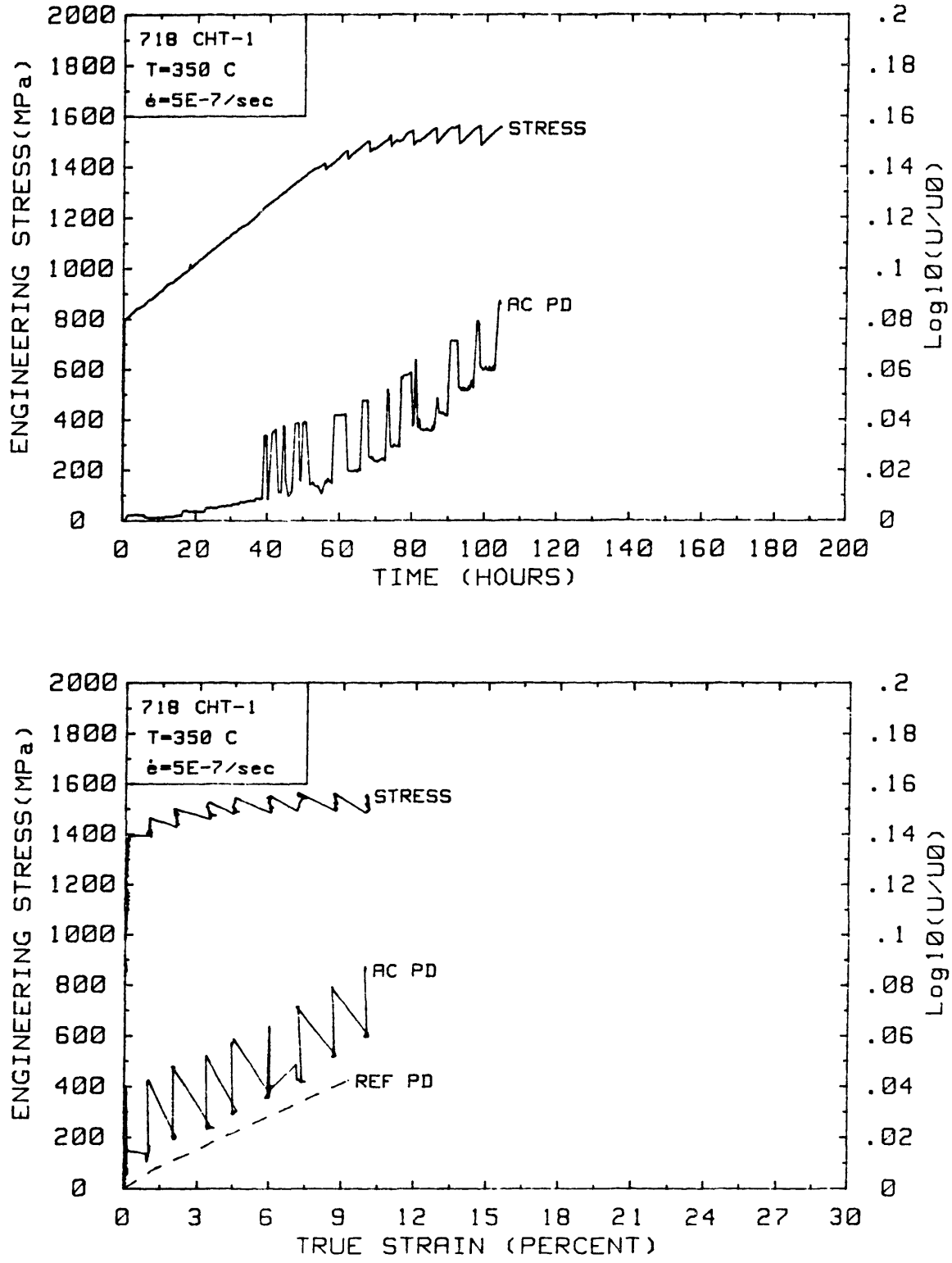

Figure 6.215 Stress and ACPD versus Time (upper) and Strain (lower) for CHT Condition of Alloy 718 During a SSRT at a Strain Rate of 5 x 10^{-7} sec^{-1} in a High Purity Deaerated Water at 350 C.

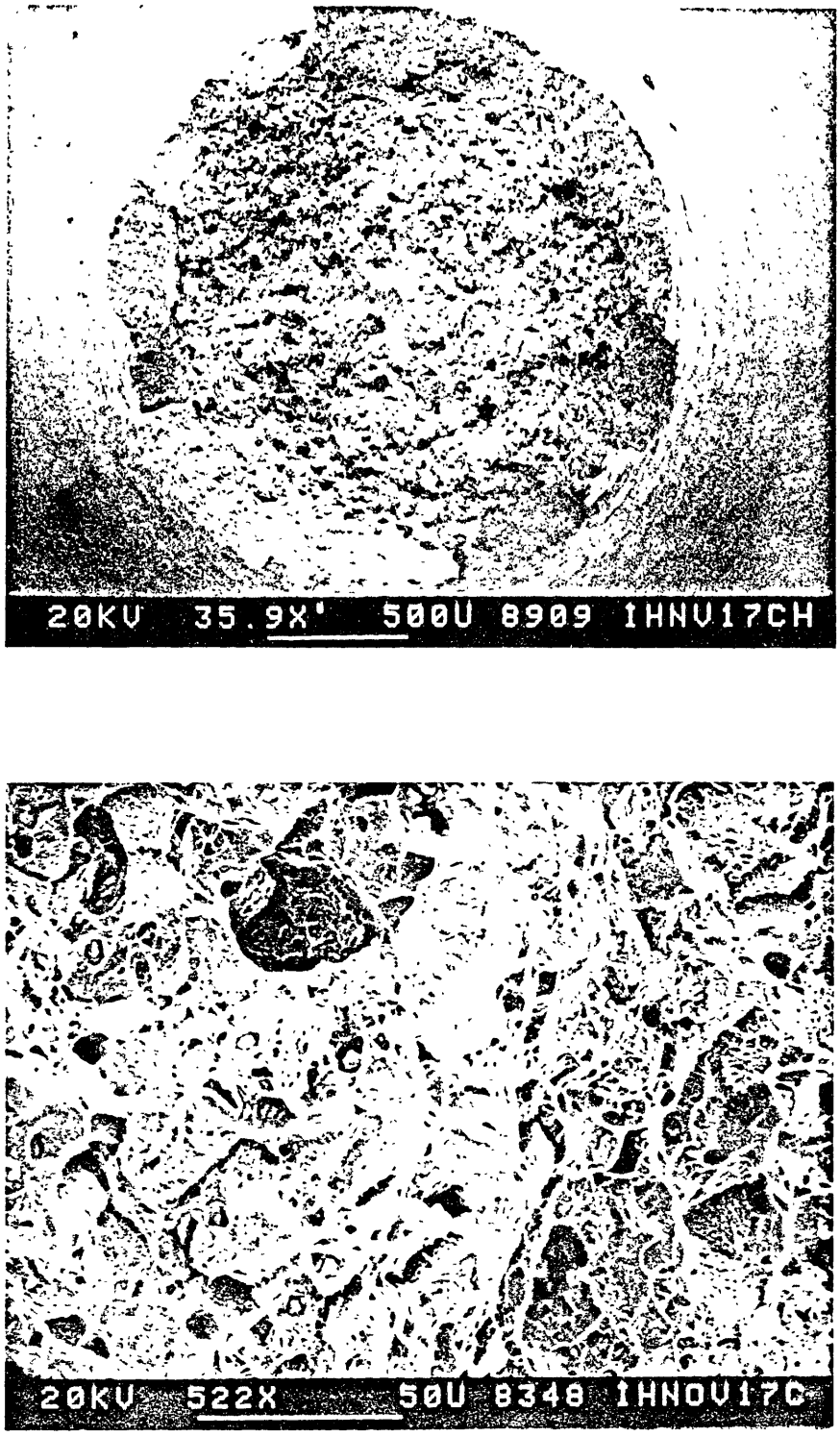

Figure 6.216 SEM Fractographs for the SSRT Specimen of CHT Condition of Alloy 718 Tested at a Strain Rate of 5×10^{-7} sec^{-1} in a High Purity Deaerated Water at 350 C (lower micrograph shows grain boundary cavities).

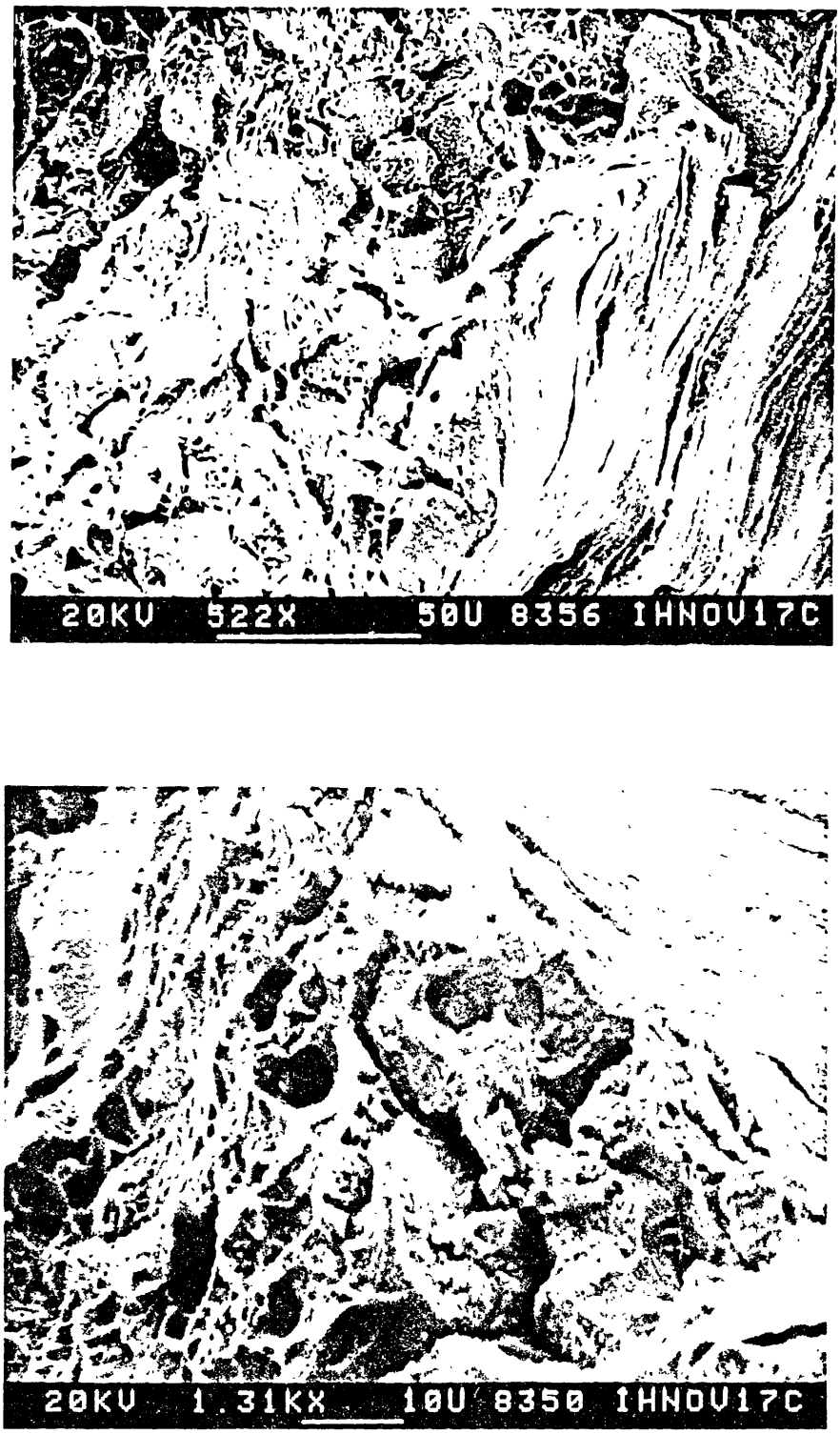

Figure 6.217 SEM Fractographs for the SSRT Specimen of CHT Condition of Alloy 718 Tested at a Strain Rate of 5×10^{-7} sec^{-1} in a High Purity Deaerated Water at 350 C (lower micrograph shows featureless intergranular cracks in contrast with typical edge grains with microvoids in upper micrograph).

due to poor stability in the signal.

The results with DA condition are shown in Figure 6.218. A small amount of serrated yielding is observed near the end of test. An UTS of 1758 MPa and an elongation of 14.3% are obtained. The UTS and elongation of the DA condition are, respectively, 30% and 10% higher than those of the CHT condition. The SEM fractographs are shown in Figure 6.219. The fracture is cup-and-cone. A few surface oxide fissures were observed to emerge from the scratches made by polishing. However, there is no evidence of environment assisted intergranular crack initiation. The ACPD shows the three-stage pattern although the stage of ramp is conspicuously diminished. The slope of the ramps are low and unchanged in agreement with the fractographic observation.

6.6.4 Summary

The susceptibility of environmental embrittlement of alloys 600, X-750 and 718 were studied by using the slow strain rate test. Alloys 600 and X-750 specimens were tested in the deaerated high purity water at 93 C with a range of strain rates corresponding to a fatigue crack tip strain rate between 0.1Hz and 1 Hz. No evidence of embrittlement was observed with either materials. Data for the strain dependence of ACPD were obtained from the low temperature tests. Due to lack of environment-induced cracks, the obtained data were used as the reference value for high temperature tests.
The high temperature behaviors were obtained at a temperature around 350 C for alloys 600, X-750 and 718. Due to an appreciable contribution of seal friction forces to the measured strengths, the stress data was corrected based on the differences in yield strength between the SSRT and the tensile tests in air. This method was found to be successful since the corrected UTS agree well with expected values based on the fractography and the tensile test results.

The results on the maximum intergranular crack depth are summarized in Figure 6.220. In case of alloy 600, environment assisted cracking was observed from the heat NX1638 and the LTMA condition of heat 96834 when

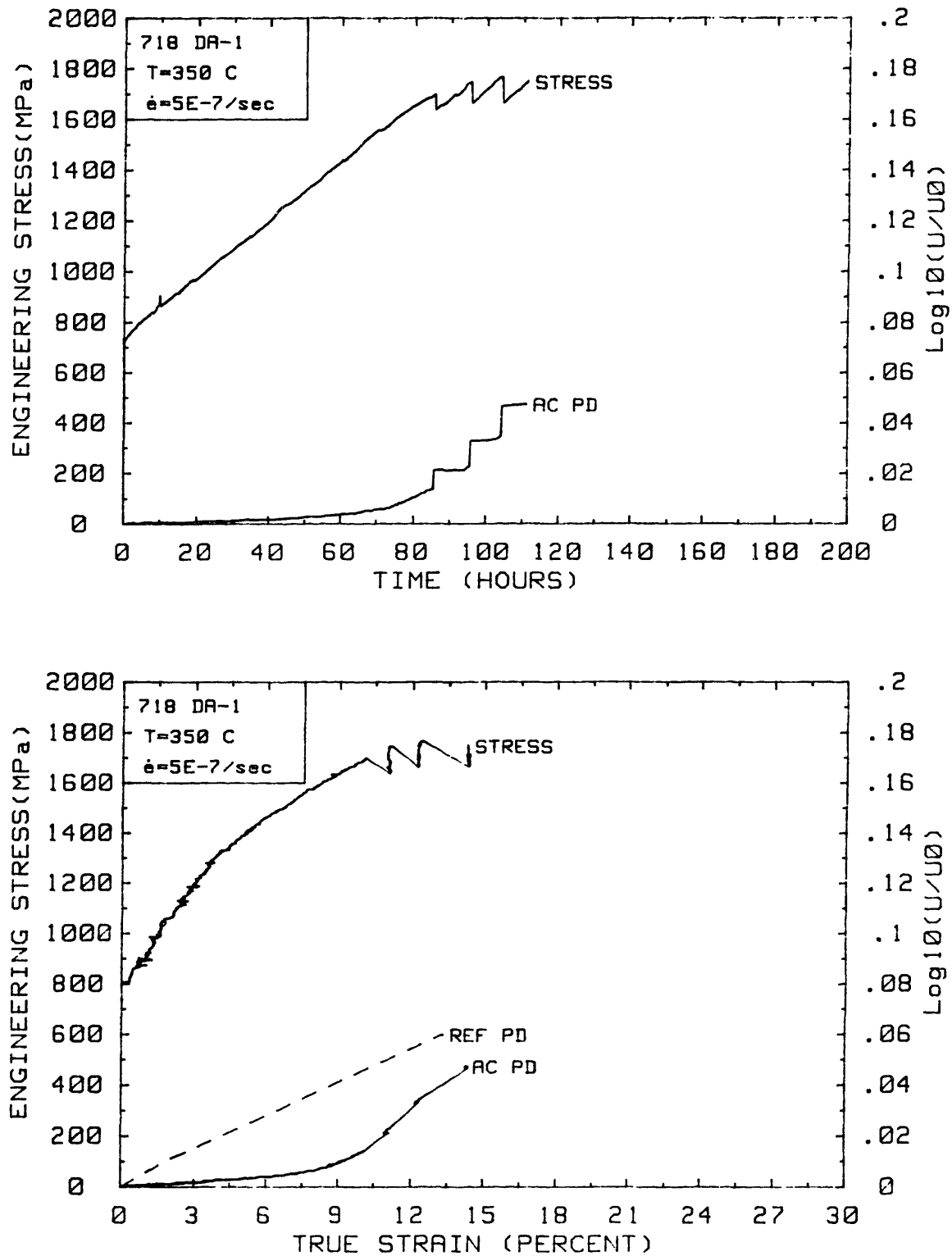

Figure 6.218 Stress and ACPD versus Time (upper) and Strain (lower) for DA Condition of Alloy 718 During a SSRT at a Strain Rate of 5 x 10^{-7} sec^{-1} in a High Purity Deaerated Water at 350 C.

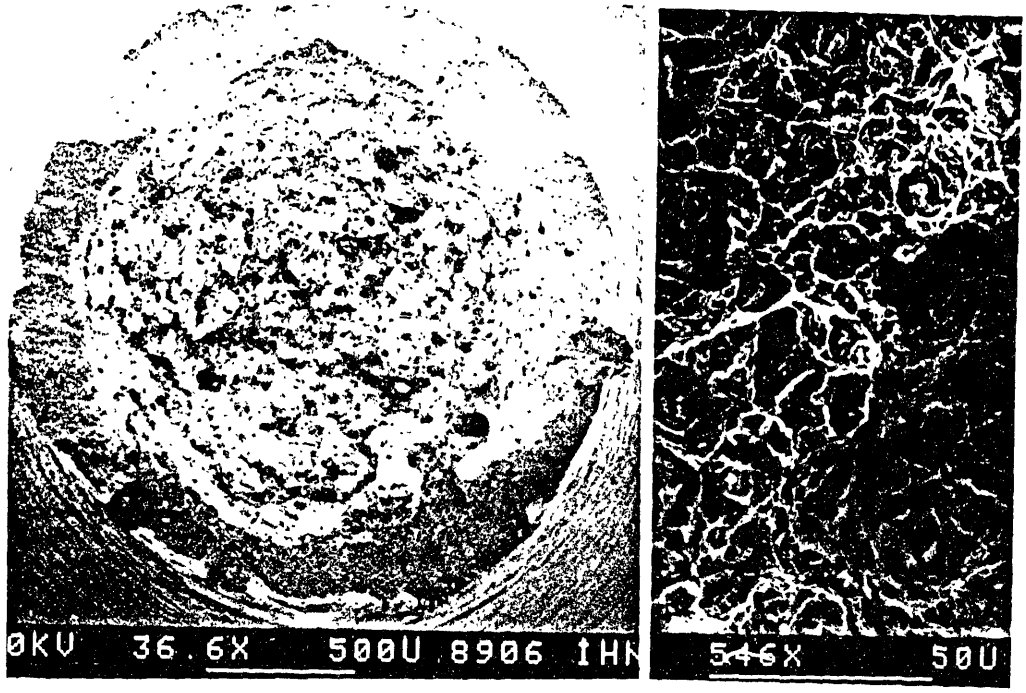

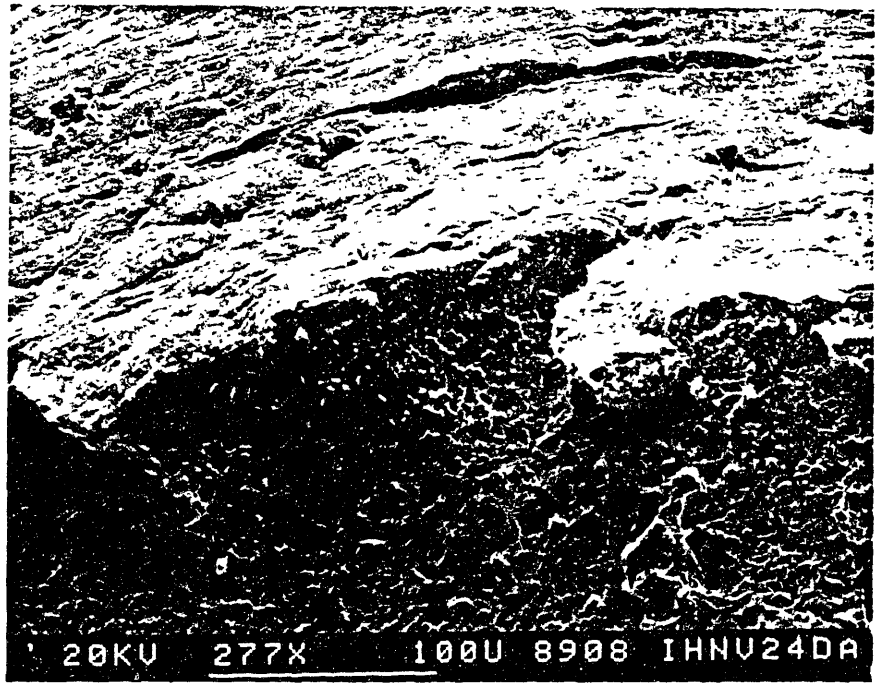

Figure 6.219 SEM Fractographs for the SSRT Specimen of DA Condition of Alloy 718 Tested at a Strain Rate of 5×10^{-7} sec^{-1} in a High Purity Deaerated Water at 350 C.

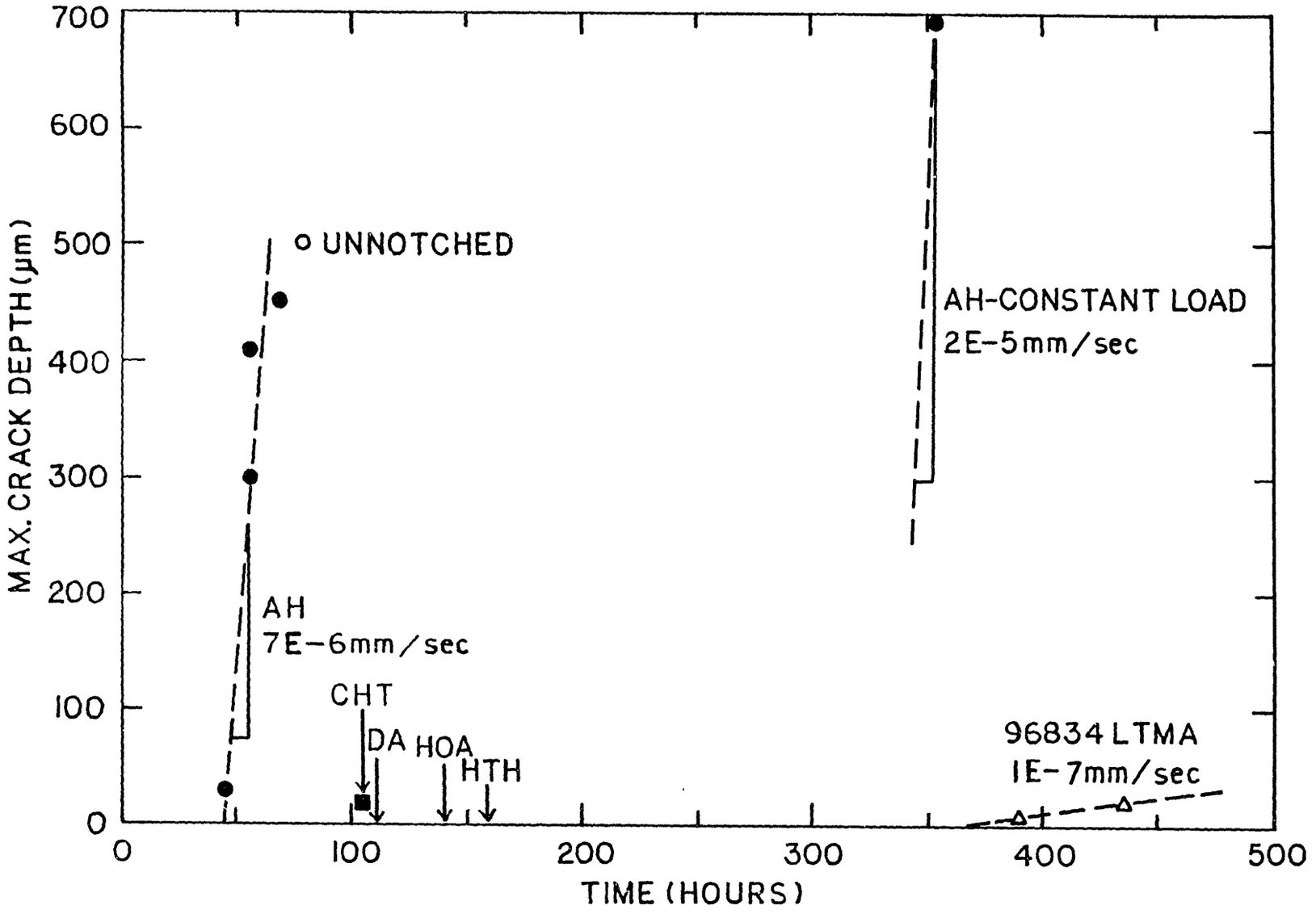

Figure 6.220 Summary of Crack Initiation and Growth Behaviors of Alloys 600, X-750 and 718 in High Temperature Water with 0.18 MPa Dissolved Hydrogen.

the specimens were exposed to 340 C or above with a strain rate of $2x10^{-7}$sec. Heat NX1638 showed, however, only 10μm deep cracks after 405 hours. About three times deeper cracks were observed with the LTMA condition of 96834 during the same period. Assuming a linear crack growth rate with time, the growth rate was determined to be $1x10^{-7}$mm/sec with an initiation time of 350 hours. Due to the smaller crack size and probe failures, ACPD information was not obtained.

In case of alloy X-750, a significant difference in the susceptibility was observed at 360 C with a strain rate of $5x10^{-7}sec^{-1}$. The AH condition showed a crack growth rate of $7x10^{-6}$mm/sec with an initiation time of 40 hours. The HTH and HOA conditons failed after about the same exposure time and strain with little evidence of the environment assisted cracking, as shown in Figure 6.220.

In case of alloy 718, a smaller difference in the susceptibility was observed between two heat treatments. The CHT condition showed about a 10% decresae in the UTS and about 30% decrease in the elongation whereas, essentially no change was observed with the DA condition. The fractographs of CHT condition revealed only a negligible amount of environemtnal effect. The evidence of an extensive grain boundary caviation in CHT condition is attributed to the degradation of proerties by a creep crack growth process.

The sensitivity of the ACPD system to multiple crack initiation in alloy 600 was not verified during SSRT in water due to the fact that the produced crack depth was much shorter than the expected sensitivity of 70μm. For alloys X-750 and 718, environment assisted cracks initiated only at a few sites resulting in a lower sensitivity which was determined to be 300μm with a probe spacing of 1.6mm and 200kHz. Sensitivity is expected to be improved by reducing th probe spacing, and minimizing the occurrence of internal crack formation. The constant load test on the X-750 AH specimen with a laser-induced pit led to an ACPD sensitivity of 60μm with a probe spacing of 1.2mm and 200 kHz.

Chapter 7

DISCUSSION OF RESULTS

The results from this work are discussed in an effort to provide a detailed understanding of embrittlement mechanisms. As the first step Results of microstructural charaterization are analyzed in order to determine general relationship between process variables and grain boundary chemistries as well as fundamental microstructural charateristics. The electrochemistry of important grain boundary constituents is then discussed to determine its role and kinetics during the microprocess of the embrittlement. Finally, embrittlement mechanisms and associated rate-controlling steps are to be determined for two temperature regimes; below and above 200 C. Considerable evidences support that there are different rate-controlling process of embrittlement in the different regimes.

7.1 MICROSTRUCTURAL EVOLUTION

Alloy 600

In agreement with earlier works [22,27], the microstructures of mill annealed alloy 600 tubings are determined primarily by the carbon content and the final anneal temperature. The five heats studied in this thesis are compared as a function of the two variables, as shown in the carbon solubility curve in Figure 7.1. The temperature of HTMA process was 1024C which is expected to be high enough for carbon solutionization in heats NX3857 and 763675 while heat 96834 is not completely solutionized. Heats NX1638 and NX2650 are presented in Figure 7.1 based on reported furnace temperature. Actual tubing temperature, although not determined, is expected to be about 50 C [22] to 100 C lower than the furnace temperature. Heat NX1638 containing 0.014% carbon by weight appears to have been solutionized while heat NX2650 containing 0.038 % carbon could not be solutionized. Hence heat

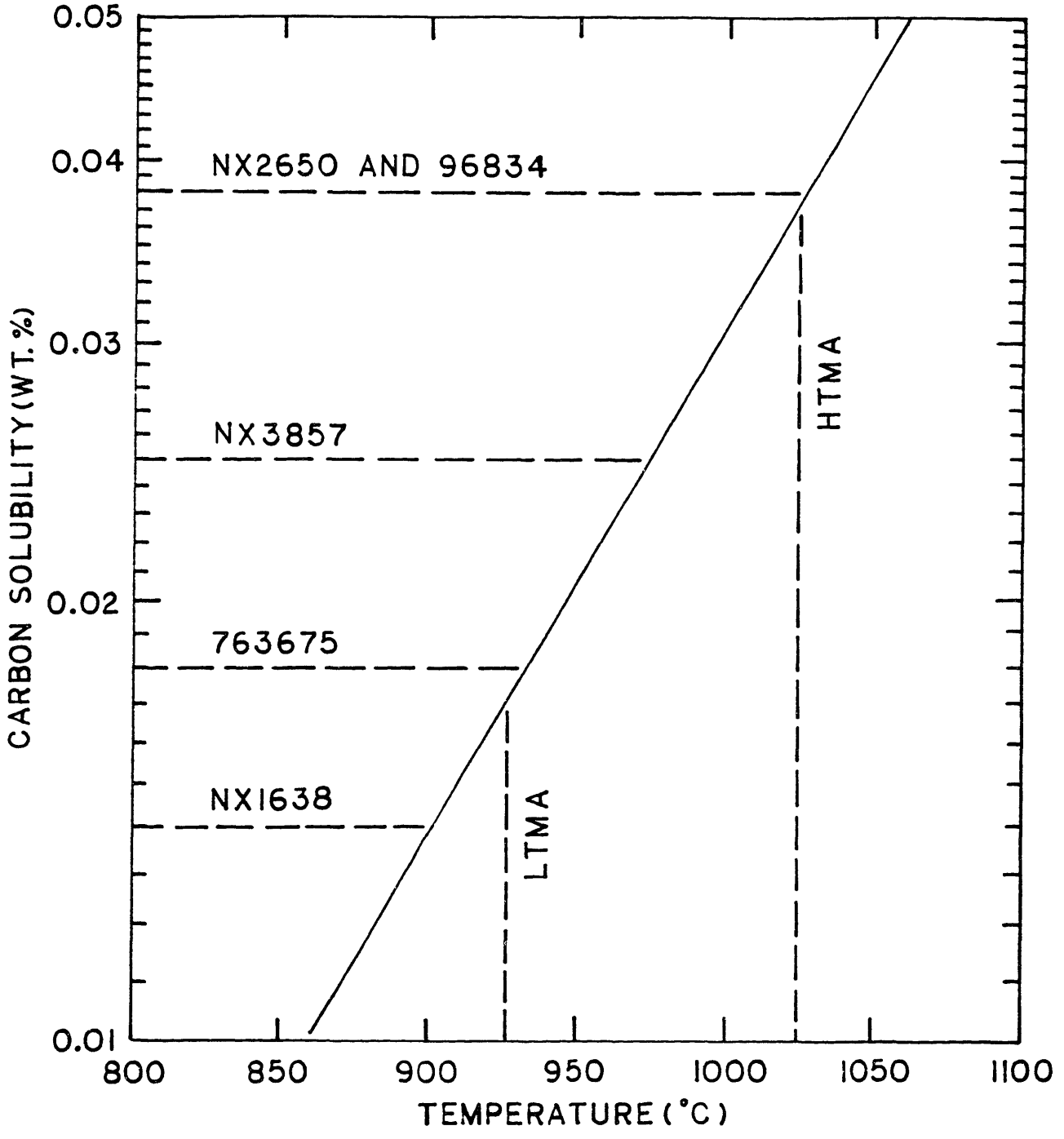

Figure 7.1 Carbon Solubilities of Alloy 600 Tubings at Final Anneal Temperatures

NX2650 should be classified to LTMA material. All LTMA conditions of heats 96834, 763675, and NX3857 are expected to be less than solutionized.

Microstructure of fully solutionized HTMA heats is charaterized by 1) a larger grain size (35 μm), 2) presence of intergranular carbide and 3) little intragranular carbides. Amount of intergranular carbides appears to be proportional to carbon content. Microstructure of less than solutionized LTMA heats is charaterized by 1) a small grain size (10 μm), 2)little intergranular carbides and 3) preponderance of intragranular carbides.

These microstructural differences can be understood by varying importance of four major steps in the final anneal; 1) carbide precipitation along the cold worked grain boundaries during the initial heatup, 2) recrystallization, 3) dissolution of carbides and grain growth, and 4) carbide precipitation along the final grain boundaries during the cooldown. All four steps occur in the HTMA process while the latter two steps are less active in the LTMA process due to the lower temperature and therefore the lower carbon inventory in solution.

It should be noted that the incompletely solutionized NX2650 responded to the thermal treatment. This suggests that the slower cooling after the HTMA or LTMA can produce more intergranular carbides although greater benefit is expected for a higher carbon heat. The effect of bulk carbon content is observed by comparing heats 96834, 763675 and NX3857 which received an identical process; the EPRI Special Process. The heat 96834 containing more carbon showed the greater extent of both intergranular and intragranular carbides after the HTMA process. All the lower carbon heats, 763675 and NX3857, showed however almost as much intragranular carbides as the high carbon heats after the LTMA process. This suggests that carbon inventry is determined by bulk carbon content for HTMA heats and by anneal temperature for LTMA heats.

When the chromium depletion at grain boundaries are compared between HTMA and LTMA of a given heat there are two patterns observed . The

first pattern is that the LTMA is only slightly depleted while the HTMA is appreciably depleted, as shown in heats 96834 with a 2.2cm diameter and NX3857. The second pattern involves heats 96834 with a 1.9cm diameter and 763675 of which the LTMA is appreciably depleted and the HTMA is replenished. Difference between HTMA and LTMA is explained by the fact that the longer time-at-temperature was available for the HTMA for the chromium depletion. The HTMA condition of NX1638 may be characterized by the first pattern for HTMA while NX2650 is again described by the LTMA condition of the second pattern. No general rule is established to explain difference between the patterns in terms of carbon content, anneal temperature and cooldown rate. Hence there is another unidentified process variable which affect chromium depletion behavior. This variable, however, appears to be not important in determination of grain size and carbide distribution.

The difference between two tubing diameters of heat 96834 can also be understood by the longer time-at-temperature of the smaller tubing due to the lower ratio of heat transfer surface area to volume. It is suggested that a subtle difference in the cooldown rate between heats can produce such a variation. The sensitivity to cooling rate is manifested by the different chromium depletion levels between the inner diameter and outer diameter regions. Therefore the final anneal temperature and the carbon content are found to be inadequate to describe the detailed microstructural evolution of alloy 600 tubings. One additional variable identified to be important is the cooling rate which was already suggested by Owen[27].

The grain boundary segregation study shows that a Mclean-type equilibrium relation holds for phosphorus in the three heats of alloy 600 tubing including NX1638, NX2650 and 96834 with a free energy of phosphorus segregation between 56 and 60kJ/mole. No significant variation is observed in the measured phosphorus concentration among the heats. Hence, the cooling rate after the final anneal is fast enough compared with the kinetics of impurity segregations. There is a site competition between phosphorus and boron in the temperature range between 700C and 1100C. At high temperatures which encompass both the

HTMA and LTMA conditions, boron is found to be primary segregant while at 700C or in the thermally treated condition, phosphorus is the major element to segregate.

Alloys X-750 and 718

The optical metallography on the X-750 heat 96457E6 shows that the microstructural evolution of all the heat treatment agree with the corresponding conditions of heat 94051. The grain sizes of HTH, HOA, and AHTH conditions are slightly smaller than that of heat 94051. This suggests that a small variation in the solution anneal conditions can result in a measurable difference in the degree of grain coarsening. Grain boundary segregation of phosphorus and boron are observed. No systematic difference in the segregation behavior exists among the finally aged conditions.

The plate heat of X-750 has a grain size of 30μm after the AH treatment. The grain boundaries are decorated with $M_{23}C_6$ carbides as well as γ'. No MC carbide is observed, suggesting that the presence of MC carbide is not essential to the embrittlement.

The CHT condition of alloy 718 contains semi-continuous precipitates of Laves phase along the grain boundary. The DA condition shows a significantly reduced amount of these precipitates.

7.2 ELECTROCHEMICTRY OF GRAIN BOUNDARY.

Important Galvanic Couples

Due to approximately same amount of chromium in the three nickel base alloys, similar passivation behavior is expected. The potentiodynamic polarization results and the measured corrosion potentials support this contention. The microstructural constituents at grain boundaries are, however, shown to exhibit a wide range of electrochemical behaviors. The present results on electrochemical characterization together with

the previous observation by Hosoya et al.[57] on the behavior of γ' and the chromium depleted chemistries confirm that galvanic corrosion would occur at significant current densities between the more active grain boundary chemistries and adjacent matrix.

The most significant galvanic couple is between the intergranular γ' and adjacent grain faces. The activity of γ' is shown to be a strong function of titanium content which may substitute for aluminum up to 70% [23] and STEM analysis on electrolytically extracted γ' of X-750 indicates that the real γ' can be approximated by the $Ni_3Al(Ti=0.15)$. There is a possibility that the composition of γ' surface layers is more active and may have been lost during the electrolytic extraction. However, the aluminum-to-titanium ratio of both fine γ' and coarse γ' are comparable and such a compositional gradient appears to be not significant. The consideration, thus, supports the validity of approximating real γ' properties based on $Ni_3Al(Ti=0.15)$.

It is found that polarization studies by slow scan rates are not sufficient to characterize rapid electrochemical transient on bare surfaces. Surface passivation during a slow scan can result in a gross underestimation of electrochemical activities during a short period after fracture. Therefore passivation kinetics studies should complement polarization experiments. For the same reason it is suggested that during the experiments where the fresh surface behavior is desired for a prolonged period of time, a non-passivating substitute material should be used. The galvanic current measurments, and the straining electrode tensile tests (SETT) with $Ni_3Al(Ti=0)$ are typical examples for the situations where the non-passivating substitute material is more useful. The substitute material should be judiciously chosen so that this can approximate the real material for both initial corrosion potential and current density. Since the platinum cathode was used, this condition is satisfied with $Ni_3Al(Ti=0)$ provided that anodic Tafel slope is the same as that of $Ni_3Al(Ti=0.15)$. The measured anodic Tafel slopes of both γ' chemistries are, indeed, very similar as shown

in Table 6.4. Therefore, the corrosion potential of fresh Ni_3Al(Ti=0.15) is believed to be close to that of Ni_3Al(Ti=0).

The galvanic current density of 0.5mA/cm^2 determined from the SETT is taken as a realistic initial current density on fresh grain boundaries in the X-750 AH condition since the surface area ratio between the matrix and γ' is about 10. The fresh surface condition of the matrix would have a larger hydrogen exchange current density. Therefore the cathodic current density is likely to be much higher than the value obtained by using a cathodically cleaned surface. The effect of the larger cathodic area and the fresh surface condition altogether can be expected to increase the cathodic current density at least by a factor of ten from the measured value of 7×10^{-5} A/cm^2.

It is shown that cathodic reaction controlled by hydrogen adsorption and anodic reaction following a parabolic passivation kinetics compete for rate control depending on cathodic to anodic surface area ratio. It is possible to determine the rate controlling reaction by comparing the cathodic and anodic current densities based at grain boundaries. The anodic current density is described by the initial current density of 0.5mA/cm^2 and the kinetics of Eq.(6-3) and cathodic reaction is described by Eq.(6-4). The cathodic to anodic area ratio in X-750 AH condition may be approximated by the inverse of γ' volume fraction at grain boundary which is about 10. Due to the lower initial current and the faster current decay kinetics, the anodic current density is found to be lower than the cathodic current density. Therefore the rate controlling reaction of the galvanic coupling between the intergranular γ' and surrounding matrix is expected to be the anodic reaction. In this consideration hydrogen combination is assumed to be negligible. When recombination is significant either due to higher temperature or by plastic straining, cathodic reaction rate would be further increased. Hence it is suggested that overall galvanic current at grain boundary of AH condition also follows parabolic kinetics described by Eq.(6-3).

The passivation kinetic study on the solution annealed X-750 also shows

the evidence of an increased activity of the fresh matrix surface. Hence, a question may be raised concerning the accuracy of the results of galvanic current measurements and the SETT where already passivated condition is assumed for the matrix composition. The error in the differential potential is likely to be insignificant since the initial current density of the matrix composition, after correction for solution oxidation effect, is shown to be much smaller than that of $Ni_3Al(Ti=0)$.

The consideration of galvanic corrosion should also be given to other important precipitates such as carbides, nitrides and Laves phases. There are some results of electrochemical studies on $M_{23}C_6$ type carbide [63]. Although detailed quantitative analysis is not possible due to extremely aggressive environments used in those studies, they provide a considerable evidence that the corrosion potential of carbides are much higher and corrosion currents are much lower than typical matrix of nickel-base alloys. Hence, it is expected that the carbides at grain boundaries would anodically polarize surrounding matrix. One typical situation with the intergranular carbides is that the chromium depleted chemistries are the surrounding compositon. Since the $M_{23}C_6$ carbides show significantly lower corrosion current when compared with matrix, it is reasonable to assume that the cathodic current density is also significantly lower. In microstructures containing a discrete or sparse carbide morphology, the galvanic effect of the carbides is expected to be negligible and the anodic current density is equal to the corrosion current density of the grain faces. As the surface coverage of carbide increases as in cases of semi-continuous or continuous carbide morphology averaged current density is reduced. This suggests that there is electrochemical benefit of the extensive intergranular carbide by reducing localized corrosion rate.

The galvanic couple between the chromium depleted chemistry and matrix may to be discussed. Although a current density of $5x10^{-5} A/cm^2$ is predicted by using the mixed potential theory in section 6.2, STEM analysis shows that the width of chromium depleted region is about a few tenth of micrometers. Therefore galvanic coupling between the chromium

depleted region and matrix is expected to be difficult due to the isolation of matrix from the environment. Hence the realistic anodic current density of the chromium depleted chemistry is determined by the corrosion current. However the predicted galvanic coupling is likely to occur in an environment with a high conductivity where external surfaces would provide as efficient cathode.

Electrochemical data on Laves phases is not available in open literatures. Although the Laves phase is described by Fe_2Ti, the exact chemical composition and its ranges has not been determined. Therefore, further experimental work is necessary a to allow a basis for any speculation on the electrochemical nature at grain boundaries in alloy 718.

7.3 EMBRITTLEMENT IN LOW TEMPERATURE WATER

Summary of Observations

The observed behaviors of nickel-base alloys in the water below 200 C are summarized. Results from the straining electrode tensile tests, the corrosion fatigue tests and the slow strain rate tests provide the basis. Due to the limited test temperatures and small number of microstructure used, a systematic functional dependence is not obtained for the variables. Earlier results by Elliot [23] and Prybylowski [26] are also employed to summarize the dependences on microstructures, temperature and strain rate.

Microstructures susceptible to the intergranular embrittlement in the low temperature high purity water include AH, AHTH and BH conditions of X-750. Hence foregoing summary assumes these conditions unless otherwise described. First two conditions contain an extensive γ' precipitates along grain boundaries. The AHTH condition has a larger grain size and a less amount of γ' which relate with slightly lower susceptibility than the AH condition. The BH condition, having a duplex grain size with intergranular carbide precipitates, revealed the

intergranular fracture only in regions of smaller grain [50]. Huey test indicates a limited amount of chromium depletion at grain boundaries of the BH condition which is less extensive than the HTH condition [50]. Hence a necessary microstructural characteristics involve the extensive amount of intergranular γ', small grain size and the chromium depleted grain boundary. However, the characteristics can not be considered as adequate to result in the embrittlement. The HOA condition contains both $M_{23}C_6$ and γ' on grain boundaries without showing the susceptibility. The sensitized grain boundaries including the SAS condition of alloy 600 and the HTH condition of X-750 do not support the embrittlement.

Even with the susceptible microstructures, a sharp notch geometry is necessary to result in the intergranular embrittlement. The tensile testing on the unnotched AH specimen in the high purity water at 93C produces a ductile fracture. The pre-cracked specimens in the same susceptible condition always show the intergranular crack growth during the fatigue test and the rising load test in the low temperature high purity water.

Striking temperature dependences are shown during the fatigue test with the susceptible microstructures. Both AH and AHTH condition have peak crack growth rates near 93C at which the crack growth rate is significantly higher than at 288C. The detailed temperature dependence is not available for the BH condition but the crack growth rate at 93C is about a factor of two to three higher than at 288C. The fracture surfaces shows a transition from transgranular to intergranular mode as the temperature decreases below about 120C. Therefore, there appears a transition in the fracture mechanism near the temperature.

A strong frequency dependence is observed during the fatigue tests for both AH and AHTH conditions. The cyclic crack growth rate (da/dN) increases with frequency between 0.01 Hz and 1 Hz. When the frequency is further increased to 10 Hz, the growth rate is slightly decreased with the SEN specimen but unchanged with the CT specimen of heat 94051.

A transition to transgranular fracture made is shown below 0.3 Hz [26]. The rising load test is equivalent to about 20 Hz of cyclic loading in terms of crack tip strain rate which is translated by Eq. (2-3). At very low strain rate occuring in the WOL SCC test, no crack growth is observed with both AH and AHTH conditions in the high purity water at 93C. Therefore it appears that a relatively high crack tip strain rate is a necessary condition for accelerated crack growth.

The low conductivity appears to be a necessary condition for the intergranular crack growth of the susceptible X-750 conditions. The SEN fatigue tests in electrolytes show a crack growth rate with transgranular mode. The externally applied current is found to affect the crack growth rate only in the electrolytes including the sodium sulphate solution and the dilute chromate solution. The crack growth rate increases with cathodic charging current density and decreases with anodic charging current density. The extensive branching cracks on the sidewall during tests in the high purity water is consistent with the observation during the cathodic charging in the sodium sulphate solution. The straining electrode tensile tests with cathodic charging show an increasing embrittlement with increasing current density. Brittle transgranular crackings are observed at a current density which is expected to occur by localized galvanic coupling at the crack tip. At a much higher current density, most of the microstructures are embrittled with an intergranular mode. The passive films are found to be broken at a very small plastic strain.

By sidewall observation during the SEN fatigue tests, a conspicuous difference in the crack tip deformations is found between two different modes of crack growth. During an intergranular crack growth, the plastic zone size appears to be much larger than for the case of transgranular crack growth. There is extensive crack branching ahead of the crack tip which is observed both in the high purity water and in the sodium sulphate solutions with cathodic charging. Plastic zone sizes during tests in sodium sulphate solution under free corrosion compare well with that of the air tests.

Identification of Low Temperature Mechanism

Based on the observed characteristics of environment assisted cracking of alloys 600, X-750 and 718, it is possible to identify the most likely mechanism. For the sake of brevity, four representative mechanisms are included in the foregoing discussions. These are (1) the active path corrosion mechanism (APCM); (2) the film-rupture mechanism (FRM); (3) the adsorption (or stress-sorption) related surface mechanism (SM) caused by other than hydrogen adsorption and (4) hydrogen embrittlement mechanism (HEM).

The APCM can not explain the two most important characteristics of embrittlement which are:

1) all grain broundary chemistries of the susceptible conditions show passivation behaviors and no continuous dissolution is possible;
2) the embrittlement is increased by cathodic chargings and decreased by anodic chargings.

These contradictions with the APCM make detailed discussions unnecessary.

The FRM assumes that the cracking process requires a balance between the film rupture rate and subsequent passivation rate. When this mechanism is applicable, it is possible to find a potential in a passive or an active-passive transition range which results in the maximum crack growth rate. The SEN corrosion fatigue test and the SETT results with nickel-base alloys show increasing crack growth rates with decreasing potential even far below the corrosion potentials. As the applied potential further decreases, the crack growth rate reaches a plateau near -600 mV (SHE) without showing any maximum as evidenced by the corrosion fatigue tests on alloy X-750 in this work and on alloy 600 by Was [99]. The anodic current density predicted by the measured electrochemical parameters in Table 6.4 is about 10^{-10} A/cm^2 for Ni_3Al (T_i = 0) at -600 mV (SHE). Other chemistries show about 10^{-15} A/cm^2 at the potential. The film ductility (ϵ_F) is found to be less than the

strain for yielding which is about 1%. A more accurate study indicates the film ductility by about 0.2% for iron-base alloys at temperature near 100C [152]. It is useful to apply these parameters to estimate a crack growth rate based on the FRM model as follows [101]:

$$\frac{da}{dt} = \frac{M}{3\rho F} \frac{Q_F}{\epsilon_F} \dot{\epsilon}$$

where M is atomic weight, z is number of electron per reaction, ρ is density of metal, F is the Faraday constant, Q_F is total charge of dissolution after film rupture, and ϵ_F is film ductility. The predicted crack growth rate is about the order of 10^{-14} cm/sec for alloys 600 and X-750. The large discrepancy between the predicted and observed crack growth rates of the two nickel-base alloys is, hence, an evidence against this mechanism. The second important contradiction with FRM arises from the discontinous crack growth pattern which is observed during the SEN corrosion fatigue test. The FRM assumes a step-wise crack growth but only on a firlm thickness scale which is a few tens of angstrom in this enviroment [43]. Therefore, it is believed that FRM can not describe the observed characteristics.

The surface mechanism (SM) assumes that adsorption of surface active elements lowers fracture strength. There are evidences that oxygen is not involved in the embrittlement of nickel-base alloys at low temperatures. These are:

1) the crack growth rate is unaffected by bulk oxygen content;
2) oxygen solubility in water shows a minimum near 100C [149] where the maximum crack growth rate is observed;
3) oxygen adsorption pins dislocations while the plasticity is increased during the fast crack growth;
4) discontinuous crack growth was observed;
5) smooth specimen, having an easier access to oxygen, does not show the embrittlement.

The SM, by other than oxygen, may be either due to water molecules or by

anionic metal hydroxides. No strong interaction with these elements are observed at low temperature. The cathodic removal of the anionic species resulted in the increase in embrittlement while the opposite effect is expected with the SM as pointed out by Uhlig [113]. Therefore, the SM is believed to be inappropriate to explain the behaviors of nickel-base alloys.

The HEM is consistent with all the observed characteristics of the low temperature embrittlement. The galvanic coupling of anodic phases such as γ' and low chromium chemistry with cathodic matrix is shown to result in a large anodic current density of 0.5 mA/cm^2 at 93C in the deaerated pH 3 solution. The high anodic current density is consistent with the crack tip acidity as indicated by Taylor et al [75, 76]. The localized environment at crack tip allows hydrogen discharges as the cathodic reaction in the oxygen depleted and acidified galvanic cell. The localized cathodic reaction in the low conductivity water would result in high concentration of adsorbed hydrogens at the crack tip where dislocations intersect with the surface. The cathodic reaction occurs over a wider area in the high conductivity solution resulting in a low hydrogen concentration at the crack tip which accounts for the low observed crack growth rate under free corrosion state. The HEM is further supported by the increased embrittlement with increasing cathodic current density during the SEN corrosion fatigue test as well as the straining electrode tensile test. It should be noted that occuluded geometry is not necessary in the latter cases where hydrogens are externally supplied.

The strong dependence of embrittlement on the microstructure and its correlation with the extent of intergranular γ' precipitation indicate that the crack growth rate is a strong function of the hydrogen generation rate by galvanic corrosion. Therefore it is assumed that the dependence of crack growth rates on temperature and fatigue loading frequency (or strain rate) should be consistent with the hydrogen source term characteristics. No data is available on the temperature dependence of the galvanic current density of γ'. However, the peak anodic current density measured by the polarization study by Hosoya et

al [57] provides a good basis for speculation. The peak current densities of both γ' (Ni_3Al (T_i = 0.15)) and chromium depleted chemistry increase with temperature monotonously. The hydrogen concentration would be expected to increase with temperature if there is no hydrogen loss process.

The maximum crack growth rate near 100C, however, suggests that these may be an increasing effect of hydrogen loss process at higher temperatures. Consistent evidence of such a loss process can be found from the fatigue loading frequency dependence. Total amount of hydrogen generation during each fatigue loading cycle increases with decreasing frequency whereas the crack growth rate increases with increasing frequency. This is often explained by the growth of passivating layer which may block the hydrogen adsorption [122]. The galvanic corrosion study in this work shows that the deterioration of the cathodic surface is slow enough so that overall reaction is governed by the anodic reaction rate. Therefore, the explanation by the passivating film as the rate controlling step is not appropriate.

The hydrogen loss process may be similar to that in HEM process for high strength low alloy steels where the hydrogen adsorption and desorption are believed to be the rate controlling processes [115, 120]. As evidenced by the literature review in Chapter 2, there is a similiarity in the embrittlement behaviors at low temperature between nickel-base alloys and the precipitate hardened iron-base alloys such as 4340 steel and 18 Ni-maraging steel. A recent adsorption study by Pasco and Ficalora [120], shows that the dissociative adsorption and plasticity assisted desorption after surface diffusion are the source and loss process of crack tip hydrogen in gaseous hydrogen embrittlement process, respectively. Data of Wei et al [115] on 18 Ni-maraging steel which have a maximum crack growth rate near 30C are closely predicted by the adsorption/desorption kinetics [120].

For nickel-base alloys in high purity water, there are important differences in the hydrogen adsorption and desorption nature from the

system of iron-base alloys and the gaseous hydrogen environment. No dissociative barrier exists in adsorption since the electrochemical reaction generates protons not the molecular hydrogens. Also the electrostatic repulsion between protons on the surface step would maximize the hydrogen interspacing so that recombination is minimized before the charge transfer reaction step. In the absence of plastic deformation, the galvanic corrosion study indicates no significant recombination at 93C. Hence, it is reasonable to assume that the adsorbed hydrogen concentration increases with time during a short period after an exposure of fresh surface which is determined purely by the galvanic current density. During the corrosion fatigue test in water, however, the recombination due to the plastic strain and the hydrogen leakage by surface diffusion out of the crack tip may become significant processes of the hydrogen loss.

If the recombination and surface diffusion are truely significant enough to affect the hydrogen source term and the resultant crack growth rate, the activation energies for the above processes should be such that the observed maximum crack growth rate at 93C can be explained. A quatitative analysis given in the next section supports this belief.

Knowing that the HEM is responsible for the observed intergranular embrittlement of nickel-base alloys it is necessary to show that the high cracke growth rate can be explained from the kinetic viewpoints of hydrogen transport. There are three classes of opinions as to the extent of hydrogen transport in the HEM process; 1) adsorption, 2) near surface transport by diffusion and 3) dislocation assisted transport into the plastic zone.

High crack growth rate can also be achieved by adsorption effect as evidenced by a high growth rate of 40μm/sec in mercury [153]. However the observed increase in crack tip plasticity and the incremental crack growth can not be explained by the adsorption effect. The increased plasticity is suggested as the result of hydrogen assisted removal of $NiOH^+$ which may pin the dislocation egress at surfaces [154]. Since the plasticity in the nitrogen gas was observed to be much smaller the

latter explanatioon appears not to apply to the present system. Due to the low hydrogen diffusion coefficient in the nickel-base alloys, the hydrogen absorption by diffusion, if significant, is suggested to occur in the near surface region. Due to significantly faster diffusion along grain boundaries [155] it is expected that the higher intergranular concentration leads to the observed fracture mode. The increased crack tip plasticity is also attributed to the influence of near surface hydrogen atoms which may ease to overcome solute barriers [156]. The size of enhanced plasticity observed during the SEN corrosion fatigue tests is about 500μm. It is not likely that the near surface effect on the plasticity can affect such a broad region. One may question that the observed plasticity may actually be limited to the near surface layer on the side wall of the SEN specimen. However the plasticity is believed to extend through entire thickness of specimen considering that the hydrogen generation takes place mostly inside the crack rather than on the side wall in the high purity neutral water.

The dislocation transport of hydrogen into the plastic zone is consistent with the observation. The increased plastic zone size is attributed to the catalytic interaction of hydrogen with mobile dislocations. The observed pattern of discontinuous crack growth is attributed to a relatively uniform increase in the hydrogen concentration at grain boundaries over significant fraction of plastic zone which results in simultaneous fracture of the area. The hydrogen concentration at grain boundaries near crack tip is expected to increase since hydrogen delocalization processes such as detrapping and intergranular diffusion at low temperatures are much slower than the hydrogen transport process.

Galvanically Induced Hydrogen Embrittlement Mechanism (GIHEM)

In the previous section, the dislocation assisted GIHEM is identified as the responsible mechanism for the intergranular cracking of nickel-base alloys in low temperature water. A more detailed description of microprocesses is given as follows:

1) Hydrogens are generated as the cathodic partial process of

microstructural galvanic corrosion at the oxygen-depleted and acidified crack tip. The localization of the hydrogen source is dictated by the electric conductivity of the crack tip environment.

2) During a short period after an exposure of fresh grain boundaries, the adsorbed hydrogen concentration increases. Both the strain-assisted recombination and the surface diffusion removes the adsorbed atomic hydrogens from the crack tip. The recombination poisons at grain boundaries would reduce only the former hydrogen loss process.
3) Remaining hydrogens are transported to inside the plastic zone by mobile dislocation which results in further promotion of the mobile dislocations and the increase in plastic zone size.
4) As the mobile dislocations intersect with grain boundaries within the plastic zone, the hydrogens are delivered. There are some hydrogens which are trapped intragranularly at immobile dislocations or particle interfaces.
5) Intergranular fracture occurs over a characteristic length within the plastic zone when the hydrogen concentration reaches a critical value which is a function of stress, stress state and impurity concentrations. Detailed mechanism of fracture is, however, not determined in this thesis. A significantly higher supersaturation is likely due to much slower delocalization by the grain boundary diffusion. Hence both γ-hydride formation and decohesion are likely to be responsible. The internal pressure theory is not supported due to absence of microvoids on the fracture surface.

The correlation between the crack growth rate with the predicted galvanic corrosion rate and with cathodic charging current density indicate that the hydrogen generation and loss processes are rate controlling. Based on the hydrogen concentration analysis, the crack growth rate of the GIHEM may be quantitatively explained.

In the low conductivity environment, all the hydrogens are assumed to be generated at the crack tip where dislocations intersect. A generalized

treatment of the conservation equation is as follows:

$$\frac{dC}{dt} = -k_r C^2 + D\frac{d^2C}{dX^2}, \text{ in } -\infty < x < \infty \text{ and } t > 0 \qquad (7\text{-}1)$$

$$S(t) = i_o(t_o/t)^{1/2}, \text{ at } x = 0 \text{ and } t > 0 \qquad (7\text{-}2)$$

where C = concentration of adsorbed hydrogens
D = surface diffusion coefficient
X = distance along crack flanks from the crack tip
S = hydrogen generation rate
k_r = proportional constant for recombination reaction

The recombination is expressed by the second order function of C. Since an understanding of functional dependences is the primary goal of this model, a simpler approximation is made by assuming that the hydrogen leakage by surface diffusion is negligible. Then the hydrogen concentration at the crack tip is governed by:

$$\frac{dC}{dt} = i_o(t_o/t)^{1/2} - k_r C^2, \text{ at } X = 0 \qquad (7\text{-}3)$$

Due to the non-linearity, a closed-form solution is not available. However, it is possible to expect a maximum hydrogen concentration at a certain intermediate time since the first term of hydrogen generation decreases while the second recombination rate would increase until the maximum concentration is reached. Hence, a short term and a long term approximation are made by neglecting each unimportant term.

$$C(t) = \begin{cases} i_o\sqrt{t_o \cdot t} & \text{for small } t \\ c_o/(k_r D t) & \text{for large } t \end{cases} \qquad (7\text{-}4)$$

The crack growth rate by HEM can be related with the surface concentration of hydrogens. The above results suggest that at high frequencies the crack growth rate would follow $1/\sqrt{\nu}$-dependence while a linear dependence is expected at low frequencies. These are actually

observed in the corrosion fatigue data of alloy X-750, as shown in Figure 6.142.

The microstructural dependence of the crack growth rate may also be explained by the importance of galvanic current density of the maximum concentration. Recombination poisons such as P and S would lower k_r and increase the maximum concentration. Since the recombination reaction is important in a longer time scale, the grain boundary segragants would broaden the range of frequency of embrittlement. At high frequencies, their role is expected to be less important.

The temperature dependence may also be understood by using Eq (7-3). As shown in Figure 6.142, the crack growth rate of AH condition at 10 Hz shows a maximum at about 93C. The activation energy below 93C is found to be 23kJ/mole which is in a reasonable agreement with the activation energy of γ' peak current density, as shown in Figure 2.1. Thus the activation of the galvanic current density (i_o) is approximated by this value. The activation energy for the strain-assisted recombination reaction is not known at the time of this work. Considering that the rate controlling step of the recombination process is the surface diffusion of hydrogen to the favorable recombination sites, the activation energy of hydrgen diffusion in nickel, 50kJ/mole, is taken. From Eq (7-3), the competition between the hydrogen generation and the recombination is examined. At low temperature where the recombination is less significant the hydrogen generation process is rate controlling. At higher temperature the recombination term is expected to be dominant. Although no detailed analysis can be made due to lack of data, the temperature dependence of the crack growth rate is believed to support the above descriptions.

In order to explain the observed crack growth behavior in 0.05 M Na_2SO_4 (pH = 3) solution, it is suggested that the high electric conductivity of the environment would increase useful cathodic surface area. Consequently, an effective hydrogen generation current density at the crack tip is proportionally reduced. The measured conductivity shows

that the attenuation can be by several orders of magnitude. By cathodic charging at the galvanic current density, the initial value is expected to be restored. One important difference from the galvanically generated hydrogen is that the imposed overpotential minimizes the hydrogen loss by recombination or surface diffusion due to uniform generation of hydrogen on all the surfaces. As a consequence, the surface concentration of hydrogens would monotonously increase with time. This expectation is consistent with the increasing crack growth rate with decreasing frequency under the cathodic charging in the conducting environment.

Therefore the GIHEM model with the assumption that the rate limiting process is the hydrogen generation and recombination is found to explain most important functional dependences of experimental observations of the crack growth rate. Dependences on the frequency, microstructure, temperature and environments are consistently explained.

There are a few observed characteristics which are not explained by the source term analysis. One of these is the grain size dependence. Comparison between BH condition of X-750 with different grain size leads to the higher crack growth rate. There appears one reasonable explanation for the behaviors; the higher yield strength would increase the stress concentration at grain boundaries. There are several supporting evidences for the stress concentration as follows:

1) Hydrogen-charged AES specimens of EAH, EBH and EHTH conditions contain more transgranular regions than their finally aged conditons (AH, BH and HTH) with the same grain size. The yield strengths are significantly increased by the final ages.
2) Hydrogen-charged AES specimens of alloy 600 require much longer charging time than X-750 specimens to obtain the same amount of intergranular fracture area.

Another factor is the effect of grain boundary impurities on the fracture strength. Although a strong correlation is found between the sulphur level and the fracture strength, no confirming basis has been established for phosphorus and boron which are important segregants in nickel-base alloys.

7.4 EMBRITTLEMENT IN HIGH TEMPERATURE WATER

Summary of Observations

Due to experimental difficulties associated with long test time and high temperature, data obtained in this work alone are not sufficient to identify systematic dependences of the embrittlement on various parameters. Hence the obtained data are compared with other results in literature in order to draw consistent bases for mechanistic understandings.

For alloy 600, an extensive data base is produced using the slow strain rate tests. The crack growth rate of heat 96834 agrees with the data by Bandy and Van Rooyen [60] within a factor of three when compared with 0.03% carbon mill annealed tubings. The crack initiation time also shows a good agreement with available data with 0.02% carbon tubings [42]. Hence it is assumed that the alloy 600 tubings tested in the developed SSRT follow the same functional dependence on temperature, strain rate and microstructures as other mill annealed materials tested by Bandy and van RooyenL. For alloys X-750 and 718, SSRT data are scarce. Result by Miglin et al [20], Daret [157] and Hirano et al [158] provides the only basis for direct comparison. Microstructural dependence of the embrittlement is discussed by including data from other testing methods, although the dependences on temperature and strain rate are examined based on the SSRT results.

One distinct microstructural characteristic common to most susceptible conditions of nickel-base alloys is that grain size is small with preponderous intragranular strengthening precipitates. Low temperature anneals for alloy 600 and low temperature anneals or equalization for alloy X-750 lead to such conditions. High temperature anneals appear to improve performance of both alloys primarily by introducing semi-continous and coherent carbide along grain boundaries. Reduction in the yield strength is believed to be a secondary factor. A microdeformation study on alloy 600 heat 96834 by Bruemmer et. al [53]

confirms that dislocations can be easily injected toward matrix from the coherent carbides so that a crack tip can be effectively blunted. In the high purity water, considerably sensitized conditions do show a good performance probably for this reason. In precipitation hardened alloys, intergranular γ' particles are correlated with high susceptibility.

There are evidences that a small phosphorus segregation to grain boundaries increases the susceptibility in alloy X-750 [36]. Results from this work, however, support a group of researchers with an opposite opinion [25, 33]. In alloy 600 the significant phosphorus segregation is observed in the thermally treated condition which is more resistant than mill annealed condition with lower phosphorus segregation level. In alloy X-750, the phosphorus level is low in all the finally aged conditions without any correlation with the observed susceptibility. Therefore, the intergranular segregation is believed to be a contributing factor to the susceptibility rather than a necessary factor.

Cracks can initiate from smooth surfaces at high temperatures. The initiation process is much slower than the subsequent crack growth process. In alloy 600, about 350 hours is taken for initiation while only about 40 hours is taken in the AH condition of alloy X-750. There appears a distinct difference in the initiation process between the two alloys. In alloy 600, the intergranular cracks initiate from the surfaces. Hence the initiation and growth may be an identical process. In alloy X-750, the cracks initiate from grooves which usually form by mechanical fissures in the surface oxide layer. The thickness of the layer is about 0.5 μm to 1 μm. The composition is similar with oxides formed at low temperatures.

An Arrhenius-type temperature dependence of the crack initiation time is well-characterized with alloy 600. The activation energy varies between 84 kJ/mole and 336 kJ/mole in the temperature range above 330C [42,44,155]. In the AH condition of alloy X-750, data are not sufficient to show any relation with temperature. The present results suggest that the susceptibility increases with temperature for a range

between 288C and 350C. The average crack growth rate in this work at 350C is significantly higher than Miglin's data at 363C. Daret [157] observed a crack growth rate of $3x10^{-6}$mm/sec in a temperature range between 320 and 360. No detailed temperature dependence is reported. Wilson's 400C steam tests showed a slower crack growth than 350C SSRT.

In alloy 600, the crack growth rate increases with decreasing strain rate of the SSRT. It appears that a strain rate of 2×10^{-7} sec^{-1} is close to the highest strain rate allowed for the intergranular cracking at 340°C in the hydrogenated water. In AH condition of alloy X-750, a certain slow strain rate appears necessary which is evidenced by a complete dutile failure at 350°C with a strain rate of 2×10^{-5} sec^{-1}. At 1×10^{-6} sec^{-1}, Daret obtained the crack growth rate of 3×10^{-6} mm/sec. Wilson and Mager showed much lower crack growth rate at 365C by using WOL SCC specimens which had an estimated strain rate of 2×10^{-7} sec^{-1}. Hence there seems to be a range of strain rate for high crack growth rate. This range is between 4×10^{-6} sec^{-1} and 2×10^{-7} sec^{-1}.

There appears that alloy 600 shows a varying degree of susceptibility in different environments. The crack initiation time of susceptible heats of alloy 600 decreases in the order of the high purity deaerated water, the PWR primary water and the hydrogenated high purity water. Hence the increasing concentration of boric acid and lithium hydroxide favorably compensates for the hydrogen effect in the PWR primary water. It is not clear whether this is the effect of increased electric conductivity or a specific ionic effect. A future work is necssary to identify a time factor. The susceptibility of alloy 600 increases with the hydrogen overpressure up to a certain value near 76 kPa. The higher pressure is shown to reduce the susceptibility suggesting that there is a hydrogen pressure for the maximum susceptibility.

For alloy X-750, the effect of hydrogen overpressure is not demonstrated, at least, for the AH condition. The crack growth rate at 363 C in the PWR primary water [26] is much lower than that at 350 C in the pure water determined in this work. Since the specimens tested in

the PWR primary water have about three times larger grains than the heat 96457E6, it is not possible to make a direct comparison. The crack depth-number density profile of alloy 600 tested in the hydrogenated water is characterizd by a typical multiple initiation. Hirano et al. [158] showed the increased susceptibility with increasing pH by LiOH addition in 350C water. The microstructure X-750 condition of this work is expected to be similar with AHTH condition. The crack growth rate of the observed small cracks, as discussed earlier, agrees well with those reported for longer crack size. This provides another evidence for the identical controlling process in both small and long cracks. The crack number density appears to depend on testing methods. The reverse U-bend tests usually produce a crack number density which is significantly lower than that of SSRT. The nonuniformity of the strain rate in the former tests may be responsible for the difference. In the AH condition of alloy X-750, the crack number density is very small even in unnotched specimen geometry. The cold work due to specimen flattening accelerates the crack growth rate [62] but without changing the activative energy for alloy 600. However, cold pressed hump design used in the SSRT by Totsuka et al. [158] lowers the activation energy and increases crack growth rate.

Based on the above discussions on the high temperature behaviors of nickel-base alloys, it becomes apparent that there are significant differences between alloy 600 and alloy X-750 as to the functional dependence of susceptibility on major variables. Therefore, experimental observations are summarized separately for two alloys in Tables 7.1 and 7.2

Mechanisms of Embrittlement in High Temperature Water

The APCM is not supported due to the observed passivity of all the intergranular phases. Although the susceptibility is well correlated with more active intergranular γ' precipitates, the chromium-depleted microstructures such as the SAS condition of alloy 600 and the HTH condition of X-750 do show a lower susceptibility than non-sensitized microstructures. Hence, no consistent evidence is observed in support

Table 7.1

Summary of Observations on the
Embrittlement in High Temperature of Alloy 600

Variables	Observations
Microstructures	· Smaller grain size and more matrix carbides increases susceptibility (LTMA) · G.B. carbides reduces susceptibility · No positive correlation with P-segregation or with chromium-depletion at G.B.
Specimen Geometry	· Complex stress state increases susceptibility · No crevice or notch necessary
Temperature	· Arrhenius type with Q between 80 and 330 kJ/mole
Strain Rate	· The lower strain rate increases growth rate · The strain rate to produce IGSCC decreases with decreasing temperature
Environment	· H-overpressure increases susceptibility but the maximum occurs at intermediate pressure · B and Li addition reduces susceptibility
Crack Pattern	Multiple initiation in SSRT · Lower crack density in reverse U-bond tests

Table 7.2

Summary of Observations on the
Embrittlement of alloy X-750 in High Temperature Water.

Variables	Observations
Microsturctures	· Intergranular γ' and small grain size increases susceptibility · Extensive carbides along G.B. reduces susceptibility · P-segregation correlates with susceptibility in some heats
Specimen Geometry	· No initial notch is necessarry because thick oxide fissure provide crevice geometry
Temperature	· Susceptibility increases with temperature up to 363C No data above 363C.
Strain Rate	· Slow strain rate (lower than $2x10^{-5}sec^{-1}$) is required for intergranular cracking · A maximum crack growth rate may occur at an intermediate strain rate
Environment	· Comparable susceptibility in aerated or deaerated water · No clear dependence on hydrogen overpressure
Crack Pattern	Low crack number density both in initiation and in growth stages

of the APCM.

The surface mechanism(SM), on the other hand, may be postulated although no detailed description has been made for the process, since a number of different adatoms are available due to hydrolysis at high temperature. The temperature and strain rate dependence are not contradictory with this mechanism considering an activation barrier for adsorption and the requirement of kinetic balance between adsorption and crack opening. However, the long initiation period for both alloys provides crucial evidence against it. Therefore only the film rupture mechanism (FRM) and the HEM are discussed in detail.

Alloy 600

It is proposed that the FRM is responsible for the intergranular embrittlement of alloy 600 in deaerated high temperature water. The supporting evidences are summarized as follows:

1) Cracks initiate from smooth surfaces in direct contact with the bulk neutral water in which hydrogen discharge is unlikely.
2) Activation energy in the range between 80 kJ/mole and 330 kJ/mole is much higher than that of hydrogen diffusion (50 kJ/mole). This suggests that the rate controlling process has much higher dependence on temperature. At 400C, the maximum crack growth rate is comparable with the hydrogen diffusion speed. At 350^{o}C, the crack growth rate is about two orders of magnitude slower than the hydrogen diffusion speed ($\sqrt{Dt}$). A significant delocalization of hydrogen is expected during the slow process.
3) The microstructural dependence of susceptibility is identical to that in caustic environments. IGSCC in caustic environments is well correlated with the active/passive transition potential region.
4) No positive correlation hydrogen overpressure is observed at high overpressure whereas the HEM leads to a linear or a square-root correlation between the crack growth rate and the hydrogen pressure.

5) A negative correlation is observed between the susceptibility and phosphorus segregation.
6) A strain rate dependence is consistent with the FRM since the upper limit for IG embrittlement incrases with temperature.

Therefore, there are sufficient evidences for the FRM and against the HEM as the responsible mechanism for alloy 600 embrittlement. Assuming that the FRM is responsible for the observed embrittlement behavior, it is necessary to explain the microstructural and environmental dependence of susceptibility. The susceptible microstructures characterized by the high yield strength and little intergranular carbides appear to induce a higher stress concentration at grain boundaries which may lead, to preferential film rupture along the grain boundary. The intergranular carbides reduce the stress concentration by facilitating the dislocation injection into matrix. The type of coherency between carbides and adjacent grains is believed to be an important factor of the effectiveness of carbides.

Another microstructural role may be the modification of film structure. Pathania et al [70] observed that the more resistant TT condition of alloy 800 has a thicker film. The same relation between the susceptibility and film thickness is reported by Airey [43]. The consistent observation on the TT condition of NX2650 is made by the anodic polarization at 93C. Since the FRM requires a balance between the film rupture rate and dissolution rate, the increased resistance with thicker films can be rationalized. However it is not yet known that what kind of microstructural features influence the film structures. In the high temperature water (363C) with hydrogen overpressure, Airey observed a typical alloy 600 film which is thinner than the case of high purity water [43]. The compositional analysis revealed the dominance of NiO and depletion of chromium exides. Hence it is suggested that the formation and rupture of NiO layer is primarily related with the crack growth kinetics.

Alloy X-750

Based on the summary of experimental observations in the high temperature water the HEM is suggested as the responsible mechanism for the intergranular cracking of the AH condition of alloy X-750. Supporting evidences are as follows:

1) Crack depth is slightly lower than $\sqrt{Dt}$. The less than 10 times difference may be the result of the trapping effect. The hydrogen diffusion coefficient of nickel-base alloys at 350 C is about 100 times lower than that of iron-base alloys at 25 C. Hence, hydrogen localization is possible at the observed crack growth rate.
2) Cracks initiate from an occuluded cell formed by the fissuring of the outer oxide layer. Electrochemical potential data show that microstructural galvanic coupling at grain boundaries can result in sufficient dissolution rate for crack tip acidification.
3) Due to small plastic strains, the strain-induced recombiantion is absent.
4) A good correlation exists in the microstructural dependence between the high temperature embrittlement and the low temperature embrittlement. Convincing evidences for HEM in the low temperature water have already been shown.
5) Specimen bake-out experiment after an exposure to high temperature water but before a crack initiation restores the initial life-time [36].
6) In some heats, there is correlation between the susceptibility and phosphorus segregation[36].

Assuming that these observations are sufficient to support the HEM, it is possible to describe detailed microprocesses. As with the case of low temperature water, the hydrogen is generated as the cathodic reaction of galvanic couple in the oxygen-depleted acidified crack tip. Most of the hydrogen is adsorbed at the localized crack initiation site. Although the desorption by the strain-assisted recombination would be negligible due to slow strain rate significant fractions are removed by the leakage and recombination by surface diffusion. Hence a much smaller amount of hydrogen atoms are introduced to the crack tip mostly

by the grain boundary diffusion process. The chemical potential gradient due to the stress localization would increase the hydrogen concentration at the crack tip. The intragranular precipitates trap hydrogens to help delay the crack initiation as well as the growth. Intergranular fracture is assumed to take place when the hydrogen concentration at grain boundaries at the crack tip reaches a certain critical value. The critical value is, again, dependent on the stress level and impurity concentration.

There are two possible rate controlling processes; 1) hydrogen generation and 2) hydrogen diffusion. It should be stressed that these two processes occur in series. The overall rate is determined by the slower process which may depend on a specific combination of microstructure and environment.

In the AH condition of X-750 where corrosion of intergranular γ' is expected to result in a high hydrogen generation rate. As a result, it may be assumed that the diffusion process is slower and thus rate controlling. In fact, there is a good agreement between the crack depth in the AH condition and that predicted by $\sqrt{Dt}$. Several factors which lower the actual crack depth are explained by a reduced diffusion rate in the presence of traps.

In a more resistant condition of X-750 such as HTH or HOA, the hydrogen generation rate is proposed as the rate controlling process. If the hydrogen generation rate is below a certain critical rate, a critical hydrogen concentration may never be reached at the crack tip and the crack tip environment would be neutralized. This implies that another mechanism viable in the neutral environment is substituted for the HEM. The alternative mechanism is likely to be the film rupture mechanism (FRM) since it operates in a similar nickel-base alloy with active intergranular chemistries; i.e., alloy 600.

The role of microstructure in the high temperature embrittlement is important in both elctrochemical and mechanical processes. The presence of electrochemically active phases or hydrogen recombination poisons

would increase the amount of hydrogen which is available for entry into the crack tip. Hydrogen traps such as intragranular precipitates can slow down matrix diffusion. However their effectiveness would be significantly reduced in the more likely situation of the grain boundary diffusion. Semi-continuous carbides along the grain boundaries would inject dislocations and blunt the crack tip geometry. The role of these carbides is as effective in the HEM as in the FRM.

In summary, both HEM andFRM are viable and evidenced in alloy X-750 in high temperature water. In the AH condition, the diffusion controlled HEM is believed to occur while the FRM is the more likely mechanism for the HTH or HOA conditions. A detailed description must await more data from mechanistic approaches.

For alloy 718, the present work failed to produce any embrittlements at high temperature. Available data in the literature is insufficient to allow any mechanistic speculation. Therefore no discussion is made as to the high temperature embrittlement of alloy 718.

Chapter 8

CONCLUSIONS AND RECOMMENDATIONS

Fundamental Aspects of Environment Assisted Cracking Process

Based on the data analysis and discussion presented in previous chapters it is clear that microstructure and environment interact strongly to influence a material's susceptability to environmentally assisted cracking. For the specific case of intergranular cracking of nickel-base alloys it has been proposed that two different cracking mechanisms are active and competing. These are hydrogen embrittlement (HEM) and a film rupture based mechanism (FRM).

In many cases one or the other mechanism is dominant. Which mechanism dominants will depend on (1) grain boundary chemistry, (2) temperature, (3) crack tip echemistry and (4) strain rate. The electrochemical response of the grain boundary constituents to its aqueous environment depends on a number of factors which include: (1) the presence of second phases, (2) segregation of contaminants, (3) any bulk chemistry gradients between the near grain boundary rejoin and the surrounding matrix, and (4) local area ratios for anodic and cathodic processes. The type of the grain boundary precipitate that will be present is controlled by heat treatment. More active grain boundary precipitates such as $\gamma'(Ni_3(A\ell, Ti))$ can act as anodes with respect to the adjacent matrix whereas other precipitates including $M_{23}C_6$ carbides can act as cathodes. Kinetics as well as thermodynamics of grain boundary reactions are a strong function of temperature. The reactions can be localized to crack tip envirment depending on conductivity, geometry and strain rate.

The complex processes that lead to fracture almost always involve a rate controlling step. Identification of the rate controlling step includes fundamental insight into the basic process. In many cases the cathodic

reaction is hydrogen evolution which provides a local source of hydrogen to the material which may lead to embrittlement. The anodic process will, in many cases, result in the formation of a surface film. The stability of this film, mechanically and electrochemically will govern a material's resistance to film rupture based crack advance. In addition to electrochemical and microstructural features the mechanics of crack propagation are also influenced by the nature of the deformation that occurs at the grain boundary. Slip dispersal can blunt a crack tip and lower grain boundary stress concentrations and thus reduce the possibility of fracture. Also, transport of hydrogen by dislocations during deformation can provide for a supply of hydrogen to the grain boundaries and promote embrittlement.

For the purposes of this investigation the performance of several nickel-base alloys were investigated. The materials chosen, alloy 600, alloy X-750. and alloy 718, can be processed such that a range of grain boundary chemistry and microstructure can be obtained. This was a critical factor in those choice for this thesis. The fact that these materials are of technological importance to the nuclear industry provides for an opportunity to connect fundamental understanding to practical application and to provide advances in both areas.

Embrittlement Mechanisms of Nickel-base Alloys

1. Hydrogen embrittlement is responsible for intergranular cracking of susceptible microstructures of alloy X-750 in low temperature high purity water. Hydrogen is generated in the crack tip environment as the cathodic partial process of galvanic corrosion of active γ' which acts as the anode in a galvanic cell with the material. Hydrogen adsorption/desorption are proposed as the rate controlling process. Dislocation transport of hydrogen into the crack tip plastic zone is proposed as the dominent transport process. This is supported by: (1) the observed incremental crack growth behavior, and (2) an increased crack tip plastic zone size during cathodic charging. Both γ-hydride formation and decohesion at grain boundaries are suggested as possible fracture mechanisms.

2. The intergranular cracking mechanism for nickel-base alloys with active grain boundary chemistries in high temperature water is also proposed to be galvanically induced hydrogen embrittlement. In this cases crack tip acidity is required for hydrogen reduction. This acidity is provided for by dissolution of strained material at the crack tip. For this process a critical strain rate is required to: (1) support anodic dissolution and at the same time (2) prevent excessive strain induced hydrogen recombination. Thermally activated recombination is believed to be significant. Recombination poisons such as phosphorous or boron, present at the grain boundaries strongly influence the kinetics of recombination and will this influence the overall process.

3. If the galvanic current density is below the critical value necessary for the development of crack tip acidity a hydrogen mechanism can not operate. The film rupture mechanism is an alternative but slower process. Crack growth rate is approximately two orders of magnitude lower when the film rupture mechanism is controlling.

4. Since two embrittlement mechanisms operate in significantly different electrochemical conditions, they have different microstructural dependences. Intergranular γ' and segregated phosphorus support the hydrogen embrittlement mechanism. The film rupture mechanism is unaffected by their presence. Slightly reduced passivity may blunt the crack tip and retard embrittlement by the film rupture mechanism. The reverse dependence on the electrochemical acitivity suggests the existence of an optimal condition at some intermediate activity.

5. Extensive intergranular carbides promote slip dispersal and are thus expected to reduce stress concentrations at grain boundaries. Larger grain size and the absence of shearable precipitates also lowers stress concentrations at grain boundaries. Mechanical factors affect both mechanisms (HEM, FRM) in the same manner.

Relation between Process and Grain Boundary Chemistry

The alloy 600 material used for this study was processed as tubing. The fabrication process was adjusted to produce several different tubing microstructures with variable grain boundary carbide morphology. In addition to conclusions drawn with respect to the effect of carbide morphology on cracking resistance the following conclusions were drawn with respect to the effect of processing variables on resulting microstructure.

1 The microstructural evolution of mill annealed alloy 600 tubing can be characterized by the carbon content and final annealing temperature provided metal temperature is used for process specification. In general, material annealed at temperatures below the carbon solibility limit (low temperature mill anneal) will contain an extensive amount of intragranular carbide at the expense of intergranular carbide. Material annealed at a temperature above the carbon solibility limit will contain a preponderance of intergranular carbide. Use of furnace temperature in process specification is undesirable due to difficulty in control of microstructural evolution.

2. The degree of chromium depletion at grain boundaries of mill annealed alloy 600 due to carbide precipitation is higher at the tubing inner surface due to a slower cooling rate than the outer wall. The difference in chromium concentration between the inner and outer surfaces can be up to 3 wt %.

3. Phosphorus and boron segregate to grain boundaries of alloys 600 and X-750. The phosphorus segregation in alloy 600 follows McLean-type equilibrium behavior with a free energy of segregation of 58 ± 2kJ/mole for the temperature range between 700C and 1100C. In alloy X-750, phosphorus segregation appears to be impeded by simultaneous γ' precipitation during thermal treatment near 700C. There is a site competition between phosphorus and boron at grain

boundaries at temperatures between 700 C and 1100 C.

AC PD Crack Detection System

As part of the experimental program a sensitive crack detection technique has been developed based on AC potential drop techniques. The following conclusion reflects to this development. A sensitivity of 50 μm is possible during constant load tests and low temperature slow strain rate tests at an AC frequency of 200 kHz with a probe spacing of 1cm. Discontinuous emergence of slip bands at high temperature significantly reduces sensitivity. Its surface crack detection sensitivity is optimized through the use of the so called "skin" effect whereby the majority of the current can be forced to pass through the region of the specimen near the surface. The potential drop is thus increased for a given total current than that of DC techniques.

Recommendations for Alloy Design

Finally implications of mechanistic understanding advanced in this work are applied to formulate principles for alloy development, as follows;

1. Active intermetallic precipitates should be avoided at grain boundaries.

2. Phosphorus segregation should be reduced if hydrogen embrittlement mechanism is dominant.

3. Extensive intergranular carbide morphology should be used if possible.

4. If film rupture mechanism dominates, film passivity should be lowered so that crack tip is blunted by distributed dissolution. Excessive reduction in passivity, however, may induce hydrogen embrittlement mechanism. Hence the film passivity should be optimized.

REFERENCES

1. Copson, H.R. (1959) Physical Metallurgy of Stress-Corrosion Fracture, Interscience, New York, pp. 247.

2. Stahlkopf, K.E., Smith, R.E. and Marston, T.U. (1978) "Nuclear Pressure Boundary Materials Problems and Proposed Solutions," Nucl. Eng. Des., Vol. 46, pp. 65-79.

3. Hunyadi, L. (1986) "Ringhals No. 2 - Steam Generator Repair/Replacement Options," Int. J. Pres. Ues. & Piping, Vol. 25, pp. 75-87.

4. Green, S.J. (1986) "Methods for Preventing Steam Generator Failure or Degradation," Int. J. Pres. Ves. & Piping, Vol. 25, pp. 359-391.

5. Green, S.J. and Paine, J.P.N. (1984) "Steam Generator Materials - Experience and Prognosis," Proceedings of Intl. Symp. on Environmental Degradation of Materials in Nuclear Power Systems - Water Reactors, NACE, pp. 53-68.

6. Potter, E.C. and Mann, G.M.W. (1965) "The Fast Linear Growth of Magnetite on Mild Steel in High Temperature Aqueous Conditions," Br. Corros. J., Vol. 1, pp. 26-35.

7. Taylor, G.F. and Dautovich, D.P. (1981) "Materials Performance in CANDU Nuclear Steam Generators," Nucl. Tech., Vol. 55, No. 1, pp. 30-36.

8. Frederick, G. and Hernalsteen, P. (1986) "Comparative Evaluation of Preventive Measures Against Primary Side Stress Corrosion Cracking of Mill Annealed Inconel 600 Steam Generator Tubes," Int. J. Pres. Ves. & Piping, Vol. 25, pp. 47-67.

9. Burghard, H.C. and Bursle, A.J. (1978) "Final Report - SWRI Project 02-5839-001."

10. Page, R.A. (1983) "Stress Corrosion Cracking of Alloys 600 and 690 and Nos. 82 and 182 Weld Metals in High Temperature Water," Corrosion, Vol. 39, No. 10, pp. 490-421.

11. Mager, T.R. (1986) "Fastener and Bolting Materials for Westinghouse Design Internals," Presented at EPRI Workshop on Advanced High Strength Materials for LWR Vessel Internal Applications, Clearwater Beach, FL.

12. Rubel, H. (1986) "KWU Experience with Inconel-X-750 and Today's Philosophy for High Strength Materials Selection," Presented at EPRI Workshop on Advanced High Strength Materials for LWR Vessel Internal Applications, Clearwater Beach, FL.

13. Benhamou, C. and Poitrenaud, P. (1986) "Framatome Experience and Programs in Relation with Guide Tube Support Pin Cracking," Presented at EPRI Workshop on Advanced High Strength Materials for LWR Vessel Internal Applications, Clearwater Beach, FL.

14. Hayner, G.O., Smith, Jr., J.L. and Garder, G.L. (1986), "High Strength Alloy Field Failures and Successes," Presented at EPRI Workshop on Advanced High Strength Materials for LWR Vessel Internal Applications, Clearwater Beach, FL.

15. Carnahan, R.A. and Gordon, G.M. (1986) "Summary of Alloy X-750 Behavior in General Electric BWRs," Presented at EPRI Workshop on Advanced High Strength Materials for LWR Vessel Internal Applications, Clearwater Beach, FL.

16. McIlree, A.R. (1984) "Degradation of High Strength Austenitic Alloys X-750, 718 and A-286 in Nuclear Power Systems," Proceedings of Intl. Symp. on Environmental Degradation of Materials in Nuclear Power Systems - Water Reactors, NACE, pp. 838-850.

17. Yahr, G.T. (1985) "Preloading of Bolted Connections in Nuclear Reactor Components," in Pressure Vessel and Piping Technology: A Decade of Progress, ASME, pp. 9-27.

18. Merrick, E.A., Rivers, A., Bickford, J. and Marston, T.U. (1986) "Prevention of Bolting Degradation or Failure in Pressure Boundary and Support Applications," Int. J. Pres. Ves. & Piping, Vol. 25, pp. 333-357.

19. Scarberry, R.C., Pearman, S.C. and Crum, J.R. (1976) Corrosion, Vol. 32, No. 10, pp. 401.

20. Sarver, J.M., Crum, J.R. and Mankins, W.L. (1987) "Effect of Carbide Precipitation on the Corrosion Behavior of Inconel Alloy 690," (Paper Number 95), Corrosion, Vol. 87, San Francisco, CA.

21. Takemoto, M. (1985) "The Effect of Processing Variables on the Microstructure of Alloy 600," unpublished work at MIT.

22. Airey, G.P. (1981) "Carbide Dissolution and Precipitation Kinetics of Inconel 600," EPRI/NP-2093, EPRI, Palo Alto, CA.

23. Sheeks-Elliott, C.K. (1985) Effects of Thermal Treatment on the Fracture Properties of Alloy X-750 in Aqueous Environments, Sc.D. Thesis, MIT.

24. Miglin, M.T. and Domian, H.A. (1987) "Microstructure and Stress Corrosion Resistance of Alloy X-750, 718 and A-286 in Light-Water-Reactor Environments," submitted for publication in J. Mater. for Energy Systems.

25. Yonezawa, T., Onimura, K., Sakamota, N., Sasaguri, N., Nakata, H. and Suskida, H. (1984) "Effect of Heat Treatment on Stress

Corrosion Cracking Resistance of High Nickel Alloys in High Temperature Water," Proceedings of Intl. Symp. on Environmental Degradation of Materials in Nuclear Power Systems - Water Reactors, NACE, pp. 345-367.

26. Prybylowski, J.W. (1986) The Influence of Microstructure on Environmentally Assisted Cracking of Alloy 718, Ph.D. Thesis, MIT.

27. Owens, C.M. (1986) "Stress Corrosion Cracking Performance of Mill-Annealed, Inconel-600 Tubing in Steam Generators," (Paper Number 93), Corrosion '86, Houston, TX.

28. Hosoi, K., Hattori, S., Urayama, Y., Masaoka, I. and Sasaki, R. (1984) "Relation Between Susceptibility to Stress Corrosion Cracking in High Temperature Water and Microstructure of Inconel Alloy X-750," Proceedings of Intl. Symp. on Environmental Degradation of Materials in Nuclear Power Systems - Water Reactors, NACE, pp. 334-344.

29. Airey, G.P. (1979) "The Effect of Carbon Content and Thermal Treatment on the SCC Behavior of Inconel Alloy 600 Steam Generator Tubing," Corrosion, Vol. 35, No. 3, pp. 129-136.

30. Kowaka, M., et al. (1981) "Effect of Heat Treatment on the Susceptibility to Stress Corrosion Cracking of Alloy 600," Nucl. Tech., Vol. 55, No. 2. pp. 394-404.

31. Pement, F.W. and Graham, N.A. (1974) "Stress Corrosion Cracking in High Purity Water," in Corrosion Problems in Energy Conversion and Generation, ed. by Tedmon, C.S. Jr., The Electrochemcial Soc., Princeton, NJ.

32. Guttmann, M. Dumoulin, P., Tan, Tai, N. and Fountaine, P. (1981) "An Auger Electron Spectroscopic Study of Phosphorus Segregation in the Grain Boundaries of Nickel-Base Alloy 600," Corrosion, Vol. 37, No. 7, pp. 416-425.

33. Briant, C.L., O'Toole, C.S. and Hall, E.L. (1986) "The Effect of Microstructure on the Corrosionand Strss Corrosion Cracking of Alloy 600 in Acidic and Neutral Environments," Corrosion, Vol. 4, No. 1, pp. 15-29.

34. Was, G. and Latanision, R.M. (1981) "The Influence of Thermal Treatment on the Chemistry and Structure of Grain Boundaries in Inconel 600," Metall. Trans. A., Vol. 12A, pp. 1397.

35. Was, G. and Martin, J.R. (1985) "The Influence of Grain Boundariy Precipitation on the Measurement of Chromium Redistribution and Phosphorus Segregation in Ni-16Cr-9Fe", Metall. Trans. A., Vol. 16A, pp. 349-359.

36. Grove, C.A. and Petzold, L.D. (1984) "Mechanism of Stress Corrosion Cracking of Alloy X-750 in High Purity Water,"

Proceedings Intl. Conf. on the Corrosion of Nickel Base Alloys, ASM, Cincinatti, OH, pp. 165-180.

37. Ljungberg, L.G. and Bergtsson, B. (1984) "Grain Boundary Segregation in Alloy X-750 of Varying Heat Treatment and Stress Corrosion Susceptibility," Presented at EPRI Workshop on Advanced High Strength Materials for LWR Vessel Internal Applciations, Clearwater Beach, FL.

38. Shinoda, T. (1983) "Theoretical Estimates of Phosphorus Concentration Profiles Across Grain Boundaries in Fe-P and Fe-Ni-P Systems," Acta Metall., Vol. 31, pp. 2051-62.

39. Coriou, H., Grall, L. and LeGrall, M., and Vettier, S. (1959) "Stress-Corrosion Cracking of Inconel in High-Temperature Water," 3e Colloque De Metallurgie sur la Corrosion, North Holland Publishing Co., 1960, pp. 161-169.

40. Blanchet, J., Coriou, H., Grail, L., Mahieu, C. Otter, C. and Turluer, G. (1975) "Influence De La Contrainte, Des Traitements Thermiques Et Des Couplages Sur La Fissuration Intergranulaire Des Alliages Inconel 600 Et X-750," J. of Nucl. Mater., Vol. 55, pp. 187-206.

41. Domian, H.A., Emanuelson, R.H., Sarver, L.W., Theus, G.J. and Katz, L. (1971) "Effect of Microstructure on Stress Corrosion Cracking of Alloy 600 in High Purity Water," Corrosion, Vol. 33, No. 1, pp. 26-37.

42. Bulischeck, T.S. and Van Rooyen, D. (1981) "Effect of Environmental Variables on the Stress Corrosion Cracking of Inconel 600 Steam Generator Tubing," Nuclear Technology, Vol. 55, No. 2, pp. 383-393.

43. Airey, G.P. (1984) "The Stress Corrosion Cracking (SCC) Performance of Inconel Alloy 600 in Pure and Primary Water Environments," Proceedings of Intl. Symp. on Environmental Degradation of Materials in Nuclear Power Systems - Water Reactors, NACE, PP. 462-478.

44. Economy, G., Jacko, R.J. and Pement, F.N. (1986) "IGSCC Behavior of Alloy 600 Steam Generator Tubing in Water or Steam Tests Above 360°C," (Paper Number 250), Corrosion '86, Houston, TX.

45. Yonezawa, T., Yamaguchi, N., Okada, Y. and Igarashi, M. (1986) "Effect of Chemical Compositions and Heat Treatment Conditions on the SCC Resistance of Nickel-Base High Strength Alloys," Presented at EPRI Workshop on Advanced High Strength Materials for LWR Vessels Internal Applications, Clearwater Beach, FL.

46. Airey, G. (1983) "Optimization of Metallurgical Variables to Improve Corrosion Resistance on Inconel Alloy 600," EPRI NP-3051, EPRI, Palo Alto, CA.

47. De, P.K. and Ghosal, S.K. (1981) "A Comparative Study of Stress Corrosion Cracking of Steam Generator Tube Materials in Water at 315°C," Corrosion, Vol. 37, No. 6, pp. 341-349.

48. Hayner, G.O. and Ballinger, R.G. (1984) "Evaluation of Alloy X-750 Holddown Spring Service Failures," Final Report EPRI RP-2058 (Task 4), EPRI, Palo Alto, CA.

49. Wilson, F.L.N. (1986) "SCC Behavior of Alloys 718 and A-286," Presented at EPRI Workshop on Advanced High Strength Materials for LWR Vessel Internal Applications," Clearwater Beach, FL.

50. Sheeks, C.K. (1983) Fatigue Crach Growth Behavior of Alloy X-750 Under Simulated BWR Conditions, S.M. Thesis, MIT.

51. Kekkonen, T. and Hänninen, H. (1985) "The Effect of Heat Treatment on the Microstructure and Corrosion Resistance of Inconel X-750 Alloy," Corr. Sci., Vol. 25, No. 8/9, pp. 789-803.

52. Bengtsson, B., Dahlbaeck, M., Jansson, C. and Morin, U. (1986) "Constant Load Tests of Age-Hardened Ni-Base Alloys in Oskarshamn 2 BWR," Presented at EPRI Workshop on Advanced High Strength Materials for LWR Vessel Internal Applications, Clearwater Beach, FL.

53. Bruemmer, S.M., Charlot, L.A. and Hennger, Jr., C.H. (1987) "Microstructure and Microdeformation Effects on IGSCC of Alloy 600 Steam Generator Tubing," (Paper Number 88), Corrosion '87, San Francisco, CA.

54. Raymond, E.L. (1967) "Effect of Grain Boundary Denudation of Gamma Prime on Notch-Rupture Ductility of Inconel Nickel-Chromium Alloys X-750 and 718," Trans. Metall. Society of AIME, Vol. 239, pp. 1415-1422.

55. Floreen, S. and Nelson, J.L. (1983) "The Effects of Heat Treatment and Composition on the Stress Corrosion Cracking Resistance of Inconel Alloy X-750," Metall. Trans. A., Vol. 14A, pp. 133-139.

56. Silcock, J.M. (1983) "Transgranular Stress Corrosion Cracking in γ'-forming Austenitic Steels," Br. Corr. J., Vol. 18, No. 3, pp. 132-137.

57. Hosoya, K., Ballinger, R., Prybylowski, J.W. and Hwang, I.S. (1987) "The Role of Microstructure in Environmentally Assisted Cracking of Nickel-base Alloys," (Paper Number 101) Presented at Corrosion '87, San Francisco, CA.

58. Tsubota, M., Hattory, K., Kaneko, T. and Okada, T. (1986) "SCC Susceptibility of Inconel 718," Presented at EPRI Workshop on Advanced High Strength Materials for LWR Vessels Internal

Applications, Clearwater Beach, FL.

59. Totsuka, N., Lunarska, E., Cragnolino, G. and Szklarska-Smialowska, Z. (1986) "A Sensitive Technique for Evaluating Susceptibility to IGSCC of Alloy 600 in High Temperature Water," Scr. Metall., Vol. 20, pp. 1035-1040.

60. Bandy, R. and Van Rooyen, D. (1984) "Initiation and Propagation of Stress Corrosion Cracking of Alloy 600 in High Temperature Water," Proceedings of Intl. Symp. on Environmental Degradation of Materials in Nuclear Power Systems - Water Reactors, NACE, pp. 763-774.

61. Wilson, I.L.W. and Aspden, R.G. (1976) "The Influence of Specimen Type and Heat Treatment on the Caustic Stess Corrosion Cracking of Some Stainless Alloys," Corrosion, Vol. 32, No. 5, pp. 193-201.

62. Bandy, R. and Van Rooyen, D. (1985) "Mechanisms of SCC and IGA in Alloy 600 in High Temperature Caustic and Pure Water," J. Mater. for Energy Systems, Vol. 7, No. 3, pp. 237.

63. Gill, T.P.S. and Gnanamoorthy, J.B. (1982) "A Method for Quantitative Analysis of Delta-ferrite, Sigma and $M_{23}C_6$ Carbide Phases in Heat Treated Type 316 Stainless Steel Weldments," J. Mater. Sci., Vol. 17, pp. 1513-1518.

64. Cihal, V., Desestret, A., Froment, M. and Wagner, G.H. (1970) Corrosion-Traitement-Protection, Vol. 18.

65. Latanision, R.M. and Opperhauser, Jr., H. (1974) "The Intergranular Embrittlement of Nickel by Hydrogen: The Effect of Grain Boundary Segregation," Metall. Trans. A., Vol. 5A, pp. 483-487.

66. Latanision, R.M. and Opperhauser, Jr., H. (1975) "Further Observations on the Effect of Grain Boundary Segregation in the Hydrogen Embrittlement of Nickel," Metall. Trans. A., Vol. 6A, pp. 233-234.

67. Fukushima, H. and Birnbaum, H.K. (1984) "Surface and Grain Boundary Segregation of Deuterium in Nickel," Acta Metall., Vol. 32, No. 6, pp. 851-859.

68. Cowan, R.L. and Gordon, G.M. (1973) "Intergranular Stress Corrosion Cracking and Grain Boundary Composition of Fe-Ni-Cr Alloys," in Stress Corrosion Cracking and Hydrogen Embrittlement of Iron Base Alloys, Firminy, France, G-14.

69. Jones, R.H. Danielson, M.J. and Baer, D.E. (1986) "Role of Segregated P and S in Intergranular Stress Corrosion Cracking of Ni," J. Materials for Energy Systems, Vol. 8, No. 2, pp. 185-196.

70. Pathania, R.S. and Cleland, R.D. (1985) "The Effect of Thermal Treatments on Stress Corrosion Cracking of Alloy-800 in a Caustic Environment," Corrosion, Vol. 41, No. 10, pp. 575-581.

71. Chen, C.M., Aral, K. and Theus, G.J. (1983) "Computer-Calculated Potential pH Diagram to 300°C: Volume 2. Handbook of Diagrams," EPRI NP-3137, EPRI, Palo Alto, CA.

72. Gabetta, G. and Rizzi, R. (1983) "Electrochemical Potentials Measured at the Tip of A Growing Fatigue Crack in Demineralized Water 93°C: The Effect of Frequency, Wave Form and Oxygen Content," Corr. Sci., Vo. 23, No. 6, pp. 613-620.

73. Turnbull, A. (1983) "A Theoretical Evaluation of the Oxygen Concentration in a Corrosion-Fatigue Crack," Corrosion Fatigue: Mechanics, Metallurgy, Electrochemistry and Engineering, ASTM STP 801, ASTM, pp. 351-366.

74. Taylor, D.F. (1979) "Crevice Corrosion of Alloy 600 in High Temperature Aqueous Environments," Corrosion, Vol. 35, No. 10, pp. 550-559.

75. Taylor, D.F. and Caramihas, C.A. (1982) "Crevice Corrosion in High-Temperature Aqueous Systems Potential/pH Measurements in Alloy 600 Crevices at 288°C," J. Electrochem. Soc., Vol. 129, No. 11, pp. 2458-2464.

76. Taylor, D.F. and Caramihas, C.A. (1983) "High Temperature Aqueous Crevice Corrosion in Alloy 600 and 304L Stainless Steel," in Embrittlement by the Localized Crack Environment, Edited by Gangloff, R.P., Proceedings of an Intl. Symp. Metallurgical Soc., Philadelphia, PA.

77. Shuck, R.R. and Swedlow, J.L. (1974) "Analysis of Transport in Crack-like Regions - Part I" in Localized Corrosion, NACE, Houston, TX.

78. Turnbull, A. (1983) "The Solution Composition and Electrode Potential in Pits, Crevices and Cracks," Corr. Sci., Vol. 23, No. 8, pp. 833-870.

79. Bandy, R., Roberge, R. and Newman, R.C. (1983) "Low Temperature Stress Corrosion of Inconel 600 Under Two Different Conditions of Sensitization," Corr. Sci., Vol. 23, No. 9, pp. 995-1006.

80. Matsushima, S. and Shimizu, Y. (1983) "Effect of Environmental Factors in Stress Corrosion Cracking of the Ni-Base Alloy 600 in Oxygenated High Temperature Water," Trans. Japan Inst. Metals, Vol. 24, No. 8, pp. 149-153.

81. Airey, G.P. and Pement, F.W. (1983) "A Comparison of Intergranular Attack in Inconel Alloy 600 Observed in the

Laboratory and in Operating Steam Generators," Corrosion, Vol. 39, No. 2, pp. 46-55.

82. Theus, G.J. (1976) "Relationship Between Acid Intergranular Corrosion and Caustic Stress Corrosion Cracking of Alloy 600," Corrosion, Vol. 33, No. 1, pp. 20-25.

83. Boateng, A., Begley, J.A. and Staehle, R.W. (1983) "Corrosion Fatigue of Type 304 Stainless Steel and Inconel 600 in a Boiling (140°C) Concentrated Caustic Solution," Metall. Trans. A., Vol. 14A, pp. 67-73.

84. Serra, E.T. (1981) "Stress Corrosion Cracking of Ni-Cr-Fe Alloy 600 in Steam Generator Environments: A Review," Trans. ANS, pp. 447-450.

85. Bandy, R., Roberge, R. and Van Rooyen, D. (1985) "Intergranular Attack and Stress Corrosion Cracking of Alloy 600 in High-Temperature Caustic Solutions Containing Contaminants," EPRI/NP-4051, Interim Report. EPRI, Palo Alto, CA.

86. Eastman, J., Heubaum, F., Matsumoto, T. and Birnbaum, H.K. (1982) "The Effect of Hydrogen on the Solid Solution Strengthening and Softening of Nickel," Acta Metall., Vol. 30, pp. 1579-1586.

87. Thompson, A.W. (1982) "Hydrogen-assisted Fracture in Single-phase Nickel Alloys," Scr. Metall., Vol. 16, pp. 1189-1192.

88. Igarashi, M., Mukai, S., Kudo, T., Okada, Y. and Ikeda, A. (1987) "Precipitation Hardened Nickel-Base Alloys for Sour Gas Environments," (Paper Number 387), Corrosion '87, San Francisco, CA.

89. Thompson, A.W. and Wilcox, B.A. (1972) "Deformation and Fracture of Dispersion-strengthened Nickel Charged with Hydrogen," Scr. Metall., Vol. 6, pp. 689-696.

90. Fricker, V., Janser, G.R. and Brown, J.A. (1971) in Space Shuttle Materials, Vol. 8, pp. 90-97.

91. Cornet, M., Bertrand, C. and Da Cunha Belo, M. (1982) "Hydrogen Embrittlement of Ultra-Pure Alloys fw the Inconel 600 Type: Influence of the Additions of Elements (C, P, Sn, Sb)," Metall. Trans. A., Vol. 13A, pp. 141-144.

92. Price, C.E. and Morris, J.A. (1985) "The Comparative Embrittlement of Example Nickel Alloys by Hydrogen and Mercury," J. Mater. for Energy Systems, Vol. 7, No. 3, pp. 246-255.

93. Kekkonen, T., Hänninen, H. and Tähtinen, S. (1986) "A Comparison of HE and SCC Susceptibility of an Age Hardenable Nickel-base Alloy," Presented at EPRI Workshop on Advanced High Strength

Materials for LWR Vessel Internal Applications, Clearwater Beach, FL.

94 Lee, T.F. (1982) A Straining Electrode Study on the Hydrogen Embrittlement of Nickel and Nickel-base Alloys, Sc.D. Thesis, MIT.

95. Hinotani, S., Ohmori, Y. and Terasaki, F. (1985) "Effect of Nickel on Hydride Formation and Hydrogen Embrittlement in Ni-Cr-Fe Alloys," Mater. Sci. & Eng., Vol. 74, pp. 119-131.

96. Bauer, H.J. and Baranowski, B. (1977) "Hydride Formation in Ni-Fe Alloys in High Pressure Gaseous Hydrogen Followed by Magnetization Measurements," Hydrogen in Metals, Vol. 3, Proc. of the 2nd International Cong., Pergamon Press.

97. Goniszewski, T. and Smith, G.C. (1961) "A Note on Nickel Hydride," Letter to the Editor, J. Phys. Chem. Solids, Vol. 21, pp. 115.

98. Jones, R.H., Bruemmer, S.M., Thomas, M.T. and Baer, D.R. (1983) "Hydrogen Pressure Dependence of the Fracture Mode Transition in Nickel," Metall. Trans. A., Vol. 14A, pp. 1729-1736.

99. Was, G.S. and Ballinger, R.G. (1980) "Hydrogen Induced Cracking Under Cyclic Loading of Nickel Base Alloys Used in PWR Steam Generator Tubing," Fourth Semi-annual Progress Report, EPRI NP-4613, EPRI, Palo Alto, CA.

100. Moshier, W.C.J. (1983) The Corrosion Fatigue Behavior of Alloy 600 in Steam Generator Environments, Sc.D. Thesis, MIT.

101. Ford, F.P., Taylor, D.F., Andersen, P.L. and Ballinger, R.G. (1985) "Environmentally-controlled Cracking of Stainless and Low Alloy Steels in Light-Water Reactor Environments," EPRI RP-2006-6, Supplementary Report, EPRI, Palo Alto, CA.

102. Kuruwilla, A.K. (1987) Unpublished work at RPI.

103. Wilson, I.L.W. and Mager, T.R. (1985) Corrosion '85.

104. Latanision, R.M., Gastine, O.H. and Compeau, C.R. (1979) "Stress Corrosion Cracking and Hydrogen Embrittlement: Differences and Similarities," Environment-Sensitive Fracture of Engineering Materials, TMS-AIME, Warrendale, PA, pp. 48-70.

105. Prybylowski, J. and Ballinger, R.G. (1986) "A Overview of Advanced High Strength Nickel Base Alloys for LWR Applications," Presented at EPRI Workshop on Advanced High Strength Materials for LWR Vessel Internal Applications, Clearwater Beach, FL.

106. Marcus, P., Teisseier, A. and Oudar, J. (1984) "The Influence of Sulphur on the Dissolution and Passivation of a Nickel-iron Allloy - II. Surface Analysis by ESCA," J. Corr. Sci., Vol. 24,

No. 4, pp. 259-278.

107. Marcus, P., Teissier, A. and Oudar, J. (1984) "The Influence of Sulphur on the Dissolution and the Passivation of a Nickel-iron Alloy - Electrochemical and Radiotracer Measurements," Corr. Sci., Vol. 24, No. 4, pp. 259-268.

108. Vermilyea, D.A. and Diegle, R.B. (1976) "Concerning Strain-Enhanced Corrosion Mechanism of SCC," Corrosion, Vol. 32, No. 1, pp. 26-29.

109. Pessall, N. (1980) "Prediction of Stress Corrosion Cracking in 10% Caustic Soda Solutions at 315°C (600°F)," Corr. Sci., Vol. 20, pp. 225-242.

110. Indig, M.E. and Weber, J.E. (1985) "Effects of H_2 Additions on Stress Corrosion Cracking in a Boiling Water Reactor," Corrosion, Vol. 41, No. 1, pp. 19-30.

111. Garud, Y.S. and McIlree, A.R. (1986) "Intergranular Stress Corrosion Cracking Damage Model: An Approach and Its Development for Alloy 600 in High-Purity Water," Corrosion, Vol. 42, No. 2, pp. 99-105.

112. Petch, N.J. (1956) "The Lowering of Fracture-Stress Due to Surface Adsorption," Phil. Mag., Vol. 1, pp. 331.

113. Uhlig, H.H. (1967) "An Evaluation of Stress Corrosion Cracking Mechanisms," in Proc. Conf. Fund. Aspects of Stress Corrosion Cracking, NACE, OSU, pp. 86-97.

114. Betrocci, U. and Pugh, E.N. (1985) "Modeling of Crack Chemistry in Copper Alloys," Corrosion '85, Boston, MA.

115. Wei, R.P., Simmons, G.W. and Chou, Y.T. (1984) "Fracture Mechanics and Surface Chemistry Investigations of Environment-Assisted Crack Growth," in Hydrogen Embrittlement and Stress Corrosion Cracking, Edited by Giblala, R. and Hehemann, R.F., ASM, Metals Park, OH, pp. 103-133.

116. Simmons, G.W., Pao, P.S. and Wei, R.P. (1978) "Fracture Mechanics and Surface Chemistry Studies of Subcritical Crack Growth in AISI 4340 Steel," Metall. Trans. A., Vol. 9A, pp. 1147-1158.

117. Asyama, Y (1984) "The Behavior of Delayed Failure in Ultra-High Strength 18% Ni Maraging Steels," Trans. Japan Inst. Metals, Vol. 25, No. 6, pp. 390-400.

118. Latanision, R.M. (1983) "General Overview: Atomistics of Environmentally-Induce Fracture," in Atomistics of Fracture, Plenum Press, New York, pp. 3-38.

119. Bockris, J. O'M. and Reddy, A.K.N. (1970) Modern Electrochemistry, Vol. 2, Plenum Press, New York, pp. 1156.

120. Pasco, R.W. and Ficalora, P.J. (1983) "A Work Function - Chemisorption Study of Hydrogen on Iron: Kinetics and Strain Effects," Acta Metall., Vol. 31, No. 4, pp. 541-558.

121. Steinruck, H.P., Luger, M., Winkler, A. and Rendulic, K.D. (1985) "Adsorption Probabilities of H_2 and D_2 on Various Flat and Stepped Nickel Surfaces," Phys. Rev. B, Vol. 32, No. 8, pp. 5032-5037.

122. Marichev, V.A. (1985) "Degree of Coverage by Adsorbed Hydrogen Atoms of the Surface of the Passivating Film on the Metal at a Crack Tip in Corrosion Cracking of Constructional Materials," Fiziko-Khimicheskaya Mekhanika Materialov, Vol. 21, No. 1, pp. 7-14.

123. Lacombe, P., Aucouturier, M. and Chene, J. (1984) "Hydrogen Trapping and Hydrogen Embrittlement," in Hydrogen Embrittlement and Stress Corrosio Cracking, Edited by Giblala, R. and Hehemann, R.F., ASM, Metals Park, OH, pp. 83-102.

124. Hirth, J.P. and Jhonson, H.H. (1983) "On the Transport of Hydrogen by Dislocations," in Atomistics of Fracture, Edited by Latanision, R.M. and Pickens, J.R., Plenum Press, NY, pp. 771-787.

125. Birnbaum, H.K. (1983) "Hydrogen Related Fracture of Metals," in Atomistics of Fracture, Edited by Latanisim, R.M. and Pickens, J.R., Plenum Press, NY, pp. 733-769.

126. Birnbaum, H.K. (1984) "Hydrogen Related Second Phase Embrittlement of Solids," in Hydrogen Embrittlement and Stress Corrosio Cracking, Edited by Giblala, R. and Hehemann, R.F., ASM, Metals Park, OH, pp. 153-177.

127. Ballinger, R.G. (1982) Corrosion Fatigue in Nickel Base Alloys for Nuclear Steam Generator Applications, Sc.D. Thesis, MIT.

128. ASME (1980) "Heating Boiler," in The 1980 ASME Boiler and Pressure Vessel Code - Section IV, ASME, New York, NY.

129. Timoshenko, A.V., Vasil'ev, V.Y. and Isaev, N.I. (1978) "Effect of Alternating Current on the Electrochemical Behavior and Corrosion Cracking of Steel 40Kh13 in Neutral Media," Moscow Institute of Steel and Alloys, Vol. 14, No. 4, pp. 406-409.

130. Verpost, I., Aernoudt, E. and Deruyttere, A. (1981) "An Improved A.C. Potential Drop Method for Detecting Surface Microcracks During Fatigue Tests of Unnotched Specimens," Fatigue of Eng. Mater. and Structures, Vol. 3, pp. 203-217.

131. Congleton, J., Olieh, R.A. and Parkins, R.N. (1982) "Corrosion-Fatigue Crack Nucleation in 1.5 Mn - 0.5 Si Steel," Metals Tech., Vol. 9, pp. 94-103.

132. Charlesworth, F.D.W. and Dover, D. (1982) "Some Aspects of Crack Detection and Sizing Using AC Field Measurement," in The Measurement of Crack Length and Shape During Fracture and Fatigue, Edited by Beevers, C.J., EMAS, West Midlands, U.K.

133. Berge, P. and Donati, J.R. (1981) "Materials Requirement for Pressurized Water Reactor Steam Generator Tubing," Nucl. Tech., Vol. 55, No. 1, pp. 88-104.

134. Stein, A. (1984) Presented at EPRI Meeting on Tube Processing, Boston, MA.

135. Cliff, G. and Lorimer, G.W. (1975) "The Quanttitative Analysis of Thin Specimens," J. Microscopy, Vol. 103, pp. 203-207.

136. Wood, J.E., Williams, D.B. and Goldstein, J.I. (1984) "Experimental and Theoretical Determination of K_{AFe} Factors for Quantitative X-ray Microanalysis in the Analytical Electron Microscope," J. Microscopy, Vol. 133, Pt. 3, pp. 255-274.

137. Goldstein, J.I., Costley, J.L., Lorimer, G.W. and Reed, S.J.B. (1977) "Quantitative X-ray Analysis in the Electron Microscope," Scanning Electron Microscopy, Vol. 1, pp. 315.

138. Hagi,H. and Ohtani,N.(1984) "Effect of Arsenic on Electrochemical Penetration of Hydrogen into Iron," J. Japan Inst. Metals, Vol. 48, NO. 4, pp397-404

139. Was, G.S., Tischner, H.H. and Martin, J.R. (1983) "An in situ Slow Extension Rate Fracture Stage for Auger Electron Spectroscopy," J. Vac. Sci. Tech., Vol. A1, No. 3, pp. 1477-1479.

140. Clough, S.P. (1983) "Detectability Limits for Auger Analysis." Interface, Vol. 6. No. 1, pp. 7-9.

141. Baboian, R. (1976) "Electrochemical Technique for Predicting Galvanic Corrosion," in Galvanic and Pitting Corrosion - Field and Laboratory Studies, ASTM STP 576, ASTM, pp. 5-19.

142. Andresen, P.L. (1982) "Assembly Instructions for Andresen External AgCl Reference Electrode," presented at the Int'l Cyclic Crack Growth Rate (ICCGR) meeting, Cambridge, MA.

143. Baratta, F.I., Bluhm, J.I., Driscoll, G.W. and Matthews, W.T. (1971) "Elastic Energy Release Rates Determined from Nonlinear Load-Deflection Curves," Int. J. of Fracture Mech., Vol. 7, No. 2, p. 203.

144. Andresen, P.L. (1984) "Switched DC Potential Drop Technique for

Crack Following on Compact Tension Specimens," Memorandum, General Electric Co., Corporate Research and Development Center.

145. Johnson, H.H. (1965) in Material Research and Standard, Vol. 5, No. 9, p. 442.

146. Guttmann, M. and McLean, D. (1977) "Grain Boundary Segregation in Multi-component Systems," in ASM Seminar on Interfacial Segregation, Chicago, ASM. pp. 261-348.

147. Dumoulin, Ph., Guttmann, M., Foucault, M., Palmier, M., Wayman, M. and Biscondi, M. (1980) Metal Sci. Vol. 14, p. 1.

148. Uhlig, H.H. (1986) private communication.

149. Himmelblau, D.M. (1960) "Solubilities of Inert Gases in Water: 0 C to near the Critical Point of Water," J. of Chem. & Eng. Data, Vol. 5, No. 1, pp. 10-14.

150. Suresh, S. (1981) "Mechanisms of Environmentally-Infllluenced Fatigue Crack Growth in Lower Strength Steels," Ph.D. Thesis, MIT.

151. Andresen, P.L. (1979) "The Effect of Environmental Variables on the Stress Corrosion Cracking Behavior of Type 304 Stainless Steel in High Temperature Water Environments," Ph.D. Thesis, Rensselaer Polytechnique Institute.

152. Ford, F.P.(1982) "Mechanisms of Environmental Cracking in Systems Peculiar to the Power Generation Industry," Final Report, EPRI-NP 2589, EPRI, Palo Alto, CA.

153. Stoloff, N.S. (1984) "Metal Induced Embrittlement - A Historical Perspective," in Embrittlement by Liquid and Solid Metals, ed. by Kamdar, M.H., Metall. Soc., pp. 3-26.

154. Craig, Jr., J.H. (1984) "Adsorption of Hydrogen and Carbon Monoxide on Nickel," Surf. Sci., Vol. 141 pp. L291-294.

155. Tsuru, T. and Latanision, R.M. (1982) "Crain Boundary Transport of Hydrogen in Nickel," Scr. Metall., Vol. 16, pp. 575-578.

156. Kimura, A. and Birnbaum, K. (1987) "On the Kinetics of Intergranular Embrittlement of Nickel by Hydrogen Transport from the External Surface," Scr. Metall., Vol. 21, pp. 219-222.

157. Daret, J. (1986) "CEA Experience on Alloy X-750 and Alternative Materials after 27000 Hours Testing of Actual Pins and Tensile Specimen," Presented at EPRI Workshop on Advanced High Strength Materials for LWR Vessel Internal Applications, Clearwater Beach, FL.

158. Totsuka, N. and Smialowska, Z. (1987) "Activation Energy for

IGSCC of Alloy 600 in an Aqueous Solution Containing Dissolved H_2 at 300 to 350C," Scr. Metall., Vol. 21, pp. 45-47.